信安儀器有限公司

美國EMS電顯用品總代理

TEL:886-2-23654317
FAX:886-2-23680650
E-MAIL:
hsinanin@ms27.hinet.net
www.emadiasum.com
台北市羅斯福路3段244巷10弄6-1號1樓(台電大樓右後方)

DUMONT
SWISSMADE

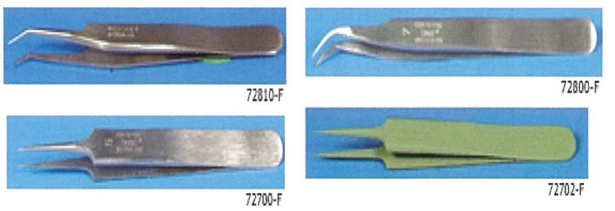

生物級及電子級不銹鋼鑷子

EMS Fiber Tip Tweezers

BEEM®Capsule Holders

包埋板

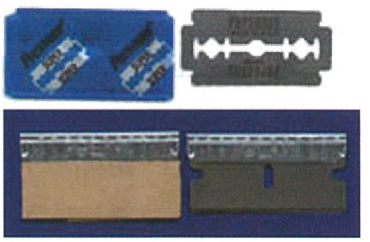

銅網 . 鎳網 . 鉬網

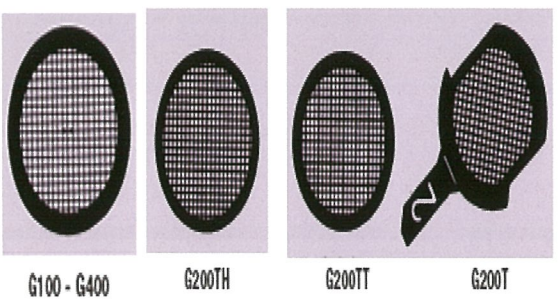

包埋

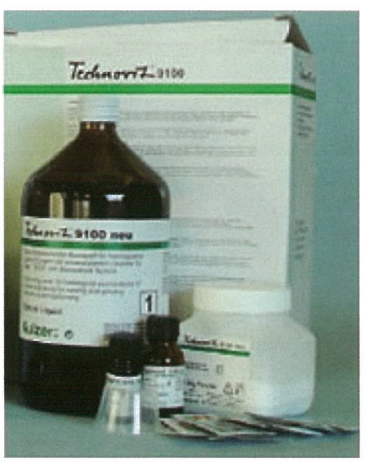

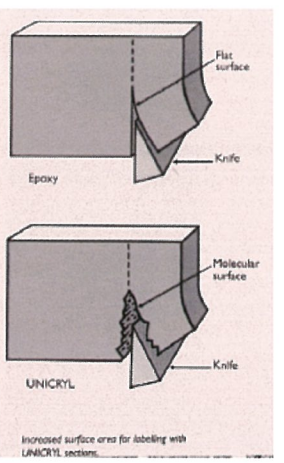

浮游生物網

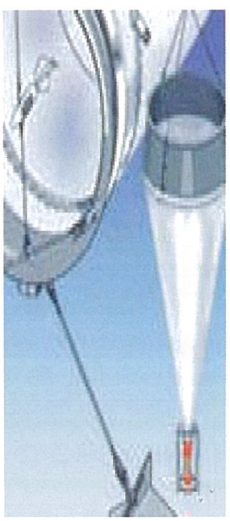

流量計

第七屆海峽兩岸顯微鏡學術研討會

主辦單位

新竹　清華大學
台灣顯微鏡學會

協辦單位

台灣大學生命科學院"TechComm 5,生物影像平台"
中央研究院物理研究所
中國醫藥大學附設醫院
東華大學奈米科技研究中心
國立東華大學材料科學與工程學系

補 助 單 位

行政院國家科學委員會.
教 育 部

贊 助 廠 商

JEOL Ltd.
Gatan Inc.
FEI Company
OXFORD INSTRUMENTS
NANOFACTORY INSTRUMENTS
益弘儀器股份有限公司
美嘉儀器股份有限公司

籌辦委員：

姓 名	服 務 機 構	職 稱
陳福榮	清華大學工程與系統科學系	教授
黃玲瓏	台灣大學生命科學系	教授
李英雄	中國醫藥大學	教授兼研發長
張　澤	北京工業大學	教授兼院士
韓曉東	北京工業大學	教授
李寧春	中國電子顯微鏡學會電子顯微學報編輯部	編輯

議程委員：

姓 名	服 務 機 構	職 稱
陳福榮	清華大學工程與系統科學系	教授
張嘉升	中央研究院物理研究所	研究員
陳香君	台灣大學 生命科學系	講師
胡宇光	中央研究院物理研究所	研究員
葉恒強	中國科學院瀋陽金屬研究所	教授兼院士
李方華	中國科學院物理研究所	教授兼院士
薛其坤	北京清華大學	教授兼主任
朱　敏	廣州華南理工大學	教授

論文編輯委員：

姓 名	服 務 機 構	職 稱
李志浩	清華大學工程與系統科學系	教授
張　立	交通大學材料科學與工程學系	教授
歐陽浩	清華大學材料工程科學系	教授
許並社	山西太原工業大學	教授
丁明孝	北京大學	教授
李寧春	中國電子顯微鏡學會電子顯微學報編輯部	編輯

海峽兩岸電鏡會之歷史

李英雄

中國醫藥大學 副校長

西元1989年10月23日本人應中國科學院瀋陽分院院長及中國電鏡學會理事長郭可信先生之邀請參加「第三屆北京分析測試學術報告暨展覽會」，這是中國大陸破冰之旅，在北京十日備受禮遇，真是終身難忘。該研討會之本質是以物理與化學領域為主題的國際性學術會議。來自世界各國的專家學者使用英語作50分鐘之專題報告，本人的演講題目是：「高解析度電子顯微鏡在生物醫學領域原子層次結構之應用研究」。在1980年代全世界利用高解析度電子顯微鏡從事生物醫學領域在原子層次之研究可說是鳳毛麟角、屈指可數。因此，這場演講是語驚四座，令與會學者專家是由衷欽佩。經由此次的演講開啟台灣與中國大陸學術交流之大門。本人主動向中國電鏡學會的領導提議共同舉辦學術研討會之可能性。因雙方對於使用的名稱有所顧忌，經數次協商終於塵埃落定，以「海峽兩岸」的名稱拍板訂案。西元1991年3月28日至3月30日在福建省廈門市隆重舉行「第一屆海峽兩岸電子顯微鏡學術研討會」。本人親自率領台灣地區從事電子顯微鏡學相關領域研究之學者專家共60餘人與中國大陸之同道們齊聚一堂共襄盛舉，當時的場景可謂盛況空前。本人是開啟海峽兩岸學術交流之先鋒，台灣與中國大陸舉辦學術研討會之名稱冠上「海峽兩岸」乃緣起於本人在西元1989年之倡導，爾後兩岸的學術會議都是蕭規曹隨沿用本人的創意而已。此後，每隔1~2年就舉辦一次海峽兩岸的學術研討會。從西元1991年至2004年共舉辦六屆海峽兩岸電子顯微鏡學術研討會，除第三屆及第五屆在台北市，其餘四屆都在中國大陸的都市，遠至西北新疆省的烏魯木齊市(第四屆)及東北黑龍江省的哈爾濱市(第六屆)。茲將六屆海峽兩岸電子顯微鏡學術研討會列於下表：

研討會名稱	地點	日期
第一屆海峽兩岸 電子顯微鏡學術研討會	福建省 廈門市	1991年3月27日
第二屆海峽兩岸 電子顯微鏡學術研討會	北京市	1992年10月
第三屆海峽兩岸 電子顯微鏡學術研討會	台灣省 台北市	1993年11月27 日
第四屆海峽兩岸 電子顯微鏡學術研討會	新疆省 烏魯木齊市	1999年8月28日
第五屆海峽兩岸 電子顯微鏡學術研討會	台灣省 台北市	2002年11月
第六屆海峽兩岸 電子顯微鏡學術研討會	黑龍江省 哈爾濱市	2004年8月2日

In situ Ultrahigh Vacuum Transmission Electron Microscope Investigations of Nanostructures

Lih-Juann Chen（陳力俊）

Department of Materials Science and Engineering, National Tsing Hua University, Hsinchu.
（清華大學材料科學工程學系）

Low-dimensional nanostructures, such as nanodots, nanowires and nanotubes, are especially attractive candidates for developing a bottom-up paradigm for nanotechnology-enabled architectures. In situ ultrahigh vacuum transmission electron microscope (UHV-TEM) is a powerful tool to investigate the dynamic changes of nanostructures. By observing growth and phase transitions in situ, understanding of their mechanisms can be used to model relevant processes. Recent development of UHV-TEM further enables the investigation on atomic-scale materials systems in a clean environment. With the precise knowledge of the changes occurred on an atomic level, accurate control of the growth process can be achieved [1]. The appropriate utilization of the UHV-TEM will be beneficial in studying the fundamental mechanisms of dynamic reactions, formation of transient phase, solid-state amorphization, epitaxial growth, growth kinetics and evolution of defects.

The dynamical changes occurred on the nano scale are often unexpected, which also underscores the importance of the approach. In this presentation, we will highlight several examples to demonstrate the unique capability of in situ TEM to study the dynamical changes. The examples include

1. Growth of high-density titanium silicide nanowires in a single direction on a silicon surface [2]: Merging of the two NWs in the same direction and collapse of one NW on a competing NW in different directions when they meet at the ends were observed. On the other hand, as one NW encounters the midsection of the other NW in different direction, it recedes in favor of the bulging of the other NW at the midsection. The crucial information has been fruitfully exploited to grow a high density of long and high aspect-ratio Ti silicide NWs on Si(110) in a single direction.
2. Controlled growth of atomic-scale Si layer with huge strain in the nano-heterostructure NiSi/Si/NiSi through point contact reaction between nano-wires of Si and Ni and reactive epitaxial growth [3]: Point contact reactions between a Si nanowire and a Ni nanowire are reported in which the Si nanowire is transformed into single crystal NiSi with an epitaxial interface which has no misfit dislocation. The growth of the NiSi occurs by the dissolution of Ni into the Si nanowire and by interstitial diffusion from the point of contact to the epitaxial interface. The point contact reactions have enabled us to fabricate single crystal

NiSi/Si/NiSi heterostructures of atomically sharp interfaces for nanoscale devices.

3. Observation of repeating events of nucleation in epitaxial growth of nano $CoSi_2$ in nanowires of Si [4]: The $CoSi_2$ has undergone an axial epitaxial growth in the Si nanowire and a stepwise growth mode was found. We observed that the stepwise growth occurs repeatedly in the form of an atomic step sweeping across the $CoSi_2$/Si interface. It appears that the growth of a new step or a new silicide layer requires an independent event of nucleation. We are able to resolve the nucleation stage and the growth stage of each layer of the epitaxial growth in video images. In the nucleation stage, the incubation period is measured, which is much longer than the period needed to grow the layer across the silicide/Si interface. So the epitaxial growth consists of a repeating nucleation and a rapid stepwise growth across the epitaxial interface. A discussion of the kinetics of supply-limited and source-limited reaction in nanowire case by point contact reaction is given.
4. Observations of electromigration in copper lines at room temperature [5]: Grain boundary affects migration of atoms and electrons in polycrystalline solids, hence it controls many mechanical and electrical properties of the solids. By introducing nano-twins into Cu grains, we show here that we change the grain boundary structure and atomic diffusion behavior along the boundary. Using *in-situ* UHV-TEM, we observed directly electromigration induced atomic diffusion in the twin-modified grain boundaries in Cu lines. The triple point where a twin boundary meets a grain boundary was found to slow down grain boundary and surface electromigration by one order of magnitude. We propose that it is due to the incubation time of nucleation of a new step at the triple points. The finding shall lead to the effective strategy to suppress electromigration by introducing a high density of nano-twins in the Cu interconnects.

Acknowledgment

The research was supported by the National Science Council through grants No. NSC 97-2120-M-007-003.

References

[1] F. M. Ross, R. M. Tromp, and M. C. Reuter, Science 286, 1931-1934 (1999).

[2] H. C. Hsu, W. W. Wu, H. F. Hsu, and L. J. Chen, Nano Lett. 7, 885-889 (2007).

[3] K. C. Lu, W. W. Wu, H. W. Wu, C. M. Tanner, J. P. Chang, L. J. Chen, and K. N. Tu, Nano Letts. 7, 2389-2394 (2007).

[4] Y.C. Chou, W.W. Wu, S.L. Cheng, B.Y. Yoo, N. Myung, L.J. Chen, and K. N. Tu, Nano Lett. 8, 2194-2199 (2007).

[5] K.C. Chen, W.W. Wu, C.N. Liao, L.J. Chen, and K.N. Tu, Science 321, 1066-1069 (2008).

New technologies and trends of TEM

Y. Kondo, E. Okunishi, S. Motoki, H. Sawada and F. Hosokawa

JEOL, Ltd., 1-2 Musashino 3-chome, Akishima, Tokyo 196-8558, Japan.

It is apparent that the microscopic information is useful for studies fo and industry. Especially, the electron microscope, which was invented in 1 Ruska, has been contributing to biology, materials science, chemistry and recently, to nano science and structural biology. And the electron microscope required by industries, especially by the microfabrication-related industry semi-conducting materials.

From the point of view of instrumental progress, during past few decade progress has been brought in. It is the invention and realization of a aberration correction system (Cs corrector) by Rose [1] and Haider et al spherical aberration, which proved to be unavoidable with the axial s electron lens, has limited the resolution of the scanning and conventional tra electron microscopies (STEM and TEM). The invention enabled us to do high-resolution observation in TEM and STEM but also highly sensitive an materials. These brought fruitful results for high-resolution microscopy as 6 47 pm resolution [3][4] and for analysis of materials science as an 'Atomic map' [5][6][7].

After the conquests of atomic resolution and high brightness of analytic the next problems are image contrast and specimen damage. With Cs correc defocus zero, it mathematically brought zero contrast of image for thin sp which is usually used in high-resolution electron microscopy, since the abso specimen of electrons is negligibly small. To overcome this problem, phase- electron microscopy has been tried Zernike phase plate. Nagayama succe image unstained biological sample with this method by using carbon film ph [8]. Other mediums to realize the phase contrast imaging, which are elec phase plate, have been tried and submitted by Taiwan [10] and American grou

The specimen damage problems strongly relate the nature of specimen. materials such as carbon nanotube related materials, it is effective to accelerating voltage microscopy. Quite recently, Suenaga group succeeded t single atom inside the fullerene using an aberration corrected 60 kV microscope. [11]

For methodology, we conclude that 'trends in TEM' is not only resolu also atomic level analysis, visualization of beam sensitive materials and enhancement of biological sample. For instrumental requirement, it is nece add ease-of-use and stability.

Reference

[1] H. Rose, Optik **85** (1990) 19.
[2] M. Haider et al Nature (1998) **392**: 768–769.
[3] H. Sawada et al., Jpn. J. Appl. Phys. **46**, L568 (2007).
[4] H. Sawada et al, J. electron microscopy (2009) on-line published.
[5] E. Okunishi et al Proc. of microsc. & microanal. (2006) p1150.
[6] M. Bosman et a., Phys. Rev. Lett. (2007) **99**, 086102 .
[7] K. Kimoto et al., Nature (2007) **450**, 702.
[8] R. Danev and K. Nagayama, Ultramicroscopy **88** (2001) 243-252.
[9] R. Cambie et al Ultramicroscopy (2007) **107**, 329-339.
[10] J. Shiue et al: J electron microscopy (2009);**58**(3):137-45.
[11] K. Suenaga et al: Nature Chemistry (2009) **1**, 415 - 418 .

維多利亞宴會廳平面配置圖

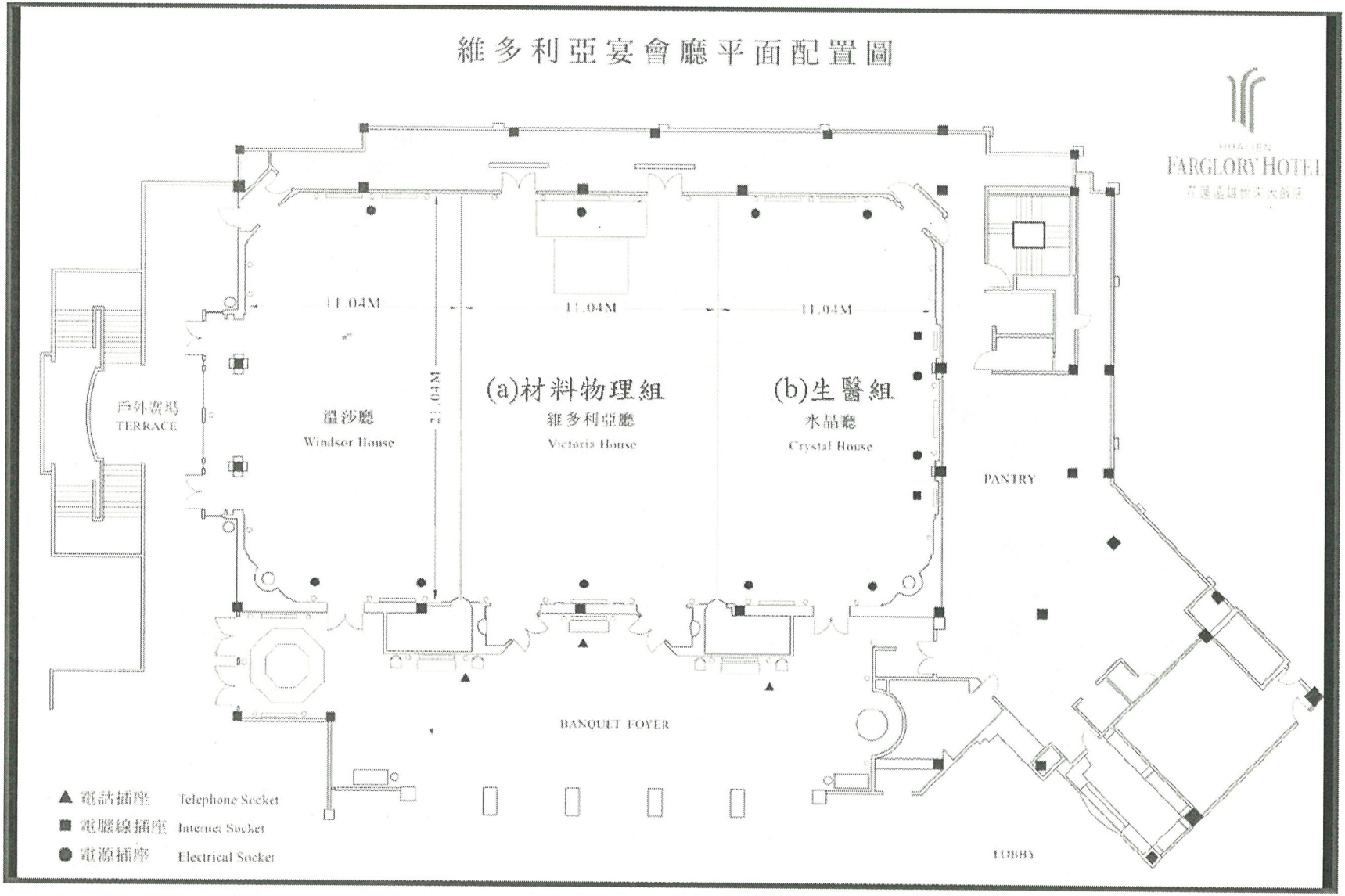

第七屆海峽兩岸顯微鏡學術研討會

Date	Aug.28(Fri.)
Place	維多利亞宴會廳
台灣顯微鏡年會	
14:30-15:00	會員報到
15:00-16:00	會員大會
第七屆海峽兩岸顯微鏡學術研討會	
16:30-18:00	報到註冊
18:00-18:10	大會開幕
18:10-18:30	李 英 雄
18:30-19:00	陳 力 俊
19:00-19:20	吳 建 國
19:20-20:30	歡迎晚宴

Date	Aug.29(Sat.)
Place	維多利亞廳
8:00-8:30	Dr. Don Kania FEI CEO
8:30-8:35	Dr.Yoshiyasu Harada
8:35-8:55	Yukihito Kondo
Schedule	(a) Cs corrected TEM
9:00-9:15	朱 靜
9:15-9:30	李 方 華
9:30-9:45	陳 福 榮
Schedule	(b) Diffractive Imaging
9:45-10:00	李 定 國
10:00-10:15	DRONYAK, Roman
10:15-10:30	Break & Exhibition
Schedule	(c) Microscopy on Phase Transformation
10:30-10:45	葉 恒 強
10:45-11:00	黃 英 碩
11:00-11:15	隋 曼 齡
Schedule	(d)Special talk in Scanning Probe Microscopy
11:15-11:35	張 嘉 升
11:45-13:30	LUNCH
Schedule	(e) NanoMaterials and Science (I)
13:30-13:45	張 澤
13:45-14:00	劉 全 璞
14:00-14:15	俞 大 鵬
14:15-14:30	沈 博 彥
Schedule	(f)New Materials for Energy
14:30-14:45	開 執 中
14:45-15:00	朱 敏
15:00-15:15	Break & Exhibition
Schedule	(g) Thin Film and Interface
15:15-15:30	李 建 奇
15:30-15:45	張 立
15:45-16:00	王 建 波
16:00-16:15	薛 富 盛
16:15-16:30	盧 朝 靖
16:30-16:45	歐 陽 浩
16:45-17:00	韓 曉 東
17:00-17:15	黃 榮 潭
17:15-17:30	孫 威
17:30-18:00	Poster
18:00~	Dinner

Date	Aug.30(Sun.)
Place	維多利亞廳
Schedule	(h)Industrial Application: Nano-electronics
8:30-8:45	蘇 紘 儀
8:45-9:00	謝 詠 芬
9:00-9:15	江 正 誠
Schedule	(i)Microscopy Techniques
9:15-9:30	Sohei Motoki
9:30-9:45	羅 聖 全
9:45-10:00	林 芳
10:00-10:15	黃 祖 緯
10:15-10:30	Break & Exhibition
Schedule	(j) Spectroscopy
10:30-10:45	薛 其 坤
10:45-11:00	朱 明 文
Schedule	(k) Nano-particles
11:00-11:15	殷 廣 鈐
11:15-11:30	朱 信 華
11:30-11:45	張 庶 元
11:45-12:00	王 建 義
12:00-13:30	LUNCH
Schedule	(l) Microscopy related Techniques
13:30-13:45	陳 清
13:45-14:00	李 志 浩
14:00-14:15	劉 慶
14:15-14:30	鮑 忠 興
14:30-14:45	丁 澤 軍
14:45-15:00	Break & Exhibition
Schedule	(m) Materials Science
15:00-15:15	李 吉 學
15:15-15:30	張 六 文
15:30-15:45	白 樸 存
15:45-16:00	顧 輝
16:00-16:15	馬 秀 良
16:15-16:30	敖 寧 建
16:30-17:00	閉 幕 式

第七屆海峽兩岸顯微鏡學術研討會

Date	Aug.28(Fri.)
Place	維多利亞宴會廳
台灣顯微鏡年會	
14:30-15:00	會員報到
15:00-16:00	會員大會
第七屆海峽兩岸顯微鏡學術研討會	
16:30-18:00	報到註冊
18:00-18:10	大會開幕
18:10-18:30	李 英 雄
18:30-19:00	陳 力 俊
19:00-19:20	吳 建 國
19:20-20:30	歡迎晚宴

Date	Aug.29(Sat.)
Place	水晶廳
8:00-8:30	Dr. Don Kania FEI CEO
8:30-8:35	Dr.Yoshiyasu Harada
8:35-8:55	Yukihito Kondo
Schedule	(a) Medical Science
8:55-9:15	高 甫 仁
9:15-9:35	王 素 霞
9:35-9:55	董 成 淵
9:55-10:15	楊 勇 驥
10:15-10:30	Break & Exhibition
10:30-10:50	楊 琇 雯
10:50-11:10	陳 德 蕙
11:10-11:30	錢 宗 良
11:30-11:50	崔 麗
11:50-13:25	LUNCH
Schedule	(b)BiogicalChemistry
13:30-13:45	張 俊 哲
13:45-14:05	隋 森 芳
14:05-14:25	林 弘 萍
14:25-14:40	朱 蔡 豈
Schedule	(c)Biological Technology
14:40-15:00	胡 宇 光
15:00-15:15	Break & Exhibition
15:15-15:35	武 一
15:35-15:55	孫 啓 光
15:55-16:15	李 超 煌
16:15-16:35	章 爲 皓
16:35-16:55	劉 清 標
16:55-17:15	蔡 錦 盛
17:30-18:00	Poster
18:00~	Dinner

Date	Aug.30(Sun.)
Place	水晶廳
Schedule	(d) Animal Science
8:35-8:55	王 重 雄
8:55-9:15	丁 明 孝
9:15-9:35	黃 榮 南
9:35-9:55	張 勤 奮
9:55-10:15	黃 宏 圖
10:15-10:30	Break & Exhibition
10:30-10:50	何 翰 蓁
10:50-11:10	鄭 穹 翔
Schedule	(e) Plant Science
11:10-11:30	鍾 美 珠
11:30-11:50	洪 健
11:50-13:25	LUNCH
13:25-13:45	陳 榮 銳
13:45-14:05	楊 秉 耀
14:05-14:25	簡 萬 能
14:25-14:45	王 學 東
14:45-15:00	Break & Exhibition
15:00-15:20	黃 玲 瓏
15:20-15:40	陳 淑 華
15:40-16:00	何 小 曼
16:00-16:15	許 秋 容
16:15-16:30	陳 香 君
16:30-17:00	閉 幕 式

主題演講目錄

(1)Physics and Materials Science

(a) Cs corrected TEM

(b) Diffractive Imaging

(c) Microscopy on Phase Transformation

(d) Special talk in Scanning Probe Microscopy

(e) NanoMaterials and Science (I)

(f) New Materials for Energy

(g) Thin Film and Interface

(h)Industrial Application: Nano-electronics

(i) Microscopy Techniques:

(j) Spectroscopy

(k) Nano-particles

(l) Microscopy related Techniques

(m) Materials Science

(2) Biological Science

(a) Medical Science

(b) Biogical Chemistry

(c) Biological Technology

(d) Animal Science

壁報摘要目錄

(1)Physics and Materials Science

(2) Biological Science

Materials Characterization by Aberration-Corrected High Resolution Electron Microscopy
(球差校正高分辨電子顯微術在材料表徵中的應用)

ZHU Jing (朱靜), LING Tao (淩濤), LU Ning (呂寧)

Department of Materials Science and Engineering, Tsinghua University, Beijing 100871，P R China
(北京電子顯微鏡中心，清華大學材料科學與工程系，北京 100084，中國)

隨著科學技術的進步，材料表徵技術已經進入了原子表徵的時代。電子顯微鏡一直在納米和功能材料的表徵中起著重要的作用。近年來球差校正技術的出現，突破了球差對電子顯微鏡的空間解析度的限制，將空間解析度推進到亞埃尺度，給納米和功能材料的表徵帶來了新的機遇**[1~4]**。本文給出球差校正高分辨電子顯微術(*Cs*-HRTEM)在納米顆粒和鐵電材料中的應用實例。

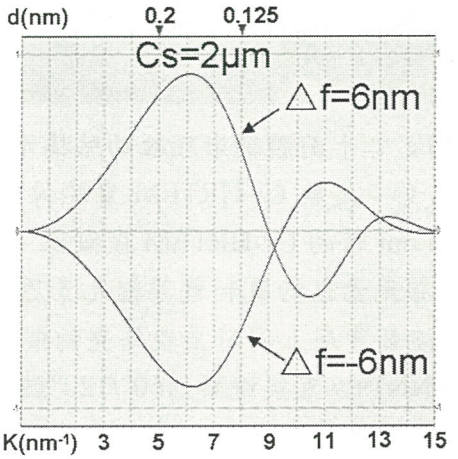

圖 1 Titan 80-300 *Cs*=2 μm 時襯度傳遞函數 (semi-angle of beam convergence: 0.1 mrad, defous spread: 2.3 nm)。

本研究組最近成功合成了直徑為 5-13 nm 的 *FCC*-Fe 二十面體納米顆粒，應用球差校正高分辨電子顯微鏡對這些小顆粒的微觀結構進行表徵[5]。圖 1 是北京電子顯微鏡中心 Titan 80-300，*Cs*=2 μm，欠焦△*f*=6 nm 和-6nm，會聚半形(semi-angle of beam convergence)為 0.1 mrad，defous spread 為 2.3nm 時的襯度傳遞函數。*FCC*-Fe 的{111}和{220}的晶面間距為 0.206 和 0.126 nm，可以在通帶平臺內傳遞。在實驗 HRTEM 拍攝中球差調整在-2~3 μm 範圍內進行成像，加速電壓為 300 kV。

二十面體是一種非常特殊的結構，由二十個四面體組成，有二次、三次和五次對稱軸，每個四面體的外表面和孿晶面均為{111}面，每個四面體的棱邊都是<110>方向。圖2A是二十面體沿五次軸取向的結構示意圖。此時，將二十面體分為兩部分，一部分是上下兩組五次對稱的十個四面體，第二部分是二十面體邊沿的十個四面體。如果只考慮二十面體上面或下面的一組五個四面體，它們都處於<110>帶軸。圖2B是這兩組五次對稱的十個四面體反對稱疊置後的原子投影圖，可以看出，只有中心的五角反棱錐顯示完整的十次對稱。其他原子，投影是沒有辦法嚴格重合的，即使勉強說靠得很近，周邊的五個原子也不是正五角形分佈。因此在中心之外，再也找不到嚴格的十邊形投影。圖2C是欠焦時拍攝的HRTEM圖，此時的高

分辨圖像不再具有"週期性"的晶格像，而是如同一朵盛開的美麗花朵，雖然顆粒週邊有十次對稱的條紋，但是顆粒內部的HRTEM花樣並沒有五次對稱性，只呈二次對稱性。圖2D是二十面體納米顆粒位於"准"五次軸，即二十面體的原子模型繞Y軸從X軸往Z軸轉1.2°時得到的$\triangle f$=-6 nm時模擬像，同圖2C的實驗像是非常吻合的。

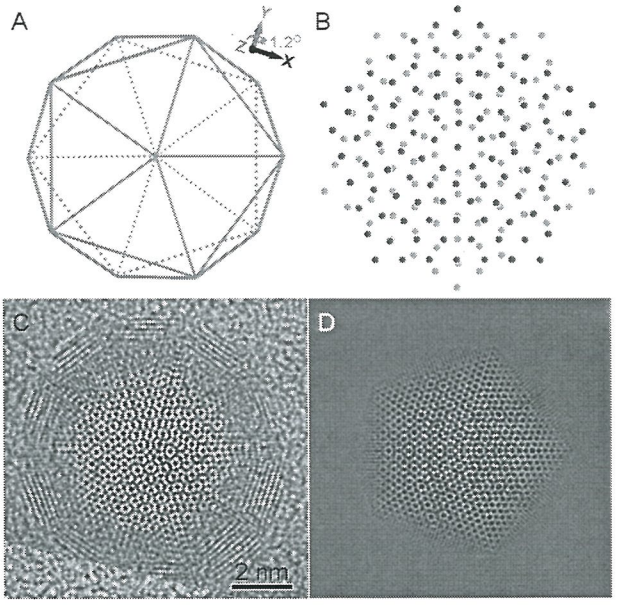

圖 2　A：五次軸取向時 FCC-Fe 二十面體納米顆粒的結構示意圖；B：上下兩組五次對稱的十個四面體原子投影圖；C：欠焦 *Cs*-HRTEM 實驗像；D："准"五次軸取向時 FCC-Fe 二十面體納米顆粒$\triangle f$=-6 nm 時的 *Cs*-HRTEM 模擬像。

負球差成像技術可以使所有元素包括氧和氮等輕元素原子同時成像[1]。負球差和物鏡過焦條件，使所有原子柱在黑色襯度背底上同時呈現為亮的襯度。利用該成像技術，在新型無鉛壓電陶瓷($K_{0.46}Na_{0.54}$)NbO_3(KNN)中，直接觀察到60°/120°鐵電疇壁兩側氧原子相對陽離子的位移。此外，作者還利用第一性原理計算方法，優化得到正交相KNN結構中原子相對位置。基於計算得到原子位置所類比的高分辨圖像與實驗得到的圖像非常吻合。進而，作者推斷出鐵電疇壁及其兩側疇的極化方向。這種負球差成像技術和第一性原理計算相結合的方法為鐵電極化理論的進一步研究提供了原子尺度上的依據。

References

1. Jia C L, Lentzen M, Urban K. Science，2003，299：870-873.
2. Jia C L, Urban K. Science，2004，303：2001-2004.
3. Muller D A, Kourkoutis L F, Murfitt M, et al.　Science，2008，319：1073-1076.
4. Batson P E, Dellby N, Krivanek O L. Nature，2002，418：617-620.
5. Ling T, Xie L, Zhu J, et al. Nano Lett，(Accepted).

Image Contrast and Deconvolution Processing of Spherical Aberration- corrected High-resolution Electron Microscope Images (球差校正高分辨電子顯微像的像襯和解卷處理)

LI Fang-Hua (李方華), WAN Wei (萬威)

Beijing National Laboratory for Condensed Matter Physics, Institute of Physics, Chinese Academy of Sciences, Beijing 100190，P R China（北京凝聚態物理國家實驗室，中國科學院物理研究所，北京 100190，中國）

弱相位物體近似（WPOA）簡單明瞭地解釋了高分辨電子顯微像（以下簡稱高分辨像或像）與襯度傳遞函數的關係，特別是與物鏡球差係數及離焦量的關係，但未能給出像襯隨試樣厚度的變化規律。借助較嚴格的理論，包括廣泛應用於高分辨電子顯微學的多片理論[1]，有助於從模擬像瞭解不同厚度試樣的像襯。為了得出普遍的規律，曾從多片理論出發，將每片近似為弱相位物體，忽略片與片之間的多次散射，但考慮菲涅爾衍射，得出了一個比 WPOA 較為高級的像襯理論，稱贗弱相位物體近似（PWPOA）。該理論給出像襯隨晶體厚度變化的普遍規律，而且指出輕重不同原子像襯隨厚度變化規律之差異。還指出，只要樣品不太厚，例如在中等電子加速電壓下，對於中等原子序數原子組成的晶體，厚度為數納米時，WPOA 的公式仍然有效，但需把電勢投影函數$\varphi(\boldsymbol{r})$置換為贗電勢投影函數和$\varphi'(\boldsymbol{r})$[2]。後者是一個假想晶體的電勢投影，假想晶體的結構與被測晶體類型相同，僅組成原子不同，其重原子較真實晶體的輕，而輕原子則較真實晶體的重。

贗弱相位物體近似的像強度公式是針對傳統電子顯微鏡（以下簡稱電鏡）推導的，即認為物鏡球差像數 C_S 為正。本工作將其擴展至球差校正電鏡的情形，C_S 可正可負，得 Scherzer 聚焦條件下的像強度公式為：

$$I(\boldsymbol{r}) = 1 \mp 2\sigma\varphi'(\boldsymbol{r}) \text{ ，} \qquad (1)$$

$$\varphi'(\mathbf{r}) = \varphi(\mathbf{r}) + \Delta\varphi(\mathbf{r}) \text{ ，} \qquad (2)$$

其中$\sigma = \pi/\lambda U$，λ 和 U 分別表示電子波長和加速電壓，$\Delta\varphi$ 與樣品厚度有關。$C_S > 0$ 時，公式（1）等號右端的符號"∓"取負號；$C_S < 0$ 時取正號。$C_S > 0$ 時無論其值如何，像襯規律與傳統電鏡相同，即晶體足夠薄時，原子在像上顯示為黑[3, 4]。隨著晶體厚度加大，輕原子襯度相對增加，而重原子襯度相對降低，且當樣品厚度超過臨界值時重原子襯度發生反轉，顯示為白。$C_S < 0$ 時輕重不同原子隨樣品厚度的變化規律同前，但在薄晶體的結構像上原子始終顯示為白，重原子襯度不發生反轉。因此，相對於正球差而言，負球差對樣品厚度的要求有所放寬，更有利於直接拍攝結構像。

上述像襯規律說明解卷處理方法同樣可應用於球差校正電鏡拍攝的高分辨像。圖 1 是有 I2 型層錯的六方 GaN 晶體沿$(\boldsymbol{a}+\boldsymbol{b})$方向的投影結構模型。圖 2 上排給出圖 1 結構模型的類比像，下排是對應的解卷像。類比參數為電子加速電壓 300 kV，由色差引起的離焦擴展 3 nm，電鏡點分辨本領和資訊極限分別為 0.086 nm 和 0.096 nm 試樣厚度 3.2nm,球差係數（左）0.04 和（右）-0.04 mm，離焦量列於圖的下端。由圖可見，模擬像均不直接反映 GaN 晶體完整區和 I2 層錯區的結構，而經解卷處理後均顯示了完整區和缺陷區原子解析度的結構。這說明對於球差校正電鏡，解卷處理方法依然是從高分辨像中恢復原子解析度晶體結構和缺陷的有力

手段。結合上一段關於球差校正高分辨像襯度的討論，欲借助解卷處理將實驗像轉換為結構像時，不妨在負球差下拍攝高分辨像。

對球差校正電子顯微鏡拍攝的外延 SiC/Si 實驗高分辨像的解卷處理正在進行中。

References

1. Cowley J M， Moodie A F. Acta Cryst，1957，10：609-619.
2. Li F H，Tang D. Acta Cryst，1985，A41 ：376-382.
3. 李方華. 電子晶體學與圖像處理. 上海：科學技術出版社，2009.
4. Li F H. Effect of diffraction crystallography on HREM. Zeit Kristallogr，2003，218：279-292.

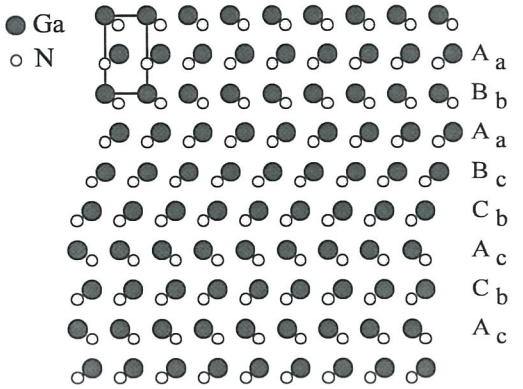

圖 1 六方 GaN 晶體沿($\boldsymbol{a}$ + $\boldsymbol{b}$)方向的投影結構模型，其中有 I2 型層錯。圖右側分別用大寫和小寫字母標注了 Ga 和 N 原子的堆垛順序。

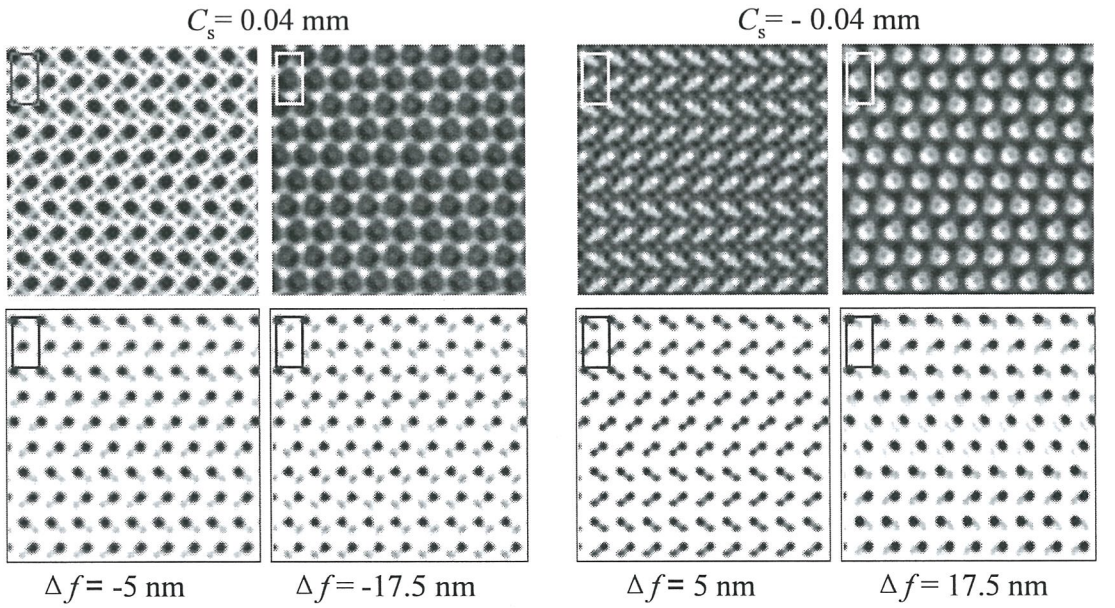

圖 2 含 I2 層錯 GaN 晶體的球差校正高分辨類比像的解卷處理。上排是圖 1 結構模型的類比像，下排是對應的解卷像。模擬像的試樣厚度為 3.2nm，球差係數為（左）0.04 和（右）-0.04 mm，離焦量列於圖的下端。

Toward Qusai-Atomic Resolution Tomography

Fu-Rong Chen[1](陳福榮), Roar Kilaas[2], Christian Kisielowski[3], Dirk Van Dyck[4]

1. Dept. of Enginering and System Science, National Tsing Hua University, Hsin Chu, 300 Taiwan
（新竹清華大學工程與系統科學系）
2. Total Resolution, Berkeley, CA 94707 USA
3. NCEM, Lawrence Berkeley National Lab., CA 94707 USA
4. Vision Lab., University of Antwerp, Groenenborgerlaan 171, U316 2020 Antwerp Belgium

As the electron travels through the sample, it suffers from the dynamical scattering such that phase in exit wave is altered according to the atomic structure and the thickness. The exit wave may bear no simple one to one relationship with the structure. The phase in exit wave is further complicated by the lens aberrations such as the spherical aberration and focus. The Cs corrector basically severs as a phase plate that corrects the the phase distortion from the spherical aberration. The phase distortion arising from the spherical aberration can also be removed by the exit wave reconstruction process. However, due to the presence of dynamical scattering and local variation of focus in sample, the atomic structure of sample is still encoded in the images or the reconstructed exit wave even recorded from a Cs corrected TEM.

Before the dynamical scattering can be reversed, the geometry of the exit surface of the sample has to be deduced. The development of the "numerical focus plate" is to correct the phase terms from local variation in focus in the sample. Possible approaches to the problem of local variation in focus will be presented. Simulation case of wedge Au crystal will be used as a test example. After correction of the "focal" plate, then the quantification of the exit wave can be carried out by reversion prcess of the dynamical scattering either by the reversing multislice algorithm or 1s state model. Examples from C_s corrected TEM will be shown to demonstate the concept of "focal phase plate" and reversing of dynamical scattering that will lead to quantification of the structure from Cs corrected TEM.

As the exit wave propagates in the free space, it forms a circle in the Argand plot. Fig. 1 shows Argand plot of the propagated exit wave from simulated exit waves of Au and Si crystals. In my talk, I will present methods (1) to determine the "focal plate" based on the propagation circle of the exit wave and (2) to retrieve the potential map from the exit wave based on reversing multi-slice (RMS) calculations. For crystalline materials containing single element, the 3 dimensional atomic structure can be reduced after the geometry of exit surface and the potential map are analyzed. Quasi-atomic resolution tomography will be demonstrated using simulated wedge Au crystal. Fig. 2 (a) shows a defocus map obtained from a simulated wedge-shape Au structure with atom columns containing 1 to 5 atoms. The side-view of the structure is shown in the insert of (a). Fig. 2(b) shows the defocus circles for every atom column. Each atom column is defocused from -30°A to +30°A.

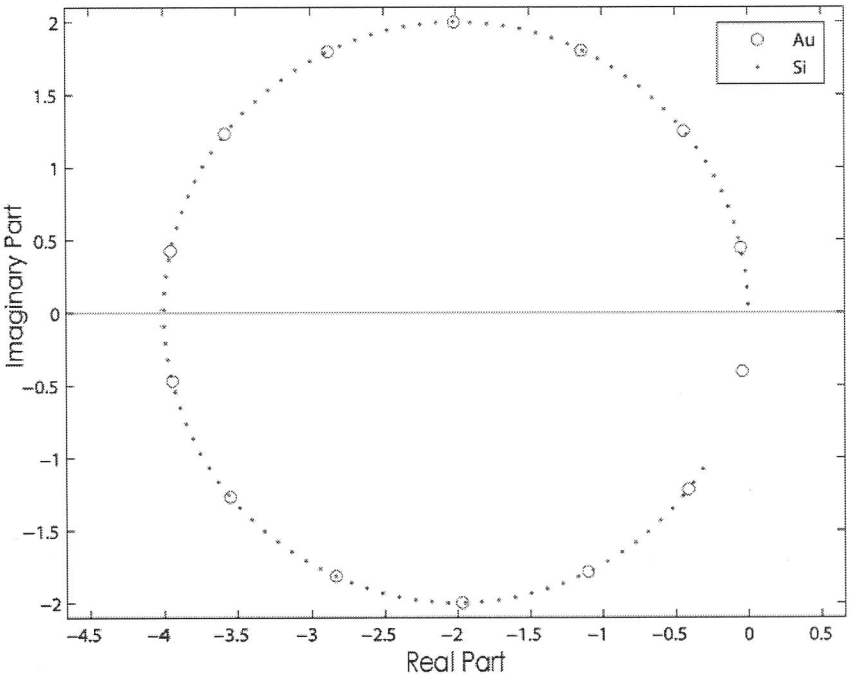

Fig. 1 Argand plots for Si and Au in [100] orientation obtained from simulated exit waves using the channelling theory.

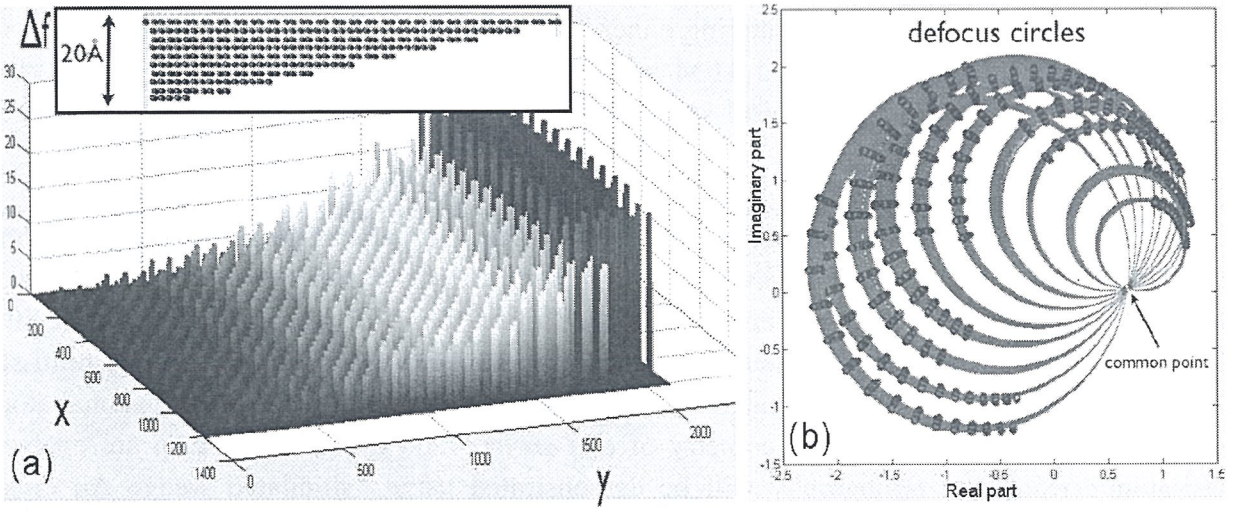

Fig. 2 (a) a defocus map obtained from a simulated wedge-shape Au structure with atom columns containing 1 to 5 atoms. The side-view of the structure is shown in the insert of (a). (b) The defocus circles for every atom column. Each atom column is defocused from -30°*A* to +30°*A*.

A new method to study three-dimensional structures of radiation-sensitive samples by using X-ray or electron diffraction microscopy

T. K. Lee(李定國), C. C. Chen and C. H. Lu

Institute of Physics, Academia Sinica(中央研究院物理所), Taiwan

A new method to reconstruct a three-dimensional image by using measured x-ray or electron diffraction intensities is presented. The method is specially designed to study radiation-sensitive samples with data taken at a limited number of angles. The method combines the ideas of Pseudo-Polar Fourier transform and 3D Hybrid Input-Output method. For both theoretical models and experimental data, it is shown to provide a much improved accuracy for the reconstructed 3D images at all angles than previous methods.

ELECTRON DIFFRACTIVE IMAGING OF A SINGLE NANOPARTICLE

Roman Dronyak(卓亞克)[1,2], Keng S. Liang(梁耕三)[2], Ting-Kuo Lee(李定國)[3], Chi-Kai Feng(馮祺凱)[1], and Fu-Rong Chen(陳福榮)[1,2]

[1]*Department of Engineering and System Science, National Tsing Hua University(清華大學工程與系統科學系), Hsinchu, Taiwan*

[2]*National Synchrotron Radiation Research Center(同步輻射研究中心), Hsinchu, Taiwan*

[3]*Institute of Physics, Academia Sinica(中央研究院物理所), Nankang, Taipei, Taiwan*

In diffraction experiments the phase information is encoded in diffraction intensities and, in principle, can be recovered using a coherent diffractive imaging (CDI) commonly known as the oversampling method. Electron CDI is promising to achieve diffraction-limited resolution, and is particularly challenging for characterization of disordered materials and biological samples.

Here we present a phase-recovery technique that utilizes a guiding method with a dynamic support **[1 - 3]** to reconstruct the shape and the exit wave of a single MgO nanoparticle (Fig. 1a). The proposed optimization method provides an optimal solution deduced from the experimental electron diffraction pattern alone (Fig. 1b). The recovered shape of a hydrated nanocrystal (Fig. 2a) has a spatial resolution 3.1 nm, limited by the measurable diffuse scattering intensities about Bragg peaks. The modulus of the recovered exit wave has a fine periodic structure of spacing 0.15 nm (Fig. 2c). The estimated error of solution (Fig. 2b, d) is smaller than 10% except in the region of width about 1.6 nm at the edges of the sample. Note, the modulus of exit wave decreases linearly in a width about 3.5 nm at the edges (Fig. 2e), consistent with the presence of {110} facets at an early stage of hydration of MgO smoke cubes.

The important requirement of electron CDI is the coherent nature of illumination that is shown in the strong interference fringes over the beam profile (Fig. 1a). We quantify the coherence length in the sample plane by fitting a simulated partially coherent beam to the experimentally recorded beam profile. A minimal discrepancy was obtained for the electron probe (see upper inset of Fig. 1a) having coherence length 15 nm. Therefore, the partial coherence of the beam can be treated quantitatively in the CDI. Further details will be discussed during the workshop.

References

1. C. C. Chen, J. Miao, C. W. Wang, and T. K. Lee, Phys. Rev. B 2007 (76) 064113.
2. R. Dronyak, C.-K. Feng, K. S. Liang and F.-R. Chen. Acta Cryst. A 2008 (64) C130.
3. R. Dronyak, K. S. Liang, T.-K. Lee, C.-K. Feng, J.-S. Tsai, and F.-R. Chen, submitted.

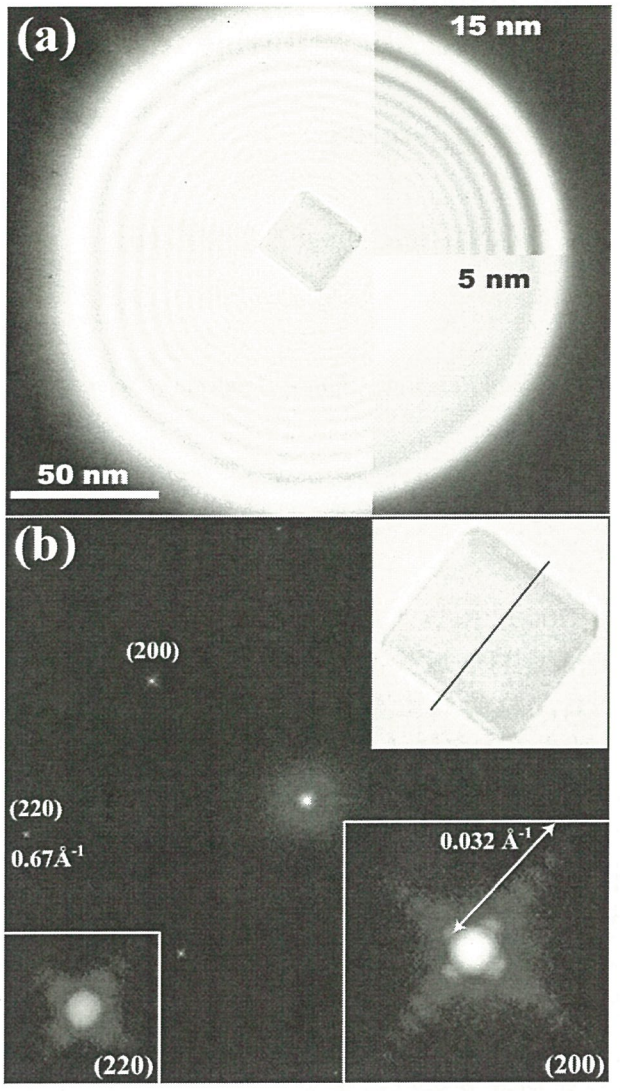

Figure 1 (a) TEM image of the electron probe illuminating a sample. Insets show a simulated beam assuming partially coherent illumination with spatial coherence length 15 nm and 5 nm correspondingly. (b) Electron diffraction pattern recorded on the imaging plate near the [001] zone axis. The upper inset shows an enlarged image of an eroded 24-nm MgO nanoparticle shown in (a). The lower insets are enlarged views of intensities about (200) and (220) Bragg peaks.

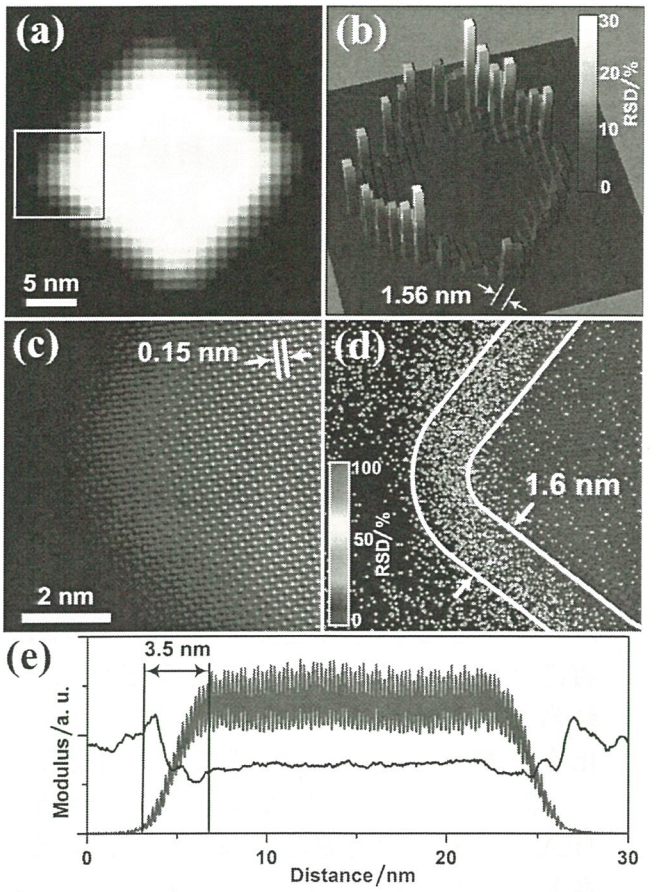

Figure 2 (a) Modulus of the shape of the MgO nanoparticle recovered from intensities about the (200) Bragg peak. . (b) Spatial accuracy of a solution showing the relative error of the recovered shape that is greater within 1.56 nm at the edges of the sample. (c) Modulus of the reconstructed exit wave at the edge of the sample indicated by the square in (a). (d) Spatial accuracy of the part of the exit wave shown in (c). The region at the edges of the sample at which error is great (~35 %) has width about 1.6 nm. (e) Comparison of the contrast profile (black line) obtained from a TEM image of the sample along the line shown in the upper inset of Fig. 1(b) with the modulus of the exit wave (red line) along the same region

An Electron Microscopy Analysis and Computational Simulation for Deformation-Induced Phase Transformation of TiAl Alloys During Room Temperature Compress
(TiAl 合金室溫形變誘導相變的電子顯微與計算類比研究)

LIU Yong-Li(劉永利)[1,2], CHEN Chun-lin(陳春林)[1,3], WANG Shao-qing(王紹青)[1], HE Lian-long(賀連龍)[1], YE Heng-qiang(葉恒強)[1*]

1.Shenyng National Laboratory for Materials Science, Institute of Metal Research, Chinese Academy of Sciences, Shenyang Liaoning 110016, P R China(中國科學院瀋陽金屬研究所)

2.School of Sciences, Northeastern university, Shenyang Liaoning 110006, P R China ;3. Center of Electron Microscopy, Osaka University, Japan)

TiAl 合金具有密度低、強度高的優點，適於 700°C 附近溫度應用，一直被認為是有潛力的高溫結構材料。但由於其室溫塑性低、韌性也未能符合服役要求，這類合金的實用化進程較為緩慢。近年來，在汽車引擎的活塞杆和航空發動機的低壓渦輪葉片採用 TiAl 合金的工程化應用有了進展。深入瞭解該合金的變形行為，對改善其室溫力學性能可提供理論上的支援。

具有較好綜合力學性能的 TiAl 合金都是由 TiAl（γ 相，面心四角結構，*c/a* 接近於 1）和 Ti_3Al（α_2 相，六角密堆結構）片層相間的雙相組織。兩相片層間的 $(111)_\gamma$ 與 $(0001)_{\alpha_2}$ 相聯接。在熱處理時，相之間轉變是經常發生的。近年來，TiAl 合金中室溫形變誘導相變時有報導**[1]**。$\gamma \Leftrightarrow \alpha_2$ 相變屬於 *fcc* ⇔ *hcp* 類型，從基面切變機制很易瞭解，滑移方向是 1/6<112> //1/3<10$\bar{1}$0> $_2$。但是，鈦鋁比在 TiAl 是 1：1, 在 Ti_3Al 是 3：1，且基面的有序方式也不同。在室溫切變改動基面堆垛次序的同時，有否誘導基面內成份的改變，在室溫狀態是個問題**[2]**。本文旨在原子尺度上用電子顯微學和計算模擬的手段，對 TiAl 合金室溫形變誘導相變的顯微結構進行研究，以求為合金綜合性能的改善提供依據。

在名義成份為 Ti-45Al-8Nb(at.%)的合金中，觀察到室溫形變誘發 $\gamma \rightarrow \alpha_2$ 相變發生在形變孿晶交截區。分析表明**[3]**，形變誘生的具有六角堆垛特徵（ABAB...）的相變產物從高分辨像看十分類似 α_2－Ti_3Al 相，但相應傅立葉變換得到的衍射譜表明它的基面的有序結構與 Ti_3Al 的不同，而可以用 TiAl 的 {111} 面有序結構解釋。進一步的成份分析也說明，誘生相變的產物與 γ 相有類似的組分。

在同一種合金中，還觀察到室溫壓縮（～10%）過程中發生於 α_2 片層內的形變誘發 $\alpha_2 \rightarrow \gamma$ 相變。圖 1a 是其高分辨像，電子束方向為 $[11\bar{2}0]_{\alpha_2}$ //$[\bar{1}01]_\gamma$。形變誘生的 γ 薄片只有三層原子面厚。形變誘生的　相點陣常數稍大一些。X 射線能譜測量結果表明，形變誘生的 γ 相（Ti+Nb）/Al 值為 1.52，而 α_2 基體的為 1.56。可以認為室溫誘生的 γ 相與基體 α_2 有相同的成分。

Ti-Al 二元相圖顯示，Ti_3Al，TiAl 都不是成分比十分確定的相，例如，Ti_3Al 的 Ti/Al 可以從 3.35 變化到 1.85，TiAl 相則從 1 到 0.79。為了考察不同成份的 γ，α_2 相形變誘發另一方的難易程度，設計了不同成分相剪切變形的能量計算**[4]**。計算模型分為兩組，TiAl 面心四角結構(*fct*)組，Ti/Al：1，1.25，1.4，1.57，2，2.43，3。在 Ti_3Al(*hcp*)組，Ti/Al 變化為 1, 1.29，1.5，1.67，2，2.43，3。計算表明，各成分構型不同原子占位優化的超單胞參數隨 Ti 含量增加而增大。這與實驗相符。圖 2 是剪切變形模擬，那裏存在一個成分軟化區，即最大剪切應力普遍比較小的區域（Ti:Al 在 1.25～2 附近），且 *hcp* 構型的 τ_{max} 要小於相應 *fct* 結構的最大剪切應力，這也符合既有的實驗報導。各成分構型的位錯形核參數 D 隨成分的變化的計算表明，在 Ti:Al≈2 時，*fct* 和 *hcp* 的 Ti_2Al 構型的 D 值均為負，且最小。這說明 Ti_2Al 構型可能是

合金應力誘發相變中較易形成的中間相。

總之，高分辨電子顯微像和相應衍射圖確證了室溫壓縮形變誘發了從T
相的轉變。沒有成分變化。計算表明，化學成分在形變誘導相變中起驅動
接近 1.5 的區間，$\alpha_2 \rightarrow \gamma$ 的轉變很可能發生。加了外力的剪切變形模擬表明
的區域，雙向相變 $\gamma \Leftrightarrow \alpha_2$ 容易進行。鑒於 γ 相很難達到這個成分區域，而
存在於此區域，所以 $\alpha_2 \rightarrow \gamma$ 被形變誘發的可能性更大。

References

1. Gao Y，Zhu J. Stress-induced phase transformation in two-phase TiAl i
   Scripta Metall Mater，1993，28：651-655.
2. Liu Y L，Liu L M，Wang S Q，Ye H Q. The first principle study of shear
   and Ti_3Al. Intermettallics，2007，15: 428.
3. 陳春林，魯偉，賀連龍，葉恒強. 鈦鋁合金中的形變誘發 γ→DI-α_2 相
   2007，26 (4)：276-287.
4. Liu Y L，Liu L M，Wang S Q，Ye H Q. First-principles study of shear
   alloys. Journal of Alloys and Compounds，2007，440：287–294.

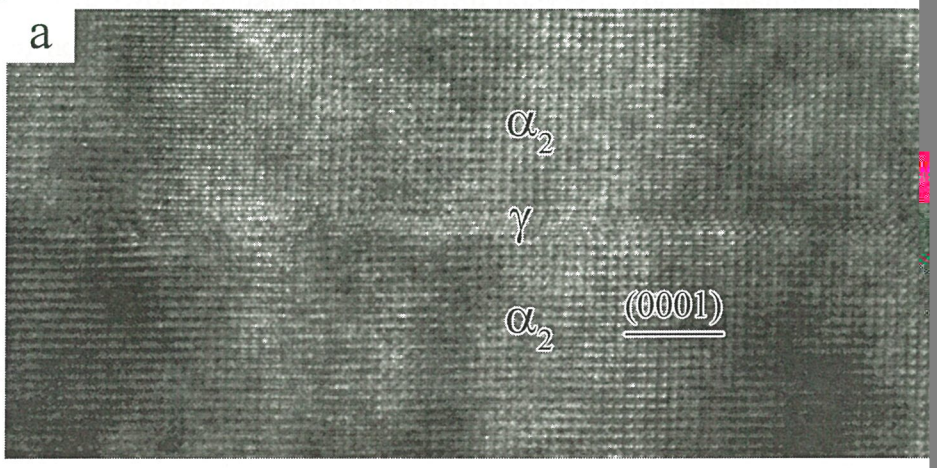

圖 1 室溫壓縮過程中發生於 α_2 板條內的形變誘發 $\alpha_2 \rightarrow \gamma$ 相變。高分辨像
小薄片在 α_2 板條內形核長大，電子束入射方向為$[11\bar{2}0]_{\alpha_2}//[\bar{1}01]_r$ 。

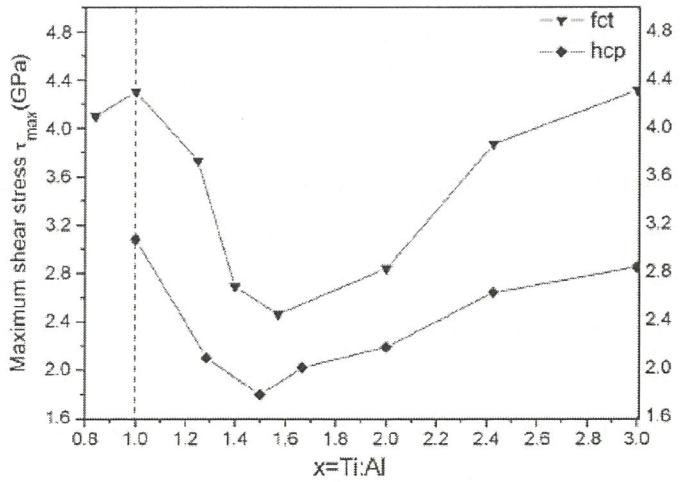

圖 2 *fct*（▼）和 *hcp*（◆）結構的各成分構型的最大剪切應力隨成分的變化

Effects of boundaries and point defects on a surface phase transition

Ing-Shouh Hwang(黃英碩) , Chung-Kai Fang , Shih-Hsin Chang , Tien T. Tsong(鄭天佐)

Institute of Physics, Academia Sinica(中央研究院物理所), Nankang, Taipei, Taiwan, R.O.C.

A reversible, temperature-driven structural surface phase transition of Pb/Si(111) is studied with a variable-temperature scanning tunneling microscope (STM). At a coverage around one monolayer, there exists a 1×1-Pb phase at room temperature. The 1×1-Pb phase undergoes a reversible structural transformation into a row-like $\sqrt{7}\times\sqrt{3}$ -Pb reconstruction at low temperatures. Since the Si(111) substrate has three-fold symmetry, there are three different row orientations. We also find that an elongated boundary shape tends to favor the $\sqrt{7}\times\sqrt{3}$ row structure with orientation aligned with the long axis of the elongated compact region. Our STM study of many Pb-covered Si(111) compact nanoislands at several different temperatures shows that the transition temperature decreases with decreasing region (island) size **[1,2]**. Near the transition temperature, sudden change in the row orientation or the sudden translation of the low-temperature $\sqrt{7}\times\sqrt{3}$ phase can be seen. Neither domain walls nor traces of their motions can be seen in these compact nano-regions (or nanoislands). This suggests that the domain wall motions are much too fast for STM imaging. The phase transition may involves only small lateral displacements of Pb atoms without breaking the covalent Pb-Si bonds, which can explain the small activation energies for domain wall motions **[1,2]**. We believe that the disordering transition may be caused by prolific creation and very rapid migration of domain walls at high temperatures. Another interesting observation is pre-disordering near boundaries at temperatures slightly below T_c.

Fortunately, through proper sample preparation, the trapping of domain walls by certain boundary conditions or by point defects allows us to capture domain walls and their motions at a time scale reachable by STM. Thus, the interactions of domain walls with boundaries and point defects can be studied. We find that domain walls can be pinned at constrictions. Through introduction of atomic hydrogen, we find that H-induced point defects may facilitate formation of domain walls and trap their motions. In addition, we often see enhanced structural fluctuations or even loss of the long-ranged order on the Pb-covered nano-regions after higher H exposures. This indicates that introduction of point defects can reduce the transition temperature. We also observe pre-disordering in defective areas, where the local defect density is significantly higher than the average. Here we propose that most of the defects and boundaries may provide attractive potentials for domain walls. A qualitative picture based on these potentials can explain the observed phenomena, such as strong pinning of domain walls at constrictions and/or by point defects, finite-size effects on the phase transition temperatures, pre-disordering in areas near boundaries or

in defective areas, enhanced structural fluctuations after introduction of point defects. Many concepts may be extended to understand other domain-wall based systems.

Work supported by the National Science Council of ROC and Academia Sinica.

References

1. I.-S. Hwang, S.-H. Chang, C.-K. Fang, L.-J. Chen, T. T. Tsong, Phys. Rev. Lett. **93**, 106101 (2004).
2. I.-S. Hwang, S.-H. Chang, C.-K. Fang, L.-J. Chen, T. T. Tsong, Surf. Sci. Lett. **572**, L331 (2004).

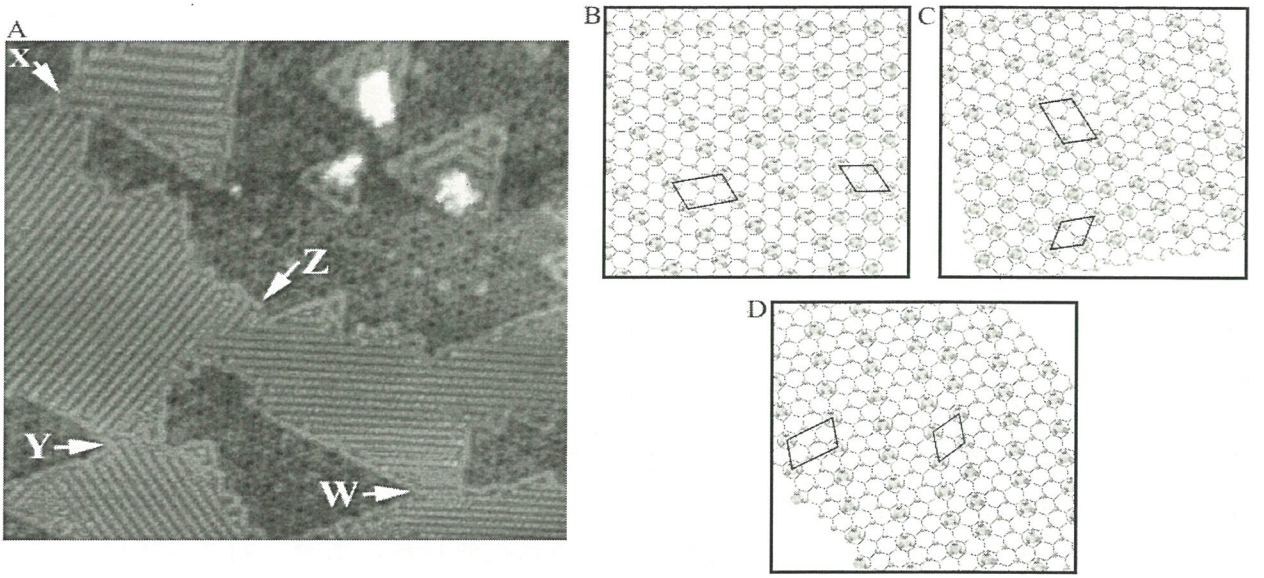

Fig. 1 (A) STM images of compact Pb-covered regions connected by constrictions, taken at 96 K. Atomic model for 60° and 120° orientational domain walls are shown in (B) and (C), respectively. The unit cells for each $\sqrt{7}\times\sqrt{3}$ domain are illustrated with black dashed lines, and a unit cell of the $\sqrt{3}\times\sqrt{3}$ is indicated with a blue dashed lines. (D) Atomic model for a phase domain wall.

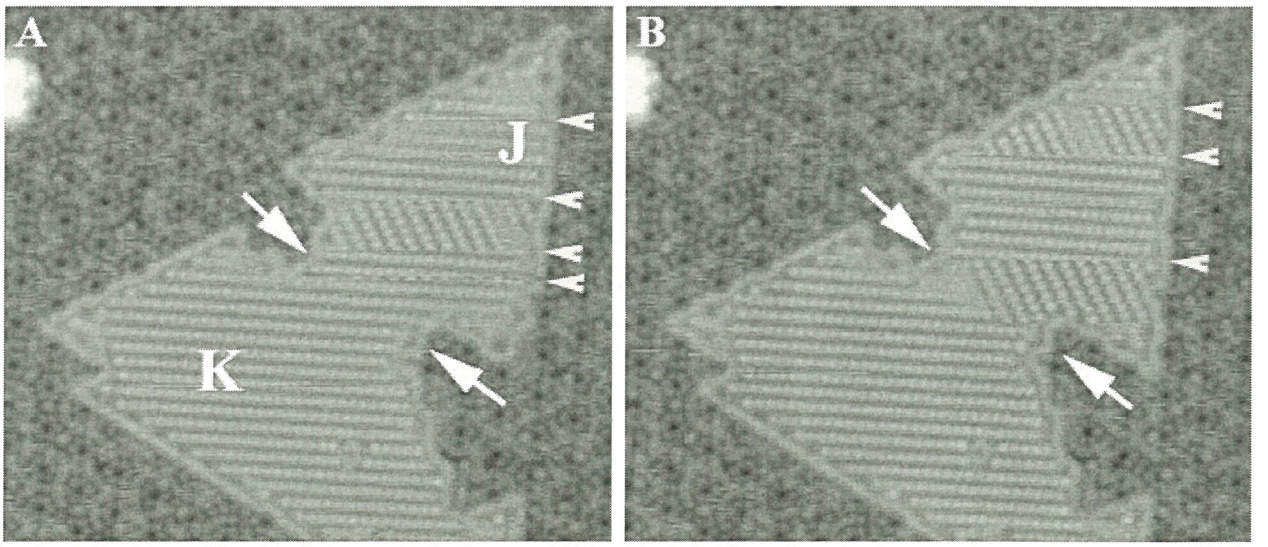

Fig. 2 Pinning effects of a constriction. (A) and (B) show two consecutive STM images of a Pb-covered region taken at 190 K and the sample bias of +2 V. The duration between two images is ~ 1 min.

Novel Deformation Mechanisms Discovered by *in situ* HREM Observations (利用原位高分辨觀察揭示新材料形變機制)

SUI Man-Ling (隋曼齡)

(Shenyang National Laboratory for Materials Science (SYNL), Institute of Metal Research, Chinese Academy of Sciences, Shenyang Liaoning 110016, P R China)

(中國科學院金屬研究所瀋陽材料科學國家(聯合)實驗室,遼寧 瀋陽 110016,中國)

伴隨著新材料新性能的出現,必然會產生新的材料科學研究問題。對於一些高性能新材料所表現出的特殊力學行為,其形變機理的研究顯得至關重要,因為對其機理的認知是能夠有效地控制材料性能、有目的地發展高性能新材料的基礎。利用透射電鏡(TEM)進行形變機理的研究通常是分別對形變前和形變後的樣品進行微觀結構觀察,通過對比研究相結構和位元錯組態等變化,間接獲得對形變過程的認識,從而揭示其形變機制,如典型的位錯機制、形變孿晶機制、形變誘導的相變機制等。然而,這種通過對應力卸載後樣品的形變結構觀察研究,只能獲得該材料的塑性形變資訊,而無法解釋材料在彈性形變過程的行為;而且,這種非原位觀察的方法也不利於研究納米晶體材料的晶界滑移/遷移和晶粒旋轉長大等形變機制。

在高分辨透射電鏡(HRTEM)下的原位拉伸實驗是研究材料形變機制的直接而有效的方法。通過在原子尺度上直接觀察應力應變作用下晶體結構的演變以及位元錯的產生和運動等,直觀地揭示材料在彈性及塑性階段的形變機理,有利於人們對材料本征特性的認識。

本工作利用透射電鏡原位拉伸技術揭示了幾種高性能材料的形變機制 **[1~4]**。

以往對於孿晶界在材料變形中作用的研究主要集中在孿晶界是如何像普通晶界一樣阻礙位錯運動而提高材料的強度;而對大量孿晶界的存在是如何提高材料的塑性和延伸率這方面研究得甚少。在研究具有高強度和高延伸率特點的納米片層孿晶銅的形變機理時發現,應力作用下在基體中產生的擴展位錯儘管在滑向孿晶界時其擴展距離逐漸減小(圖1),但還是可以通過與孿晶介面發生交互作用後穿過孿晶界,位錯反應分解出的不全位元錯沿著孿晶介面滑移,從而導致孿晶介面移動(圖2)**[1]**。此外,孿晶介面在有位元錯臺階的情況下還可以作為位元錯源發射位錯**[2]**,從而揭示了納米片層孿晶銅的孿晶介面提高塑性的本征機理。

對於納米晶材料的變形機制,大量的分子動力學模擬計算已經把納米晶材料的形變機制按照晶粒尺寸的不同分為三類,即晶界協調變形、位錯協調變形和兩者共同協調變形機制。本文通過透射電鏡原位拉伸變形納米晶鎳,獲得了形變誘發納米晶粒旋轉和形變誘發納米晶粒之間合併長大的實驗結果**[3]**,為晶界協調變形機制提供了即時有利的證據。

最近發展出的一種新型醫用鈦合金(Ti2448)兼具低彈性模量和高強度等特點,但這類合金所具有的非線彈性形變行為不能簡單地用已有的非線彈性形變機制(如應力誘發馬氏體相變)加以解釋,因此有必要研究其非線彈性本質。本文將透射電子顯微鏡下原位拉伸的實驗方法用於揭示該合金在彈性形變階段的微觀結構變化。為便於和應力誘發可逆馬氏體相變機制進行直接比較,實驗選用了容易誘發馬氏體相變的低合金化的Ti2448合金。動態實驗和觀察發現:薄膜樣品中的應力誘發可逆馬氏體相變只發生在擴展裂紋附近的高應力應變區,因此不能視為主要的非線彈性形變機制;在低外加應力的初期形變階段,晶粒內部普遍產生沿(110)面的具有微小剪切應變的局域晶格扭曲,這些晶格扭曲進而演變成位錯環,兩者均為可逆過程(圖3)**[4]**。具有可逆特徵的位元錯環均勻成核的發現,不僅揭示了新型鈦合金

的非線彈性變形機制，而且豐富了人們對固體形變行為的認識，對運用該機制設計新合金具有重要的參考價值。

致謝：本工作的主要完成者王豔波博士和崔靜萍博士及有關合作者。本工作得到中國科學院“百人計畫”、國家自然科學基金和國家“九七三”專案的資助。

References

1. Wang Y B，Sui M L.　Appl Phys Lett，2009，94:021909.
2. Wang Y B，Wu B，Sui M L.　Appl Phys Lett，2008，93:041906.
3. Wang Y B，Li B Q，Sui M L，Mao S X.　Appl Phys Lett，2008，92:011903.
4. Cui J P，Hao Y L，Li S J，Sui M L，Li D X，Yang Y. Phys Rew Lett，2009，102: 04.

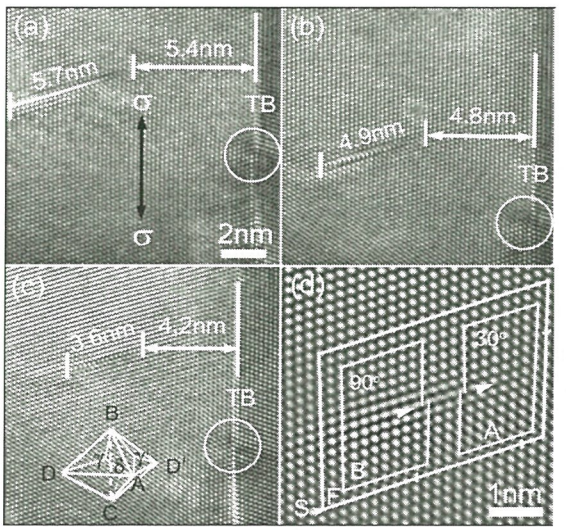

圖 1 a-c：擴展位錯隨著應變增加向孿晶界滑移的系列原位 HRETM 像；d：擴展位錯放大的 HRETM 像（畫出三個 Burgers 回路）。

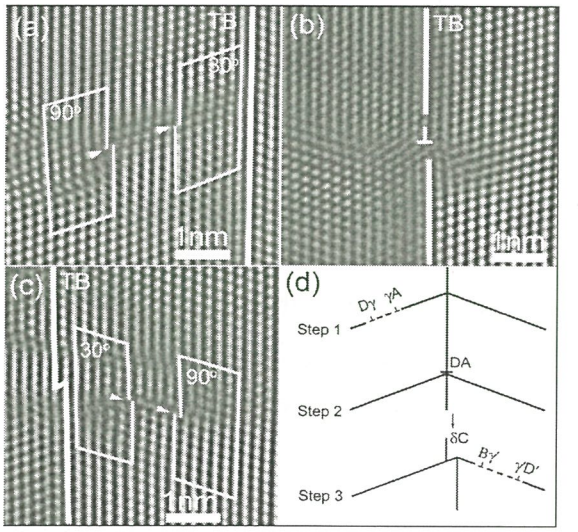

圖 2 a-c：分別為擴展位錯在穿過孿晶界過程中接近、進入和離開孿晶界時的 HRETM 像；　d：為位錯穿過孿晶界的示意圖。

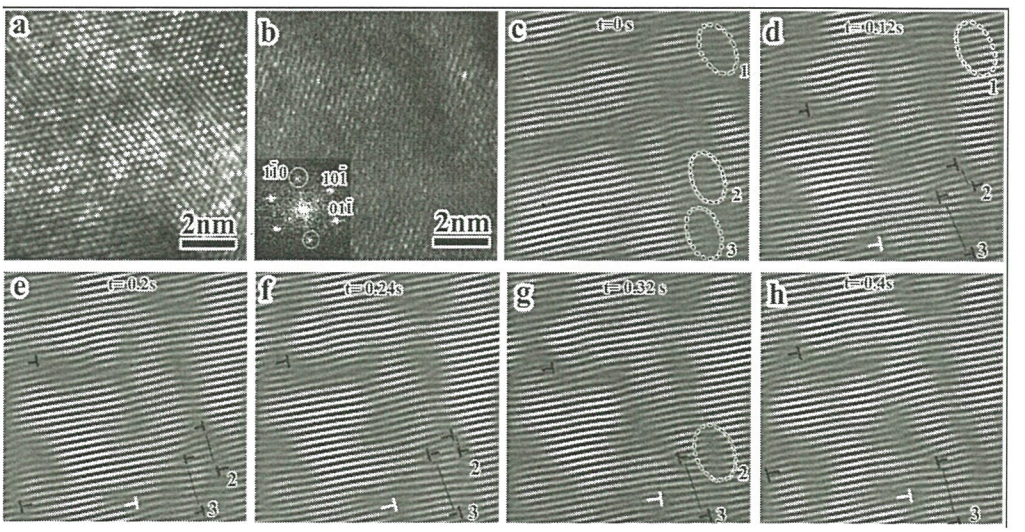

圖 3 低合金化的 Ti2448 合金形變前（a）和彈性形變範圍內載入時（b）的 HRTEM 像。(b) 中左下角插圖為所給區域的傅利葉變換圖。(c) 為 (b) 的一維傅利葉過濾像，從中可見明顯的晶格畸變區域(1, 2, 3)。(d-h)是載入條件下繼(c)之後不同時刻的系列 HRTEM 像的一維傅利葉過濾像，從中可見區域 2 內位元錯偶的產生、擴展運動及逆過程。

Surface and interface properties of ultrathin metal films on Si and Cu substrates

C.S. Chang[a,b](張嘉升), W.B. Su[a], and Tien T. Tsong[a]

[a]*Institute of Physics, Academia Sinica, Nankang, Taipei, Taiwan(中央研究院物理所)*

[b]*Department of Physics, National Taiwan University, Taipei, Taiwan*

When the thickness of a metallic film approaches a few atomic layers, the wavevector of its Fermi electrons along the surface normal becomes discrete due to the boundary confinement. This occurrence can have a profound effect on various nanoscale physical properties. For instance, electronic state densities, surface potential and work function of the film will all be affected. In addition, as the effect of discrete lattice is taken into account, this quantum effect can even induce the structural variations and play a key role in the film growth. Furthermore, the potential variation at the metal/semiconductor interface can mediate a subtle interplay between the screening and confinement effects in the metallic thin film. And at low temperatures the interfacial information can even be convoyed to the surface.

Higher order peaks of Gundlach oscillation in scanning tunneling spectroscopy can be employed to measure the work function difference between a thin film and a metal substrate with very high precision. We use this technique to measure the work functions of a few metal thin films grown on different metal substrate. Referring to the figures below, we demonstrated the cases of Ag/Au(111) and Ag/Cu(111), and the spectra on the right showed a constant energy shift for the higher-order Gundlach oscillation peaks. These measurements show a very high precision comparable to the photoemission measurements. For the Pb films grown on the Cu(111) surface, the results reveal that the work function varies in oscillation with island thickness, which can be attributed to the existence of the quantum well states within the thin film.

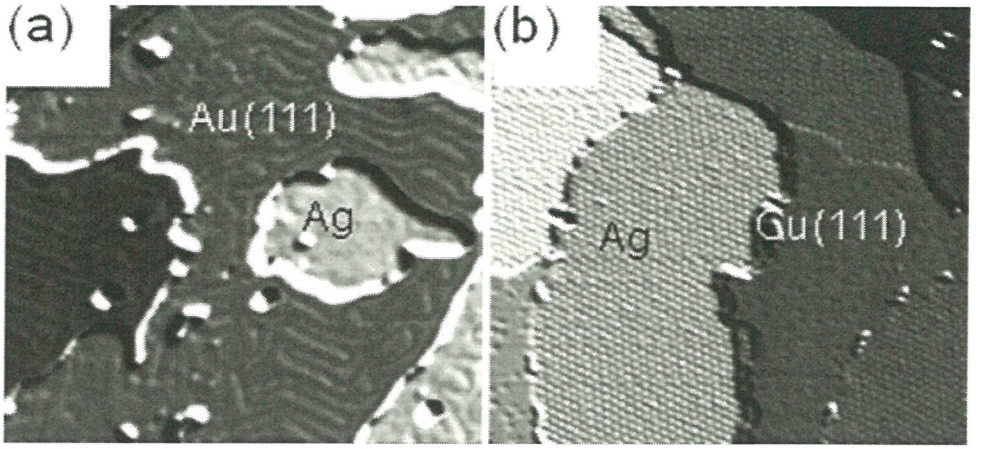

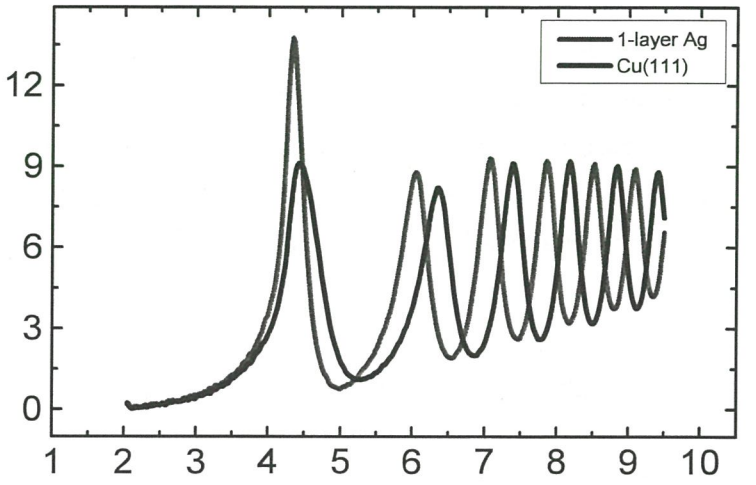

Metallic thin films can also act as narrow potential wells to the incident electrons. Under the configuration of scanning tunneling microscope, when the bias applied to the tip is raised beyond the vacuum level of the sample, emitted electrons will experience transmission resonances, which can be detected in both the dI/dV and dI/dZ spectra. In this presentation, we will review our recent investigations on the individual 2D lead (Pb) and silver (Ag) islands grown on the Si(111), Si(100), and Cu(111) surfaces. Most of the studies were performed concurrently with scanning tunneling microscopy and spectroscopy at low temperature.

Aberration Corrected TEM for materials science ~The atomic revel elemental analysis~

Eiji Okunishi, Isamu Ishikawa, Hidetaka Sawada and Yukihito Kondo

JEOL, Ltd., 1-2 Musashino 3-chome, Akishima, Tokyo 196-8558, Japan.

Recently, the performance of STEMs is greatly improved by the realization of Cs corrector for the probe forming system. The Cs corrector mainly offers two advantages: a small probe size and high current probe density. As to the former advantage, the smallest probe size was measured to be less than 0.1 nm at 200kV with Cs corrector. The small probe size, which serves as a high-resolution capability in imaging, has already been reported by the Pennycook's group **[1, 2]**. As to the latter advantage, the current probe density is about ten times higher than the one in ordinary STEMs. The higher current probe density enables us to analyze with higher sensitivity reaching an atomic level resolution. The present paper reports atomic resolution imaging and elemental analysis by the combination of EELS/EDS and Cs-corrected STEM.

Figure 1 shows a high resolution image of Si[112] taken by high-angle annular dark-field (HAADF) method, using a aberration corrected microscope (JEM-ARM200F) equipped with the STEM Cs corrector. The image shows 0.078nm dumbbell. The image was obtained with a 10pA probe current. Figure 2 shows elemental maps of $SrTiO_3$, by EELS. These images were obtained with a probe current of 150 pA and an acquisition time of 0.03 second per pixel, (total acquisition time being 3.5 minutes). The thickness of the specimen was estimated to be 24 nm by EELS. (A) shows a HAADF image acquired simultaneously with the EELS spectra. The atomic position can be clearly seen. (B) shows the element map by an RGB display. (C), (D) and (E) show strontium, titanium and oxygen maps. Each atom position can be seen definitely.

References

[1] P.D. Nellist et al., *Science* **305**, 1741 (2004)
[2] E. Abe et al., *Nature* **421**, 347 (2003)

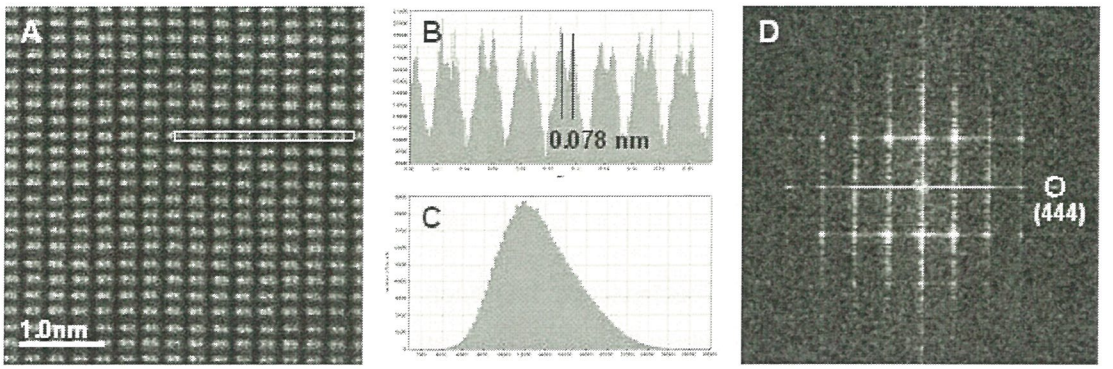

Fig.1 A) High-angle annular dark-field image of Si [112] taken by JEM-200F with STEM Cs Corrector. B) Line profile of the white square area of A (Raw data). C) Histgram of intensity in A, the horizontal and vertical axes being intensity and number of pixels. D) Fourier transform of image A, the lattice spacing of (444) being 0.078nm.

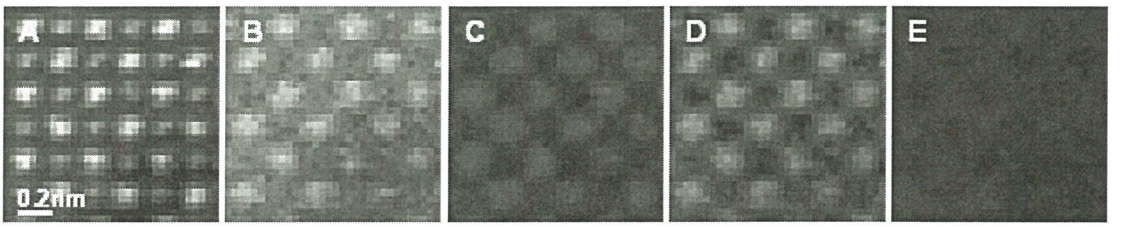

Fig.2 EELS maps of $SrTiO_3$ obtained by JEM-ARM200F with STEM Cs Corrector. A) HAADF image acquired simultaneously with EELS signal. B) EELS map with an RGB display. C) Sr-M map, D) Ti-L map and E) O-K map.These images were taken at a probe current of 150pA with an acquisition time of 0.03 second per pixel, total acquisition time being 3.5min with the use of drift compensation. The images are shoen with 32 x 32 pixels.

Recent developments in EELS analysis

A.Maigné[1]

[1]*Nippon Gatan 3F Sakurai bldg. 2-8-19 Fukagawa, Koto-ku Tokyo 135-0033*

amaigne@gatan.com

Energy Electron Loss Spectroscopy has been proven many times to be the state of the art analysis method for material characterization. TEM and STEM performances have increased drastically with the development of Cs correctors as well as monochromators. To be part of this technological revolution, Gatan has decided has decided to redesign fro, the ground up our spectrometers. For the first time in Asia, we will present the new GIF Quantum™ series which represents Gatan's 4th and most advanced generation of post-column energy filters. The GIF Quantum combines advanced dodecapole-based electron optics with a blazing fast CCD camera system to yield an imaging filter that defines the new state-of-the-art in the capture of both highly detailed EELS and EFTEM data sets with maximum throughput.

With the GIF Quantum, there is no compromise between EFTEM and EELS. It combines 3 state of the art equipment in one: a full frame high-quality CCD camera, a ultra-fast EELS detector for spectrum imaging and a 5th order aberrations corrected post column filter for EFTEM analysis.

Spectrum-Imaging is a powerful approach in data acquisition for materials characterisation whereby a spectrum is recorded at each pixel position in an image to form a '3-D data-cube'. As a technique it is a powerful means for rapid materials characterisation at the nanometre level and is well established, especially in the field of materials science. Rapid increases in computing power, increased ease of use, and the advent of high sensitivity and high throughput detectors have enabled acquisition of higher dimensional data sets within a practical time-scale. Advances in control software and systems integration has allowed simultaneous capture of multiple spectral signals, as well as providing complementary information in spatial correlation to further increase the ability of this powerful tool. With an atomic resolution, combined EELS and HAADF spectrum-imaging is a formidable approach for solving materials science problems. Furthermore , diffraction-imaging allows the measurment of the diffraction pattern during the scanning process and extends STEM-mode data acquisition to another dimension, opening up new possibilities in advanced materials science characterization at the nanoscale.

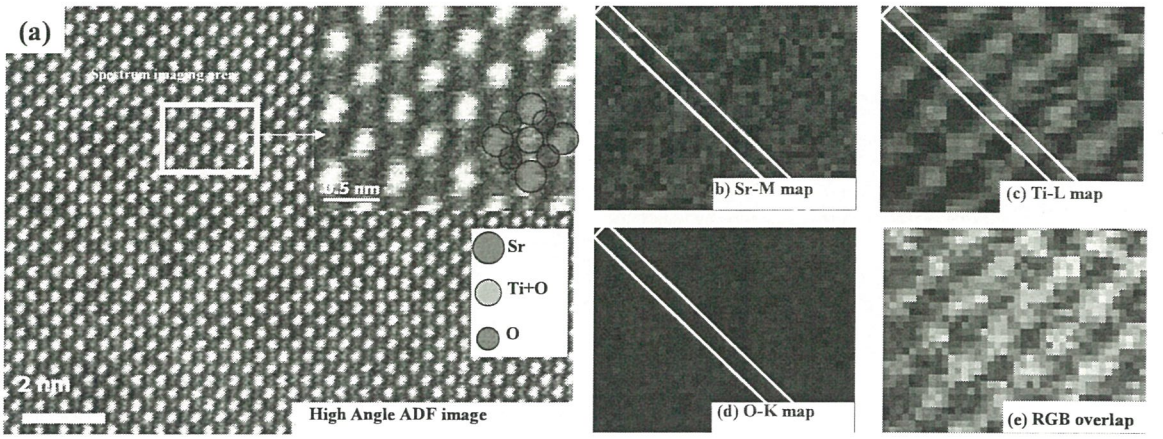

Fig 1. Atomic column by column EELS mapping of $SrTiO_3$ using JEOL 2100F with Cescor and Gatan Tridium. The High angle ADF image shows clearly the $SrTiO_3$ structure. The EELS elemental map of Ti and Sr shows clearly the same pattern

By combining a new high-speed detector (1000 spectra per second) and ultra-fast 1μs shutter and a very large collection angle due to the 5mm entrance aperture (in EELS mode), STEM-SI can be recorded with high resolution with an incredible speed. Real EELS is now achievable via dual-EELS. DualEELS™ allows the operator to acquire two optimized EELS spectra from different energy ranges (typically one core-loss and one low-loss) in rapid succession. By having both the core-loss and the low-loss signal from the identical area of the sample, absolute quantification can be performed. More importantly, DualEELS™ is fully integrated into Gatan's spectrum imaging application creating a new standard in data acquisition and quantification. The new precision offset of up to 2kV and switching times less than 50μs allows hysteresis free energy offsets beyond the Si-K edge enabling accurate core level shifts to be measured for elements across the periodic table.

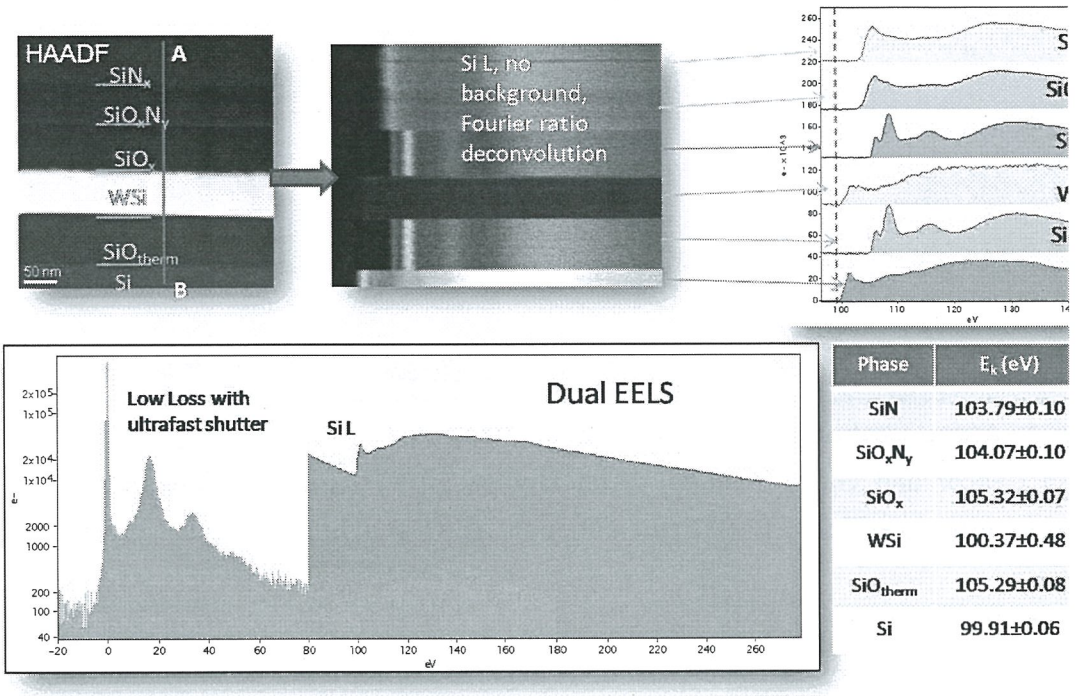

Phase	E_k (eV)
SiN	103.79±0.10
SiO_xN_y	104.07±0.10
SiO_x	105.32±0.07
WSi	100.37±0.48
SiO_{therm}	105.29±0.08
Si	99.91±0.06

FIG 2. Si L edge chemical shift within the different Silicon phase, using Dual EELS and the ultrafast shutter, the low loss and the core loss region can be acquired together and the chemical shift measured extremely accurately, moreover the plural scattering can be remove with ease using Fourier Log deconvolution.

Of course, EFTEM performance are critically improved too with an increased field of view up to 36 μm (with the 9mm entrance aperture), dodecapole based electron-optics with an isochromaticity as low as 1eV at 200keV and 0.75% maximum image distortion and of course, the new dual EELS mode. Moreover, EFTEM measurement can be done easily with the all new advanced AutoFilter suite choosing all the measurement parameters to get the best data with the minimum electron radiation

Direct Atomic Mechanisms of Stress-Induced Unusual Large Strain Plasticity of Semiconductor Nanowires[1]

(應力誘發的半導體納米線超大塑性的直接原子機制)

ZHANG Ze(張 澤)，ZHANG Yue-Fei(張躍飛)，ZHENG Kun(鄭 坤)，YUE Yong-Hai(嶽永海)，HAN Xiao-Dong(韓曉東)

(Institute of Microstructure and Properties of Advanced Materials, Beijing University of Technology，Beijing 100124，P R China) (北京工業大學 固體微結構與性能研究所，北京 100124，中國)

Employing mechanical tests on individual nanowires via a newly developed in-situ atomic-lattice resolution electron microscopy method, we have, for the first time, successfully observed the brittle materials SiC and Si even Si_xO_{1-x}-nanowires (NWs) become highly ductile at room temperature. A crystalline structural evolution corresponding to the occurrence of unusual high ductility of the brittle materials includes the dislocation initiation, dislocation accumulation and the amorphous phase transition, finally the extended nano amorphous ductility processes at the necking region of the one dimensional nanowires. A corresponding deformation mechanism for these one dimensional nanowires under an external tensile force has been proposed based on MD simulations and it agrees well with our experimental results.

Amorphous solid materials as silicate glass or metallic glasses are usually with high hardness but brittleness in nature. The deformation mechanism of amorphous materials has two modes: at high stress and low temperature, the plastic deformation in metallic glass is inhomogeneous: the strain is concentrated in a few thin shear bands, while for silicate glass the plastic deformation is even much smaller before brittle failure. At lower stress and higher temperature, the deformation is homogeneous, which is atomic diffusion process for both types of glasses. The homogeneous flow regime includes liquid flow, which occurs above or near the glassy transition temperature, T_g. Above T_g superplasticity will occur for glasses with the nature of visco-plasticity.

We have reported, for the first time, a new phenomenon of large tensile plasticity of semiconductor nanowire through a phase transition of single crystal to amorphous under an external stress. These unusual mechanical properties of one-dimensional semiconductor nano materials with covalence bonds are fundamental important for understanding the nano-scale fracture and stress-induced band structure variation for high temperature semiconductors.

References

1. Han X D，Zhang Z，Wang Z L. Experimental nanomechanics of one-dimensional nanomaterials by in situ microscopy. Nano，2007，2：249
2. Han X D，Zhang Y F，Zheng K，Zhang X N，Zhang Z，Hao Y J，Guo X Y，Yuan J，Wang Z L. Low-temperature in situ large strain plasticity of ceramic SiC nanowires and its atomic-scale mechanism. Nano Letters，2007，7： 452.

3. Han X D，Zheng K，Zhang Y F，Zhang X N，Zhang Z，Wang Z L. Low-temperature in situ large-strain plasticity of silicon nanowires. Adv Mater，2007，19：2112.
4. Zhang Y F，Han X D，Zheng K，et al. Direct observation of super-plasticity of beta-SiC nanowires at low temperature. Adv Func Mater，2007，17：3435.
5. Han X D，et al. Lattice bending, disordering, and amorphization induced plastic deformation in a SiC nanowire. J Appl Phys，2005，98：124307.

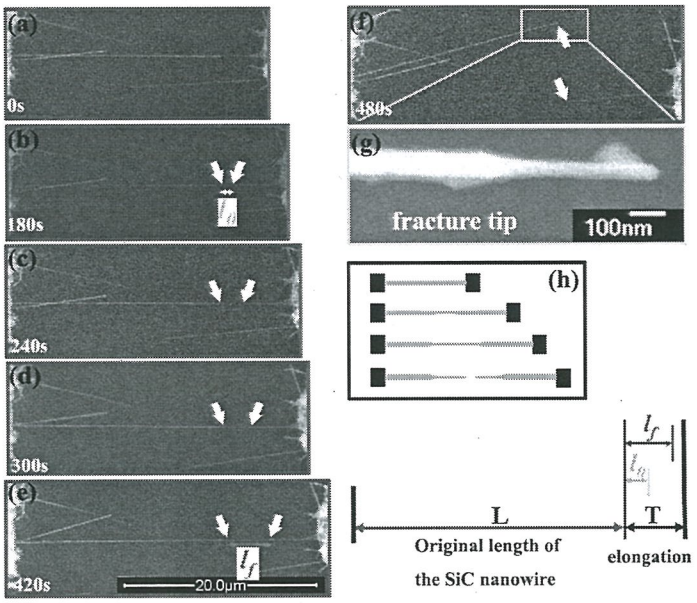

Fig.1 In situ investigation of the superplasticity of SiC NWs at room temperature. (a) – (g) are a series of SEM images when conducting the axial-tensile experiments on an individual SiC NW. (h) is a schematic illustration of the deformation process.

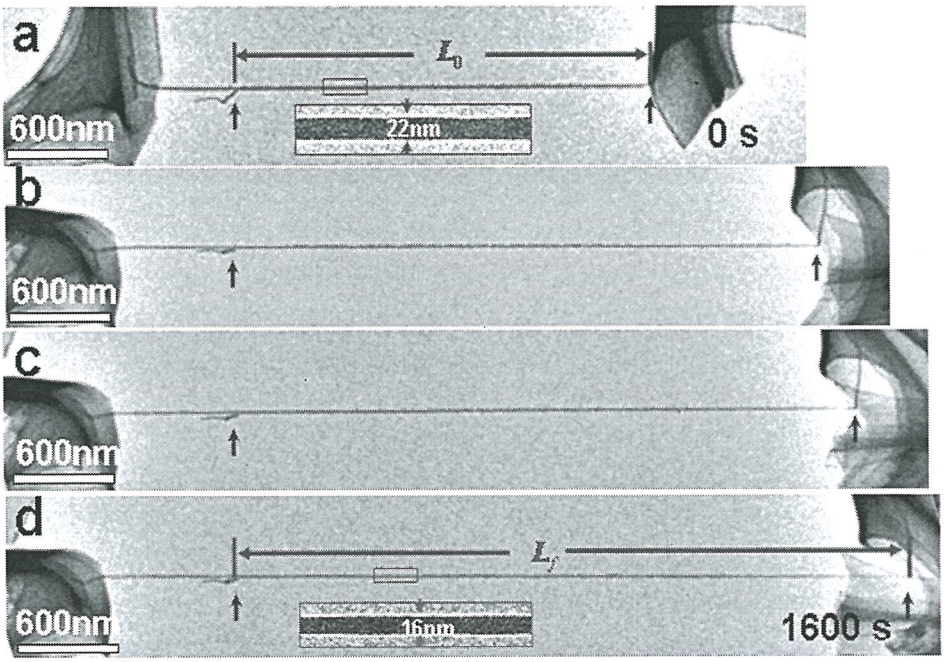

Fig.2 Direct atomic scale *In-situ* study of the silica NW large strain plasticity at room temperature.

Characterization of In-Ga intermixing in InAs/GaAs Quantum Dots by HRTEM and EFTEM

Hung-Chin Chung[a], Yi-Feng Lai[a], Chuan-Pu Liu(劉全樸)*[a], Yen-Lin Lai[a], Yu-Ching Fang[b], and Li Hsu[b]

[a] *Department of Materials Science and Engineering and Center for Micro/nano Science and Technology, National Cheng Kung University(成功大學材料科學與工程學系), Tainan, Taiwan, Republic of China*

[b] *Materials & Electro-Optics Research Division, Chung-Shan Institute of Science & Technology, Tao-Yuan, Taiwan, Republic of China*

Semiconductor quantum dots (QDs) have important potential applications in optoelectronic and transport devices.**[1]** Among the QD families, InAs QDs have received the most attention because of their specific applications in lasers,**[2]** optical memories,**[3]** and infrared photodetectors.**[4]** For implementation in devices, both the formation and capping processes are crucial for the structural and optoelectronic properties of QDs, however, dot morphology and composition tend to be modified in post-growth process through interdiffusion and has not completely understood yet**[4.5]**. Therefore, we attempt to investigates shape and composition profiles of both buried and surface InAs/GaAs quantum dots (QDs) by combining three-window and spectrum imaging (SI) methods with energy-filter transmission electron microscopy (EFTEM) and high-resolution (HRTEM). Both of the surface and capped QDs were grown by molecular beam epitaxy via S-K growth mode.

Fig.1. shows a plan-view 220 dark-field TEM image of the surface InAs QDs. Coherently strained QDs are clearly observed. The typical lateral sizes of the uncapped InAs QDs are 17±2nm. Fig. 1(b) shows a cross-sectional 400 dark-field TEM image. In this image, both surface and buried QDs are apparent, as labeled. It also shows that the typical height is about 8 nm. In comparison to the surface QDs, the buried QDs typically have similar widths and densities, but their heights are reduced by the capped GaAs. For the surface dots, an off-zone bright-field image is shown in Fig. 2(a) and the indium elemental map from EFTEM SI is shown in Fig. 2(b), where the degree of brightness should be proportional to the indium content. Fig. 2(b) reveals that the contrast within the dot is constant with an abrupt interface, implying that the dot had the same In concentration and no obvious indium inter-diffusion. For the buried dots, an off-zone bright-field image is shown in Fig. 2(c), and the In elemental map is shown in Fig. 2(d). These demonstrate that these dots are characterized by inhomogeneous indium compositions with indium-rich centers in the form of truncated cones. Detailed analysis of the [In] in the vicinity of the surface and buried QDs is shown in Figs. 2(e)-2(f). The gray shaded area in Fig. 2(e) represents the In concentration variation in a typical buried dot in Fig. 2(d). The dot is found to have an indium-rich content at its base with a thickness of 3.7±0.1 nm. Furthermore, the vertical height of the dot that still shows In signals is estimated to be 10 nm, which was longer than the average buried dot height of 5 nm. The added

height suggests the presence of In-Ga intermixing above the QD. On the other hand, the In concentration variation in the lateral direction is shown in Fig. 2(f) for the base regions of the dot. The lateral dimension of each dot appears approximately the same, as it is affected less by the capping process than by the growth direction. Moreover, asymmetric photoluminescence is observed from the buried InAs QDs, which is attributed to the confinement effect of the pure InAs QDs for the main emission and the strain-driven In/Ga intermixing between the QDs and the matrix layer for the side peak. The significant blue-shift in the main emission coincides with a calculation by taking the dot height from the indium map. These results prove that the photoluminescence of the buried InAs dots is the result of In/Ga intermixing during post-growth.

References

1. K. Eberl, Phys. World. 10, 47 (1997)
2. S.-W. Lee, K. Hirakawa, and Y. Shimada, Appl. Phys. Lett., 75, 1428 (1999).
3. A. Barabasi, Appl. Phys. Lett., 70, 2565 (1997).
4. H. Y. Liu et al, J. Appl. Phys., 98, 083516(2005)
5. H. S. Lee et al., J. Appl. Phys., 91, 5195 (2002)

Acknowledgement

The work was supported by Research Grant No. NSC 95-2221-E-006-080-MY3, National Science Council of Taiwan.

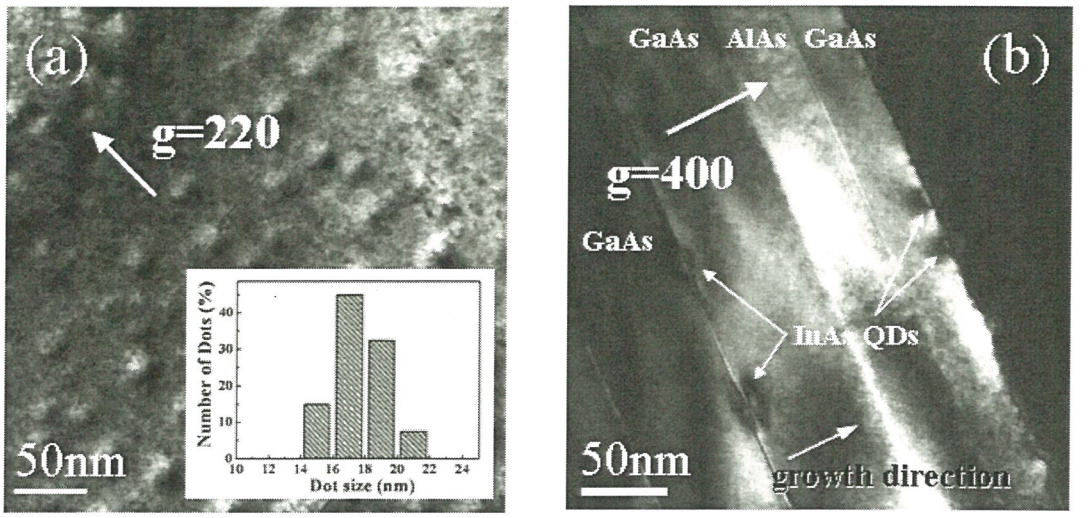

Fig. 1 TEM images of the 1.75 ML InAs/GaAs QDs for (a) plan-view dark-field (g=220) and (b) cross-sectional dark-field (g=400).

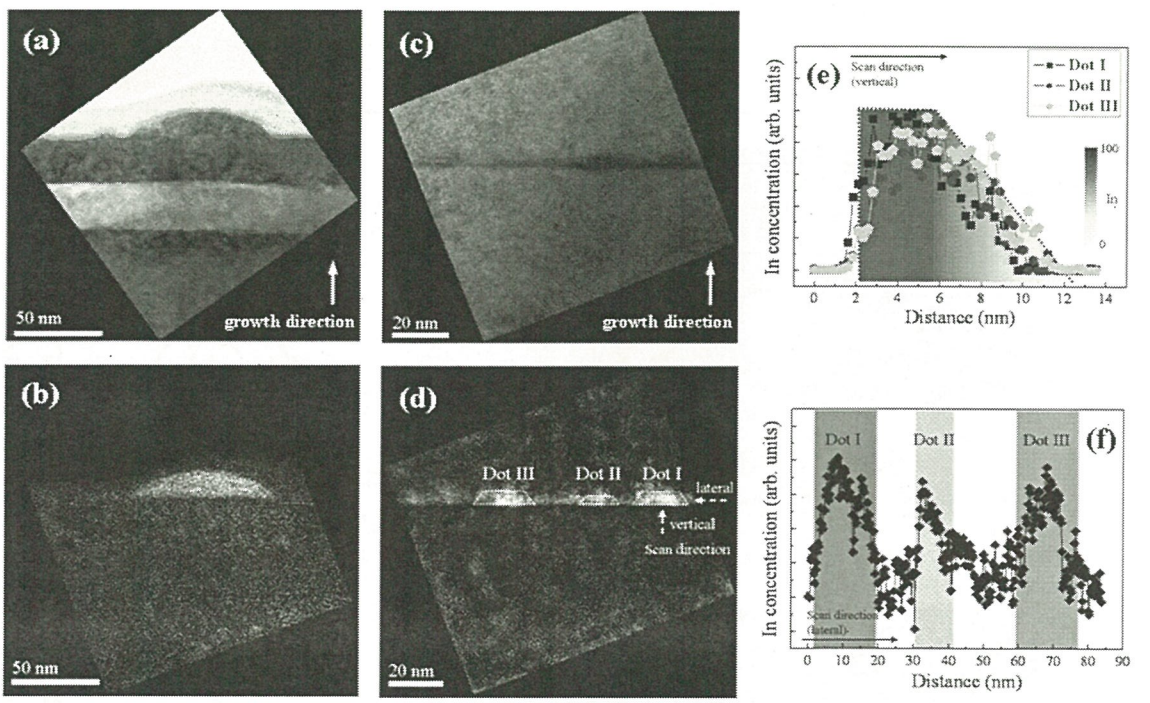

Fig. 2 EFTEM elemental maps from the SI technique, (a) zero-loss image and (b) indium map of a surface-dot; (c) zero-loss image and (d) indium map of a buried-dot. Images are calculated using the In M-edge at 443 eV threshold energy, where the indium concentration profiles along the (e) growth and (f) lateral direction of the dots, as a function of position across the dots I-III, are projected directly. As indicated in (d), the gray shaded areas in (e) mark the indium concentration variations from the InAs dots to the GaAs cap layer.

Electronic and Mechanical Coupling in Bent ZnO Nanowires
(單體納米材料的力電耦合性質的掃描電鏡原位研究)

YU Da-Peng (俞大鵬), HAN Xiao-Bing (韓曉冰), XU Jun (徐軍), CHEN Li (陳莉), ZHU Xin-Li (朱新利)

Department of Physics, Peking University，Beijing 100871，P R China(北京大學 物理學院 電子顯微鏡實驗室，北京 100871，中國)

材料的許多物理性質是相互關聯的，只是在塊體下難以顯示出來。本文系統在掃描電子顯微鏡中利用陰極研究了單根 ZnO 納米線在彎曲應力作用下的力電耦合效應。研究發現，在彎曲應力作用下， 納米線的近邊 UV 發光峰會發生明顯的紅移，在室溫下最大可達 50meV，如圖所示。利用第一性原理方法從理論上對上述現象進行了解釋，認為是由於應力作用，量子化的導帶子能級發生展寬所致。

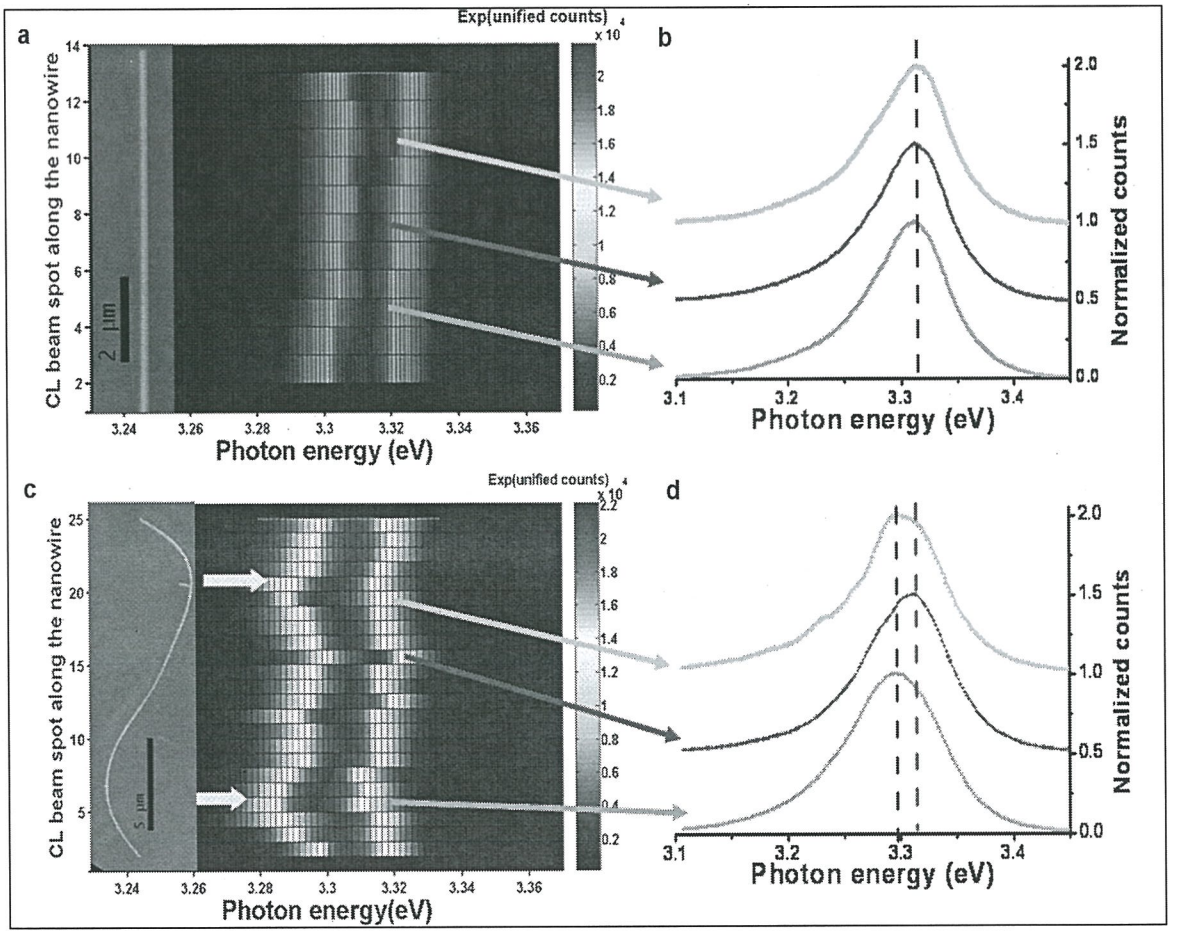

圖　單根 ZnO 納米線的 UV 發光譜對應力的依賴關係：(a) 無應力狀態下直的納米線的陰極螢光譜沒有變化；(b) 彎曲應力下彎曲納米線的陰極螢光譜發生顯著的紅移。

TEM study of the structure and phase behavior of gold nanocondensates: Effects of laser ablation parameters and carbon catalysis

Chang-Ning Huang,[1] Shuei-Yuan Chen,[2] Yuyuan Zheng[1] and Pouyan Shen(沈博彥)[1]

[1] *Department of Materials and Optoelectronic Science, Center for Nanoscience and Nanotechnology, National Sun Yat-sen University(國立中山大學) Kaohsiung, Taiwan, R.O.C.*

[2] *Department of Mechanical and Automation Engineering, Shou University Kaohsiung, Taiwan, R.O.C.*

The small Au clusters fabricated by a vacuum-evaporation process typically form multiply twinned particles (MTP) with pentagonal arrangement of decahedral (Dh, 10-faced) and icosahedron (Ih, 20-faced) types **[1, 2]**. The Ih and Dh particles 3-14 nm in size, via such a vapor condensation route with purified helium gas, are unable to transform to fcc even near the bulk melting point (1337 K) due to a high activation energy **[3]**. Here, Au nanocondensates in the form of amorphous clusters, MTPs, and fcc with progressive larger particle size, as characterized by transmission electron microscopy (TEM, FEI Tecnai G2 F20 at 200 kV), were fabricated by pulsed laser ablation on Au in vacuum with or without argon gas flow at 1.5×10^{8} vs. 1.4×10^{12} Watt/cm^2 power density for a rapid heating/cooling effect.

Our observed critical size ca. 2 nm for the amorphous to MTP transformation of the Au condensates thus prepared **[4]** implies a minimum {111} surface area of ca. 4 nm^2 for MTP. Coarsening and {111}-specific coalescence of the MTPs and fcc to form defects were also found to be competitive under the influence of laser parameters and Ar gas flow **[4]**. The size and phase changes of the Au nanocondensates were further observed to be sensitive to electron irradiation. Electron dosage in fact activates {hkl}-specific coalescence of the impinged nanoparticles to form MTP and even fcc structure under the influence of graphite-like catalysis. Such in-situ TEM observations (Fig. 1) indicated that the MTP→ fcc transformation occurred for a surprising small particle size of 5 nm due to the catalytic effect of graphite-like materials (G) with varied extent of rolling following the habit plane $(0001)_G/(111)_{fcc}$, i.e. via a partial epitaxial relationship. The ultimate relationship would be $(2\bar{1}\bar{1}0)_G//(2\bar{1}\bar{1})_{fcc}$; $[0\bar{1}10]_G//[0\bar{1}1]_{fcc}$ for a minimum misfit strain with perfectly crystallized graphite according to theoretical calculation using the CASTEP module in Materials Studio software.

Acknowledgment. Supported by Center for Nanoscience and Nanotechnology at NSYSU and partly by National Science Council, Taiwan, ROC.

References

1. S. Iijima, T. Ichihashi, Phys. Rev. Let. 56 (1986) 616.
2. P.A. Buffat, M. Flüeli, R. Spycher, P. Stadelmann, J.P. Borel, Faraday Discuss. 92 (1991) 173.
3. K. Koga, T. Ikeshoji, K. Sugawara, Phys. Rev. Lett. 92 (2004) 115507.
4. C.N. Huang, S.Y. Chen, Y. Zheng and P. Shen, J. Phy. Chem. C 112 (2008) 14965.

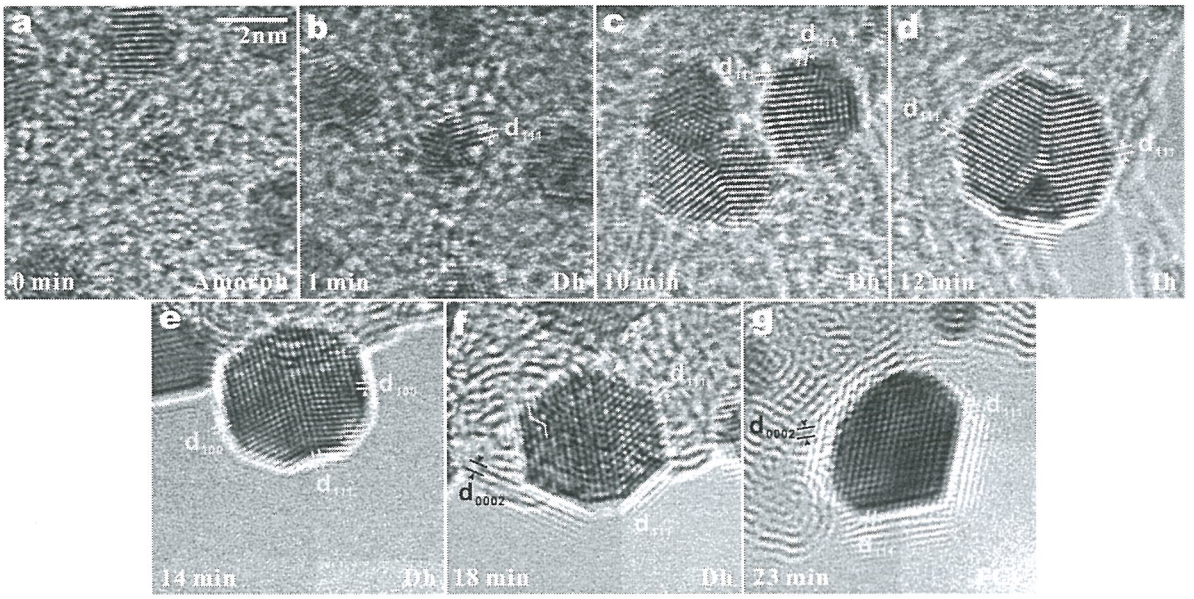

Figure 1. Lattice images showing the phase behavior of the Au nanocondensates during electron irradiation for a specified time: (a) as-deposited amorphous nanoparticles (i.e. time setting t = 0), (b) turned into faceted Dh and approaching each other at t = 1 min, (c) Dh nanoparticles underwent (111)-specific coalescence upon impingement at t = 10 min, (d) transforming into larger sized Ih at t = 12 min, (e) back transformed into Dh at t = 14 min, (f) graphite basal layers were developed epitaxially on the (111) facets of Dh at t = 18 min, (g) further transformed into fcc by partial epitaxial nucleation on graphite-like basal layers with varied extent of rolling at t = 23 min. The d spacings of (111) in Dh/Ih/fcc and/or (0002) of graphite-like flakes are denoted in b to g.

The Newly Developed Method using High Resolution TEM to Quantify The Structural Integrity of Nuclear Grade Graphite in Very High Temperature Gas Cooled Reactor (VHTGR) Core Environments

Ji-Jung Kai(開執中), Shuo-cheng Tsai(蔡碩承) and Yi-Tsang Hsieh

Department of Engineering and System Science National Tsing Hua University(清華大學工程與系統科學系), Hsinchu

With the increase of importance of nuclear energy, the newly designed generation IV reactor (G-IV) has incorporated hydrogen production into the reactor design. The most promising type of G-IV reactor for both electricity and hydrogen production is the very high temperature gas-cooled reactor (VHTGR). In this type reactor design, nuclear grade graphite is the major core internal structural material serving as reflector and moderator to maximize the neutron economy. Due to the high temperature and high neutron flux in the reactor core, graphite will face very serious challenge in terms of structural integrity, especially, the irradiation creep and Wigner energy stored in the damaged matrix.

Graphite will store Wigner energy inside the crystalline lattice and cause the expansion of c-axis and shrinkage of a-axis and b-axis during irradiation. The amount of irradiation creep can become a critical factor to limit the lifetime of graphite used in the in-core structure. Also the crystalline lattice of damaged graphite may release enormous amount of defect energy when the temperature reaches the critical annealing temperature which may cause serious problem in reactor safety during abnormal accident conditions.

We have developed a new method to quantify the radiation damage effect on the microstructural evolutions of graphite by using the High Resolution Transmission Electron Microscopy (HRTEM) images. By this method, we can define the degree of expansion and distortion of the c-axis which indicates the amount of irradiation creep and the stored energy in the lattice. Compare our results with the previous published graphite experimental data from other groups, we will be able to quantify the effect of irradiation on the lifetime of graphite in the VHTGR core environments.

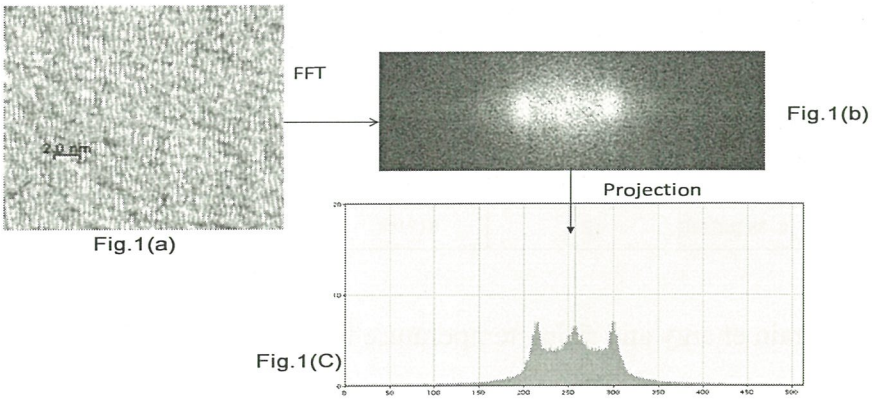

Fig.1(a) HRTEM images of irradiation graphite (10dpa)
1(b) Fast Fourier Transform of HRTEM image
1(c) The projection of FFT intensity

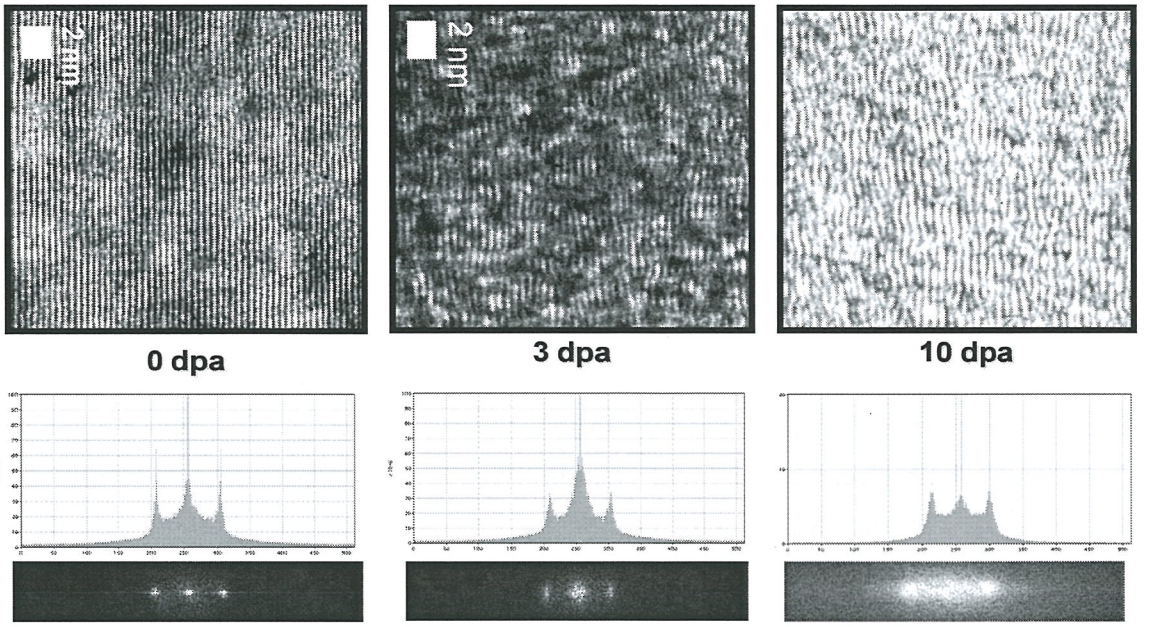

Fig.2 HRTEM images from the region of different doses

				only c- axis		a+c axis	
	dose(dpa)	d spacing(nm)	strain of c spacing(%)	strain energy(cal/g)	rising temperature(℃)	strain energy(cal/g)	rising temperature(℃)
500	0.6	0.344±0.002	2.4	40±4	105±11	81±9	215±22
	3	0.355±0.002	5.7	222±24	536±55	518±52	1368±128
	5	0.361±0.003	7.6	279±20	735±54	847±59	2087±146
	10	0.381±0.007	13.5	791±47	2087±123	2681±158	7073±417
600	0.6	0.358±0.002	6.7	108±11	264±27	397±38	1008±93
	3	0.362±0.002	7.7	289±28	670±66	793±83	2014±223
	5					±	±
	10					±	±
700	0.6	0.357±0.002	6.3	83±8	199±20	316±33	777±79
	3	0.359±0.002	7	209±19	483±47	584±59	1434±145
	5	0.365±0.003	8.6	249±21	612±53	845±73	2076±176
	7	0.371±0.004	10.7	421±45	1035±111	1315±141	3232±346
	10	0.389±0.01	16.1	691± 76	1697± 187	2828±311	6947±764
	40					±	±
800	0.6	0.355±0.002	5.8	63±8	160±18	263±30	630±65
	3	0.357±0.003	6.3	160±18	366±39	447±42	1069±96
	5						
	10	0.382±0.006	13.6	617±94	1475±226	2125±330	5166±790

Table.1 The strain energy and rising temperature for different temperature and dose.

Microstructure and Hydrogen Storage Properties of $MmNi_{3.5}(CoAlMn)_{1.5}$/Mg Multi-layers for Hydrogen Storage
(MmM_5/Mg 複合薄膜的顯微結構和儲氫性能的關係)

OUYANG Liu-Zhang (歐陽柳章), YE Su-Yun (葉素雲), ZHU Min * (朱敏)*

College of Mechanical Engineering, South China University of Technology, Guangzhou, 510641, P R China
(華南理工大學 材料科學與工程學院，廣東 廣州 510641，中國)

Mg 的理論儲氫量高達 7.6%，但普通 Mg 基合金的吸氫動力學性能差，吸氫需在約 300℃－400℃、30 個大氣壓的條件下才能進行。如何改善其動力學是十分重要的問題。Zalaski 等[1]用高能球磨製備出不同晶粒尺寸的鎂，發現隨晶粒尺寸細化到 50 nm，鎂的吸氫速率明顯加快。晶粒越細，吸/放氫動力學性能改善的效果越顯著。有研究者[2，3]發現機械合金化製備的 Mg 基納米複合儲氫合金中存在自催化效應和脫氫協同機制,大大降低了 Mg 的吸/放氫溫度，這與納米複合體系內高密度的相界有關。因此，需要進一步研究納米晶晶界對儲氫材料性能的影響。多層膜的一個重要特點就是存在高密度的介面(包括晶界和相界)，同時薄膜中的介面密度和相可以通過工藝進行有效調製。因此用多層膜可以用來揭示微觀結構特別是介面對儲氫性能的影響。近年來，本課題組對不同儲氫材料構成的多層膜結構對 Mg 的儲氫性能的影響進行了初步的研究[4~6]，並計算了納米晶 Mg 基儲氫合金的介面能[7][i]，指出納米結構儲氫合金中高的介面能是其儲氫特性變化的重要原因。本文綜述了本課題組用磁控濺射工藝製備的 Mg/MmM_5 多層膜的微觀結構和儲氫性能之間的關係。

本文用 X-射線衍射（XRD）方法研究了磁控濺射製備的 $MmNi_{3.5}(CoAlMn)_{1.5}$/Mg（簡寫為 Mg/MmM_5)複合薄膜吸/放氫前後的結構變化和儲氫性能之間的關係。XRD 表明 Mg/MmM_5 多層膜中 Mg 層的儲氫性能有一定程度的改善，吸/放氫溫度分別為 473K 和 523K。用透射電鏡（TEM）研究了 Mg/MmM_5 多層薄膜的微觀結構。Mg/MmM_5 多層膜中 Mg 層和 MmM_5 層的結構與襯底的性質有密切關係。Mg 層由納米晶和沿垂直於襯底表面的[001]方向生長的柱狀晶組成；MmM_5 層則由納米晶和非晶組成。Mg/MmM_5 多層膜在吸氫過程中表現為(103)面平行於襯底生長的柱狀晶先吸氫，然後是(001)面生長的柱狀晶再吸氫。

圖 1 是 5 層的 Mg/MmM_5 多層膜的橫截面 TEM 像。在 TEM 像中，亮襯度區域是厚度約 2μm 的 Mg 層，而深色襯度區域是厚度約 400 nmMmM_5 層。整個多層膜的厚度約為 4.2 μm。由圖可以看到 Mg 層和 MmM_5 層之間的介面較平直整齊，未發現其他合金相，說明不同膜層材料之間沒有發生固態反應，故磁控濺射法製備的 Mg/MmM_5 多層膜的結構不同於蒸鍍法製備的 Mg/$MmNi_x$ 薄膜[8]，也不同於機械合金化製備的 Mg-MmM_5 複合合金[9]。

圖 2a, b 分別是沉積在 Mg/MmM_5 多層膜中 MmM_5 層上的 Mg 膜層的明、暗場像，可以看出 Mg 層的結構由兩部分組成。在靠近 MmM_5 層一側，Mg 層具有納米晶結構；在納米晶 Mg 區域上繼續沉積的 Mg 層則具有柱狀晶結構，柱狀晶的寬度約為 100 nm，長度約為分別對應著各自鎂層的厚度，其長軸方向基本與襯底表面垂直。對圖 2 中的 Mg 晶粒進行微區衍射分析，即：將每個晶粒的[110]晶向傾轉到與電子束平行，然後記錄下雙傾台的傾轉位置 X, Y，根據公式 $\cos\theta=\cos(X_2-X_1)\cdot\cos(Y_2-Y_1)$ 就可以計算出各個 Mg 柱狀晶的[110]晶向之間的取向差 θ。通過計算，Mg 柱狀晶之間的最大取向差約為 9°，這說明不同 Mg 柱狀晶之間的取向差很

小, Mg 柱狀晶之間互成小角度排列。

圖 3 是 5 層 Mg/MmM_5 多層膜氫化後的 XRD 圖。與未氫化前多層膜的 XRD 圖相比，Mg/MmM_5 多層膜在 473K 氫化後的 XRD 圖(圖 3a)中出現了強度很弱的 MgH_2 的衍射峰，Mg 的(103)衍射峰消失，而（001）強度仍然很高，說明 Mg 在此氫化條件下不同的晶粒取向具有不同的氫化能力。當氫化溫度升高到 523K，氫化後的 XRD 圖如圖 3b 所示，儘管 Mg 的（001）衍射峰仍然存在，但 MgH_2 的衍射峰的強度提高，表明 Mg 的氫化程度有所增加。圖 3c 是多層膜在 523K 氫化後並在相同溫度和氫壓(~10^{-1} Pa)條件下脫氫後的 XRD 圖。可以看到 MgH_2 的衍射峰完全消失，只剩餘 Mg 的衍射峰，說明 MgH_2 已完全分解。Mg/MmM_5 多層膜吸氫後微觀結構的改變主要是由於 Mg/MmM_5 多層膜經過吸放氫迴圈後，薄膜在脫氫過程中原有的柱狀晶結構被破壞，吸/放氫的相變過程導致了 Mg/MmM_5 多層膜中 Mg 相改變為 MgH_2 相。Mg 的儲氫性能改善與多層膜中易氫化的 MmM_5 插層有關，插層起到了離解和輸送氫的作用，促進了 Mg 氫化反應的進行。

References

1. Zaluska A, Zaluski L and Ström–Olsen J. O. Nanocrystalline magnesium for hydrogen storage . Alloys Comp, 1999，288：217.
2. Zhu M, Gao Y, Che X Z, Yang Y Q, Chung C Y. Hydriding kinetics of nano-phase composite hydrogen storage alloys prepared by mechanical alloying of Mg and $MmNi_{5-x}(CoAlMn)_x$. Alloys and Comp, 2002, 330-332: 708-713.
3. Fujii H, Orimo S, Ikeda K. Cooperative hydriding properties in a nanostructured Mg_2Ni–H system. Alloys and Comp, 1997, 253-254: 80-83.
4. Wang H, Ouyang L Z, Peng C H, Zeng M Q, Chung C Y, Zhu M. MmM_5/Mg multi-layer hydrogen storage thin films prepared by dc magnetron sputtering . Alloys and Compounds, 2004, 370: L4-L6.
5. Ouyang L Z, Wang H，Zhu M, Zou J, Chung C Y. Microstructure of MmM_5/Mg multi-layer hydrogen storage films prepared by magnetron sputtering. Microscopy Research And Technique，2004，64：323.
6. Ouyang L Z, Wang H，Zhu M, Zou J, Chung C Y. Alloys and Comp，accepted.
7. Ouyang L Z, Ye S Y, Dong H W, Zhu M. Effect of interfacial free energy on hydriding reaction of Mg–Ni thin films. Appl Phys Lett，2007，90：021917.
8. Wang H, Ouyang L Z, Zeng M Q, Zhu M. Hydrogen sorption properties of Mg/Mm–Ni multi-layer film prepared by thermal evaporation . Alloys and Comp, 2004，375：313-317.
9. Zhu M, Zhu W H, Chung C Y, Che X Z, Li Z X. Microstructure and hydrogen absorption properties of nano-phase composite prepared by mechanical alloying of $MmNi_{5-x}(CoAlMn)_x$ and Mg . Alloys and Comp, 1999, 293-295：531-535.

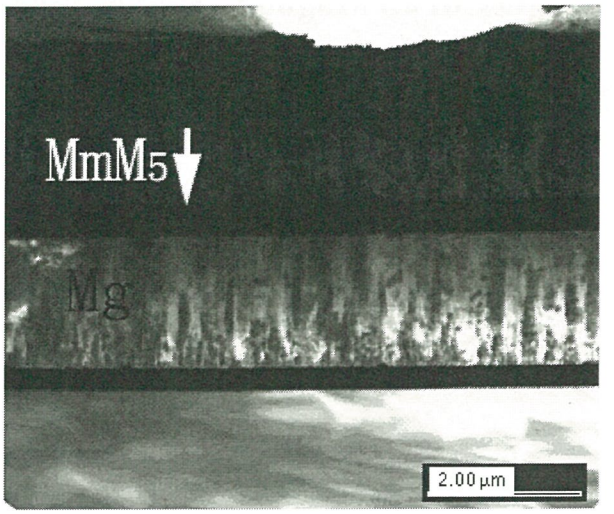

圖1 :5層的Mg/MmM_5多層膜的截面TEM像。

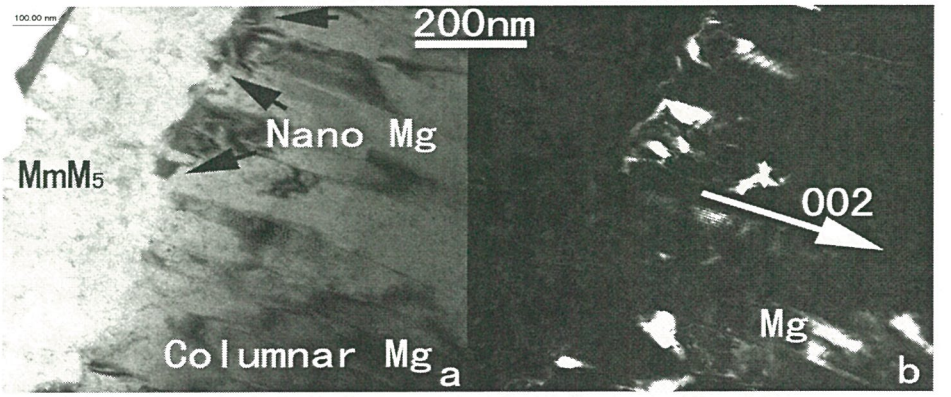

圖2 :a, b分別為沉積在MmM_5層上的Mg膜層的明、暗場像。

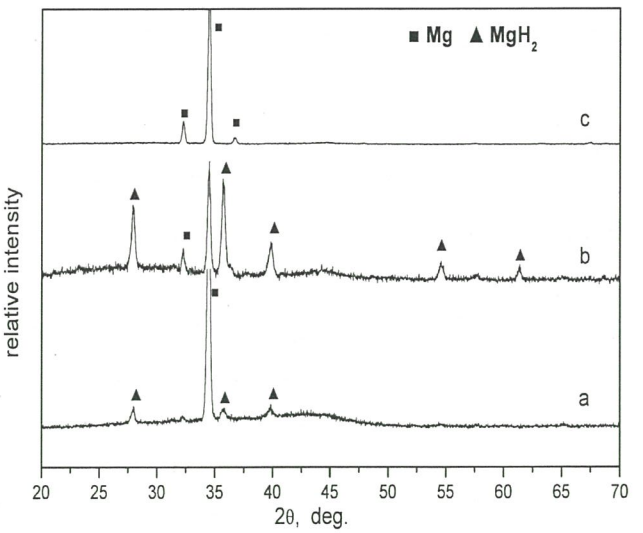

圖3: Mg/MmM_5多層膜吸/放氫後XRD圖。a：在473K氫化；b：在523K氫化；c：在523K脫氫。

Investigations of CoFeB/MgO/CoFeB Magnetic Tunnel Junctions by TEM and Electron Holography
(CoFeB/MgO/CoFeB 磁隧道結的透射電鏡和電子全息研究)

TIAN Huan-Fang (田煥芳), YANG Huai-Xin (楊槐馨), MA Chao (馬超), LI Ying (李瑩), LI Jian-Qi* (李建奇)

Institute of Physics Chinese academy of Science, Beijing 100190, P R China
(中國科學院物理研究所，北京凝聚態國家實驗室，北京 100190，中國)

以 MgO 為基的磁性隧道結具有巨大的室溫磁電阻效應，在磁隨機記憶體和感測器中表現出很好的應用前景[1，2]。 實驗分析發現，退火效應在提高隧道結的磁電阻比中發揮了重要作用，退火後室溫磁阻效應可達 604%[3]。 微結構觀測表明，退火可使隧道結和鐵磁電極的介面粗糙度降低，減少介面缺陷，從而可以提高磁電阻。本文主要利用高分辨電子顯微術研究了原位生長和退火後的磁隧道結微結構特性，利用電子全息方法研究了鐵磁電極/非晶氧化勢壘層之間的勢場分佈差異，進而分析了介面微結構對磁電阻的影響。

隧道結多層膜結構為 Ta(30 nm) /$Co_{50}Fe_{50}$(3 nm) /IrMn(15 nm) /$Co_{50}Fe_{50}$(2 nm) /Ru(0.8 nm) /$Co_{50}Fe_{50}B_{20}$(3 nm) /MgO(1.2 nm)/ $Co_{40}Fe_{40}B_{20}$(3 nm) /Ta(10 nm) /Ru(5 nm)。圖 1 a 和 1b 分別是製備態和退火後截面樣品的 HRTEM 像。從圖中可以看出，在製備態樣品中，CoFeB 頂底電極主要為無定形結構，偶爾出現一些小晶粒， CoFe 層為多晶結構，MgO 勢壘層也沒有明顯的結晶現象，CoFeB 和 MgO 之間的介面比較粗糙。但在經過 380°C 退火後，樣品介面變的比較光滑，頂部 CoFeB 層、CoFe 保護層和 CoFeB 底電極都發生了明顯的晶化現象。這一晶化現象可以提高 CoFeB 層和 IrMn 層之間的磁相互作用，起到很好的釘軋作用。實驗結果表明，退火處理明顯地影響了 CoFeB/MgO/CoFeB 勢壘層的介面和 CoFeB 電極的性質，樣品具有很高的 TMR 值。

圖 2a 和 2c 為 CoFeB/MgO/CoFeB 隧道結製備態(a)和退火後(c)的相位變化圖，圖中黑色條帶為 MgO 勢壘層。沿垂直勢壘層的方向作一個一定寬度的線掃描（寬度約為 50 Pixel）可得到相位的分佈曲線（圖 2 b 和 2d)。圖 2 b 相位變化曲線顯示 MgO 層兩側的 CoFeB 電極相對於 MgO 勢壘層是不對稱的，而且 CoFeB 和 MgO 之間的介面不明銳，勢壘層的寬度約為 4nm。從圖 2 d 中可以看出，相對於製備態樣品，退火後的相位變化更均勻，除了 MgO 勢壘層，Ru 的保護層的相位變化更明顯了； CoFeB 電極的對稱性相對於 MgO 勢壘層明顯提高，而且有兩個 CoFeB 層的平臺。這一結果說明退火後 CoFeB 和 MgO 勢壘層之間存在清晰的介面。這一變化和 CoFeB 的晶化有關。這和 HRTEM 像結果基本一致。

References

1. Parkin S S P，et al. Nat Mater，2004，3：862.
2. Yuasa S，et al. Nat Mater，2004，3：868.
3. Ikeda S，et al. Appl Phys Lett，2008，93：082508.

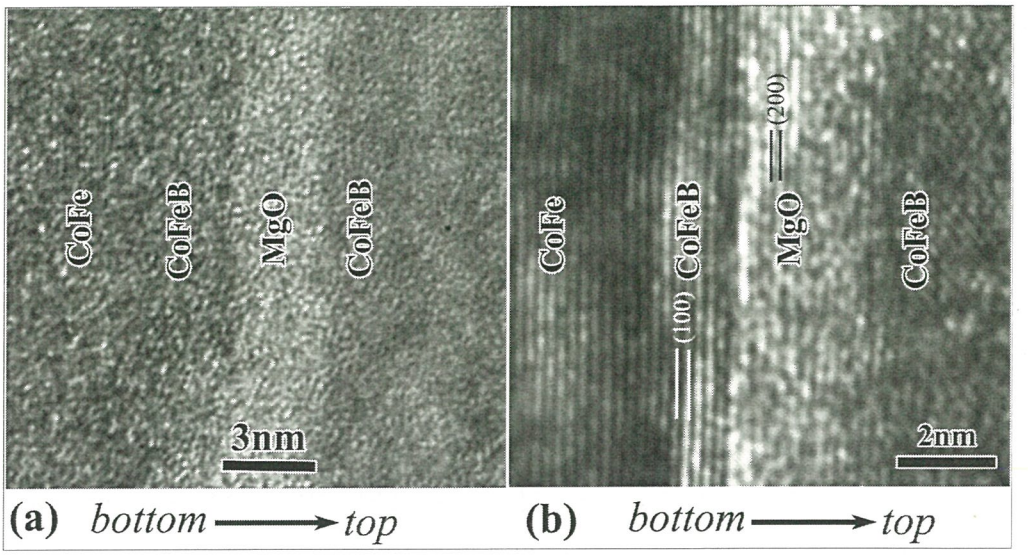

圖 1 CoFeB/MgO/CoFeB 磁隧道結的 HRTEM 像。a：製備態樣品；b：退火後樣品。

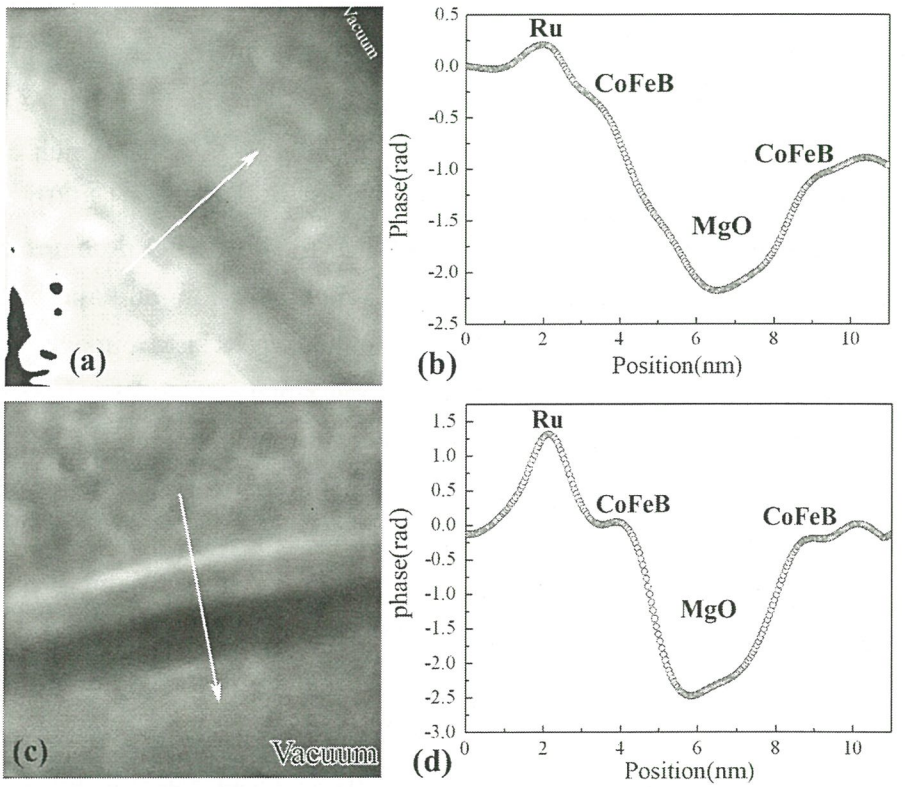

圖 2 CoFeB/MgO/CoFeB 隧道結的電子全息相點陣圖和穿過勢壘層的相位變化曲線。(a)和(b)為製備態樣品，(c)和(d)為退火後樣品。

TEM investigation of interface between non-polar ZnO and $LaAlO_3$

Wei-Ling Wang, Yen-Tang Ho, Li Chang(張立)

Department of Materials Science and Engineering, National Chiao Tung University(交通大學材料科學與工程系), Hsinchu 300

Non-polar ZnO films were grown on (001) and (112)$LaAlO_3$ (LAO) substrate by pulsed laser deposition. The structure properties of the non-polar ZnO films were investigated in detail through using transmission electron microscopy (TEM). According to the results of selected area diffraction patterns in cross-sectional TEM (XTEM) and plan-view TEM (PVTEM), ZnO grown on (001) and (112)LAO substrates, respectively, form in a-plane and m-plane orientations.

For a-plane ZnO on (001)LAO, the ZnO film consists of two in-plane orientations which are perpendicular to each other. The crystal orientation relationships of ZnO deposited on (001)LAO substrate can be identified as $[0001]_{ZnO\,I}$ // $[110]_{LAO}$ and $[0001]_{ZnO\,II}$ // $[\bar{1}10]_{LAO}$, with $(0001)_{ZnO\,I}$ // $(\bar{1}100)_{ZnO\,II}$. In the correlation between a ZnO domain and (001)LAO substrate, LAO has an in-plane translation period of 5.361 Å ($\sqrt{2}a_{LAO}$) along $[110]_{LAO}$ which can nearly match with ZnO in 5.206 Å along $[0001]_{ZnO}$ and 5.627 Å ($\sqrt{3}a_{ZnO}$) along $[1\bar{1}00]_{ZnO}$. Based on the observations in high-resolution (HR) images in PVTEM, most of ZnO domains coalesce to form inversion domain boundaries and twin boundaries. The inversion domain boundaries can be unambiguously defined as m-plane $(\bar{1}100)$. From PV-HRTEM image and its Fourier transformation pattern, the twin boundaries extend along r-plane $(\bar{1}102)$. However, r-plane twin boundary is found to be an incoherent twin boundary because of the effect of strain and distortion in ZnO lattices.

The crystallographic orientations of m-plane ZnO grown on (112)LAO are verified to be $[0001]_{ZnO}$ // $[\bar{1}10]_{LAO}$ and $[\bar{1}2\bar{1}0]_{ZnO}$ // $[\bar{1}\,\bar{1}1]_{LAO}$ without other oriented domains. For the adjoining behaviors of interface in ZnO/(112)LAO, the in-plane translation periods of LAO surface are 2.681 Å ($a_{LAO}/\sqrt{2}$) along $[\bar{1}10]_{LAO}$ and 6.577 Å ($a_{LAO}/\cos 54.8$) along $[\bar{1}\,\bar{1}1]_{LAO}$ which can match with ZnO in 2.603 Å ($c_{ZnO}/2$) and 6.498 Å ($2a_{ZnO}$), respectively. As exhibited in HRTEM image viewed along the zone axis of $[\bar{1}2\bar{1}0]_{ZnO}$, basal stacking faults (BSFs) with the displacement of $a/6<20\bar{2}3>$ are found to generate from the interface between ZnO and (112)LAO. A BSF appears to elongate the mean distance between two misfit dislocations for about two times. On the other hand, the appearance of BSFs is able to release the strain caused by lattice mismatch between ZnO and LAO. It is evident that BSFs can not only form after growth accident, but also generate for the strain relaxation at ZnO/LAO hetero-interface.

Fabrication and Characterization of ZnSe Nanostructures and Related Interfaces (ZnSe 纳米材料及介面的製備與表徵)

JIN Lei(金 磊)[1,2,3]，WANG Jian-Bo(王建波)[1,2*]，JIA Shuang-Feng(賈雙鳳)[1,2]，XU Zhong-Ling(徐中領)[1,2]，YAN Xue(嚴 雪)[1]，DENG Liang-Zi(鄧量子)[1]，CAI Yao(蔡 瑤)[1]，LU Ping(盧 萍)[1]，LEUNG Y P[3]，CHOY W C H[3]

1. Department of Physics and Key Laboratory of Acoustic and Photonic Materials and Devices of Ministry of Education, Wuhan University；

2. Center for Electron Microscopy, Wuhan University, Wuhan Hubei 430072；

3. Department of Electrical and Electronic Engineering, University of Hong Kong, Hong Kong，P R China

（武漢大學 1.物理科學與技術學院和聲光材料與器件教育部重點實驗室，2. 電子顯微鏡中心，武漢 430072；3. 香港大學電機與電子工程學系，香港；中國）

通常，ZnSe 具有面心立方閃鋅礦和六角密堆纖鋅礦兩種晶體結構，長久以來，對其研究主要集中在穩定相閃鋅礦結構上。早在上世紀 90 年代初，基於閃鋅礦 ZnSe 製備的發光二極體和半導體雷射器就已面世，然而，由於材料內部大量缺陷（尤其是面缺陷）的存在，使得基於閃鋅礦 ZnSe 構建的光發射器件的壽命受到了極大制約。因此，如何獲得高品質的 ZnSe 材料及特殊的介面組態，同時對材料內部介面與缺陷的微結構進行深入研究，成為擺在研究者們面前最為緊迫的任務之一。相比於閃鋅礦，纖鋅礦 ZnSe 具有十分接近的禁帶寬度，但由於對稱性較低被認為能有效提高器件的發光壽命。但是，纖鋅礦 ZnSe 卻因其亞穩相的特性研究十分匱乏。為此，本研究旨在討論 ZnSe 納米材料的相控合成，並通過改變實驗參數獲得了多種同質與異質介面，同時利用 TEM 對其進行系統研究，為大量合成與提高其性能打下基礎。

為實現相控合成，首先基於熱動力學原理對氣相法合成的平衡相圖進行了探討。圖 1 給出了平衡相圖的一部分，可知存在兩條途徑得到纖鋅礦結構：（1）提高生長溫度 T。當 T 高於穩定相與亞穩相轉變溫度 T_{tr} 時，纖鋅礦將取代閃鋅礦成為該溫度下的穩定相。由於亞穩相的平衡蒸氣壓 $P_m(T)$始終大於穩定相 $P_s(T)$，故穩定相將始終保持較高的成核幾率，使得纖鋅礦結構最終成核並生長。（2）對於 $T<T_{tr}$，則需降低實際反應壓強。此時，蒸發源的飽和蒸氣壓 P 將因此提升，當 P 大於臨界壓強 P_{cr} 時，Ostwald's step rule 得到滿足，最終導致亞穩纖鋅礦以較高幾率成核析出。

基於上述討論，本工作進行了相控合成，這裏僅選取樣品 A~D 作為例子進行說明（圖 1），它們分別對應于納米線、納米圈、納米輪和三晶納米帶。ZnSe 納米線（圖 2a）尺寸均一，具有閃鋅礦晶體結構，遵照氣－液－固（VLS）機制在 Au 顆粒的催化下沿[111]方向生長而成。分別通過降低反應壓強和提高生長溫度，成功製備出納米圈（圖 2b）和納米輪（圖 2c），它們均主要由鋅礦結構組成，沿著[01$\bar{1}$0]方向快速生長並保持[0001]始終指向圓心。需要指出的是，納米輪由一圈狀基底和其內側生長出的無數齒狀結構組成，其中基底具有完整的纖鋅礦結構，而齒狀區域則富含面缺陷，說明樣品在生長過程中存在較大擾動，可能與生長溫度

相比於亞穩相生長來說仍然偏低有關。故進一步提高生長了溫度並進行了參數優化，獲得了ZnSe 三晶納米帶（圖 2d）。系列傾轉選區電子衍射（SAED）表明 ZnSe 三晶納米帶的任一子帶均具有亞穩纖鋅礦結構，子帶間通過{01$\bar{1}$3}孿晶加以聯繫（圖 2e），證實了提高生長溫度的可行性。

在相控合成基礎上，通過兩階段合成法成功獲得了 ZnSe 複合孿晶納米帶與 ZnSe 納米螺旋，並利用 TEM 對兩者進行了深入研究。首先，通過明、暗場方法以及系列傾轉 SAED 系統地研究了複合孿晶納米帶的結構和長軸方向，確定了孿晶變體間的晶體學取向關係。採用會聚束電子衍射技術並結合衍射動力學模擬確定了複合孿晶納米帶沿<111>方向的極性，揭示其在<111>孿晶介面處極性並不存在反轉，據此判定了{113}和<111>孿晶的類型分別為鏡面和旋轉孿晶，進而提出了初步的原子結構模型，並對 ZnSe 複合孿晶納米帶的形成機制進行了討論，為大量合成與深入研究提供了可能。與通常報導的 II-VI 族半導體盤繞狀納米材料不同，ZnSe 納米螺旋（圖 3）展現出面內彎曲的外形特徵。高分辨透射電子顯微學研究表明：該面內彎曲源于 ZnSe 納米螺旋內部大量存在的具有刃型分量的 Lomer-Cottrell 不滑位錯，從而進一步強調並完善了位錯機制在納米材料生長中所起的作用。

除了同質介面外，在大量合成過程中也獲得了其他幾種具有閃鋅礦－纖鋅礦多型介面的 ZnSe 納米異質結構，其內部閃鋅礦和纖鋅礦多型變體間均具有$<111>_{ZB}//<0001>_{WZ}$取向關係，深入研究正在進行當中。

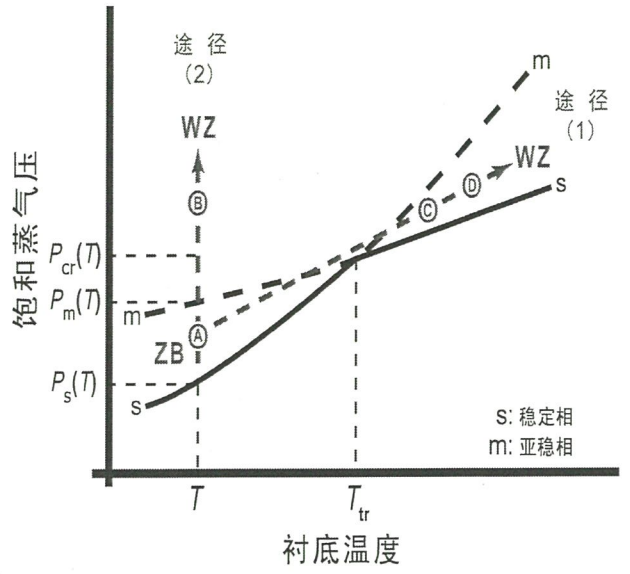

1

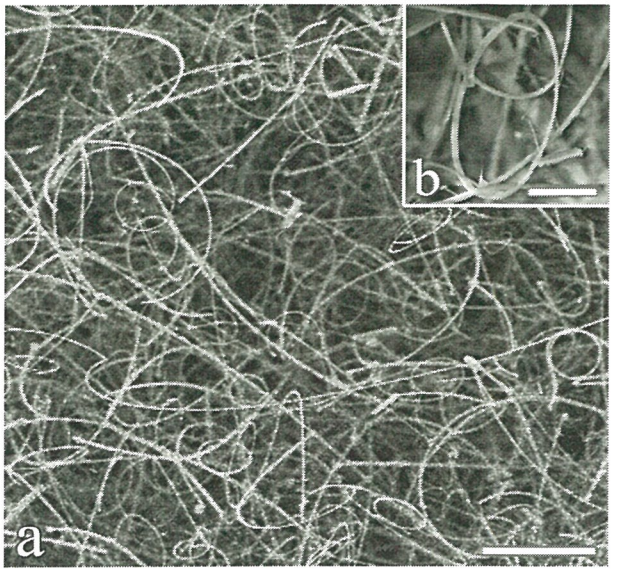

3

圖 1　平衡相圖的一部分。實線 s 代表氣相與穩定相平衡；虛線 m 代表氣相與亞穩相平衡。P_s 和 P_m 分別對應穩定相和亞穩相的平衡蒸氣壓，$P_{cr}(T)$為發生穩定相與亞穩相轉變的臨界壓強。箭頭指出了發生閃鋅礦—纖鋅礦轉變的途徑。圖 3　不同放大倍數下納米螺旋的 SEM 圖像。a：Bar = 40 m；b：Bar = 5 m

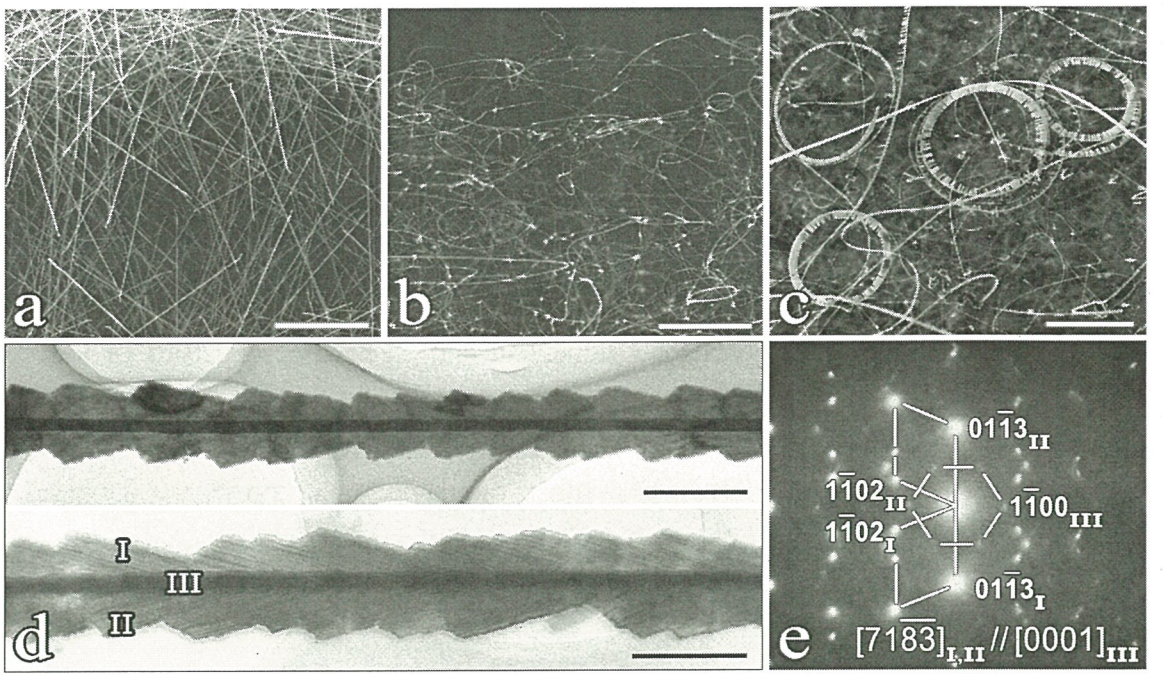

圖 2　a，b，c：樣品 A，樣品 B，樣品 C 的 SEM 形貌圖。d：樣品 D 的 TEM 明場像；ZP e：與 D 對應的 SAED 花樣。　a：Bar = 15 m；b：Bar = 15 m；c：Bar = 25 m；d：Bar =4m.

Characteristics of TiVCr and TiVCrZrY films prepared by dc magnetron sputtering

D. C. Tsai and F. S. Shieu(薛富盛).

Department of Materials Science and Engineering, National Chung Hsing University, Taichung, Taiwan 402（中興大學材料科學與工程學系）

TiVCr and TiVCrZrY alloy and nitride films were deposited on Si wafer by dc magnetron sputtering. Effect of the rf power ranging from 0 to 25 W and N2 flow ratio (RN) ranging from 0 to 100 % on the microstructure and characteristics of the films was investigated in detail. Results indicate that the deposited TiVCr and TiVCrZrY alloy films exhibit body-centered cubic (BCC) and hexagonal close-packed (HCP) crystal structures, respectively. The TiVCr and TiVCrZrY nitride films show sodium chloride type (NaCl) solid solution structure. When applying a moderate rf power of 5 W, it was observed that the structure changes from a porous columnar microstructure to a large-sized columns with no micro-voids. When the rf power was further increased to 15 W, a fully dense and equiaxial microstructure was obtained. However, when the rf power is 25 W, the films peels off the substrate due to excessive residual stress. When introducing more nitrogen gas, the original porous columnar structure with the pyramid-like surface features is gradually substituted by dome-shaped grains. A clear correlation between the void density and the physical properties of the films can be drawn. The void density decreases with the bias voltage and RN, which, in turn, improves the mechanical and electronic properties of the films. When the rf power is 15 W, the TiVCr and TiVCrZrY alloy films showed the highest hardness of 11.2 and 13.95 GPa and the lowest resistivity of 7.72×10-5 and 1.02×10-4 Ω-cm, respectively. When RN=100 %, the TiVCr and TiVCrZrY nitride films revealed he highest hardness of 15.06 and 17.49 GPa and the resistivity of 3.33×10-3 and 4.28 Ω-cm, respectively.

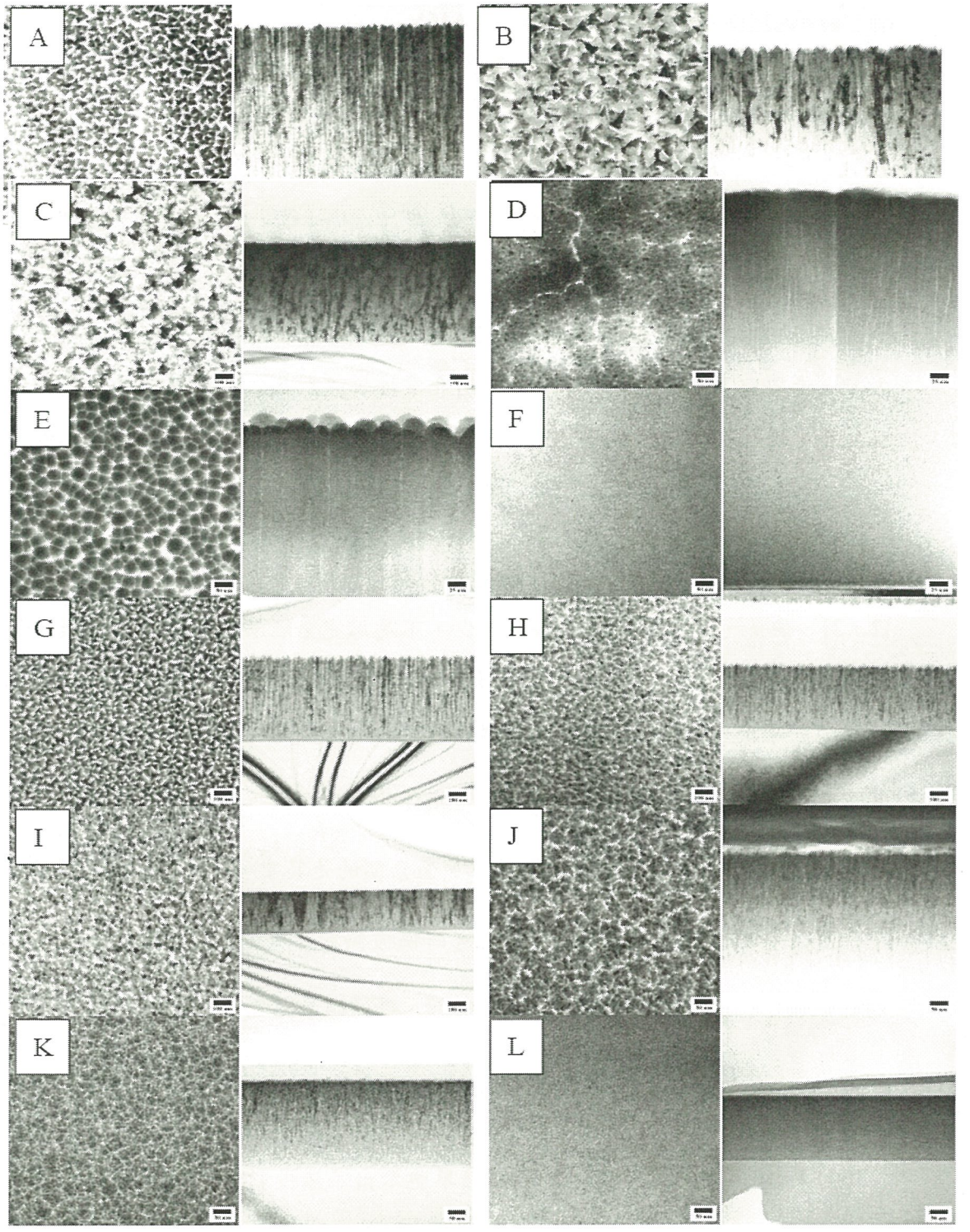

A-C TiVCr alloy films deposited at substrate biases of (A) 0 W, (B) 5 W, and (C) 15 W. **D-F** TiVCrZrY alloy films deposited at substrate biases of (D) 0 W, (E) 5 W, and (F) 15 W. **G-I** TiVCr nitride films deposited at RN= (G) 33 %, (H) 66 %, and (I) 100 %. **J-L** TiVCrZrY nitride films deposited at RN= (J) 33 %, (K) 66 %, and (L) 100 %.

Five Types of Dissociated Misfit Dislocations in Epitaxial Thin Films of Perovskite Grown on (001)$LaAlO_3$
(鈣鈦礦型外延薄膜中五種分解失配位錯的 HRTEM 研究)

LU Chao-Jing (盧朝靖)

(Laboratory of Fiber Materials and Modern Textile, the Growing Base for State Key Laboratory, Qingdao University, Qingdao Shandong 266071, P R China)
（青島大學 纖維新材料與現代紡織國家重點實驗室培育基地，山東 青島 266071，中國）

鈣鈦礦型固溶體 $Ba_{1-x}Sr_xTiO_3$ (BSTO)在微波電子元件方面應用前景十分誘人。大量研究表明，BSTO 外延薄膜的介電性質強烈依賴於薄膜中的內應力與缺陷結構。因此，研究其應變鬆弛十分重要。在鈣鈦礦外延薄膜中，人們已觀察到柏格斯向量 $\boldsymbol{b}$ = [100]的刃型失配位錯，伴隨(001)層錯 $\boldsymbol{b}=\frac{1}{2}$<101>的不全失配位錯**[1]**，還在 $SrRuO_3$–$LaAlO_3$ 介面觀察到與{111}層錯相伴的梯棒位錯和超位錯**[2，3]**。但是，現有的觀察報導還太少，不足以完全理解鈣鈦礦外延薄膜的失配調整機制。本文用傳統的和 HRTEM 研究了生長在(001) $LaAlO_3$ 上 $Ba_{0.3}Sr_{0.7}TiO_3$ 外延薄膜中的缺陷結構**[4，5]**。在薄膜的近介面層發現了高密度的穿透位元錯，其中大部分穿透位錯是與$\frac{1}{2}$<101>層錯相伴的不全位錯。本文擬介紹在該薄膜中觀察到的五種新型的分裂失配位錯，下面介紹的是其中一種有趣的失配位錯。

圖 a 中靠近 BSTO–$LaAO_3$ 介面有四個被標為 1-4 的不全位錯和一被標為 5 的螺位錯。不全位錯 2 和 3 間有層錯襯度。跨過該層錯面，(101)面平移$\frac{1}{4}[10\bar{1}]$，$(10\bar{1})$面平移$\frac{1}{4}[\bar{1}0\bar{1}]$。因此，該層錯的位移向量投影 $\boldsymbol{R}_{2proj}=\frac{1}{4}[10\bar{1}]+\frac{1}{4}[\bar{1}0\bar{1}]=\frac{1}{2}[00\bar{1}]$。圖 b 中用星號標注的鈣鈦礦單胞示出了該投影分量。$\frac{1}{2}[00\bar{1}]$層錯在晶體學上不穩定。考慮到在[010]方向可能有一未被分辨的位移分量，本文作者認為不全位錯 2 和 3 間夾層錯的位移向量 $\boldsymbol{R}_2=\frac{1}{2}[01\bar{1}]$。

圖 a 中不全位錯 1 和 4 的柏格斯向量分別為 $\mathbf{b}_1=\frac{1}{2}[101]$和 $\mathbf{b}_4=\frac{1}{2}[10\bar{1}]$。不全位錯 3 和 4 間應夾有一層錯，儘管難見其襯度。圖 b 中星號示出了該層錯的位移

向量 $\mathbf{R}_3=\frac{1}{2}[101]$。相同的層錯存在于不全位錯 1 和 2 間。類比高分辨像已證實這類層錯的襯度非常弱[4]。圖 b 中繞不全位錯 3 的柏格斯回路有兩個不閉和的分量，一是位移向量 $\boldsymbol{R}_3$，用黑箭頭表示；其二為位移向量投影 $\boldsymbol{R}_{2\text{proj}}$，用白箭頭表示。所以不全位錯 3 的柏格斯向量投影 $\boldsymbol{b}_{3\text{proj}}=\boldsymbol{R}_3+\boldsymbol{R}_{2\text{proj}}=\frac{1}{2}[100]$。類似地，可以確定不全位錯 2 有相同的柏格斯向量投影。如上所述，不全位錯 2 和 3 間夾層錯的位移向量在[010]方向有一分量。因此，兩位錯的柏格斯向量應有螺分量 $\frac{1}{2}[010]$或$\frac{1}{2}[0\bar{1}0]$。如果二者的螺分量同號，則圖 a 中四個不全位錯屬於按下式分裂的複性失配位錯

$$[210]\rightarrow \frac{1}{2}[101]+\frac{1}{2}[110]+\frac{1}{2}[110]+\frac{1}{2}[10\bar{1}]\text{--.(1)}$$

另一種可能性是不全位錯 2 和 3 柏格斯向量的螺分量反號。在此情況下，圖 a 中四不全位錯屬於按下式分裂的刃型失配位錯

$$[200]\rightarrow \frac{1}{2}[101]+\frac{1}{2}[110]+\frac{1}{2}[1\bar{1}0]+\frac{1}{2}[10\bar{1}]\text{. --(2)}$$

分裂反應(1)在能量上比(2)更有利。此外，圖 a 中螺位錯 5 建議分裂的失配位錯柏格斯向量很可能有反號的螺分量。因此，反應(1)更可能發生。關於鈣鈦礦型外延薄膜中失配位錯的這兩種分解方式尚未見報道。

圖 a 中四個不全位錯對應變鬆弛都有貢獻，因為它們的柏格斯向量都有刃分量。這些不全位錯的發生與 BSTO 薄膜的島狀成核與莫紮克生長有關。薄膜生長初期少許過量 TiO_2 促進了與不全位錯相伴的$\frac{1}{2}$<110>層錯形成。

References

1. Suzuki T, Nishi Y，Fujimoto M. Phil Mag A，1999，79：2461.
2. Wu J S，Jia C L，Urban K，Hao J H，Xi X X.　Philos Mag Lett，2001，81：375.
3. Wu J S，Jia C L，Urban K，Hao J H，Xi X X.　J Cryst Growth，2002，234：603.
4. Lu C J，Bendersky L A, Chang K，Takeuchi I.　Philos Mag，2003，83：1565.
5. Lu C J，Bendersky L A，Chang K，Takeuchi I.　J Appl Phys，2003，93：512 .

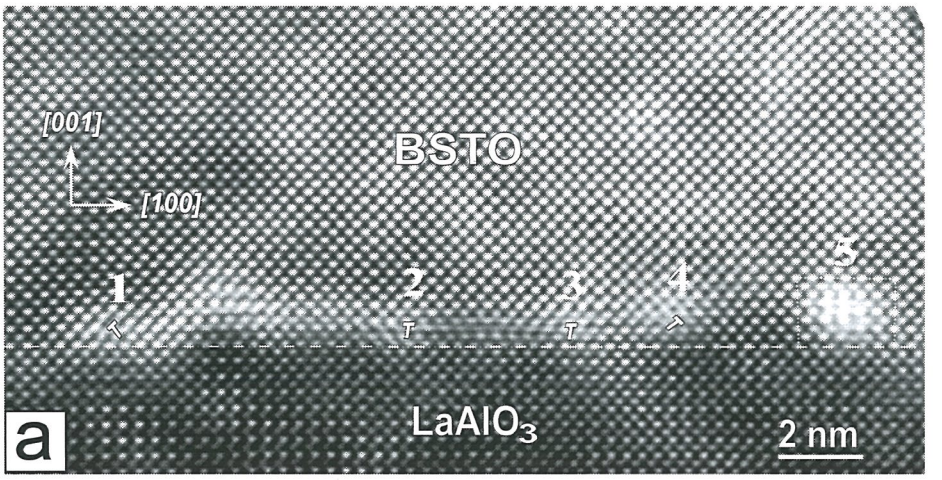

圖 a　包括四個不全失配位錯 1-4 和螺型介面位元錯 5 的 HRTEM 像。

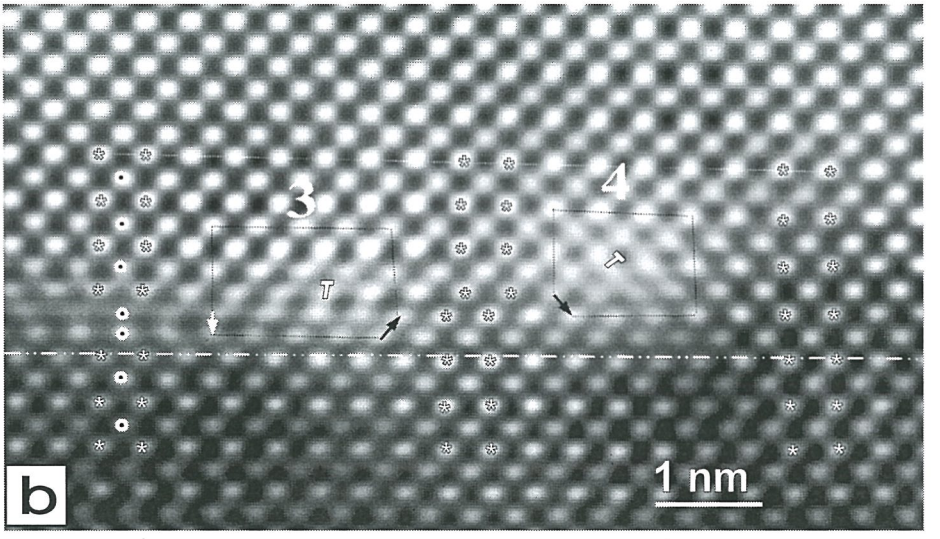

圖 b　圖 a 中不全位錯 3 和 4 附近區域的放大像。繞不全位錯 3 的柏格斯回路上兩箭頭表示左右兩層錯的位移向量投影。星號示出了鈣鈦礦單胞的不同堆垛順序。

The origin of perpendicular magnetic anisotropy in ultrathin Co/Pt multilayers

Chyun-H. Su[a], Yung-Ruei Shiu[a], Shen-Chuan Lo(羅聖全)[b], K.-W. Lin[a], and H. Ouyang(歐陽浩)[c*]

a) *Department of Materials Science and Engineering, National Chung Hsing University(中興大學材料科學與工程系), Taichung, Taiwan 402, R.O.C.*

b) *Material and Chemical Research Laboratories and Nanotechnology Research Center, Industrial Technology Research Institute(工業技術研究院), Hsinchu, Taiwan 310, R.O.C.*

c) *Department of Materials Science and Engineering, National Tsing Hua University(清華大學材料科學與工程系), Hsinchu, Taiwan 300, R.O.C.*

As individual layers in Co/Pt multilayers become thinner the role of surface and interface properties can dominate the bulk magnetism. It has been observed that a perpendicular interface contribution to the magnetic anisotropy can rotate the easy magnetization direction from within the film plane to perpendicular to the film plane when the Co thickness is below a critical value that is in the range of (sub)nanometers. In this work, mixed CoPt phases consisting of disordered fcc CoPt and ordered L10 CoPt, were found to be responsible for the perpendicular magnetic anisotropy (PMA), as shown in the plot, for the film deposition End-Hall voltage (V_{EH}) equal to 140 V. However, the interfacial hybridization between Co and Pt can be the origin of PMA, for the V_{EH} of 100 V, by lowering the interfacial energy. Estimates of mechanisms that could be responsible for the PMA such as "orange peel" coupling, exchange bias and magnetostriction indicate that they are too weak. We believe that this PMA is driven by the negative heat of mixing and relatively unstable interfacial structure as the thickness of Co is below 1 nm.

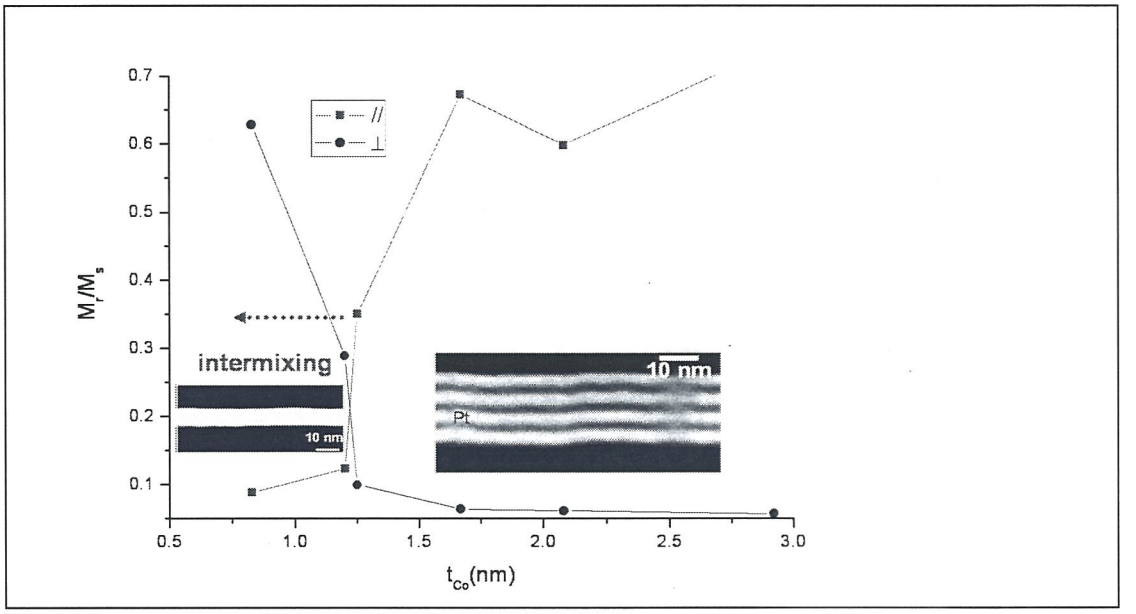

Fig.1 Dependence of the remanence to saturation ratio M_r/M_S from both in-plane (//) and perpendicular (⊥) hysteresis loops on the Co thickness, t_{Co}, for the V_{EH} of 140 V. The insets are the results from HAADF (high-angle annual dark-field), which identify that onset of intermixing and PMA when t_{Co} is less than 1.2 nm.

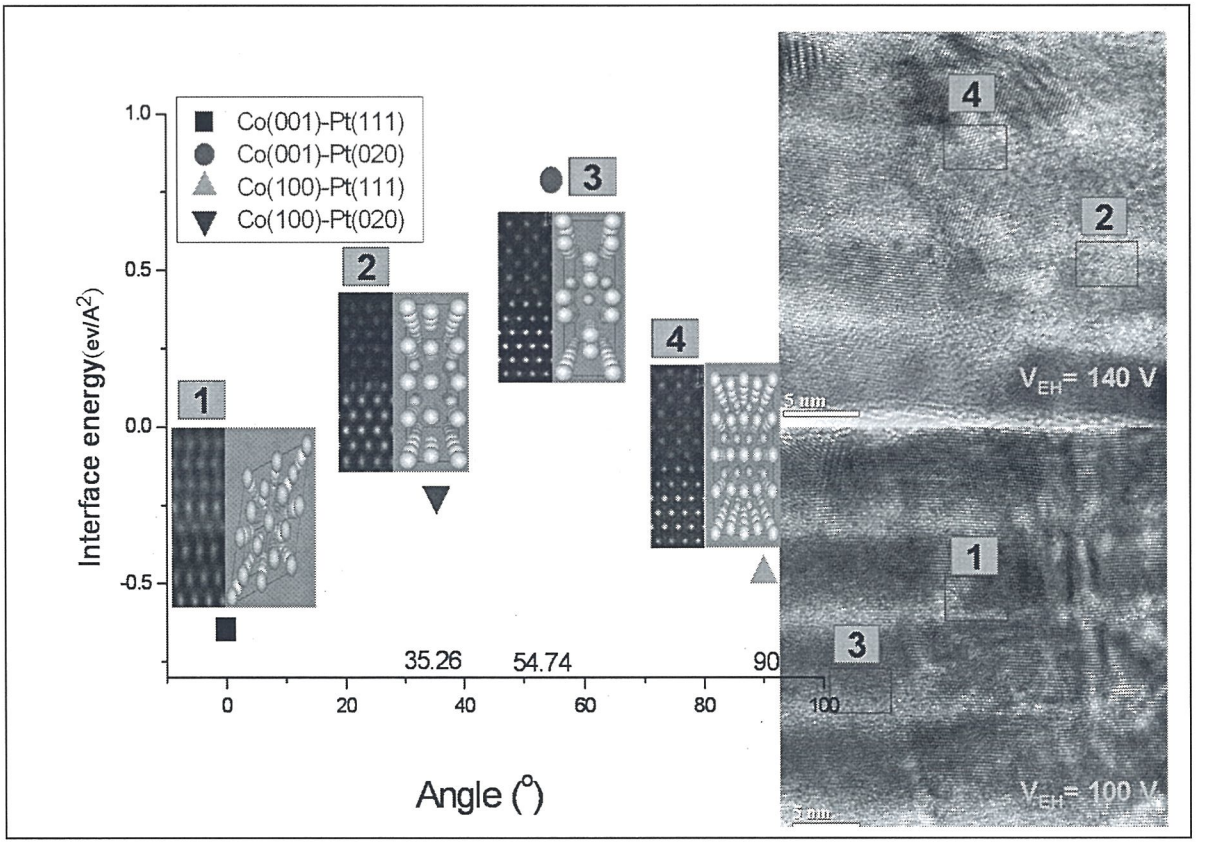

Fig.2 Interfacial energy calculations based on the analyses of HRTEM (High-resolution transmission electron microscopy).

Atomic Structure of the As-Sputtered $Ge_2Sb_2Te_5$ Amorphous Alloy (濺射的 $Ge_2Sb_2Te_5$ 非晶合金的原子結構研究)

ZHANG Lei (張 雷)，HAN Xiao-dong (韓曉東)，ZHANG Ze (張 澤)

(Institute of Microstructure and Property of Advanced Materials, Beijing University of Technology, Beijing 100124, P R China)

(北京工業大學 固體微結構與性能研究所，北京 100124，中國)

In the 21 century, the demanding of high capability of data storage is increasing day by day. Especially, with the rapid development of multi-media techniques, high speed and high density of data storage memory techniques are highly desirable. For the optical storage, the standard 4.7G bit DVD disc could not meet the rapid requirement increasing of next generation data storage. As a candidate of next generation storage technology, the rewritable digital versatile disk-random access memory (DVD-RAM) has been developed based on Ge-Sb-Te thin films. However, one of the most important scientific questions is remained unsolved: the amorphous structure of the record thin film has not been completely decoded.

We investigated the structure of the as-sputtered amorphous Ge-Sb-Te 20nm-thin film using conventional selected area electron diffraction (SAED) and the total pair distribution function g(r) which was calculated from those SAED data. A theoretical Reverse Monte Carlo simulation (RMC) was carried out to deduce the simulated partial g(r)s. The results revealed that Ge-Te and Sb-Te were the majority nearest neighboring bonds. Sb-Sb and Te-Te distances in the first coordination shell were consistent with their crystalline counterpoints. The analysis of band angle distribution suggests that Ge atoms also form a structural unit, in which the angle distributions were the same with tetrahedral configuration. The most probability of angle distributes at about ninety degrees. The detailed atomic structures according to the angle distribution are constructed.

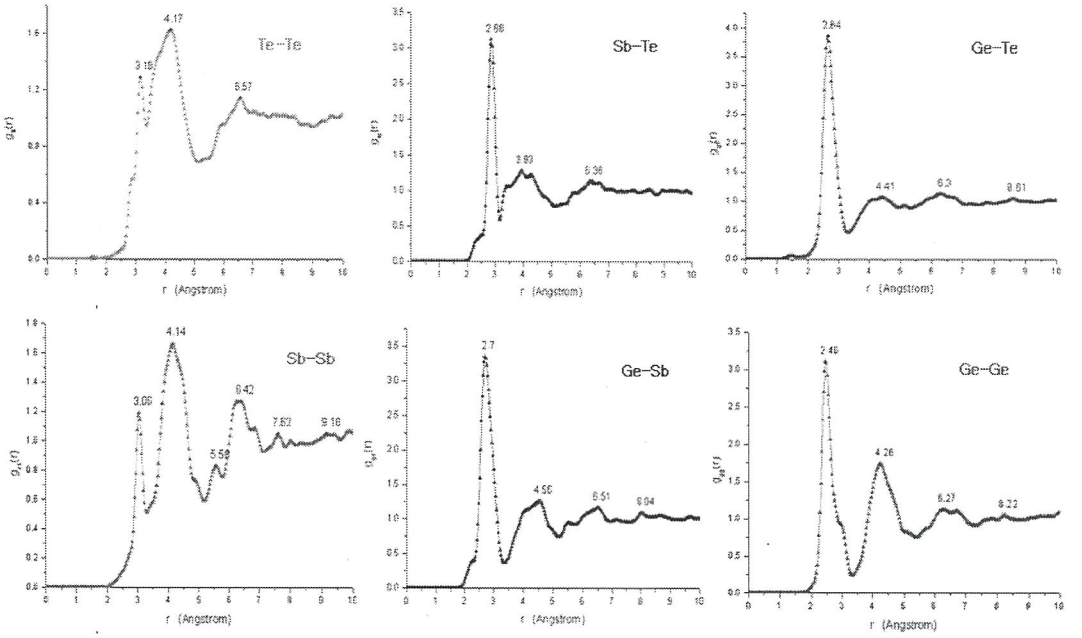

Fig.1 Partial gij(r)s of sputtered amorphous Ge2Sb2Te5. Six partial pair distribution can be deduced.

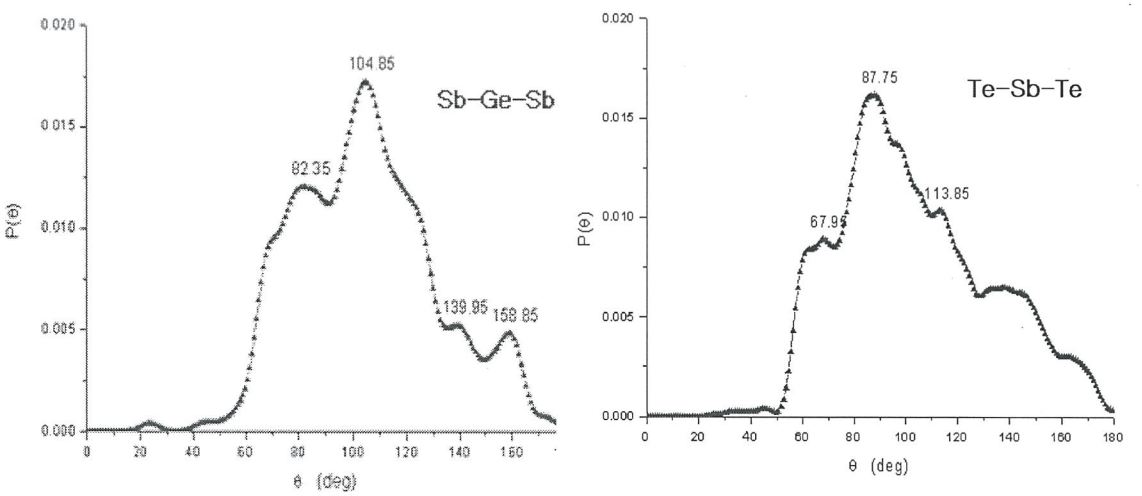

Fig. 2 Configuration of RMC simulation of amorphous $Ge_2Sb_2Te_5$.

Characterization of Fatigue Behavior and Microstructure for Cu-based Glass-forming Metallic Thin Film

Rong Tan Huang(黃榮潭),* Zhe Zhi Liang(梁哲誌),* and Jinn P. Chu**

* *Institute of Materials Engineering, National Taiwan Ocean University(海洋大學材料工程學系), Keelung, 20224, Taiwan*

** *Department of Polymer Engineering, National Taiwan University of Science and Technology, Taipei, 106, Taiwan*

Glass-forming materials with relatively high thermal stability and low critical cooling rates have attracted great attentions to the fundamental and applied research due to their potential use in engineering applications. These materials in bulk form, or so-called bulk metallic glasses (BMGs), are known to possess distinctive properties, including extraordinarily high strength, high thermal stability, and excellent wear resistance **[1-3]**. Thus, the deposition of thin glass-forming films onto structural materials to enhance the fatigue behavior is of great interest for scientific studies. The glass-forming metal films, $Cu_{51}Zr_{24}Hf_{18}Ti_7$ and $Cu_{31}Zr_{47}Al_{13}Ni_9$ (atomic percent, at.%), deposited respectively on the two substrates of 316L and Ni-based alloy using magnetron sputtering, have been investigated by using high resolution transmission electron microscopy (HRTEM) coupled with nanobeam energy dispersive x-ray spectroscopy (EDX). The as-deposited specimens were first proceeded fatigue test. Accordingly, the fatigue strength and life of the specimens coating with one of the two glass-forming metal films are all clearly better than the specimens without coating any glass-forming metal films, as shown in Table I. To clearly study the relationship of fatigue property improvement and microstructure, these specimens are divided into two groups: I). Two different substrates, 316L and Ni-based alloy, coated with the same 200 nm $Zr_{47}Cu_{31}Al_{13}Ni_9$ film, respectively; II). 316L substrate coated with a 200 nm $Zr_{47}Cu_{31}Al_{13}Ni_9$ and $Cu_{51}Zr_{24}Hf_{18}Ti_7$ film, respectively. From the analysis of cross-sectional and plan-view TEM images, group I shows the same microstructure, i.e. amorphous matrix surrounding crystalline grain. However, the 316L substrate shows a thicker interface layer (~ 5 nm), as shown in Fig. 1(a)&(b). It seems to be an oxygen-rich interlayer from the nanobeam EDX analysis. Expectably, it could make 316L substrate surface roughness even smoother. It will be beneficial to enhance the adhesion of film and results in showing a better fatigue property improvement. For group II, it shows the same thickness of oxygen-rich interlayer. There is also no apparent difference of the nanobeam EDX analysis across interface layer for the two specimens. Nevertheless, $Cu_{51}Zr_{24}Hf_{18}Ti_7$ film shows the microstructure, made up of amorphous matrix surrounding nano-crystal, but the microstructure of $Zr_{47}Cu_{31}Al_{13}Ni_9$ film, was composed of amorphous matrix surrounding coarse crystal, as shown in Fig. 2(a)&(b). Since the coarse crystal would be subject to the "transgranular" behavior; on the contrary, the nano-crystal could

reinforce the strength of the thin film. Consequentially, it is useful for Cu film to perform better improvement of fatigue strength and life than Zr film.

References

1. A. Inoue, B. Shen, H. Koshiba, H. Kato, and A. R. Yavari, Nat. Mater 661.
2. A. L. Greer, Science **267**, (1995) p. 1947.
3. A. Inoue, Acta Mater. **48**, (2000) p. 279.

4. Acknowledgement: This work was supported by a grant from Nati Council Foundation under Contract 95-2221-E-019-023-

Table I. The improvement of fatigue life and strength for substrate c Cu-based metallic glass-forming thin film.

Film, Thickness	Substrate	Fatigue Life Improvement	Fatigue Endurance Limit Improveme
$Zr_{47}Al_{13}Cu_{31}Ni_9$, 0.2 μm	316L SS	3,224 %	27 %
$Cu_{51}Zr_{24}Hf_{18}Ti_7$, 0.2 μm	316L SS	4,490 %	53 %
$Zr_{47}Al_{13}Cu_{31}Ni_9$, 0.2 μm	Ni-based alloy	390 %	56 %

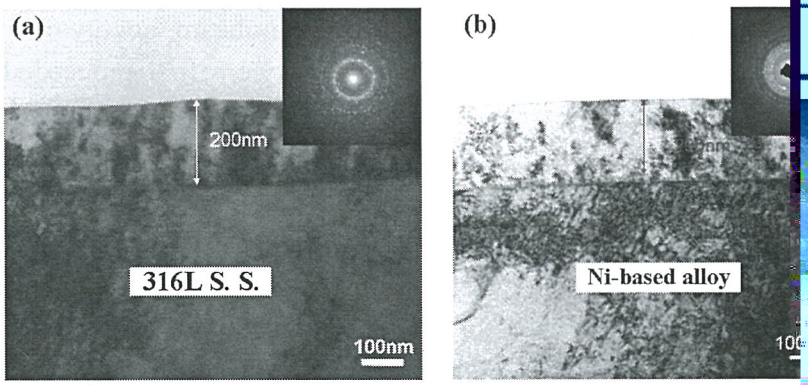

Fig. 1. Cross-sectional TEM images of (a) 316L S.S. coated with $Zr_{47}Cu_3$ film and (b) Ni-based alloy coated with $Zr_{47}Cu_{31}Al_{13}Ni_9$ thin film.

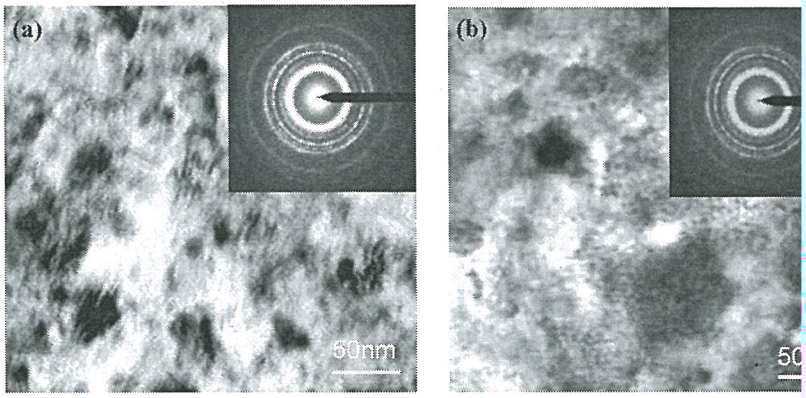

Fig. 2. Plan-view TEM images of (a) 316L S.S. coated with $Zr_{47}Cu_{31}Al_{13}$ and (b) Ni-based alloy coated with $Zr_{47}Cu_{31}Al_{13}Ni_9$ thin film.

Ormation of Long Period Stacking Structure in Mg-Gd-Y-Zn Alloy Heat Treated at 400℃
(Mg-Gd-Y-Zn 合金 400℃熱處理過程中長週期堆垛結構的形成)

WANG Fei (王飛), SUN Wei (孫威*), LIU Lin-Lin (劉林林)

Institute of Microstructure and Property of Advanced Materials, Beijing University of Technology, Beijing 100124, P R China(北京工業大學 固體微結構與性能研究所，北京 100124，中國)

近年來，能源與環境問題正日益受到人們的廣泛重視。作為一種環境友好的輕型材料，鎂合金已在航空、航太、汽車製造及 3C 產品等領域得到廣泛應用。其中鎂稀土系列合金在高溫下具有良好的力學性能及熱穩定性，因而受到人們更多的關注。通過研究發現，Mg 稀土合金中可以形成多種結構不同的納米強化相，例如納米析出相**[1]**和長週期堆垛結構強化相（LPS）**[2]**。選取合適的 Mg 稀土合金系（如 Mg-Gd-Zn 或 Mg-Gd-Y-Zn），並進行適當固溶時效處理以及熱軋加工，可以實現彌散強化相和 LPS 強化相的共存，從而有效地提高合金的強度和綜合性能**[3]**。目前，對於各種不同 Mg 稀土合金中彌散強化相的形成和演變過程的研究已經有很多報導，而對其中 LPS 強化相的形成過程和演變機制仍然有很大的爭議。尤其是在四元 Mg-Gd-Y-Zn 合金體系中，要做到有效地調控納米強化相（包括彌散析出相和 LPS）的綜合強化效果，對 LPS 強化相形成條件和形成過程的研究就變得十分必要。作者的前期研究發現，熱處理可以導致 $MgGd_{1.8}Y_{0.8}Zn_{0.8}$（at.%）合金中 LPS 的明顯形成。本文利用掃描電鏡背散射電子技術、透射電鏡觀察和能譜分析，研究了 $MgGd_{1.8}Y_{0.8}Zn_{0.8}$ 合金 400℃熱處理前後第二相附近的微結構變化，發現鑄態合金中富含稀土及 Zn 的初生第二相在熱處理過程中的分解，與 LPS 的形成有密切關聯。

鑄態 $MgGd_{1.8}Y_{0.8}Zn_{0.8}$ 合金中觀察到大量的層錯缺陷(SF)的存在，但沒有形成明確的 LPS 結構。圖 1a 為鑄態合金在$[11\bar{2}0]_{Mg}$方向的 TEM 明場像，從中可以清楚地看到呈黑襯度的第二相以及其附近的層錯缺陷襯度。從層錯缺陷區（C 區）的電子衍射花樣上可以看到（見圖 1c），在 Mg 基體倒空間 沿[0001]*方向上有明顯的芒線，說明層錯的分佈呈無序的分佈。納米束 EDS 分析表明，SF 區的 Zn 和 RE 原子明顯比 Mg 基體多，說明 SF 的形成與 Zn 和 RE 原子的擴散密切相關。鑄態合金中的初生相可以標定為具有面心結構(fcc)的 Mg_3RE 型相，晶格常數為 $a = 0.76nm$。EDS 分析 Mg_3RE 型相給出的平均成分為：$Mg_{69}Gd_{16}Y_5Zn_{10}$ (at.%)。

鑄態 $MgGd_{1.8}Y_{0.8}Zn_{0.8}$(at.%)合金在 400℃的時效處理可以導致長週期堆垛結構的形成。圖 1b 所示為鑄態 $MgGd_{1.8}Y_{0.8}Zn_{0.8}$ 合金 400℃熱處理 20h 後沿$[11\bar{2}0]_{Mg}$方向觀察的 TEM 明場像。在 Mg 基體上（見圖 1b 的 D 區）可觀察到與圖 1a 中 C 區十分類似的 SF 分佈；從對應的電子衍射譜（見圖 1c 和圖 1d）上可以看出，

D 區的結構與 C 區的結構特徵相同，沒有 LPS 存在的跡象。但與鑄態不同的是，400℃熱處理 20h 後，在第二相和基體之間存在一個與 D 區襯度不同的 E 區。從其對應的電子衍射譜（圖 1e）上看，Mg 基體的 0000 透射斑和 0002 衍射斑之間除了存在芒線外，還存在等間距分佈的 5 個弱斑，將其等分為 6 等份，表明 E 區除了 SF 外，還存在 6 層週期的 LPS 結構。能譜分析表明，該區的稀土和 Zn 含量明顯高於其前沿的 SF 區（D 區）。

以上的實驗觀察和更長時間熱處理後的結構演變分析表明，可以通過控制第二相的分佈，達到調節 LPS 分佈的目的，這樣可以將力學性能較差的第二相轉變成更多的可以強化鎂合金的 LPS 結構，從而提高鎂合金性能。

References

1. NIE J F，MUDDLE B C.　Acta mater，2000，48: 691-1703.
2. Kawamura Y，Hayashi K，Inoue A，Masumoto T.　Mater Trans，2001，42: 1172-1176.
3. Yamasaki M，Sasaki M.　Acta Materialia，2007，55: 6798–6805.

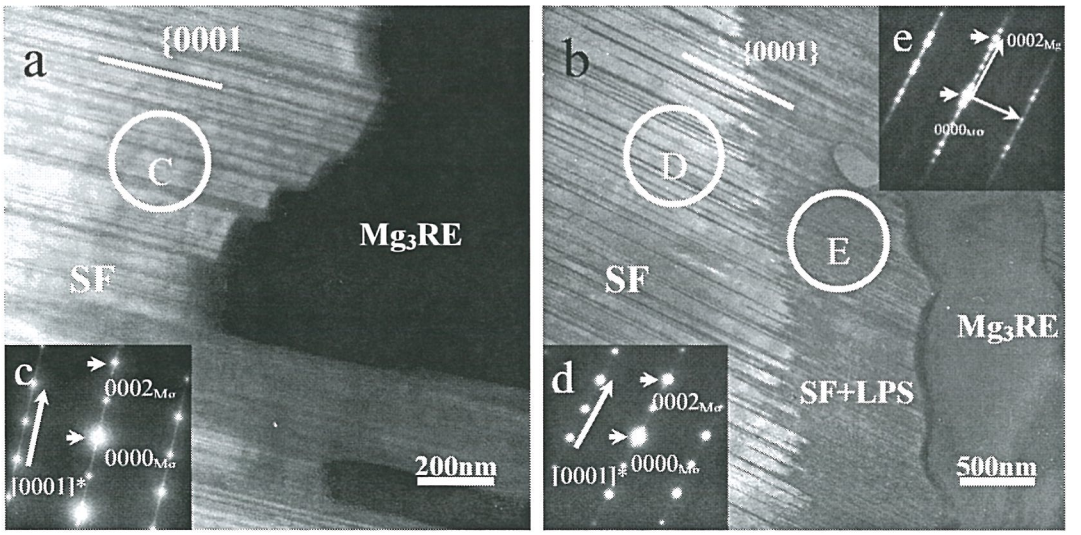

圖 1　a：$MgGd_{1.8}Y_{0.8}Zn_{0.8}$ 鑄態合金沿$[11\bar{2}0]_{Mg}$方向觀察的 TEM 明場像；b：鑄態合金經 400℃＋20h 熱處理後沿$[11\bar{2}0]_{Mg}$方向的 TEM 明場像；c，d，e：分別為對應明場像中 C，D，E 區的選區電子衍射譜。

Application of TEM in the Semiconductor Industry

David H. Su, (蘇紘儀)Li-Chien Chen, Kai-Min Yin, Bonnie Huang, F.Y. Tseng, M.N. Yu, C.M.

Huang

Taiwan Semiconductor Manufacturing Co. Inc., Hsinchu Science Park, Taiwan 300

(台灣積體電路股份有限公司 故障分析處)

Abstract

Over the past 30 years, Transmission Electron Microscopy (TEM) has evolved from a research tool to a combination of research and failure analysis tool in the semiconductor industry. In this work, the main uses and challenges of TEM in the semiconductor industry will be discussed.

Introduction

In the modern day semiconductor industry TEM is used in different roles: materials characterization in the research and development (R&D) phase, monitoring and metrology during production and finally failure analysis to resolve yield and reliability problems during qualification, product ramp and to handle customer returns. Each one of these areas requires a different mode of operation and has different demands on the skill set of the TEM laboratory.

Independent of which role it is playing in the semiconductor industry one key feature of industrial mode of TEM usage is the need for rapid turnaround time. Instead of providing a TEM result in two weeks, nowadays it is routine to provide 24-hour TEM turnaround and it is not uncommon for TEM results to be provided a few hours after the samples are submitted to the laboratories.

Another notable difference between performing TEM work in the semiconductor industry compared to TEM work done in academic institutions is the requirement for TEM laboratories in industry to "hit" specific features or locations, this need is present even during the R&D phase. Thus, the semiconductor industry has been one of the main drivers of site-specific TEM sample preparation techniques including site specific dimpling and ion milling techniques **[1]**, the wedge technique using the tripod polisher **[2]**, culminating with the use of focused ion beam (FIB) systems dedicated to the preparation of site-specific TEM samples **[3, 4]**.

TEM As A Materials Characterization Tool in the Semiconductor Industry

The more traditional use of TEM in R&D in the semiconductor industry is to use it to perform materials characterization, especially when new types of materials are involved such as the introduction of Cu interconnects and low-k dielectrics in the 0.13um technology node, the introduction of SiGe stressors in the 45nm node and the introduction of high dielectric constant gate dielectrics and metal gates in the 28nm technology node.

Some of the more challenging applications that currently need to be addressed by TEM or other techniques include strain measurement with high spatial resolution, dopant profiling for ultra-shallow junctions, and high spatial resolution chemical analysis.

Adding strain to an integrated circuit (IC) device can improve the performance of the device. For example, adding compressive strain to the channel region of a p-type transistor improves the

performance of the device. However, measuring the local strain in a 45nm transistor is a challenge due to the small geometries involved. Attempts have been made to use different techniques to address this problem including convergent beam electron diffraction (CBED) **[5]**, electron beam backscattered electron diffraction **[6]** and nano-beam diffraction (NBD) **[7]**. As of now, NBD shows the most promise in terms of spatial resolution (Fig. 1).

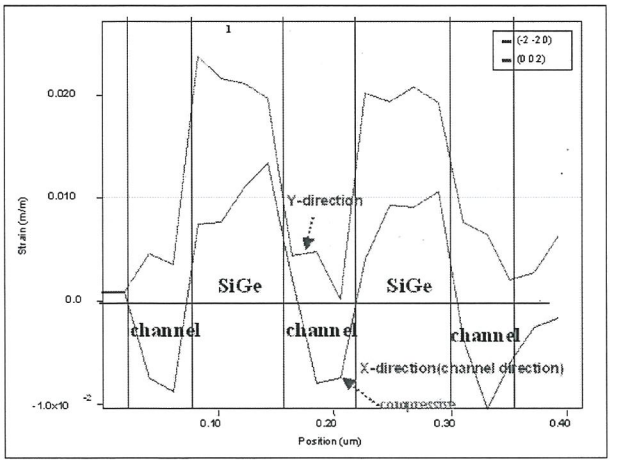

Fig. 1: NBD results of a device showing changes in strain in x- and y- directions generated by SiGe stressors.

Two-dimensional dopant delineation has been studied for many years **[8]**. Unfortunately, most techniques are only suitable for qualitative measurements and are frequently not reproducible. Furthermore, p-type dopants are especially difficult to delineate. A newly developed technique using well-controlled electrochemical etching has been used to delineate junctions successfully and reproducibly.

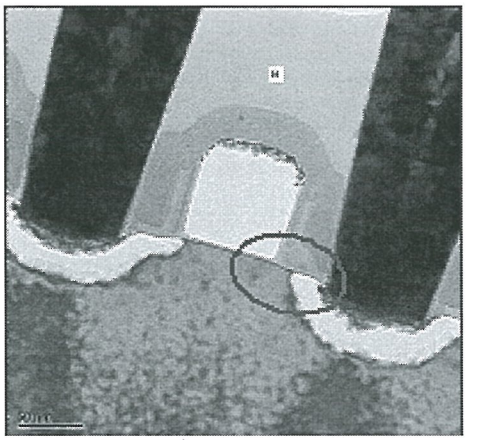

Fig. 2: Chemical junction delineation showing problems with LDD implant in NMOS probably caused by presence of a particle during implantation.

TEM As A Failure Analysis Tool

One of the most challenging tasks for TEM in the modern semiconductor company is failure analysis. Unlike ramp-up yield-related problems, there are very few failing samples and localization of the area of failure is very difficult. Thus, one of the techniques being used more and more frequently is to use plan view TEM to identify defects that could be the cause of the failures and then prepare cross-sections of these plan view TEM samples to understand these defects better and to confirm that they were in fact responsible for the failure (Fig. 3).

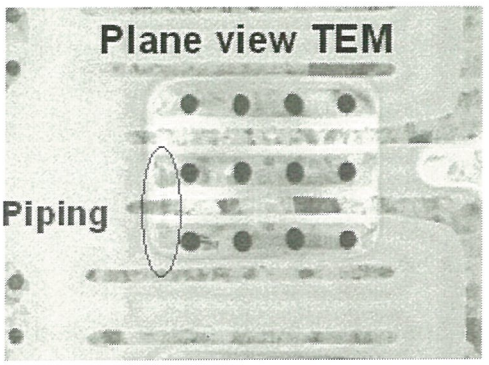

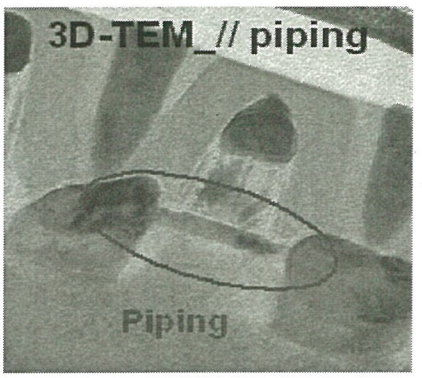

Fig.3a: Plan view TEM used to identify likely cause of a failure. Fig.3b: Cross-section of the sample shown in Fig. 2a showing a "piping" defect.

The most common method of preparing these TEM samples for 3D observation is very elaborate involving first preparing the plan view sample by conventional means or by FIB thinning and lift-out, examining the plan view sample in the TEM, identifying the area of interest and marking it, then gluing a support film to the bottom of the plan view sample, thinning the cross-section with an FIB and finally lifting the cross-section lamella out. The whole process can take 5 to 8 hours. A newly developed method used to produce the results shown in Fig. 3, reduces the sample preparation time down to 3 hrs or less.

Summary

TEM laboratories in the semiconductor industries are continuously challenged with demand for quicker turnaround, smaller dimensions and new materials. However, new innovative techniques are also being developed to address these challenges.

Acknowledgements

The authors would like to thank Dr. Erwan Sourty from FEI for performing the NBD analysis shown in this work.

References

1. Helen L. Humiston , MRS Proceedings Volume: **480,** San Francisco, California, 1997, pp117~126
2. R. M. Anderson, et al., Microscopy of Semiconducting Materials 1989
3. R.J. Young, E.C.G., D.A. Williams, and H. Ahmed, in Specimen Preparation for Transmission Electron Microscopy of Materials - II, edited by R. Anderson (Mater. Res. Soc. Proc. **199**, San Francisco, California, 1990), pp. 205-216.
4. D.Basile, R. Boylan, B. Baker, Kathy Hayes, and David Soza, in Specimen Preparation for Transmission Electron Microscopy of Materials - III, edited by R. Anderson, B. Tracy, J. Bravman (Mater. Res. Soc. Proc. **254**, Boston, Massachussetts, 1992), pp. 23-41.
5. C.J. Humphreys et. Al., Ultramicroscopy, **26**, (1998) 13
6. A. J. Wilkinson, Ultramicroscopy **62** (1996), p.237
7. K. Usuda. et al, SOI conference 2003. IEEE. 138
8. R. B. Marcus and T. T. Sheng, Transmission Electron Microscopy of Silicon VLSI Circuits and Structures (Wiley, New York, 1983), Chap. 5, p. 124.

Advanced Nano-electronic TEM analysis, challenges and applications

謝詠芬

閎康科技股份有限公司，新竹

Versatile TEM applications have been widely applied in novel materials study and process development with the aids of FIB sample preparation techniques. Owing to atomic resolution capability, TEM analysis is known to be the most powerful tool for nano device/materials research among all kinds of microstructure study. Sample preparation is thus the key to make successful imaging of the targeted features.

In this lecture, excellent demonstration has been realized in ICs, CMOS image sensor, solar cell, TFT-LCD, LED, laser diode, MR-head, DVD, organic materials, magnetic nano powders, and carbon nano tube. The challenging skills include precise cutting of ultra-small feature size (<45nm), deep and long trench of large view size (>10um x 30um), uniform thinning of huge size features (100um x 150um), proper material choice of protection layer before FIB cutting, and multi-layer stacked structure with different FIB sputtering yield (FIB cutting prints). Currently, supporting methods, such as mechanical polishing prior to FIB cut and thermal evaporation coater/metal sputtering/spin-on-glass, have been employed to solve the fore-mentioned issues to some extent as complementary alternatives to FIB techniques. Innovative system design of FIB is still mandatory to establish an all-in-one process and to improve sample quality and shorten the working time.

TEM sample preparation by FIB cutting

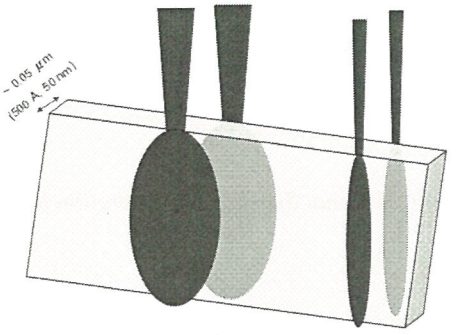

CMOS image sensor analysis

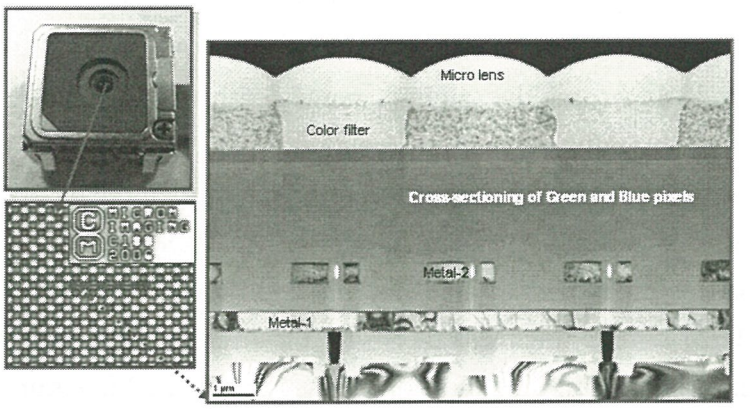

MR Head Analysis

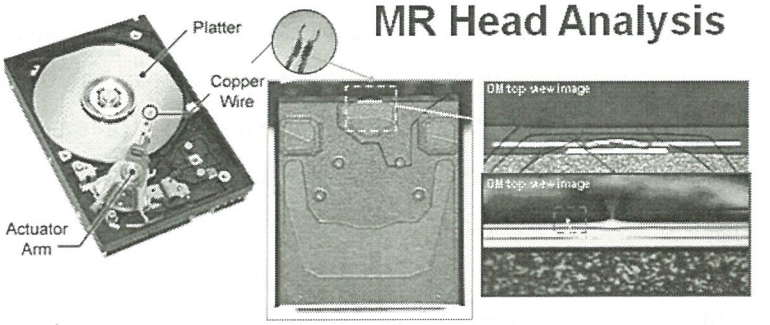

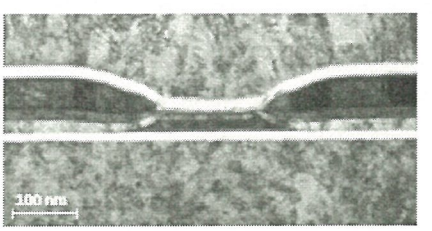

EDX mapping

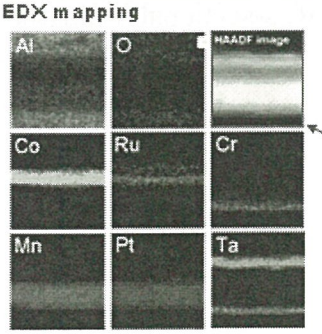

X-S TEM image

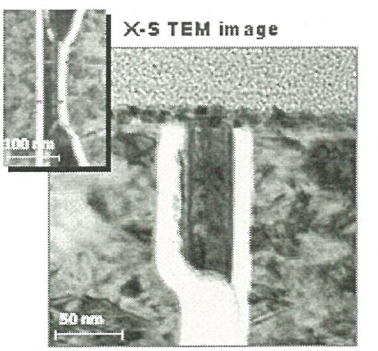

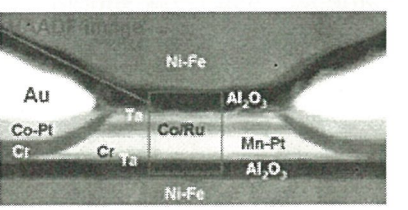

A Novel Preparation Method of Mechanical polishing for Cross-sectional TEM Specimen with 10 nm Thickness

Cheng Cheng Chiang(江正誠)* and Rong Tan Huang**

* *Industrial Application Group of Beamline Division, National Synchrotron Radiation Research Center(國家同步輻射研究中心), Hsinchu, 30076, Taiwan, R.O.C.*

** *Institute of Materials Engineering, National Taiwan Ocean University, Keelung, 20224, Taiwan, R.O.C.*

The need for cross-sectional preparation of materials for transmission electron microscope (TEM) study is always great because both thin films and interfaces of the coated materials can be analyzed and photographed down to the atomic range with this method preparation **[1]**. Nevertheless, this method is normally very time-consuming and/ or expensive, e.g. focused ion beam technique **[2]**. Therefore, the development of more effective methods is always one of aims for TEM sample preparation. In general, the objective of TEM sample preparation is to create an electron transparent region containing large thin area of feature interested without contamination and artifacts. Hence, the TEM sample thickness of electron transparent is usually smaller than 100 nm and even thin to 20 nm for photographing the atomic level image. In this report, based on wedge technique **[3]**, a newly developed preparation method called optic four-point adjustment method referring to the operated process of regular optical microscope is used to prepare high quality TEM sample with large thin area and very thin thickness. Figure 1 shows operated process of the optic four-point adjustment technique. To make a cross-sectional sample, a piece of thin cover glass is glued on the surface of the specimen to protect the feature of interest. The sample is then mounted on the holder for first side polish. The holder is placed on the stage of an optical microscope. The cross-section line can be adjusted by turning the two adjusting screws. Meanwhile, when the holder is lain on the stage of an optical microscope, the planar surface also can be adjusted by turning the two adjusting screws to focus four-point, as shown in Fig. 1(a), (b) and (c). For the second side polish, the optic four-point adjustment method is also used to prepare a very plane region. Consequentially, the resulting TEM image of copper dual-damascene structure with six metal layers was shown as Fig. 2. Besides, a so-called three-dimensional (3D) TEM, which refers to the examination of the same feature in TEM from two perpendicular directions, is used to verify that the TEM sample thickness is thin up to 10 nm. The cross-sectional TEM sample with Cu grid is then mounted on small piece of silicon wafer with epoxy. Subsequently, the regular optic four-point adjustment technique is applied again. As shown as Fig. 3, the sample thickness smaller 10 nm is successfully prepared and the depth could be reached to 900 nm. The details will be presented in the conference.

References

[1] Hong Zhang, Micron **33**, (2003) p. 515.

[2] S. Morris, et al., Proceedings of ISTFA, (1991).
[3] J. P. Benedict, S. J. Klepeis, W. G. Vandygrift, R. M. Anderson, EMSA Bulletin, (1989)
[4] Acknowledgement: This work was supported by a grant from National Science Council Foundation under Contract 95-2221-E-019-023-

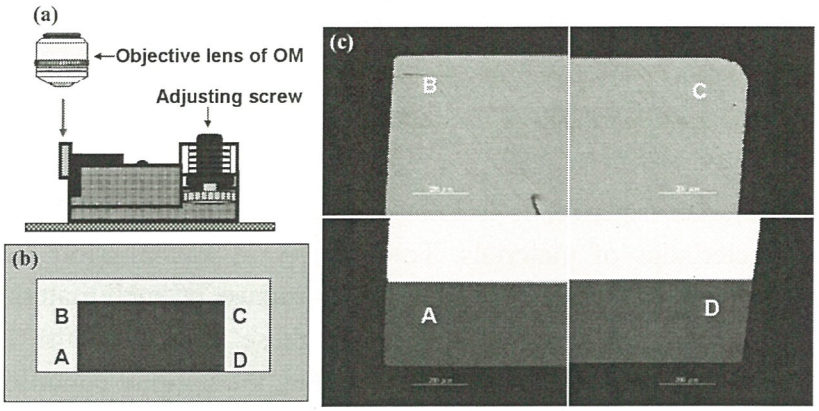

Fig. 1. The schematic procedure of optic four-point adjustment method. (a) The holder is lain on the stage of an optical microscope, then the planar surface also can be adjusted by turning the two adjusting screws to focus four-point of (b). (c) The corresponding OM image of (b).

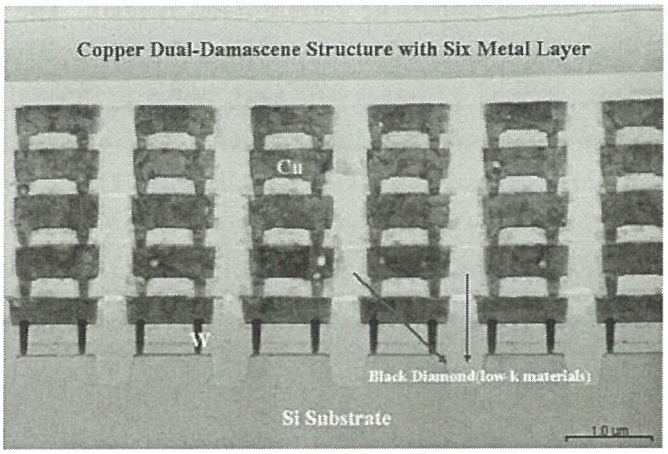

Fig. 2. The TEM image of copper dual-damascene structure with six metal layers.

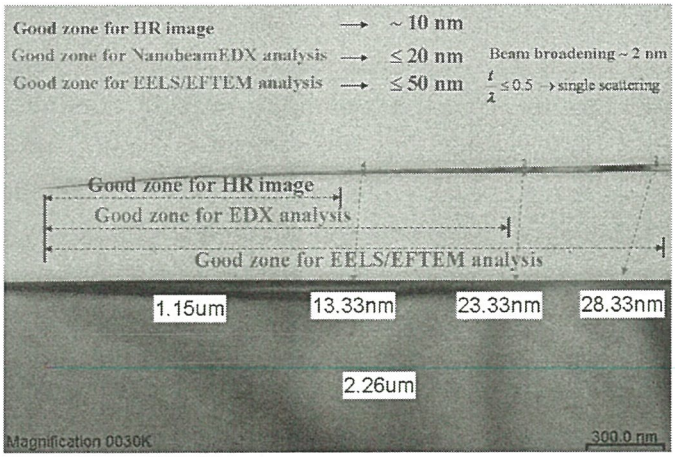

Fig. 3. A so-called three-dimensional (3D) TEM, which refers to the examination of the same feature in TEM from two perpendicular directions, is used to verify that the TEM sample thickness is thin up to 10 nm.

The latest development of 3D tomography for soft materials

S. Motoki[1], T. Kaneko[1], Y. Aoyama[1],H. Nishioka[1], Y. Ohkura[1], Y. Kondo[1], H. Jinnai[2,3]

[1]*JEOL Ltd., 3-1-2 Musashino, Akishima Tokyo 196-8558, Japan,*

[2]*Department of Polymer Science and Engineering, Kyoto Institute of Technology, Matsugasaki, Kyoto 606-8585, Japan*

[3]*WPI Advanced Institute of Materials Research, Tohoku University,2-1-1 Katahira Aoba-ku, Sendai 980-8557, Japan*

In the soft materials science, it is known that the inclusion of 10 ~ 100 nm order scale influence the characteristics of materials. Tomography in transmission electron microscopy is powerful for the analysis of three-dimensional(3D) structure of such materials. Structural analysis of those materials needs thick sample to involve these. However, the dynamics of scattered electrons inside the thick specimen is so complicate that the optimal condition for observation of it is uncertain. In this study, we compared bright field transmission electron microscopy (BF-TEM), bright field scanning transmission electron microscopy (BF-STEM) and dark field scanning transmission electron microscopy (DF-STEM) as a tomographic imaging method for such thick sample.

We employed an acylonitrile butadiene styrene (ABS) resin. The ABS resin was stained by OsO_4 vapor to enhance the contrast and then microtomed for 3D observations. The thick section of ca. 1 μm thick was transferred onto a Copper grid with polyvinylformal as a supporting film. Prior to the tomographic observations, 40-nm-sized Au particles were deposited on the sample as markers. The tilt series of the electron images were taken with 200 kV TEM/STEM (JEM-2100). The pixel resolution was 4 nm resulting in the effective focal depth of 1.6 μm, which is substantially larger than the sample thickness. The detection angles of BF- and DF-STEMs were 6.5 mrad and 150 mrad, respectively. All reconstruction procedures were carried out using a software:"TEMography" **[1]**.

To evaluate reconstructed tomograms by BF-TEM, BF-STEM and DF-STEM, we compared images sliced from their volumes at three heights, *i.e*, near the top, at the middle and near the bottom of the volume. The images from BF-TEM show almost the same degree of blur at three heights. The reason for the blur is considered to be a chromatic aberration due to increase of energy spread of image forming electrons, orginated from inelastic scattering. Analysis on the sliced images of STEMs shows that the spatial resolutions decrease continuously from the top to the bottom of the volume. This related to the electron beam broadening caused by the multiple-scattering of the electrons passing through the specimen. The broadened width estimated from the blur of the sliced image accords with that predicted by a theory **[2]**. The spatial resolution of DF-STEM tomograms tends to lose faster than that of BF-STEM, since the electrons within the small detection angle have lower probability of multiple scattering than those in large angle. From these results, we conclude that the BF-STEM with small detection angle is advantageous for tomograms of thick specimen.

References

[1] TEMograpy, http://www.temography.com

[2] J. I. Goldstein, Introduction to Analytical Electron Microscopy, Plenum Press, New York, 1979.

The Development of 3D TEM/STEM Tomography in ITRI

Shen-Chuan Lo(羅聖全)[1,2] Ming-Wei Lai,[1] Shi-ri Lee, Shu-Jan Chen[1] and Li-Jiaun Lin [1]

[1] *Material and Chemical Research Laboratories, Industrial Technology Research Institute(工業技術研究院), Hsinchu, Taiwan.*

[2] *Nanotechnology Research Center, Industrial Technology Research Institute(工業技術研究院), Hsinchu, Taiwan.*

TEM is an important tool to study the microstructure of materials. In the past decade, several hardware such as new field emission electron guns, aberration corrector, monochromator has been developed with sub-Å image and sub-eV energy resolution. However two-dimensional (2D) image projects from three-dimensional (3D) object will loss the information along thickness direction of sample. With recent developments of electron tomography, TEM tomography is becoming a powerful tool for visualization of nano-structure in 3D space in biology, chemistry and materials science **[1]**. Using conventional TEM samples and specimen holders, a tilt may be reached beyond which the sample is too thick. A 'missing wedge' information will be occur and reconstructions can be elongated in the direction of missing wedge. Basically, there are two method to overcome the missing wedge problem, one is dual-axis method, the other is rod-shape specimen method.**[2,3]**

In this report, a dedicated home made complex holder for 3D Tomography will be presented in this conference (Fig.1). This complex holder is designed for UHR mode FETEM (model: JEOL JEM-2100F) with pore piece around 2mm, and the throughput of sample preparation using FIB-based method will be speed up two times **[4]**. The rod-shape specimen has been fabricated using DB-FIB without surface amorphous layer as shown in Figure 2. A JEOL JEM-2100F electron microscope equipped with Gatan multi-scan CCD was used for 3D TEM/STEM tomography. The preliminary results of tilt series images were recorded at tilt angles ranging from $+75^{o}$ to -75^{o} in a 1^{o} step with automated controlled function. The tilt series alignment and 3D reconstruction were done with program developed by JEOL System Technology Co., Ltd **[5]**. Finally, commercial Avizo^{TM} software was used for 3D model visualization. Figure 3 is the HAADF image of the PCM device in rod-shape. This kind of specimen can be reach to ±90 tilt degree (this paper now is ±75) without any missing wedge and geometry elongated problems. Figure 4 presented the reconstructed 3D model of rod-shape PCM device. The preliminary results showed that the detail 3 dimensional PCM microstructure can be resolved with less missing wedge but no geometry elongated problems. We will keep going to modified our TEM facility to reach ±90 tilt degree and the detail results will be presented in this conference.

Keyword: electron tomography,.missing wedge, dual-axis, rod-shape, complex holder

References

1. J. Frank editor. Electron tomography: three-dimensional imaging with the transmission electron microscope. New York: Plenum; 1992.
2. P.A. Midgley and R.E. Dunin-Borkowski, Natural materials, vol.8, (2009) p.271-280

3. M. Koguchi et al., Journal of Electron Microscopy, 50, (2007) p.235-241
4. Shen-Chuan Lo et al., R.O.C. Patent apply no.097151170, (2008) submitted.
5. Acknowledge: Thanks for 3D reconstruction program provided by M. Shimizu and H. Furukawa from JEOL System technology Co. Ltd.

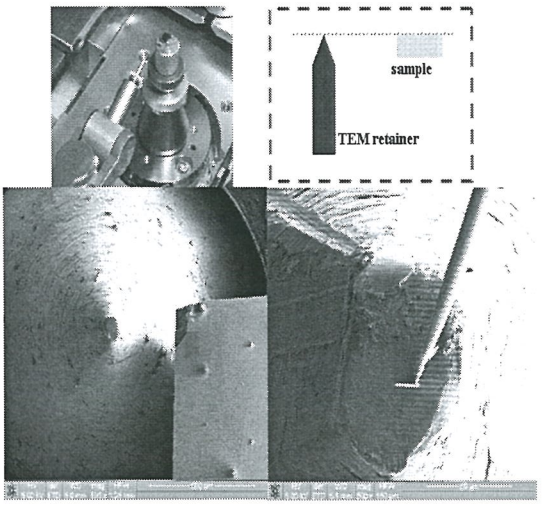

Fig.1 The dedicated home made complex holder for UHR mode TEM.

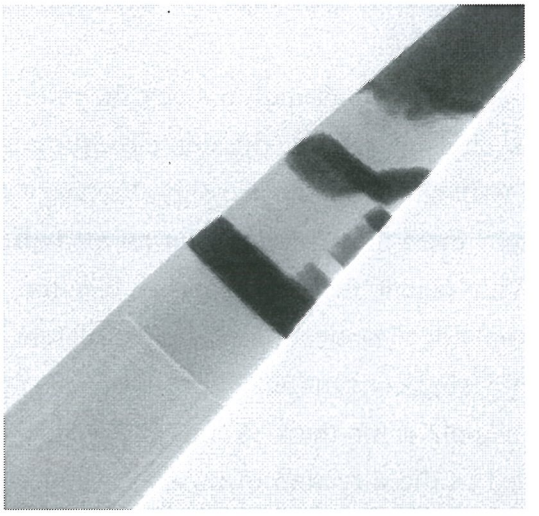

Fig.2 The rod-shape 3D TEM specimen with surface amorphous free for full 3D tomography

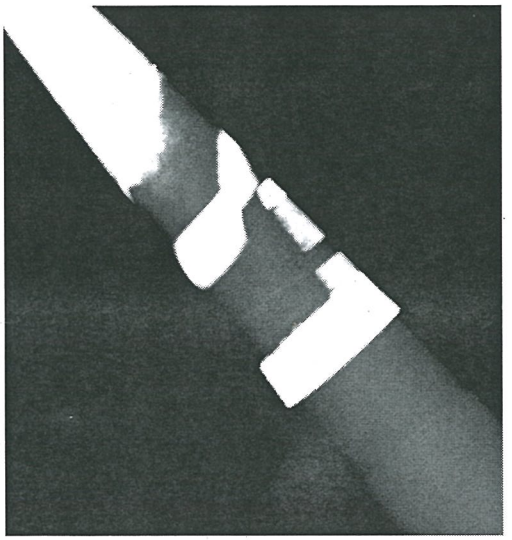

Fig.3 HAADF image of the rod-shape 3D TEM specimen.

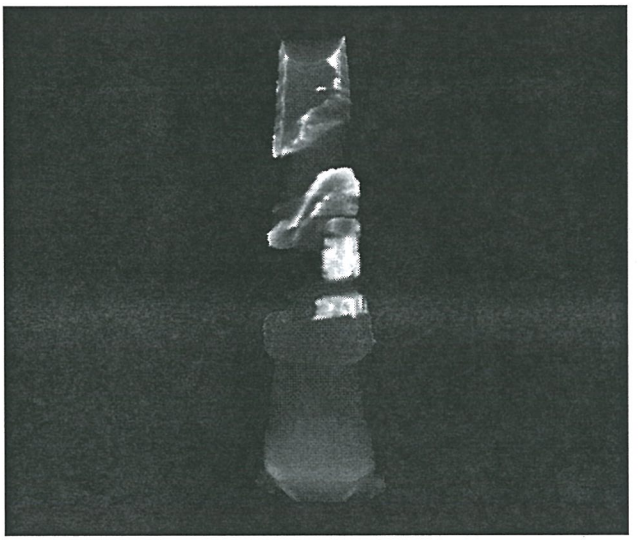

Fig.4 3D visualization of the rod-shape 3D TEM specimen.

Resolving the Individual Carbon Atoms of Graphene Monolayer by REW Software (利用 REW 軟體實現石墨烯的單個碳原子分辨)

LIN Fang[1] (林芳), JIN Chuan-Hong[2,3] (金傳洪)

1. 華南農業大學理學院，廣東 廣州 510642，中國

2. Nanotube Research Center, National Institute of Advanced Industrial Science and Technology (AIST), Tsukuba 305-8565, Japan

3. Department of Materials Science and Engineering, Meijo University, Tenpaku-ku, Nagoya 468-8502, Japan

單層原子厚度的二維石墨烯具有特殊的電子輸運現象，並有望在未來成為新的半導體晶體材料，因此是近幾年理論研究、實驗研究的熱點材料。石墨烯是由單個碳原子以六角網格結構構成的二維材料，通常在垂直於六角網格的方向上，以 ABAB...形式堆剁成較為穩定的多層石墨體材料。石墨體材料較易獲得，但是要製備出能夠在電子顯微鏡下觀測的石墨烯，則需要特殊的製備方法。在透射電鏡中，利用電子束對多層的石墨材料進行輻照減薄，成功地獲得了具有嚴格二維結構的石墨烯。通常，電鏡能夠在原子量級上成像，但所成的像實際上是原子列的投影像。當獲得了石墨烯後，就可以真正地實現單原子成像。

儘管實驗中採用了配備球差矯正器的 JEOL-2010F 型電鏡，但直接獲得單個碳原子的像仍較困難。其原因是：(1) 碳原子散射能力很弱，所採集的實驗像噪音很大；(2) 石墨烯對高能電子束敏感，電鏡的操作電壓僅為 80kV，電鏡解析度有所下降。針對這兩個問題，本文採用系列離焦像的重構方法：通過多張圖像資訊的疊加，重構出位於樣品後表面的波函數，從而提高高頻部分的圖像資訊，並獲得高品質的、能直接分辨單個碳原子的波函數相位像。圖 1 是獲得石墨烯後拍攝的高分辨像，單張像是由同條件的 30 幀的圖像疊加而成，單幀圖像的曝光時間為 0.5s。其中 A 區域為真空，B 區域為單層的石墨烯，其餘區域的石墨厚度大等於兩層。由於從單張的實驗像難以分辨到單個碳原子，9 張系列離焦的高分辨像被採集，供波函數重構使用。

在進行波函數重構之前，需要完成系列像的對中以及圖像拍攝條件的估算。所有這些像處理工作均在自編軟體 REW 下進行。軟體具有如下幾方面的重要功能：由結構類比 HRTEM 像、系列像的對中、最大似然法（MAL：maximum likelihood method）的系列離焦像重構以及 IWFR（iterative wave function reconstruction）的系列離焦像重構等功能。

圖 2 顯示的是與圖 1 方框標注區域一致的系列離焦像。這 9 張實驗像的球差係數為 0 mm，離焦量在-11 到-27nm 之間，離焦間隔為-2nm。圖像參數估算是利用類比像與實驗像的比對得到的，圖 3 所示的是與實驗像近似條件的模擬像。圖 4 所示為重構後的波函數的相點陣圖，從相位像上可直接清晰地分辨出單個碳原子。

本工作的意義在於：(1) 首次利用可控的電子束輻射辦法成功製備了石墨烯樣品；(2) 利用波函數重構的方法，從石墨烯上分辨出了清晰的單個碳原子，而非傳統實驗中獲得的碳原子列，波函數重構的方法將在未來石墨烯缺陷的研究上發揮重要作用；(3) 在 REW 軟體下可方便地實現像類比、系列離焦像的對中以及波函數重構等像處理操作，本文結果是使用 REW 軟體的一個實例*。

關鍵字：石墨烯；高分辨電子顯微像；REW 軟體；波函數重構；單原子分辨

*林芳感謝國家自然科學基金（No.60802003）及華南農業大學校長基金（No. 4900-K07417）的資助。金傳洪感謝 JSPS 和 International Balzan Foundation 的資助。

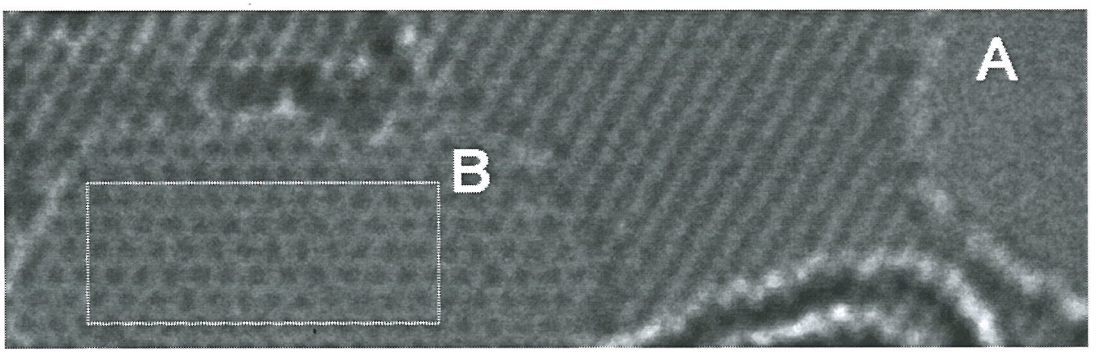

圖 1 石墨樣品的實驗高分辨像。實驗時的球差係數為 0 mm，離焦約為-11nm。A 區域為真空，B 區域為石墨烯。

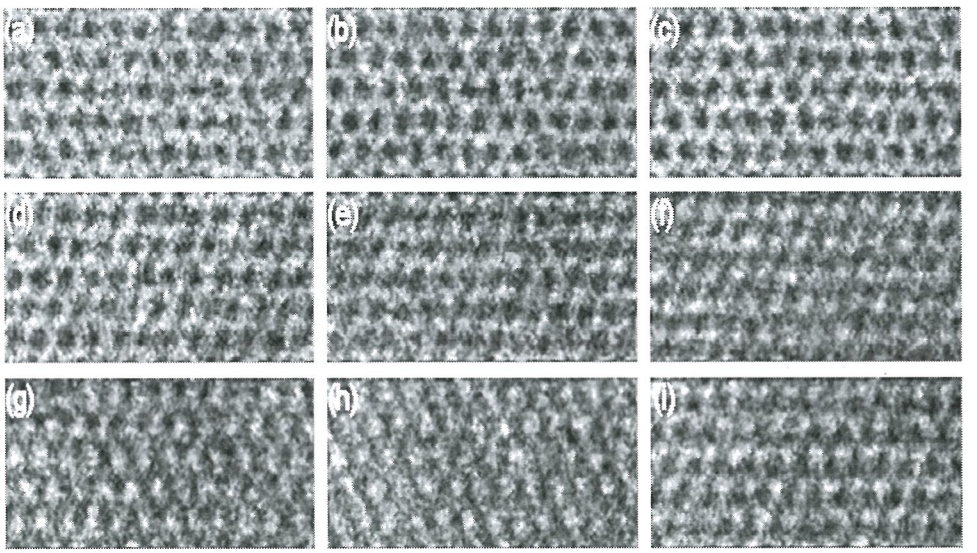

圖 2 石墨烯的系列離焦高分辨像。各子圖的離焦條件不同，對應著圖 1 方框標注區域。

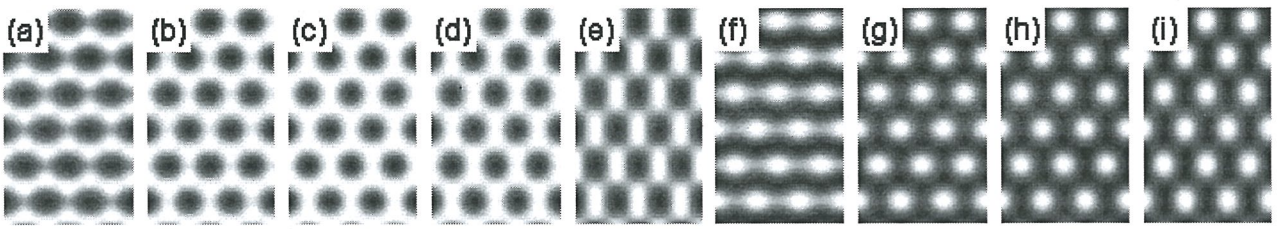

圖 3 石墨烯的模擬像。

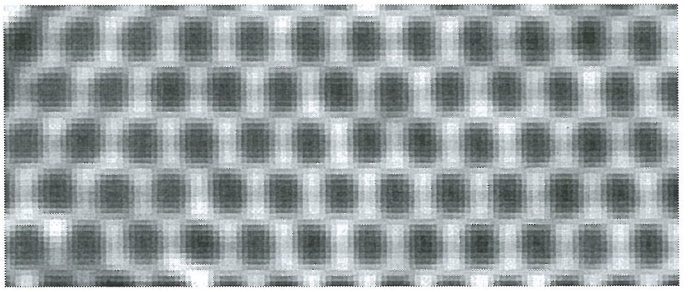

圖 4 利用系列離焦的 HRTEM 像重構得到的波函數的相點陣圖，從中可清晰分辨出單個碳原子。

Dynamic observation of wet specimen in Electron Microscopy or X-ray Microscopy using Wet-Cell

Tsu-Wei Huang (黃祖緯)[1], Cheng-His Chu[1], Cheng-Li Fan[1], Shu-Ting Jhuang[1], Gung-Chian Yin (殷廣鈐)[2], Fan-Gang Tseng (曾繁根)[1,3] and Fu-Rong Chen (陳福榮)[1]

[1]*Engineering and System Science Department, National Tsing Hua University(清華大學工程與系統科學系), Taiwan*

[2]*National Synchrotron Radiation Research Center(同步輻射研究中心), Taiwan*

[3]*Division of Mechanics, Research Center for Applied Science, Academia Sinica(中央研究院應科中心), Taiwan*

The purpose of this research is to develop a wet-cell sealing the specimen in a liquid environment to carry out living cells examination under X-ray or electron-beam Microscopy. This device fabricated with MEMS technology can be used in conventional TEM holder directly, need not install any hardware additional.

Transmission X-ray microscopy or electron microscopy provide very high resolution images (in nm) on material study. However, to apply these powerful tools for cell observation under their nature conditions, it is important to seal the wet bio-samples in a shallow chamber (wet-cell) with special shielding mechanism for reducing radiation energy loss, preventing liquid evaporation, and decreasing energy absorption during the observation in vacuum or atmosphere environment. As a result, there have been two type wet-cells developed in the past years, including open and close ones **[1]**. In the open type wet-cell, very complex aspiration/circulation system and tedious process were adopted to isolate the top and bottom open windows from vapor leakage **[2]**. This system has been employed to study microbial reduction of Cr(VI) in bacteria in a environment cell transmission electron microscope (EC-TEM) **[2]**. On the other hand, close type wet-cell was also developed by simply gluing two bulk micromachined chamber of silicon nitride membrane for cell study inside cryo scanning transmission X-ray microscope (CSTXM) **[3]** or TEM **[4]**. However, challenges including tedious alignment/package process, liquid leakage issue, and chamber charging/heating problems were still left unresolved. As a result, a new type MEMS wet-cell is developed for circumvent the aforementioned issues.

The design of the MEMS wet-cell is shown in Fig. 1. This wet-cell combined two complementary compartments fabricated by bulk micromachining process, which allows self alignment for chamber engagement and gap control (in μm range) between two 50 nm thick silicon nitride membrane, very important for X-ray or electron beam penetration (Fig. 2). To reinforce the membrane and release the charge or heat generated by the X-ray or electrons and absorbed on the wet-cell, metal grids were fabricated on the membrane surface. Due to elongated sealing path on the inclined surfaces between two frames and glue stop mechanism at the end of the incline surface, the MEMS wet-cell can provide better sealing capability without liquid leakage for more than 24 hours and easier alignment/package process than those of the prior works.

To verify the performance of the wet-cell, 100nm polystyrene beads (PBs) and 500 nm silver nano particles (SNPs) were first suspended in DI water and then dropped into the wet-cells. The

images were acquired under 100 keV in TEM and SEM for PBs and SNPs, respectively, as shown in Fig. 3 and 4. The low contrast in Fig. 3 was resulting from the light atoms in PBs, while Fig. 4 gave a very clear image of clustered SNPs. Brownian motion was also observed dynamically for 500 nm gold nano particles inside TXM (Fig. 5), and cell viability test was also performed for living cell in wet-cell inside TXM environment for at least 60 seconds under 8keV X-ray radiation. Fig. 6 shows the optical images of the cell before and after the radiation and reveal reasonable cell living condition.

References

1. "In situ studies of gas – solid reactions," Audrey M. Glauert, Practical Methods in ELECTRON MICROSCOPY, 9, 239 (1981).
2. "In-situ Environmental Cell - Transmission Electron Microscopy Study of Microbial Reduction of Chromium(VI) using Electron Energy Loss Spectroscopy," Tyrone L. Daulton, Microscopy and Microanalysis, 7, 470 (2001).
3. "Sealed Cell For In-Water Measurements," K. Kaznacheyev, X-RAY MICROSCOPY: Proceedings of the VI International Conference. AIP Conference Proceedings, 507, 395 (2000).
4. "Novel microchip for in situ TEM imaging of living organisms and bio-reactions in aqueous conditions," Kuo-Liang Liu, Chien-Chen Wu and Tri-Rung Yew, Lab on a Chip, 8, 1915 (2008).

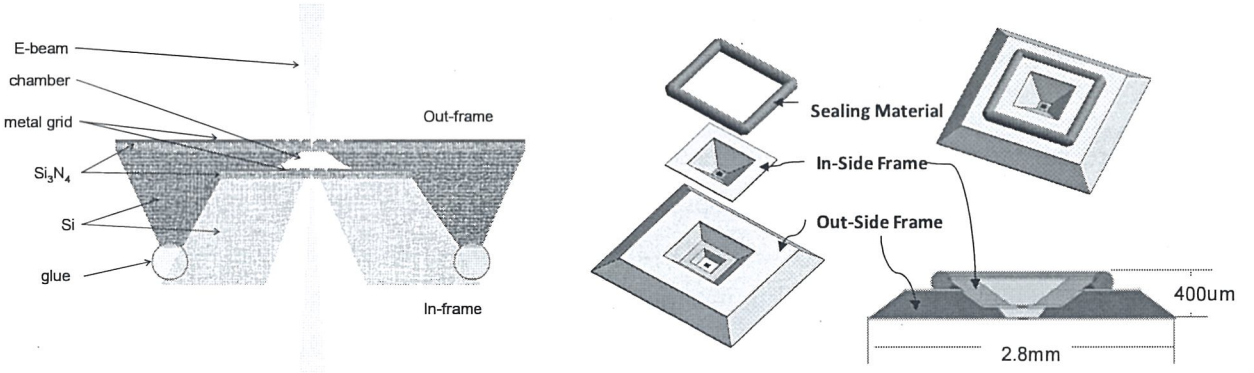

Figure 1. Schematics of the WetCell structure

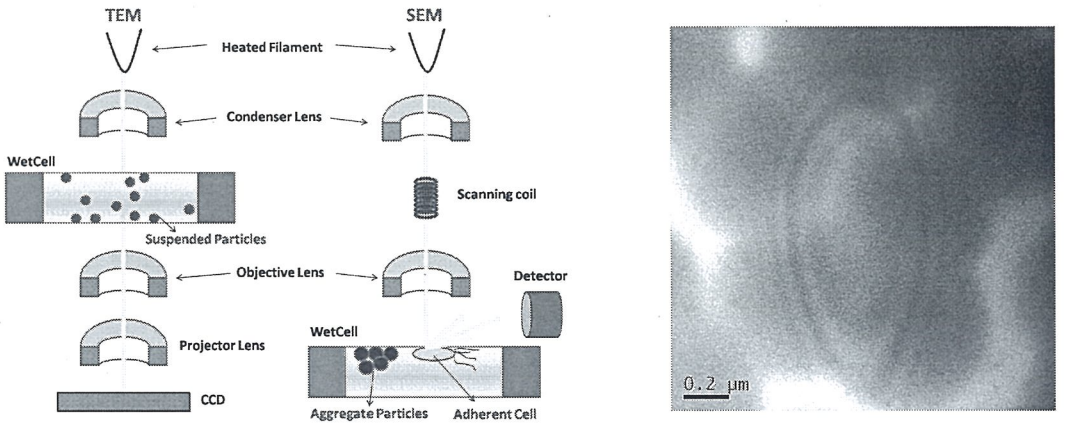

Figure 2: Diagram of the WetCell application in TEM and SEM

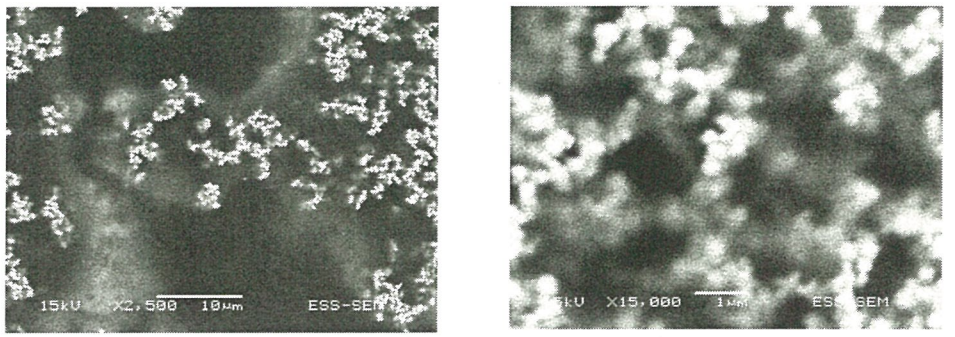

Figure 4. SEM Image of 500nm Ag particles sealed in wet-cell.

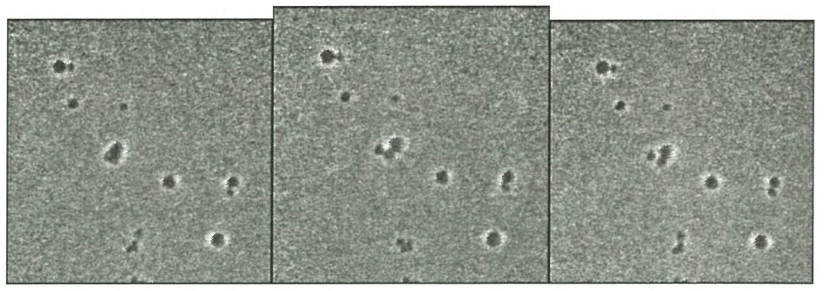

Figure 5. TXM Images of the Brownian movement of 100nm PS and 500nm gold particles mixed solution.

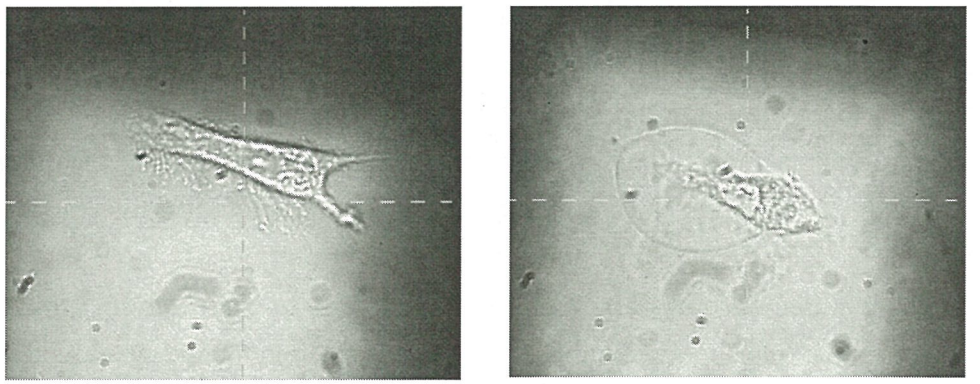

Figure 6. Optical Microscopy Images of HeLa cell before (left) and after the 8keV X-ray radiation (right) for 60s inside wet-cell.

Spin Detection with a Low Temperature Scanning Tunneling Microscope[1]
(單自旋態的探測)

XUE Qi-Kun (薛其坤)

(Department of Physics, Tsinghua University, Beijing 100871 , P R China)
(清華大學物理系，北京 100871，中國)

A magnetic impurity in a superconductor breaks the time-reversal symmetry and induces low energy bound states in the superconducting gap **[1~3]**. Probing the response of superconductors to magnetic impurities has been one of the important methods for revealing the nature of the superconducting pairing **[4]**. On the other hand, the intra-gap states offer a sensitive mechanism to detect the spin states of the magnetic impurities. The magnetic impurity-induced bound states in a conventional superconductor were previously observed in a scanning tunneling microscopy (STM) study **[5]**. The tunneling spectra in the experiments reveal an enhancement of the density of the excitations within the superconductor's gap near the magnetic adsorbates. However, it remains challenging to make use of these intra-gap resonances in analyzing the spin states of adsorbates, in part because of the insufficient energy resolution. For example, the splitting of the intra-gap states induced by magnetic coupling between impurities is typically one order of magnitude smaller than the superconducting gap and cannot be easily resolved by an STM.

In this work, tunneling spectra for individual atoms and dimers of Mn and Cr adsorbed on superconducting Pb thin films (see the schematic in Fig. 1(a) and Fig. (b)) were measured by a sub-Kelvin temperature scanning tunneling microscope. Multiple-resonance structures within the superconducting gap on the adsorbates were resolved and interpreted as the magnetic impurity induced bound states associated with different scattering channels (Figs. 1(c)-(f)) **[6]**.

The experiment demonstrates a spectroscopic approach to characterizing the spin states of magnetic structures and exploring the competition between superconductivity and magnetism at the nanometer scale. The present method can be applied to various systems, ranging from transition metals to rare earths, on a superconductor, which is not necessarily to be Pb, as long as the local magnetic moment of the adatom is not quenched and can create bound states in the superconducting gap. We expect that the present experiments will also motivate further theoretical studies and stimulate more measurements, such as on the quantum phase transitions associated with multiple impurities

The work was carried out in collaboration with Xi Chen, Xucun Ma, Jinfeng Jia, S. H. Ji, Y. S. Fu, R. Wu, T. Zhang, P. Cheng, and Wenhui Duan, under financial supports from National Science Foundation and Ministry of Science and Technology of China.

E-mail: qkxue@mail.tsinghua.edu.cn

References

1. Yu L. Acta Phys Sin，1965，21：75.
2. Shiba H. Prog Theor Phys，1968，40：435.
3. Rusinov A I，Eksp Zh. Teor Fiz，1969，56：2047[Sov Phys JETP，1969，29：1101].
4. Balatsky A V，Vekhter I，Zhu J X. Rev Mod Phys，2006，78：373.
5.Yazdani A，Jones B A，Lutz C P，et al. Science，1997，275：1767.
6. Ji S H，et al. Phys Rev Lett，2008，100：226801.

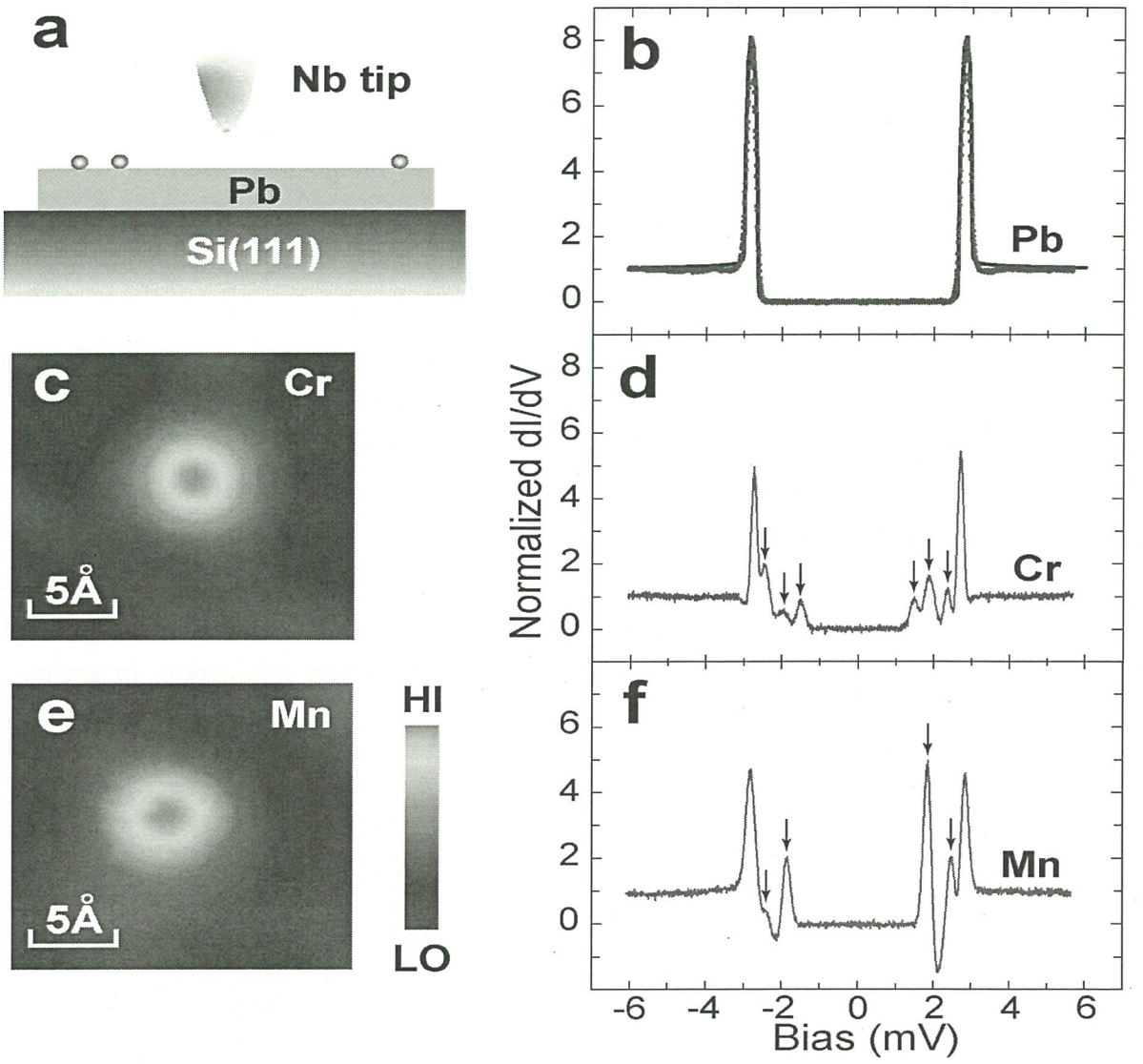

Fig. 1 Single magnetic atom induced bound states in the superconducting gap of Pb thin flms. (a) Schematic and (b) differential conductance of the S-S tunneling junction. (c)-(f) Topographic images and normalized dI/dV spectra of single Mn and Cr atoms at 0.4K. For a Mn atom (c), the four peaks at energies of -2.35 meV, -1.84 meV, +1.86 meV and +2.47 meV, correspond to the first two angular momentum channels, respectively. For a Cr atom (e), the bound states are evidently different and six peaks (f) were detected at energies of -2.44 meV, -1.92 meV, -1.49 meV, +1.49 meV, +1.89 meV and +2.38 meV, respectively.

Probing Bright and Dark Surface-Plasmon Modes in Individual and Coupled Au Nanoparticles Using an Electron Beam

M.-W. Chu (朱明文)[1], V. Myroshnychenko[2], C. H. Chen (陳正弦)[1], J.-P. Deng (鄧金培)[3], C.-Y. Mou (牟中原)[4], and F. Javier García de Abajo[2]

[1] *Center for Condensed Matter Sciences, National Taiwan University, Taipei 106, Taiwan(台灣大學凝態中心)*

[2] *Instituto de Óptica CSIC and Unidad Asociada CSIC-Universidade de Vigo, Serrano 121, 28006 Madrid, Spain*

[3] *Department of Chemistry, Tamkang University, Taipei County 25137, Taiwan*

[4] *Department of Chemistry, National Taiwan University, Taipei 106, Taiwan*

The rich structure of bright and dark surface-plasmon (SP) modes localized in individual and coupled Au nanoparticles is unveiled by electron energy-loss spectroscopy (EELS) performed in a scanning transmission electron microscope (STEM) equipped with a monochromator [1], STEM-EELS. Spatially-resolved STEM-EELS maps of SP modes in the ~1.5-2.5 eV range (wavelengths ~500-800 nm), collected for individual nanorods, coupled nanorod dimers, and touching nanosphere dimers, are in excellent agreement with theory. SP maps constructed from the spatially and spectrally resolved EELS signals are shown to mimic rather well the near fields calculated for external illumination in the case of bright SP modes (i.e., those coupling to external light). Dark SP modes that cannot be excited by optical means are also found (see FIG. 1), and our electron probing technique provides further insight into their corresponding spatial distribution and symmetry, which are not accessible to any other existing techniques. Our results initiate the study of a whole set of new dark SP modes that should become a source of new applications in sensing and microscopy, but have escaped experimental scrutiny so far.

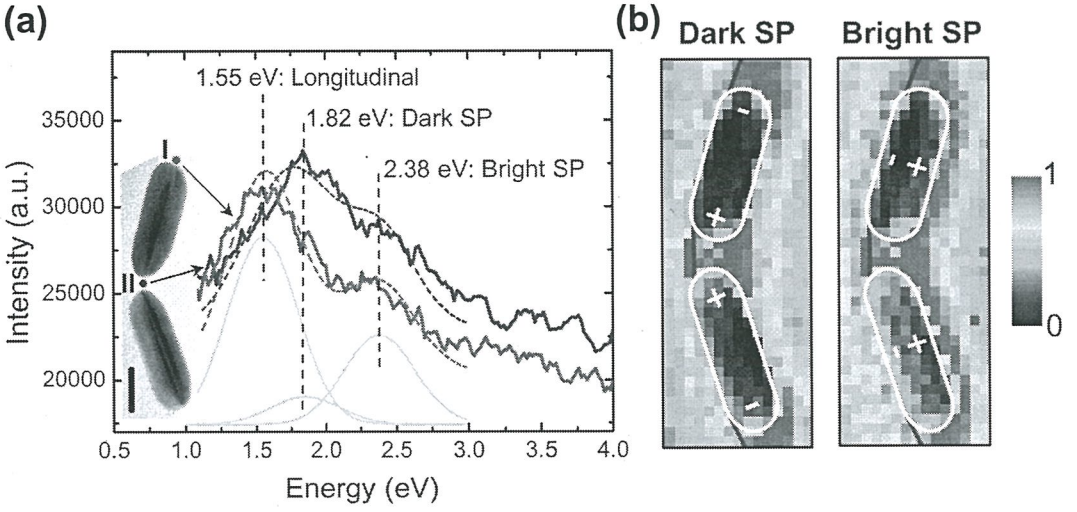

FIG. 1. (a) Experimental STEM-EELS excitations of bright longitudinal, dark, and bright SP modes in a coupled nanorod dimer (scale bar, 25 nm; inter-rod coupling gap, 8 nm). (b) SP maps constructed from STEM-EELS excitation intensities. Reproduced from **[1]**.

Reference

[1] M.-W. Chu *et al.*, *Nano Lett.* 9 (2009) 399.

Surface Exciton Polaritons in Individual Au Nanoparticles in the Far-UV Spectral Regime

M.-W. Chu (朱明文)[1], C. H. Chen (陳正弦)[1], F. Javier García de Abajo[2], J.-P. Deng (鄧金培)[3], and C.-Y. Mou (牟中原)[4]

[1] *Center for Condensed Matter Sciences, National Taiwan University, Taipei 106, Taiwan(台灣大學凝態中心)*

[2] *Instituto de Óptica CSIC and Unidad Asociada CSIC-Universidade de Vigo, Serrano 121, 28006 Madrid, Spain*

[3] *Department of Chemistry, Tamkang University, Taipei County 25137, Taiwan*

[4] *Department of Chemistry, National Taiwan University, Taipei 106, Taiwan*

Interests in surface excitations of Au are mainly focused on the well-known surface plasmon (SP) in the visible spectral regime **[1]**. The existence of surface exciton polaritons (SEPs) is believed to be pristine to the spectral regimes showing strong excitonic absorptions **[2]**. The presence of SEPs in far-UV in Au (≥ 10 eV), where the optical and electronic properties of Au are dominated by broad interband transitions that display characters of weak and diffused excitonic oscillator strengths, is not expected and has never been discussed. Reexamining Ref. 2 and using electron energy-loss spectroscopy (EELS) with a 2-Å electron probe in aloof (optical near-field) setup and energy filtered mapping (FIG. 1), we firmly establish the existence of SEPs in individual Au nanoparticles in the far-UV spectral regime **[1]**. These results indicate that SEPs indeed can be excited in weak excitonic onsets in addition to their general believing for the sharp excitonic oscillations. Our experimental observations are further confirmed by the theoretical calculations of EELS spectra. The unmatched spatial resolution (2 Å) of the electron spectroscopy technique enables an investigation of individual nanomaterials and their surface excitations in aloof setup. The SEPs in individual Au nanoparticles thus represent an example of surface excitations of this type beyond the visible spectral regime and could stimulate further interests in SEPs in various materials and applications in novel plasmonics and nanophotonics at high energies via manipulations of the associated surface near fields.

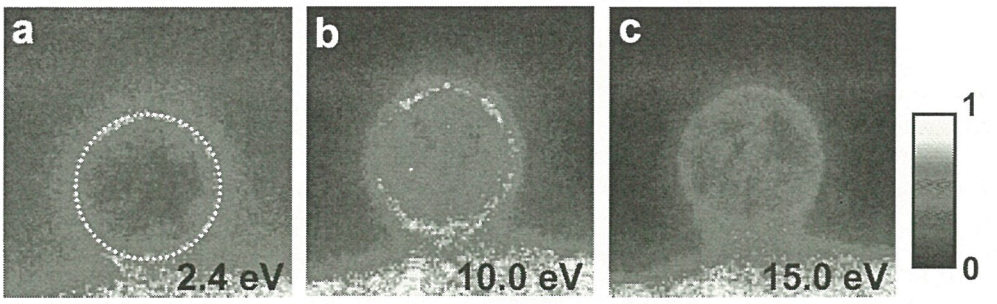

FIG. 1. (a) EELS mapping of SP near fields in an individual Au nanoparticle (radius, 13 nm; dotted circle, the projected surface of the nanoparticle). The intensity maximum encircling the surface is well known to signify the surface-excitation nature, which is also observed in (b) and (c) for SEP excitations in Au in the far-UV spectral regime (10.0 and 15.0 eV, respectively). Reproduced from **[1]**

References

[1] M.-W. Chu *et al.*, *Phys. Rev. B* 77 (2008) 245402.

[2] F. Yang *et al.*, *Phys. Rev. Lett.* 64 (1990) 559.

Probing Surface Plasmons in Individual Ag Nanoparticles in the Ultra-violet Spectral Regime

Ming-Wen Chu (朱明文)[1], Pradeep Sharma[2,3,4], Ching-Pin Chang (張景斌)[1,5], Sz-Chian Liou (劉思謙)[1], Kun-Tong Tsai[2], Juen-Kai Wang (王俊凱)[1,2], Yuh-Lin Wang (王玉麟)[2,4], and Cheng Hsuan Chen (陳正弦)[1,2,4]

[1]*Center for Condensed Matter Sciences, National Taiwan University, Taipei, Taiwan (台灣大學凝態中心)*

[2]*Institute of Atomic and Molecular Sciences, Academia Sinica, Taipei 106, Taiwan*

[3]*Taiwan International Graduate Program, Academia Sinica, Taipei 106, Taiwan*

[4]*Department of Physics, National Taiwan University, Taipei 106, Taiwan*

[5]*Department of Materials Science and Engineering, National Taiwan University, Taipei 106, Taiwan*

The previous investigations of surface plasmons in Ag were largely focused on their excitations in the visible spectral regime. Using scanning transmission electron microscope with an electron beam of 0.2 nm in conjunction with electron energy-loss spectroscopy, we spectrally and spatially probe the surface plasmons in individual Ag nanoparticles (~30 nm), grown on Si, in the ultra-violet spectral regime [1]. The nanomaterials show respective sharp and broad surface-plasmon resonances at ~3.5 eV (~355 nm) and ~7.0 eV (~177 nm), and the correlated spectral calculations established their multipolar characteristics. The near-field distributions of the surface plasmons on the nanoparticles were also mapped out (Fig. 1), revealing the predominant dipolar nature of the 3.5-eV excitation with obvious near-field enhancements at one end of the nano-object. The unveiled near-field enhancements are of potential plasmonics and molecular sensing applications.

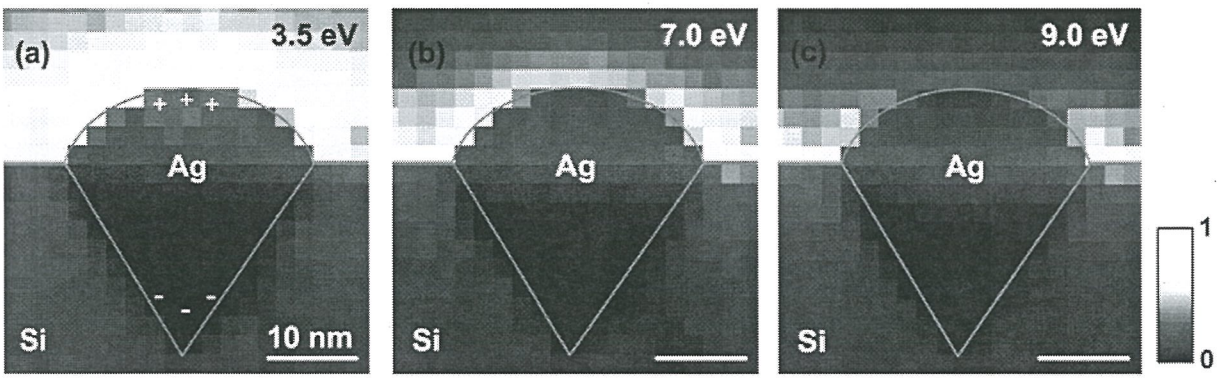

FIG. 1. STEM-EELS mapping of (a) 3.5-, (b) 7.0-, and (c) 9.0-eV surface resonances in the material with the contrast maxima signifying the most prominent excitation locations for the given spectral features. Color scale bar, the linearly normalized image contrast.

References

[1] M.-W. Chu *et al.*, Nanotechnology 20, 235705 (2009).

Surface Exciton Polariton in Monoclinic HfO_2: Electron Energy-Loss Spectroscopy Study

S. C. Liou (劉思謙)[1], M.-W. Chu (朱明文)[1], Y. J. Lee (李毅君)[2], M. Hong (洪銘輝)[2], J. Kwo (郭瑞年)[3], and C. H. Chen (陳正弦)[1]

[1] *Center for Condensed Matter Sciences, National Taiwan University, Taipei 106, Taiwan(台灣大學凝態中心)*

[2] *Department of Materials Science and Engineering, National Tsing Hua University, Hsinchu 300, Taiwan*

[3] *Department of Physics, National Tsing Hua University, Hsinchu 300, Taiwan*

We have recently revisited the conventional understanding in surface exciton polaritons (SEPs) and established their excitations in materials displaying an otherwise weak excitonic oscillator strength **[1,2]**. The existence of SEPs is thus not limited to materials with a sharp excitonic absorption **[3]**, and the collective nature of SEPs upon weak excitonic absorption originates from oscillations of loosely defined delocalized excitons, which are correlated with broad interband transitions in materials (e.g., FIG. 1). The weak excitonic absorption and the associated interband transitions can be observed in practically all semiconductors and insulators above the band gap, suggesting the existence of SEPs in the materials. Using scanning transmission electron microscope (STEM) in conjunction with electron energy-loss spectroscopy (EELS) with an ultimate spatial resolution of 0.2-2 nm, we have firmly established the existence of SEP (~7.5 eV) in monoclinic, insulating HfO_2 upon the weak excitonic excitation, ~6.2 eV, above the optical band gap (~5.1 eV), FIG. 1. Interband transitions can be found in almost all semiconductors and insulators above the band gap, and this work could stimulate future interests in SEPs in various materials, where the SEP excitations may find unexpected optics applications via manipulations of their surface wave fields analogous to surface plasmons for plasmonics.

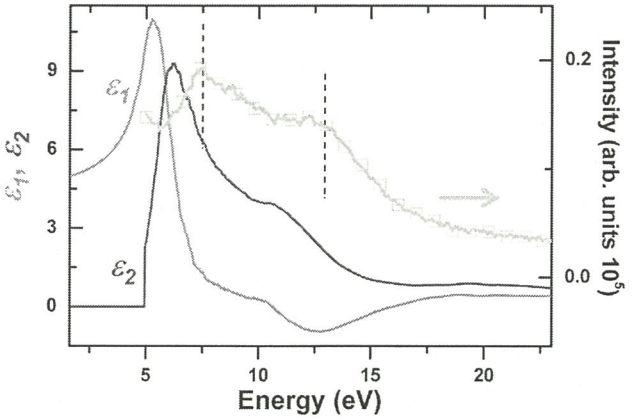

FIG. 1. The real (ε_1) and imaginary parts (ε_2) of the complex dielectric function of monoclinic HfO_2, displaying a broad, weak excitonic absorption (maximum in ε_2) at ~6.2 eV above the optical band gap. SEP onset at ~7.5 eV and that for surface plasmon (SP) at ~13.4 eV are indicated by dashed lines. Gray, STEM-EELS excitations of SEP and SP taken at 4 nm from the surface of an HfO_2 bulk ceramic.

References

[1] M.-W. Chu *et al.*, *Phys. Rev. B* 77 (2008) 245402.

[2] S. C. Liou *et al.*, *New Journal of Physics*, revised.

[3] F. Yang *et al.*, *Phys. Rev. Lett.* 64 (1990) 559.

Micro-dynamics of nano-particle in liquid in Transmission X-ray Microscope

Gung-Chian Yin(殷廣鈐)[1], HUANG, Tsu-Wei(黃祖緯)[2] and CHEN, Fu-Rong(陳福榮)[1,2]

1.National Synchrotron Radiation Research Center(同步輻射研究中心), 101 Hsin-Ann Road, Hsinchu 30076

2. Department of Engineering and System Science National Tsing Hua University(清華大學工程與系統科學系) Hsinchu, 30013

The transmission x-ray microscope (TXM) has been subsequently improved since its first invention in 1970s. The resolution of TXM was close to tens of nanometer by the great progress of the zone plate fabrication **[1]** and the other imaging mode has been develop since a capillary based condenser **[2]** was used in TXM with Synchrotron source. **[3,4]**

Transmission x-ray microscopy (TXM) is able to directly observe the micro-dynamics of nano-scaled particles suspended in a glassy forming liquid. In order to content the liquid and wet samples for TXM, we have designed and fabricated an environmental cell which can be used under normal air pressure and have high penetration depth for 8 to 11 keV x-ray. This environmental cell in TXM allows the sample can be visualized in the liquid phase and stable temperature.

The nano-particles in glycerin filled in the wet cell are used to perform the motion observation. The image is captured with 0.5 seconds exposure time in our TXM system, however, as shown in the Fig.1. The trajectories of the nano-particles between each frame can be traced; therefore the motion of the particles can be analyzed. Through measuring correlation of the collective behavior and local bond-orientation order, we identify the relation of dynamic heterogeneity and slow dynamics. A temperature control device will be implemented in near future to help this study.

References

1. Yu-Tung Chen, et al. Nanotechnology **19** (2008) 395302
2. G. C. Yin ,et al. Appl. Phys. Lett. **88** , 241115 (2006)
3. U. Neuhäusler,et al. J. Phys. D: Appl. Phys. **36** 79 (2003)
4. G. C. Yin, et al. PROCEEDINGS OF SPIE **6317** , 631703 (2006)

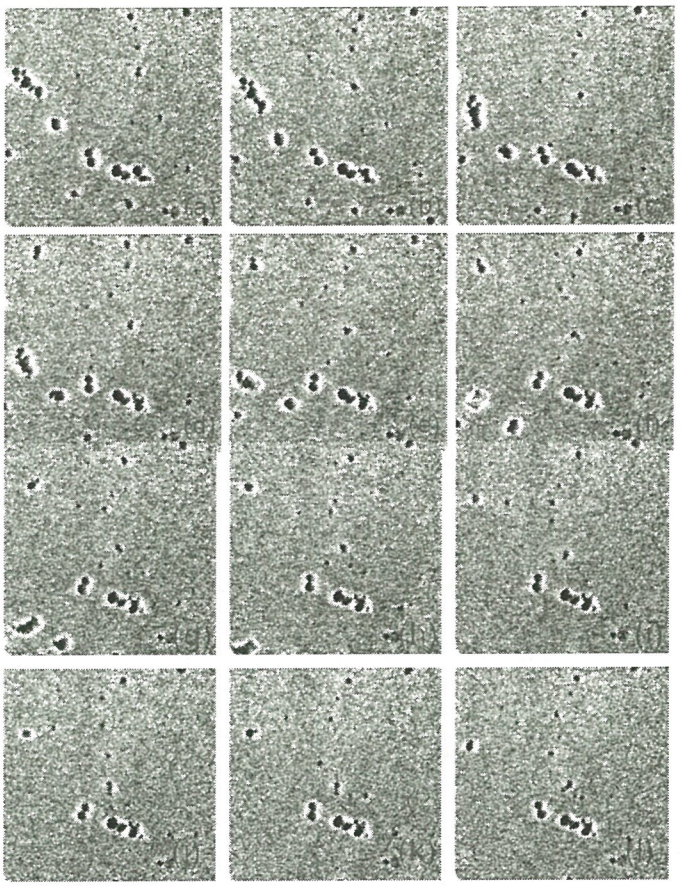

Fig. 1: Image (a) to (l) show the typical snapshots of real image with increasing time frames- (a) 0 sec (b) 10 sec (c) 20 sec (d) 30 sec (e) 40 sec (f) 50 sec. (g) 60sec (h) 70 sec (i) 80 sec (j) 90sec (k) 100 sec (l) 110sec. The gold nano-particles are in the glycerin. The photon energy is 8 keV.

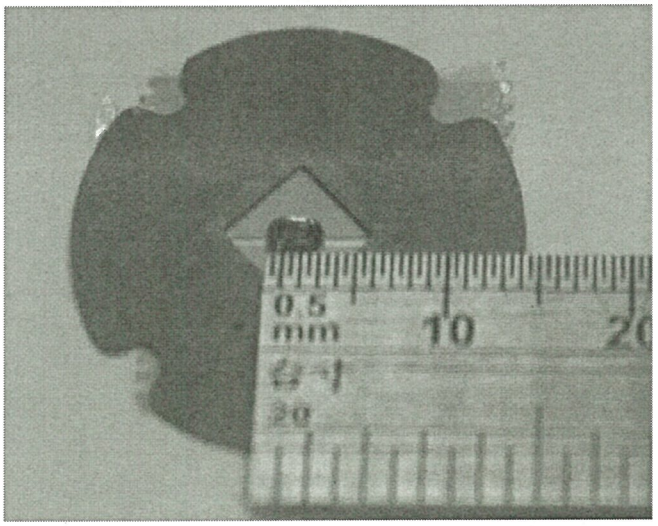

Fig.2 : The outlook of the wet cell for TXM. The transparent region is 1300 μm × 300 μm. The thickness –the distance between silicon nitride is 85 μm.

The Influences of Reactive Conditions on the Formation of Hydrothermal $BaTiO_3$ Nanoparticles and Their Atomic-Scale Surface Structures
(水熱反應條件對 $BaTiO_3$ 納米晶的形成影響及其原子尺度表面結構)

ZHU Xin-hua(朱信華)，ZHU Jian-min(朱健民)，SONG Ye(宋 曄)，ZHOU Shun-hua(周舜華) ，LIU Zhi-guo(劉治國)

National Laboratory of Solid State Microstructures, Department of Physics, Nanjing University, Nanjing Jiangsu 210093, P R China

(南京大學物理系固體微結構物理國家重點實驗室，南京大學物理系，江蘇 南京 210093，中國)

$BaTiO_3$陶瓷具有良好的介電特性，在多層陶瓷電容器(multilayered ceramic capacitors，MLCCs)方面具有重要的應用價值。隨著微電子通訊技術的發展，人們對器件的微型化要求越來越高，這就要求用於製備新一代MLCCs 器件的$BaTiO_3$陶瓷粉料具有高純、超細 (幾十個納米)、粒徑分佈窄等特性。$BaTiO_3$陶瓷粉體的傳統製備方法是固相合成，但這種方法製備的粉體顆粒粗細不均勻且易團聚，無法滿足新一代MLCCs 器件的微型化要求。溶液化學法是製備超細粉體的一種重要方法，其中水熱法最適合於製備尺寸均勻、結晶度高的納米粉體。

本文採用水熱法製備了$BaTiO_3$納米晶，並研究了不同水熱反應條件對$BaTiO_3$納米晶的尺寸和形貌形的影響（見圖1，圖2），並揭示其原子尺度的表面結構。結果表明採用Ba/Ti摩爾比較大的前驅體容易獲得立方狀大尺寸的$BaTiO_3$納米晶體；而採用乙二醇作為水熱反應介質可獲得小尺寸弱團聚的$BaTiO_3$納米晶（與純水溶液或水-乙二醇的混合液相比較）。立方狀或矩形狀的$BaTiO_3$納米晶外表面被{100}晶面所包圍，而{110}晶面條紋與納米晶體的邊界相交呈45°角。在粗糙的$BaTiO_3$納米晶表面，經常可觀察到臺面臺階扭折（terrace-ledge-kink）的表面結構，臺面（terrace）和臺階 (ledge) 位於{100}晶面。由於表面結構的重構，{110}晶面通常被分解成由許多小的{100}晶面相連接的扭折結構。而在球狀的$BaTiO_3$納米晶邊緣，沒有觀察到表面臺階結構（圖3，圖4）。

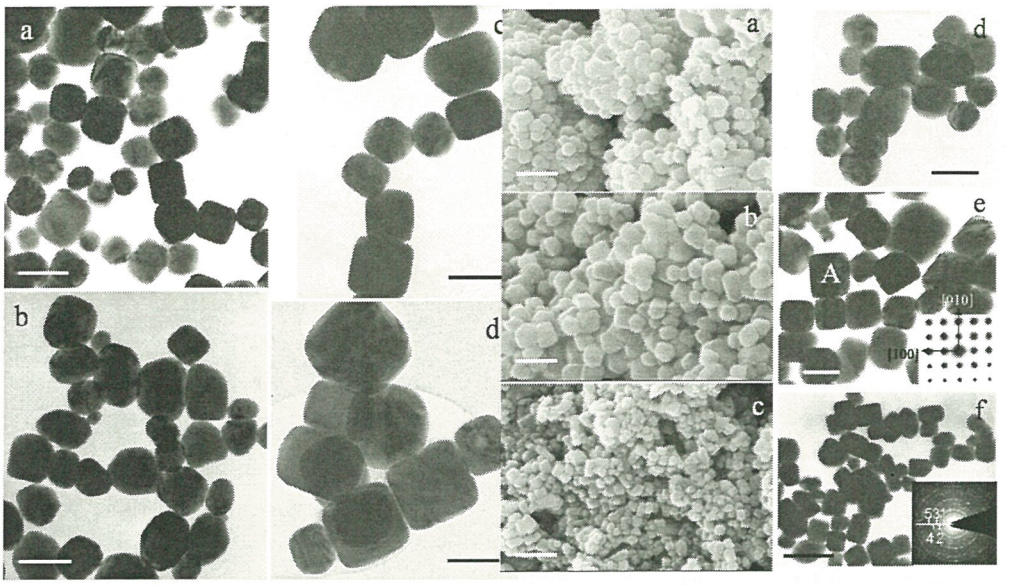

圖 1 採用不同 Ba/Ti 摩爾比的前驅體水熱合成 $BaTiO_3$ 納米晶體的 TEM 照片。 樣品 a：BT1 (1:1)；b：BT2 (2:1)；c：BT3 (3:1)；d：BT4 (4:1) (Bar = 200 nm)。

圖 2 不同水熱反應介質條件下合成 $BaTiO_3$ 納米晶的 SEM (a~c)和 TEM (d~f) 片(前驅體的 Ba/Ti 摩爾固定為 3:1)。圖片(a, d)：純水溶液(BT5 樣品)；(b, e)：-乙二醇的混合液（體積比 1:1）(BT3 樣品)； (c, f)：純乙二醇 (BT6 樣品)。 e 中的插圖為單個 BT 晶粒（用字母 A 標注）的[001]帶軸選區電子衍射花樣；f 中的插圖為樣品 BT6 多個 BT 納米晶的選區電子衍射花樣，前五個多晶衍射的面指數分別標定為(100), (110), (111), (200), 和 (210)。a~c：SEM 照片：Bar =500 nm；d~f：TEM 照片：Bar = 200 nm。

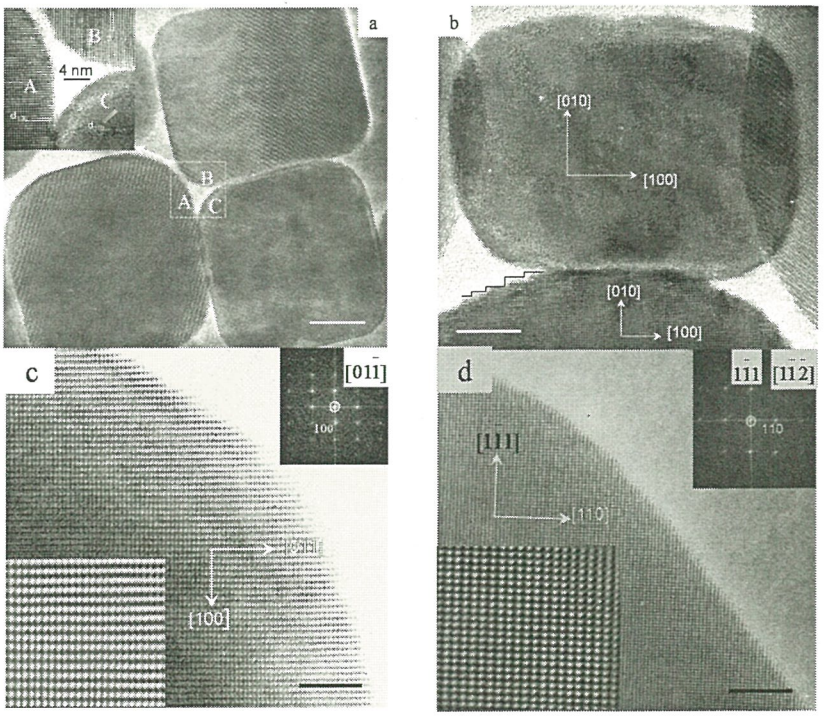

圖 3 樣品 BT1 不同形貌的納米晶高分辨 TEM 照片。圖片 a：立方體 (Bar = 20 nm)；b：長方體 (Bar = 10 nm)；c，d：球形 (Bar = 4 nm)。

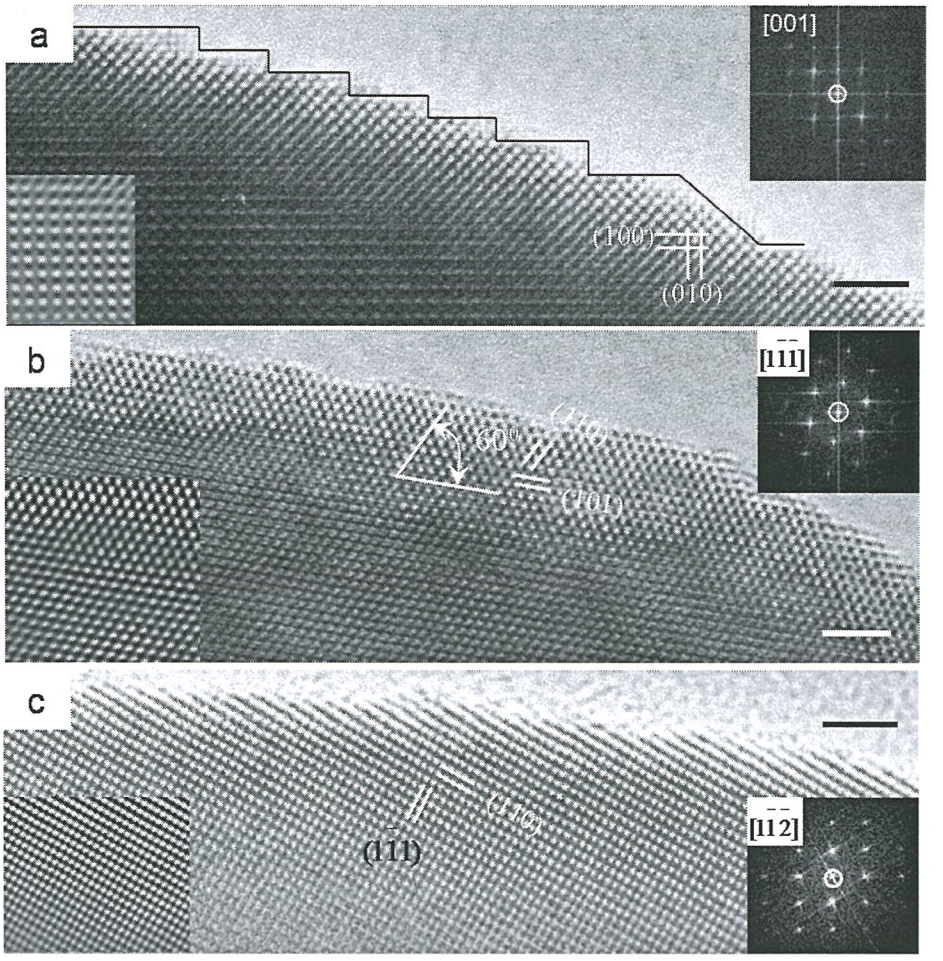

圖 4 不同方向觀察的三個晶粒（樣品 BT3）的高分辨 TEM 照片。圖片 a：[001]；b：[$\bar{1}\bar{1}\bar{1}$]；c：[$\bar{1}\bar{1}2$] 方向；Bar = 2 nm。

Microstructure Characterization and Optical Properties of Au-based Multi-Component Heterostructrue Nanoparticles
(Au 基多組元異質納米顆粒的顯微結構表徵及光學特性)

ZHANG Shu-Yuan(張庶元)，ZENG Jie(曾 傑)，LIN Yue(林 岳)，WANG Xiao-Ping(王曉平)

(Hefei National Laboratory for Physical Science at Microscal, University of Science and Technology of China, HeFei Anhui 230001，P R China)

（中國科學技術大學微尺度國家實驗室，安徽 合肥 230001，中國）

多組元耦合型納米晶粒，特別是金屬基納米異質結構，近年來已引起國際學術界的廣泛關注。本文探索了 Au 基異質型納米顆粒的製備方法，製備出多種二組元和三組元的 Au 基異質型納米顆粒。同時，對試樣的光學特性進行了研究。

圖 1（A~D)給出 4 幅 TEM 圖像，分別為滴加不同數量 Au 源溶液(比例為 1：2：3)獲得的 3 個 CdSe-Au 試樣（A~C)。由圖可見，隨 Au 源溶液的增加，CdSe-Au 中 Au 顆粒部分逐漸增大。圖 1D 為單個異質納米顆粒的 HRTEM 像，Au 顆粒沿 CdSe 表面生長，其取向關係為 Au{111}//CdSe{101}。基於試樣製備，TEM 和 HRTEM 的觀測，CdSe-Au 異質納米結構的形成過程可歸結為相分離和介面反應機制。該機制為 Au 基異質納米結構的製備提供了一個較為普適的方法。採用這一方法，製備了 PbSe-Au, FePt –Au, Cu_2O-Au 和 FePt-CdS-Au 等多種異質納米結構。

圖 2 給出 FePt-Au(A), PbSe-Au(B，C)和 Cu_2O-Au(D~F)三種異質納米結構的電子顯微像。從圖像中可以看出，Au 顆粒在 PbSe 顆粒上形貌酷似“帽子”，以多晶狀態為主。FePt –Au 異質納米顆粒的形貌呈“葫蘆”狀，Au 顆粒尺寸大於 FePt 顆粒，也以多晶狀態存在。Cu_2O-Au 的形態介於“帽形”和“葫蘆”之間，Au 顆粒大多為單晶。在 Cu_2O-Au 異質納米顆粒中，發現有相當數量的 Cu_2O 納米顆粒上長出 2 個和 3 個 Au 顆粒的現象（圖 2D，E)，分析認為這可能與 Cu_2O 納米顆粒表面曲率的不對稱性有關。表面曲率半徑較小的地方，會因尺寸效應形成活性很高的催化區域，更容易使 Au 核形成長大。基於這一設想，製備了方塊形 Cu_2O 納米顆粒為前驅物，進而製備 Cu_2O-Au 異質納米顆粒。實驗結果表明，Cu_2O 納米晶的每個角上幾乎都形成了一個很小的 Au 顆粒（圖 2F)，這一結果證實了本文作者的假設。作為一個擴展，以 FePt-CdS 異質納米顆粒為前驅物，還製備出三組元的 FePt-CdS-Au 異質納米結構。

圖 3 給出 CdSe-Au 異質納米顆粒的 XPS 價帶譜(A)、吸收光譜(B)和 PL 譜(C)，從試樣 a-d, Au 的組分逐漸增加。圖 3(A)中譜線 E 對應 2 nm 的 Au 顆粒試樣，作為分析的參考。從譜中可見，隨 Au 顆粒長大，試樣 a-d 中的 Cd 4d 峰相對降低，而 Au 5d 雙峰逐漸增強，展現了 CdSe-Au 異質結構中兩種組元相互耦合調控的效應。從吸收光譜(圖 3B)中可以看出，純量子點 CdSe 樣品 a，其長波段是典型的半導體零吸收特性，在 555 nm 附近出現第一個吸收峰。隨 CdSe 量子點上生長的 Au 顆粒長大，吸收光譜在長波段逐漸表現出金屬吸收特徵，而 CdSe 顆粒的第一吸收峰也逐漸變得平緩，這體現了金屬和半導體顆粒耦合之後的二元化吸收光譜特性。螢光光譜(圖 3C)的資料表明，隨著顆粒中 Au 組分的增大，其螢光效率急劇下降。對試樣 d，螢光已完全淬滅，這是因為金屬－半導體異質結構體系會造成半導體組分上的光生載流子分離，降低了電子和空穴輻射複合的幾率。

References

1. Gu H W, Zheng R K, Zhang X X, Xu B. J Am Chem Soc，2004，126(18)：5664-5665.
2. Robinson R D，Sadtler B，Demchenko D O，Erdonmez C K，Wang W，Alivisatos A P. Science，2007，317：355-358.

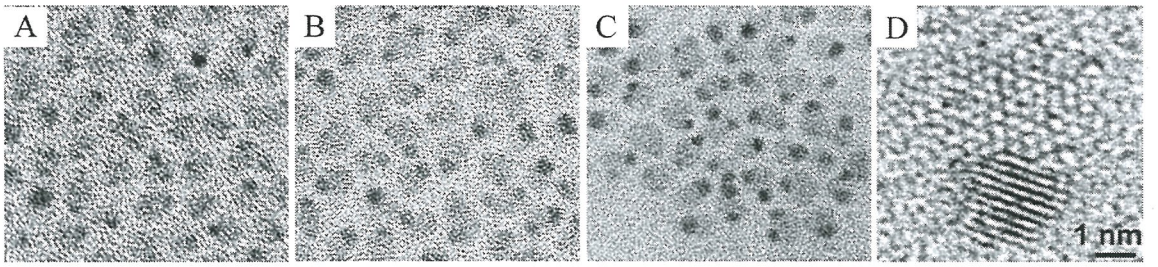

圖 1 A~C：Au 組分逐漸增多的 CdSe-Au 異質納米顆粒 TEM 像；D：CdSe-Au 的 HRTEM 像。

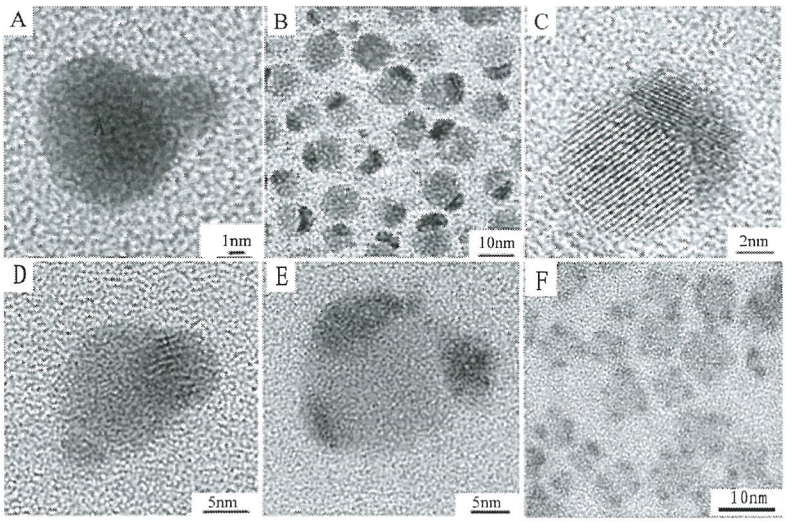

圖 2 異質納米顆粒 FePt-Au(A)，PbSe-Au(B，C)和 Cu_2O-Au(D~F)的 TEM 和 HRTEM 像。

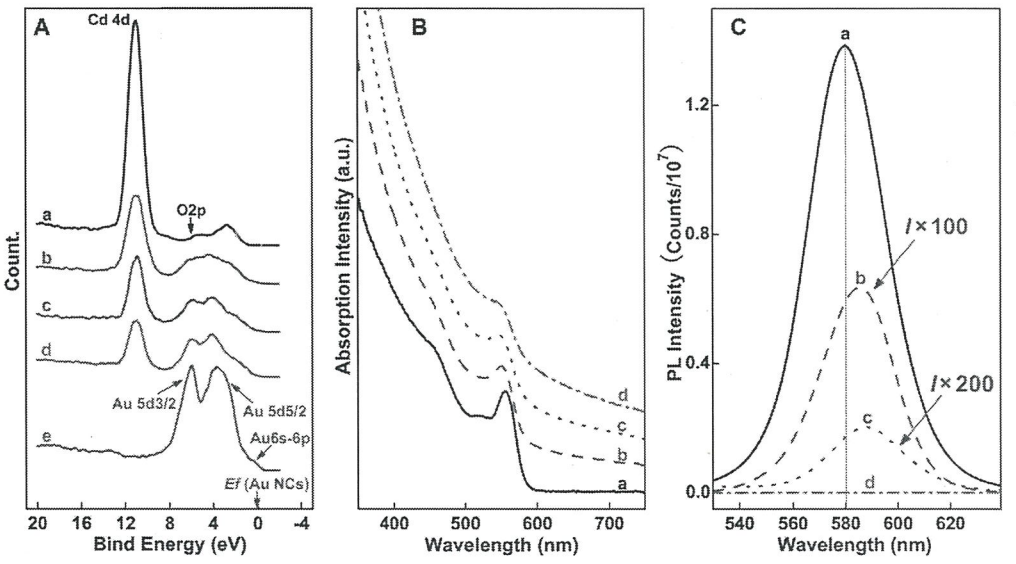

圖 3 CdSe-Au 異質納米顆粒的 XPS 價帶譜(A), 吸收譜(B)和 PL 譜(C)。

MgLi 合金之室溫析出行為與機械性質

王建義

國立東華大學材料工程學系

Mg-Li-Al-Zn 合金擠製狀態之顯微組織呈現 α+β 兩相組織，兩種不同型態之 α 相，原先存在 α 相顆粒因擠製而沿擠製方向排列，晶內及晶界上之針狀 α 相，則是因高溫擠製之動態析出。固溶處理後形成單一 β 相，雖然晶粒成長 1.6 倍，但機械強度則因固溶強化而提升 1.6 倍。自然時效處理 48 h 即達尖峰值，此時係析出寬 2~3nm 長約 10nm 的小片狀準安定析出物，其結構接近 β 相。時效時間越長，θ-phase 析出，同時 α 相析出。但是 α 相之析出對機械性質提升並無貢獻。

1. 前言

鎂合金是密度最低且具有回收性之結構用材料。在輕量化與環保訴求上，更成為眾所矚目之輕合金[1)]。Mg 合金中添加 Li，更可以使密度降低，Mg-12 mass% Li 合金之密度只有市販鎂合金的 3/4 左右。此外，MgLi 合金之結晶構造，隨 Li 添加，由室溫下滑移系不足的 HCP 結構，形成含有易加工之 BCC 結構[2)]。然而其機械強度仍無法滿足一般結構上之用途。近年來，大部份研究以合金化及強塑性變形方式來提高 MgLi 合金機械性質[3-7)]。前者以添加合金元素及熱處理方式，藉由析出強化或固溶強化而改善機械強度。後者則以冷軋+退火[8)]或 ECAP[3,5)]等，利用晶粒微細化來提高 Mg-Li 合金之機械性質與強度。然而，對於機械強度改善之機構，仍然各有不同說法。Alamo et al[9)]在 MgLiAl alloy 之合金之析出，以 XRD 做了詳細研究，認為在 30 h 之室溫時效即可達尖峰時效，此時析出相為 θ phase($MgLi_2Al$)。提出室溫析出之相的變化順序為 β→β+θ+α；而在高溫析出之相變化則為 β→β+θ+α→β+θ+α+AlLi。然而對析出相之形貌未能以 TEM 來深入觀察。本研究，針對 MgLiAlZn alloy 之室溫時效，除以 XRD 鑑定相結構外，嘗試以 TEM 直接觀察及解析相之形貌，進而推測 MgLi 合金之強化機構。

2. 實驗方法

高純度合金元素稱重後，在真空感應爐中，抽真空後通 Ar 保護熔煉。充分熔解之合金再澆鑄於圓柱狀鋼模內，可獲得直徑 203.2mm，長度約 450mm 之鑄錠。合金之組成經分析結果為 Mg-11.2mass%Li-0.95mass%Al-0.43mass%Zn。在 623K 均質化後，高溫擠製成厚度 10mm 寬 110mm 之板材，擠製比約為 29.4:1。以光學顯微鏡(OM)及穿透式電子顯微鏡(TEM)與 X 光繞射儀(XRD)分析顯微組織及相結構。使用顯微硬度機測試各種處理試片之微硬度。拉伸試驗用則為 ASTM E8M 之標準試片，Gage length 為 25mm，夾頭走速為 0.1mm/min。

3. 實驗結果與討論

Fig.1 為擠製狀態之 OM。平均晶粒大小為 52μm。同時沿擠製方向可見粒狀 α 相之分布，大小約 0.1-0.2μm 寬，1-10μm 長，約占 2.3 %。由相圖知此合金應為單一 β 相。G. S Song[10)] 認為合金組成非常接近(α+β)/β 境界，因凝固誘起偏析而形成 α+β 兩相組織。Fig. 2 為固溶狀態之 OM。由於 α 相溶入 β-matrix 中而呈現單一 β 相，但晶粒成長相當明顯，大小約 83μm，為擠製狀態晶粒的 1.6 倍左右。Fig. 3 為擠製狀態及固溶狀態之 XRD。擠製狀態為 β 相及少量 α 相，此結果與 OM 相同。然而仍有許 extra peaks，可知為 MgLi2Al 之 θ 相。此 θ-phase

因為量或形狀太小，以至於在 OM 中未發現。固溶狀態則呈現單一 β 相。由插入之(200) β 相繞射峰，可知固溶處理後，繞射角度偏向較低角度，係因固溶而使晶格變大。由 3.5176Å 變成 3.5334Å 約增加 0.45%，此晶格改變造成之晶格應變，使固溶強化效果提升明顯增加。Fig. 4 為合金之室溫時效曲線。很明顯地，時效 48 h 左右達尖峰值，之後隨時效時間增加即呈現過時效現象，而在 840 h 之時效，合金之機械強度趨向水平。

由一系列室溫時效之 OM，可知在時效 336h 開始有 α 相析出，而在達 840h 時效時，α 相之析出達飽和。此即在時效曲線所見，840h 時效時強度趨近一定值之原因。由此可知 α 相之析出並非 Mg-Li 合金之強化相。此結果與 Alamo et al 之推測相同 [9]。由自然時效不同時間之 XRD。可知 48 h 之尖峰時效仍然維持單一 β 相。此時除固溶強化因素外，析出強化仍被考慮。由後續之 TEM 分析可知準安定相析出而達最高強度。在 840h 過時效可見明顯之 θ-phase 析出。而且隨時效時間增加，θ-phase 更為明顯。同時可見 α phase 析出。Fig. 5 為尖峰時效之 TEM。詳細觀察可見 β-matrix 中，呈現大小 2~3mm，長 10nm 之板狀析出物。由 SADP，可知其(110)之面距為 2.56Å，由此可計算出此板狀 particles 之晶格常數為 a=3.62Å 之立方晶。此 SADP 在 Song[11]之研究報導中亦曾出現，但未加以探討。此晶格常數 3.62Å 與 θ phase(MgLi2Al)之 6.36 Å 不同，而與 β 相之 a=3.52Å 相近，其差異約 0.3%，與固溶處理之面距增加 0.45%之 XRD 的結果相近。此板狀顆粒為析出初期之非穩定相，暫稱為 pre-θ phase。

擠製狀態之抗拉強度 123.2MPa，硬度 58.2HV，而延伸率高達 96%。400 ℃ 固溶處理後，抗拉強度提升至 205MPa 之高值，硬度也達 HV90，但伸長率下降至 39%。由顯微組織比較，可知固溶後晶粒成長 1.6 倍，但強度反而由 124.2 升高達 205MPa，增加了 1.6 倍，此增加之因素，推測為 α 相之固溶強化之貢獻外，室溫析出強化是另一因素。在 48 h 時效即達尖峰時效，可見 pre-θ phase 析出相。尖峰時效強度可達 226MPa，此時伸長率仍有 34 %。而在 168h 以後過時效，則因 α-phase 析出，使得固溶強化效果降低而強度下降，此時伸長率則高達 53 %。

4. 結論

Mg-11 mass%Li-1 mass%Al-0.5 mass%Zn 合金擠製狀態之顯微組織，呈現 α+β 兩相組織。固溶處理後，因過飽和而形成單一 β 相，雖然晶粒成長 1.6 倍，但機械強度則因固溶強化及析出強化而提升 1.6 倍。自然時效處理，48 h 即達尖峰時效，此時係析出寬 2~3nm 長約 10nm 片狀的 pre-θ-phase 析出物。其結構接近 β 相，推測為過飽和固溶體與 θ phase 間之過渡相。時效時間越長，pre-θ-phase 消失而 θ-phase 析出，同時 α 相析出。但是 α 相之析出對機械性質提升並無貢獻。840 h 之時效，合金之機械強度趨向水平，而不再下降，係因 α 相析出已達飽和所致。

References

1. J.Y. Wang, W.P. Hong, P.C. Hsu, C.C. Hsu, S. Lee, Mater. Sci. Forum 419–422 (2003) 65–170.
2. A.A. Nayeb-Hashemi, J.B. Clark, A.D. Pelton, in: A.A. Nayeb-Hashemi, 236 J.B. Clark (Eds.), Phases Diagrams of Binary Magnesium Alloys, ASM 237 International, Ohio, USA, 1998, pp. 184–194.
3. T. C. Chang, J. Y. Wang, C. L. Chu, S. Lee, Materials Letters, 60(2006) 3272-3267.
4. C. C. Chiu, J. Y. Wang, H. Y. Wu, Mater. Sci. Forum 546-549 (2007) 229-232.
5. J. Y. Wang, T. C. Chang, L. Z. Chang, S. Lee, Mat. Trans. V.47 N.4(2006) 971-976.
6. C. H. Chiu, J. Y. Wang, H. Y. Wu, Mat. Trans.V.47 N.4(2006) 966-970.

7. G.V. Raynor, J.R. Kench, J. Inst. Met. 88 (1959-1960) 209-216.
8. P. Crawford, R. Barrosa, J. Mendez, J. Foyos and O. S. Es-Said, Journal of Materials Processing Technology, Volume 56, Issues 1-4, January 1996, Pages 108-118.
9. Alamo, A.D. Banchik, J. Mater. Sci. 15 (1980) 222-229.
10. G. S. Song, M. Staiger, M. Kral, Mater. Sci. Eng. A 371 (2004) 371.
11. G. S. Song, M. Staiger, M. Kral, Magnesium Technology 2003, ed. H. I. Kaplan, TMS, (2003) 77.

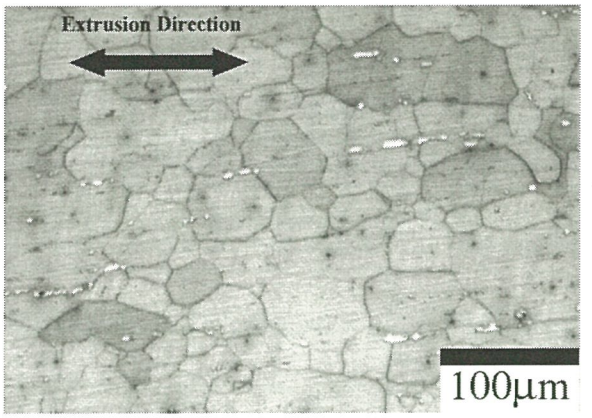

Fig. 1 擠製狀態之金相組織。

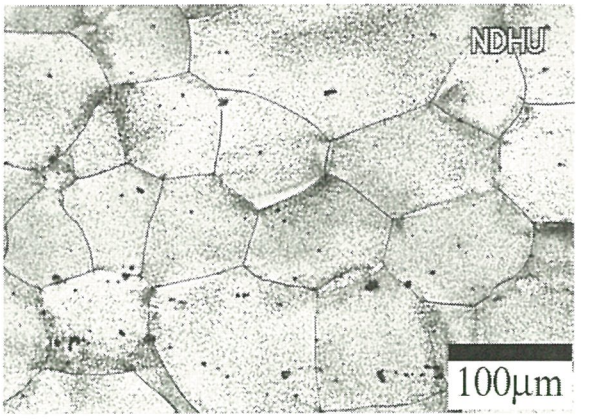

Fig. 2 固溶狀態之金相組織。

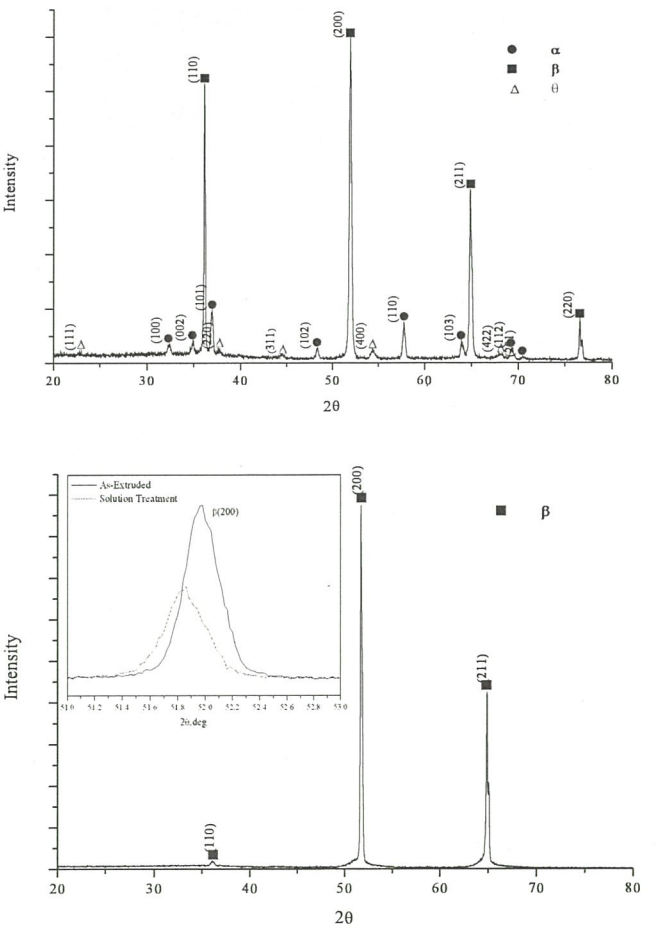

Fig. 3 擠製狀態(a) 及固溶狀態(b)之 XRD 圖。插入 XRD 為 β(200)面繞射峰放大比較。

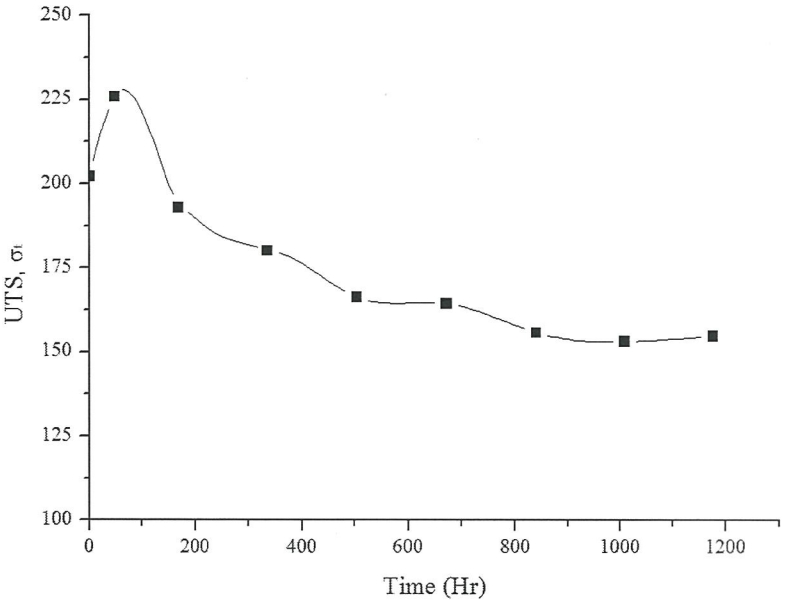

Fig. 4 自然時效曲線。

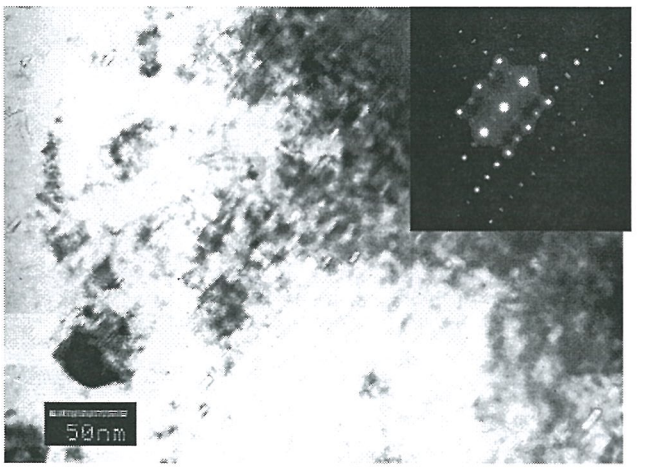

Fig. 5 尖峰時效時之 TEM Bright image 及析出相之 SADP。

Pus
area

DR.

Oxfor

F
excel
(SDD
the ad

A
of the
that s
which
manu
provi
energ
up ne

Benef

-
-
-
-
-
-
-
-

In
silico
vary f
the de
both S

In
also b
nano-
across

Measurements and characterization with in situ SPM-TEM instruments.

Oleg Lourie

Nanofactory Instruments AB, Goteborg, Sweden

In situ SPM-TEM instruments such as AFM-TEM, STM-TEM and TEM-NanoIndenter are used for characterization of the electrical and mechanical properties of various nanomaterials. Piezo actuated and having force or current feedback, the SPM probe in these instruments is also employed for sample surface imaging combined with conventional TEM imaging of the samples. The concept of such instrumentation is to correlate the electro-mechanical measurements with the HRTEM observations of structural changes in the materials. The combination of SPM and TEM techniques in one instrument becomes especially valuable for in situ studies of nanoscale structures such as nanotubes, nanoparticles or nanowires. It also widely used to investigate the formation and propagation of the defects and dynamic phenomena such as fracture and deformation in many bulk materials.

This brief presentation will outline the recent progress in the instrumentation development aimed to expand the range of available SPM-TEM systems. Some experiments for the nanostructures, bulk samples, and semiconductor applications will also be discussed.

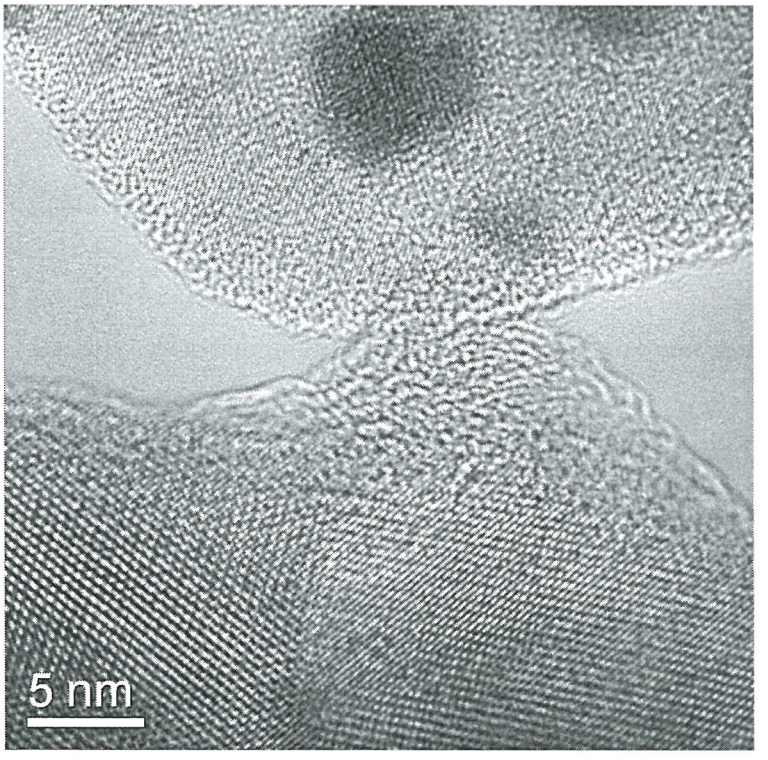

In Situ Study on the Mechanical and Electronic Properties of Individual Carbon Nanotubes Inside a SEM
(在掃描電鏡中原位研究單根碳納米管的力學和電學特性)

CHEN Qing (陳清)

(Key Laboratory for the Physics and Chemistry of Nanodevices and Department of Electronics, Peking University, Beijing 100871, P R China)

(納米器件物理與化學教育部重點實驗室 北京大學電子學系，北京 100871, 中國)

碳納米管是納米電子器件和納米電機系統的理想材料。研究顯示碳納米管可用于多種納米諧振器。這些器件都是利用外電場調節碳納米管的受力來調諧碳納米管的諧振頻率。但至今為止，碳納米管在受力情況下的振動特性還沒有被定量研究過。另一方面，碳納米管受力會引起其能隙變化，發生金屬性向半導體性的轉變。但已有的實驗結果還缺乏一些定量資料，不好跟理論類比結果進行定量比較。

本文作者發展了在掃描電鏡中原位測量單根單壁和單根少壁碳納米管的方法和原位搭建碳納米管諧振器的方法**[1]**，定量且同時地測量了單根碳納米管的諧振頻率、軸向應力和幾何尺寸。並定量研究了碳納米管受到軸向力時的振動特性；觀察到諧振特性從多壁碳納米管到單壁碳納米管逐漸從梁模型向弦模型的轉變；原位測量了單根雙壁管的楊氏模量、斷裂強度和受力下的電輸運特性，觀察到碳納米管受力時從金屬性向半導體性的轉變；發展了將測量後的碳納米管轉移到透射電鏡微柵上進一步在透射電鏡中表徵原子尺度結構的方法，將性能與結構真正對應起來。

原位實驗是在掃描電子顯微鏡 FEI XL30F 中利用 Kleindiek 的納米探針操縱系統完成的。碳納米管是利用化學氣相沉積方法製備的。本文將原子力顯微鏡的針尖或一根矽納米線引入掃描電鏡中並與納米探針結合用於準確測量碳納米管所受的力。還利用了電位輔助襯度增強技術**[2]**實現了在掃描電鏡中較低放大倍數下觀察並操縱只有 1-2 納米直徑的單根單壁或單根少壁碳納米管。本文利用焦耳熱來避免電子束誘發非晶碳的沉積**[3]**，保證了原位測量的可重複性。

實驗和模擬結果如圖 1-圖 4 所示。

致謝：特別感謝主要合作者魏賢龍同學。本工作中還受到彭練矛教授、李彥教授、張錦教授、左建民教授、許勝勇副教授、王鳴生博士、劉洋同學和崔榮麗同學等人的幫助。研究項目受到科技部、基金委和北京大學的經費支持。

References

1. Wei X L，Chen Q，Xu S Y，Peng L M，Zuo J M. Adv Funct Mater，2009，in Press.
2. 彭練矛，梁學磊，王勝，張志勇，姚昆，胡又凡，高旻，陳清. 電子顯微學報，2007，26（5）：395-400.
3. Wei X L，Liu Y，Chen Q，Peng L M. Nanotech，2009，19：355304.

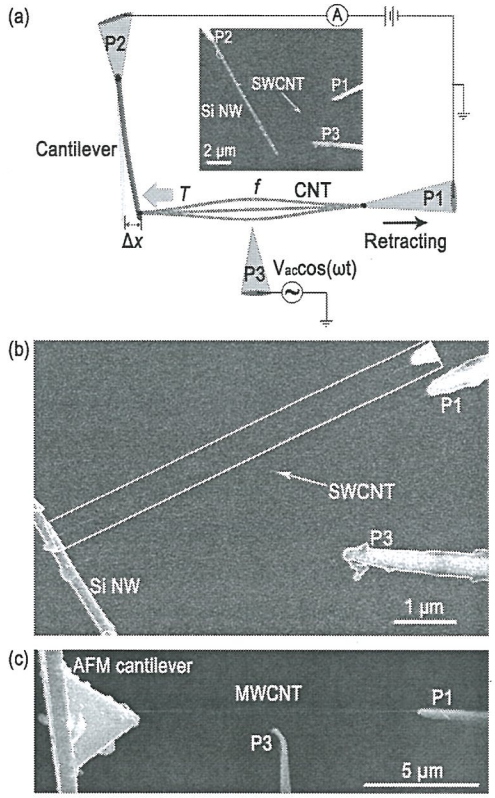

圖 1 原位搭建碳納米管諧振器的結構示意圖和中心部分的掃描電鏡照片(a),單根單壁(b)和單根多壁(c)碳納米管諧振時的掃描電鏡照片。

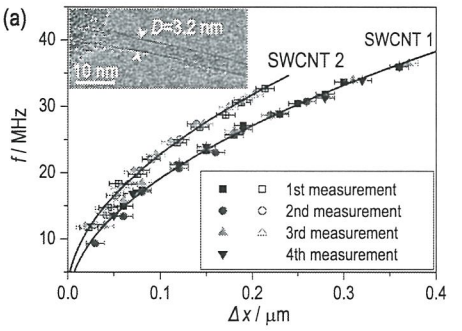

圖 2 單壁碳納米管的諧振頻率隨測力懸臂的位移（正比于碳納米管的受力大小）變化。

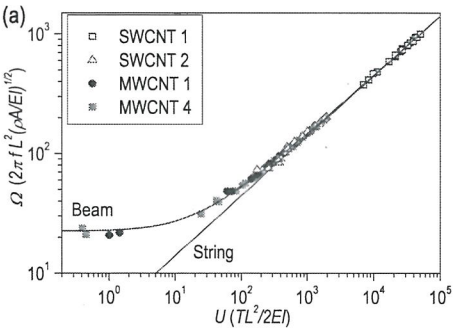

圖 3 碳納米管的諧振特性從梁模型向弦模型轉變的情況。

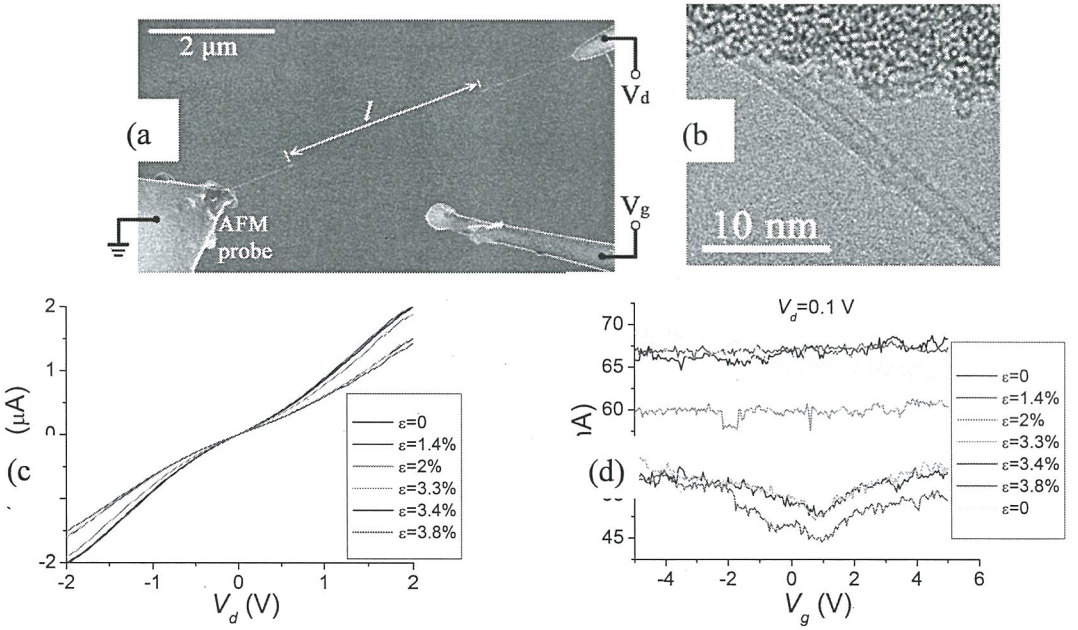

圖 4 a：測量碳納米管受軸向拉力時的電學特性的掃描電鏡照片；b：被測碳納米管的透射電鏡照片顯示這是一根雙壁碳納米管；c：碳管受力不同時電流隨源漏電壓的變化；d：碳管受力不同時電流隨柵壓的變化，顯示碳納米管從金屬性向半導體性的轉變。

The synchrotron radiation microscopy-a complementary tool for SEM/TEM

Chih-Hao Lee (李志浩)

Department of Engineering and System Science, National Tsing Hua University, Hsinchu.
(清華大學工程與系統科學系) & National Synchrotron Radiation Research Center(同步輻射研究中心)

Microscopy using the advanced light source, such as synchrotron radiation, gains many advantages over the traditional light sources. It is also a complementary tool to the TEM and SEM. Synchrotron radiation light source is better than the traditional light source due to its continuous spectrum, high intensity, highly collimated beam, polarized beam, and pulse beam. In recent advanced light source, high coherent X-ray is also possible. Microscopies based on these advantages are invented in the past. They are not only taking the advantage of high intensity and sub-micro beam, they also adopted the highly collimation beam technology of phase contrast image. One of the major advantage is the microspectroscopy or spectromicroscopy technique which combines the technology of spectroscopy and microscopy together. Furthermore, the properties of polarized beam can be used to probe the magnetic materials and chirality of molecules. Although, the spatial resolution of synchrotron radiation is much worse than a high resolution TEM, the better penetration of X-ray provides a chance of doing the in-situ and in-vivo experiments without worrying about the vacuum environment, in addition, select the right X-ray energy to the interesting element to eliminate the background is also a great advantage and a complementary tool to the SEM/TEM.

The Taiwan Light Source (TLS, 1.3 GeV, circumference 120 m) located in NSRRC(National synchrotron Radiation Research Center) was commissioned by in 1993. Since then, several microscopy beamlines were constructed and installed. These beamlins are IR microscopy beamline, PEEM (Photoemission electron microscopy), SPEM (Scanning photoemission microscopy), X-ray microscopy. In the near future, a more advanced synchrotron project, the Taiwan photon source (TPS, 3 GeV, circumference 518.4 m), with much better beam quality, will provide not only higher intensity X-ray, but much higher beam divergence for the coherent X-ray scattering and diffraction measurement. This project was granted by the government and the TPS is to be commission at 2014, also at the site of NSRRC. New beamline with coherent scattering beamline and nanoprobe beamlines are proposed also to be commissioning at the first day of light available. The properties of beamlines are highlighted will be described in the following:

The IR microscopy is useful especially for biological image. Most of biological sample consists of only organic material with almost very low density contrast. However, different chemical bonds give different vibration frequencies which can be easily revealed in the IR spectra. The IR microscopy gives a mapping image of IR

vibrational spectroscopy. The IR intensi
than the conventional light source. The re
by the long wavelength of IR using the f
technology can be applied, 10 times bette

The SPEM is an experimental static
spectroscopy) and XANES (X-ray absor
Tunnel Microscopy) which is similar t
generated from the undulator of TI
nano-translation stage to load the sample
XPS and XANES, the chemical prope
characterized. The spatial resolution is
states of art instrument in NSRRC. It v
which is capable of producing hig
photoemission electron generated from
similar principle of electron microscopy
and left-handed circulated polarized ligh
ferromagnetic transition metal atoms, an
can be obtained. An in-vacuum MBE s
in-vacuum MOKE system to character
spatial resolution of PEEM is 100 nm,
domain. Energy scan across the absorptio
chemical properties of each element in t
20 nm in spatial resolution in the near fut

Two X-ray microscopy beamlines
down to a resolution of 50 nm were also
be selected to match the K-edge of
microscopy beam covered different mag
contrast image can be obtained using
capability is all available in these beamli

In the future, the high coherent bea
image of single nanoparticle. One coh
beamline were proposed by National Tsi
The highly coherent beam of TPS is cap
shape and image of a single nanopa
nano-probe beamline with capability of 3
70 m at TPS using a KB mirror system. A
at the goal of 10 nm resolution.

Acknowledgement – A team work of NS
榮, 魏德新, 許瑤真, 李耀昌, 宋豔芳, l
acknowledged.

EBSD Study on Microstructure and Texture of Deformed and Annealed Metals (形變及退火金屬微觀組織與織構的 EBSD 表徵)

LIU Qing (劉 慶)

(School of Materials Science and Engineering, Chongqing University, Chongqing 400044，P R China)
(重慶大學材料科學與工程學院，重慶 400044，中國)

塑性變形是金屬材料製備加工成型的主要方式，在複雜的塑性加工及退火處理過程中材料內部組織結構將發生巨大的變化；同時，材料內部的晶粒要發生擇優取向而形成織構。除材料微觀組織結構外，金屬材料在形變及退火過程中形成的織構也是決定材料性能的關鍵因素之一。所以，對金屬形變及退火過程中微觀組織與織構演化進行定量表徵研究具有重要的理論及實際意義。電子背散射衍射（electron back scattered diffraction，EBSD）技術的發展，特別是近幾年來速率及空間分辯率的提高，已成為研究形變及退火金屬微觀組織及織構演變的最有效的分析方法之一。

對於大多數單相金屬（特別是高層錯能金屬）形變過程中的微觀組織結構演變主要是基於位元錯滑移而形成的形變位元錯介面。圖 1 示出了鋁單晶在經 30% 軋製變形後形成繞 TD 方向選擇具有不同取向的兩類區域及各區域中的位元錯介面。與透射電子顯微（TEM）分析技術相比，除具有樣品製備簡單、觀察分析區域大的優點外，無論在位錯介面的觀察還是在微區取向及介面取向差的分析方面都更加簡便。圖 2 是結合掃描電鏡中各晶粒位元錯介面的表徵及利用 EBSD 技術對晶粒取向的測定，總結出形變位元錯介面的特徵受晶粒取向影響分為三種典型類型，並與所開動的位錯滑移系密切相關的結果。其中，按形變位元錯介面特徵分類的表徵晶粒取向的極圖資料來源與 151 個不同晶粒的統計結果。機械孿生是密排六方結構金屬塑性變形的主要方式之一。對形變金屬孿生類型、孿晶界特徵及孿生百分比例的表徵對於揭示這類金屬塑性變形機理具有重要的意義。圖 3 示出具有較強初始織構的 AZ31 鎂合金材料，在沿與原織構 C 軸成垂直方向壓縮 5% 後，晶粒內部形成大量的孿晶界(彩色)，同時由於機械孿生引起的晶粒取向轉動，織構也發生了較大變化。

形變金屬在退火過程中形核位置、形核晶粒的取向及其與形變基體之間的關係對於揭示再結晶的機理，實現再結晶織構的控制具有重要意義。圖 4 示出了經 98%形變量軋製工業純鎳（99.97%），經 300℃保溫 40 分鐘後，具有 S 取向區域的高分辨 EBSD 掃描的取向成像圖及介面圖。介面圖中，紅線表示 Σ3 孿晶 60°<111> 介面，紫紅線表示 Σ9 孿晶 40°<101>介面。可以看到，再結晶優先在 S 取向形變區域的 LGB 中形成，並沿 LGB 優先長大，晶粒/晶核之間絕大多數為 60°<111>孿生介面。

退火過程中再結晶晶粒長大速率及各種取向晶粒長大行為的差異對最終材料的晶粒尺寸及再結晶織構具有重要的影響。EBSD 技術由於其具有的統計意義以

及能在確定晶粒尺寸的同時確定該晶粒的取向，是研究比較不同取向晶粒長大行為的非常有效的工具。圖 5 示出經 98%軋製變形超高純 Ni（99.999%），在 300℃退火不同時間晶粒尺寸及取向的變化。晶粒長大的分析研究結果表明，立方取向晶粒長大速率約為非立方取向晶粒的 3 倍，立方取向晶粒的擇優長大是立方織構形成的主要原因。

本文舉例闡述了 EBSD 技術在幾種典型金屬材料形變及退火過程中微觀組織結構與織構演變研製中的應用。EBSD 技術對於形變位元錯介面、機械孿生產生的各種孿晶介面、退火過程中再結晶形核及晶粒長大等各種微觀組織結構特徵演變的研究都是一個非常有效的分析工具。特別是在將微觀組織結構與晶粒取向進行對應以及具有統計意義的表徵方面具有獨特的優勢。

致謝

本項目研究獲得國家自然科學基金項目 50231030、50620130096 和 50890172 的資助；感謝課題組同事 Godfrey A 和劉偉教師，研究生陳宏生、李增傑、曹文權、蔣佳及李曉玲的貢獻。

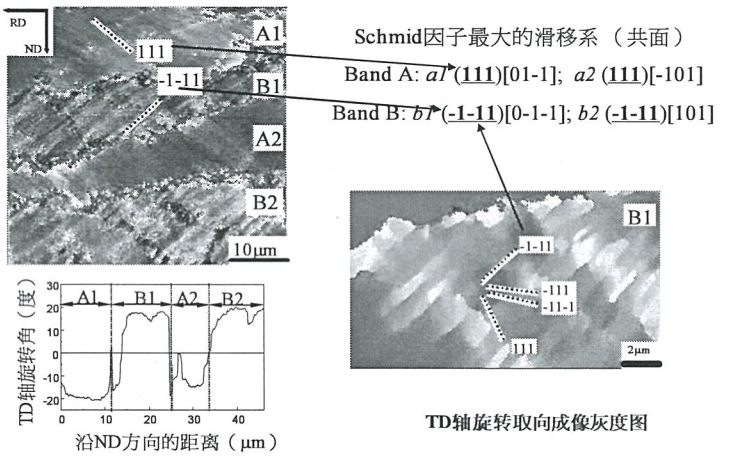

圖 1 初始取向為旋轉立方取向的鋁單晶經 30%軋製變形後的 EBSD 分析。

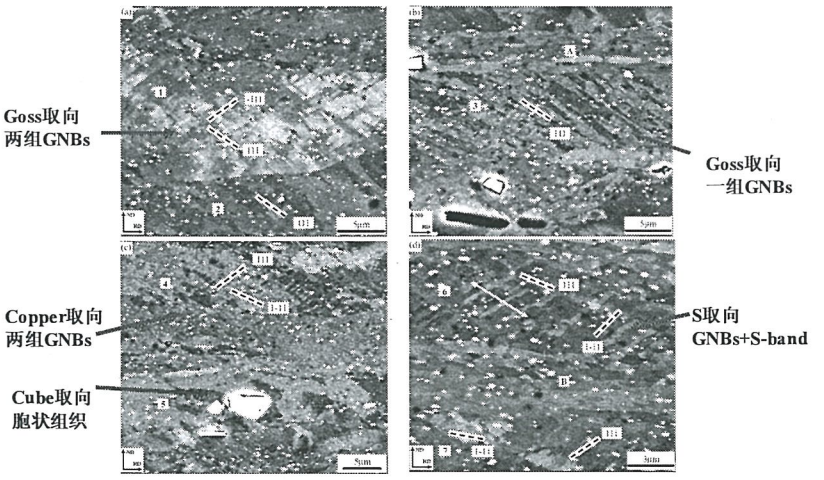

圖 2 AA3104 合金經 30%冷軋變形後各晶粒內部形成的三類位元錯介面結構：Type A：兩組 GNBs；Type B：一組 GNBs；Type C：胞狀組織的顯微照片及其應的晶粒取向。

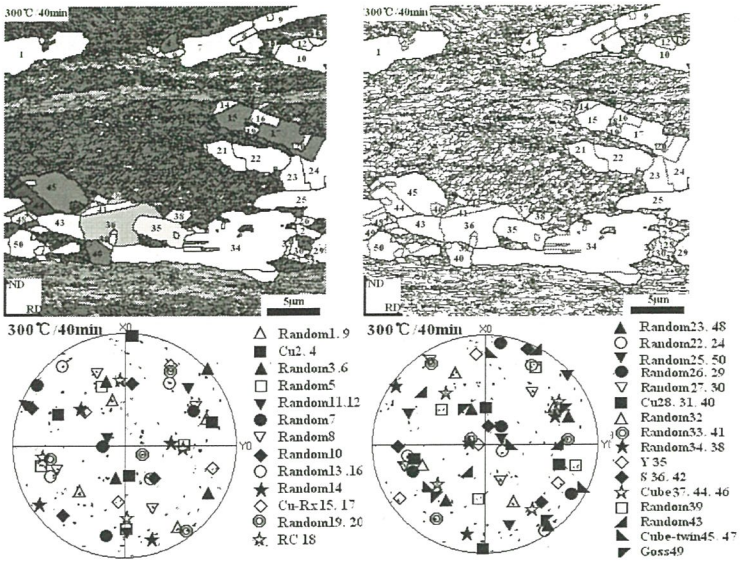

圖 3　AZ31 鎂合金壓縮變形 5%後的各種晶界的顯示及壓縮前後織構變化。

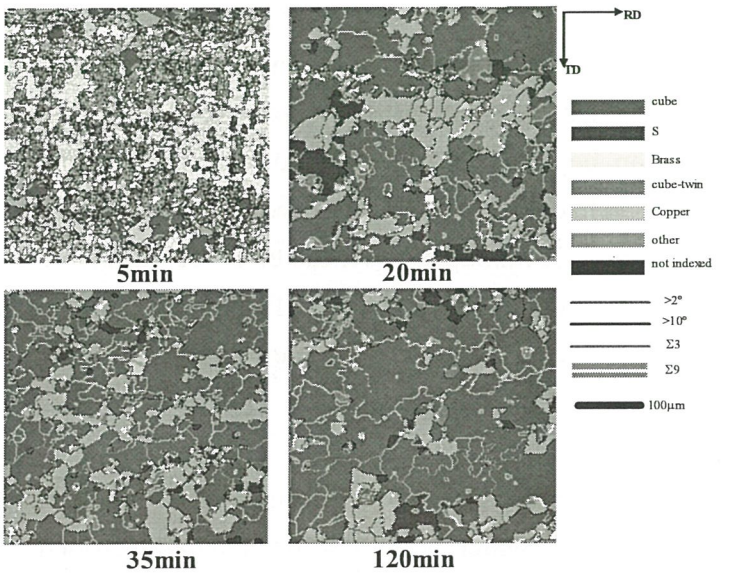

圖 4　98%形變量軋製工業純純鎳，經 300℃保溫 40 分鐘材料經 EBSD 進行面掃描分析後重構的取向成像圖及介面圖，以及各形核晶粒的取向。

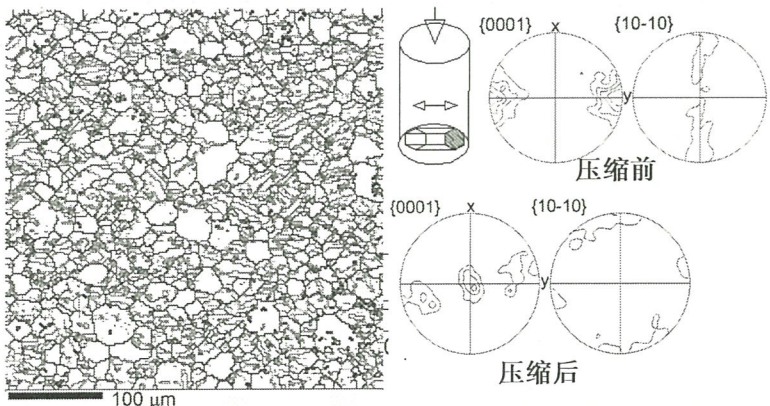

圖 5　98%軋製變形超高純 Ni（99.999%），在 300℃退火不同時間的 EBSD 取向成像圖。

Quantitative Analysis in AEM by Self-calibration Method

Bow, Jong-Shing (鮑忠興)，Wang, Hong-Wen(王宏文)

1. *E. B. Tech Co. Ltd., Taipei, Taiwan, ROC*
2. *Department of Chemistry, Chung-Yuan Christian University, Chungli 320, Taiwan, ROC*

TEM has been proved to be a very attractive and powerful analytical tool for nano-materials research. Modern TEM has put the image resolution and the spatial resolution down to 0.1 nm [1, 2], some advanced TEMs even down to 0.05 nm [3]. In composition analysis, elements from a single array of atoms could be identified [3]. However quantitative analysis from specified phases is still an annoyed work. From literatures, the most accurate way to perform quantitative EDS analysis is to analyze the unknown sample and a standard sample with similar composition and crystal structure in the same TEM/STEM operation condition. It is easy to keep same operation condition for current delicate TEM/STEM, but it is very consumptive to get standard samples for so diverse materials studied today. It will be an easy way to perform quantitative analysis if the standards can be found in the analyzed sample itself [4]. We will call this method to be the self-calibration quantitative analysis technique, SCQAT. From a previous work in an Al-Ti-Ni super alloy, the error was found to be as low as 2%. It is therefore worth to develop this technique for further advanced material analysis in the future. In this paper, we evaluate this technique by using a simple and common material system, Si-glass-SiO_2.

Three different samples were cut and ground to be thin slabs, and were bound to a sandwich, Si/glass/quartz, which was then mechanically ground and polished to be a XTEM sample, as shown in Fig. 1, in order to explore the possibility and accuracy of the SCQAT. In TEM, this sample was tilted to be away from strong diffraction condition for both Si and quartz firstly, then EDS spectra were collected in TEM mode with various probe sizes to eliminate the probe size effect. EDS spectra were first quantitatively analyzed by the TIA program installed in the TEM, and then exported to be text files which were further analyzed by Excel, a standard Microsoft Office software. Both peak intensity and integrated intensity were used to calculate the composition ratio. The ratios of Si/O from Si and quartz were taken to be standards to calculate the composition of the glass. Fig.2 shows the EDS spectra of Si, glass, and quartz. The atomic ratios of O/Si calculated from these spectra are 0.03, 1.16, and 1.09 correspondingly. Detail results will be discussed in the conference.

Reference:

1. B. Freitag, S. Kujawa, P. M. Mul, J. Ringnalda, and P. C. Tiemeijer, Ultramicroscopy 102, 209-214 (2005).
2. FEI Application note (2007)
3. C. Kisielowski et. al. Microsc. Microanal. 14, 469-477 (2008).
4. Zhiqing Yang, Wim Tirry, Dominique Schryvers, Scripta Mat. 52, 1129-1134 (2005).

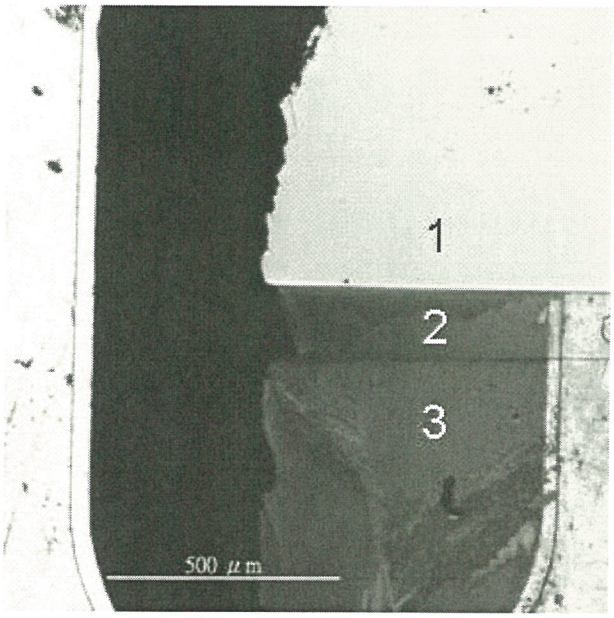

Fig.1 OM image shows the geometry of the XTEM sample, adhered upon a Cu-ring, consisted of three parts. "1": Si; "2": glass (unknown); "3": quartz (SiO_2).

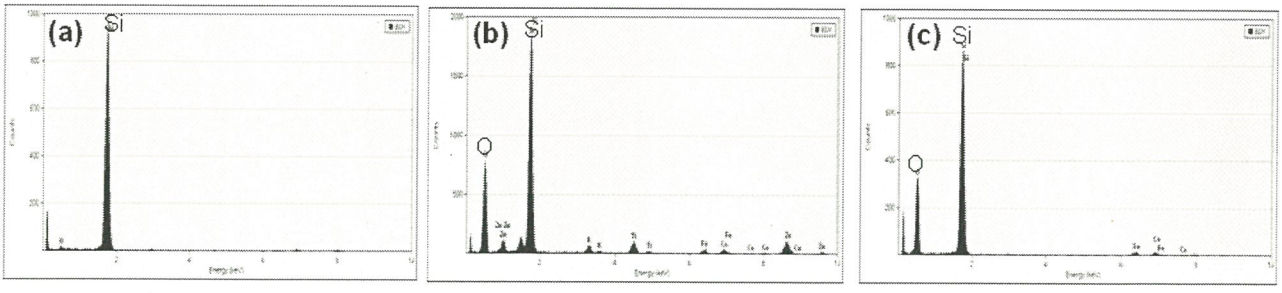

Fig.2 EDS spectra. (a) Si, (b) glass, (c) quartz.

Application of Monte Carlo Image Simulation to Linewidth Measurement with CD-SEM
(Monte Carlo 成像模擬方法應用於 CD-SEM 的線寬測量)

LI Yong-Gang(李永鋼), DING Ze-Jun (丁澤軍)

Hefei National Laboratory for Physical Sciences at Microscale and Department of Physics, University of Science and Technology of China, Hefei, Anhui 230026, P R China
（合肥微尺度物質科學國家實驗室、中國科學技術大學物理系，安徽 合肥 230026，中國）

半導體大型積體電路技術的發展使得刻蝕線寬已經降到 30 nm 以下，但其進一步發展亟待納米級精確測量技術的支援。因此，納米尺度的精確測量已成為半導體行業未來發展的關鍵和極具挑戰性的工作。由於 SEM 有著較高的解析度與吞吐效率、普適性好等優點，可以實施對樣品的實施監控和圖像分析，並且利用 SEM 可以實施對線寬的正面（Top－Down）、截面甚至是三維成像分析，而 Top－Down 方式下可以實施對樣品的無損傷、高分辨、快速測量，因此在半導體行業中已經發展成一種專門的測長掃描電鏡（即臨界尺度掃描電鏡 CD-SEM）技術，它被認為是即時監控與測定納米級線寬的最為高效和準確的方法。

通常，利用 CD-SEM 獲得線寬的二次電子掃描圖像，相應的線寬確定演算法是精確測量的關鍵。然而，隨著體系線寬尺度逐漸降到幾十 nm 範圍，幾種常用幾種經驗的線寬確定演算法都已變得不再適用，其根本原因在於 SEM 中二次電子信號發射的本身物理效應：二次電子信號發射的邊沿效應（edge effect）使得二次電子信號的線掃描曲線會呈現一個有相當展寬的包絡線型，展寬尺度約為 10 nm 量級。這種展寬對於幾十 nm 的結構來說是最為重要的誤差來源，因為這時人們很難從圖像中確定準確的線邊沿位置，而應用中所需的測量精度要求在 1 nm 以下。因而，目前對於無週期性的絕對線寬測量仍然是急待學術上解決的問題。

由於二次電子信號產生涉及電子束與固體的相互作用基本物理過程，因此解決這個問題必須要從理論上進行全面研究。該問題的複雜性在於：實際的掃描電鏡成像中，影響襯度的因素非常多。其中一些因素是普適性的，它與入射電子散射、二次電子激發以及發射過程的基本物理有關，如納米結構樣品幾何參數、表面帶電性質、可控電子束參數等；而另外一些因素還與具體儀器有關，如探測器幾何配置和樣品外電場分佈等。為瞭解各種因素對 CD-SEM 圖像進而對線寬測量的影響，人們已付諸了大量精力。實驗上對標準樣品和 AFM 等其他手段進行了對比研究，而理論上則用 Monte Carlo 方法對 SEM 進行了初步模擬研究，試圖找出一種精確的線寬確定方法。然而，由於國際上其他小組的理論研究中採用的 Monte Carlo 計算模型有相當的局限性，目前還未有能得到普遍接受的結果。由此可見，CD-SEM 中半導體線寬的確定問題（以及更一般的 SEM 中納米結構測量問題）對納米測量技術的發展起著重要的作用。

本文作者採用的 Monte Carlo 物理模型在原來的基礎上主要做了三大改進：1）

用 Mott 彈性散射截面處理電子彈性散射過程和用全 Penn 介電函數方法計算電子非彈性散射截面；2）採用基本構造體組合模型以及三角形網格法組建具有任意複雜三維結構的樣品模型，由此構造了粗糙樣品表面模型；3）利用光線追蹤演算法處理電子散射步長，更加合理地處理電子出射幾率和折射過程；並利用空間分割演算法以加速計算效率。利用 Fortran 語言編寫的 MPI 並行根源程式可運行於各種平行電腦系統。

作者由此系統詳細地研究了線寬隨納米結構各種參數（寬度、高度、邊牆角、頂端圓弧、拖尾、粗糙度等）、入射電子束條件（加速電壓、入射角）、探測器條件（幾何配置、樣品外電場分佈）而變化的規律。這將有助於進一步總結經驗線寬分析公式，可以更加精確和高效地確定線寬，對半導體工業大型積體電路生產中納米線寬的確定具有重要的實際應用價值。

關鍵字：測長掃描電鏡；Monte Carlo 模擬；線寬測量；二次電子；成像模擬

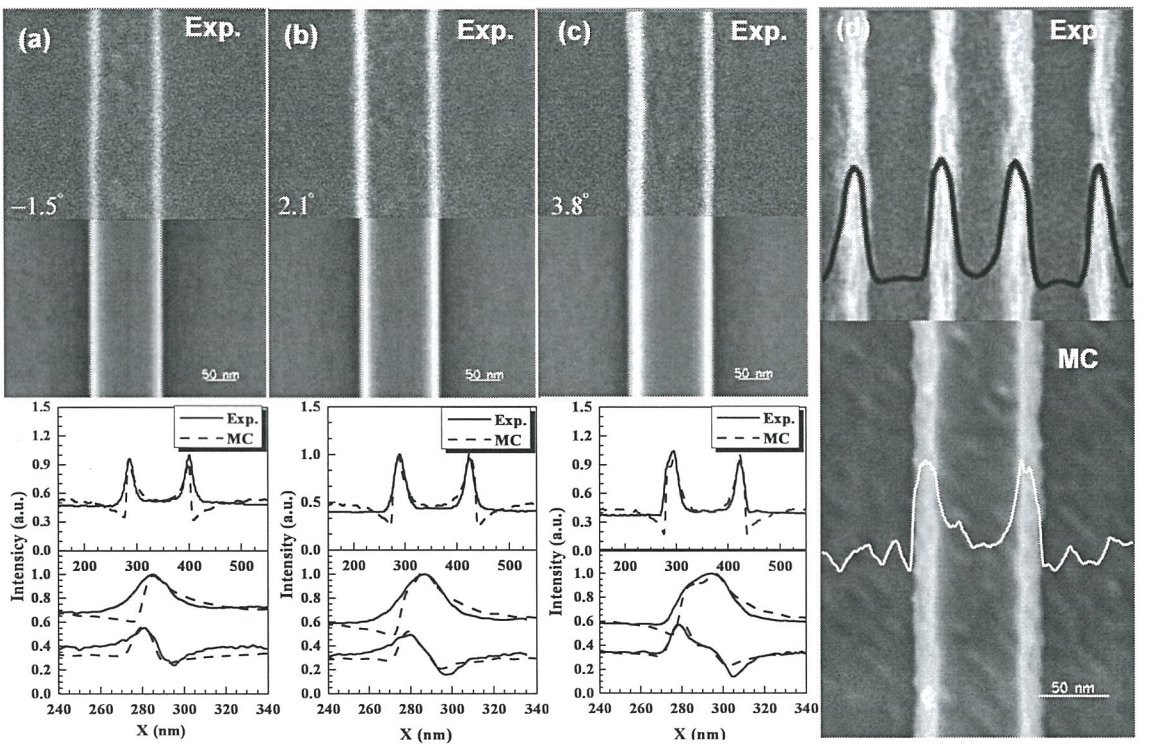

圖 1 掃描電鏡線掃描及圖像的類比結果與實驗結果的對比。參數為：a：高度 H = 240 nm，上底寬 W = 120 nm，邊牆角 α =-1.5°；b：H = 240 nm，W = 120 nm，α =2.1°；c：H = 240 nm，W=120 nm，左邊角 α =3.8°，右邊角 α =2.1°；d：H = 150 nm，W = 65 nm，α =5°，粗糙邊緣振幅 3σ =6 nm，密度間隔 a=10 nm；粗糙上底面和基底 3σ =1.5 nm，a = 2 nm。a, b, c 中電子束寬為 8 nm，d 為 3 nm；a, b, c 入射電子束能量為 0.8 keV，d 為 1 keV。

In-situ studies of solid-state reaction between Au and ZrO2 nano-particles by TEM
(原位 TEM 研究金與二氧化鋯納米粒子快速固相反應)

LI Ji-Xue (李吉學), GE Xin (葛欣), ZHU Xing-Fu (朱幸福), XIA Bai-Ying (夏柏營)

State Key Laboratory of Inorganic Synthesis and Preparative Chemistry, Jilin University，Changchun Jilin 130012,P R China(無機合成與製備化學國家重點實驗室，吉林大學，吉林 長春 130012, 中國)

納米粒子之間的固態反應，直接影響納米材料的實際應用。尤其是在異種納米材料共同使用中，納米粒子之間的固態反應，可以直接改變材料的物理化學性能，決定材料的實際應用前景。對於兩種金屬的納米粒子固態反應過程，人們研究發現類似於塊狀材料相圖中的合金化過程。原位研究金屬納米粒子與金屬氧化物納米粒子的固態反應過程，至今還報導的不多。本文報導應用透射電子顯微鏡，原位研究金納米粒子與二氧化鋯納米粒子固態反應過程。

應用水熱合成的方法合成製備出粒徑分佈在 2nm~20nm 的二氧化鋯納米粒子。應用真空濺射的方法將金納米粒子濺射到二氧化鋯納米粒子的表面，使金納米粒子與二氧化鋯納米粒子之間形成外延生長的介面。依據金納米粒子具有納米性質時的臨界尺寸為 5nm，將實驗研究的體系分為金納米粒子尺寸小於 5nm 和大於 5nm 兩種情況。原位實驗在 JEOL JSM-3010 型透射電鏡上執行。加速電壓為 300 kV，選擇進行輻照區域的電子束密度在 150~240A/cm^2。在整個的觀測中，樣品台始終保持在室溫下。Gantan 794 CCD 逐時的對樣品進行高分辨透射電鏡照片的拍攝。

研究結果表明：當金納米粒子粒徑小於 5nm 時，納米粒子反應可有分為三個階段即粒子相對位置的調整；快速合金化和形成新相。金粒子尺寸大於 5nm 時，固相反應形成以 Au 為核的核殼結構，殼為 $AuZr_4$ 新相。由於金粒子的尺寸從小於 5nm 變化到大於 5nm 時金與二氧化鋯納米粒子形成的介面是從浸潤性介面變化到非浸潤介面，也將影響固態反應過程。

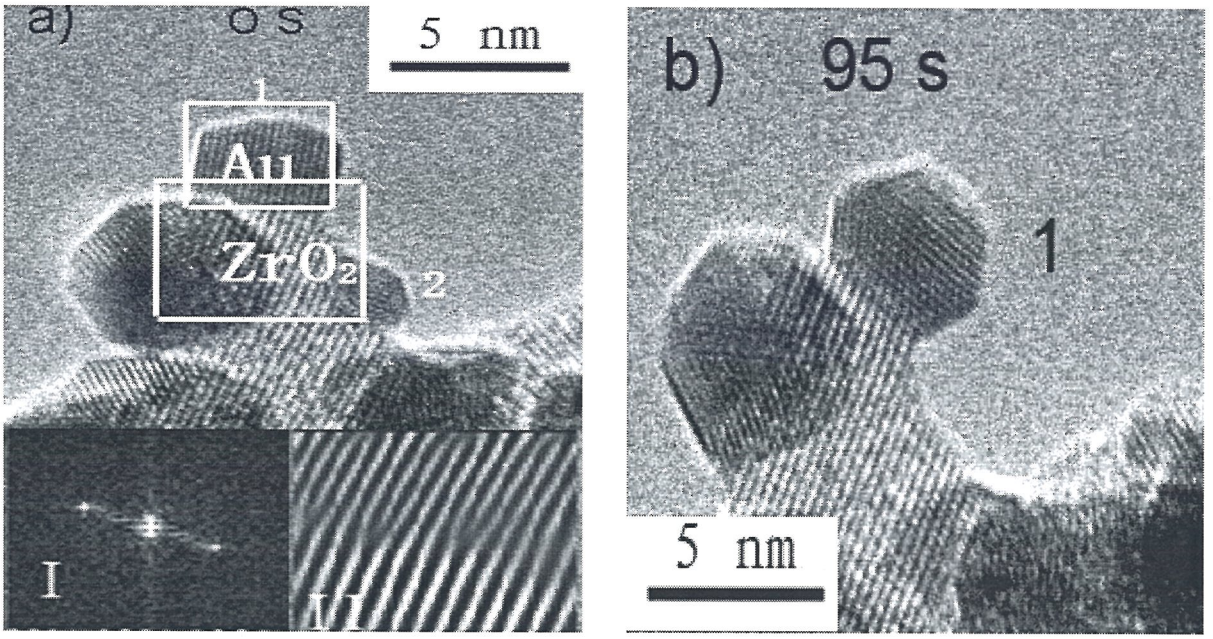

圖1 a：電子束輻照前小於5 nm Au納米顆粒與二氧化鋯納米顆粒形成的介面結構。圖中I表示介面區的傅立葉變換，圖中II為反傅立葉變換。1b：輻照95s後$AuZr_4$新相生成，相介面平直。

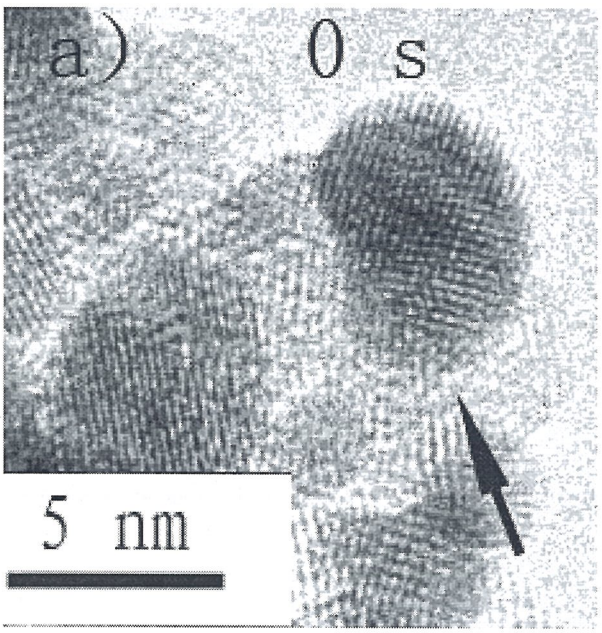

圖2 粒徑大於5nm粒子金顆粒。

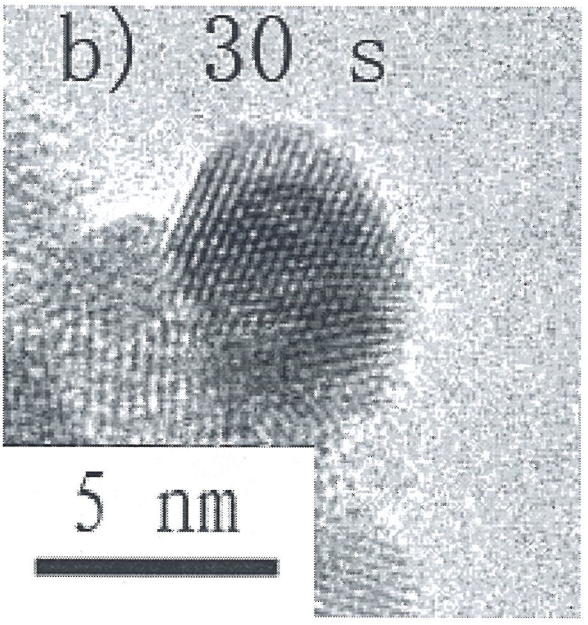

圖3 經過30s輻照後形成Au為核$AuZr_4$為殼的結構。

Formation Kinetics of the Inhibition Layer of Galvanized Steels

Kuang-Kuo Wang, Hung-Ping Wang, Liuwen Chang(張六文)*, Dershin Gan

Department of Materials and Optoelectronic Science, National Sun Yat-Sen University(中山大學材料科學系), Kaohsiung 80424,Taiwan, R. O. C.

The formation of a nano-sized Fe-Al inhibition layer with a uniform thickness at Fe/Zn interface during continuous hot-dip galvanizing process is a crucial issue for industrial production of galvanized and galvannealed steel strips. However, the extremely rapid nature of the reactions makes the formation mechanism of the Fe-Al (-Zn) inhibition layer still elusive. This work presents a characterization result on the inhibition layer formed on a interstitial-free (IF) steel and two dual-phase (DP) steels after a short time galvanizing. Instead of preparing cross-section specimens for transmission electron microscopy (TEM) analysis, the present work prepare plane view TEM specimens by dissolving chemically the Fe and Zn away to reveal the thin inhibition layer. This way large area of it is available for microscopic observation, and some steel substrate can be intentionally retained for interfacial analysis.

For the IF steel, the Fe-Al and steel interface is free from oxide, indicating that the Fe-Al crystals can directly nucleate on ferrite grains. TEM electron diffraction shows that only Fe2Al5-xZnx intermetallic compound was formed and it possesses a well-defined orientation relationship with Fe substrate as: [110]FA// [111]Fe, (001)FA// (011) Fe and (110)FA// (211)Fe whereFAstandsforFe2Al5-xZnx(seeFig.1). Themostpopular interface is (001)FA/(011) Fe which is a low energyinterface with good match of lattice sites. Another interface is suggested to be (110)FA/(233)Fe. The still large lattice mismatch prohibits 2D growth and results in a very small grain size involving multiple crystallographic variants. The Fe2Al5-xZnx islands grow rapidly from an initial size of 20 nm or less on the Fe side to 500 nm or more on the Zn side.

For the case of the DP steels, the steel surface is partially covered by manganese oxides and Cr or Si containing oxides prior to the galvanizing (see Fig. 2). Fig. 3a shows a bright field image for the inhibition layer formed on the galvanized C-Mn-Si DP steel. It is evident that the layer is composed of coarse grained Fe2Al5-xZnx (>200 nm) in thick region and fine grained Fe2Al5-xZnx (<100 nm) in thin region. Two EDS spectra acquired from positions 1 (thick region) and position 2 (thin region) are shown in Fig. 3b. The spectrum acquired from position 1 is free from oxygen. In contrast, the oxygen content in the thin region (position 2) is high and a Si peak is also detected. The depletion rate of Al on reducing manganese oxides thus plays a key role on retarding the nucleation and growth of Fe2Al5-xZnx at the interface, resulting in a motley

inhibition laye
Fe2Al5-xZnx
observed betw

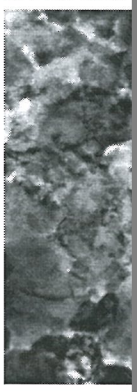

Fig. 1 (a) TE
the correspon
of three varian

Fig. 2 Bright fi

Fig. 3 (a) Brig
C-Mn-Si steel
and position 2

Characterization of Structure of Spray Forming Mg–12.55Al–3.33Zn–0.58Ca-1Nd Alloy
(噴射沉積 Mg–12.55Al–3.33Zn–0.58Ca-1Nd 合金組織與結構表徵)

BAI Pu-Cun(白朴存)[1], DONG Tai-Shang(董太尚)[1], HOU Xiao-Hu(侯小虎)[1], ZHANG Xiu-Yun(張秀雲)[1], CHEN Wei(陳 偉)[2]

1.School of Materials Science and Engineering, Inner Mongolia University of Technology, Huhehaote Neimenggu 010051; 2.The 52nd Institute of China Ordnance Industries, Baotou Neimenggu 014000,P R China
(1. 內蒙古工業大學 材料科學與工程學院，內蒙古 呼和浩特 010051，中國)
(2. 中國兵器工業第 52 研究所，內蒙古 包頭 014000，中國)

鎂是所有金屬及合金中密度最低的結構材料，具有比強度和比剛度高以及減震性好、電磁遮罩性好和抗輻射能力強等特點，且易切削加工和回收。近年來，隨著很多金屬礦產資源的日益枯竭以及節能、環保和工業產品輕量化的迫切要求，鎂以其資源豐富而日益受到重視。鎂合金在汽車、電子、電器、交通、航空航太和國防工業等領域存在潛在的開發與應用價值，目前壓鑄鎂合金已得到較廣泛的應用。但是,具有高性能的變形鎂合金品種及其產品還很少，因此,發展新型變形鎂合金的製備工藝和加工技術成為近年來開發新型輕質結構材料的重要研究方向之一。經過30多年的發展，噴射沉積已發展成為一種成熟的商業化快速凝固技術，它可以製備Ni、Ti、Fe、Cu、Al、Mg等金屬及其複合材料，具有廣闊的應用前景。噴射沉積鎂合金於1987年在美國開始首次研究，隨後法國、德國及英國等國家也加入噴射沉積鎂合金的研究行列，並取得一定的研究成果，但國內的相關研究報導不多。

本文利用噴射沉積技術製備了含稀土的鎂合金，對鎂合金的組織和結構進行了分析與表徵，利用噴射沉積技術製備了 Mg–12.55Al–3.33Zn–0.58Ca-1Nd 鎂合金，對其進行了熱擠壓。利用 X 射線衍射儀、掃描電子顯微鏡、透射電子顯微鏡和能譜儀對鎂合金的組織、結構與成分進行了分析與表徵，結果表明擠壓態鎂合金中主要包括 α-Mg 和 Al_2Ca 相，稀土元素 Nd 可促進 Al_2Ca 相的形成，Nd 以固溶的方式存在於 Al_2Ca 中，Al_2Ca 相中存在孿晶結構。研究結果為製備高性能鎂合金提供理論與實驗技術基礎。

部分研究結果如下：

（一）噴射沉積 Mg–12.55Al–3.33Zn–0.58Ca-1Nd 鎂合金 X 射線衍射結果如圖 1 所示，衍射峰明銳，說明合金結晶良好，合金中主要包括 α-Mg 和 Al_2Ca 兩種相。

（二）圖 2a 為一 Al_2Ca 顆粒 TEM 形貌像，Al_2Ca 顆粒尺寸約為 300 nm 左右，圖 2b 為圖 2a 中 Al_2Ca 顆粒的高分辨像，圖 2b 中的插圖為高分辨像的傅立葉變換，電子束沿 Al_2Ca 顆粒的[112]晶向

（三）圖 3 a 為另一 Al_2Ca 顆粒的高分辨像，具有明顯的孿晶結構特徵，其中雙向箭頭所示為孿晶面，圖 3 b 為 3 a 的傅立葉變換，孿晶面為{111}面，該孿晶結構可能是在鎂合金的擠壓變形過程中形成的。

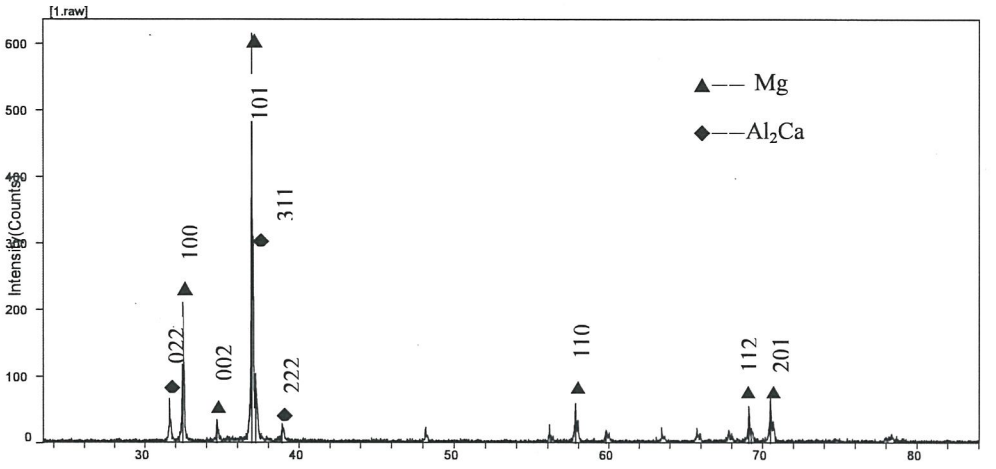

圖 1　鎂合金 X 射線衍射圖。

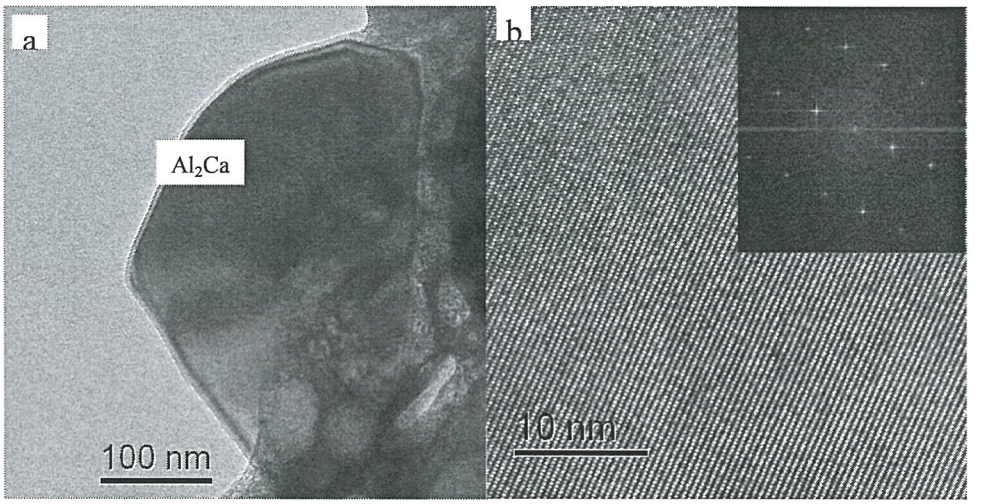

圖 2　a：Al_2Ca 相形貌；b：高分辨像（電子束沿[112]方向）。

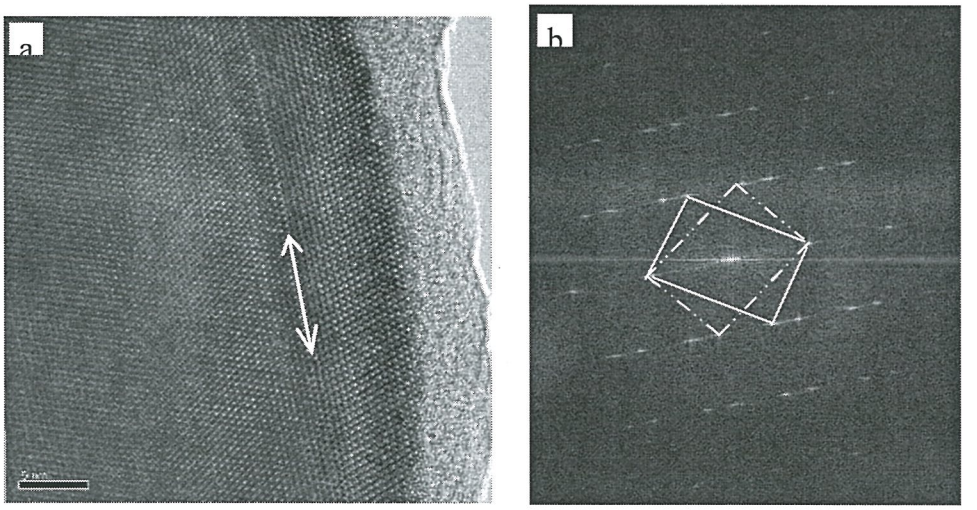

圖 3　a：Al_2Ca 孿晶結構高分辨像(Bar=5 nm)；b：a 的傅立葉變換。

A Self-Correction Method in Quantitative EDS Analysis for Complex Niobates (鈮酸鹽結構的透射 EDS 定量分析及自校正方法)

WANG Xian-Hao (王賢浩)，GU Hui (顧 輝)*

（中國科學院上海矽酸鹽研究所高性能陶瓷和超微結構國家重點實驗室，上海 200050，中國）

由於薄試樣厚度的未知，能譜（EDS）峰強度的校正難以有效開展並造成很多微分析只能定性。基於一種吸收、螢光等厚度效應自校正的方法，可以不需要測量試樣厚度也可進行經校正的 EDS 定量分析：該方法要求在譜線中包含同一元素兩個不同線系，其強度比與理論值的差異就會體現出厚度效應，從而"間接"進行厚度效應的定量校正。應用該方法驗證具有固定組分的鎢青銅結構鈮酸鋇鈉微晶，發現鈮的自校正效應可有效地作用於修正重元素鋇的含量，而對於輕元素鈉的修正還需更多地考慮其他誤差來源。同樣方法去定量分析鎢青銅結構的鈮酸鍶鋇織構化陶瓷，可精確測定晶粒內部組分，從而為開展陶瓷材料內部微觀"擴散相圖"的研究工作提供必要的微分析技術基礎。

作為分析電鏡的主要探測技術，X 射線能譜（EDS）被廣泛應用於材料等研究領域並成為透射電鏡的常規附件。但在大多數微分析中，EDS 主要用於元素識別這種定性工作，其主要原因在於定量分析還需要額外瞭解探頭和試樣的參數。因此，EDS 定量分析也就是相關參數的規律、特點乃至其新的應用方法研究，從而可以有效解決材料研究中的很多有趣或關鍵問題[1~3]。與掃描 EDS 相比，透射 EDS 不但具有高得多的空間解析度，其定量分析也相對直觀、簡單，可採用無標樣的薄樣品近似只進行厚度效應校正（或稱 ZAF 修正，包含原子序數、吸收和螢光發射等過程）。而厚度的測量，成為 EDS 定量分析的瓶頸難題。測量或計算消光距離或平均自由程等變通手段也會帶來其他問題，不是根本的解決辦法。近年來 Watanabe 發明的 ζ 因數的方法從能譜實驗本身包含入厚度效應，但其操作與思路較為複雜並且依賴於特定的標準樣品[4]。20 年前 Horita 等發展了同一元素多線系間的"本征"修正方法[5]，作者用同樣思路來測量薄試樣厚度並進行定量分析的必要修正。本研究將該方法驗證和應用于成分已知和未知的兩種鎢青銅結構的鈮酸鹽材料。

鎢青銅型鈮酸鹽是重要的多功能複雜氧化物，兼具良好的電光、熱釋電、壓電性質，但固溶原子種類和含量會對其產生根本影響，而織構化的陶瓷製備工藝和範本反應等化學控制過程使得其固溶成分經歷多重變化。由於鈮有 K 和 L 兩套特徵峰，低能的 L 系可被高能的 K 系所吸收，而它們之間的吸收比率變化規律與薄試樣的厚度有關，由此可以進一步推算出其他原子被鈮 K 系吸收的程度並進行矯正。作者針對其中的兩種結構進行定量分析：一是用作範本成分確定的鈮酸鋇鈉 BNN 晶種（$Ba_2NaNb_5O_{15}$），二是織構化陶瓷成分未知的鈮酸鍶鋇 SBN 主相（$Sr_xBa_{1-x}Nb_2O_6$）[2/6]。作為充滿型鎢青銅結構，BNN 中三種陽離子各自佔據結構

中特定的位置並在通常製備條件下形成化學配比的相，這為我們對比能譜定量校正前後的效果提供了很好的條件。

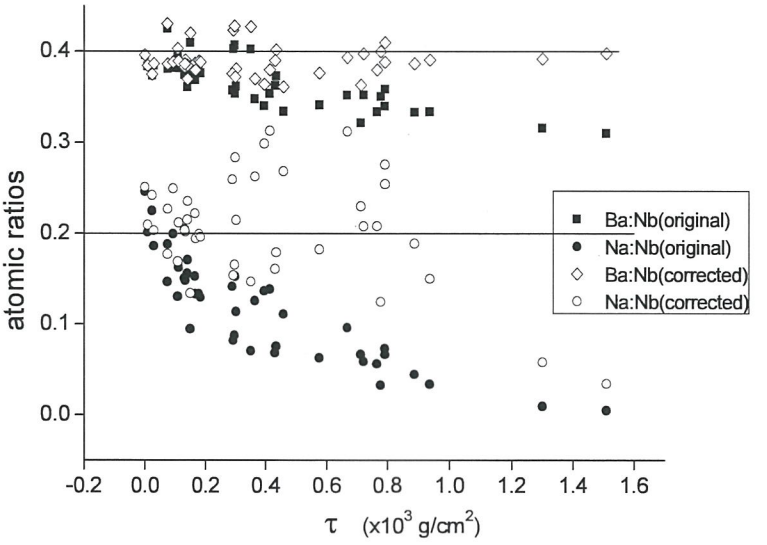

從右圖可以發現，原始和經校正（實心、空心符號）的 Ba:Nb 和 Na:Nb 的比值隨與厚度相關τ值的變化行為不同。經過校正的 Ba:Nb 非常接近理論值 0.4，偏差更小，而且基本不再隨厚度而變化。但是 Na:Nb 的校正結果不太理想，雖然校正後的平均值更接近理想值 0.2，但其彌散程度被擴大，反映出推算過程中有其他誤差被引入。

經高溫燒結的 SBN 陶瓷中主相是未充滿的鎢青銅結構，包含有多種成分和結構缺陷。作者對 Sr:Nb 和 Ba:Nb 比值均進行了厚度吸收效應的校正，發現前者不經過校正的結果已足夠好，而後者校正結果與 BNN 相同。由此推論出兩元素的特徵峰能量比較接近時，厚度效應相對接近並基本相互抵消，所以可不用進行校正；而對待校正的特徵峰能量較低情況，厚度校正是很有效的提高定量分析精確度和準確性的辦法；但對於能量過低的特徵峰，來自探頭等其他的效應也會開始對結果產生負面影響，單使用該方法可能效果不夠好。

References

1. Chi M F, Gu H, Wang X, Wang P L. J Am Ceram Soc，2003，86：1953.
2. Wang X H, Gu H, Huang Q W, Čeh M. Acta Materialia，2007，55：5304.
3. Xing J J, Gu H, Gloter A, Shen H, Pan X M, Wang P C. Acta Materialia，2007，55：5323.
4. Watanabe M, Williams D B. Z Metallkd，2003，94：307.
5. Horita Z, Ichitani K, Sano T, Nemoto M. Phil Mag，1989，A 59：939.
6. Wang X H, Gu H, Huang Q W, You L P. Inter J Mater Res，2007，98：228.

Deformation Induced Fe_3C Dissolution in Pearlite Steel
(形變導致 Fe_3C 分解機制研究)

LI Zi(李智), MA Xiu-Liang* (馬秀良)

Shenyang National Laboratory for Materials Science,Institute of Metal Research, Chinese Academy of Sciences, Shenyang Liaoning 110016,P R China

(中國科學院金屬研究所瀋陽材料科學國家（聯合）實驗室， 遼寧 瀋陽 110016，中國)

室溫下塑性變形導致珠光體鋼中 Fe_3C 相分解的現象早在上世紀 70 年代就引起了普遍關注**[1，2]**。 過去幾十年人們致力於研究 Fe_3C 分解的原因, 提出了一些可行的機制**[3~5]**，但依然存在較大的爭議，目前有兩種機制得到一定的認可：其一是位錯機制[1]，即認為珠光體鋼在變形時，體素中形成大量位錯纏結在 Fe_3C 的周圍，由於碳原子和鐵素體位錯的交互作用能高於 Fe_3C 中的鐵原子和碳原子的結合能，位錯將碳原子從 Fe_3C 顆粒表面拖出，導致其分解。另外一種機制是熱力學機制**[4]**，他們認為由於變形導致 Fe_3C 細化，表面積增加，使熱力學上 Fe_3C 變得不穩定，Fe_3C 通過 Thompson-Gibbs 效應發生分解。且認為辨別兩種機制的判據[5]是碳原子最後溶於鐵素體晶格中還是鐵素體位錯或晶界等缺陷中，溶於鐵素體中則造成鐵素體晶格的膨脹，溶於缺陷中則應看不到這種現象。

本工作實驗材料採用 AISI52100 鋼板材，成分為(wt.%)：1.0% C，1.5% Cr，0.31% Mn，0.24% Si，0.08% Ni，0.15% W，0.03% Mo，其餘為 Fe。經過熱處理獲得粒狀和片狀珠光體鋼，再分別對兩種珠光體鋼進行了軋製變形處理，對粒狀珠光體鋼還做了表面機械研磨處理，X 射線實驗採用用矽粉作為標準樣品校正實驗資料。

對於片狀珠光體鋼，變形後鐵素體衍射峰向低角發生明顯漂移，見圖 1（a），在 90%軋製變形後漂移達到 0.06 度，由布拉格公式可知鐵素體晶格發生了膨脹，這種膨脹是碳原子溶於鐵素體晶格中造成，0.45at.%的碳原子固溶在鐵素體晶格間隙內, 計算可知有 10%的滲碳體發生了分解。而經過同樣處理的粒狀珠光體鋼卻沒有發現這種現象，見圖 1（b）。

為了解釋兩種形態珠光體鋼 XRD 實驗結果的差異，本文對變形後的樣品進行了透射電鏡觀察。發現片狀珠光體鋼在承受變形時，滲碳體片的表面形成大量臺階，Fe_3C 相和鐵素體一同發生變形，這將利於熱力學機制發生作用**[4]**，碳原子溶於鐵素體晶格間隙中造成鐵素體晶格發生膨脹。而粒狀珠光體鋼變形時基本不發生剪切變形，沒有形成新的表面，變形過程是鐵素體晶粒細化和滲碳體顆粒直徑減小的過程，最後滲碳體顆粒要麼完全分解要麼保持原始形狀，這是位錯機制發生作用的結果**[1]**，因而鐵素體晶格常數沒有明顯的變化。也就是說滲碳體的形態影響滲碳體的分解方式。

但根據他人的研究**[1，2]**，嚴重塑性變形後，片狀珠光體中碳原子應該偏聚於

位錯中，本實驗也發現粒狀珠光體樣品細化成納米晶後鐵素體的晶格也發生了一定的膨脹。作者認為只有小變形後的碳原子位置才能真實反應 Fe_3C 的分解方式，而不能以發生嚴重塑性變形後的碳原子位置作為 Fe_3C 分解方式的判據，形變是一個動態的過程，經歷嚴重塑性變形時，就不能不考慮 Fe_3C 的形態在變形的過程中發生的變化。粒狀珠光體鋼在變形的早期是位錯機制發揮作用，而當其細化到一定程度後熱力學機制和毛細現象也會發揮作用，片狀珠光體鋼也同樣存在這一複雜的變化。

References

1. Gridnev V N，Gavriljuk V G. Metal Phys，1982，4: 531.
2. Gavriljuk V G. Phys Metals Metallogr，1978，45(5): 59.
3. Yu Ivanisenko，Lojkowski W，Valiev R Z. Acta Mater，2003，51: 5555.
4. Languillaume J，et al. Acta Mater，1997，45: 1201.
5. Sauvage X，Copreaux J，Danoix F，Blavette D. Philos Mag A，2000，80:781.

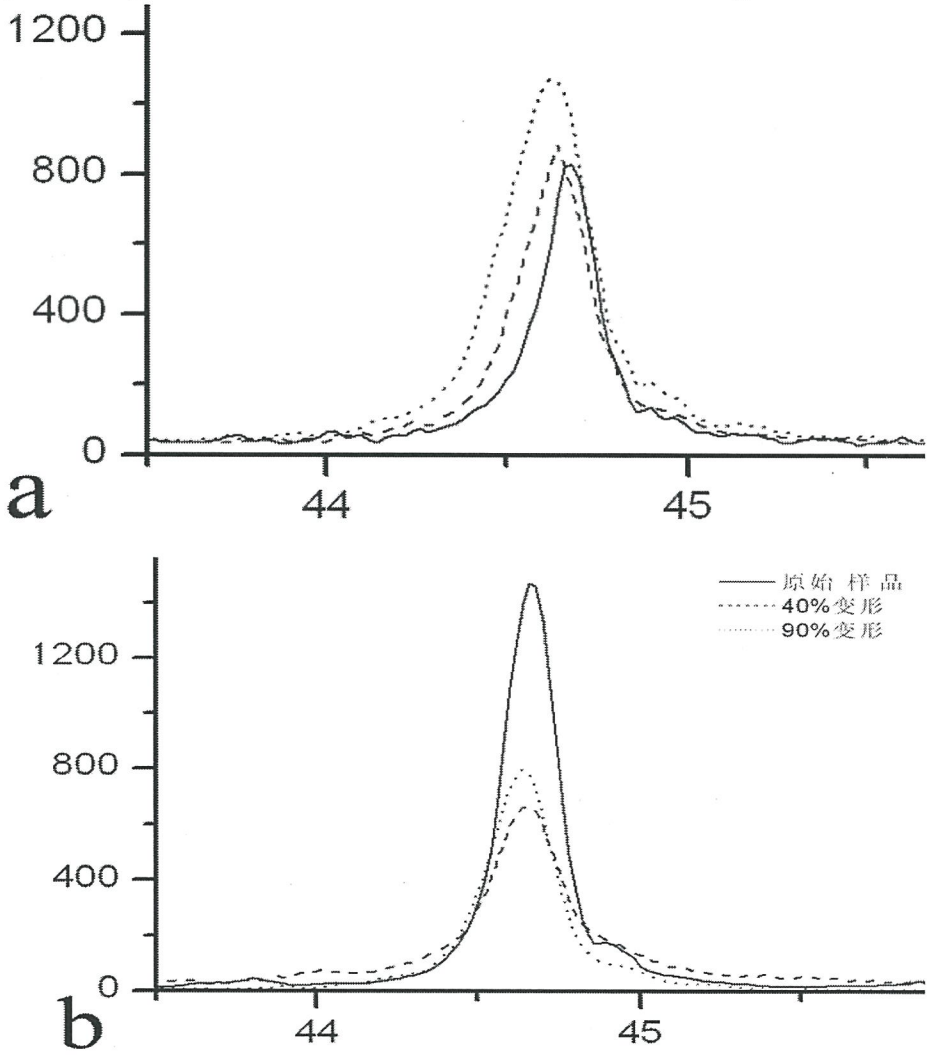

圖 1 a，b 分別為片狀和粒狀珠光體鋼軋製變形後的 XRD 實驗結果，圖中僅顯示了經過 Si 標樣校正的 Fe（110）衍射峰。

Study on the Grafting of Titanate Coupling Agent/Silane Coupling Agent onto Wheat Straw by Microwave Radiation (微波接枝鈦酸酯/矽烷處理秸稈纖維微觀結構的分析)

DENG Hua(鄧 華)，SUN Rong(孫 蓉)，YAN Tuo(嚴 拓)，AO Ning-Jian*(敖寧建*)

Life Science and Technology College, Jinan University, Guangzhou Guangdong 510632, P R China
(暨南大學 生命科學技術學院 ，廣東 廣州 510632，中國)

由於天然纖維具有許多突出的優點，如：來源豐富、價格低廉、可再生、可降解、高性能比等，使對高性能天然纖維及其複合材料的研究、開發與應用亦已成為全球研究熱點。作者選用微波接枝鈦酸酯/矽烷偶聯劑對秸稈進行表面處理，對經表面處理後的秸稈纖維進行 FTIR（傅立葉變換紅外）分析；用 SEM 觀察處理前後秸稈纖維表面形貌變化，並將處理後秸稈纖維與 HDPE（高密度聚乙烯）製成複合材料，對其力學性能及其在複合材料中微觀分佈情況進行了分析。

秸稈纖維經粉碎、過標準篩篩選統一粒徑，用鈦酸酯/矽烷偶聯劑進行微波接枝改性處理，經表面處理後的秸稈纖維與 HDPE 粒料混合輥煉，將混合好的物料放入模具中壓制成型。對經表面處理後的秸稈纖維進行 FTIR 分析；採用 XRD 表證秸稈纖維處理前後去結晶化的結果；用 SEM 觀察處理前後秸稈纖維表面形貌變化及樣品的斷層形態。

秸稈在複合材料中的分散狀態，包括分散均勻程度、有無定向等對複合材料的物理力學性能和加工性能的較大影響。圖 1 a 為秸稈未處理的複合材料形態，圖 1b 為秸稈用鈦酸酯偶聯劑處理的複合材料形態，圖 1c 為秸稈用矽烷偶聯劑處理的複合材料形態。可見，未處理的秸稈表面較為光滑，與塑膠相的相互作用較弱。相反，用偶聯劑進行活化處理後的秸稈表面覆蓋一層偶聯劑，變得比較粗糙，因此與塑膠相的相互作用較強。

秸稈纖維與高分子基體形成介面時，要通過“接觸”、“浸潤”與“固化”等過程才能成形。物質的表層分子狀態與它內部的分子狀態不同，表層分子能量比內部分子能量高，當固態物質表面與其他物質接觸時，一旦形成介面，就會發生降低表面能的吸附現象。在複合材料中，當纖維與基體相接觸時，就會首先吸附那些能降低表面能的物質形成介面，從宏觀上看，就是基體相會沿增強材料表面向四方流動、鋪展，這就是“浸潤”。浸潤性好，就會在兩相材料介面上形成最緊密的結合狀態(圖 1e，1f)。而後經過“凝結”、“固化”等過程，使介面區達到基體的分子能量最低、結合穩定的狀態，這樣複合材料介面就取得了良好的結合。對製備的複合材料按 GB/T 1040-92 進行拉伸性能測試，發現經鈦酸酯處理的秸稈纖維，填充量高達 30%時，拉伸性能保持率仍保持在 82.3%；而經矽烷處理的秸稈纖維，填充量在 20%時，拉伸性能保持率高達 96%。

* 通訊作者 E-mail：taonj@jnu.edu.cn

由 FTIR(圖 2a)可以看出，在 2920cm^{-1} 左右處的吸收峰為-CH_2 基團的 C-H 反對稱伸縮振動；在 2400cm^{-1} 左右處的強吸收峰是由碳甲基及次甲基基團中的 C-H 對稱伸縮振動引起，此處峰的明顯加強意味著反應後甲基和次甲基增多 730cm^{-1}、890cm^{-1} 為 P-O-P 和 P-O-Ti 的特徵吸收譜帶；圖 2b 中可以看出在 1750cm^{-1} 處為中心的寬吸收帶為水分子形成氫鍵的變形振動、木質素中與芳香環相連的 C=O 伸縮振動及醯胺化合物的特徵吸收譜帶；在 1100cm^{-1} 附近為 Si-O-Si 的特徵伸縮振動峰；在 1160cm^{-1} 左右處為醚鍵的非對稱伸縮振動，980～1100cm^{-1} 為磷-氧-碳鍵的特徵吸收譜帶，此處峰的加強表明醚鍵增多，秸稈纖維中部分羥基已被醚鍵所取代。因此，可以看出，經微波改性處理，鈦酸酯及矽烷都較好的接枝在秸稈纖維上，使秸稈纖維複合材料介面問題得到很好的改善。

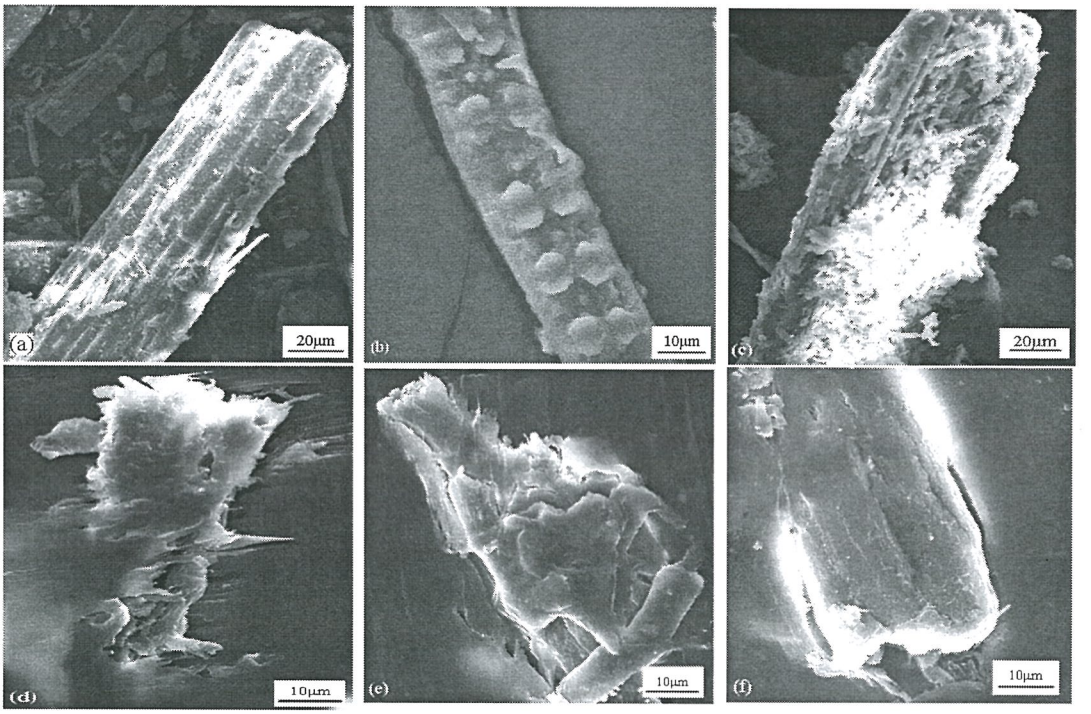

圖 1 不同處理條件下秸稈纖維的表面情況。a：未處理秸稈纖維組；b：鈦酸酯偶聯劑處理組；c：矽烷偶聯劑處理組。秸稈纖維/高密度聚乙烯複合材料的 SEM 照片。d：填充未處理秸稈纖維組；e：填充鈦酸酯偶聯劑處理組；f：填充矽烷偶聯劑處理組。

2a

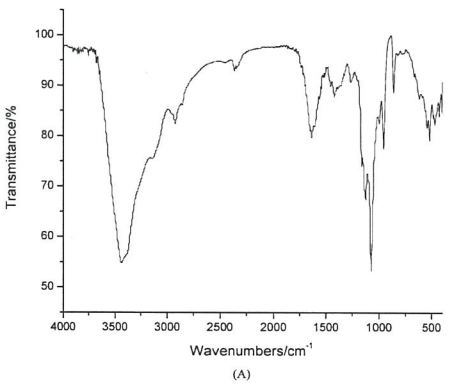

2b

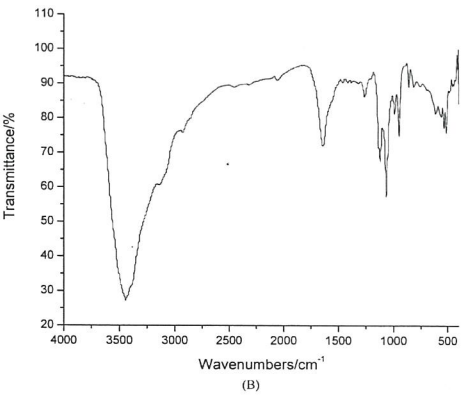

圖 2 秸稈纖維經微波接枝鈦酸酯(a)和矽烷偶聯劑(b)的紅外光譜圖。

Monitoring Cellular Metabolism with Fluorescence Lifetime of Reduced Nicotinamide Adenine Dinucleotide

Vladimir Gukkasyan[a], Tatyana Buriakina[a], Jim Hsu[a], and Fu-Jen Kao（高甫仁）[a, b]

[a]*Institute of Biophotonics, National Yang-Ming University（陽明大學生醫光電研究所）, Taipei 11221, Taiwan*

[b]*Department of Photonics, National Sun Yat-sen University, Kaohsiung 80424, Taiwan*

* Corresponding author: fjkao@ym.edu.tw

As a minimum invasive technique, autofluorescence spectroscopy has found its applications in the characterization of tissues and diagnosis of diseases. The major distinguishing power arises from the change of the nano-environment, quantities and functional/conformational states of the endogenous fluorophores.

Formulation of the oxidative phosphorylation and its' first observation by means of fluorescence spectroscopy in the 60s of the previous century led to the acceptance of bioenergetics as a new field of studies. The new discipline grew fast with the increasing number of papers, related to the energy generation in mitochondria, advancement of the instrumentation and improvement of observation techniques. As such, fluorescence lifetime imaging microscopy (FLIM) has gained popularity as a sensitive technique to monitor the functional/conformational states of NADH– one of the main compounds of the oxidative phosphorylation. We hereby present a brief review on the development and current application of cellular metabolism observation via NADH FLIM, illustrating it with the examples of both physiological (cell density, apoptosis, necrosis) and pathological states (inhibition of the electron transfer chain).

References

[1] D. H. Williamson, P. Lund, and H. A. Krebs, Biochem J. 103, 514 (1967).

[2] A. Mayevsky, N. Zarchin, H. Kaplan, J. Haveri, J. Haselgroove, and B. Chance, Brain Res. 276, 95 (1983).

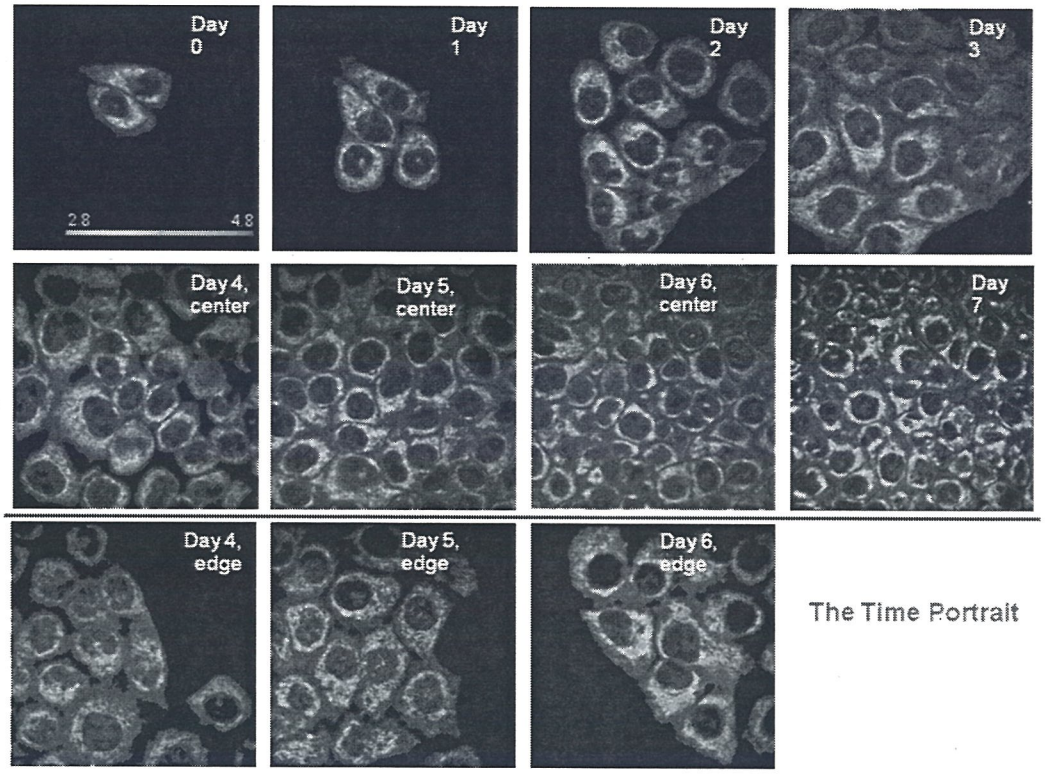

Figure 1. NADH free/bound ratio mapping at the center and at the border of a HeLa cell colony in a culture. The images, color coded with the free/bound ratio, reveals different metabolical conditions at the edge and in the middle of a colony. The scale bar is 100 μm.

The Electron Microscopic Diagnosis of Thrombotic Microangiopathy Associated Nephropathy

血栓性微血管病腎損傷的電鏡診斷

WANG Su-Xia（王素霞）, ZOU Wan-Zhong, XIE Yan-Ling, CHAI Li-Jun, WANG Shu-He

Department of Electron Microscopy, Peking University First Hospital（北京大學第一醫院電鏡室）, Beijing 100034, P R China

血栓性微血管病（thrombotic microangiopathy, TMA）臨床表現為微血管病性血管內溶血、血小板減少和急性腎功能不全；多數病例急性起病，病情嚴重，預後較差。多種不同的病因均可引起 TMA， 包括細菌和病毒的感染、遺傳性、自身免疫、腫瘤、藥物、妊娠等，其中經典類型為溶血性尿毒癥綜合症（HUS）和血小板減少性紫癜（TTP）[1~4]。TMA 的病理改變以微血管內皮損傷、微血栓形成及臟器缺血性改變為特徵。雖然根據臨床表現可以推測 TMA 的存在，但其確診需要觀察到活檢組織的特徵性病理改變。腎臟是 TMA 最常累及、且病變較重的器官之一，因此，進行腎活檢組織的病理檢查是診斷 TMA 的重要手段，對於指導臨床治療和改善病人的預後具有重要意義。其中，透射電鏡檢查對於觀察血管內皮損傷的病理改變具有不可替代的作用。本文分析了我室近四年來診斷的 TMA 病例的臨床病理特點，探討電鏡檢查在 TMA 的診斷及其鑒別診斷中的作用。

物件和方法：收集北京大學腎臟病研究所 2005 年 1 月至 2008 年 12 月間的腎活檢病例共計 7562 例，均具備完整的臨床病理資料，腎活檢標本進行了光鏡、免疫螢光和電鏡檢查，其中，20 例診斷為 TMA 腎損傷。分析其臨床病理特點，將根據臨床症狀和光鏡檢查的初步診斷與最終的電鏡診斷結果進行比較。

結果與討論：(1) 臨床特點：發病年齡 19-66 歲，平均年齡 42±14 歲。以女性比例較高，男：女為 6：14。均表現有血尿、蛋白尿，其中 12 例合併急性腎功能不全；貧血 8 例，高血壓 6 例。根據臨床表現懷疑為 TMA 的病例 8 例，其餘病例均是通過病理檢查發現和診斷的。已知的原發病或合併的系統性疾病分別為：抗磷脂抗體綜合征 1 例，造血幹細胞移植術後 1 例，Castleman 病 2 例，系統性紅斑狼瘡 3 例，乳腺癌術後化療 1 例，其他病例的病因不明。(2)病理改變：TMA 的病理診斷依據如下：病變部位主要以腎小動脈和腎小球毛細血管壁的內

皮細胞損傷為主。光鏡下
可見纖維素樣壞死或血栓
胞增生及腫脹，基底膜增
檢查可見腎小球內皮細胞
絨毛樣結構，並伴有紅細
中 3 例合併狼瘡性腎炎。
血管內增生性腎小球病或
管損傷 2 例，原發性 I 期
一步確診為 TMA。分析光
有特異性，如腎小球內皮
或內皮細胞病；基底膜增
致雙軌征，與膜增生性腎
甚至腎小管壞死，與其他
他疾病合併發生時，其病
中，4 例合併狼瘡性腎炎

結論：透射電鏡檢查
用，對於光鏡病理改變不
可防止其誤、漏診。

參考文獻

[1] Moake J L. New Engl J
[2] Tsai H M. J Am Soc Nep
[3] Tostivint I, et al. Nephro
[4] Renolds J C, et al. Am J

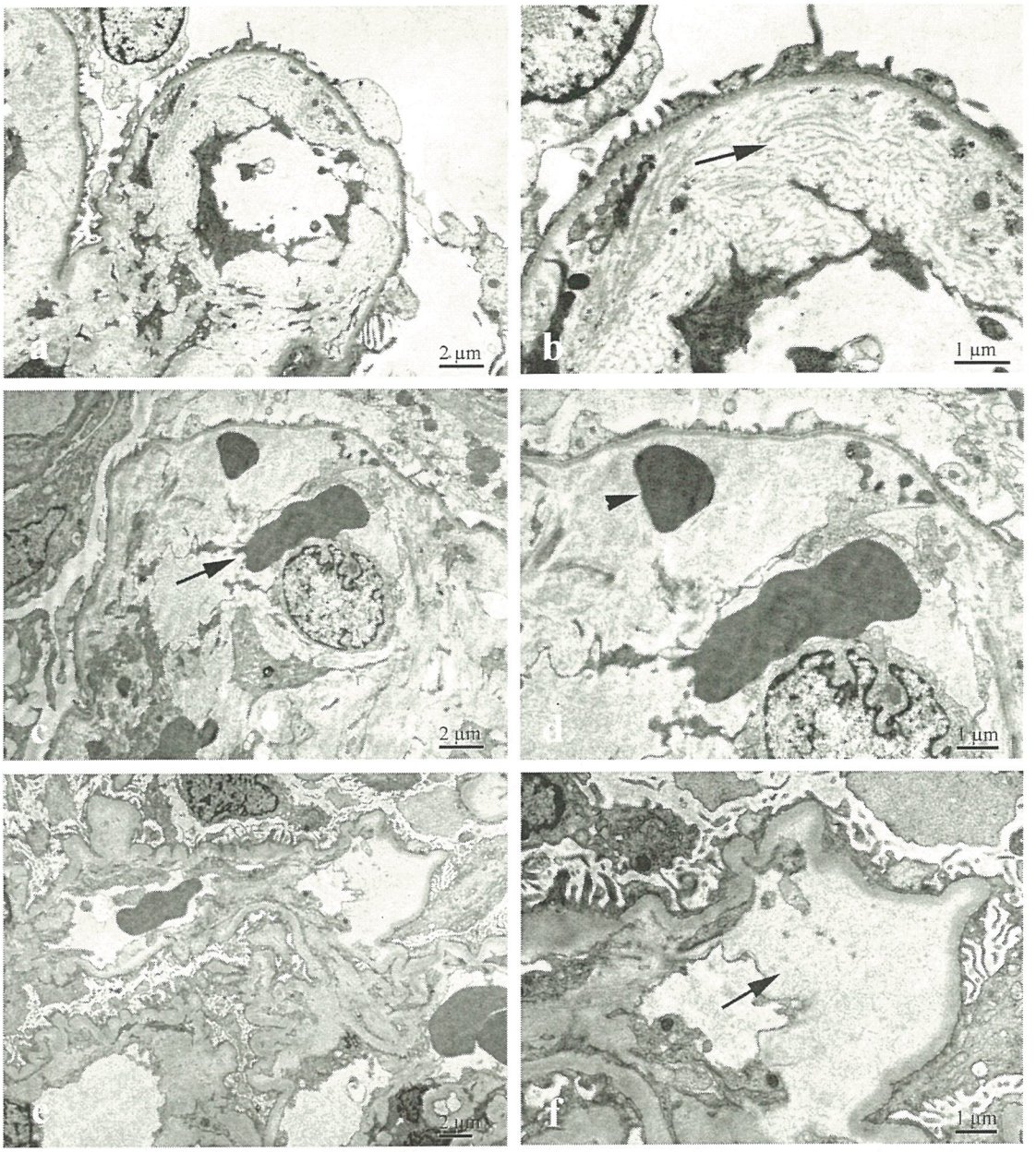

圖 a，b：腎小球基底膜內疏鬆層增寬，毛細血管腔狹窄，內皮下可見電子透明的顆粒狀、纖維狀結構(↑)（a：Bar＝2 μm，圖 b：Bar＝1 μm）；圖 c，d：腎小球毛細血管腔嚴重狹窄，可見毛細血管腔內紅細胞(↑)及滲入內疏鬆層內的紅細胞(▲)（圖 c：Bar＝2 μm, 圖 d：Bar＝1 μm）；圖 e，f：腎小球基底膜缺血性皺縮，節段性內疏鬆層增寬，可見電子透明的顆粒狀結構(↑)（圖 e：Bar＝2 μm, 圖 f：Bar＝1 μm）。

Intravital Multiphoton Hepatic Microscopy for Elucidating Liver Metabolic Activities *in vivo*

Chen-Yuan Dong（董成淵）, PhD

Department of Physics, National Taiwan University（臺灣大學物理學系）

Abstract

The ability to image within living organisms can reveal important dynamic information of physiological systems and provide insights in dealing with diseases. In an attempt to achieve intravital optical microscopy, we employ the minimally invasive imaging technique of multiphoton microscopy which allows *in vivo* imaging to be achieved with improved depth penetration and minimal photodamage. In order to validate the application of multiphoton imaging in studying pathological tissues, we performed *ex vivo* characterization of normal and pathological liver tissue specimens. Furthermore, we developed and implemented intravital imaging chambers that allow the direct visualization of physiological phenomena *in vivo*. In this presentation, I will present results in hepatology demonstrating the progress we have made in imaging and quantifying physiological dynamics of hepatobiliary metabolism in normal and pathological mouse livers *in vivo*. Our results may lead to an improved understanding of basic liver physiology and treatment procedures of liver diseases in the future.

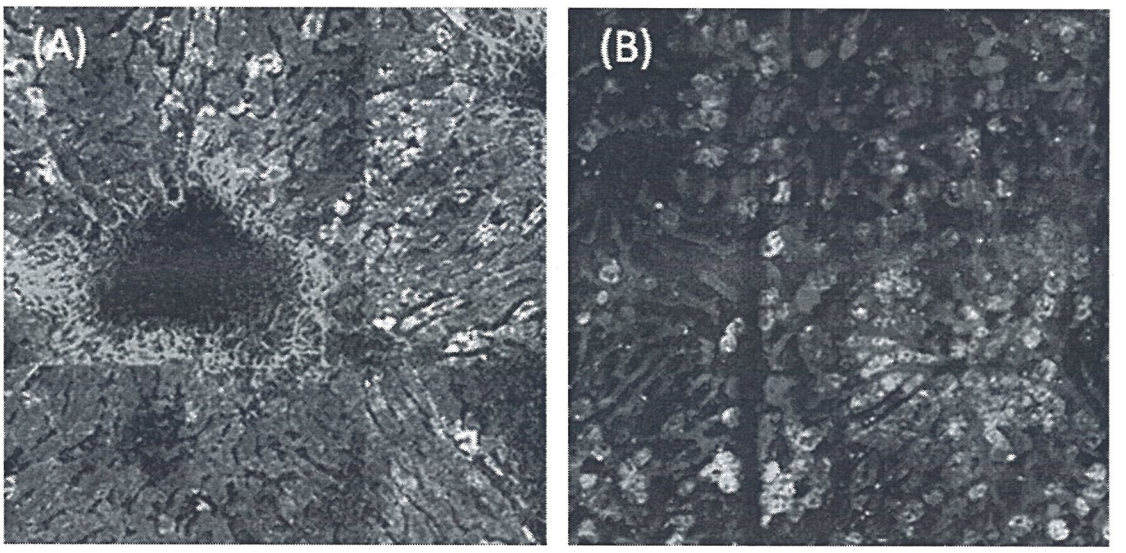

In vivo multiphton imaging of: (A) the effects of liver fibrosis on hepatobiliary metabolism and (B) acetaminophen induced hepatic pathology.

Research on the Change of the Sarcoplasmic Reticulum Ultrastructure and Ca^{2+} Concentration During Excitation-Contraction Coupling in Muscle

肌收縮偶聯時肌漿網結構及 Ca^{2+} 變化的研究

YANG Yong-Ji（楊勇驥），TANG Ying，LEI Chang-hai，SHEN Ya-feng，LIU Guan-sheng

Department of electron microscope, Second Military Medical University（第二軍醫大學基礎部生物物理研究所）, Shanghai 200433, P R China

本文報導了採用紅外探測-電腦控制的超低溫快速冷凍固定技術、冷凍置換技術、電鏡技術、膜片鉗技術及鐳射掃描共聚焦技術對肌興奮收縮偶聯時肌漿網結構及肌漿網內 $Ca2^{+}$釋放進行了分析，從顯微結構、超微結構形態學的角度對肌興奮-收縮偶聯發生時，$Ca2^{+}$的作用進行了研究，這對揭示肌興奮-收縮偶聯時，肌漿網內 $Ca2^{+}$的釋放機理研究有重要意義。

肌漿網（SR）及 Ca^{2+}在肌興奮-收縮偶聯機制中起著重要作用，但在肌興奮-收縮偶聯時，Ca^{2+}如何在肌漿網中被"刺激"後而釋放，是多年來生理學及細胞生物學最感興趣的研究熱點之一，也是一直未能在形態學上得到證實的難題。由於肌興奮-收縮偶聯發生時的時間歷程極短（以毫秒計）,常規化學固定（固定時間以分鐘計）無法保留其瞬間經歷時的超微結構形態及 Ca^{2+}位點變化，因此現有的細胞超微結構研究方法,無法對其在毫秒級功能變化時的結構作同步研究，因而很難對其進行形態上的觀察及證明，這也是超微結構形態學、細胞生物學、細胞生物物理學亟待解決的難題。採用超低溫快速冷凍固定並結合透射電子顯微鏡（TEM）及膜片鉗-鐳射掃描共聚焦顯微鏡技術是唯一能夠解決該問題的方法。本文採用電腦控制電刺激-超低溫快速冷凍同步固定技術及膜片鉗-鐳射掃描共聚焦顯微鏡技術對肌興奮-收縮偶聯時，肌漿網的結構及肌漿網內 Ca^{2+}釋放進行了分析。

採用透射電子顯微鏡對電刺激後 2.4ms 及 3.8ms 後的骨骼肌肌漿網進行觀察分析，發現骨骼肌肌漿網內膜上存在排列整齊的跨膜樣物質，其尺寸為：，這與肌漿網膜上存在的鈣離子通道-RyR 受體蛋白的尺寸相同，肌漿網記憶體在高電子密度的物質（稱為 core cylinder），如圖 1、圖 2 所示。

採用鐳射掃描共聚焦顯微鏡觀察到骨骼肌在單次電刺激後 6.4s 時 Ca^{2+} spark 開始明顯增大，說明此時胞漿內的游離 Ca^{2+}濃度開始增高。在骨骼肌肌細胞中，胞漿內游離 Ca^{2+}增多必然要與肌鈣蛋白結合引起肌纖維收縮，而根據興奮收縮偶聯發生時的 CICR 機制，此時骨骼肌已進入舒張狀態，兩者相違背。國外也有文獻報導骨骼肌電刺激後在 5.52s-7.1s 時間段內 Ca^{2+} spark 體積最大、強度最強，但對於其發生的原因目前還不太清楚。

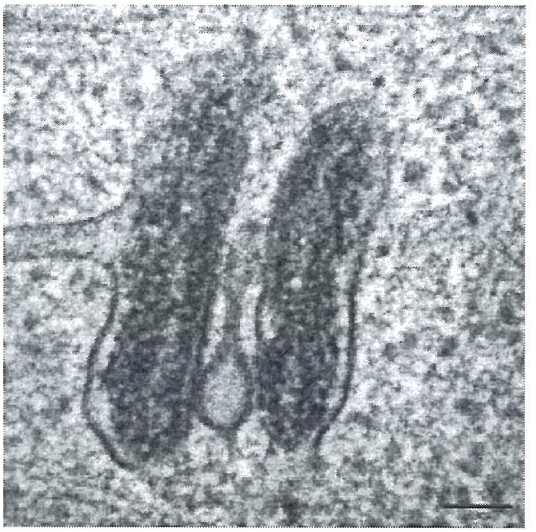

圖 1 電刺激後 2.4 毫秒後的骨骼肌肌漿網，肌漿網內膜上存在排列整齊的跨膜樣物質（箭頭所指）。Bar=100nm

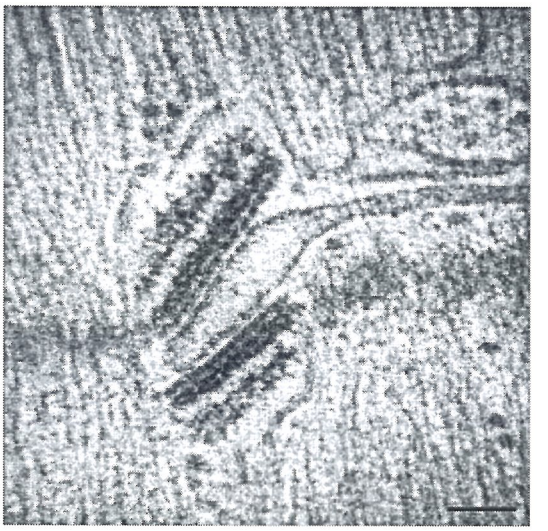

圖 2 電刺激後 3.8 毫秒後的骨骼肌肌漿網，肌漿網內膜上存在排列整齊的跨膜樣物質（箭頭所指）。Bar=100nm

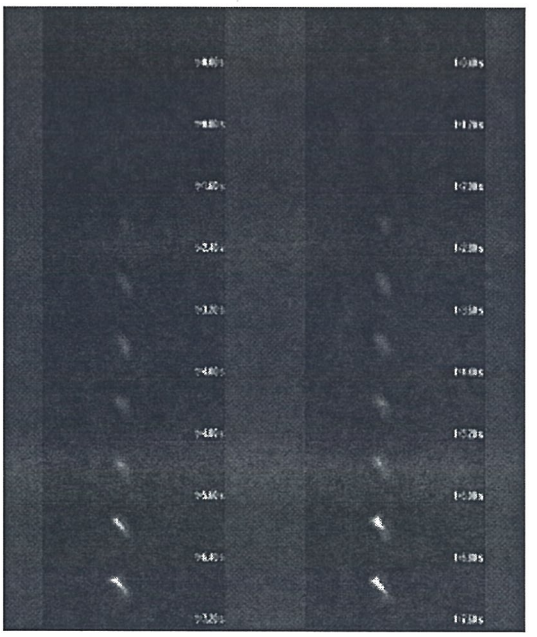

圖 3 採用鐳射掃描共聚焦顯微鏡獲得的骨骼肌鈣火花圖像。

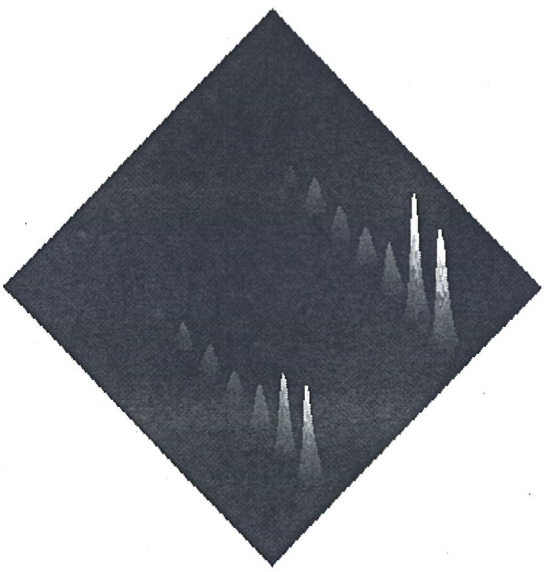

圖 4 骨骼肌鈣火花圖像的強度圖，骨骼肌在單次電刺激後 6.4s 時 Ca^{2+} spark 開始明顯增大，說明此時胞漿內的游離 Ca^{2+} 濃度開始增高。

Light and Electron Microscopic Immunocytochemical Analysis of Noradrenergic Terminals in the Rat Trigeminal Motor Nucleus

YANG, Hsiu-Wen（楊琇雯）[1] and MIN, Ming-Yuan[2]

[1] *Department of Biomedical Sciences, Chung-Shan Medical University（中山醫學大學生物醫學科學系）, No.110, Sec. 1, Chien-Kuo N. Road, Taichung 402, Taiwan.*

[2] *Department of Life Science, College of Life Science, National Taiwan University, 1, Sec 4, Roosevelt Rd. Taipei 106, Taiwan.*

The noradrenergic (NA) innervation in the trigeminal motor nucleus (Mo5) of postnatal and adult rats was examined by light microscopic (LM) and electron microscopic (EM) immunocytochemistry using antibodies against dopamine-β-hydroxylase (DBH) or tyrosine hydroxylase (TH), which are synthesis enzymes for norepinephrine and are commonly used as biomarker for NAergic neurons. The DBH-immunoreactive (ir) fibers, presumed to be NA fibers, were identified in the Mo5 as early as postnatal day 0 (P0). A continuous increase in the density of labeled fibers was observed during development up to P20, with a slight decrease at P30 and in the adult. EM analysis of serial ultrathin sections revealed that, at P5, nearly half (46%) of the examined NA terminals (TH-ir terminals) made synaptic contact with other neuronal elements with membrane specializations. The percentage of examined NA varicosities engaged in synaptic contacts increased at P15 (74%), then decreased in the adult (64%). At all developmental ages, the majority of contacts made by these boutons were symmetrical, with the postsynaptic elements being mainly dendrites and occasionally somata. Interestingly, some of the NA terminals made axo-axonic contacts with other unidentified boutons. These results show that, although the density of NA fibers increases during postnatal development, functional NA boutons are present in the Vmot at early postnatal ages. Some of these fibers might exert their effect via non-synaptic release of noradrenaline, so-called volume-transmission[1], but, in the main, they form conventional synaptic contacts with dendrites, somata, and other axonal terminals in the Mo5[2]. These results are consistent with previous electrophysiological studies that propose an important role for the NA system in modulating mastication[3].

References

1. Katakura, N. and Chandler, SH. J Neurophysiol. 1990 (63) 356
2. Min, MY., Hsu, PC., Lu, HW., Lin, CJ. and Yang, HW. Anat. Rec. 2007 (290) 96
3. Vizi, ES., Kiss, JP. and Lendvai, Neurochem. Int. 2004 (45) 443

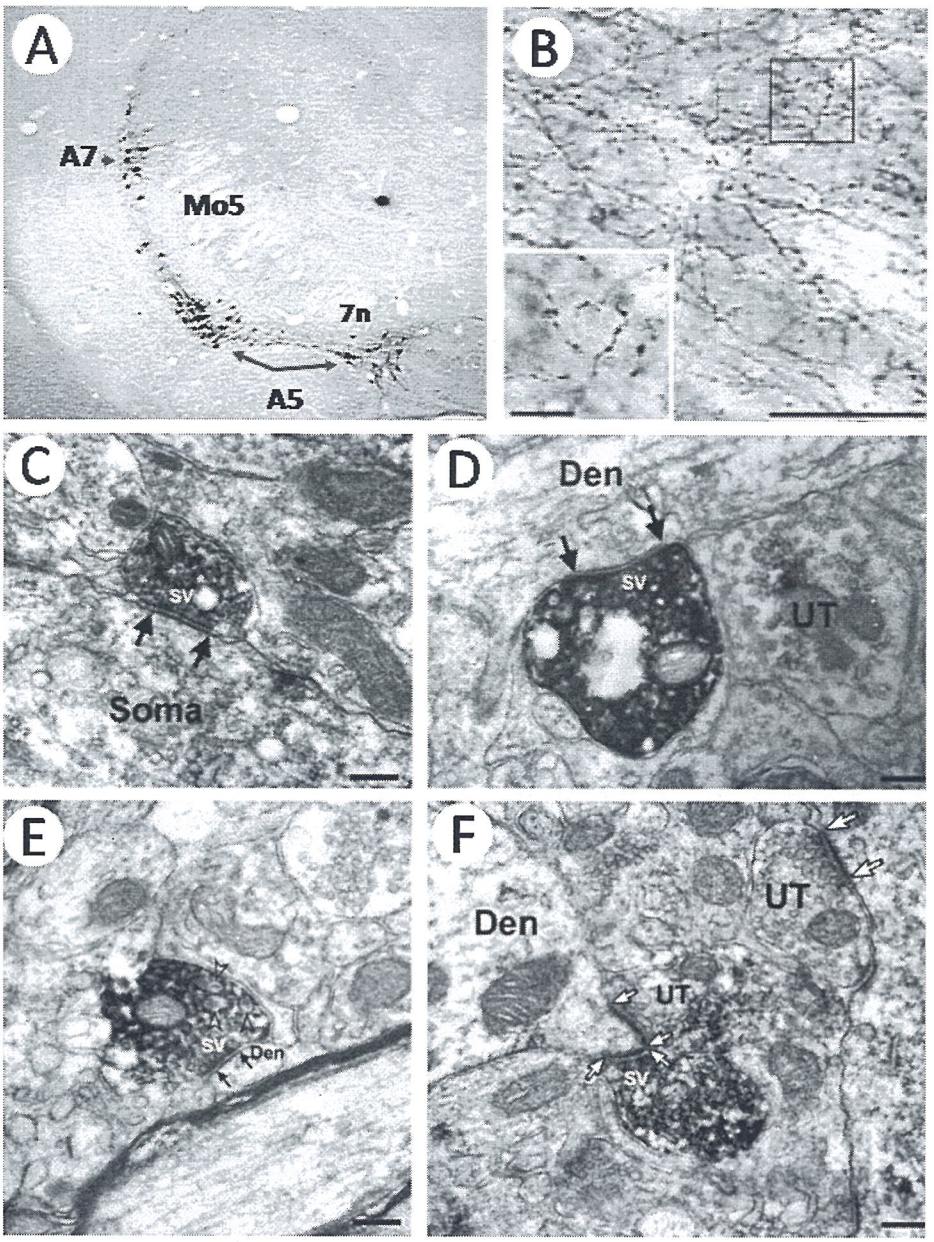

A Immunostaining of DBH shows two populations of noradrenergic neurons, the A7 and A5 catecholamine cell groups, which project to trigeminal motor nucleus (Mo5) in adult rat. **B** High power magnification shows DBH-ir fibers in Mo5 at P15 rat pup. **C-E** EM photomicrographs illustrating three TH-IR varicosities in the Mo5 at P15 which make symmetrical synaptic contacts with a cell body (C), a primary dendrite (D), and a distal dendrite, respectively (E). Note the less prominent density on the face of the postsynaptic membrane indicated by the two parallel arrows in all three cases. Bouton in E contains dense-cored vesicles indicated by white arrowheads. **F** A TH-IR bouton and an unlabeled bouton (UT) forming asymmetrical synapses (white arrows) with a dendritic spine. Note the prominent postsynaptic density of the active zone indicated by four arrows. Another unlabeled bouton (UT) also forms a asymmetrical synapses (white arrows) with another dendrite. Scale bars = 0.2 μ m.

Morphological Evidence of Coinfection of Viruses in Cultured Cell
培養細胞病毒共感染的形態學證據

CHEN De-Hui（陳德蕙）[1], YANG Yi[2]

1. Institute of Basic Medical Sciences, Academy of Military Medical Sciences（軍事醫學科學院基礎醫學研究所）；

2. National Center of Biomedical Analysis，Beijing 100850, P R China）

電鏡是檢出動物和人體組織細胞感染病毒與發現新病毒的重要研究工具。根據電鏡下病毒的形態和形態發生學的特徵，可以鑒定分類病毒到科（Family）。作者在上世紀 70 年代曾報導過，從 134 份送電鏡檢查的感冒患者鼻分泌物或/和咽漱液分離病毒可疑的體外培養細胞中發現 7 份有兩種病毒的混合感染（或稱共感染），它們是：腺病毒與副粘病毒 2 份；皰疹病毒與副粘病毒 2 份；鼻病毒與冠狀病毒 1 份；鼻病毒與正粘病毒 1 份以及鼻病毒與副粘病毒 1 份。2003 年 SARS 暴發期間，我們又意外地從一例女性患者及其母親（搶救無效死亡）生前咽拭子分離病毒陽性的細胞（Hep）培養物中檢出冠狀病毒與呼腸病毒的共感染。電鏡下，超薄切片中培養細胞內共感染病毒的形態學特徵如下。

（一）副粘病毒與腺病毒共感染：在感染細胞核中可查見呈晶格狀排列或散在的裸露的腺病毒粒子，其直徑在 70~90nm；有時在細胞外也有數目不等的散落的病毒粒子。在同一視野中還查見細胞外有少數副粘病毒的病毒粒子和胞漿內的核衣殼絲，前者大致呈球形或多形態，有包膜，直徑在 150~500nm，後者呈細絲狀，直徑約 13~14nm，偶見在細胞表膜下胞漿內聚集形成包涵體（圖 1）。

（二）副粘病毒與皰診病毒共感染：在感染細胞中除了查見具有上述副粘病毒形態特徵的病毒粒子和核衣殼絲及其包涵體外，在鄰近的感染細胞核內還查見皰診病毒核衣殼，其直徑約為 100nm，散在或呈晶格狀排列,病毒粒子呈球形，直徑在 150~160nm，包膜在核膜上芽生成熟。

（三）鼻病毒與冠狀病毒共感染：鼻病毒是微小核糖核酸病毒科的成員，病毒粒子呈球形，直徑在 24 ~30nm，裸露，無包膜，在胞質內排列呈晶格狀，在核周胞漿內可查見大量聚集的直徑在 200~300nm 的液泡和空泡。冠狀病毒的病毒粒子呈球形或多形態，有包膜，直徑在 80~160nm，核衣殼絲直徑在 9~13nm，

包膜雙層表面有纖突，在胞質內膜芽生成熟，在擴大的核周間隙和內質網池中及細胞外均可查見大量病毒粒子。但由於在感染細胞內很難找到晶格狀排列的鼻病毒，所以在同一視野中見到兩種病毒的機遇很少（圖 2）。

（四）鼻病毒與副粘病毒共感染：在不同視野中可查見具有上述兩種病毒的形態特徵的病毒粒子和副粘病毒的核衣殼絲。

（五）鼻病毒與正粘病毒共感染：鼻病毒的形態特徵同前。正粘病毒的病毒粒子呈球形或絲狀，直徑在 80~120nm，有包膜，包膜表面有穗狀纖突，核衣殼直徑在 9~15nm，病毒粒子在細胞表面芽生成熟。在不同視野中可查見上述兩種病毒粒子。

（六）冠狀病毒與呼腸病毒的共感染：在同一感染細胞內同時查見兩種病毒十分罕見。呼腸病毒具有獨特的形態特徵，核衣殼裸露，直徑在 60～80nm，有 1 或 2 層蛋白外衣殼，核心緻密約 52nm，病毒粒子有實心的和空心的，常排列晶格狀，在核周胞漿內形成無定形包涵體，它與共感染的冠狀病毒在形態上較易鑒別（圖 3）。

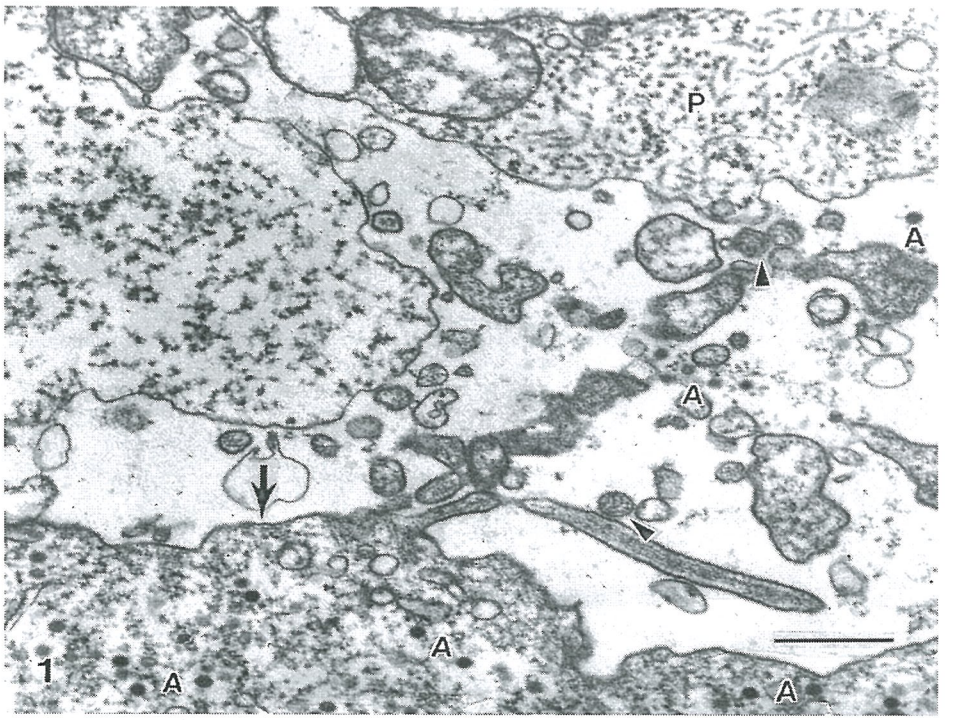

圖 1 培養細胞中共感染的副粘病毒與腺病毒。胞漿內聚集的副粘病毒核衣殼絲（P），副粘病毒粒子（▶），細胞核內（→）和細胞外散在的腺病毒粒子（A）。 Bar＝500nm

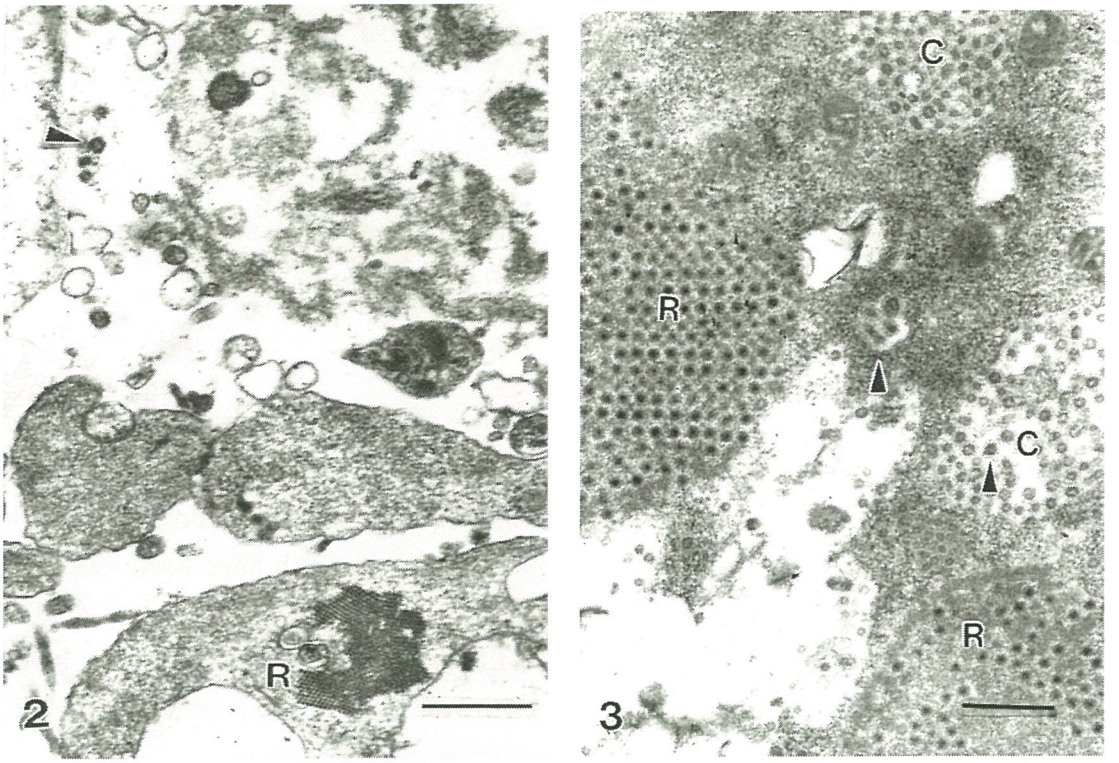

圖 2 培養細胞中共感染的晶格狀排列的鼻病毒（R）和細胞外散在的冠狀病毒（►）。Bar＝500nm

圖 3 同一感染細胞胞漿中的冠狀病毒（C）顯示包膜表面的纖突（►）和胞漿內呈晶格狀呼腸病毒（R）。Bar＝500nm

Animal Models for the Neuronal Degeneration

CHIEN, Chung-Liang（錢宗良）

Department of Anatomy and Cell Biology, College of Medicine, National Taiwan University（台灣大學醫學院解剖與細胞生物學研究所）, 1 Section 1, Jen-Ai Road, Taipei 10051, Taiwan

The spatial and temporal expression patterns of neuronal intermediate filaments in the developing and mature neurons could be found in both central and peripheral nervous systems. The accumulation of intermediate filament proteins in the degenerating neurons and subsequently induced neuronal death have been found and characterized in some neurological diseases. In previous transgenic studies, pathological accumulations of intermediate filaments (IF) were also found in the cytoplasm or axons of degenerating neurons. However, it still needs to be clarified the pathological role of cytoskeletal accumulation in the neuronal death.

We have investigated *Dystonia musculorum* (*dt*) mutant, an animal model for the neuronal degeneration. It has been showed that a defective bullous pemphigoid antigen 1 (BPAG1) gene is responsible for this nature mutation. We found that not only BPAG1deficiet, but also a neuronal IF protein, internexin, was absent in the dorsal root ganglia (DRG) neurons in adult *dt* mice. The progressive degeneration of both central and peripheral processes of DRG neurons could be characterized not only in *dt* homozygotes but also in heterozygotes. In this study, we demonstrated the phenotyping method to distinguish heterozygous *dt* from wild type mice using a behavioral hot-plate test. Immunocytochemical assay of cultured DRG neurons from *dt* embryos revealed that internexin was aggregated in the proximal region of axons and juxtanuclear region of the cytoplasma, yet the other IF proteins were widely distributed in all processes. The active caspase-3 activity was observed not only in the cultured *dt* neuron but also in the developing *dt* DRG neurons *in vivo*. From our observations, we suggest that (1) the interaction between BPAG1 and internexin may be one of the key factors involved in neuronal degeneration, and (2) abnormal accumulation of internexin may impair the axonal transport and subsequently turns on the cascade of neuronal apoptosis in developing *dt* mutants. Besides that, it could be also found that the accumulation of IF proteins in the swelling axons of spinal motor neurons in *dt* mice. In order to understand the pathological role of neuronal IFs in the swelling axons of spinal motor neurons from *dt* mice, we extensively examined the distribution of neuronal IF proteins. By immunofluorescence staining, our results

indicated that internexin was a major component in the swelling axon and showed abnormal translocation in the nuclei of spinal motor neurons in dt/dt mice. This abnormal translocation of internexin in the nuclei of spinal motor neurons was also confirmed by Western blotting and immunoelectron microscopy. Instead of the 10-nm filamentous structure, a diffuse immunopositive pattern of internexin was observed in the nucleus of spinal motor neurons in *dt* mutants. We further examined the cell death of spinal motor neurons by TUNEL assay, and no TUNEL-positive cells could be identified from spinal motor neurons in *dt* mice. From these observations we suggest that abnormal accumulation of neuronal IFs in the swelling axons and abnormal translocation of internexin in the nuclei of the spinal motor neurons from *dt* mice may not directly cause cell death of the spinal motor neurons.

References

1. Tseng KW, Lu KS, and Chien CL . *J. Neuropathol. Exp. Neurol.* 2006; 65:336-347.
2. Tseng KW, Chau YP, Yang MF, Lu KS, and Chien CL. *J. Comp. Neurol.* 2008. 507:1053-1064.

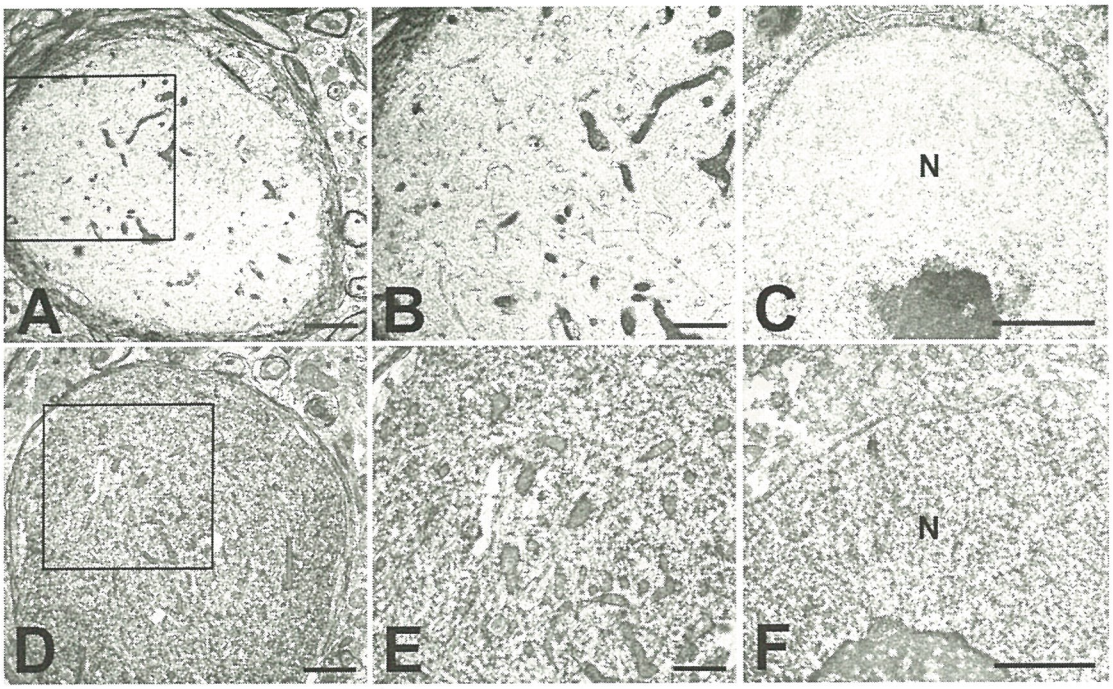

Figure1. Pre-embedding immunoelectron microscopy of the swelling axon and the nucleus of motor neuron from *dt* mutant. Ultrathin sections obtained from *dt* spinal cords were stained with uranyl acetate and lead citrate (A-C), or stained with antibody to internexin (D-F), and examined by electron microscopy. Randomly orientated intermediate filaments and axonal organelles were found in the swelling axons (A and B), yet the morphology of the cell nucleus looked normal in the spinal neuron of the *dt* (C). Internexin (dark DAB reaction products) was detected in the swelling axon (D and E) and also in the nucleus (F) of spinal motor neuron by immunoelectron microscopy. N: nucleus. Scale bars = 1 μm (A and D); 500 nm (B, C, E and F).

Effects of Ginsenoside Rg2 on Structure and Expression of Synaptophysin of Neurons in Hippocampus of Rats with Alzheimer's Disease

人參皂苷 Rg2 對阿爾茨海默病大鼠海馬神經元結構及突觸素表達的影響

CUI Li（崔麗）[1]，PAN Li[1]，LI Yan-Ru[1]，ZHUANG Ying[1,2]

1. Baiqiuen Medical College，Jilin University（吉林大學白求恩醫學院），Changchun Jilin 130021

2. Department of histology and embryology，Jilin Medical College，Jilin Jilin 132013；P R China)

阿爾茨海默病（Alzheimer's disease,AD）又稱為老年性癡呆，臨床上表現為不可逆的進行性記憶減退以及認知、語言功能障礙。經實驗證實大鼠海馬內注射 Aβ 可成功模擬 AD 患者海馬神經元的變性和壞死。有文獻報導人參皂苷 Rg1 能使 AD 模型海馬中的突觸數目增加，改善神經元膜的流動性，從而起到保護神經元的作用。人參皂苷 Rg2 與 Rg1 同屬於人參皂苷三醇型，分子結構相似，本實驗以銀杏達莫注射液作為陽性對照，旨在探討人參皂苷 Rg2 對 AD 大鼠模型海馬內神經元形態結構及突觸素（Synaptophysin，SY）表達的影響。

實驗選用 3~5 月齡清潔級 wistar 大鼠隨機分為 7 組，每組 12 只，雌雄各半。採用腹腔注射人參皂苷 Rg2 進行預防給藥，正常對照組和 AD 模型組大鼠腹腔注射生理鹽水（$2ml.kg^{-1}.d^{-1}$），銀杏達莫組給予銀杏達莫注射液（$3.6mg.kg^{-1}.d^{-1}$），溶媒組給予 1，2-丙二醇（$1ml.kg^{-1}.d^{-1}$），人參皂苷 Rg2 低劑量組給予人參皂苷 Rg2（$3mg.kg^{-1}.d^{-1}$），人參皂苷 Rg2 中劑量組給予人參皂苷 Rg2（$6mg.kg^{-1}.d^{-1}$），人參皂苷 Rg2 高劑量組給予人參皂苷 Rg2（$12mg.kg^{-1}.d^{-1}$）。預防給藥 2 周後，利用大鼠大腦立體定位儀進行海馬內一次性注射 $A\beta_{25\sim35}$ 建立 AD 模型，AD 模型組、銀杏達莫組、溶媒組及人參皂苷 Rg2 各劑量組大鼠海馬注射 $A\beta_{25\sim35}$，正常對照組大鼠海馬內注射等體積的生理鹽水。繼續預防給藥 3 周取材。採用蘇木精-伊紅（HE）染色法，光鏡下觀察大鼠海馬神經元的一般形態結構；採用免疫組化 SABC 法檢測大鼠海馬神經元 SY 的表達，並應用 MD-20 圖像分析系統進行定量分析；利用透射電子顯微鏡觀察大鼠海馬神經元及神經氈的超微結構。

HE 染色和 SY 免疫組化染色及定量分析結果顯示正常對照組大鼠海馬內神經元數量較多且排列整齊，細胞體積大，核大而圓，核仁明顯；SY 的陽性表達

產物呈棕黃色顆粒狀。AD 模型組和溶媒組神經元數量減少且神經元排列紊亂，神經元之間間隙增大，較多神經元壞死呈固縮狀；SY 免疫染色變淺，陽性表達減弱，吸光度值明顯下降。人參皂苷 Rg2 各劑量組大鼠海馬神經元的一般結構均較 AD 模型組均有不同程度的改善；SY 免疫染色變深，陽性表達呈現不同程度的增強，吸光度值較高。人參皂苷 Rg2 高劑量組與銀杏達莫組相似，神經元排列整齊、緊密，胞體大，核圓，核仁明顯，未見神經元壞死。透射電鏡觀察顯示正常對照組大鼠海馬內神經元胞體較大，核呈圓形，核仁明顯；胞質內可見豐富的粗面內質網、游離核糖體、高爾基複合體和線粒體；神經氈內突起排列緊密，突起結構清晰，其內可見神經絲和線粒體，突觸數量較多。AD 模型組和溶媒組可見較多暗細胞神經元，胞體變小，呈不規則形；核基質呈緻密狀、核仁可見；胞質基質緻密，細胞器不易分辨；局部神經氈內突起呈空化狀，突觸數量減少。銀杏達莫組和人參皂苷 Rg2 各劑量組暗細胞神經元減少或消失，神經氈內空化的突起。其中人參皂苷 Rg2 高劑量組海馬內神經元超微結構接近正常對照組。海馬作為大腦中執行學習記憶功能的主要部位，其神經元和突觸數量的減少以及結構的破壞均可引起認知和記憶障礙。本文實驗結果表明人參皂苷 Rg2 各劑量組和銀杏達莫組大鼠海馬神經元的一般形態和超微結構均不同程度地優於 AD 模型組；SY 均呈不同程度的陽性表達增強且定量分析具有顯著性差異。本文的形態學結果與本室另文發表的行為學檢測結果相一致，均提示人參皂苷 Rg2 對 AD 模型中海馬神經元和突觸結構均起到了一定的保護作用。

Germ Line Development, Formosa Antibody, and Cover Stories

Chang, Chun-che（張俊哲）[1]

[1] *Laboratory for Genetics and Development, Department of Entomology/Institute of Biotechnology（台灣大學 昆蟲學系）, College of Bioresources and Agriculture, National Taiwan University, No. 27, Lane 113, Roosevelt Rd., Sec. 4, Taipei 106, Taiwan.*

In animals germ cells are specified during embryogenesis; this specification relies either on a maternally inherited germ plasm in early development or induction signals from neighboring somatic cells in mid or late development. Whether the modes of germline specification are associated with embryonic pattern formation or with phylogenetic relationship is still not clear. Nevertheless, it has been demonstrated that many animals utilize two conserved germline genes, *vasa* and *nanos*, for germline development regardless which specification mode they employ. In order to examine the diversity of germline specification in insects, we produced a highly cross-reacting antibody formosa (for most Vasa) that recognize conserved Vasa-specific motifs in many species. In this presentation I shall describe how we take advantage of such an antibody to explore germline specification in the grasshopper *Schistocerca gregaria* and the pea aphid *Acyrthosiphon pisum*, two hemimetabolous insects whose body plan is determined differently from the model holometabolous insect *Drosophila melanogaster*. In addition, I will present our recent findings concerning the establishment of egg polarity and the migration of germ cells in the pea aphid. Taken together, these data allow us to shed new light on germline development in insects.

References

Chun-che Chang, Hui Chiu, and How-Jing Lee (2008) Identification of nuage-like structures in the panoistic ovarioles of the German cockroach *Blattella germanica* (Linnaeus). Formosan Entomologist 28: 1-10. **(cover article)**

Chun-che Chang, Wen-chih Lee, Charles E. Cook, Gee-way Lin, and Tschining Chang (2006) Germ-plasm specification and germline development in the parthenogenetic pea aphid *Acyrthosiphon pisum*: Vasa and Nanos as markers. Int. J. Dev. Biol. 50: 413-421. **(cover article)**

Cassandra G. Extavour (2005) The fate of isolated blastomeres with respect to germ cell formation in the amphipod crustacean *Parhyale hawaiensis*. Dev.

Biol. 277, 387-402. **(cover article)**

Chun-che Chang, Peter Dearden, and Michael Akam (2002) Germline development in the grasshopper *Schistocerca gregaria*: Vasa as a marker. Dev. Biol. 252, 110-118. **(cover article)**

Figures

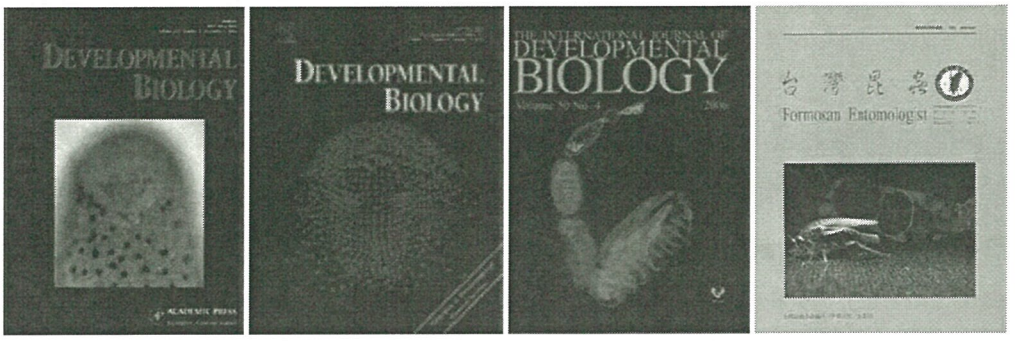

Cover pictures showing germ cells stained with the highly cross-reacting formosa antibody. From left to right: *Schistocerca gregaria* (grasshopper); *Parhyale hawaiensis* (amphipod crustacean); *Acyrthosiphon pisum* (pea aphid); *Blattella germanica* (German cockroach).

The Structure of Protease/Chaperone DegP (HtrA) on Membranes
蛋白酶/分子伴侶 DegP(HtrA)蛋白在膜上的結構

BAI Xiao-Chen，SHEN Qing-Tao，SUI Sen-Fang（隋森芳）

Department of Biological Sciences and Biotechnology, Tsinghua University（清華大學生物科學與技術系，生物膜與膜生物工程國家重點實驗室）, Beijing 100084, P R China

在諸如熱休克和病原侵害等環境脅迫下，細胞會發生蛋白的錯誤折疊或去折疊，由此進化出許多蛋白酶和分子伴侶來降解或重新修復這些非天然構象的蛋白。在蛋白質品質控制系統中，HtrA（high temperature requirement）家族代表了一類新的寡聚蛋白酶，廣泛分佈於包括細菌、植物、動物和人類的幾乎所有生物中，對清除錯誤折疊或變性的蛋白，抵抗各種應激反應及致病性，維持細胞的存活所必需。

DegP 蛋白（大腸桿菌中的 HtrA）同時具有分子伴侶和蛋白酶兩種活性，大量定位於大腸桿菌內膜的間質側。純化的 DegP 蛋白以無活性的六聚體狀態存在。在有脂膜存在的條件下，作者發現 DegP 蛋白可以與脂膜發生相互作用並自發組裝成具有四次和五次對稱性的寡聚結構(圖 A，B)，進一步用負染色電鏡及單顆粒三維重構方法對該寡聚體進行結構分析，發現它們分別是由四個三聚體和五個三聚體 DegP 蛋白組成的碗狀結構（圖 C)。大腸桿菌 DegP 蛋白在脂膜上形成的這種特殊的寡聚結構可能與蛋白酶與分子伴侶之間功能的轉變存在著聯繫。

DegP 在脂膜上形成的寡聚結構有很強的優勢取向（Preferred Orientation)，為了準確的計算出它在膜上的三維結構，本文採用隨機圓錐法（Random Conical Tilt）進行三維重構。相對於比較常用的角度重構法(Angular Reconstitution)，隨機圓錐重構法更適合應用於有優勢取向的蛋白結構，因為隨機圓錐法針對相同取向（View）的蛋白顆粒進行三維重構。對蛋白顆粒分別拍攝傾轉和非傾轉照片（圖 A)，對非傾轉照片中的顆粒進行分類（圖 B)，只需確定相同取向的非傾轉蛋白顆粒平面內的二維角度關係就可以確定傾轉蛋白顆粒在三維空間中的角度關係，從而得到蛋白結構的三維模型（圖 C)。雖然通過隨機圓錐法得到的結構解析度不高，但準確的確定 DegP 在膜上的低分辨結構為以後得到高分辨結構奠定重要基礎。

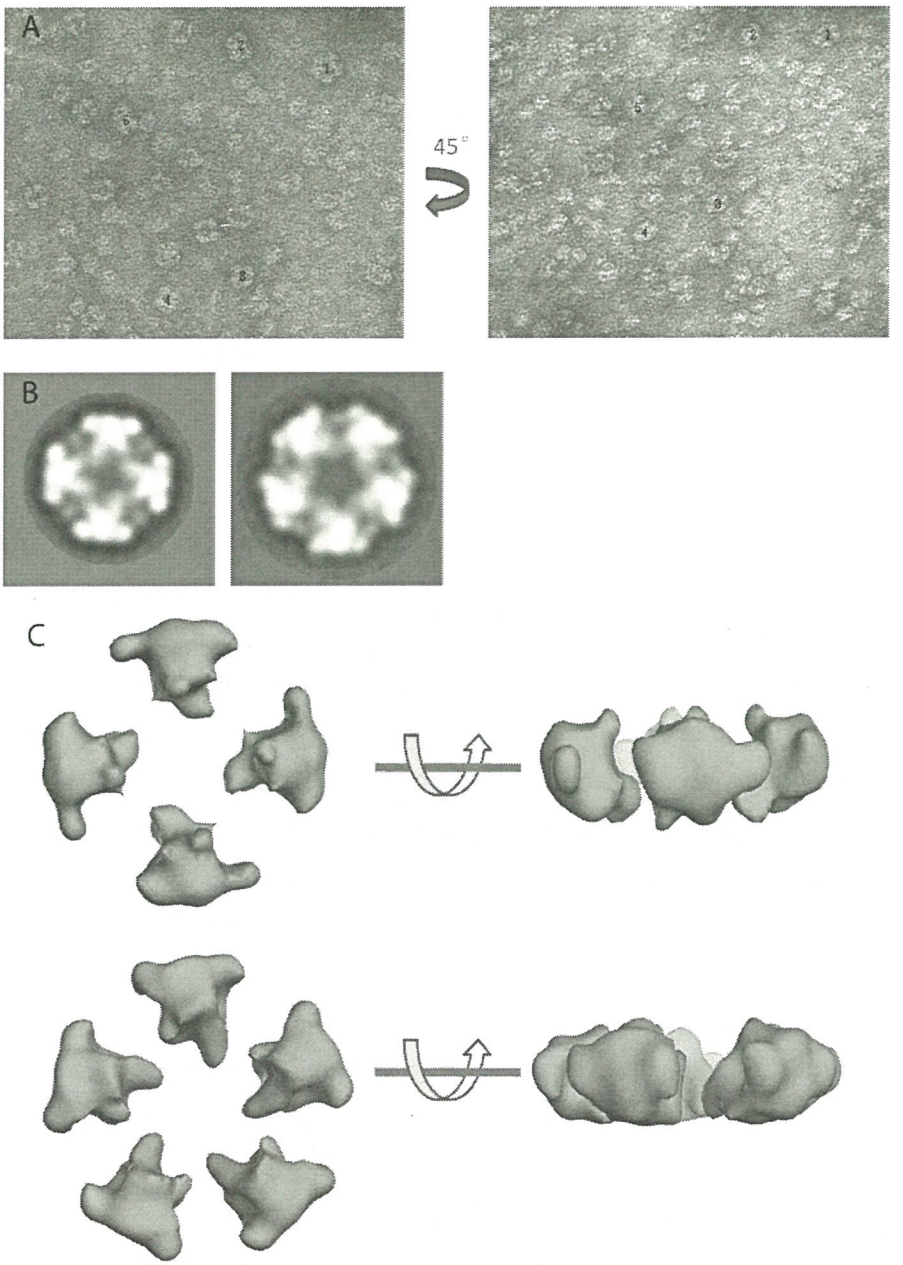

圖：用隨機圓錐法重構 DegP 蛋白在脂膜上的三維結構。

A：負染色電鏡觀察 DegP 蛋白在脂膜上的寡聚結構，分別拍攝非傾轉（左）與傾轉（右）照片。用數字標出了 5 對傾轉和非傾轉顆粒。B：對 DegP 蛋白在膜上的寡聚顆粒進行分類和平均，得到具有四次（左）和五次（右）對稱性的寡聚顆粒。它們的粒徑分別為 18 nm 和 23 nm。C：用隨機圓錐法對每一類平均的結果分別進行重構，得到具有四次（上）和五次（下）對稱性的碗狀結構。

Synthsis of Mesoporous Silicas in Different Morphologies by Using Cationic-Anionic Binary Surfactant as Templates

Gun-Chen Liu, Kai-Wen Chang, Ing-Ming Gu, Hong-Ping Lin（林弘萍）

Department of Chemistry, National Cheng Kung University(成功大學化學系), Tainan, Taiwan 701

e-mail: hplin@mail.ncku.edu.tw; phone: +886-6-2757575 ext.65342

Abstract

The skeleton, teeth in organism and the diatoms, shells in the sea and so on, are all highly joint complexes composed of inorganic and organic compounds. To understand biomineralization, this research used organic surfactant template to assemble with inorganic species into various novel shapes with well-ordered mesostructured. According to surfactant chemistry, even under very dilute condition, the cationic–anionic surfactants can self-assemble to various micelle structures, including rod micelle, vesicles micelle, and laminar structure. The binary surfactants not only can be used to simulate the property of cell membrane, but also as a template of silica microstructure which has spectacular morphologies.

In order to synthesize organic-inorganic complex material, this experiment chose surfactant as organic template and combined with inorganic species (sodium silicate solution, or tetraethyl orthosilicate). To synthesize the mesostructured silicas, firstly, cationic surfactant(C_nTMAB，n = 16，18) was mixed with anionic surfactant(SDS) at proper ratio(SDS/C_nTMAB molar ratio，***S***) to form rod micelle as organic template. Nonionic Pluronic triblock copolymer—P123 was added to combine with organic template to reduce the rigidity of organic template and increase the interaction between organic template and inorganic species. Finally, incorporating a highly dilute sodium silicate solution at pH = 1.0 ~ 1.5, 55℃ to synthesize mesoporous silicas in various morphologies including flow-like silica, helical fibers, ribbons, silica spheres, and silica vesicles.

The mesostructured silica morphologies can be tailored by changing a series of experimental conditions including CTAB/SDS molar ratio, pH value, surfactant concentration, temperature, stirring rate and so on. Using the experimental result, we tried to find out the best synthesis condition for the

mesoporous silica in the desired morphology, and extrapolation the synthesis mechanism.

In brief, we can synthesize mesoporous silica helical fibers successfully without chiral template by a simple and convenience method. The yield of products is high and the result is reproducible. Therefore, our research results have high referencing values for understanding biomineralization concepts and theories.

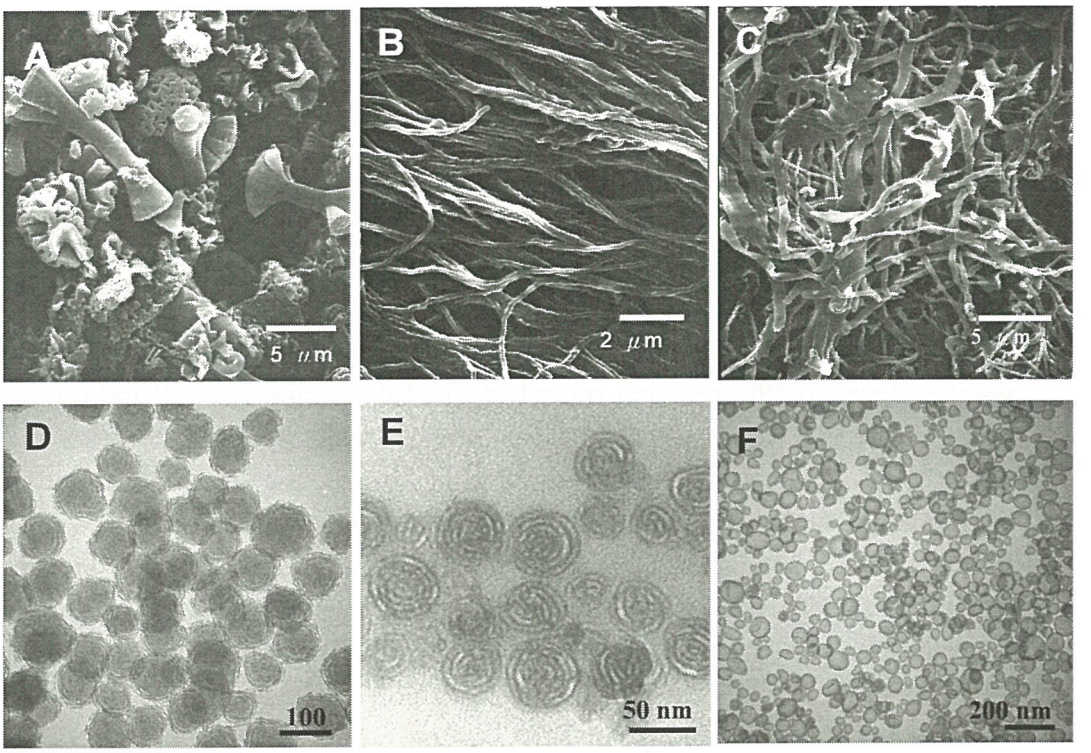

Biochemical Characterization and Structural Investigation of a Tubulin Polymerization System Originated from Carp Spermatozoa

JU, Tsai-Kai(朱蔡豈)[1, 2], CHEN, Shiang-Jiuun[1, 3], CHUANG, Yi-Chun[2], YANG, Ya-Chan[2], HUANG, Rong-Nan[4], KUO-HUANG, Ling-Long[3]

[1] *Precision Instrumentation Center, College of Science, National Taiwan University（台灣大學生科院生物細胞影像平台）, No. 1, Sec. 4, Roosevelt Rd., Taipei, Taiwan 10617*

[2] *Technology Commons, College of Life Science, National Taiwan University, No. 1, Sec. 4, Roosevelt Rd., Taipei, Taiwan 10617*

[3] *Department of Life Science, Institute of Ecology and Evolutionary Biology, National Taiwan University, No. 1, Sec. 4, Roosevelt Rd., Taipei, Taiwan 10617.*

[4] *Department of Entomology, National Taiwan University, No. 27, Lane 113, Sec. 4, Roosevelt Rd., Taipei, Taiwan 10617.*

The *in vitro* polymerizing nature of tubulin has brought about promising assay systems for the research on cytoskeletal dynamics and cell motility, as well as for the discovery of novel microtubule-associated proteins and anti-mitotic drugs. In the polymerization assay, the tubulin source is traditionally isolated from brain tissues of bovine or porcine that requires much animal care and sophisticated procedures to harvest tubulin proteins. Here, we present a flagellar tubulin-polymerizing (TBP) system isolated from carp spermatozoa (Fig 1A) that does not need complicated preparation procedures (Fig 1B) to harvest and exhibits a sigmoid polymerization curve essentially identical to those of mammalian TBP systems when kinetically measured by optical absorbance at 340 nm during microtubule reassembly (Fig 2). Although the overall TBP process requires a few longer duration than brain TBP systems do, this flagellar TBP reaction is exactly GTP-dependent (Fig 2B) and its polymerization kinetics is highly sensitive to a variety of anti-mitotic drugs, such as paclitaxel, nocodazole, and podophyllotoxin. In additional to a dynein motor subunit, the radial spoke protein Rsph1 are also co-precipitated with the reassembled flagellar microtubule (Fig 2A), suggesting that this TBP product still retains some axonemal properties and might form a more complicated structure than the brain TBP system does. Through ultrastructural inspection, it is found that the flagellar TBP system might become an amicable system for traditional TBP assay. Moreover, through two-dimemsional electrophoresis of the end product of the TBP system, it is highly promising to characterizing axonemal proteome in detail.

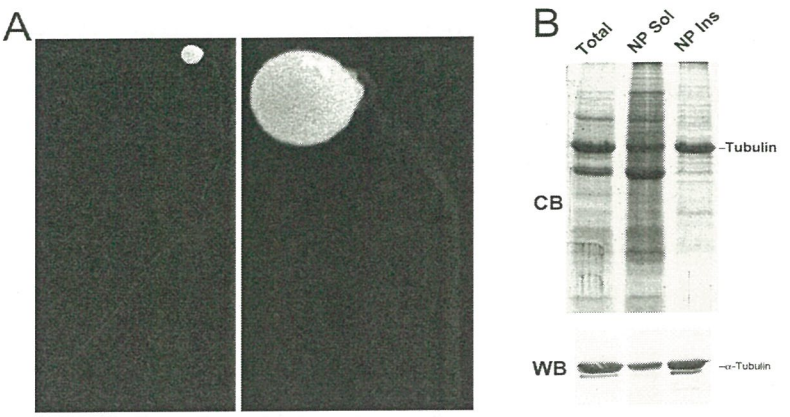

Figure 1. Morphological examination and protein fractionation of carp sperm. (A) The Carp sperm was visualized by scanning electron microscopy to show the simple configuration of the sperm tail. Unlike mammalian sperm, no auxiliary structure associates with the carp sperm flagellum. Magnification: 7,000× (left) and 40,000× (right). **(B)** Total and fractionated sperm extracts, the NP40-soluble (NP Sol) and NP40-insoluble (NP Ins) fractions, were all from 3.2× 10^7 spermatozoa and visualized by using Coomassie blue (CB). In combination with immunoblotting analysis (WB), it is revealed that the NP40-insoluble preparation is especially enriched with tubulin proteins, which account for ~80% in this protein fraction by densitometry.

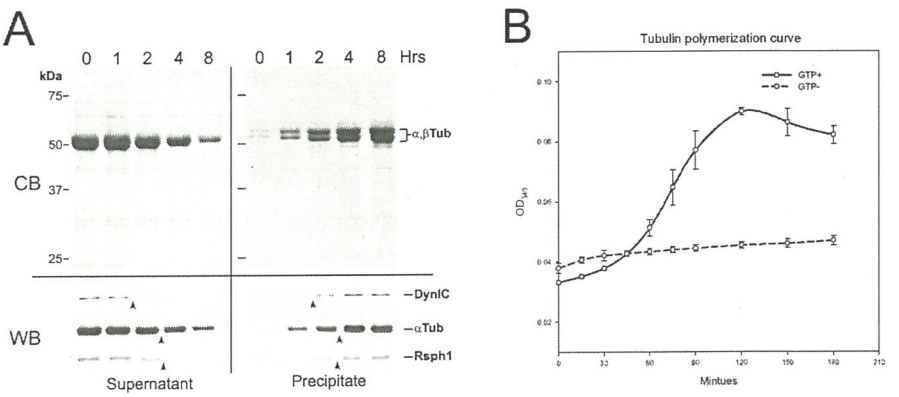

Figure 2. Sedimentation and optical properties of *in vitro* assembled flagellar microtubules. (A) Precipitation profiles of NP-insoluble proteins (8× 10^7 spermatozoa per lane) under standard tubulin-polymerizing condition were visualized by Coomassie blue staning (CB) and immunoblotting (WB). The microtubule-associated proteins, Rsph1 and dynein intermediate chain (DynIC) were co-precipitated with tubulins (, Tub in CB and Tub in WB) during the course (as indicated hours) of *in vitro* polymerization. Arrowheads indicate the time intervals where the estimated a half of the tested proteins precipitate. **(B)** Measurement of optical absorbance changes of *in vitro* polymerized tubulin at 340 nm reveals that the polymerization kinetics is consistent with the typical bovine tubulin-polymerizing system, which consists of nucleation, growth, and steady state phases. The kinetic assay also revealed that the flagellar tubulin polymerization requires GTP as a cofactor.

The Science and Technology of Synchrotron X-Ray Microscopy with 25 nm Resolution

Yeukuang Hwu（胡宇光）

Institute of Physics, Academia Sinica（中央研究院物理研究所）, Taipei 115, Taiwan

Substantial improvements in the nanofabrication and characteristics of gold Fresnel zone plates yielded unprecedented resolution levels in hard-x-ray microscopy. Tests performed on a variety of specimens with 8-10 keV photons demonstrated a first-order lateral resolution below 30 nm based on the Rayleigh criterion. Combined with the use of a phase contrast technique, this makes it possible to view features in the 20 nm range; good-quality images can be obtained at video rate, down to 50 ms per frame. The important repercussions on materials science, nanotechnology and the life sciences are discussed.

We describe the fabrication of gold Fresnel zone plates with a 25 nm outermost zone width and a 450nm thick structure by a combination of the e-beam lithography and electrodeposition. The e-beam lithography process was implemented with a careful evaluation of applied dosage, tests of different bake-out temperatures and durations for the photoresist and the use of a developer without methylisobutylketion. Electrodeposition with a pulsed current mode and with a specially designed apparatus produced the desired high aspect ratio nanostructures. The fabricated zone plates were examined by electron microscopy and their performances were assessed in a transmission X-ray microscope. The results specifically demonstrated an image resolution of 25 nm.

Architecture of Full Length AMPK Constructed by Single Particle Electron-microscopy

電鏡單顆粒方法重構全長 AMPK 的結構

ZHU Li*，CHEN Lei‡，ZHOU Xiao-Ming*，ZHAO Jing*，WU Jia-Wei‡，WU Yi（武 一）*

**School of Life Science，Lanzhou University（蘭州大學生命科學學院），Lanzhou Gansu 730000；*

‡ Department of Biological Sciences and Biotechnology, Tsinghua University, Beijing 100084, P R China

AMP 啟動的蛋白激酶（AMPK，AMP-activated protein kinase）是一種異三聚體蛋白，由 α 催化亞基、β 腳手架亞基以及 γ 調控亞基構成，在維持細胞能量平衡過程中發揮關鍵作用[1]。β 亞基可同時結合 α 及 γ 亞基，從而介導 AMPK 異三聚體的組裝。α 亞基由 N 端絲氨酸/蘇氨酸激酶區、自抑制區（AIS）和 C 端 β 結合調控區構成。γ 亞基則可感知胞內 AMP/ATP 比例的變化，通過變構啟動或壓制 α 亞基的催化活性，此即 AMPK 在體功能調控的核心機制。一般認為，γ 亞基與 AMP 結合後會通過釋放 AIS[2, 3]以及阻抑激酶區 172 位蘇氨酸去磷酸化[4, 5]，使 α 亞基激酶活性增強上千倍[4]。ATP 可拮抗 AMP 與 γ 亞基的結合，從而消除 AMP 對 AMPK 的啟動效應。

目前雖然已獲得了多個哺乳動物或酵母 AMPK 亞基或片段的晶體結構[6~8]，但由於其中存在激酶區等關鍵結構域的缺失，多個有關 AMPK 功能的基礎問題尚有待回答。例如，ATP 或 AMP 結合導致的 γ 亞基微小構象變化[6]是怎樣轉換為 α 亞基中的顯著構象切換？此外，雖然在 AMPK 核心區晶體結構中異三聚體的組裝由 β 亞基 C 端介導，但有生化證據顯示 α 亞基似乎也能起到腳手架的作用[9]。顯然，解析全長 AMPK 的結構將非常有助於回答這些問題。本文通過單顆粒電鏡技術重構了全長 AMPK（α1β1γ1）在無配體結合、AMP 結合和 ATP 結合狀態下的三維構架。在同源建模、AMPK 亞基晶體結構對接（docking）及 AMPK 突變體觀測等手段的輔助下，提出了 AMPK 複合體的亞基組裝方式以及配體結合所誘導的構象變化模型。

參考文獻：

[1] Hardie D G. AMP-activated/SNF1 protein kinases: conserved guardians of cellular energy. Nat Rev Mol Cell Biol，2007，8:774-785.

[2] Pang T, Xiong B, Li J Y, Qiu B Y, Jin G Z, Shen J K, Li J. Conserved alpha-helix acts as autoinhibitory sequence in AMP-activated protein kinase alpha subunits. J Biol Chem，2007，282:495-506.

[3] Crute B E, Seefeld K, Gamble J, Kemp B E, Witters L A. Functional domains of the alpha1 catalytic subunit of the AMP-activated protein kinase. J Biol Chem，1998，273:35347-35354.

[4] Suter M, Riek U, Tuerk R, Schlattner U, Wallimann T, Neumann D. Dissecting the role of 5'-AMP for allosteric stimulation, activation, and deactivation of AMP-activated protein kinase. J Biol Chem，2006，281:32207-32216.

[5] Sanders M J, Grondin P O, Hegarty B D, Snowden M A, Carling D. Investigating the mechanism for AMP activation of the AMP-activated protein kinase cascade. Biochem J，2007，403:139-148.

[6] Xiao B, Heath R, Saiu P, et al. Structural basis for AMP binding to mammalian AMP-activated protein kinase. Nature，2007，449:496-500.

[7] Townley R, Shapiro L. Crystal structures of the adenylate sensor from fission yeast AMP-activated protein kinase. Science，2007，315:1726-1729.

[8] Amodeo G A, Rudolph M J, Tong L. Crystal structure of the heterotrimer core of Saccharomyces cerevisiae AMPK homologue SNF1. Nature，2007，449:492-495.

[9] Wong K A, Lodish H F. A revised model for AMP-activated protein kinase structure: The alpha-subunit binds to both the beta- and gamma-subunits although there is no direct binding between the beta- and gamma-subunits. J Biol Chem，2006，281:36434-36442.

In vivo Optical Virtual Biopsy with Least Invasive Harmonic Generation Microscopy

Chi-Kuang Sun（孫啟光）

Graduate Institute of Photonics and Optoelectronics and Department of Electrical Engineering, National Taiwan University（臺灣大學光電工程學研究所）, and Research Center for Applied Sciences, Academia Sinica, Taipei, TAIWAN

In this presentation, we will report our recent development on the in vivo optical virtual biopsy based on the least invasive harmonic generation microscopy, also with a secondary focus on the developmental biology study. Optical harmonic-generations, including second harmonic generation (SHG) and third harmonic generation (THG), leave no energy deposition to the interacted matters due to their energy-conservation characteristic, providing the "noninvasiveness" nature desirable for medical studies. Combined with their nonlinearity, harmonic generation microscopy provides three-dimensional (3D) sectioning capability, offering new insights into live samples. By choosing the lasers working in the high penetration window, here we present a noninvasive *in vivo* light microscopy with submicron 3D resolution and high penetration, utilizing endogenous multi-harmonic-generation signals in live specimens. Noninvasive imaging performed in live zebrafish and mouse embryos will be presented. The complex developmental processes within >1-mm-thick zebrafish embryos can be observed *in vivo* without any treatment. No optical damage was observed even with high illumination after long-term observations and all the examined embryos developed normally at least to the larval stage. The excellent 3D resolution of demonstrated technology allows us to capture the subtle developmental information on the cellular or sub-cellular levels occurred deep inside the live embryos. This technique can not only provide *in vivo* observation of the cytoarchitecture dynamics during embryogenesis with a submicron resolution and millimeter penetration depth, but would also make strong impact in developmental and structural biology studies.

One of the most important applications of higher harmonic generation microscopy is virtual biopsy. In this talk we will present the preliminary result of in vivo optical virtual biopsy of mouse skin, hamster oral cavity, and human skin based on backward-collected harmonic signals. Our study aims for the following purposes: to detect subclinical life-threatening disease, to less invasively diagnose clinically evident disease, to reduce sampling errors before and after physical biopsy, for

presurgical and intraoperative detection of the safety margins, and to noninvasively perform follow-up examination after treatment.

Dynamical Analyses of Cell Activities Using Bright-Field Optical Profilometry and Super-Resolution Imaging

LEE, Chau-Hwang（李超煌）[1,2,3]

[1] *Research Center for Applied Sciences, Academia Sinica（中央研究院應用科學研究中心）, Taipei 11529, Taiwan.*

[2] *Institute of Biophotonics, National Yang-Ming University, Taipei 11221, Taiwan*

[3] *Graduate Institute of Clinical Medicine, National Taiwan University, Taipei 10002, Taiwan*

A cell interacts with the environment and other cells through its membrane. In addition to the ion channels, membrane dynamics and the configuration of the associate cytoskeletons are important to the identification and regulation of cell activities. Because cell membranes are extremely soft and transparent, conventional optical and probe microscopy are not very useful to reveal the membrane activities.

In this talk I shall introduce the application of a novel far-field optical microscopy, non-interferometric wide-field optical profilometry (NIWOP), on the observation and analyses of cell membrane and pseudopodium dynamics. NIWOP provides 20 nm depth profiling accuracy on cell membranes, and its image-acquisition rate can be up to 12 frames/sec with the setup using a liquid-crystal spatial light modulator. Hence it can be employed as a non-labelling and non-contact method for the studies of cell membrane dynamics. We characterize the propagation of membrane waves on a fibroblast (Fig. 1) and explain the data by an active membrane wave model. NIWOP is also able to track the 3D positions of sub-100 nm particles. We analyze 3D motion of gold nanoparticles on the membrane of a fibroblast (Fig. 2), and the intracellular transportation of liposomes coated by growth factors.

In addition, based on the nanometer topographic contrast, we improve the lateral resolution of NIWOP to the 100-nm scale by image-restoration processing. We use this "super-resolution" bright-field microscopy to analyze the filopodium activities of lung cancer cells. By quantifying the numbers and growth rates of filopodia, we identify the effect of epidermal growth factor on cancer-cell motility. We also demonstrate super-resolution imaging in a cell-culture chip for an assay of cellular responses to the chemical concentration gradients in the micro-environment (Fig. 3). These works introduce a new platform for dynamical cell analyses based on high-resolution label-free imaging.

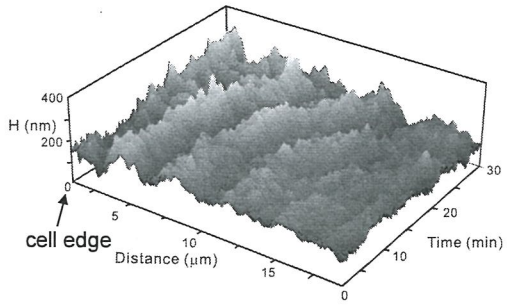

Fig. 1. Kymograph of membrane waves on a fibroblast measured by the NIWOP technique. On the distance axis, position zero represents the edge of this cell. We can see that the waves are moving away from the cell edge.

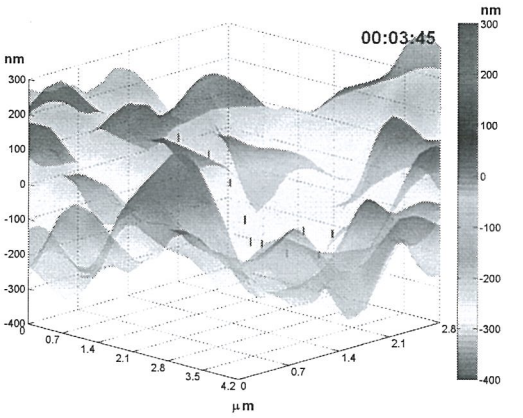

Fig. 2. The motion of a 60-nm gold particle (red dots) on the membrane of a fibroblast.

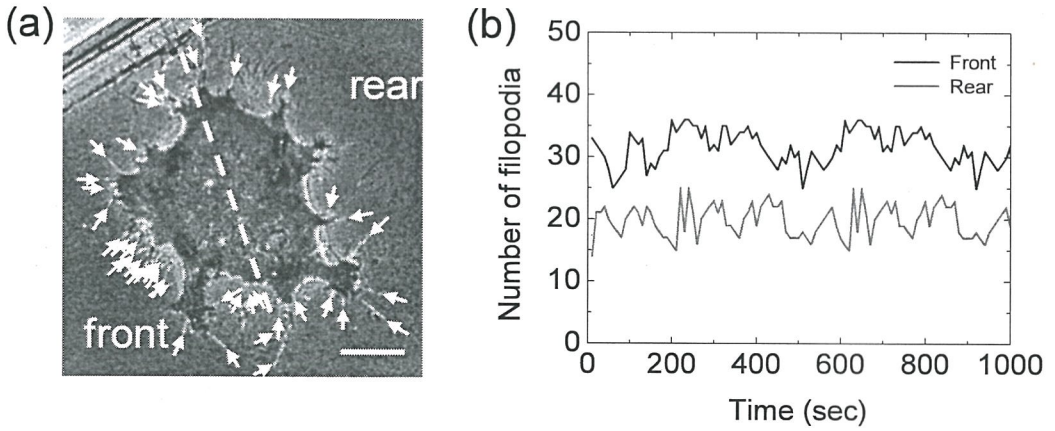

Fig. 3. (a) Super-resolution bright-field image of filopodia of a lung cancer cell in a cell culture chip. The "front" side faces to a higher concentration of epidermal growth factor. Scale bar: 10 μm. (b) Temporal variations of the filopodium numbers on the front and rear sides of the cell in (a).

Current Status of 3D Cryo-EM Structural Biology in Taiwan

CHANG, Wei-Hau （章為皓）

Institute of Chemistry, Academia Sinica（中央研究院化學所）, Taipei, Taiwan

Transmission electron microscopy aided with 3D reconstruction has emerged as an effective tool to reveal molecular details of protein complex larger than ~500 kDa. However, the resolution is much worse than that can be provided by the instrument due to the dose limit. To extend the resolution, the protein sample must be preserved in amorphous ice and millions of "structurally" homogeneous protein particles will be imaged by cryo electron microscopy that a sub-nanometer structure can be calculated. The structure is directly comparable to X-ray structure but it represents an entity of physiological interest because no high salt is used. In this talk, we will brief our progress along this line and also the combination of FRET to facilitate structural interpretation or validation.

Microencapsulated *Metarhizium anisopliae* MA126 by Low-Temperature Spray-Dryer

LIU, Ching-Piao（劉清標）and LIU, Shan-Da

Department of Biological Science and Technology, Mei Ho Institute of Technology（美和技術學院生技系）, Pingtung 91202, Taiwan

Bioinsecticides are expected to be used for controlling major species of aphids. The present study low-temperature spray drying was used to microencapsulate the conidia of the entomopathogenic fungus *M. anisopliae* MA126. In order to prolong the activity of the conidia and improve their shelf life, various polymers including HPMC, dextrin, skimmed milk, and polyvinylpyrrolidone (PVP K90) were examined as encapsulation matrices. Different inlet/outlet temperatures, compositions of the carrier systems, and conidia concentrations were examined with respect to spore viability (Fig. 1~2). Moreover, the production characteristics, such as particle size distribution, entrapment efficiency, and shape were investigated. The best encapsulated products were obtained using a matrix composed of 10% dextrin, 10% skimmed milk, and 5% PVP K90 as the coating material. The conidia exhibited 80% viability, even after storage for six months at 4°C. The microspheres obtained by spray drying were spherical with smooth or wrinkled surfaces. The mean particle size was in the range of 2.5-10 μm (Fig. 3). The yield (%) using dextrin/SM/PVP K90 as coating material having maximum viability was 68±4, while that with dextrin only as coating material was 85±3.

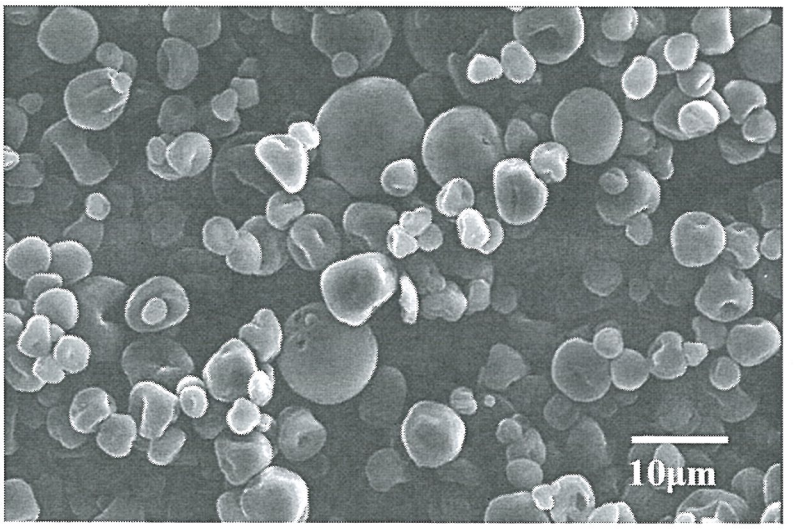

FIG. 1. *M. anisopliae* microencapsulated by the conventional spray drying technique viewed under the scanning electron microscope. Inlet/outlet temperature: 100°C/80°C; feed: 0.24 (L/h); coating materials: skimmed milk and PVP.

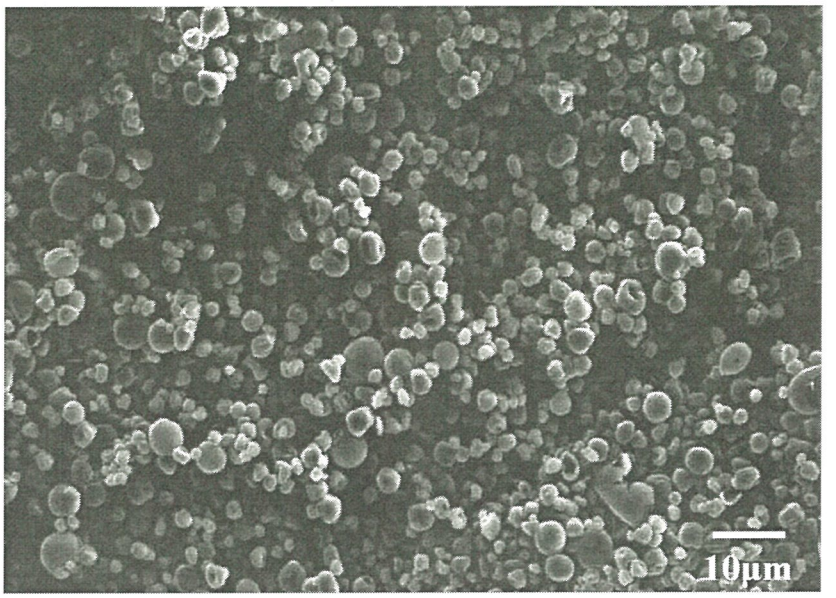

FIG. 2. Electron micrograph of the *M. anisopliae* encapsulated by the low-temperature spray drying technique. Inlet/outlet temperature: 60°C/30°C; feed: 0.24 (L/h); coating materials: skimmed milk and PVP.

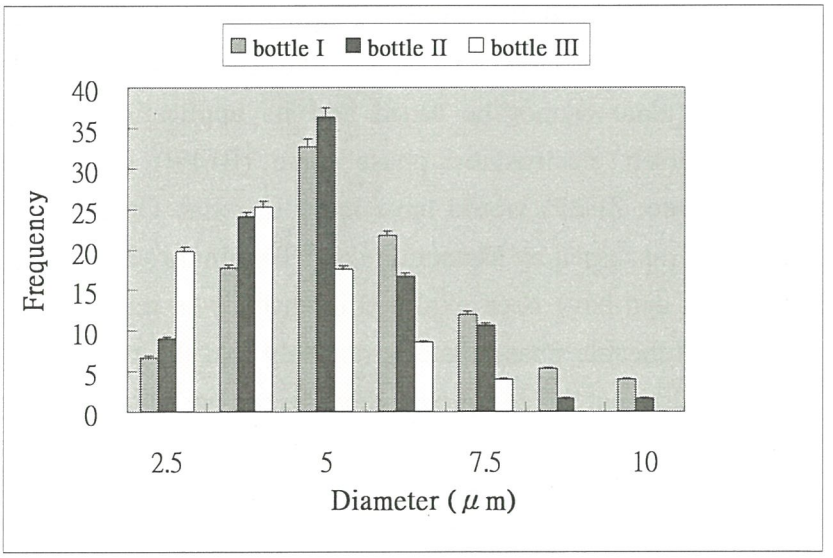

FIG. 3. Particle size distribution of the microencapsulated *M. anisopliae* collected from each of the three bottles (bottle I~ III).

Phase TEM for Biological Imaging Utilizing a Boersch Electrostatic Phase Plate

Jin-Sheng Tsai（蔡錦盛）[1], Sen-Hui Huang[2], Jessie Shiue[3],Chih-Hao Hsu[2], Chia-Seng Chang[3], Wei-Hau Chang[4], Yi-Min Wu[4], Yen-Chen Lin[4],Pai-Chia Kuo[3], Yang-Shan Huang[3], Yeukuang Hwu[1,3], Fan-Gang Tseng[4] and Fu-Rong Chen[1,2,3]

[1] *National Synchrotron Radiation Research Center（台灣同步輻射中心）, HsinChu 30076*

[2] *Department of Engineering and System Science, National TsingHua University, HsinChu 30043, Taiwan*

[3] *Institute of Physics.*

[4] *Institute of Chemistry, Academia Sinica, Nankang 11529, Taipei.*

One of the bottlenecks for biological imaging in a transmission electron microscope (TEM) is low contrast due to the weak interactions of the incident beam with materials composed of light elements. Development of electron phase plates to construct a phase contrast TEM in analogy with a phase contrast optical microscope has become an urgent research topic for biological imaging. Nagayama and Danev have successfully demonstrated the contrast improvement with the Zernike phase plate made of carbon film [1–3]. However, the phase shift provided by this thin-film-type phase plate cannot be tuned and its application is hence limited. Alternatively, a Boersch electrostatic phase plate (BEPP) (also called Zernike electrostatic phase plate, ZEPP) would have more benefits. Originally proposed by Boersch [3], and later discussed by Matsumoto and Tonomura [4], BEPPs can provide tuneable phase shifts, and have been explored intensively in recent years [5–6]. The figure of merit for a tuneable phase plate is not only that the phase contrast images can be recorded, but also that the complete exit wave can possibly be reconstructed.

Figure 1a shows the SEM image of a BEPP, where a long cantilever 2.0 μm in width and 80 μm in length is suspended across an 80 μm empty hole. Figure 1b shows the central hole (800 nm in diameter) in the middle of the cantilever, and the cross section of the hole is shown in the inset. The five-layered structure is clearly observable in the SEM image. The images recorded with zero and $\pi/2$ phase shift for a negatively stained ferritin are shown in Fig. 2. All these images were recorded at zero focus to eliminate the effect of the contrast contributed from underfocusing. Figure 2a shows an image of a negatively stained ferritin recorded without insertion of the phase plate; Fig. 2b was recorded with the phase plate inserted and with zero phase shift, while Fig. 2c was taken with the phase plate in and phase shift at $\pi/2$. Some charging effects were noticed in the images when utilizing the phase plate. As shown in Fig. 2b and c, the charging effect blurs the detail of the supporting carbon film and introduces

slight distortion in the diagonal direction (top/left to bottom/right). The charging effects can be reduced by increasing the thickness of the outer conducting layer of the BEPP. Figure 2d presents the intensity profile across the ferritin. The difference between the green and the red lines represents the gain of phase contrast, while the difference between the blue and the red lines corresponds to the contribution of absorption contrast. The phase shift produced by the Boersch phase plate is a function of the applied voltage on the electrodes of the phase plate. The phase shift was calibrated by fitting the power spectra of recorded images at a higher defocus value with calculated contrast transfer functions (CTFs). The power spectra obtained by Fourier transforms from the two images recorded at zero and $\pi/2$ phase shifts are used to demonstrate the phase shift effect from the BEPP, as shown in Fig. 2e. The left portion of Fig. 2e represents the power spectrum at zero phase shift, while the right portion of the figure demonstrates the power spectrum at a phase shift of $\pi/2$; both spectra were obtained from images recorded at a high defocus value of –1240 nm. The maxima of the squared modulus of the CTF are represented by the bright rings in the power spectrum [6]. It is clearly shown at the crossing of the two portions in Fig. 2e that the rings were shifted, indicating that the phase shift indeed occurred.

A Boersch electrostatic phase plate (BEPP) used in a TEM system can provide tuneable phase shifts and overcome the low contrast problem for biological imaging. Phase images of biological samples (negatively stained ferritin) obtained by utilizing a BEPP are reported, and the phase contrast was found to be enhanced by a factor of 1.5, based on the calculation using the Rose contrast criterion.

References

1 Danev R, and Nagayama K (2001) Transmission electron microscopy with Zernike phase plate. *Ultramicroscopy* **88**: 243–252.

2 Danev R, and Nagayama K (2008) Single particle analysis based on Zernike phase contrast transmission electron microscopy. *J. Struct. Biol.* **161**: 211–218.

3 Nagayama K (2008) Development of phase plates for electron microscopes and their biological application. *Eur. Biophys. J.* **37**: 345–358.

4 Matsumoto T, and Tonomura A (1996) The phase constancy of electro waves traveling through Boersch's electrostatic phase plate. *Ultramicroscopy* **63**: 5–10.

5 Huang S H, Wang W J, Chang C S, Hwu Y K, Tseng F G, Kai J J, and Chen F R (2006) The fabrication and application of Zernike electrostatic phase plate. *J. Electron Microsc.* **55**: 273–280.

6 Schultheiβ K, P´erez-Willard F, Barton B, Gerthsen D, and Schr ¨ oder R R (2006) Fabrication of a Boersch phase plate for phase contrast imaging in a transmission electron microscope. *Rev. Sci. Instrum.***77**: 33701.

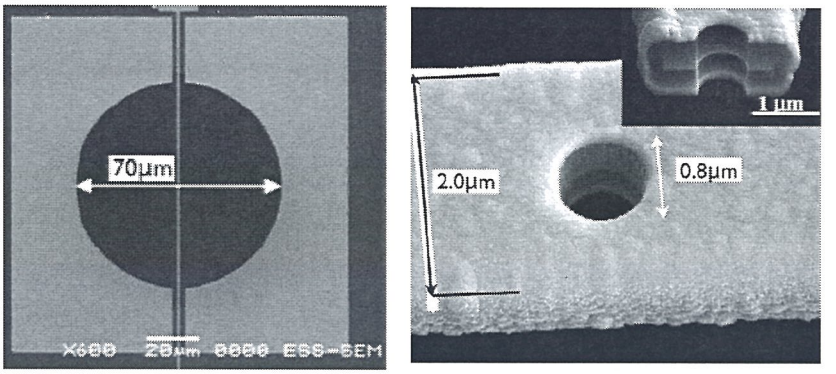

Fig.1 SEM images of a BEPP

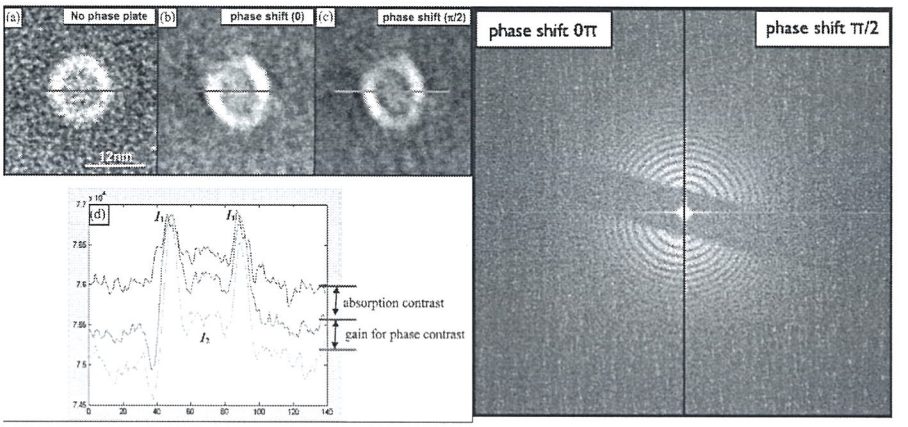

Fig.2 Images of a negatively stained ferritin, and power spectra

The Taxonomic Impact of Identification Based on Molecular Markers on Morphological Characteristics: Microsporidian Taxonomy

WANG, Chih-Yuan[1]; CHEN, Yun-Ru[1]; WANG, Chung-Hsiung（王重雄）[2]

[1]*Department of Entomology, National Taiwan University, 1 Roosevelt Rd., Sec. 4, Taipei 106, Taiwan*
[2]*Institute of Zoology and Department of Entomology, National Taiwan University（台灣大學昆蟲學系）, 1 Roosevelt Rd., Sec. 4, Taipei 106, Taiwan*

Microsporidian parasites are obligate intracellular eukaryotic pathogens. Apparently, 1,500 species are described now. Microsporidia are restricted to animal hosts, and all major groups of animals host microsporidia. Most of species are isolated from insects, then crustaceans and fishes. Some species are lethal, and a few are used in biological control of insect pests. Parasitic castration, gigantism, and change of host sex are effects of microsporidian parasitism. The traditional criteria of microsporidan taxonomy were based on biological characteristics including host range, life cycle, tissue distribution, and morphology, especially, spore ultrastructure. The microsporidian spores are unicellular spores with one or two nuclei (diplokaryon), rigid and resistant to environmental stress, the spore is only the stage can be exposed in the air and also an important stage to infect the new healthy hosts. Both shape and size (Fig. A & B) of spores are taxonomic criteria. The spore (Fig. C & D) are protected with a relative thick cover which consists of a thick, an external electron-dense expospore, a median wide and seemingly structureless endospore, containing chitin, and an internal plasma membrane. The spores are equipped with a unique infection apparatus, polaroplast, polar tube and posterior vacuole. Two important criteria that are based on the internal ultrastructure of spore, including the number of nuclei, a single nucleus or two coupled nuclei (diplokaryon), and the coiled number, slope, the length, and concentric layers of different electron density of polar tube. In addition, the replication stages and structures are also suggested to be criteria for classification, including xenoma formation (Fig. E), the bounding membrane of the vacuole which the parasites develop inside, and plasmodium (Fig. F). Apparently, most of criteria are dependent on the ultrastructural observation[3], the limitation of the observation field under electron microscope usually causes the mistaken identification and leads to several species had been changed their taxonomic position now. Furthermore, several species parasite more hosts but morphologically inconsistence occurs usually in different hosts[1].

Recently, molecular marker offers a rapid and precise tool for microsporidian identification, if the conflict occurs between molecular marker and traditional criteria. The morphological criteria are reexamined. The accumulated data of microsporidian SSUrDNA sequences in GenBank are suggested that the SSUrDNA is an important marker for microsporidian identification, taxonomy and phylogenetic analysis[2,4]. Therefore, the strategy to identify a new microsporidian isolate is examined first by light microscopy to determine their nuclear number and morphological characters, and then amplified it's SSUrDNA by PCR and phylogenetically analyzed based on the SSUrDNA sequences to determine its taxonomic position, the last is to find the important ultrastructural characters of which group it belongs.

References

1. Canning, E. U., Curry, A., Cheney, S., Lafranchi-Tristem, N. J., Haque, M. A. Parasitology 1999 (119) 273
2. Huang, W. F., Tsai, S. J., Lo, C. F., Soichi, Y., and Wang, C. H. Fungal Genet. Biol. 2004 (41) 473
3. Sprague, V., Becnel, J. J., and Hazard, E. I. Critical Reviews in Microbiol. 1992 (18) 285
4. Wang C. Y., Solter, L. F., Huang, W. F., Tsai, Y. C., Lo, C. F., and Wang, C. H. J. Invertebr. Pathol. 2009 (100) 68

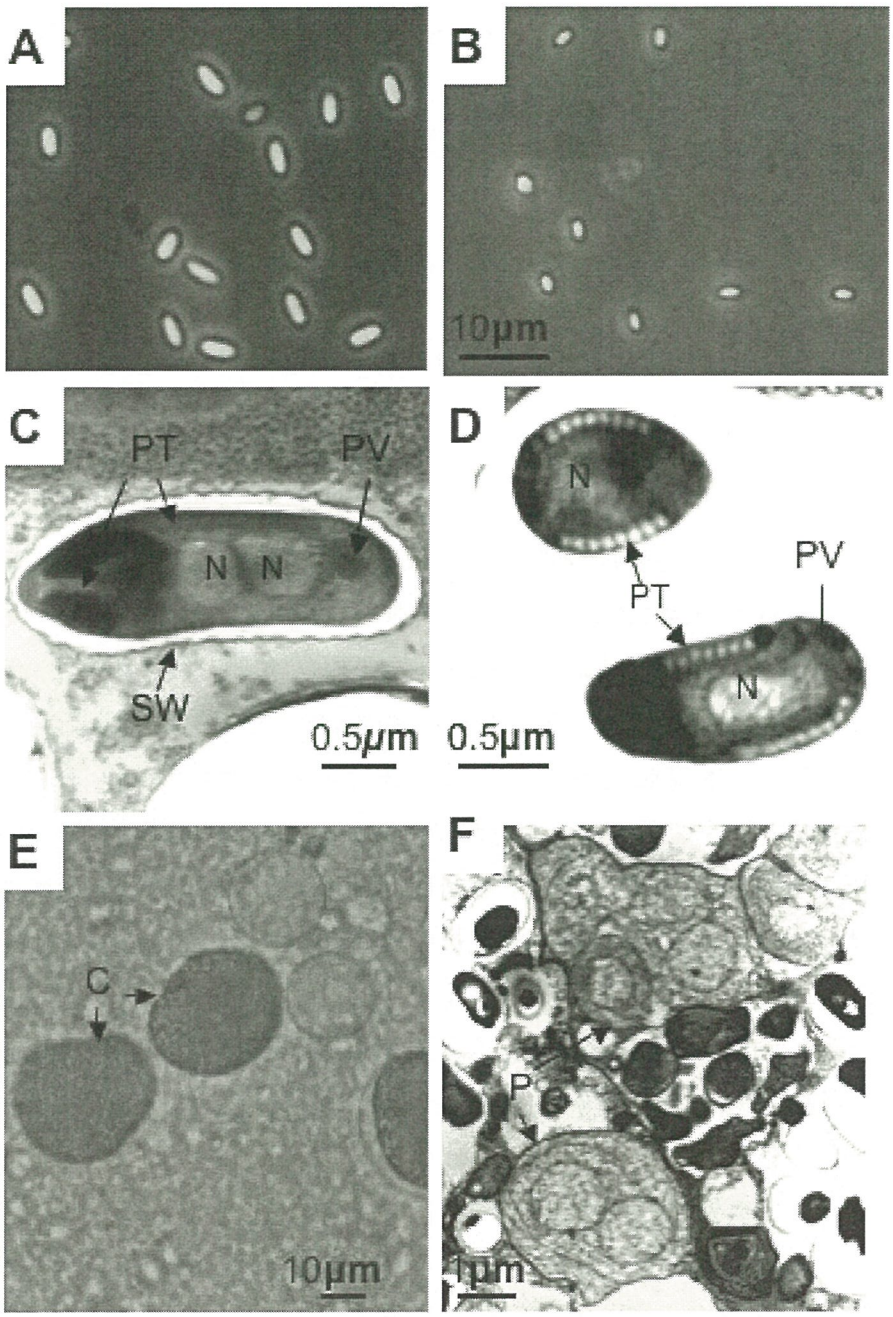

A-B Light micrographs of spores from *Vairimorpha ocinarae* and *Endoreticulatus* sp., respectively; **C-D** Electron micrographs of *Vairimorpha ocinarae* and *Endoreticulatus* sp., respectively, showing internal structure of spores; **E** Cysts of *Vairimorpha ocinarae* found in the infected tissues of *Ocinara lida*.; **F** Infected mid-gut tissue of *Ocinara lida* showing developing stages, multinuclear plasmodia, of *Endoreticulatus* sp..

C: cyst; N: nucleus; P: plasmodium; PT: polar tube; PV: posterior vacuole; SW: spore wall

Differentiation of Embryonic Stem Cells into Functional Pancreatic Beta Cells

胚胎幹細胞向胰腺β細胞體外誘導分化的研究

DING Ming-Xiao（丁明孝），Deng Hong-Kui

College of Life Sciences, Peking University（北京大學生命科學學院）, Beijing 100871, P R China

胚胎幹細胞向胰腺 β 細胞體外定向誘導分化的研究，對瞭解體內細胞分化與個體發育機理具有重要的理論意義。2000 年，加拿大科學家成功地應用人胰島移植方法治療 I 型糖尿病後，使這一研究更具誘人的應用前景。本文研究的主要內容包括：1，由胚胎幹細胞或多潛能幹細胞，在體外定向誘導分化成胰腺 β 細胞； 2，體細胞經重編程，獲得自體的胚胎幹細胞或多潛能幹細胞，用以減少移植的免疫排斥。本實驗室早期以小鼠胚胎幹細胞為實驗材料，通過作者所建立的'三步法'體外誘導途徑，成功地誘導分化成有功能的胰腺 β 細胞。在此基礎上，本文應用體細胞克隆技術，製備了小鼠胚胎幹細胞，並誘導分化成胰腺細 β 胞。與此同時，作者又率先在體外將人的胚胎幹細胞，誘導分化成有功能的胰 β 腺細胞。為了進一步在靈長類動物上進行這一工作，本文應用 iPS 技術製備了猴的多潛能幹細胞，而且，改進並極大提高了 iPS 細胞製備的效率。.這些工作，為隨後作者開展靈長類動物實驗和最終的人體應用打下基礎。在上述研究中，免疫螢光技術發揮了很重要的作用，作者正試圖在亞顯微水平上，在胚胎幹細胞向胰腺 β 細胞體外定向誘導分化研究方面，獲得一些新的有意義的資料。

關鍵字：胚胎幹細胞；iPS 細胞；胰腺 β 細胞

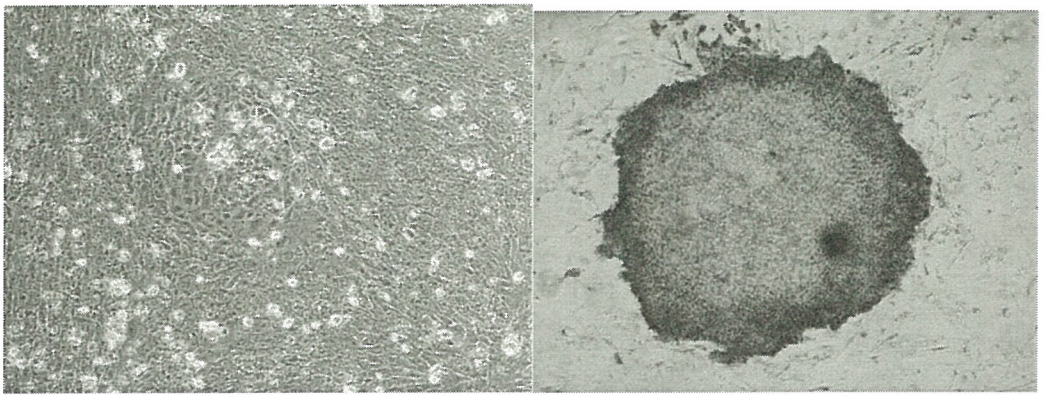

圖 1 人的胚胎幹細胞（左圖）和猴的誘導產生的多潛能幹細胞（iPSC,右圖）。

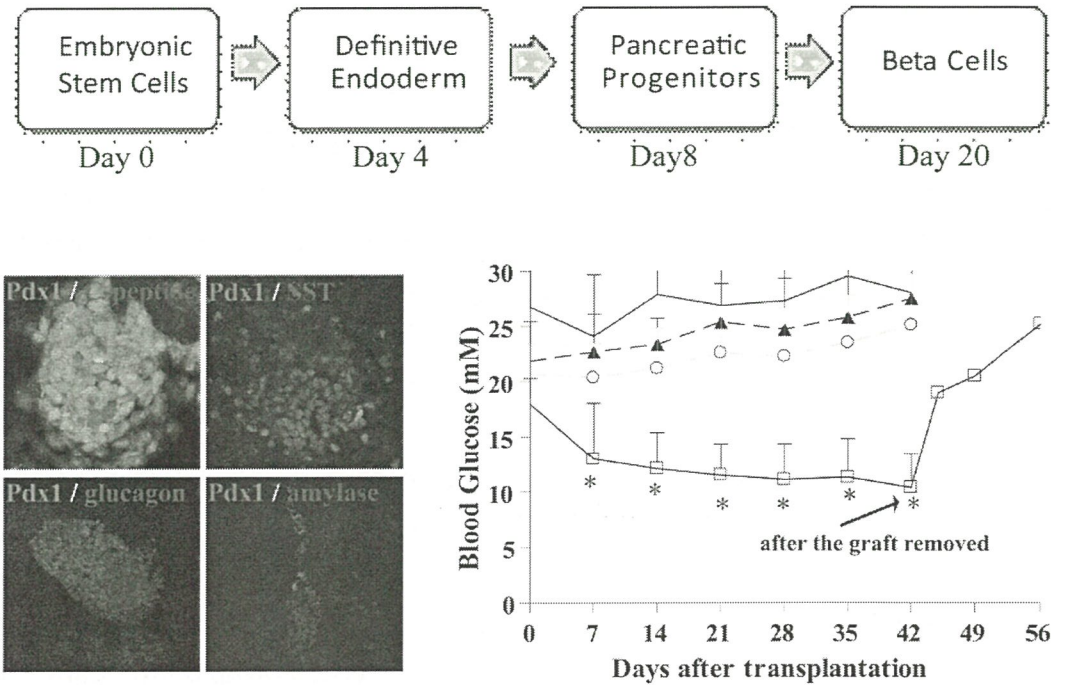

圖 2 人的胚胎幹細胞體外誘導分化成有功能的胰腺β細胞。誘導分化的程式（上圖），根據胰腺β細胞所表達的特異蛋白對誘導分化細胞的的鑒定（左圖）和小鼠體內移植後的功能檢測（右圖）。

Insecticidial Action of Galectin-1 Transfected Arabiposis to *Plutella xylostella*

Siou-Hua Wang[1], Shiang Jiuun Chen[2], Ling-Long Kuo-Huang[2], and Rong Nan Hu (黃榮南)[3]

[1] *Department of Life Science, College of Science, National Central University, Taoyuan 32054, Taiwan*

[2] *Department of Life Science, Institute of Ecology and Evolutionary Biology and TechComm-5, College of Life Science, National Taiwan University, Taipei 106, Taiwan*

[3] *Department of Entomology, College of Bioresources and Agriculture, National Taiwan University (台灣大學 昆蟲學系), Taipei 106, Taiwan*

Galectins (GALs) are a family of mammalian sugar-binding proteins specific for β-galactosides. Previous studies showed that the larval development of *P. xylostella* was significantly disturbed when fed them with *E. coli*-expressed recombinant galectin-1 (GAL1). These studies further investigate the insecticidal activity and mechanism of GAL1. The circular dichrosim (CD) spectrum shows that the secondary structure of GAL1 is not affected under pH 8-9 and below 50 ^{0}C. These results indicate that GAL1 is workable in the midgut's microenvironments of most insect (pH 8-9) and also thermo-stable below 50 ^{o}C. Moreover, GAL1 could interact *in vitro* with chitin and peritrophic membrane (PM) that are the potential targets for new bio-insecticides development. Two GAL1 over-expressed Arabidopsis (GAL1-*Arabidopsis* (whole plant) and GAL1-*Arabidopsis*-vas (vascular bundle-specific)) were established for insecticidal activity and mechanism studies. The results show that expression level of GAL1 in GAL1-*Arabidopsis* transformants ranges from 1% ~ 0.5% of total leaf soluble protein. The survival, body weight and food consumption are significantly decreased in a time-dependent manner in *P. xylostella* fed on GAL1-*Arabidopsis*. The histochemical structure and immunostaining suggest that GAL1 dose- and time-dependently bound to the midgut epithelium of *P. xylostella* fed on GAL1-containing diet or GAL1-*Arabidopsis*. The ultrastructural studies further show that disruption of the microvilli, abnormalities in epithelial cells. Moreover, Scanning electron micrographs show no PM present in *P. xylostella* fed on GAL1-containing diet or GAL1-*Arabidopsis*. Inferred from these results, the insecticidal mechanism of GAL1 involves direct binding with chitin to interfere with the structure of the PM and GAL1 could be a potential candidate for bio-insecticides development.

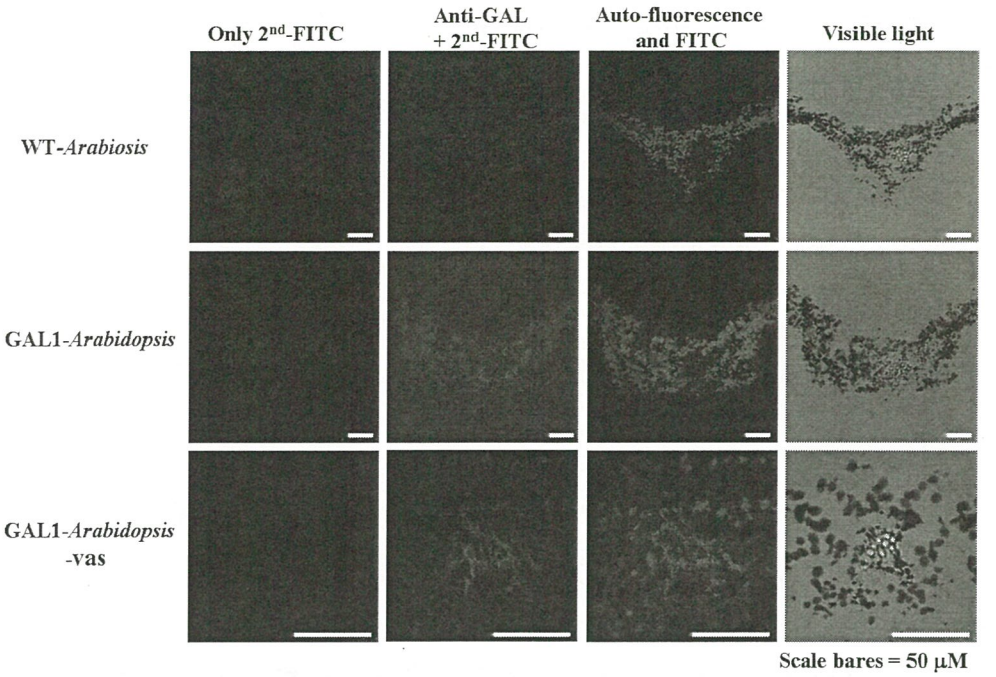

Fig. 1 Immunoloclization of GAL1 on the leaves of GAL1-*Arabidopsis* and GAL1-*Arabidopsis*-vas. Fresh leaves of WT-Arabidopsis (A) and two transgenic lines (B & C) were fixed overnight at 4 °C in 2% FA and 1.25% GA (in 0.05 M Pipes buffer), and then incubated in 3M sucrose for 2 h. At the end of incubation, the cryosections (20 m) were probed sequentially with GAL1 monoclonal primary antibody and FITC-conjugated secondary antibodies. Afterward, the fluorescence images were photographed by confocal microscopy.

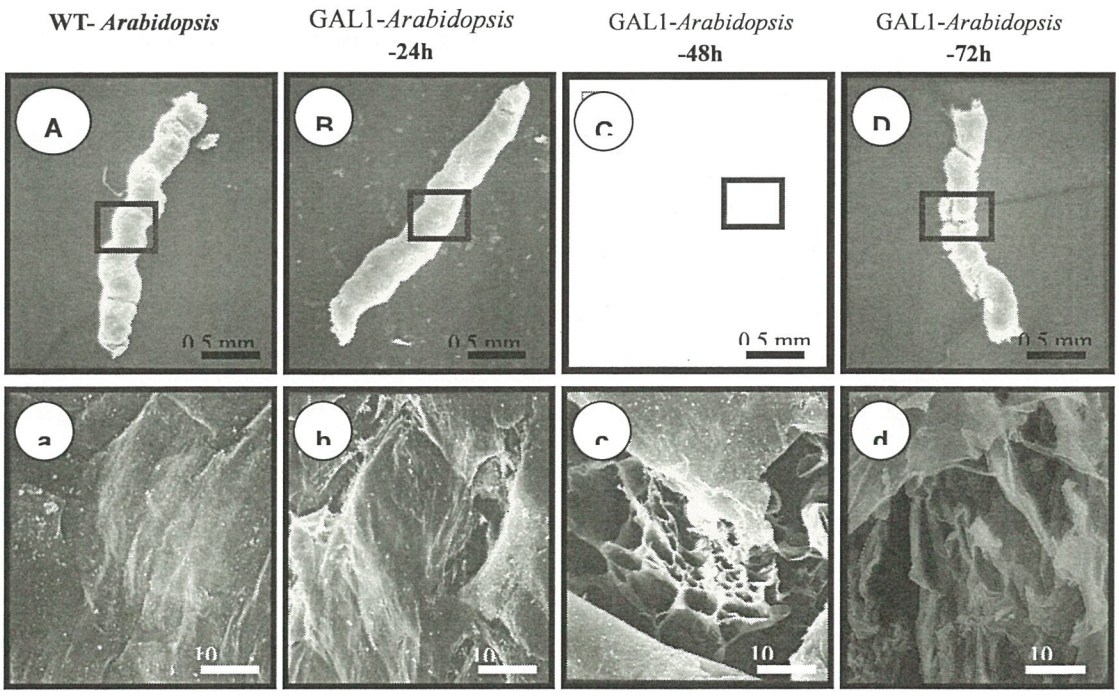

Fig. 2. Micrography of peritrophic membrane of P. xylostella reared on GAL1-tranfected *Arabidopsis*. The fourth to fifth instars larvae of *P. xylostella* were allowed to feed on GAL1-*Arabidopsis* for the time indicated. At the end of incubation, the PMs were dissected out from larvae of *P. xylostella* and fixed with 2.5% GA and 2% PFA in PBS, post-fixed in 1% OsO_4 in PBS for 2 h at 4 °C in dark and wash with PBS twice. Afterward, the PMs were photographed under Scanning Electron Microscope (Scale bars : 0.5 mm (upper panels); 10 m (lower panels)).

Electron Microscopy Study on the Structure of *Chlamydia trachomatis* 沙眼衣原體結構的電子顯微學研究

DONG Xiao-Duo[1]，CHEN Mu-Kai[2]，HUANG Zeng-Wei[1]，TANG Pei-Ping[1]，LI Kun-Peng[1]，HAN Jian-De[2]，ZHANG Qin-Fen（張勤奮）[1*]

1.State Key lab for biocontro（中山大學有害生物資源利用與控制國家重點實驗室）l

2. The first affiliated hospital, Sun Yat-Sen University, Guangzhou Guangzhou 510275, P R China

衣原體是一類細胞內寄生的原核細胞微生物，進化地位獨特，具有獨特的生長發育週期，包含了兩個不同的生長發育階段，分別對應形態和功能不同的形式：具有感染宿主細胞能力，但代謝不活躍的原體 (elementary body，EB，直徑大小約為 300nm)，以及進入宿主之後成為沒有感染能力，但是代謝活躍，具有增殖分裂能力的網狀體(reticulate body，RB，直徑可達 2000nm)。此外 RB 到 EB 的發育過程中胞質濃縮，還可出現含中等緻密的類核的中間體(intermediate body, IB)。

本文利用常溫常規電鏡制樣方法和電子斷層成像技術（electron tomography, ET)，體外對臨床上分離得到的沙眼衣原體進行了研究。沙眼衣原體（*Chlamydia trachomatis*，Ct)，可導致沙眼、感染性致盲，且是引起泌尿生殖道感染等性傳播疾病的主要病原體之一。研究發現，此種衣原體在 RB 發育成 EB 時，形態學上，有兩大方面的變化：一為體內物質的濃縮變小，二為膜形態結構的變化。RB 狀態時，衣原體胞內物質電子密度低而均一（圖 1)，而後部分物質濃縮形成 IB（圖 2)，最後形成具有高度緻密胞內物的 EB（圖 4)。伴隨胞內物質的變化，其膜也發生一系列的改變：首先 RB 的膜易皺縮(圖 1)，發育成 EB 後，其膜則較堅固，能耐受化學固定劑和脫水劑等的影響，一直能保持完整和比較光滑的形態（圖 4)，IB 狀態的膜介於兩者之間；其次 RB 發育到 EB 時，體積逐漸變小，多餘外膜會形成空的囊泡（圖 2，圖 3)；同時，外膜結構在從 RB 發育到 EB 過程中，明顯增厚。

關鍵字：沙眼衣原體；電子斷層成像技術；三維結構

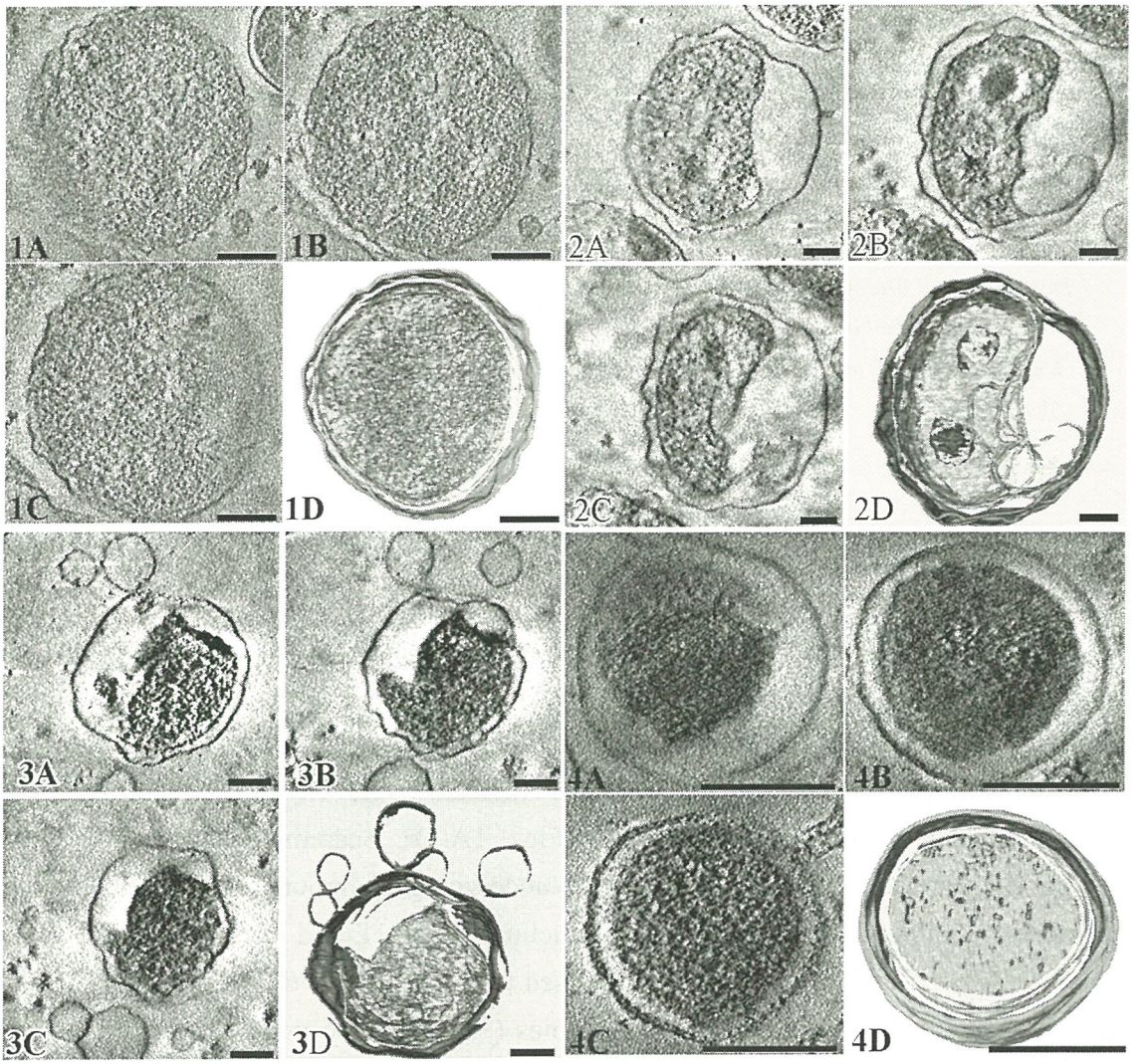

圖 1~圖 4 衣原體發育過程電子斷層成像結果。 ABC 是沿重構結果 Z 軸方向的從下到上不同位置的大約 2.7nm 的薄層二維投影圖。D 為整個衣原體厚切片三維結構。Bar＝100 μ m

Fig.1~Fig.4 Maps of Electron tomography of *Chlamydia trachomatis* at different stages. A, B, C are the 2－D projections of the slices with 2.7 nm thickness along z axis. D is the 3-D structure of *Chlamydia trachomatis*. Bar=100 μ m

Hydroxyl Radicals are Involved in Endotoxin-Induced Compound Exocytosis in Mucin-Secreting Goblet Cells of Rat Intestine

LIU, Shang-Pin[1]; CHANG, Cheng-Yu[2]; and HUANG, Hung-Tu（黃宏圖）[3,*]

[1] *Department of Biological Sciences, National Sun Yat-Sen University, Kaohsiung, Taiwan.*
[2] *Department of Pathology, Kaohsiung Veterans General Hospital. Kaohsiung, Taiwan.*
[3,*] *Departments of Beauty Science and Nursing, Meiho Institute of Technology（美和技術學院美容系）, Taiwan.*

Intravenous application of a high dose of endotoxin, also called lipopolysaccharide (LPS), results in endotoxemia in animals, that induces production of cytokines and free radicals, systemic inflammation, and mucus discharge from mucosal tissue. The present study was to investigate whether LPS application increased goblet cell secretion by compound exocytotic activity in mucosal villi of rat small intestine, and whether hydroxyl radicals were involved in LPS-induced compound exocytosis in goblet cells (Figs. 1A-D). Scanning electron microscopy showed that the numbers of goblet cells undergoing compound exocytosis (cavitated goblet cells) per mm^2 of ileal villus epithelium (Figs. 1E and F) in rats 5 minutes and 30 minutes after LPS (15 mg/kg) increased to 93±196 (N = 6) and 547±213 (N = 6), respectively, which were 5.1 and 8.4 times ($*P<0.05$) the number of corresponding value of control group receiving saline. Epithelial cell boundaries were poorly developed (Fig. 1D). Intervillous spaces contained a large amount of discharged mucus. Pretreatment with dimethylthiourea (DMTU), a hydroxyl radical scavenger, decreased the number of cavitated goblet cells to the value of saline control, suggesting that compound exocytotic activity was inhibited. LPS application strikingly increased the amount of plasma leakage in the duodenum and ileum, which was inhibited by DMTU to the baseline level. It is concluded that hydroxyl radicals were involved in LPS-induced increase in compound exocytotic activity of goblet cells, increase in plasma leakage, and villus epithelial barrier dysfunction during acute phases of inflammatory response in rat small intestine.

References

1. Cross, C. E., Halliwell, B., and Allen, A. Lancet, 1984 (16) 328.
2. Guo, J. J., Wang, D. S., and Huang, H. T. Anat. Embryol. 2003 (206) 301.
3. Huang, W. H., Chang, W. B., Liu, S. P., Lin, J. T., Fu, Y. S., Chang, M. C., and Huang, H. T. Auton. Neurosci. Basic Clin. 2009 (145) 44.

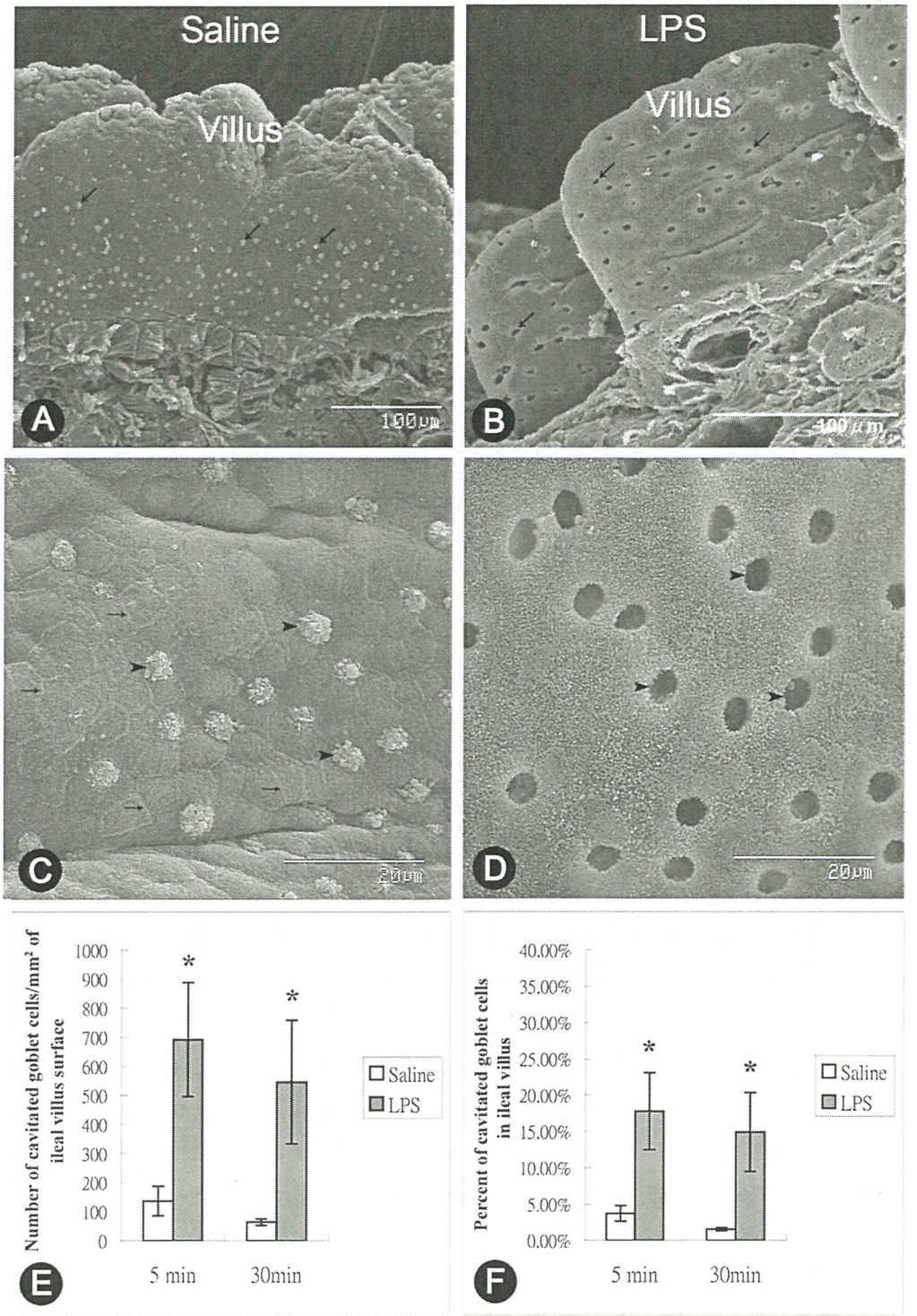

Figs. 1. A and C show the apical portion of goblet cells (arrowheads) in ileal villi after saline. Cell boundaries (arrows) are well-developed. B and D show the invaginations of goblet cells (arrowheads) after LPS. E and F show the number and percent of cavitated goblet cells.

Redistribution of Nuclear Pores during Formation of the Redundant Nuclear Envelope in Mouse Spermatids

HO, Han-Chen（何翰蓁）

Department of Anatomy, Institute of Physiological and Anatomical Medicine（慈濟大學生理暨解剖醫學研究所）, Tzu Chi University, Hualien 970, Taiwan

Extensive morphological modification occurs during mammalian spermiogenesis when spermatids change their spherical shape into cells with a compact head and a long tail [1]. In this study, freeze fracture was used to elucidate the alteration of the nuclear envelope during this process. Nuclear condensation resulted in great reduction of spermatid nuclear volume and the formation of the redundant nuclear envelope [2]. During nuclear condensation, distribution patterns of nuclear pores were greatly affected by the developing acrosome and manchette. As the acrosome enlarged to cap the nucleus, the pores redistributed caudally in the nuclear membranes and became exclusively localized to the redundant nuclear envelope (Fig 1, 2). Manchette microtubules play an important role in shaping the nucleus, and formation of the manchette was associated with exclusion of nuclear pores from the underlying nuclear envelope; therefore, it is likely that the redistribution of nuclear pores was aided by manchette development. The appearance of an electron lucent nuclear region surrounded by the nascent redundant nuclear envelope indicated a pathway for transporting degradation products through the nuclear pores to the residual cytoplasm [3]. The structured packaging of the nuclear pores into the redundant nuclear envelope (Fig 2) indicates that they play a role in late stages of sperm maturation or in fertilization, because most other unnecessary organelles of sperm are discarded during spermiogenesis or during shedding of the cytoplasmic droplet.

References

1. Russell, L. D., Ettlin, R. A., Sinha Hikim, A. P., Clegg, E. D. Histological and histopathological evaluation of the testis. 1990
2. Kerr, J. B. J Electron Microsc. Tech. 1991 (19) 215
3. Haraguchi, C. M., Mabuchi, T., Hirata, S., Shoda, T., Tokumoto, T., Hoshi, K., Yokota, S. J. Histochem. Cytochem. 2007 (55) 585

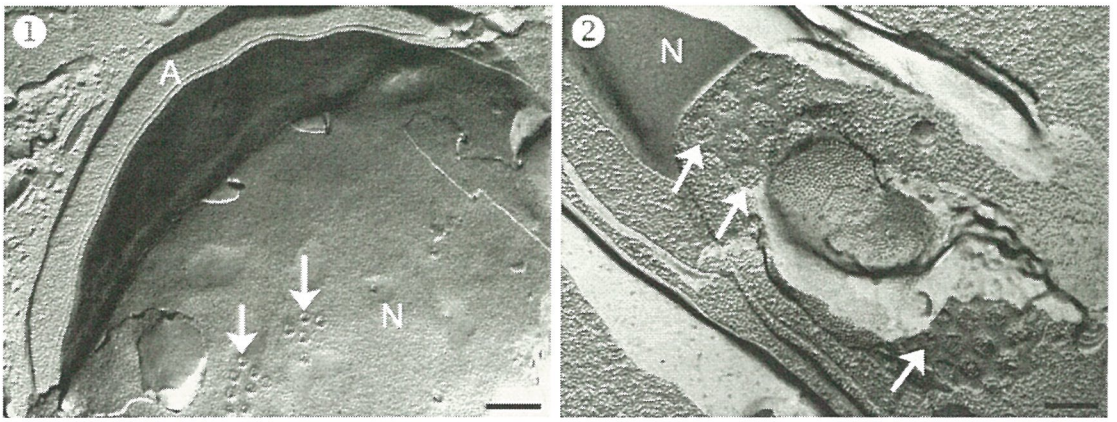

Fig. 1. Cap phase mouse spermatid. Clusters of nuclear pores (arrows) are visible at this stage in freeze-fracture replica. A: acrosomal cap; N: nucleus. Scale bar = 500 nm.

Fig. 2. Maturation phase mouse spermatid. Nuclear pores (arrows) only appear at the site of redundant nuclear envelope around the connecting piece. N: nucleus. Scale bar = 200 nm.

In vitro Ultramorphological Assessment of Apoptosis Induced by Areca Nut Extract in Murine Lymphocytes

Chiung-Hsiang Cheng（鄭穹翔）, Chia-Chi Wang and Tong-Rong Jan

School of Veterinary Medicine, National Taiwan University（臺灣大學獸醫系）, Taipei, Taiwan

Apoptosis, also called as program cell death, is involved in maintaining physiological homeostasis, such as immune balance. Lymphocytes in response to toxicants or reactive oxygen species may undergo apoptosis. Areca quid chewing is a major risk factor for oral cancer which is closely associated with poor immune surveillance. As areca nut extract (ANE) has been shown to be toxic to various oral cells, we investigated whether ANE induced lymphocyte apoptosis. Results of annexin V and propidium iodide double staining examined by fluorescent microscopy demonstrated the pro-apoptotic effect of ANE in murine splenic lymphocytes (Fig. A and B). Hoechst staining revealed that ANE induced nuclear condensation, a typical signs of apoptosis (Fig. C and D). The ultramorphological change in ANE-treated lymphocytes was examined by transmission electron microscope. Signs of apoptosis such as condensed nuclei, chromatin margination and nuclear membrane dilatation were clearly illustrated. In addition, mitochondria were affected by ANE as evidenced by the loss of cristae and swollen size (Fig. F). Based on these findings, we further determined the change of mitochondria membrane potential ($\Delta\psi_m$) and the release of cytochrome *c*. The results showed that ANE induced disruption of $\Delta\psi_m$, cytochrome *c* release and caspase-9 activation. In summary, ANE significantly induced primary lymphocyte apoptosis by the activation of mitochondrion-dependent pathway.

Splenocytes were treated with vehicle (A, C and E) or ANE (B, D and F) for 3 h. ANE-induced splenocytes apoptosis evidenced by annexin V (green fluorescence) and propidium iodide (red fluorescence) double staining (A and B). Hoechst staining showed the morphological features of apoptotic cells with nuclear condensation (C and D). Ultrastructure changes of ANE-treated cells displayed an increase in chromatin condensation and smaller, aberrantly shaped nuclei and the abnormal mitochondria with disrupted cristae (F). (Bar = 500 nm)

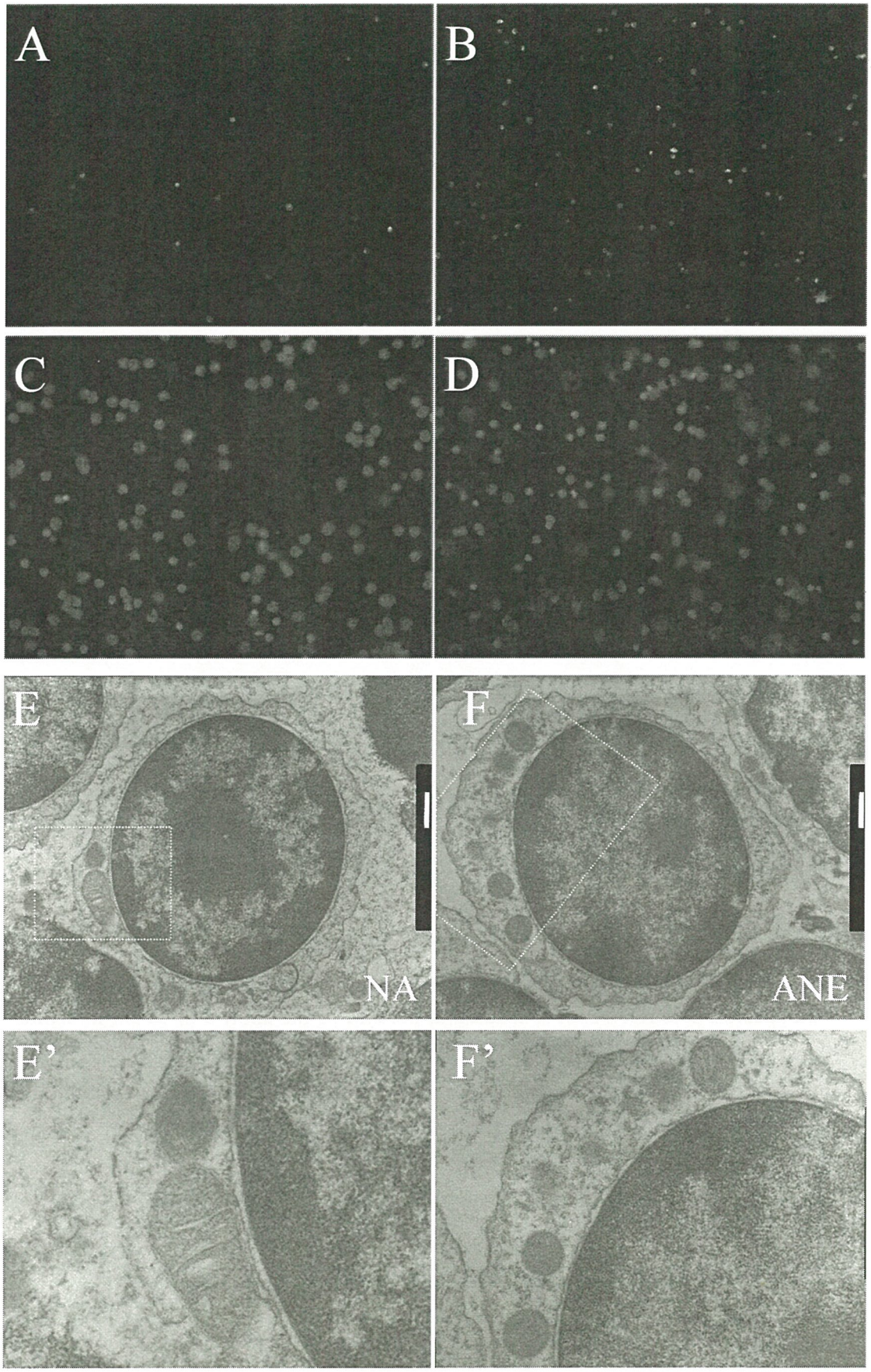
A
B
C
D
E
NA
F
ANE
E'
F'

Genome Analysis and Molecular Cytogenetics by rDNA-FISH

CHUNG, Mei-Chu（鍾美珠）

Institute of Plant and Microbial Biology, Academia Sinica（中央研究院植物暨微生物所）, Taipei, Taiwan

In higher eukaryotes, genes encoding ribosomal RNA (rDNA) are organized in two distinct multigene families, one for the 5S rRNA and another for the 45S rRNA. Highly repetitive 45S rDNAs are tandem arranged at one or a few chromosomal loci. The chromosome region bearing 45S rDNAs active in transcription is often associated with a nucleolus, this region is known as a nucleolar organizing region (NOR). The sequences in coding region of rDNAs are highly conserved among organisms, while the sequences in non-coding region are diverse even in close related species. The number and chromosome position of 5S rDNA and of 45S rDNA loci may vary in close related plant species. Fluorescent in situ hybridization (FISH) visualize 5S and 45S rDNA sites on chromosomes as reliable landmarks for chromosome identification. The results of rDNA-FISH obtained from close related species usually reveal extensively phylogenetic relationships.

The chromosome number of diploid rice is 2n=24. Both traditional cytological observation (Fig.1) and rDNA-FISH showed that there is only one 45S rDNA locus in japonica type rice (Fig. 2) and two 45S rDNA loci in indica type rice and other wild species rice with A genome type (Fig. 3). Our results reveal polymorphism in the number of rDNA loci, the number of rDNA repeats, and their chromosomal positions among *Oryza* species[1]. The numbers of rDNA loci varies from one to eight among *Oryza* species. The rDNA locus located at the end of the short arm of chromosome 9 is conserved in the genus *Oryza.* Two genome specific rDNA loci were detected in the genus *Oryza*. One locus at the end of the short arm of chromosome 4 is specific to the BB genome (Fig. 4), another in the proximal region of the short arm of chromosome 5 is specific to the CC genome (Fig. 5). A particular rDNA locus was detected at the proximal region of the short arm of chromosome 4 in tetraploid rice, *O. grandiglumis* (Fig 6). We suggest that chromosomal inversion and the amplification and transposition of rDNA might occur during *Oryza* species evolution.

References

1. Chung MC, Lee YI, Cheng YY, Chou YJ, and Lu CF. Theor Appl Genet. 2008 (116) 745.

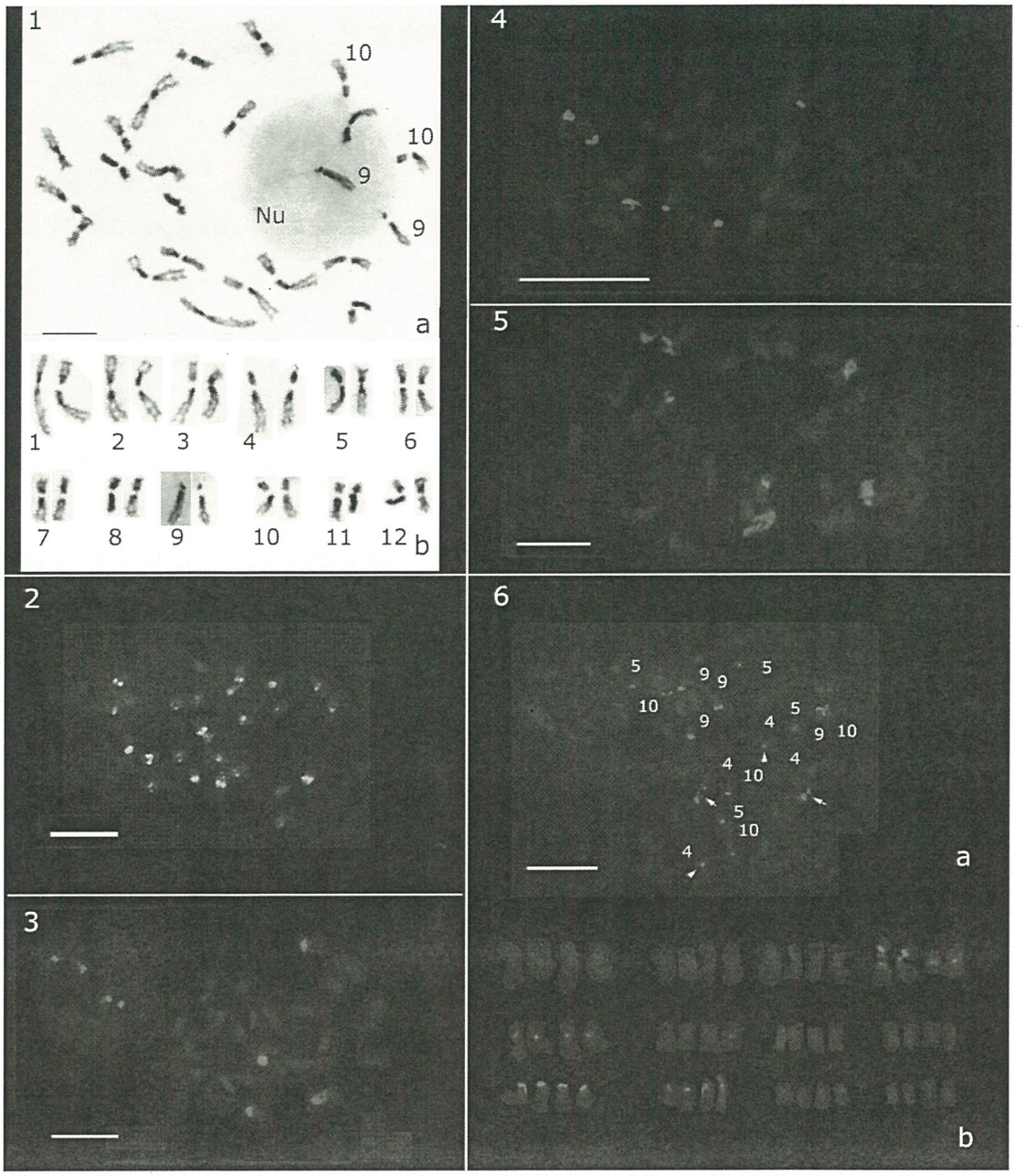

Fig. 1. Chromosome complements **(a)** and karyotype **(b)** of *O. sativa* ssp. *indica* cv. IR36.

Fig.2-6. FISH localizations of rDNA (*red*) loci on somatic chromosomes (*blue*) of *Oryza* species, **(2)** *O. sativa* ssp. *japonica* (green signals indicate the position of centromeres) **(3)** *O. ruffipogon,* **(4)** *O. punctata* , (5) *O. officinalis*, and **(6)** *O. gradiglumis.*. (scale = 10 m).

Intracellular Distribution of Broad Bean Wilt Virus 2 VP37 Protein
蠶豆萎蔫病毒 2 號 VP37 蛋白在細胞內的定位

Liu Chengke, Meng Chunmei, Zhou Xueping, Hong Jian（洪 健）*

Institute of Biotechnology, Zhejiang University（浙江大學生物技術研究所）, Hangzhou 310029，P R China）

植物病毒在寄主體內的運輸依靠短距離胞間運動和長距離維管束轉運兩個途徑，胞間運動是病毒基因產物與寄主成分相互作用的主動過程。病毒基因編碼的運動蛋白（MP）可修飾胞間連絲結構，擴大其體積排通極限（SEL），病毒以MP/RNA 或完整粒子形式通過胞間連絲進入相鄰細胞。以豇豆花葉病毒（CPMV）為代表的管狀結構運動模式病毒 MP 在細胞中形成管狀結構，病毒粒子排列在該管狀通道內穿越胞間連絲。蠶豆萎蔫病毒 2 號（BBWV-2）是豇豆花葉病毒科蠶豆病毒屬的重要成員，其胞間運動機制至今未明。本文作者通過電鏡觀察發現感染 BBWV-2 的葉片細胞中病毒排列于管狀結構穿越胞間連絲，同時應用分子生物學技術構建 VP37:GFP 融合基因並在植物細胞和原生質體中進行表達，獲得了有關 VP37 蛋白細胞定位的重要證據，為瞭解其胞間運動機制提供資料。本文報導 VP37 蛋白在 BY-2 懸浮細胞中的定位結果。

1 材料與方法

構建綠色螢光蛋白與VP37的融合基因（GFP:VP37），用pCHF$_3$植物表達載體通過農桿菌介導法轉染BY-2懸浮細胞；用ER-Tracker™ Blue-White DPX dye特異性染色內質網；以不同濃度的佈雷菲德菌素A（BFA）分別處理野生型細胞和表達GFP:VP37的細胞，再進行ER-Tracker內質網染色。所有細胞樣品均在Leica TCS SP5鐳射共聚焦顯微鏡下進行觀察，激發光488 nm、吸收光500-550 nm觀察GFP:VP37螢光，激發光405 nm、吸收光430-640 nm觀察內質網結構。ER-Tracker標記物在紫外光激發下為藍白色，為了與GFP區分比較，在共聚焦顯微鏡采圖時將內質網標記物設定為紅色。

原核表達 VP37 並製備兔抗血清；將表達 GFP:VP37 的懸浮細胞和接種 BBWV-2 的蠶豆病葉進行常溫 Spurr 樹脂包埋和 Lowicryl K4M 低溫樹脂包埋，超薄切片用 VP37 蛋白抗體進行免疫膠體金標記，JEM-1230 透射電鏡觀察，加速電壓 60-80kV。

2 結果與討論

重組表達栽體通過農桿菌介導法轉染 BY-2 懸浮細胞，48h 後共聚焦顯微鏡觀察發現 GFP:VP37 螢光主要分佈在細胞核周圍及細胞周邊，呈網路狀結構（圖 1）；不連續的螢光小點分佈在細胞邊緣（圖 2），有的成對出現在相鄰兩個細胞之間；單獨表達 GFP 的細胞螢光均勻分佈在細胞質及細胞核中（圖 3）。用 ER-Tracker 染色後可發現，這些 GFP 綠色螢光聚集的位置與內質網密切相關（圖 4~圖 6）。用 10 μmol/L 的 BFA 處理細胞後內質網結構未發生明顯變化（圖 7），濃度為 100 μmol/L 的 BFA 處理細胞後內質網被破壞（圖 8）；無論低濃度還是高濃度 BFA 處理後，GFP:VP37 大多局限在細胞核周圍，細胞周邊螢光點減少（圖 9），表明 BFA 阻止了融合蛋白在細胞邊緣的定位。

在表達 GFP:VP37 的 BY-2 細胞內，用 VP37 抗體免疫金標記可觀察到金顆粒大多分佈在細胞質及內質網部位，在細胞邊緣的細胞膜和質體周圍也有分佈（圖 10，圖 11）。

上述實驗表明，BBWV-2 的 VP37 蛋白主要定位在 BY-2 細胞邊緣胞間連絲部位以及細胞核周圍的內質網上，VP37 具有定位和穿越胞間連絲的能力，是 BBWV-2 胞間運動的關鍵因數，而細胞內質網體系對於 VP37 的胞內運輸可能起著重要作用。

基金專案：國家自然科學基金資助項目(批准號：30770091，30270873)

*通訊作者

圖 1 農桿菌法轉染 GFP:VP37 的 BY-2 細胞，螢光分佈在細胞核周圍細胞質中，呈網路狀結構；圖 2 細胞周邊形成的螢光點；圖 3 單獨表達 GFP，螢光分佈在整個細胞中；圖 4 GFP:VP37 在細胞內的分佈；圖 5 ER-Tracker 染色顯示內質網結構；圖 6 GFP 與 ER-Tracker 合成象顯示 GFP:VP37 定位在內質網上；圖 7 10 μmol/L BFA 處理細胞 ER-Tracker 染色，內質網結構完好；圖 8 100 μmol/L BFA 處理後內質網被破壞；圖 9 BFA 處理細胞 GFP:VP37 大多在細胞核周圍，細胞周邊螢光點減少；圖 10，圖 11 表達 GFP:VP37 的 BY-2 細胞免疫金標記，顯示金顆粒大多分佈在細胞質內及細胞邊緣（箭頭）。

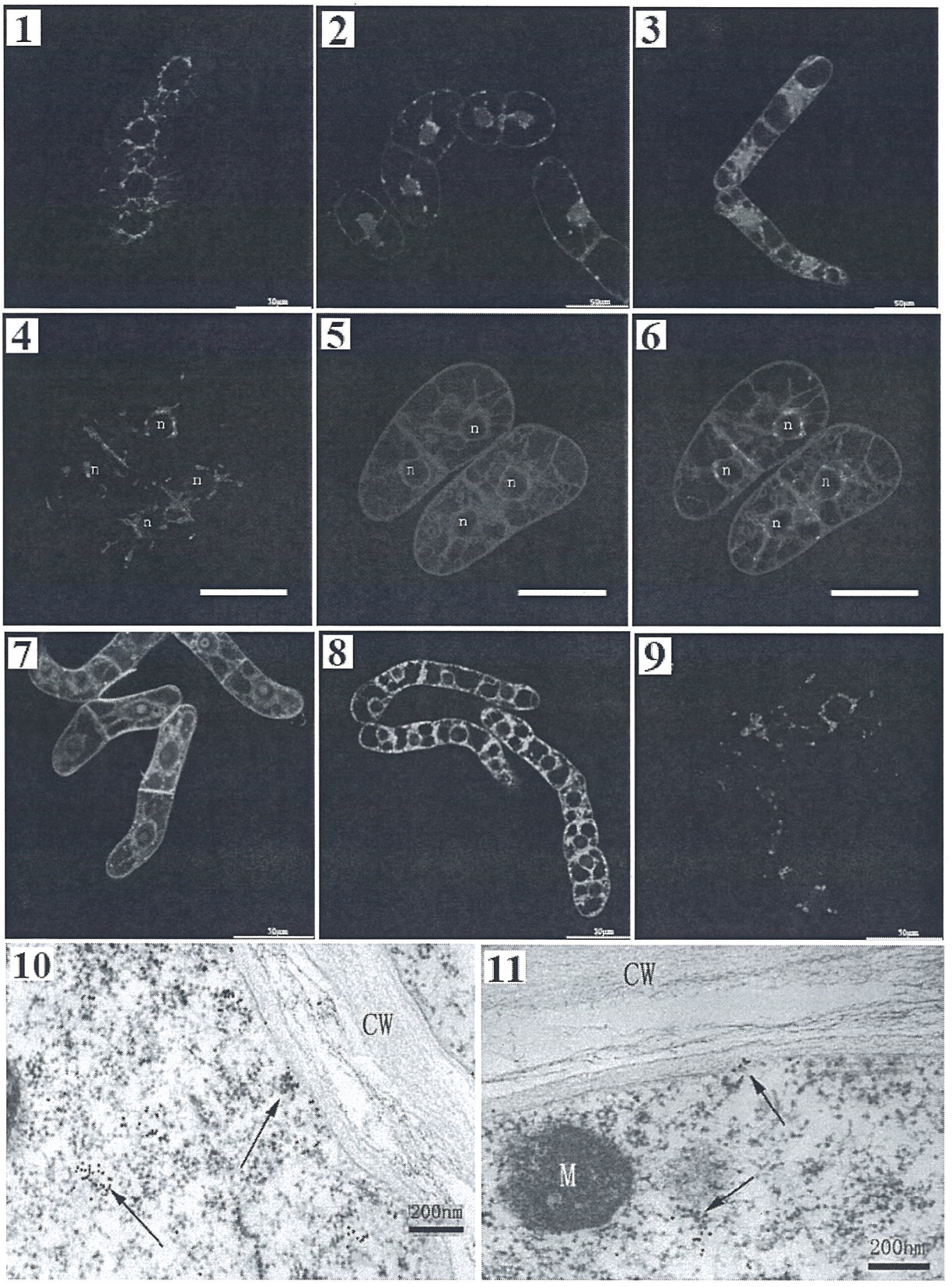
1
2
3
4
n
n
n
n
5
n
n
n
n
6
n
n
n
n
7
8
9
10
CW
200nm
11
CW
M
200nm

The latest development of 3D tomography for soft materials

S. Motoki[1], T. Kaneko[1], Y. Aoyama[1],H. Nishioka[1], Y. Ohkura[1], Y. Kondo[1], H. Jinnai[2,3]

[1] *JEOL Ltd., 3-1-2 Musashino, Akishima Tokyo 196-8558, Japan,*
[2] *Department of Polymer Science and Engineering, Kyoto Institute of Technology, Matsugasaki, Kyoto 606-8585, Japan*
[3] *WPI Advanced Institute of Materials Research, Tohoku University,2-1-1 Katahira Aoba-ku, Sendai 980-8557, Japan*

In the soft materials science, it is known that the inclusion of 10 ~ 100 nm order scale influence the characteristics of materials. Tomography in transmission electron microscopy is powerful for the analysis of three-dimensional (3D) structure of such materials. Structural analysis of those materials needs thick sample to involve these. However, the dynamics of scattered electrons inside the thick specimen is so complicate that the optimal condition for observation of it is uncertain. In this study, we compared bright field transmission electron microscopy (BF-TEM), bright field scanning transmission electron microscopy (BF-STEM) and dark field scanning transmission electron microscopy (DF-STEM) as a tomographic imaging method for such thick sample.

We employed an acylonitrile butadiene styrene (ABS) resin. The ABS resin was stained by OsO_4 vapor to enhance the contrast and then microtomed for 3D observations. The thick section of ca. 1 μm thick was transferred onto a Copper grid with polyvinylformal as a supporting film. Prior to the tomographic observations, 40-nm-sized Au particles were deposited on the sample as markers. The tilt series of the electron images were taken with 200 kV TEM/STEM (JEM-2100). The pixel resolution was 4 nm resulting in the effective focal depth of 1.6 μm, which is substantially larger than the sample thickness. The detection angles of BF- and DF-STEMs were 6.5 mrad and 150 mrad, respectively. All reconstruction procedures were carried out using a software: "TEMography" [1].

To evaluate reconstructed tomograms by BF-TEM, BF-STEM and DF-STEM, we compared images sliced from their volumes at three heights, *i.e*, near the top, at the middle and near the bottom of the volume. The images from BF-TEM show almost the same degree of blur at three heights. The reason for the blur is considered to be a chromatic aberration due to increase of energy spread of image forming electrons, originated from inelastic scattering. Analysis on the sliced images of STEMs shows that the spatial resolutions decrease continuously from the top to the bottom of the volume. This related to the electron beam broadening caused by the multiple-scattering of the electrons passing through the specimen. The broadened width estimated from the blur of the sliced image accords with that predicted by a theory [2]. The spatial resolution of DF-STEM tomograms tends to lose faster than that of BF-STEM, since the electrons within the small detection angle have lower probability of multiple scattering than those in large angle. From these results, we conclude that the BF-STEM with small detection angle is advantageous for tomograms of thick specimen.

[1] TEMograpy, http://www.temography.com

[2] J. I. Goldstein, Introduction to Analytical Electron Microscopy, Plenum Press, New York,

Plants in Response to Cadmium Toxicity

CHEN, Yung-reui（陳榮銳）

Institute of Molecular and Cellular Biology, National Taiwan University（台灣大學分子與細胞生物學研究所）, Taipei, Taiwan

Cadmium in soil is absorbed by plants and delivered to animals and humans through food chain. Bioassay and biological monitoring of cadmium pollution have been studied.[1, 2] However, the success of measurement is based upon on the chose of proper plant species and organs.[3] Morphological effects of cadmium on plants were studied with naked eye observations and image techniques. Biochemical characteristics of plant in response to heavy metal provide information not only for defensive mechanism of plant toward outside stress, but also for application on effective photoremediation to remove heavy metal from polluted soils.

Cadmium is a non-essential element for plant nutrition and affects plant growth for *Zinnia elegans*. Cadmium toxicity in susceptible plants are stunt plant body, root growth retardation and rotten in black color, small leaves with necrosis. It also affect the vascular deformation and pattern (Fig. 1). Leaf age is important in ruling the inducible ability of xylem transfer cells (Fig. 2) in cadmium-treated plants. Biochemical studies show that the best timing for plants producing phytochelatins is around 24 h after plant roots exposing to cadmium. Meanwhile, plants pretreated with 10 M cadmium were induced more sulfhydryl groups and glutathione than that of plain 45 M Cd-treated plants in their HPLC profile. Individual peaks of sulfhydryl groups did show a prominent increase in peaks 3 and 4 at 24 h, whereas they gradually decreased to initial levels of sulfhydryl group after 96 h. Both LMW and HMW complexes were collected (Table 1). Active fractions of LMW complex consisted peak 1 and peak2 and they contained histidine more than 90 % of total amino acids. HMW complex had five peaks in HPLC profile. Only peak 1 major contained histidine at percentage more than 85 %, whereas peaks 4-7 contained less than 0.1% of histidine and mainly phytochelatins whose n number were 3 and 4.

Phytochelatins are well documented in high plants, algae and fungi[3] and they sequester metals from the cellular milieu and regulate the cellular concentration of metals through the process of accumulation in vacuole.[4] The structure, organization and expressions of phytochelatin sythase genes related to cadmium have also been

reported in higher plants and fungi.[5] The approaches on effective phytoremediation through integrate researches are needed

References:

1. Woolhouse, H. W. Encyclop. Plant Physiol. II, 12C:245-300 (1983).
2. Rauser, W. E. Annu. Rev. Biochem. 59:61-86 (1990).
3. Grille, E., Winnacker, E. L. and Zenk, M. H. Science 230:674-676 (1985).
4. Wagner, G. J. Adv. Agron. 51:173–212 (1993).
5. elvama, A. and Wong, J. W. Enironmental Technology 29: 765-773 (2008)

Acknowledgements: All students participated in stress biology and these works are grateful.
Grand from National Science Council for financial support are highly appreciated.

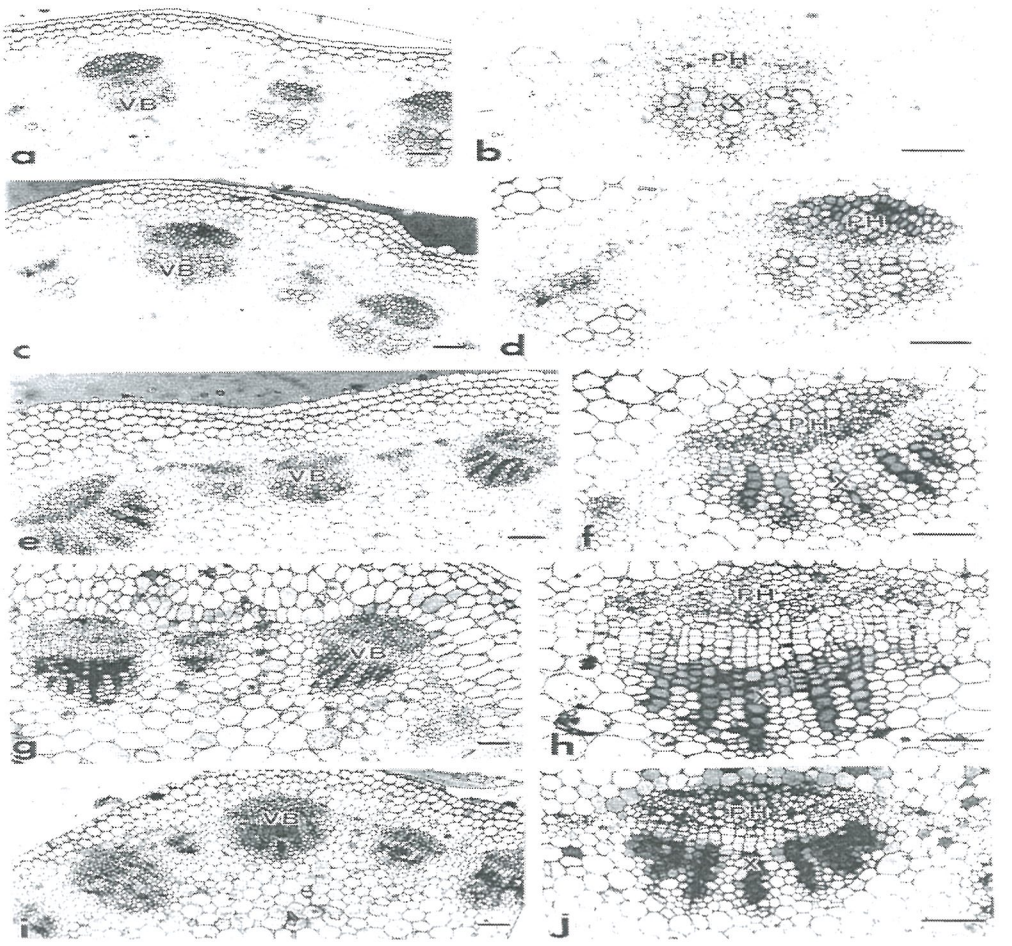

Fig. 1. Cadmium concentrations affect on the development of vascular bundles. Partial cross sections of twig showing in a and b (enlarged from a) is from control plant. Fig.1c,1e,1g, and 1i are from plants treated with cadmium concentrations at 10, 30, 60, and 100 M, respectively.

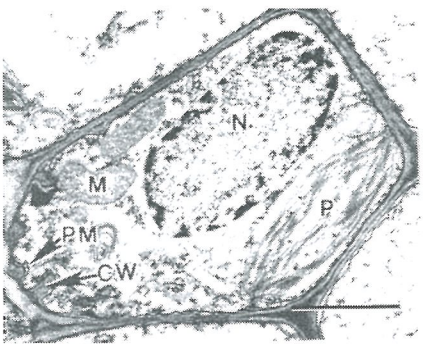

Table 1. Components of cadmium -binding complexes.

	HMW	LMW
	n mol	
Sulfurhydryl groups	700.48	129.58
Cadmium	41.00	2.00
Acid labile sulfur	1506.00	—

Fig. 2. Fine structure of induced xylem transfer cell.

Abbreviation: CW, cell wall; HMW, high molecular weight; HPLC, high performance liquid chromatography; LMW, low molecular weight; Mitochondria; N, nucleus; P, plastid; Ph, phloem; PM, plams membrane; TC, Transfer cell; VB, vascular bundle; Ve, Vessel; X, xylem

Analysis and Research of Rice Scanning Electron Microscopy of the Energy Spectrum

水稻掃描電鏡能譜分析研究

YANG Bing-Yao（楊秉耀）[1], CHEN Xin-Fang[1], Zhou Jing-Yun[1] , LIU Xiang-Dong[2], GUO Hai-Bin[2]

1. Electric Microscope Laboratory, South China Agricultural University（華南農業大學電鏡室）, Guangzhou Guangdong 510642, P R China;

2. Guangdong Provincial Key Laboratory of Plant Molecular Breeding, South China Agricultural University, Guangzhou Guangdong 510642, P R China

本文針對生物掃描電鏡能譜分析方法進行了探討，對水稻進行掃描電鏡表面形態結構觀察和對其元素含量分析。結果表明生物樣品能譜分析，鍍膜的厚度在20nm較好。在水稻根、莖、葉和穀粒中的含矽量，以穀粒表面為最多。

關鍵字：水稻矽含量；掃描電鏡；能譜分析

1 材料與方法

實驗用水稻種植於華南農業大學農學院試驗農場，品種為：矮腳南特-4x (四倍體)、廣陸矮4號-4x (四倍體)、神農265、鹽粳48、L202、玉油香粘等品種。樣品採用4%戊二醛固定48h，用乙醇30% 、50% 、70% 、80% 、90% 、100% 、梯度脫水。用CDP30型CO_2臨界點乾燥儀進行乾燥, SCD500型高真空鍍碳。用FEI XL-30型掃描電鏡進行觀察和EDAX能譜儀進行元素分析。

2 掃描電子顯微鏡能譜分析

近年來，作者對水稻進行了掃描電鏡微觀形態的觀察的同時，並在能譜分析方面做了一些工作，特別是對水稻的根部、葉片、莖杆、穗莖以及穀粒等表面進行了較詳細的分析研究。並對生物樣品能譜分析的方法進行了探討，分別在高真空鍍炭的不同厚度處理的樣品進行了比較。

水稻葉片的矽含量很高，其表面分佈著兩種形狀的矽質體，稱之為啞鈴形矽質體和“乳突”矽質體，在水稻種子穀粒表面也沉積有稱之為“乳突”的矽質體結構。 針對不同抗性的水稻品種，通過掃描電子顯微鏡觀察葉表面矽質細胞，並運用X-射線能譜分析其矽元素含量，以瞭解水稻矽化程度與多抗性的關係，為篩選多抗種質提供理論依據。

3 結果與分析

1、高真空鍍炭：水稻穗莖橫切面鍍炭 10nm 後進行掃描電鏡觀察，圖像二次電子量明顯不足，有放電現象。掃描圖像立體感差，解析度低。鍍炭 20nm 後掃描圖像二次電子量較多，沒有放電現象。掃描圖像立體感較強，解析度較高。如圖 1~圖 4 所示。

2、鍍膜厚度不同對表面元素分析的影響：在水稻葉片鍍炭不同厚度的表面元素分析中，鍍膜厚度在 10nm 時，由於樣品表面密度差，樣品對特徵能量低的特徵 X-射線益處較多，輕元素檢出率高。鍍膜厚度在 20nm 為為中。如表 1 所示。

表 1 鍍炭不同厚度葉表面元素含量

厚度＼元素	O（wt.% ）	Na（wt.% ）	Si（wt.% ）	P（wt.% ）
10nm	56.80	6.88	26.02	11.30
20nm	55.17	6.77	26.07	11.99

3、水稻不同部位元素含量：在樣品的導電處理分別用高真空鍍碳不同鍍膜厚度的比較中證明，由於生物樣品所含元素多數是 H、N、C、O 等原子序數較輕的元素，所以當用鍍碳作為導電處理時，既要考慮對輕元素的檢出率，又要考慮掃描電鏡二次電子圖像分析的導電性。在鍍膜 20 nm 導電性能好，在生物樣品進行掃描電鏡能譜進行元素分析時輕元素的檢出率也較好。

水稻的根、莖、葉和穀粒表面元素含量分析中表明，水稻穀粒表面矽元素含量為最高達 49.68（wt.% ）。其次是莖的表面矽含量為 32.48（wt.% ）。第三是葉面的表矽含量為 26.07（wt.% ）。最差是根的表面矽含量為 17.18（wt.% ）。如表 2 所示。

表 2 水稻根、莖、葉和穀粒表面元素含量

厚度＼元素	O（wt.% ）	Na（wt.% ）	Si（wt.% ）	P（wt.% ）
根	69.68	5.56	17.18	7.57
莖	53.03	7.51	32.48	6.98
葉	55.17	6.77	26.07	11.99
穀粒	41.47	1.25	49.68	7.60

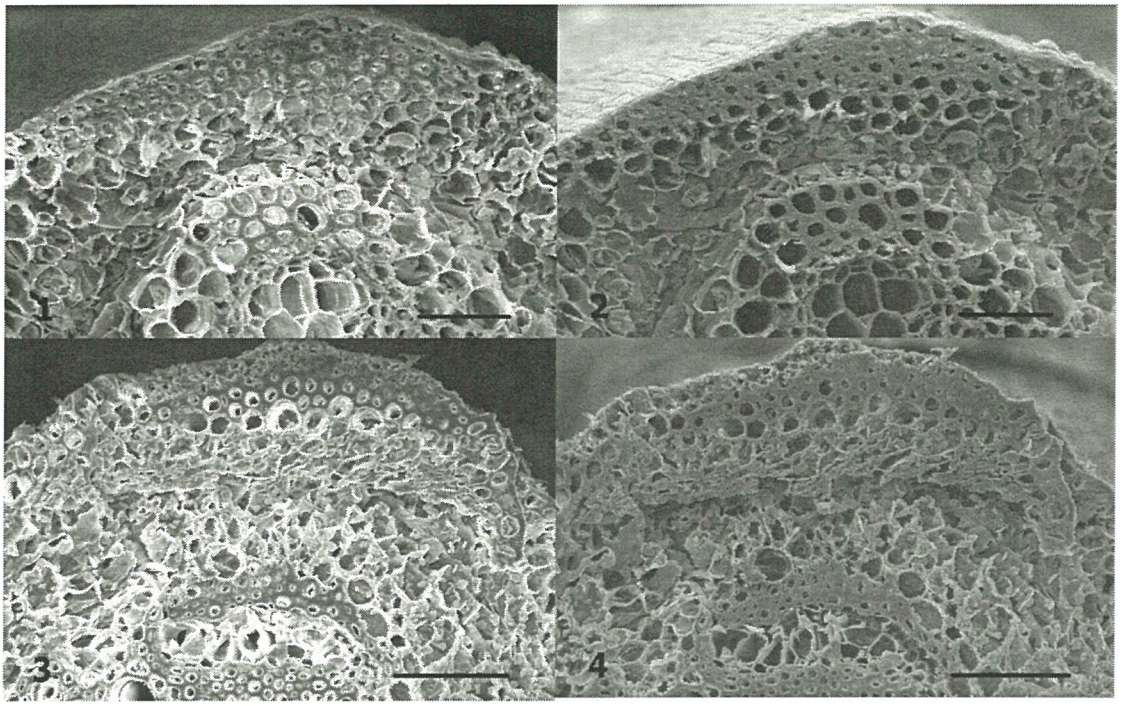

圖 1~圖 4 水稻穗莖橫切面鍍炭不同厚度二次電子圖像。

圖 1，3：鍍膜厚度 10nm； 圖 2，4：鍍膜厚度 20nm；圖 1，2：Bar＝10μm；

圖 3，4：Bar＝50μm

參考文獻略

The Pollen Ultrastructure of *Arabidopsis thaliana* During Microgametogenesis Using High Pressure Freezing Technique

HSU, Chia-Mei, MA, Feng-Yi, and JANE, Wann-Neng（簡萬能）

Institute of Plant and Microbial Biology, Academia Sinica（中央研究院植物暨微生物所）, 128 Academia Road, Sec. 2, Nankang, Taipei, Taiwan.

Sucessful cryofixation followed by freeze substitution, shows superior preservation of fine structure over that yielded by chemical fixation [1]. Using high pressure freezing/freeze substitution, we study pollen ultrastructure of ***Arabidopsis thaliana*** during microgametogenesis.

After nuclear division, the cell wall between the generative and vegetative cells is formed by cell plate. The generative cell initially attaches to the pollen wall (Fig. A), then enlarges (Fig. B, C), and finally releases to the vegetative cytoplasm (Fig. D, E). During development, the shape and vacuolation of the generative cell gradually change (Fig. G-I). The generative cell wall becomes thinning during cell enlargement (Fig. G), and disappears in the free stage (Fig. H). Some organelles, including mitochondria, plastids, dictyosomes, and RER, can be found in the generative cell (Fig. G-I). A large amount of microtubules are distributed in the peripheral region of the generative cell, adjacent to the vegetative cytoplasm (Fig. G-I). The generative cell undergoes division to form two sperm cells (Fig. J). At anthesis, two sperm cells do not take apart (Fig. K) and are close to the vegetative nucleus (Fig. F).

A large vacuole and many organelles are present in the vegetative cell (Fig. B, L) when mitosis I is finished. In following development, the vacuolation of the vegetative cell decreases (Fig. C-E), but the number of dictyosomes increases (Fig. M). When the pollen will undergo mitosis II, the amount of starch in amyloplasts reaches maximum in the vegetative cell (Fig. N). At anthesis, a large amount of polysaccharide vesicles are present in the vegetative cytoplasm (Fig. O).

Our results agree with previous studies for ultrastructural changes of ***Arabidopsis thaliana*** during pollen development[2-4]. However, we observe more detailed changes of the pollens during microgametogenesis, especially the distribution of microtubules. The microtubules should play an important role in the generative cell development.

References

1. Morphew, K. M. 2009 Unversity of Colorada
2. Owen, H. A. and Makaroff, C. A. Protoplasma 1995(185) 7
3. Kung, A. and Musgrave, M. E. Protoplasma 1996 (194) 81
4. Yamamoto, Y. Nishimura, M. Hara-Nishimura, I. Noguchi, T. Plant Cell Physiol. 2003 (44) 1192

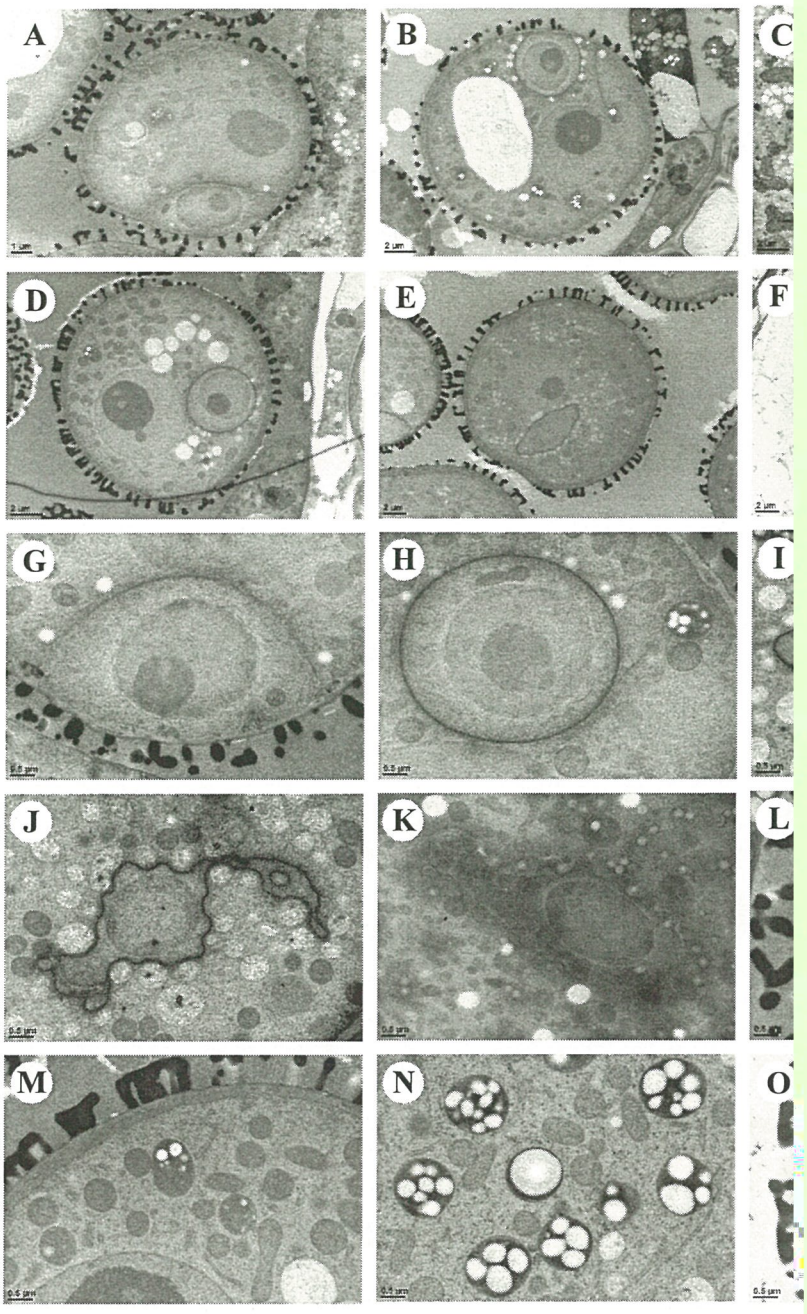

A-E Bicellular pollens in different developing stages. **F** Tricell
G-I Generative cells in different developing stages. **J** Two spe
K Sperm cell at anthesis. **L**, **M**, and **N** show cell content
developing stages **B**, **D**, and **E**, respectively. **O** Cell conten
anthesis.

Microstructural Changes of Cotyledon Cell in Soybean during Seeds Development

大豆子葉發育過程中的顯微結構變化[1]

WANG Xue-Dong（王學東），LI Ying，CUI Lin

The center of Life Science, Northeast Agricultural University（東北農業大學生命中心）, Harbin Heilongjiang 150030，P R China

本文采用光鏡組織化學、電鏡技術，結合相關生理指標測定，觀察了大豆栽培品種東農47子葉發育過程中，貯藏細胞的結構和形態變化，分析了三大類貯藏物質積累規律間的關係，旨在全面理解大豆子粒生長發育機理，為大豆種子發育生物學的研究補充有益資料。

1 質體及細胞結構變化

在光鏡和透射電鏡下觀察了子葉分化過程中結構和形態水準上的變化。開花後25-55天，細胞的體積逐漸增大。開花後65天，大豆進入成熟乾燥期，細胞體積開始變小。

開花後25天，細胞呈現不同程度的液泡化。在液泡的邊緣部分出現蛋白質沉積物，細胞質中有大量的內質網和線粒體，尤其在形成蛋白質團塊的液泡邊緣較為集中。質體直徑平均約3.0μm，含有4～5個澱粉粒，基粒片層排列整齊有序，並有嗜鐵顆粒存在。開花後45天，質體直徑平均可達5.6μm，內部充滿較大的澱粉粒，基粒片層被澱粉粒擠壓在質體的邊緣，片層數減少，質體開始表現出造粉體的特徵。蛋白質體周圍有粗面內質網分佈。開花後65天，細胞質內充滿了貯藏物質，蛋白質體周圍缺乏細胞器存在。質體平均直徑僅達2.3μm，其中僅含有1～2個澱粉粒。

2 貯藏物質積累

在透射電鏡下觀察了超薄切片中質體和澱粉粒數量及大小變化。開花後25～45天，澱粉粒在數量和體積上均呈上升趨勢。開花後45天時，澱粉粒的澱粉積累達到高峰。花後45天～65天時，澱粉含量呈下降趨勢。到花後65天時，此時處

基金專案：國家自然科學基金專案（No.30471093）

E-mail：wangxd5821@sohu.com

於生理成熟期，澱粉粒幾乎消失。可見，澱粉粒的積累經歷了從少到多，從小到大，最後又幾乎完全消失的變化過程。光鏡與電鏡下觀察到的變化趨勢是一致的。

在雙子葉植物中，貯藏蛋白主要在液泡中形成，積累在蛋白質體中。開花後25天，細胞質內開始有蛋白質積累，在液泡的周圍形成蛋白質沉積物。大液泡以出芽或在內部形成隔膜的形式變成小液泡，在小液泡內也有蛋白質沉積物出現。開花後35天，液泡內完全充滿蛋白質沉積物。隨著子葉的發育，其內的蛋白質體數量逐漸增多。花後65天，細胞內子葉貯藏細胞內通常含有多個大小不等的蛋白體，在細胞中分佈均勻。掃描電鏡下觀察了細胞內貯藏物質的積累狀況，開花後25天、45天和55天的蛋白質體平均直徑分別為1.68±0.40μm、3.71±0.89μm和5.65±0.95μm。

脂類化合物是植物種子中貯藏能量最常見的方式之一，儲存脂類的亞細胞器顆粒被稱為油體(oil body)或脂體(lipid body)。脂體通常在植物貯藏器官中積累，對大豆而言其主要積累在子葉內。在子葉發育過程，子葉貯藏細胞內的脂體成橢圓形或圓形，直徑在 0.1～1μm 之間，形態結構沒有明顯變化。花後 25 天，細胞質內的脂體較少，主要散佈在細胞壁的邊緣和液泡的周圍。花後 35~55 天，細胞質內的脂體數量增多，逐漸填充細胞質中的間隙。花後 65 天時，脂體垂直排列於蛋白體和細胞壁的周圍，排列緊密呈鑲嵌狀。細胞質中的其他脂體零散分佈於細胞中，在細胞壁附近脂體的密度大於細胞內部。同時還發現，少量脂體存在於蛋白質體中。

3 討論

3.1 大豆子葉中質體轉化與子葉發育的關係

種子作為一個庫器官，母體的其他器官供應其所需要的碳水化合物和其他的營養物質。這可能使種子自身的光合作用不具備必要性。然而，至少在不同的發育時期，許多物種的種子或者種子器官（種皮、胚乳、胚）都會變綠，並且變綠的過程總是和種子的生長以及貯藏物質的積累的過程相聯繫。在一些雙子葉植物中，特別是豆類和其他儲藏油類的種子中，主要貯藏器官胚在種子發育過程中變綠並有光合能力，例如大豆、蠶豆、擬南芥、油菜等。大豆子葉在開花後 25-45 天呈綠色，通過測定子葉內葉綠素含量高於 100μg/g。與鄭易之[6]通過螢光顯微鏡檢測大豆子葉細胞內有葉綠素的結論相一致。

在種子發育過程中，質體的發育和器官的分化是伴隨進行的。在子粒發育的中後期，子粒又經歷了與變綠相反的過程——褪綠。子粒褪綠是和葉綠素的減

少、光合器官的解體以及質體轉化成造粉體或前質體聯繫在一起的。對子葉葉綠素含量測定表明，在花後35天，葉綠素含量開始大幅下降，到花後65天生理成熟期時，子葉呈黃色，葉綠素含量很低。對大豆子葉超微結構研究表明，隨著子葉的發育，其內的質體逐漸向造粉體轉化，類囊體膜結構逐漸解體。葉綠素位於質體內的基粒類囊體膜上，基粒片層數減少導致了葉綠素含量降低。類囊體結構上的變化和葉綠素含量的測定相一致。隨著子葉內質體的轉化，質體功能的消失導致了胚胎發育遲緩，子葉由具光合活性的器官發育成貯藏器官。可見，子葉內質體轉化與子葉的發育有著密切的聯繫。

3.2 澱粉積累和蛋白質、脂類積累之間的關係

對於大多數植物，澱粉和蔗糖是光合作用的主要終產物，蔗糖是由源器官向庫器官轉移過程中主要的碳水化合物。在大豆子粒發育過程中，子粒為最終的庫，蔗糖源源不斷的向其輸入，以澱粉的形式在質體中逐漸積累。花後25～45天處於鼓粒期，植株光合作用較強，子粒中積累較多澱粉，在收穫前20天澱粉含量最高可達幹物質含量的10%～15%。在此過程中，蛋白質和脂肪逐漸合成，其合成需要大量能量。在此情況下，作為細胞主要能量和碳源貯藏庫的貯藏澱粉，就必然要加快水解，從而導致澱粉粒體積越來越小，在成熟乾燥階段澱粉含量降至種子幹重的1%～3%。透射電鏡下觀察到，正在減小的澱粉粒周圍常有蛋白質體、脂體和大量線粒體，表明線粒體正在為貯藏蛋白和脂類的合成提供能量。可見，澱粉粒體積減小很可能與細胞發育過程中能量需求有關。韓善華等在研究豌豆根瘤侵染細胞發育中造粉體形態結構變化時發現，隨著根瘤菌數量增多，細胞所需要的ATP能量隨之增多而澱粉粒的體積逐漸減小。他們認為細胞所需要的大量能量，可能來自貯藏澱粉的分解所釋放的能量。關於大豆子葉細胞中澱粉粒體積減小的原因，本實驗得出了與上述觀點相一致的結論。

參考文獻與圖略

Backscatter Electron Image (BEI) of Epidermal Silica Cells in Schizaeales

KAO, Tzu-Tong[1]; CHEN, Shiang-Jiuun[1]; CHIOU, Wen-liang[2]; and KUO-HUANG, Ling-Long（黃玲瓏）[1]

[1] *Department of Life Science（台灣大學 生命科學系）, Institute of Ecology and Evolutionary Biology, National Taiwan University, 1 Roosevelt Rd., Sec. 4, Taipei 106, Taiwan.*

[2] *Division of Forest Biology, Taiwan Forestry Research Institute, 53 Nan-Hai Rd., Taipei 100, Taiwan*

Order Schizaeales is one of the early leptosporangiate divergences in ferns with ca. 170 species in the world. This order contains three families, Lygodiaceae, Anemiaceae, and Schizaeaceae. Most of these species are tropical or southern warm-temperate species with strong climate, edaphic, and habitat preference [1]. Epidermal silica containing cells can be found in some species in this order, which might have systematically potential in this group [2].

In this study, fronds of five Schizaeales species: *Lygodium japonica*, *L. microphyllum*, *Schizaea dichotoma*, *S. digitala*, and *Anemia phyllitidis* were observed by a tabletop SEM (Hitachi, TM-1000). The tabletop SEM has a backscatter electron (BSE) detector, which can distinguish the silica containing epidermal cells from other ordinary epidermal cells by its heavier average atom mass. The samples were pretreated with a post cooling method [3] and direct observed with further fixation or coating. We found the silica containing epidermal cells are not present in the two *Lygodium* species (Fig A, D), but present in the *Schizaea* (Fig. B, E) and *Anemia* (Fig. C, F) species. In *Schizaea*, the silica containing cells present on all the epidermal cells on laminar while the cells only present on the veins of *A. phyllitidis*. They are long epidermal cells with a row of warty outgrowth, which is surprisingly similar to the epidermal silica cells in *Actinopteris radiata* (Pteridaceae, Fig. G, H). *Actinopteris* is unique taxa in which its classification position is uncertainly until Gastony treat it as a sister group of *Onychium* by *rbcL* sequence [4]. However, the silica cell morphology of *Actinopteris* is really distinct from other species in Pteridaceae even the *Onychium* species (Fig. I).

Our results agree with the previous studies that the epidermal silica cells are present in *Anemia* and *Schizaea*. However, this structure might not present in *Lygodium* and is not be found in other early leptosporangiate, so it might be a synapomorphic structure of the monophyletic group Anemiaceae and Schizaeaceae.

Further studies in silica body morphology might have potential usage in archeoecology because of the high habitat preference of species in this order.

References

1. Wikstrom, N., Kenrick, P., and Vogel, J. C. Rev. Pal. and Paly. 2002 (119) 35
2. Ribeiro, M. L. R. C., Santos, M. G., and Moraes, M. G. Rev. Bra. Bot. 2007 (30) 695
3. Tang, C. Y. Patent Pending, 2008
4. Gastony, G. J. and Johnson, W. P. Amer. Fern J. 2001 (91) 197

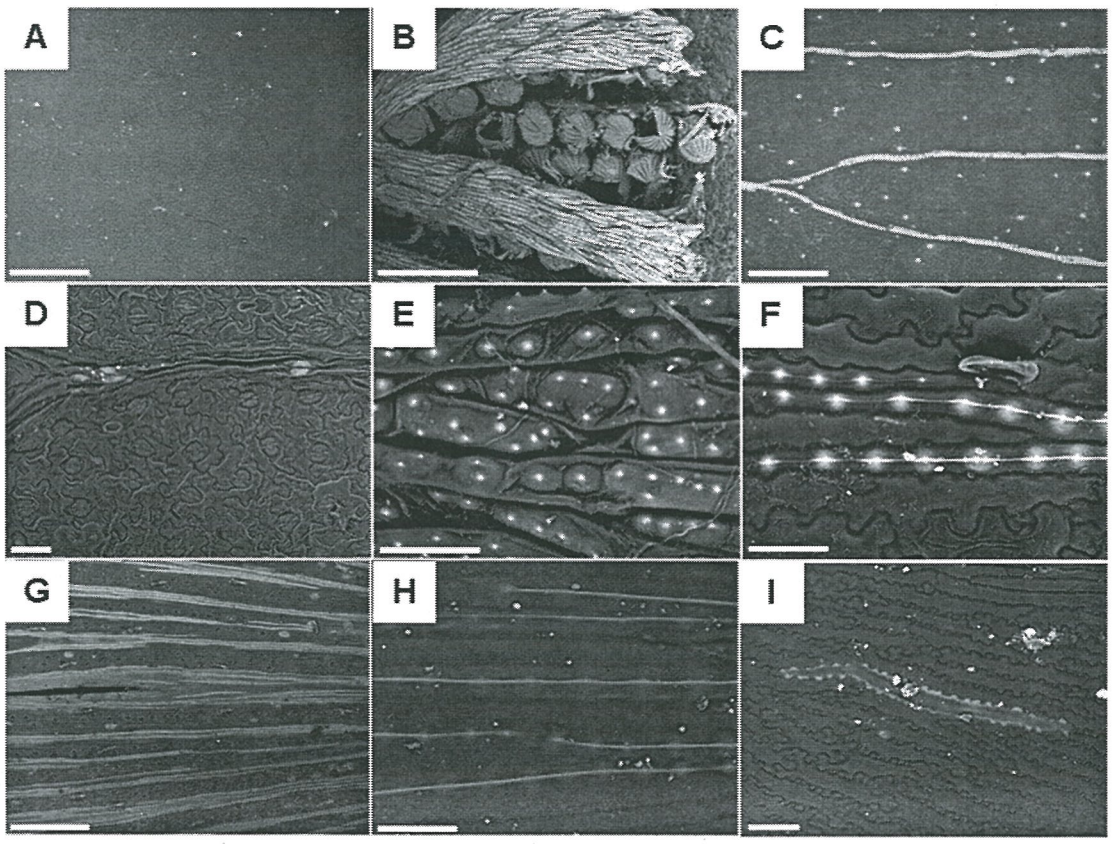

A-C Silica containing cell distribution in three different families in Schizaeales. They were not found in *Lygodium* species (A), but present on all the epidermal cells of *Schizaea* (B) and on the veins of *Anemia* (C); bars = 500μm. **D-F** Morphology of silica containing cells in Schizaeales. They are long epidermal cells with warty protrusions, but not be found in *Lygodium* (D); Bars = 50 μm. **G-H** The silica cells are similar to that of *Actinopteris radiate* (G and H), but not similar to that of *Onychium* (I). Bar = 500μm in **G** and = 50μm in **H** and **I**. A and D: *L. microphyllum*; B and E: *S. dichotoma*; C and F: *A. phyllitidis*; G and H: *Actinopteris radiate*; I: *Onychium japonica*

Microsporogenesis In *Taiwania cryptomerioides* (Tax

Su-Hwa Chen（陳淑華）

Department of Life Science（台灣大學生命科學系） & Institute of Ecology
National Taiwan University

Taiwania cryptomerioides (Taxodiaceae) is an endemic cypr
Like *Sequia, Metasequia* and *Ginkgo*, this species has been ide
rare plant in the world. It is distributed mainly in the central ric
the altitude 1800 and 2600 m. In the nature, sterile cones occurre
aim of this study is to elucidate the ontogenic processes of ferti
Sample collected from Hsitou Experimental Forest and Yeou
Orchard, National Taiwan University are observed, using LM, SE

The male strobili appeared in August. However, the sporog
recognizable first after October (Fig. 2A). The microspore mo
occurred near the end of December, while the meiosis in late Febr
the majority of male strobili contained separated microspores
pollen grains matured and were shed from the microsporangia b
(Fig. 1C).

The fertile pollen mother cells were filled with abundant vesi
first meiosis, an organelle band consisting of amyloplasts, vesic
was formed in the equatorial zone of dyad. Subsequently, like ma
the tetrad microspores were separated by the callose wall towar
(Fig. 3B). After the degradation of the callose wall, the fre
contained a large number of vesicles and vacuoles and
non-homogenously thickened intine and a thin synthesizing e
microspores divided into a large tube cell and a small ant
two-celled pollen grains contained abundant starch grains and
reduced ectexine, Ubish bodies, lamellate endexine and thick in
in the ultrastructures between fertile and sterile strobili were c
strobilus can be distinguished from the fertile one at early develop

References

Chen, S.-H. *et al*. Protoplasma 2006 (228) 137-144.

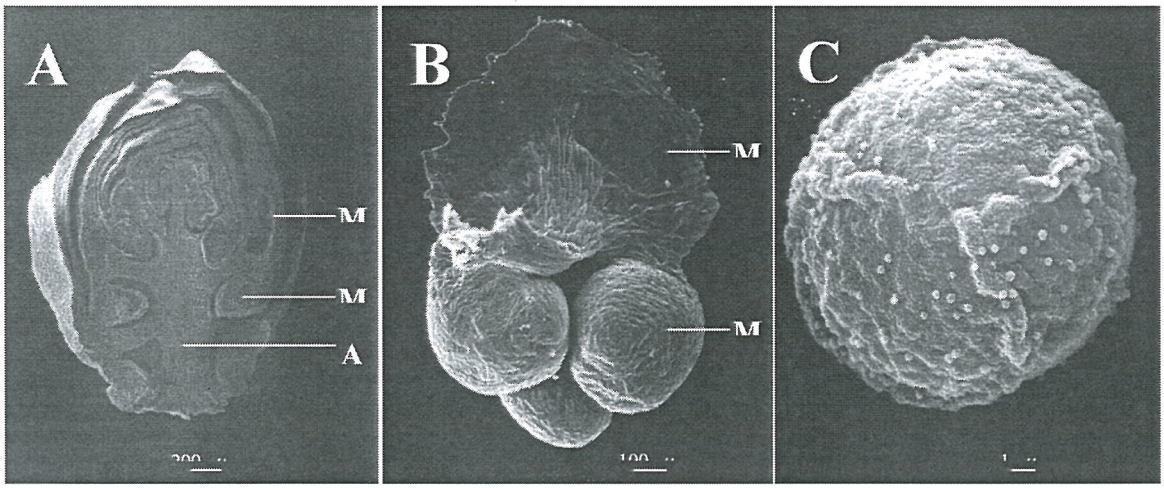

Fig. 1. A. LS of strobilus (SEM). A = axis, MG = microsporangium, MP = microsporophyll. B. A microsporophyll with three microsporangia (SEM). C. A mature pollen grain (SEM).

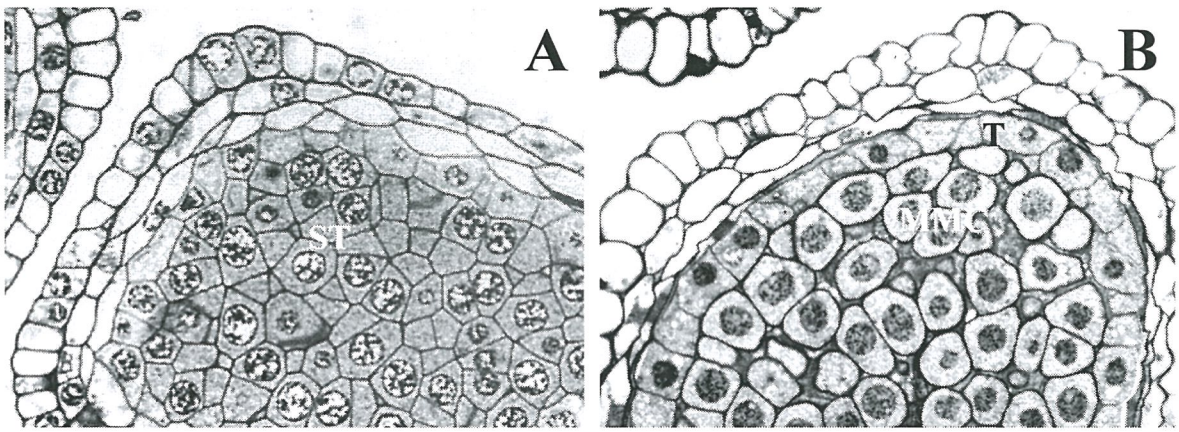

Fig. 2. A. CS of a microsporangium with sporogeneous tissue (ST) (LM). B. A part of microsporangium with early microspore mother cells (MMC) and tapetum (T) (LM).

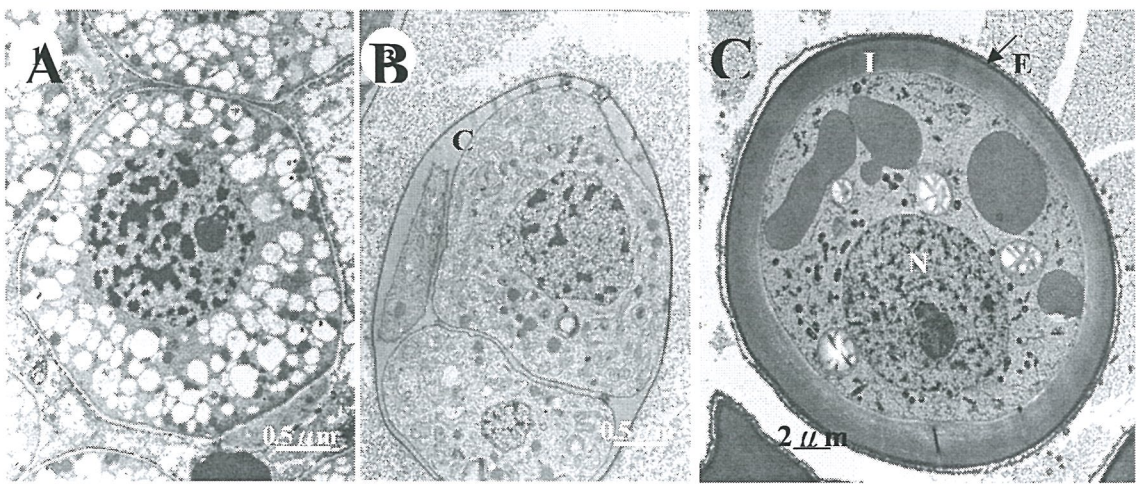

Fig. 3. A. A microspore mother cell with abundant vesicles (TEM). B. Three tetrad spores separated by callose (C). C. A microspore with thin exine (E) and thick intine (I), Nucleus (N) (TEM).

Two New Species of *Ramicandelaber* (Kickxellaceae, Kickxellales): with a Comparison to *Linderina* and *Coemansia*

CHUANG, Shu-Cheng [1], HO, Hsiao-Man（何小曼）[2] & BENNY, Gerald L. [3]

1. Agricultural Biotechnology Research Center, Academia Sinica

2. Department of Science Education, National Taipei University of Education（台北教育大學自然科學教育學系）, No. 134, Sect. 2, He-Ping E. Rd., Taipei, 10671, Taiwan.

3. Department of Plant Pathology, 1453 Fifield Hall, P.O. Box 110680, University of Florida, Gainesville, Florida 32611-0680, USA.

Kickxellales Kreisel ex R.K. Benj. is a small group of Zygomycetes composed of one family that included 12 genera and 32 species. Most members of this order are saprobes and usually isolated from mammal feces or soil, and are rarely found. The order is characterized by the vegetative hyphae and sporangiophores possess septa with median biconvex or biumbonate plug. Special fertile branches arise from sporangiophore and produce septate or aseptate branchlets (sporocladia) bearing subspherical or global sporogenous cells (pseudophialides). Asexual reproduction is by means of spore formed in unispored sporangiola borne on the apex of sporogenous cell and often immersed in liquid at maturity. Sexual reproduction is by means of nearly globose zygospore. The genera of Kickxellales can be divided into two groups based on the character of sporocladium. One is septate-sporocladium group, the other is aseptate-sporocladium group.

During a long term survey of Taiwan Kickxellalen fungi, two new *Ramicandelaber* species (aseptate–sporocladium) were isolated which are *R. fabisporus* Chuang et al. (tentative name) and *R. taiwanensis* Chuang et al. (tentative name). They all have hyphal septa with median plugs and special branchlets (sporocladia) bearing subspherical or hemispherical sporogenous cells (pseudophialide). The distinguished character of this genus is that only a single pseudophialide formed on a sporocladial element before senescence. *R. fabisporus* sp. nov. is distinguished by the bean-shaped spore and *R. taiwanesis* sp. nov. is distinguished by the smaller fusiform spore. The description of morphological characters of these two new species and a comparision of *Ramicandelaber* with *Coemansia* and *Linderina* are also going to be presented.

References

Kurihara, Y., Y. Degawa, and S. Tokumasu. 2004. Mycol Res 108:1143-1152

Linder, D. H. 1943.Farlowia 1:49-77.

Ogawa, Y., S. Hayashi, Y. Degawa and Y. Yaguchi. 2001. Mycoscience 42: 193-199.

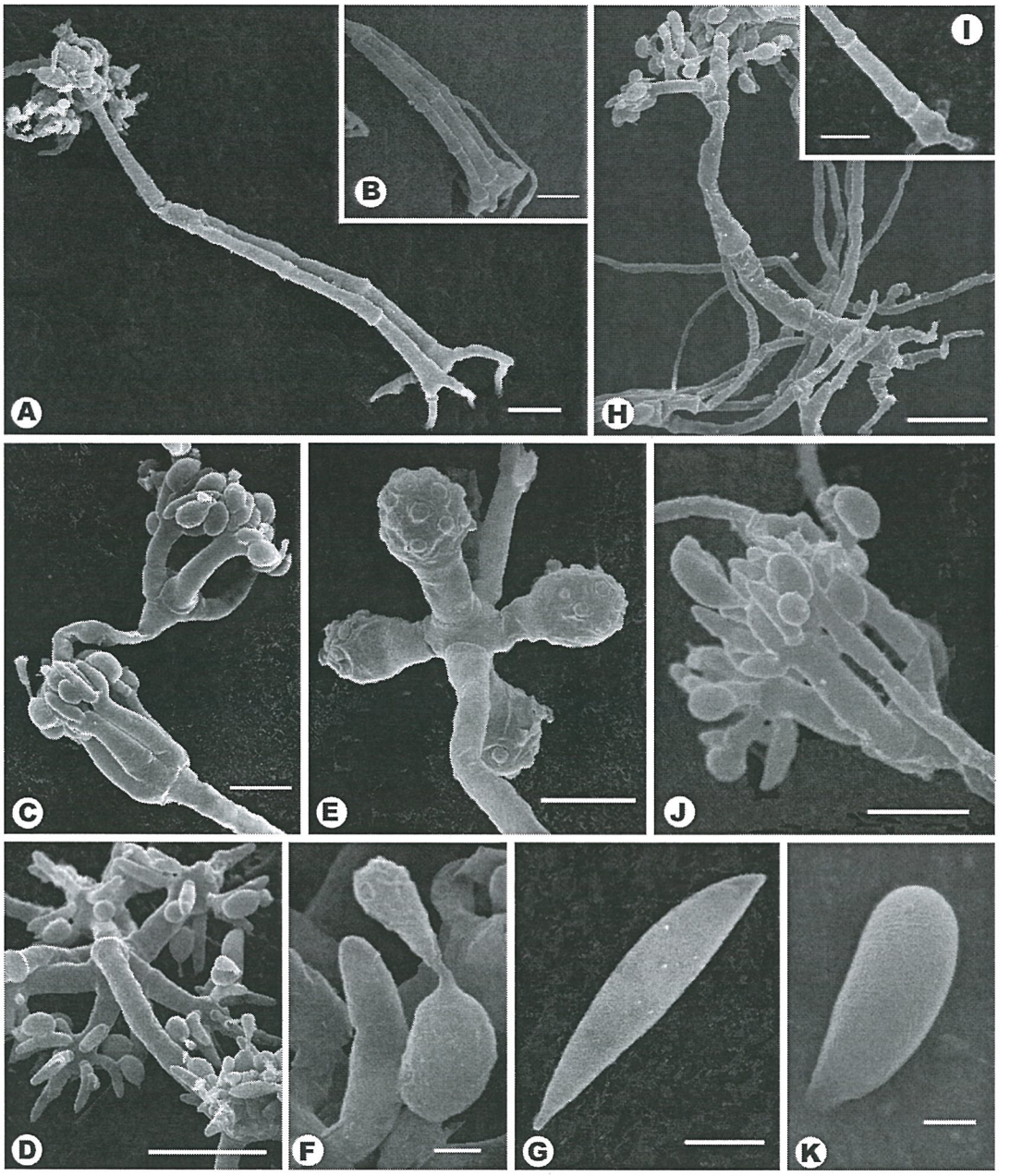

Ramicandelaber taiwanensis. A-G, SEM. A. Habitate of sporangiophore. Bar = 10μm. B. Lateral branches of sporangiophore. Bar = 10μm. C. Two verticillate fertile branches arising from sporangiophore. Bar = 5μm. D. Mature verticillate fertile branches swelling apically and bearing sporocladia and pseudophialides. Bar =10μm. E. Old swollen fertile branches leaving prominent scars after sporocladia falling. Bar =5μm. F. Aseptate sporocladium pleurogenously bearing single pseudophialide forming unispore acrogenously. Bar =1μm. G. Fusiform spore. Bar = 3μm.

Ramicandelaber fabisporus. H-K, SEM. H. Habitate of sporangiophore. Bar = 10 μm. I. Simple sporangiophore. Bar = 10 μm. J. Mature verticillate fertile branches bearing sporocladia, pseudophialides and spores. Bar = 5μm. K. Fabiform spore. Bar = 1μm.

Epidermal Chloroplasts in Deep Shade Plants of Tropical Rain Forests

SHEUE, Chiou-Rong（許秋容）[1]; PAO, Shung-Hung[1]; SARAFIS, Vassilios[2] and PENG, Ching-I[3]

[1] *Department of Biological Resources, National Chiayi University（嘉義大學生物資源學系）, 300 Syufu Rd., Chiayi 600, Taiwan.*

[2] *Institute of Physical Biology, University of South Bohemia, Zamek 136, Nove Hrady, CZ 37333, Czech Republic.*

[3] *Biodiversity Research Center, Academia Sinica, Taipei, Taiwan.*

Chloroplasts of green plants are commonly found in leaf mesophyll tissues, specifically in palisade cells and spongy cells. Twenty-two species of deep shade plants from tropical rain forests were studied for chloroplast features in epidermis with light microscopy (LM), electron microscopy (EM) and confocal scanning light microscopy (CSLM). Chloroplasts were found in the leaf epidermis of four (*Cyathodium*, *Cephalomanes*, *Selaginella* and *Begonia*) out of eight genera examined. Leaf structures are simple, with two-layered and one-layered epidermis respectively (excepting vein regions) in cave liverworts *Cyathodium* and filmy fern *Cephalomanes*. Chloroplasts with large grana and numerous stackings of thylakoid membranes per granum were observed in them. Cave liverworts has much fewer chloroplasts per cell than the filmy fern. In the three species of *Selaginella* we studied, one or two giant chloroplasts (bizonoplasts) were observed in each dorsal epidermal cell and a chain of bead-like chloroplasts appeared in each ventral epidermal cell of microphylls. Bizonoplast is a giant cup-shaped chloroplast, with a dimorphic ultrastructure: the upper zone is represented by layers of 2–4 stacked paralleling thylakoid membranes each separated by 60-90 nm, while the lower zone contains both unstacked stromal thylakoids and thylakoid lamellae stacked in normal grana structure.This unique giant chloroplast, was previously known only in the dorsal epidermis of the microphylls in *Selaginella erythropus*. Of the four genera with chloroplasts in leaf epidermis, *Begonia* is the only that has chloroplasts in the dorsal epidermis. It is noteworthy that these novel chloroplasts are much smaller than the normal counterparts in the mesophyll. Two types of such chloroplasts can be recognized based on ultrastructural features: small chloroplasts with normal structures of grana and stroma thylakoid membranes (in 6 species), and iridoplasts with 2–4 stacked membrane groups parallel to each other without grana (in 7 species). Ecological adaptations and evolutionary implications of these unusual and novel epidermal chloroplasts merit further exploration.

References

1. LEE, D. W. 2001. Malayan Nature Journal 55: 117–131.
2. Sheue C. R., Sarafis V., Kiew R., Liu H. Y., Salino A., Kuo-Huang L. L., Yang Y
   Tsai C. C., Lin C. H., Yong J. W. H. and Ku M. S. B. 2007. American Journal of
   Botany 94: 1922-1929.

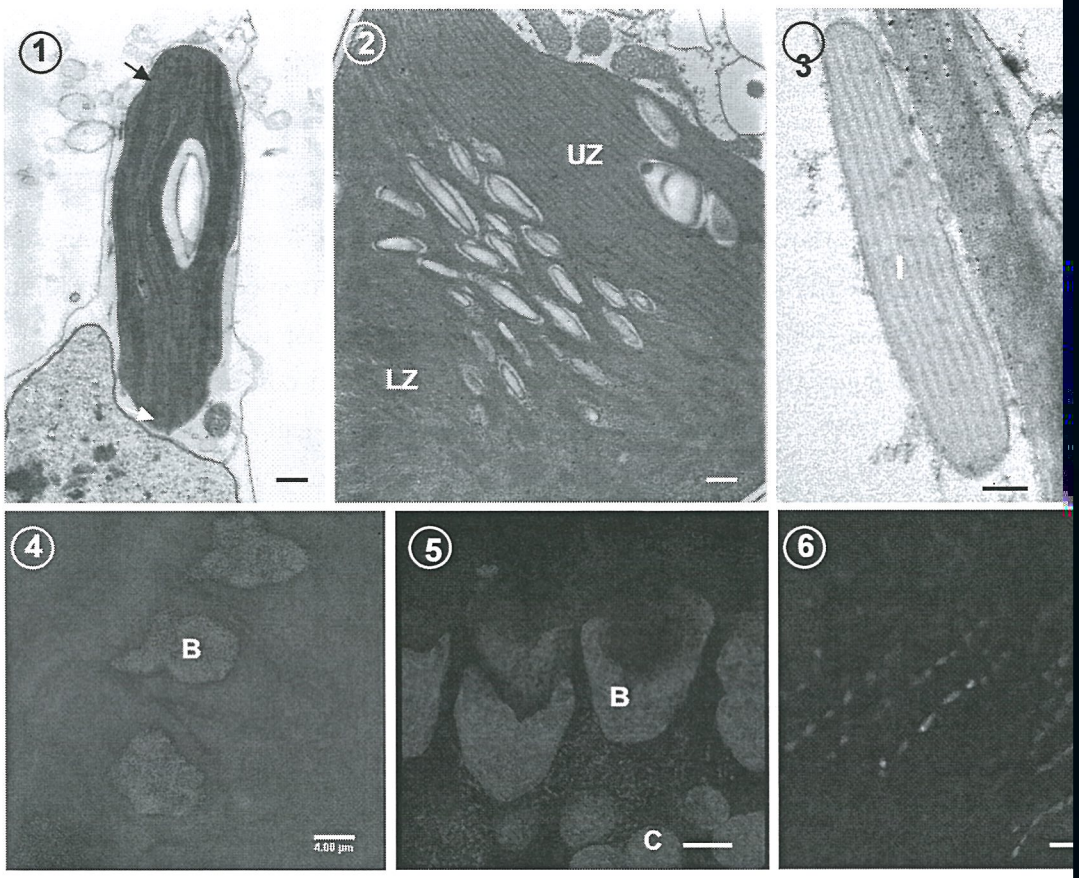

Fig. 1. Epidermal chloroplast (arrow) of *Cyathodium*. Fig. 2. TEM view o
bizonoplast of *Selaginella erythropus* in the dorsal epidermis of a microphyll show
the upper zone (UZ), with groups of paralleling thylakoid membranes, and the lo
zone (LZ), with normal chloroplast structures comprising stroma thylakoids and gr
Fig. 3. TEM view of an iridoplast (I) of *Begonia petadifida.* Fig. 4. CSLM view
bizonoplasts (B). Fig. 5. CSLM view of bizonoplasts in *S. erythropus*, show
3D-like deconvoluted image (B) with mesophyll chloroplasts (C). Fig. 6. CS
view of chains of bead-like chloroplasts in the ventral epidermis of *S. erythro*
Bars = 500 nm in Fig. 1-3; 4 µm in Fig. 4; 10 µm in Fig. 5; 25 µm in Fig. 6.

Effect of Thermochemical Pretreatment on the Cell Wall Structure of Rice Straw

CHEN, Shiang-Jiuun（陳香君）[1,2]; LIN, Hsien-Yuan[1]; CHEN, Wen-Hwa[3] and KUO-HUANG, Ling-Long[1,2]

[1] *Department of Life Science（台灣大學生命科學系）, Institute of Ecology and Evolutionary Biology, College of Life Science, National Taiwan University, 1 Roosevelt Rd., Sec. 4, Taipei 106, Taiwan.*

[2] *TechComm-5, Bio-Image Tool, College of Life Science, National Taiwan University, 1 Roosevelt Rd., Sec. 4, Taipei 106, Taiwan.*

[3] *Cellulosic Ethanol Program, Chemical Analysis Division, Institute of Nuclear Energy Research, PO Box 3-19, Longtan 325, Taiwan*

Rice straw is a potential raw material for cost-effective cellulosic ethanol. As opposed to synthetic chemicals and fossil fuels, these polymers are readily renewable, inexpensive, and environmentally benign (Lucia, 2008). The rice straw is a heterogeneous sample that consists of stems (stalk) and leaf blades. Both of these two organs of plant body contain dermal, fundamental, and vascular tissues. The upper epidermis of leaf contains five cell types: epidermal cells with thick epicuticular wax and papillae projections, guard cells and subsidiary cells to form the stomata, silica cells and rigid trichomes (Fig. 1,2).

The mature xylem of vascular tissue is a complex tissue with different cell types, including parenchyma, tracheary elements and fiber. The recalcitrant nature of lignified- secondary wall in the latter two types makes it unsuitable for cellulosic ethanol processing. We investigated the microscopic structure of cell wall in rice straw following different pretreatment (Yu, et al., 2009). Under natural dried condition, the lower epidermis of leaf shows intact protective layer on the cell wall surface (Fig. 3), however, the sample appears broken protective layer after pretreated by dried and dilute acid (Fig. 4), and exhibits more broken pieces on the wall surface following compressed and dilute acid treatment (Fig. 5). It has been shown that the deposition of "lignin" droplets could be observed in dilute acid-treated maize (Selig, et al., 2007); the present studies shows the bubble-like droplets of lignin appears to emerge from the cell wall surface (Fig.6) of rice straw heated with 180 ^{0}C. Moreover, spherical "lignin" droplets even deposited on the surface of wall when rice straw were heated with 200 ^{0}C (Fig. 7) and 220 ^{0}C (Fig. 8).

References

Lucia, L.A., BioResources. 2008, 3 (4) 981.

Selig, M.J., Viamajala, S., Decker, S.R., Tucker, M.P., Himmel, M.E. and Vinznt, T.B. Biotechnol. Prog. 2007, (23) 1333.

Yu, C.T., Chen, W.H., Men, L.C. and Hwang, W.S. Industrial Crops and Products. 2009, (29)308.

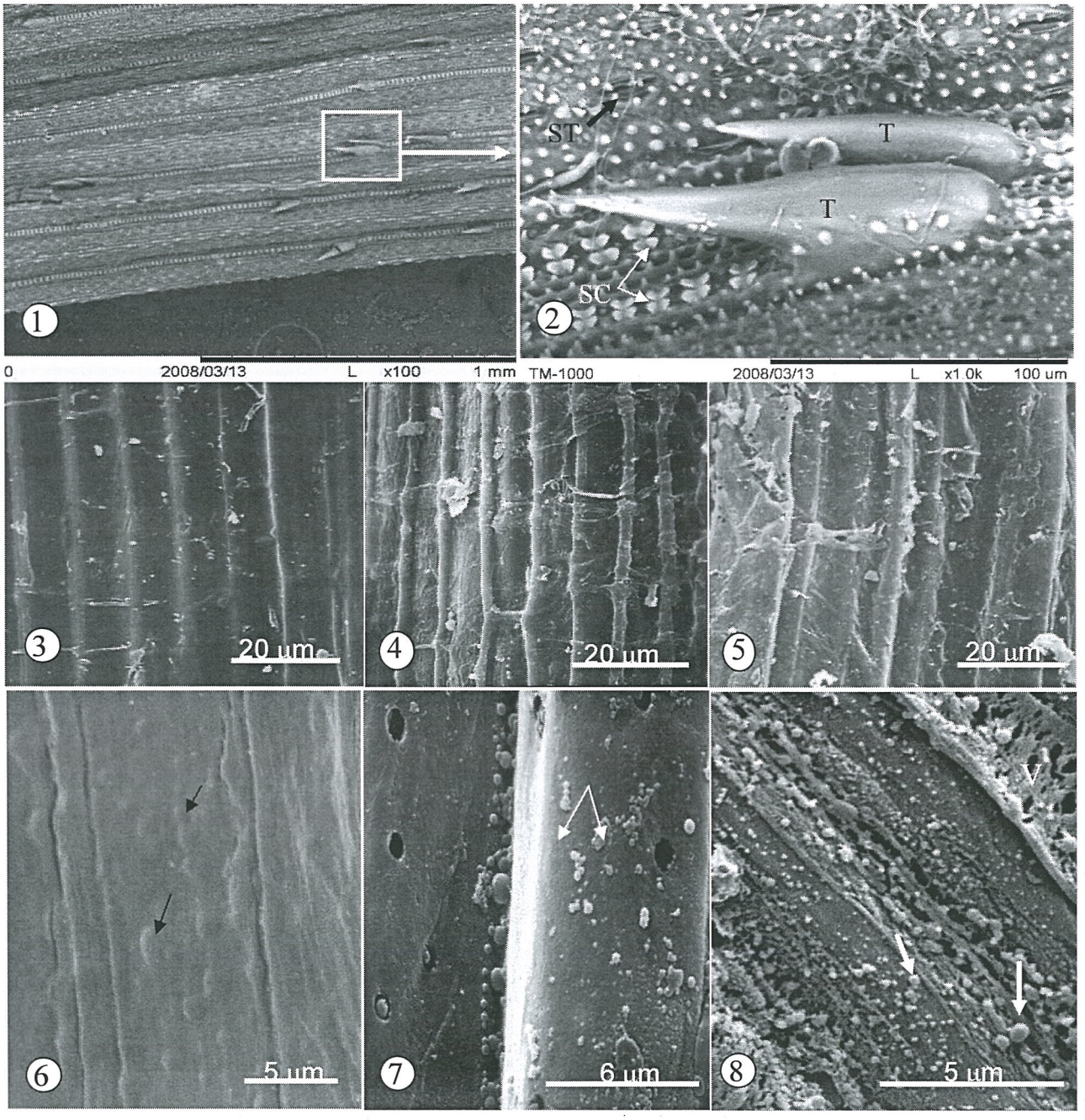

Fig. 1-3. Samples under natural dried condition. Fig.1. Upper epidermis of rice leaf; Fig.2. A SEM image showing the epidermal tissue including stoma, silica cells (SC) and two trichomes (T); Fig.3. Lower epidermis. Fig. 4. Dried and dilute acid treated, showing broken protective layer on the wall surface; Fig. 5. Compressed and dilute acid treated, showing more broken pieces of protective layer on the wall surface; Fig. 6. 180℃ boiling water treated, showing "lignin" droplets emerging from the cell wall surface (arrows). Fig. 7. 200℃ running water treated, and Fig. 8. 220℃ running water treated, showing spherical lignin droplets (arrows) on the cell wall surface.

Development and Application of Single-Axis Tilt Electron Tomography for the Structure of FePt@Fe_3O_4 Core/Shell Nanocubes

Chun-Ting Wang*(王鈞霆), Ji-Jung Kai* , Fu-Rong Chen*

Center for Electron Microscopy, Department of ESS, National Tsing-Hua University, HsinChu County, Taiwan(R.O.C.)

FePt nanoparticles containing a near-equal atomic percentage Fe and Pt are an important class of magnetic nanomaterials. At room temperature, FePt has chemically disordered face-centered cubic (FCC) structure and soft magnetic property. Thermal annealing is needed to transform the FCC structure to the chemically ordered face-centered tetragonal (FCT) structure and obtain hard magnetic property. Due to the high magnetrocrystalline anisotropy of ordered FCT FePt, it is popular for magnetic memory devices.

The nanocomposites composed of magnetically hard and soft phases are developed for permanent magnetic applications. The FePt and Fe_3O_4 particles are incorporated as nano-scale building blocks into binary assemblies and the binary assemblies can be converted into FePt-Fe_3Pt nanocomposite by annealing, where FePt is a magnetically hard phase and Fe_3Pt is a soft phase. The exchange-coupled FePt-Fe_3Pt nanocomposite have larger energy product than nonexchange-coupled isotropic FePt by over 50 per cent **[1]**.

The FePt@Fe3O4 core/shell structure nanoparticle is developed by Advanced Storage Thin Film Laboratory, National Tsing Hua University. From the TEM image in Fig.1, the real shape of Fe_3O_4 particles in three dimension can not be directly revealed, and can be one of the proposed shapes given in the right hand side of Fig.1.

The round core and cubic shell structure of FePt@Fe_3O_4 is confirmed with TEM tomography technique. Electron tomography on FePt@Fe3O4 nanoparticle wascarried out in a JEOL JEM2010F equipped with a single tilt holder with tilting range of $\pm 60^0$. Fig.2 shows a TEM image of FePt@Fe3O4 nanoparticles at zero tilt. And Fig.3 depicts the reconstructed electron tomography from three FePt@Fe3O4 nanopcubes shown in Fig.2. The Fig.4 is a transparent view of Fig.3 that shows FePt nanoparticles are indeed encapsulated in side the Fe_3O_4 nanocubes as core instead of sticking outside of surface.

We can obtain any structure information from TEM tomography to improve synthesis method, and expect this new core/shell structure can be promising for advanced applications including data storage and biomedicine.

Reference:

[1] Shouheng Sun Adv.Mater.2006, 18 393-403

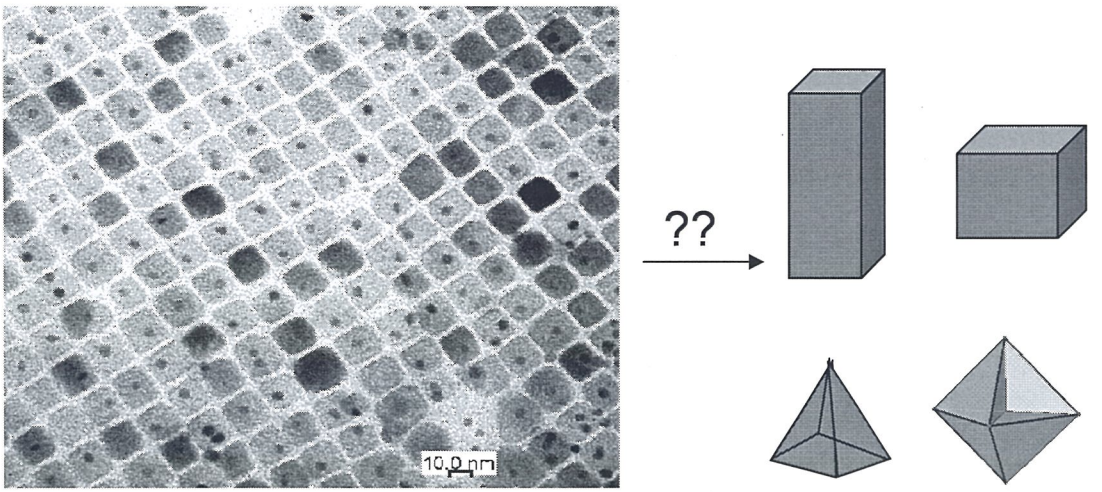

Fig.1 TEM image of a square array of $FePt@Fe_3O_4$

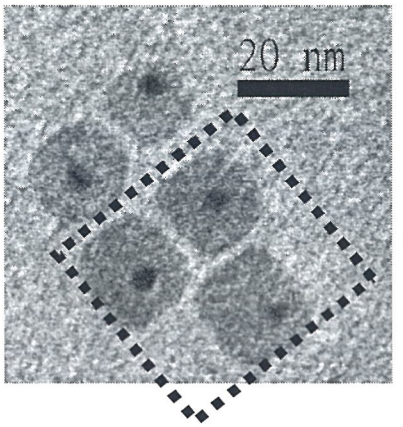

Fig.2 TEM image of $FePt@Fe_3O_4$ particles at zero tilt.

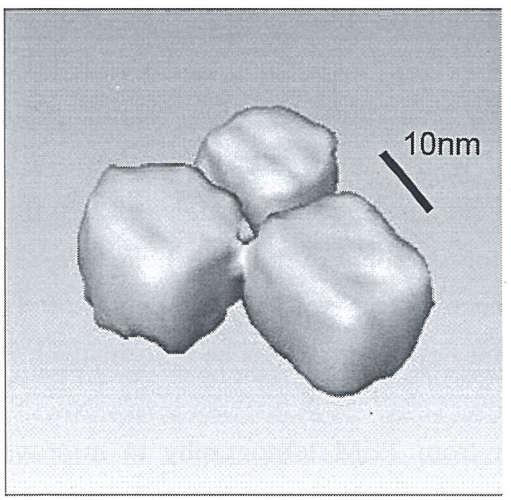

Fig.3 The images depicts the reconstructed TEM tomography from three $FePt@Fe_3O_4$ nanocubes shown in Fig.2

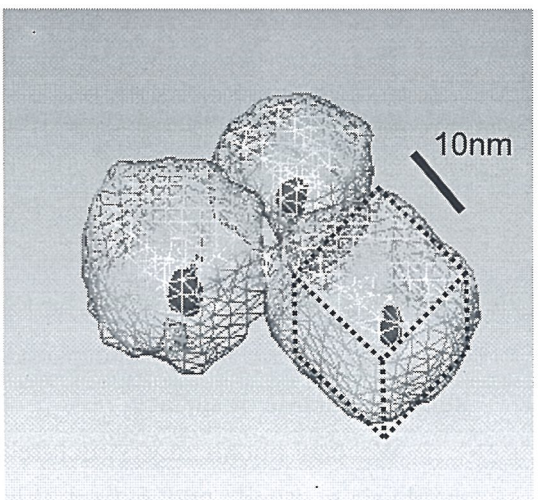

Fig.4 The transparent view of Fig.3.

Excitations of Surface Polaritons in Nano-Materials by STEM-EELS

Chien-Ting Wu (吳建霆)[1], Chun-Wei Chen (陳俊維)[1], Chuan-Pu Liu (劉全璞)[2], Kuei-Hsien Chen (陳貴賢)[3], Li-Chyong Chen (陳麗瓊)[4], Ming-Wen Chu (朱明文)[4], Cheng Hsuan Chen (陳正弦)[4]

[1] *Dept. of Materials Science and Engineering, National Taiwan University, Taipei, Taiwan*

[2] *Dept. of Materials Science and Engineering, National Cheng Kung University, Tainan, Taiwan*

[3] *Institute of Atomic and Molecular Sciences, Academia Sinica, Taipei, Taiwan*

[4] *Center for Condensed Matter Sciences, National Taiwan University, Taiwan*

Bulk and surface excitations of triangular GaN and rectangular ZnO nanorods were investigated by the conjugation of scanning transmission electron microscopy (STEM) and electron energy-loss spectroscopy (EELS), STEM-EELS. With the 0.2-nm electron probe in STEM-EELS, the excitation of surface polaritons can be thoroughly explored by brining the atomic-scale probe near the surface of nanomaterials in grazing incidence. Modern nanomaterials thus provide new opportunities for studying surface excitations. The STEM-EELS studies show that the predominant excitations at ~19 and ~14.5 eV arise from the respective resonances of bulk and surface plasmons (SP) of GaN. Furthermore, the excitations at ~18.9 and ~15.8 eV are identified respectively as bulk and surface plasmons of ZnO. In addition, the SP peak intensity was found to decay exponentially with the increase in impact parameters, e.g., from 0 to 20 nm away from the planar surface. Unexpectedly, we observed several peaks with the characteristics of surface exciton polaritons **[1]** (SEP) occurring near interband transitions in the spectral regime below the SP. The positions of these peaks correlate well with peaks in the imaginary part of the complex dielectric function of GaN and ZnO, signifying their excitonic characters **[2]**. We also note that the wave fields of these SEP-like excitations are most prominent outside the nanorod surface, while their wave-field decays exponentially at a much slower rate compared to SPs.

References

1. Fuzi Yang, J. R. Sambles, and G. W. Bradberry, PRL, **64**, 559–562 (1990).
2. Acknowledgement: This work was financially supported by the National Science Council, Taiwan.

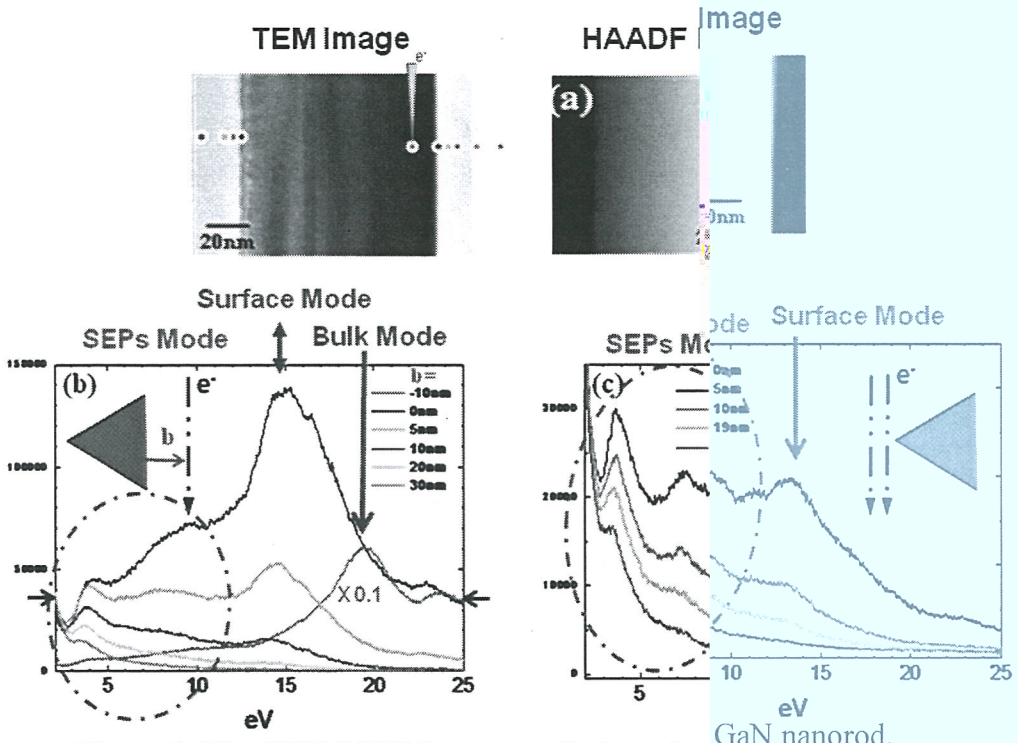

Figure 1. The STEM-EELS spectra of triangular GaN nanorod.

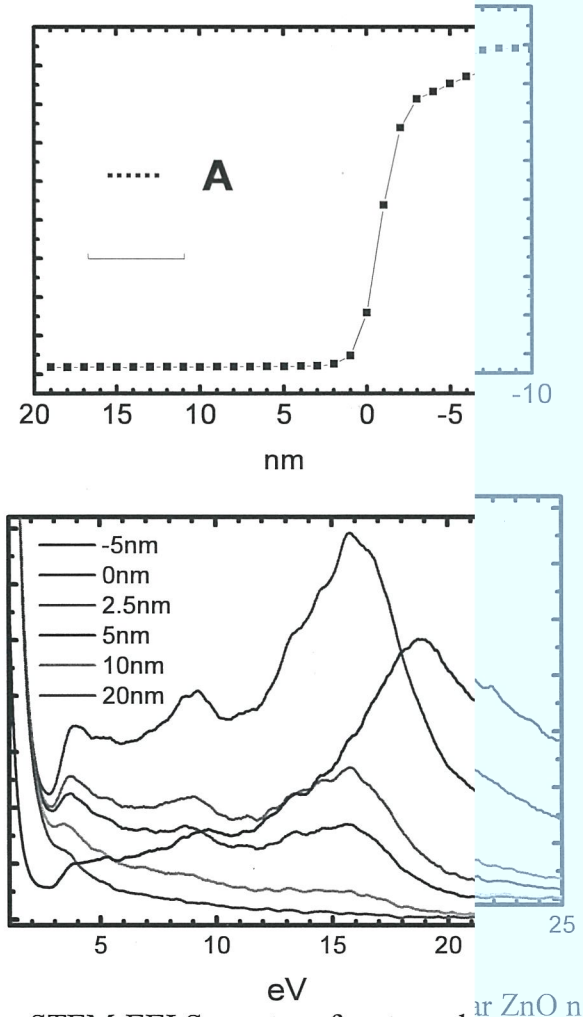

Figure 2. The STEM-EELS spectra of rectangular ZnO nanorod.

Transmission Electron Microscopy Study of Structural Phase Transition in $Lu_2Ir_3Si_5$

M. H. Lee (李明浩)[1,2] , C. M. Tseng (曾傳銘)[1], M.-W. Chu (朱明文) [1] and C. H. Chen (陳正弦)[1,2]

[1]*Center for Condensed Matter Sciences, National Taiwan University, Taipei 106, Taiwan*

[2]*Department of Physics, National Taiwan University, Taipei 106, Taiwan*

The conventional, macroscopic characterization of the rare-earth transition-metal silicide, $Lu_2Ir_3Si_5$ (orthorhombic), by electrical resistivity (ρ), Seebeck coefficient (*s*), and thermal conductivity (κ) has established the existence of a sharp structural phase transition at 130~170K in this material.**[1,2]** The corresponding microstructural details have, however, never been reported in the literature. Using electron diffraction at low temperatures, we revisited this structural phase transition and demonstrated its prominent first-order characteristic, exhibiting a large thermal hysteresis (164 K upon warming, 124 K upon cooling) and in good agreement with Ref. 2. The onset of the phase transition is characterized by the formation of incommensurate supelattice reflections along $\vec{q} = (\bar{1}21)$ and $(12\bar{1})$ of the primitive cell. Dark-field imaging employing the superlattice reflections reveals intriguing 90°-domain configurations, displaying domain contrasts perpendicular to one and another with remarkably wavy domain boundaries, further complicated by the presence of crystallographic twins. The exploration for correlation between the domain structures and the aforementioned first-order characteristic is discussed. A further examination of the extinction condition below the phase transition temperature is currently in progress.

References

1. Y. Singh, D. Pal, S. Ramakrishnan, A. M. Awasthi, and S. K. Malik, Phys. Rev. B 71, 045109 (2005).
2. Y. K. Kuo K. M. Sivakumar, T. H. Su and C. S. Lue, Phys. Rev. B 74, 045115 (2006).

This project is supported by the National Science Council of Taiwan (NSC 94-2752-M-002-006-PAE).

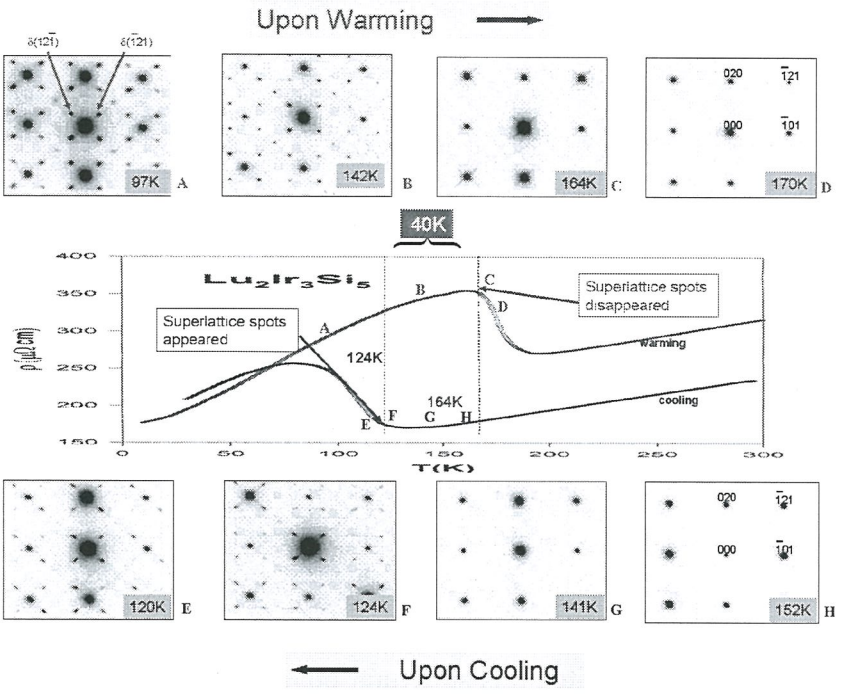
Upon Warming
δ(12̄1)
δ(1̄21)
97K
A
142K
B
164K
C
020
12̄1
000
101̄
170K
D
40K
Lu2Ir3Si5
Superlattice spots appeared
Superlattice spots disappeared
124K
164K
Warming
cooling
ρ(μΩ cm)
T(K)
120K
E
124K
F
141K
G
152K
H
Upon Cooling

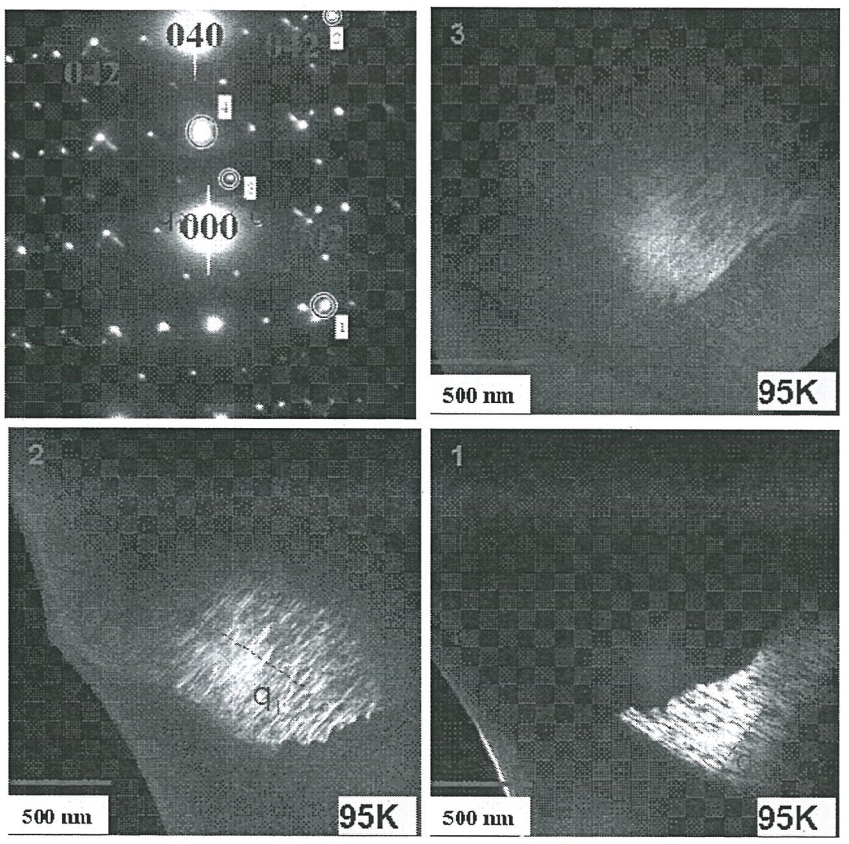
040
000
3
500 nm
95K
2
500 nm
95K
1
500 nm
95K

真空蒸鍍金汞薄膜及其穿透式電子顯微鏡檢測

Lin Yan-Fu (林彥甫)，Hsieh Peng-Han (謝鵬翰)，Hsu Tung (徐統)

Department of Materials Science and Engineering , National Tsing Hua Univerity, Hsinchu,Taiwan

金常應用在電子零件的開關及真空系統中。汞由於低熔點、可導電的特性，可做為液態電極，並應用於微機電系統。微量汞沾附在金片上做為電極，使奈米碳管與汞接觸形成通路，可進行奈米尺度操控及臨場量測**[1]**，但逸散或殘留在真空腔中的汞蒸氣可能造成汙染及真空計讀數不正常。

汞和金、銀、銅、鋅等金屬互溶形成的合金統稱為汞齊。以往的研究使用掃描式電子顯微鏡、掃描探針顯微鏡研究金汞齊**[2]**，檢測微觀形貌；使用穿透式電子顯微鏡的研究除觀察到金汞齊的繞射環之外**[3]**，並分析常溫下形成的金汞薄膜，由繞射圖形判斷含有 Au_3Hg 結構**[4]**。

本實驗以金與汞之間的反應為探討主題，將金線與鍍金鎢線以水浴法與汞反應形成灰白色合金，但金與汞的鍵結並不強，只需加熱便可讓兩者再次分離，因此在不同壓力下對金上的汞通電或加熱，將汞蒸鍍到含有金膜的直徑 3 mm 銅網上，再使用穿透式電子顯微鏡 (JEOL JEM-2100F, 200kV) 進行微結構及選區繞射分析，以研究在真空中蒸鍍汞之可行性。

在電子顯微鏡明場像下，汞沒有在金的表面上形成連續而均勻的吸附層，部份金膜與汞反應形成暗色島狀合金(圖 1)。選區繞射圖除了出現金的面心立方環，也出現其他斑點(圖 2)。量測繞射環半徑並比較斑點的位置，判定島狀合金中存在有 Au_3Hg 結構。由於 Au_3Hg 在常壓及真空下皆為穩定狀態，故可以金儲存汞做為蒸鍍源，應用於微小尺度及真空中，直接在電子顯微鏡的樣品台上蒸鍍汞。

參考文獻

1. Z. L. Wang, P. Poncharal, W. A. de Heer, *Pure and Applied Chemistry* **2000**, *72*, 209.
2. R. Nowakowski, T. Kobiela, Z. Wolfram, R. Dus, *Applied Surface Science* **1997**, *115*, 217.
3. A. E. Aylmer, G. I. Finch, S. Fordham, *Trans. Faraday Soc.* **1936**, *32*, 864.
4. T. Hsu, "Transmission Electron Microscopy Study of Gold/Mercury Amalgam," in *The 9th Asia-Pacific Microscopy Conference*, Jeju, Korea, **2008**, 574.
5. 感謝中央研究院物理研究所張嘉升研究員及奈米核心設施提供協助。

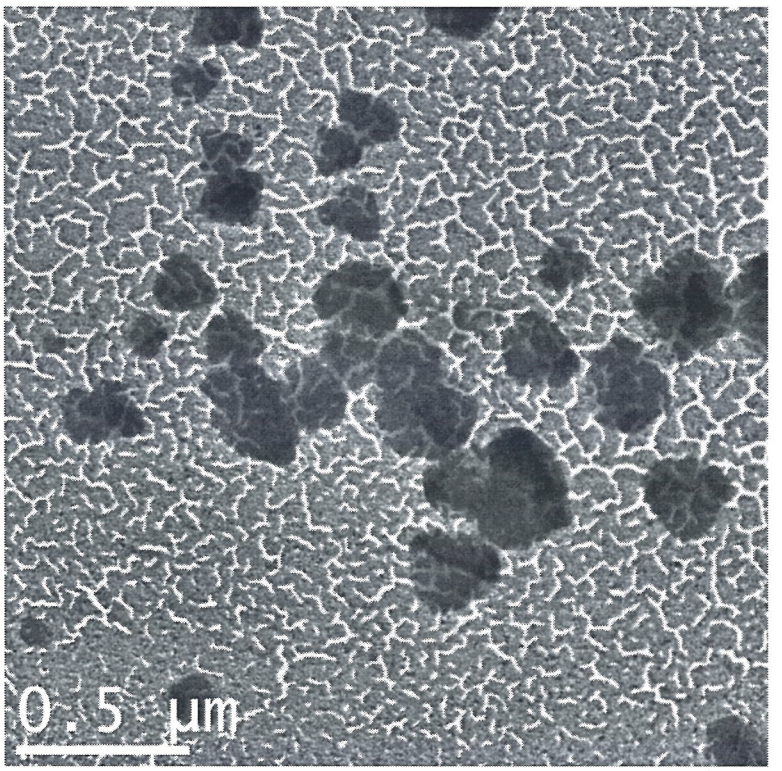

圖 1 蒸鍍汞後的金膜的明場電子顯微像。暗色區域為島狀金汞齊。

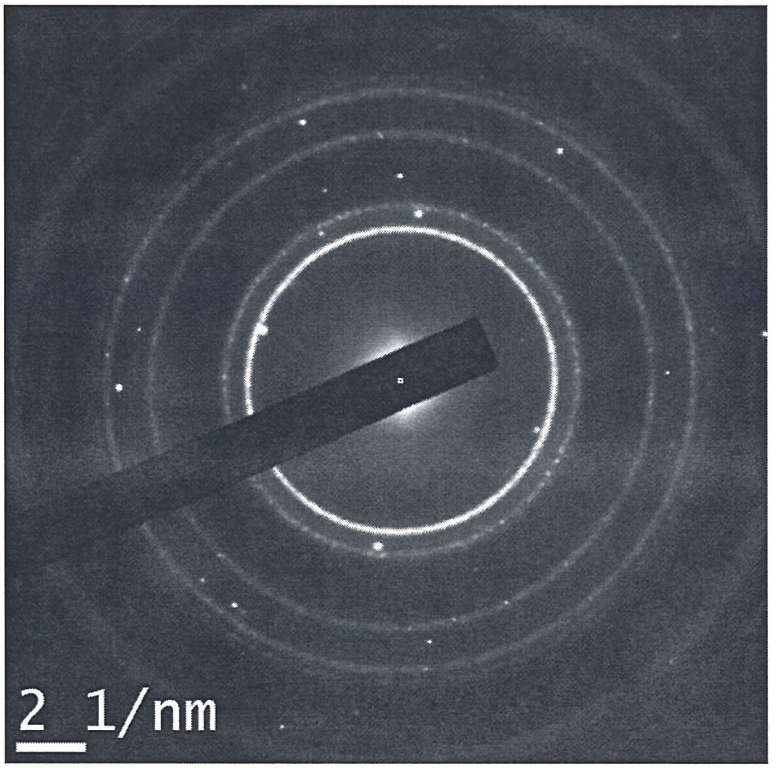

圖 2 金汞合金的繞射圖形。除金的繞射環外，還有 Au_3Hg 的繞射點。

Jahn-Teller effect on nanocheckerboard of Mn-doped $CoFe_2O_4$ spinels investigated by electron energy-loss near-edge spectroscopy

Chuan-Ming Tseng (曾傳銘)[a], Chenglin. Zhang[b], Po-Tuan Chen (陳柏端)[a], Michitoshi Hayashi (林倫年)[a], Ming-Wen Chu (朱明文)[a], Sang-Wook Cheong[b] and Cheng-Hsuan Chen (陳正弦)[a]

[a] *Center for Condensed Matter Sciences, National Taiwan University, Taipei 10617, Taiwan.*

[b] *Rutgers Center for Emergent Materials and Department of Physics & Astronomy, Rutgers University, Piscataway, New Jersey 08854, USA.*

We observed the formation of checkerboard-like nanopillars (CB) in Mn-doped $CoFe_2O_4$ spinels, with nominal composition $Co_{0.6}Fe_{0.9}Mn_{1.5}O_4$, via solid-state self-assembly. The CB pattern occurs as a result of chemical phase separation mediated by cooperative Jahn-Teller distortions. The CBs are stacked alternately with two constituent phases, tetragonal Mn-rich phase ($Co_{0.6}Fe_{0.2}Mn_{2.2}O_4$) and cubic Fe-rich phase ($Co_{0.6}Fe_{1.6}Mn_{0.8}O_4$) with compositions roughly similar to $CoMn_2O_4$ and $CoFe_2O_4$, respectively. Intriguingly, structural anisotropy of CBs gives rise to the enhancement of bulk coercivity and magnetization in $Co_{0.6}Fe_{0.9}Mn_{1.5}O_4$ **[1]**. In this study, we present the evidence of Jahn-Teller effect on the two distinct phases in CBs and compare with reference compounds by using electron energy loss spectroscopy (EELS) in conjunction with scanning transmission electron microscopy (STEM). The experimental results as shown in Fig. 1 indicate that the electron energy-loss near-edge structures (ELNES) of Mn-rich and Fe-rich phases are very similar to that of end-compounds $CoMn_2O_4$ and $CoFe_2O_4$, respectively. The ELNES spectra of $CoMn_2O_4$, based on an ideal spinel model $(Co)_A[Mn_2]_BO_4$, have been simulated theoretically using the multiple scattering code, FEFF8. The experimental and theoretical results show pronounced differences of O *K*-edge ELNES between the two constituent phases and their corresponding end-compounds. Fig.2 displays the normalized O *K*-edge and Mn L_3-edge ELNES spectra recorded from Mn-rich phase and three reference compounds. As the tetragonality of crystal structure increases from $Co_{1.5}Mn_{1.5}O_4$ to Mn_3O_4 **[2]**, two broad peaks at O *K*-edge pre-edge will split into three finely spaced peaks. This spectral evolution can be explained by Jahn-Teller energy splitting due to the elongation of the MnO_6 octahedra in spinel **[3]**. It's noted that the O *K*-edge ELNES is mainly attributed to transitions from *1s* core states to oxygen *2p* state hybridized with Mn *3d* orbitals. Compare to Fe-rich phase, the appearance of three fine-structured peaks around 530eV on Mn-rich phase is well correlated to the presence of Jahn-Teller distortions.

This work was financially supported by the National Science Council of Taiwan under Grand no. NSC97-2811-M-002- 049.

References

1. C. L. Zhang, C. M. Tseng, C. H. Chen, S. Yeo, Y. J. Choi and S. -W. Cheong, Appl. Phys. Lett. **91,** 233110 (2007).
2. J. L. Martín de Vidales et al., Chem. Mater. **7**, 1716 (1995).
3. H. -J. Noh et al., Appl. Phys. Lett. **88,** 081911 (2006).

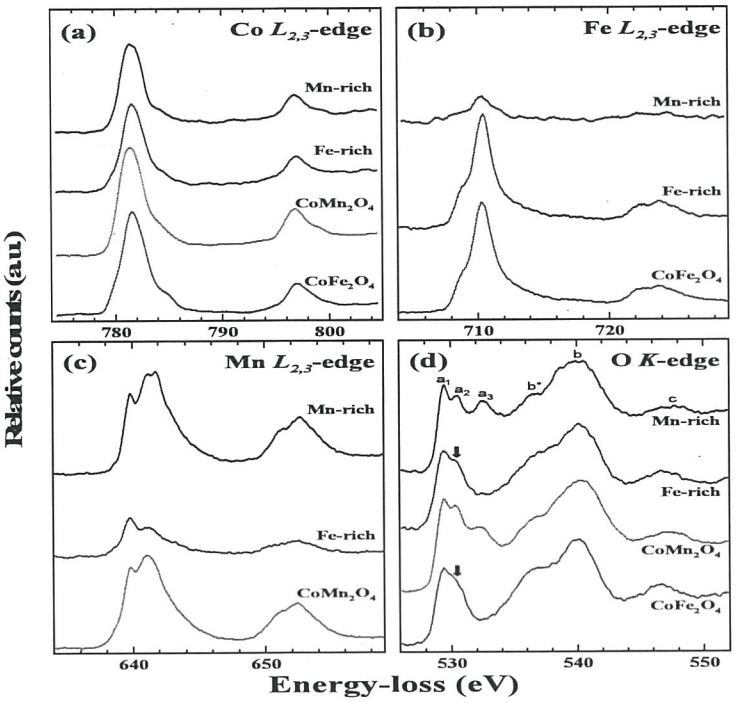

Fig. 1 The experimental (a) Co $L_{2,3}$-edge; (b) Fe $L_{2,3}$-edge; (c) Mn $L_{2,3}$-edge and (d) O K-edge ELNES spectra recorded from two constituent phases (Mn-rich and Fe-rich) on CBs in $Co_{0.6}Fe_{0.9}Mn_{1.5}O_4$ and two end-compounds, $CoMn_2O_4$ and $CoFe_2O_4$.

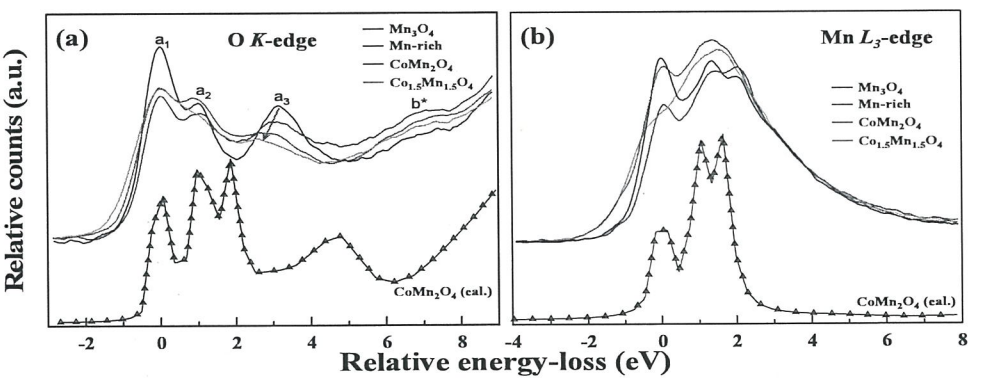

Fig. 2 (a) O K-edge and (b) Mn L_3-edge ELNES spectra recorded from Mn_3O_4, Mn-rich phase in CB, $CoMn_2O_4$ and $Co_{1.5}Mn_{1.5}O_4$. The simulated $CoMn_2O_4$ spectra calculated by FEFF8 code are employed for comparison. All spectra have been aligned to the position of first peak. The intensity has been normalized to the height of peak b around 540eV for O K-edge and the max height of L_2 peak for Mn L-edge.

Corrosion Behavior of Alloy 625 in Supercritical Water
(超合金625於超臨界水環境之腐蝕行為)

Jih-Hsuan Huang*(黃日鉉), Tsun Pin Yen(顏存濱), Ji-Jung Kai(開執中), Fu-Rong Chen(陳福榮)

Institute of Nuclear Engineering and Science, National Tsing Hua Univerity, Hsinchu,Taiwan

Department of Engineering and System Science, National Tsing Hua Univerity, Hsinchu,Taiwan

超臨界水反應器(supercritical water reactor ,SCWR)為第四代核能反應器之一，其操作環境高於水的臨界點，溫度必須超過374℃且壓力高於22.1MPa。相對於現今輕水式反應器，超臨界水反應器操作在相當高溫的環境，熱效率大約為45%(現今輕水式反應器熱效率約為33%)；並且將蒸氣產生器，汽水分離器以及乾燥器簡化除去，達到提高熱效率和降低成本兩大優點。此外，冷卻水質量小，所需進口幫浦不需太大，亦可提高安全性。

超臨界水的物理性質和低於臨界點以下的液態水有很大的不同，因此材料在超臨界水環境下的腐蝕行為值得深入研究。Inconel 625 鎳基超合金為本實驗選用之材料，將試片置於高壓釜內，實驗溫度為600℃，壓力在24.8MPa(3600psi)，溶氧濃度為8.3ppm，透過實驗前後的重量變化與微結構分析進行腐蝕測試。

相較於304L，Inconel 625 在重量變化上並無明顯改變，但在表面發現8~9μm大小之孔蝕，如圖1.；推測孔蝕與原有的(Nb,Ti)C析出相有關。經過比對ring pattern後、EDX成分分析以及XRD分析結果得知氧化層呈現兩層的結構，外層為spinel $Ni(Cr,Fe)_2O_4$，內層為spinel $Ni(Cr,Fe)_2O_4$加上Cr_2O_3組成緻密連續的氧化層。利用清華大學之串級式加速器(9SDH Tandem Accelerator)模擬輻射損傷，進行600℃，5MeV之Ni^{2+}對 Inconel 625 照射至15dpa，再經過300小時600℃的腐蝕實驗後，氧化層與未經輻照之試片相比並無明顯變化，但母材之γ”有巨凝現象發生，在電子束入射方向B=[001]方向的長度約為原γ”的13倍，圖2.。

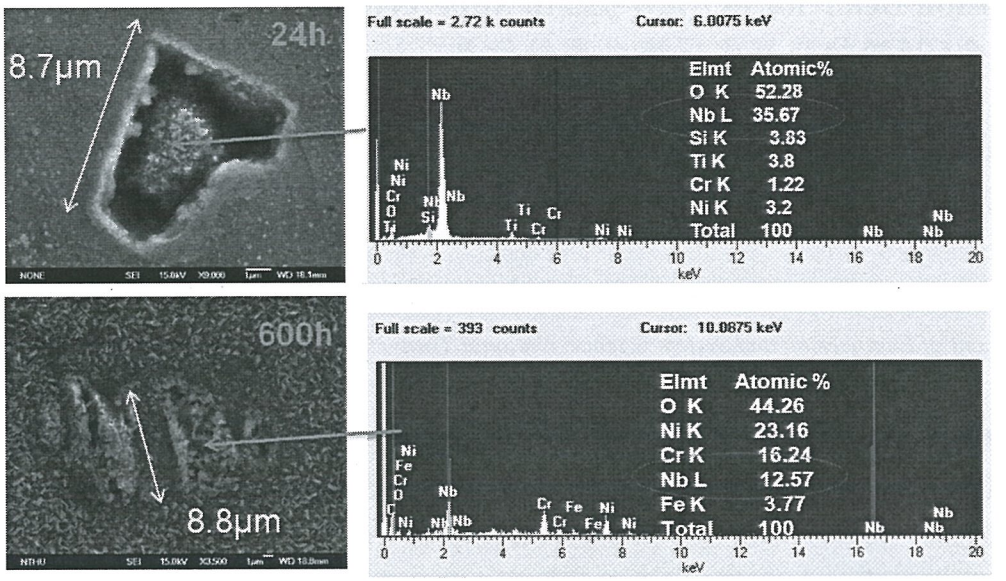

圖1. Inconel 625之 (Nb,Ti)C以及在600℃經過24與600小時腐蝕後發現之孔蝕SEM照片及EDX成分分析。

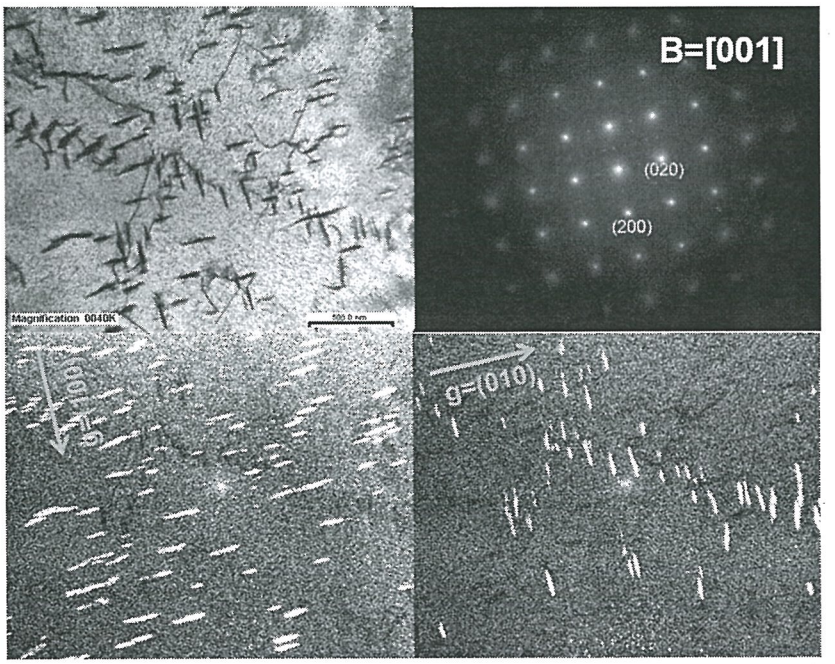

圖 2. 輻照 15dpa 之 Inconel 625 於 600℃300 小時後之明場像，B=[001]方向之電子繞射圖及 g=(100)與 g=(100)方向之暗場像，白色線條為 γ”相。

Microstructure and Composition Characterization of Gadolinium Silicate Nanocrystal

Michael R. S. Huang[1](黃榮喜), Chung Pu Liu[1], Yu Kai Chen[2], Chao Sung Lai[2], Jer Chyi Wang[2] and Yu Ching Fang[3]

[1] *Department of Materials Science and Engineering, National Cheng Kung University, Tainan, Taiwan*

[2] *Department of Electronic Engineering, Chang-Gung University, Kweishan, Taoyuan, Taiwan*

[3] *Materials and Electro-Optics Research Division, Chung-Shan Institute of Science and Technology, Longtan , Taoyuan, Taiwan*

Recently nanocrystal (NC) memory devices composed of discrete charge storage units have attracted much research interest due to its candidate for replacing conventional floating-gate memory **[1,2]**. In this study, the flash memory samples with Gd silicate NCs under different post-deposition annealing process for 30 seconds were characterized by transmission electron microscopy (TEM) for the density, distribution and microstructure of NCs, while X-ray photoelectron spectroscopy (XPS) provided the insight into composition depth profile and chemical bonding within the materials. Fig.1. illustrates the plan-view TEM images of the NCs under different conditions and the insets are the corresponding diffraction patterns (DP). The as-deposited sample reveals overlapping of nanocrystals, which is also evidenced by the observation of Moiré fringes. Through DP indexing, the NCs are assigned to FCC Gd metal and the matrix is suggested to be amorphous Gd_xO_y. The density of the NCs increases remarkably with the annealing temperature. For samples annealed at 850 and 900°C, the densities are calculated to be 6.4 x 10^{11} cm^{-2} and 9.1 x 10^{11} cm^{-2}, respectively. Therefore these two samples with high NC density can demonstrate considerably memory effect as evidenced in the previous capacitance-voltage (C-V) hysteresis results **[3]**.

Fig.2. exhibit the XPS depth profile results of the as-grown and 800°C annealed samples. Obvious interdiffusion of Si possibly from substrate or tunneling oxide into the NCs layer is noticed. Furthermore, through the deconvolution of the extracted O 1s XPS spectra (Fig.3), Gd oxide (Gd-O) and Gd silicate like (Gd-O-Si) bonding appear after annealing, while only hydroxide (O-H) and Gd oxide (Gd-O) are detected in the as-deposited sample. Consequently some diffusing Si will form Gd silicate compounds with matrix or even NCs within high-k layer. The DP of the 800°C annealed sample can then be identified as non-stoichiometric $Gd_{9.33}(SiO_4)_6O_2$ on the basis upon this consideration. For other annealed cases, the patterns are difficult to clarify as a result of their complicated and blurred characteristics. However, according

to the measured large d-spacing up to 0.6 nm and previous XPS data, it is reasonably to postulate that these NCs were also Gd silicates.

References

1. S. Tiwari, F. Rana, H. Hartstein, E. F. Crabbe, and K. Chan Appl. Phys. Lett. 68 (1996) 1377.
2. IIgweon Kim, Sangyeon Han, Kwangseok Han, Jongho Lee and Hyungcheol Shin IEEE Electron Device Letter 20(1999)1630.
3. J. C. Wang, C. S. Lai, Y. K. Chen, C. T. Lin, C. P. Liu, M. R. S. Huang, and Y. C. Fang, Electrochemical and Solid-State Letters, 12 (6) H202-H204, (2009)

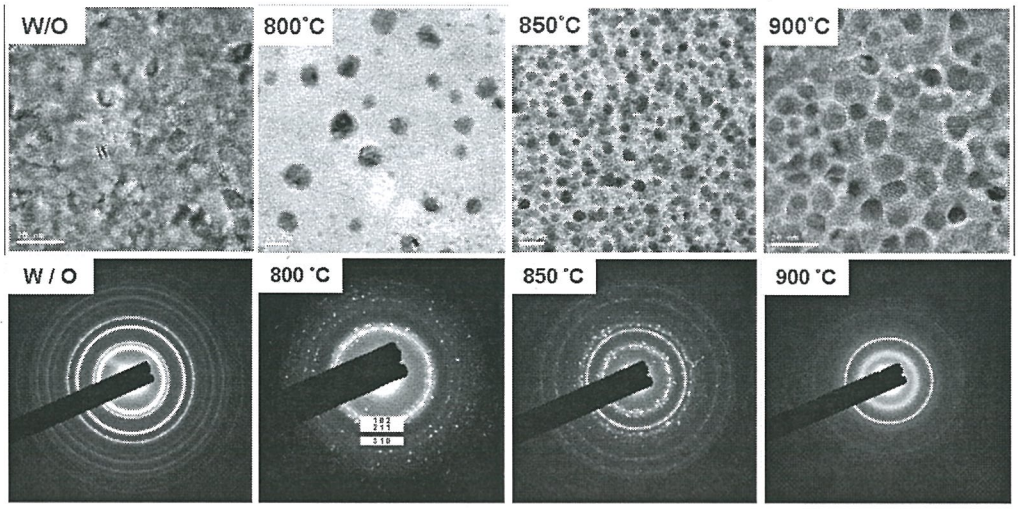

Fig. 1 TEM plan view images and diffraction patterns

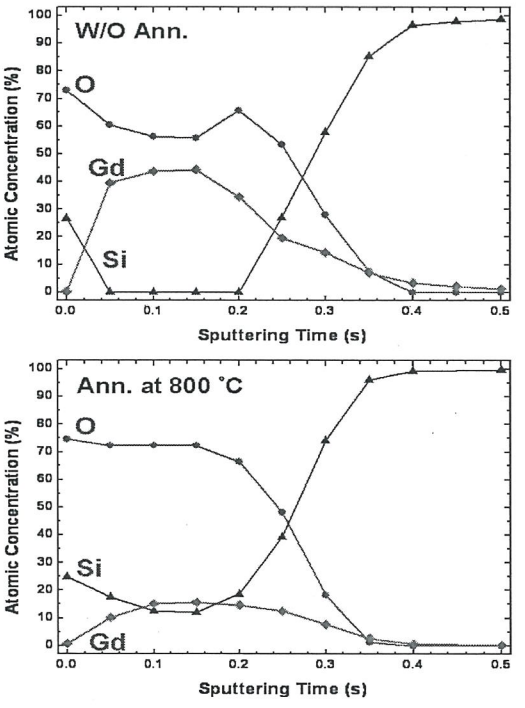

Fig.2 XPS depth profile results of the as-deposited and 800°C annealed samples.

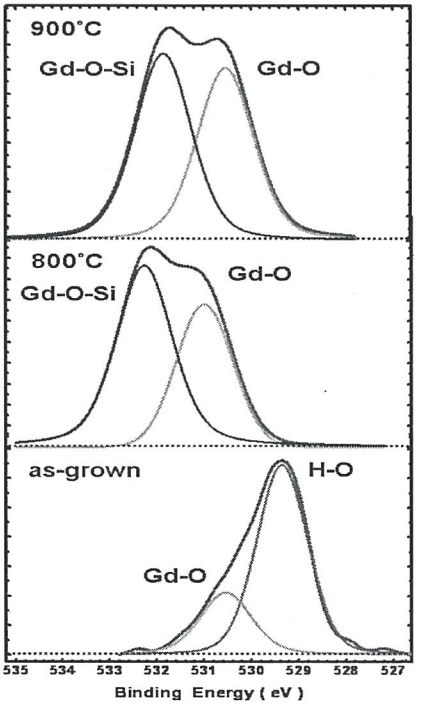

Fig.3 O 1s XPS spectra and deconvolution analysis of the as-grown, 800°C and 900°C annealed samples.

Moiré Patterns in Mesoporous Silica SBA-15 Platelet (⊥) with Perpendicular Nanochannels

Yi-Qi Yeh[a](葉亦琪), Chih-Yuan Tang[b], Chung-Yuan Mou[a]*

[a] *Department of Chemistry, National Taiwan University, Taipei 106, Taiwan*

[b] *Instrumentation Center, National Taiwan University, Taipei 106, Taiwan.*

SBA-15 is a member of mesoporous silica with one-dimensional hexagonal arrangement of uniform mesopores. The mesoporous silica SBA-15 platelets with vertical channels (denoted as SBA-15 platelet(⊥)) was prepared by using ternary-surfactant system (cationic-anionic-nonionic surfactant) as organic template. The thickness, surface area, and pore size of the mesoporous silica film are 100 nm, 450 m^2g^{-1}, and 5.0nm.

SBA-15 platelet(⊥) is characterized as platelet with 2D hexagonal mesostructure and has a six-fold rotational symmetry. The rotation moiré patterns derived from SBA-15 platelet(⊥) were observed. There might be attributed to the misorientation stacking of two layer SBA-15 platelet(⊥).

References:

1. D. Zhao, J. Feng, Q. Huo, N, Melosh, G. H. Fredrickon, B. F. Chmelka, G. D. Stucky, *Science* **1998**, 279, 548.
2. B.C. Chen, H.P. Lin, M.C. Chao, C.Y. Mou, C.Y Tang, *Adv. Mater*. **2004**, 16, 1657.

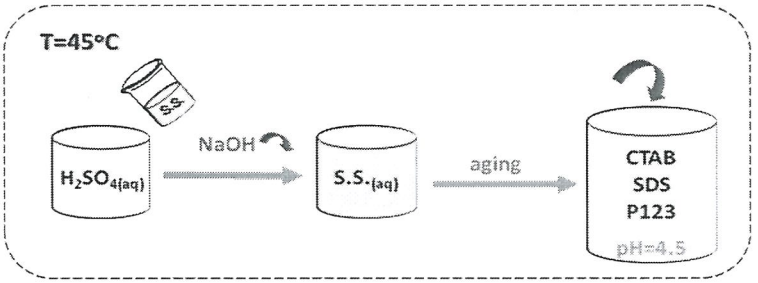

S.S. : sodium silicate, SiO_2 · NaOH
CTAB : cetyltrimethylammonium, $(C_{16}H_{33})N(CH_3)_3Br$
SDS : dodecyl sulfate sodium salt, $C_{12}H_{25}SO_4Na$
P123 : poly(ethylene glycol)-block-poly(propylene glycol)-block-poly(ethylene glycol), $EO_{20}PO_{70}EO_{20}$

Scheme 1. The preparation of SBA-15 platelet(⊥)

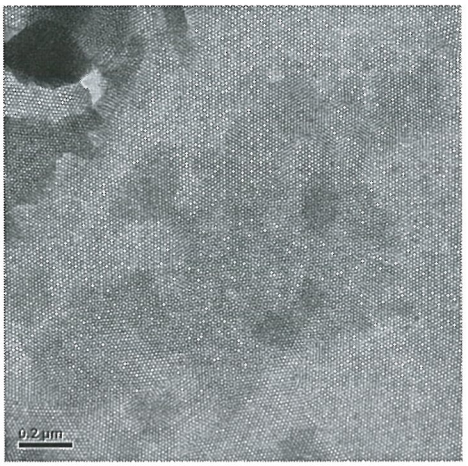

Figure 1. Typical moiré pattern derived from SBA-15 platelet(⊥).

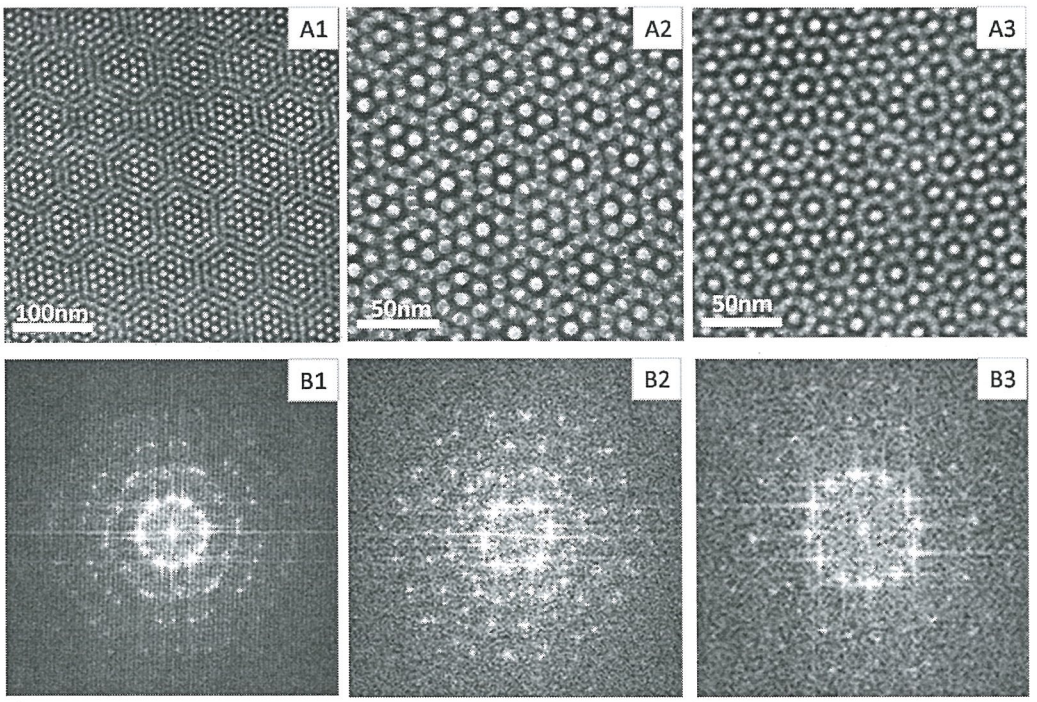

Figure 2. (left) Three rotation moiré patterns of TEM images derived from SBA-15 platelet(⊥) and (right) the corresponding FT patterns. The misorientation angles are 9°, 19°, and 28°, respectively.

Bulk and Surface Excitations in Gd2O3 : Electron Energy Loss Spectroscopy Study

S. C. Liou,*(劉思謙) M. -W. Chu,* C. H. Chen,* Y. J. Lee,** M. Hong,** and J. Kwo***

*Center for Condensed Matter Sciences, National Taiwan University, Taipei, Taiwan

**Department of Materials Science and Engineering, National Tsing Hua University, Hsinchu, Taiwan

***Department of Physics, National Tsing Hua University, Hsinchu, Taiwan

Gd2O3 with its high dielectric constant (κ~ 14) and large band gap (5.4 eV) plays as one of the most effective passivation materials in GaAs-based metal-oxide-semiconductor field-effect transistors (MOSFETs) **[1]**. Furthermore, the thermodynamic stability and the acceptable lattice matching with Si of this material also make itself as an intriguing candidate for future CMOS technology **[2]**. Indeed, thorough interface and microstructure characterizations of Gd2O3/GaAs and Gd2O3/Si heterostructures have been reported **[1,2]**. In contrast, a dedicated electronic characterization of these material systems was not documented **[3]**. Here, we reported on the bulk and surface electronic excitations of cubic Gd2O3 ceramics by electron energy-loss spectroscopy (EELS).

Figure 1a shows a high-angle annular dark filed (HAADF) image of Gd2O3 ceramics along [110] projection. Figure 1b shows the STEM-EELS spectra of the material acquired at different positions indicated in Fig. 1a. Positioning the probe at the bulk of Gd2O3 (violet, Fig. 1a), we observed several broad spectral features above the optical band gap at ~7.5, ~15, ~17.5, ~27.5, ~31.5 and ~36 eV, and the physical natures of these excitations have never been discussed before.

The experimental EELS spectra can be satisfactorily understood in the framework of the macroscopic dielectric theory for EELS excitations provided the complex dielectric function, $\varepsilon(\omega)=\varepsilon_1(\omega)+i\,\varepsilon_2(\omega)$, of the material is known. Performing Kramers-Krönig analysis on the violet spectrum in Fig. 1b, we derived the complex dielectric function of Gd2O3 as shown in Fig. 1c. At ~14 eV, the zero ε_1 and vanishing ε_2 (Fig. 1c) characteristic to the bulk-plasmon excitation clearly indicate that the excitation observed around this energy arises from bulk plasmon. Moving the probe position from the bulk to the grazing incidence near the edge (purple, Fig. 1b), the intensity for the bulk-plasmon excitation significantly reduces, while the peak at ~13.6 eV is visibly enhanced, indicating its surface-plasmon (SP) nature manifested by a negative ε_1 in the corresponding energy regime (Fig. 1c). The peaks at ~7.5, ~17.5, ~27.5, ~31.5 and ~36 eV showing sharp or diffusive corresponding oscillator

strengths (Fig. 1c) result from bulk interband transitions. With the further increase in distances from the probe to the sample edge (e.g., navy, dark yellow, etc.; Figs. 1b), significant intensity decrease at ~13.6 eV can be observed, characteristic to the exponential decay of SP wave fields from the material surface. Most importantly, the broad shoulder at ~7.5~10.5 eV (Fig.1b) persists and evolves into a prominent spectral onset at ~7.5 eV (e.g., yellow, magenta, cyan, etc.; Figs. 1b). This characteristic indicates that the 7.5-eV peak bears a strong surface excitation character, while the existence of a surface electromagnetic mode at such a sharp excitonic onset (Fig.1c) is not expected. Indeed, exciting physics underlying this unexpected phenomenon should exist and a more complete study is in progress.

References

1. M. Hong, J. Kwo, A. R. Kortan, J. P. Mannaerts and A. M. Sergent, Science 283,1897 (1999).
2. J. Kwo, M. Hong, A. R. Kortan, K. L. Queeney, Y. J. Chabal, R. L. Opila, Jr., D. A. Muller, S. N. G. Chu, B. J. Sapjeta, T. S. Lay, J. P. Mannaerts, T. Boone, H. W. Krautter, J. J. Krajewski,A. M. Sergnt, and J. M. Rosamilia. J. Appl. Phys. 89, 3920 (2001).
3. G. A. Botton, J. A. Gupta, D. Landheer, J. P. McCaffrey, G. I. Sproule, and M. J. Graham. J.Appl. Phys. 91, 2921 (2002).

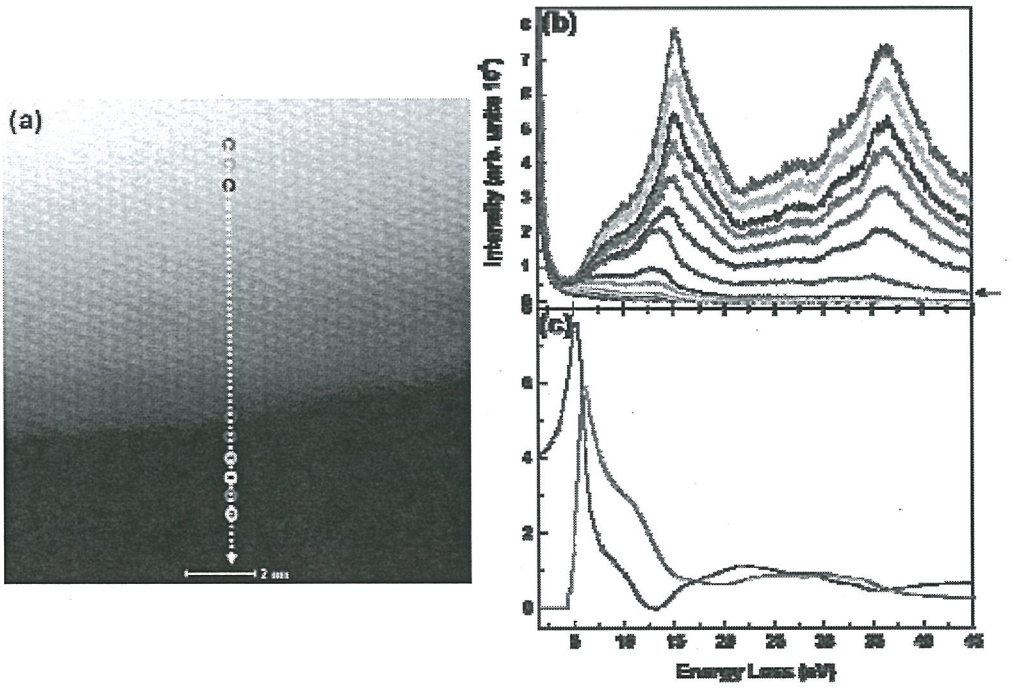

Figure 1 (a) The STEM-HAADF image of the cubic- Gd_2O_3 (001) along [110] projection. (b) STEM- EELS spectra acquired on the cubic-Gd_2O_3 with the electron probe positioned at various locations in (a). Solid arrow, the spectrum acquired in grazing incident to the sample edge. (c) The complex dielectric function of cubic- Gd_2O_3 derived from violet spectrum in (a).

The Microstructural Evolution of Nuclear Grade Graphite in Very High Temperature Gas Cooled Reactor (VHTGR) Core Environments

Shuo-Cheng Tsai (蔡碩承)*, Ji-Jung Kai, Fu-Rong Chen

Department of Engineering and System Science, National Tsing Hua Univerity, Hsinchu, Taiwan

With the importance of nuclear power go on. The newly designed generation IV reactor (G-IV) has incorporated hydrogen production into the reactor design. The most promising type of G-IV reactor for both electricity and hydrogen production is the very high temperature gas-cooled reactor (VHTGR). In this type reactor design, **nuclear grade graphite** is the major core internal structural material serving as reflector and moderator. Due to the high temperature and high neutron flux in the core, graphite will face very serious challenge in terms of microstructural evolution.

Graphite will store Wigner energy inside the crystalline lattice and cause the expansion of c-axis during irradiaton. The crystalline lattice may release enormous amount of defect energy when the temperature reaches the critical annealing temperature which may cause serious problem in reactor safety.

In this project we will study the radiation damage effect on the microstructural defects of graphite.By using the Hgh Resolution Transmission Electron Microscopy (HRTEM) images ,we can find the c-axis of graphite expanded and distorted , the degree of expansion and distortion indicates the amount of stored energy; after that , via using Fsat Fourier Transform and projection of intensity ,we can define the distance between {0000} and {0002} in reciprocal space(which equals to c-spacing).In the next step,to calculate the stored energy and raising temperature by elastic strain model.

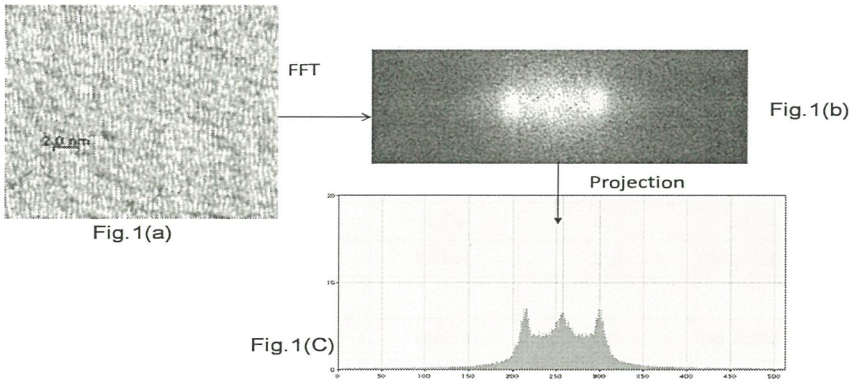

Fig.1(a) HRTEM images of irradiation graphite (10dpa)
1(b) Fast Fourier Transform of HRTEM image
1(c) The projection of FFT intensity

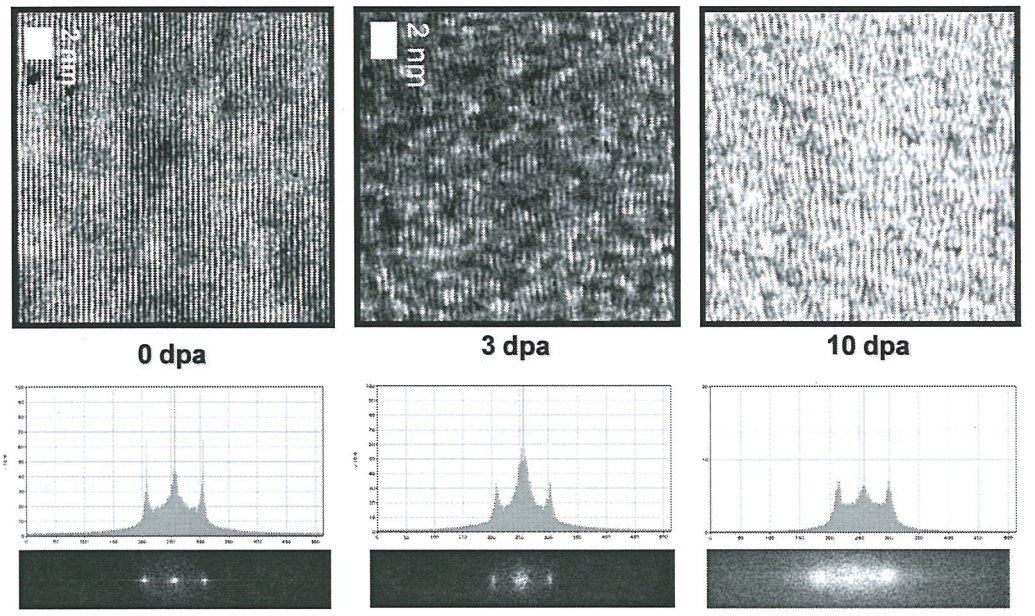

Fig.2 HRTEM images from the region of different doses

				only c- axis		a+c axis	
	dose(dpa)	d spacing(nm)	strain of c spacing(%)	strain energy(cal/g)	rising temperature(℃)	strain energy(cal/g)	rising temperature(℃)
500	0.6	0.344±0.002	2.4	40±4	105±11	81±9	215±22
	3	0.355±0.002	5.7	222±24	536±55	518±52	1368±128
	5	0.361±0.003	7.6	279±20	735±54	847±59	2087±146
	10	0.381±0.007	13.5	791±47	2087±123	2681±158	7073±417
600	0.6	0.358±0.002	6.7	108±11	264±27	397±38	1008±93
	3	0.362±0.002	7.7	289±28	670±66	793±83	2014±223
	5					±	±
	10					±	±
700	0.6	0.357±0.002	6.3	83±8	199±20	316±33	777±79
	3	0.359±0.002	7	209±19	483±47	584±59	1434±145
	5	0.365±0.003	8.6	249±21	612±53	845±73	2076±176
	7	0.371±0.004	10.7	421±45	1035±111	1315±141	3232±346
	10	0.389±0.01	16.1	691± 76	1697± 187	2828±311	6947±764
	40					±	±
800	0.6	0.355±0.002	5.8	63±8	160±18	263±30	630±65
	3	0.357±0.003	6.3	160±18	366±39	447±42	1069±96
	5						
	10	0.382±0.006	13.6	617±94	1475±226	2125±330	5166±790

Table.1 The strain energy and rising temperature for different temperature and Dose.

金汞齊的電子繞射分析

謝鵬翰(Hsieh, Peng-Han) [1] 林彥甫(Lin, Yan-Fu) [1] 徐統(Hsu, Tung) [1] 飯塚義之(Iizuka, Yoshiyuki)[2]

[1]國立清華大學材料科學工程學系2. 中央研究院地球科學研究所

汞與大部分的金屬皆能互溶形成合金，這些合金統稱為汞齊(amalgam)。金與汞的互溶速度相當快，能形成灰白色的金汞齊。在金汞齊顯微檢測研究上有利用原子力顯微鏡**[1]**、掃描穿隧式電子顯微鏡**[2]**與掃描式電子顯微鏡**[3]**做表面形貌分析。結果顯示，汞齊會以島嶼狀在金表面成長，文獻中也提出相關吸附機制**[1,2,3]**。為了觀察金膜對汞的吸附率與鑑定汞齊晶體結構，本實驗利用穿透式電子顯微鏡(JEOL JEM-2100F, 200kV 與JEOL JEM-2010, 200kV)對汞齊顆粒做繞射分析**[4]**以及電子微探儀(JEOL JXA-8500F)做元素分析。

我們希望製造一個穩定的汞源環境，讓汞氣體與金作用。故樣品製備方法為用直徑3mm 的銅網乘載厚度約100nm 金膜後，將銅網用膠帶貼於裝有一滴汞的玻璃瓶內封住，如此則金膜暴露於汞的飽和蒸汽中。實驗條件設定為室溫曝汞24小時與水浴加熱至100 ℃ 20 分鐘兩種情形。

利用電鏡選區繞射得到上述兩種條件的繞射圖形與JCPDS 數據庫做比對**[5]**。曝汞時間 24 小時的條件下可發現汞的吸附相當不均勻(圖1)，我們同時可以找到純金的面心立方環(圖2)與Au3Hg 的繞射圖形(圖3)。經過水浴後的繞射圖形(圖4)經由比對數據庫的結果也是Au3Hg。此外，根據波長分布譜(WDS)定性分結果顯示，確實有Hg 的存在(圖5)。我們的實驗結果除了發現Au3Hg 外，並沒有發現符合其他比例的汞齊合金。由實際觀察汞不均勻的吸附情形與理論計算汞的吸附率相比，差距甚遠。

參考文獻

1. R. Nowakowski, T. Kobiela, Z. Wolfram and R. Duš,*Appl. Surf. Sci.*,115 (1997) 217.
2. M. Levin, H.E.M. Niemi, P. Hautojarvi, E. Ikävalko and T. Laitinen, *Fresen.J.Anal.Chem.*,355 (1996) 2.
3. C. Battistoni, E. bemporad, A. Galdikas, S. Kaciulis, G. Mattogno, S. Mickevicius and V.Olevano, *Appl. Surf. Sci.*,103 (1996) 107.
4. T. Hsu, "Transmission Electron Microscopy Study of Gold/Mercury Amalgam",in proceedings of The 9thAsia-Pacific Microscopy Conference,Jeju, Korea (2008) 574.
5. "*PCPDFWIN*" v.2.3, 2002, JCPDS, 04-0776, 04-0780, 04-0781, 04-0784, 04-0808, 19-0522,26-0715, 46-1412.

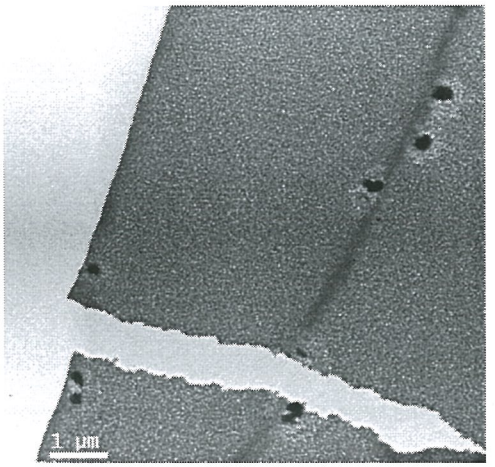

圖1. 曝汞24 小時的電子顯微鏡明場像。黑色顆粒為汞齊。

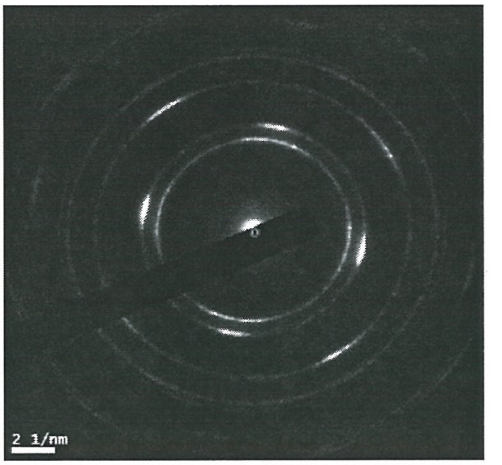

圖2. 純金繞射環。

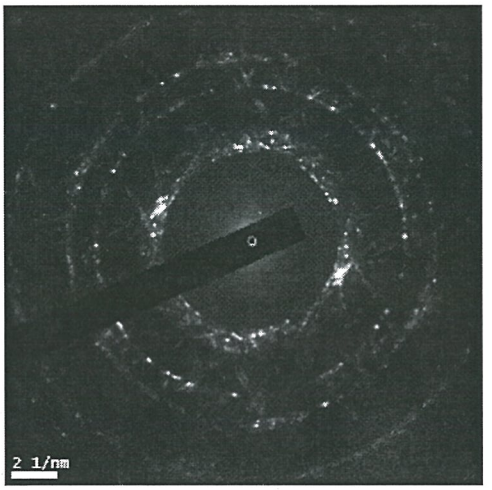

圖3. 繞射結果顯示除了本底的金環外，還可以發現有Au_3Hg的繞射環。

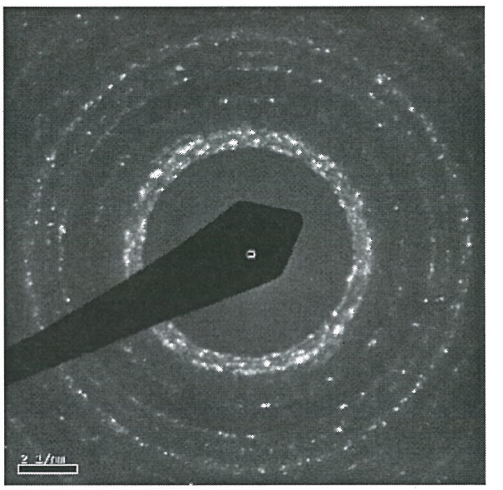

圖4. 水浴法所得到的結果。繞射環形狀更完整且發現Au_3Hg 存在。

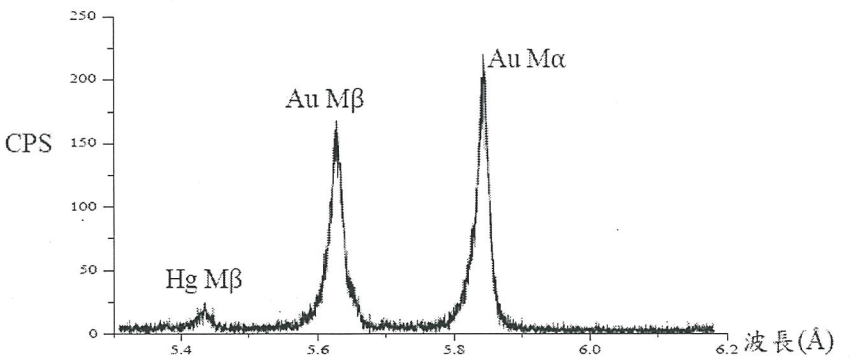

圖5.WDS 的分析結果。有汞的Mβ峰出現。

$CrSi_2$(核)/SiO_2(殼)奈米電纜之磁性質研究: 顯微結構、磁性質與第一原理摸擬分析

*韓侑宏[1] 侯德謙[1] 陳力俊[1] 歐陽浩[1]

[1] 國立清華大學材料科學工程學系

一維的奈米線、奈米管和奈米電纜，由於其低維度和表面積對體積的比增加，使得一些物理特性變得有別於塊材時的性質**[1-3]**。$CrSi_2$和 SiO_2在塊材時為反磁性材料，但在我們製備的奈米電纜 $CrSi_2$(核) /SiO_2(殼)中，我們發現這樣的奈米結構有鐵磁性質，這樣的現象引起我們極大的興趣，想深入了解其原因。

藉由常壓化學氣相沈積法，製出高密度的 $CrSi_2$(核)/SiO_2(殼)奈米電纜。並以超導量子干涉儀(SQUID)，量測出 $CrSi_2$(核)/SiO_2(殼)奈米電纜(nsnocables)的磁滯曲線(圖 4)，發現到 $CrSi_2$ 奈米線有異於塊材的磁性質。高解析穿透式電子顯微鏡(HRTEM)分析結果(圖 2)，可知奈米電纜內層 $CrSi_2$ 是以(001)平面縱向成長，而以(100)平面橫向成長並和外層 SiO_2 接觸。從掃描式電子顯微鏡(SEM，圖 3)，發現奈米電纜大致是以垂直基板方向成長，且平均長度約 12.9μm，平均直徑約 76.3nm，經過進一步分析可知佔空間密度(奈米線體積/空間體積)約 12.1%左右。

藉由第一原理摸擬計算程式 Vienna Ab-initio Simulation Package (VASP)**[4,5]** 建立出近似真實奈米線的表面結構(圖 5)，結果發現(圖 6)靠近表面的 Cr 原子有約 2μB 的磁化量，深度 0.5nm 後內部 Cr 原子磁性就跟塊材時一樣約 0μB。藉由進一步的數值估算與近似，結果得出在表面無 SiO_2 時可達 2.52×10^{-4}emu，而表面有 SiO_2 時可達 1.52×10^{-4}emu，與實驗結果飽點磁化量 3.9×10^{-4}emu 為相同數量級的磁化量，因此這樣的奈米電纜結構，主要是因為 $CrSi_2$ 表面積的增加，表面的 Cr 原子未完全鍵結及鍵結的扭曲(圖 5.(b))，使得 Cr 原子 3d 軌域的自旋向上和自旋向下的電子數不同(圖 6.(b))，而有鐵磁性材料的性質。

References

1. Xia, Y.; Yang, P.; Sun, Y.; Mayers, B.; Gates, B.; Yin, Y.; Kim, F.; Yan, H., Adv. Mater., 15, 353 (2003)
2. Cui, Y.; Lieber, C. M., Science, 291, 851 (2001)
3. Wang, Z. L.; Song, J., Science, 312, 242 (2006)
4. G. Kresse and J. Hafner, Phys. Rev. B 47, 558 (1993).
5. G. Kresse and J. Furthmüller, Phys. Rev. B 54, 11169 (1996)

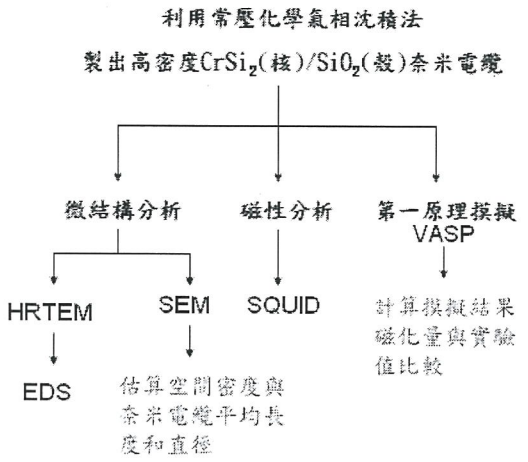

圖 1.實驗流程圖

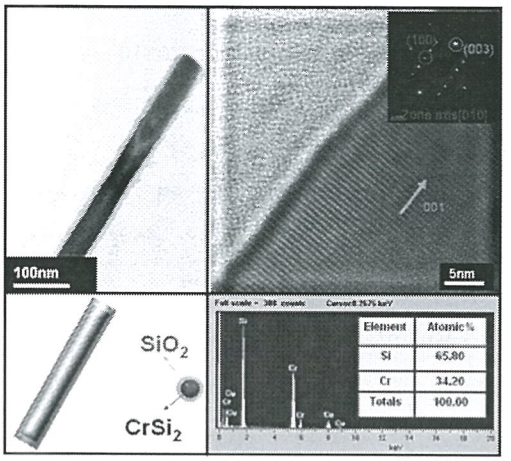

圖 2.高解析穿透式電子顯微鏡與能量散佈儀分析結果

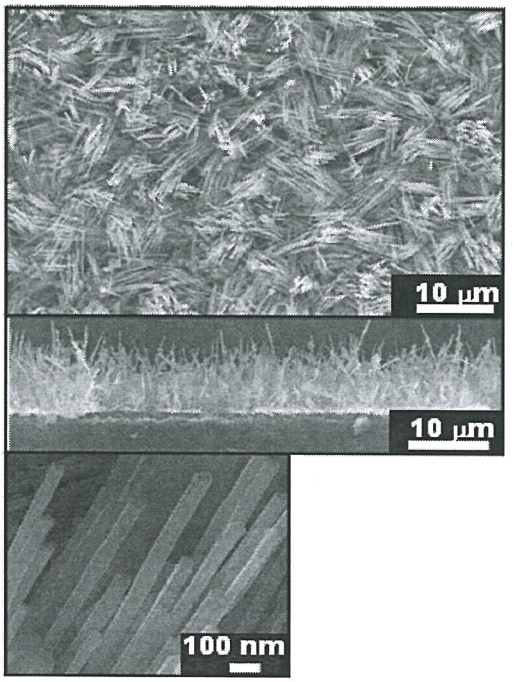

圖 3.掃描式電子顯微鏡

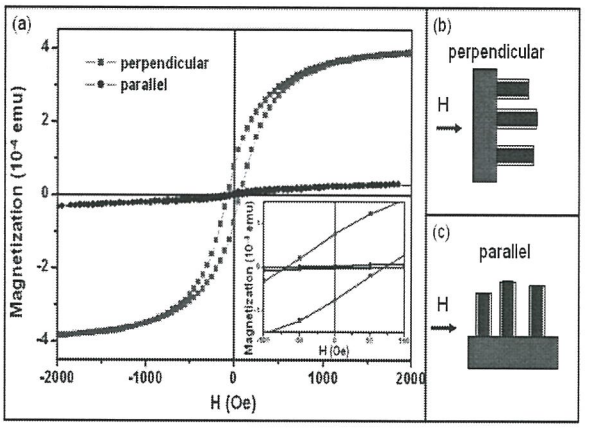

圖 4.(a)超導量子干涉儀量測結果(b)磁場與基板垂直時有易磁化現象(c) 磁場與基板平行時有難磁化現象

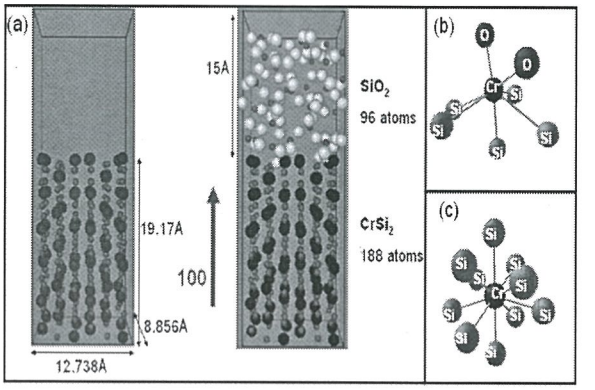

圖 5.(a)原子位置的建立(左邊 $CrSi_2$+真空層，右邊 $CrSi_2$+SiO_2)，以 $CrSi_2$ 的(100)平面向上與真空層或 SiO_2 相接(b)表面 Cr 原子的鍵結(c)內部 Cr 原子的鍵結

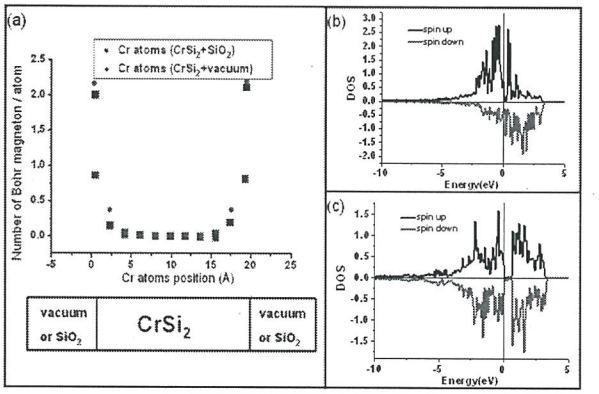

圖 6.(a)第一原子摸擬結果，Cr 原子磁化量與其位置關係，紅色為 $CrSi_2$+真空層時 Cr 原子磁化量，藍色為 $CrSi_2$+SiO_2 時 Cr 原子磁化量(b)表面 Cr 原子的態密度與能量關係作圖(c)內部 Cr 原子的態密度與能量關係作圖

添加 V 對 SmCo7 之能量穩定性及磁性質之影響

陳尹瀅[1], 謝志杰[2], 歐陽浩[1], 張文成[2], 張晃暐[3]

[1] 國立清華大學材料科學工程研究所 [2] 國立中正大學物理研究所 [3] 國立東華大學物理研究所

$RxFe_yCo_z$類型的化合物因為磁性方面的應用而受到矚目(R 為稀土元素)，此類型化合物，可能以稀土元素比上 Fe 和 Co 之原子比為 1:5，1:7，1:12，2:17 的形式出現，通常都有居禮溫度較低的缺點。但其中 $SmCo_7$ 的居禮溫度高達 770℃[1]，是一種可在高溫下應用的永久磁性材料，而引發了我們的研究興趣。本研究是以 x-ray 精算軟體 GSAS 與模擬軟體 VASP，探討鐵磁性材料 $SmCo_7$ 加入 V 之後對其能量穩定性及磁性質的影響。

在本研究中，以融熔法(melt spinning)做出 $SmCo_{6.7}V_{0.3}$ 金屬薄帶，先透過 x-ray 精算軟體 GSAS (General structure analysis system)，輸入實驗所得的 x-ray 繞射數據，利用最小平方理論，計算出 V 所佔據的晶體位置。再使用模擬軟體 VASP(Vienna ab-initio simulation package)，利用第一原理，計算出 V 所佔據能量最穩定的位置。$SmCo_7$ 的結構如圖 1 所示，其中 Co 有三種不同的晶體位置，分別是 2c，2e，3g，由於添加的 V 會在 $SmCo_7$ 的結構中取代 Co，故 V 可能佔據的位置也有三種。用 VASP 模擬發現，$SmCo_7$ 加入 V 之後能量下降，顯示 V 對此結構有穩定的作用，其中以 V 佔據 2e 位置的結構最為穩定，如表 1。而用精算軟體計算出 $SmCo_7V_{0.333}$ 中 V 也是位於 2e，兩者結果吻合，故我們推斷 V 佔據了 2e 的位置。

磁滯曲線的量測受限於儀器的極限，磁場最高只能加到 150kOe，從圖 2 中我們可以觀察到，添加 V 使 $SmCo_7$ 的磁化量下降。在 150kOe 的磁場下，磁化量從 $SmCo_7$ 的 75emu/g 下降為 $SmCo_{6.7}V_{0.3}$ 的 55emu/g，約下降了 27%；而從模擬的結果，如表 1，飽和磁化量從 $SmCo_7$ 到 $SmCo_{6.7}V_{0.3}$(2e)只下降了約 1%，實驗與模擬的結果不符。推測其原因，由於融熔法是一種以高速轉輪冷卻金屬液滴來製成金屬薄帶的方法，此法因冷卻速度快，原子擴散慢，所以在薄帶中存在大量的晶體缺陷，應力也無法釋放而留在薄帶中，而模擬時是以完美且經過鬆弛(relaxation)的晶體來做計算，兩者條件不同。由 $SmCo_7$ 和 $SmCo_{6.7}V_{0.3}$ 的 x-ray 分析可發現，繞射峰的相對強度改變，特別是晶面 $\bar{2}10$，如圖 3，說明兩者之晶體成長優選方向不同，顯示從 $SmCo_7$ 到 $SmCo_{6.7}V_{0.3}$ 其微結構可能已經發生變化，故實驗量測到的磁化量與模擬結果之飽和磁化量不相符合；但兩者都顯示出同樣的趨勢，即添加 V 使 $SmCo_7$ 的磁化量下降。

我們將用以模擬之 $SmCo_7$ 和不同位置的 $SmCo_{6.7}V_{0.3}$ 結構輸入電子顯微鏡模擬軟體 JEMS(Java electron microscopy software)中，以 multi-slice method 模擬出這四種結構之高解析電子顯微鏡影像(HRTEM image, high resolution transmission electron microscopy image)，如圖 4，發現其差異並不明顯，之後的研究中會實際拍攝 HRTEM 的影像來與模擬的影像比對。

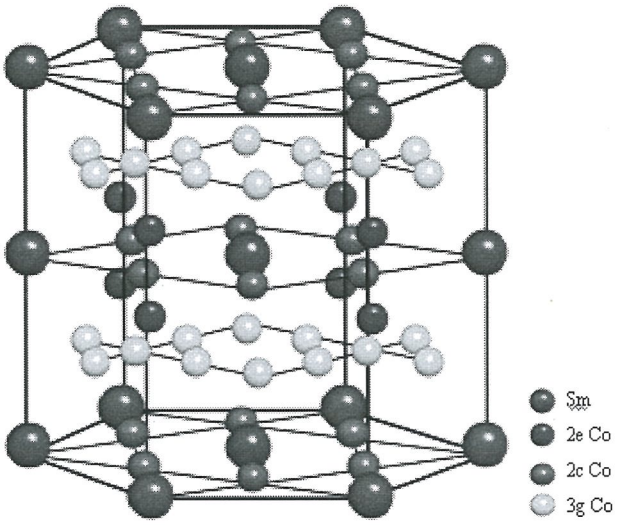

圖1 $SmCo_7$結構圖

	Energy (eV)	Magnetization per unit cell (μ_B)
$SmCo_7$	-184.23223	34.86
$SmCo_7V_{03}$(3g)	-184.86624	29.01
$SmCo_7V_{03}$(2c)	-184.98030	18.49
$SmCo_7V_{03}$(2e)	-187.78903	34.51

表1 模擬軟體VASP計算出單位晶胞之能量(eV)與磁性(Bohr magneton)

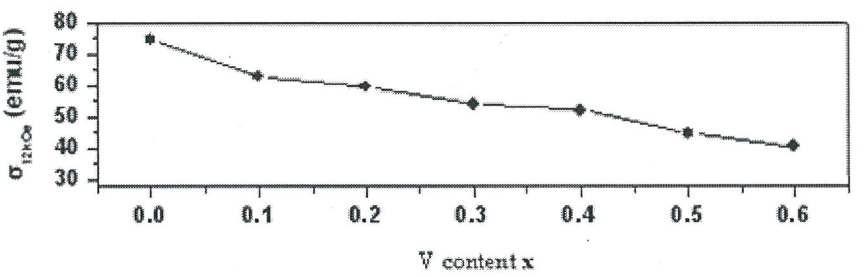

圖2 在150kOe的磁場下量測之$SmCo_{7-x}V_x$之磁化量(emu/g)

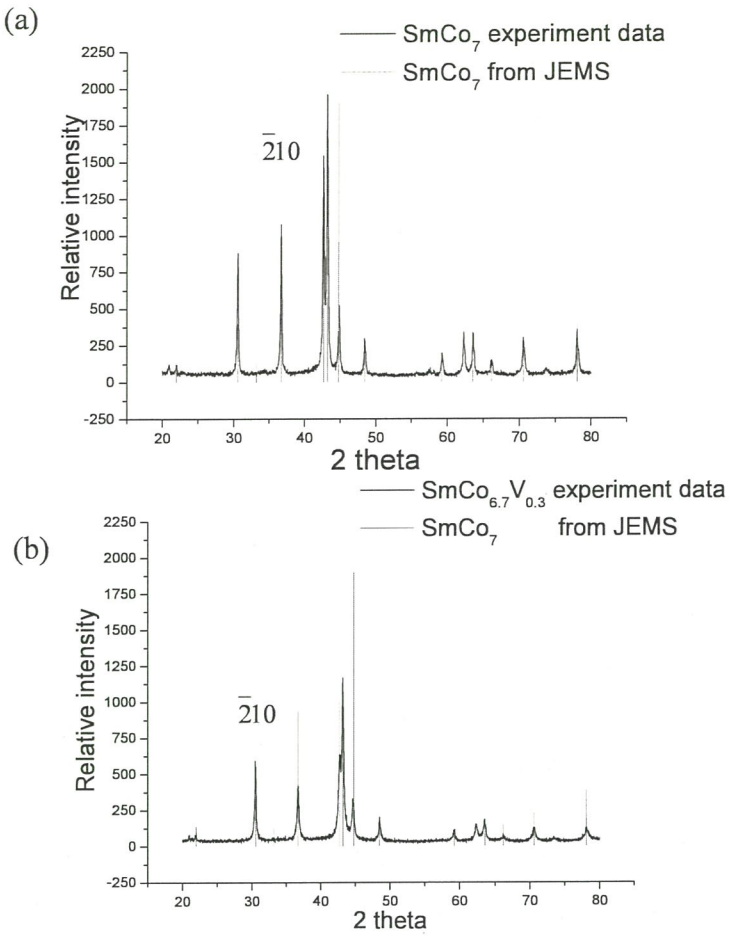

圖 3　(a)$SmCo_7$ 和(b)$SmCo_{6.7}V_{0.3}$ 的 x-ray 繞射峰之比較，其中 $\bar{2}10$ 的繞射峰相對強度有明顯變化(紅色是以電子顯微鏡模擬軟體 JEMS，Java electron microscopy software 模擬出的 $SmCo_7$ 單位晶胞繞射峰)

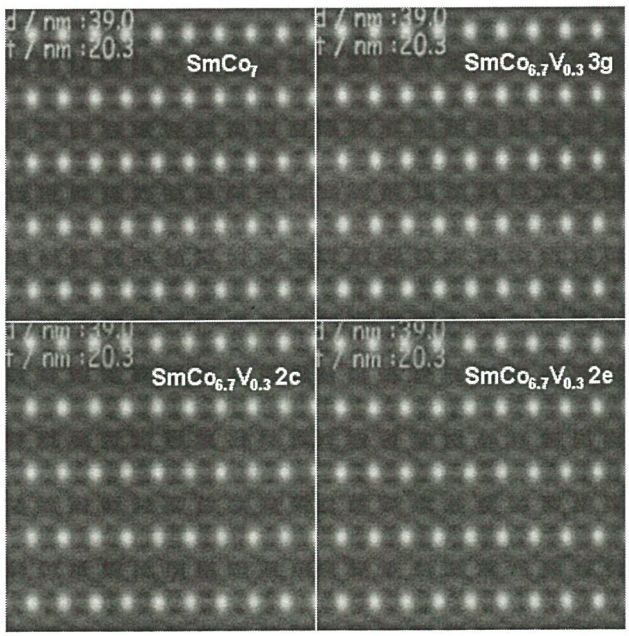

圖 4 $SmCo_7$ 和 V 佔據 3g/2c/2e 位置的 $SmCo_{6.7}V_{0.3}$ 之模擬 HRTEM image

Geomtric phase analysis of buried 2.4 monolayer InAs/GaAs quantum dots

Yue-Han Wu[a] (吳岳翰), Li Chang[a] and Fu-Rong Chen[b]

(a) Department of Materials Science and Engineering, National Chiao-Tung University, Hsinchu, Taiwan, R.O.C.

(b) Department of Engineering and System Science, National Tsing-Hua University, Hsinchu, Taiwan, R.O.C.

**Correspondence:yhwu.mse91g@nctu.edu.tw*

Geometric phase analysis (GPA) [1] from lattice images in HRTEM can accurately reveal the local strain field in atomic spatial resolution. The GPA measurement is performed by the reciprocal spatial frequency of g vectors from the Fourier transform of an HRTEM image. The strain distribution of the buried quantum dot (QD) has strong effects on structural and optical properties of QD structures which are still not well understood despite of the intensive studies over the past decade. In this study, we present the strain field of a buried InAs/GaAs QD with 7% lattice mismatch using GPA.

The nanostructure consists of 2.4 monolayer (ML) InAs self-assembled quantum dots and the GaAs capping layers, which were grown at 485 and 600 °C, respectively, by molecular beam epitaxy. HRTEM images were acquired at an accelerating voltage of 200 kV in a JEOL 2010F field-emission transmission electron microscope using auto tuning for astigmatism correction and accurate coma-free alignment. Geometrical phase calculation with displacement field and strain distribution was carried out by using MacTempas program.

Fig. 1(a) shows an HRTEM image of one buried InAs/GaAs QD without any digital processing in $[010]_{GaAs}$ zone axis. Following the processes of GPA, the phase x and y images of lattice shifts are calculated in Figs. 1(c) and (d) from two diffraction spots, {200} and {002}, respectively. Meanwhile, the corresponding amplitude and Bragg filter images are displayed in Figs. 1(e), (f), (g), and (h). As shown in the above results, the shape of this QD is roughly like truncated pyramid, which is about 3.5nm in height. The wetting layer (WL) around QDs is about 1.0nm in thickness. Figs. 2(a), (b), and (c) show the e_{xx}', e_{xy}', and e_{yy}' strain of Fig. 1(a). Most of strong tensile and compressed strains in Figs. 2 appear around QD and WL, and the strain distributions in different symmetric strain elements illustrate the diversity.

Reference:

[1] M. J. Hytch ,Microsc. Microanal. Microstr. 8 (1997) 41-57.

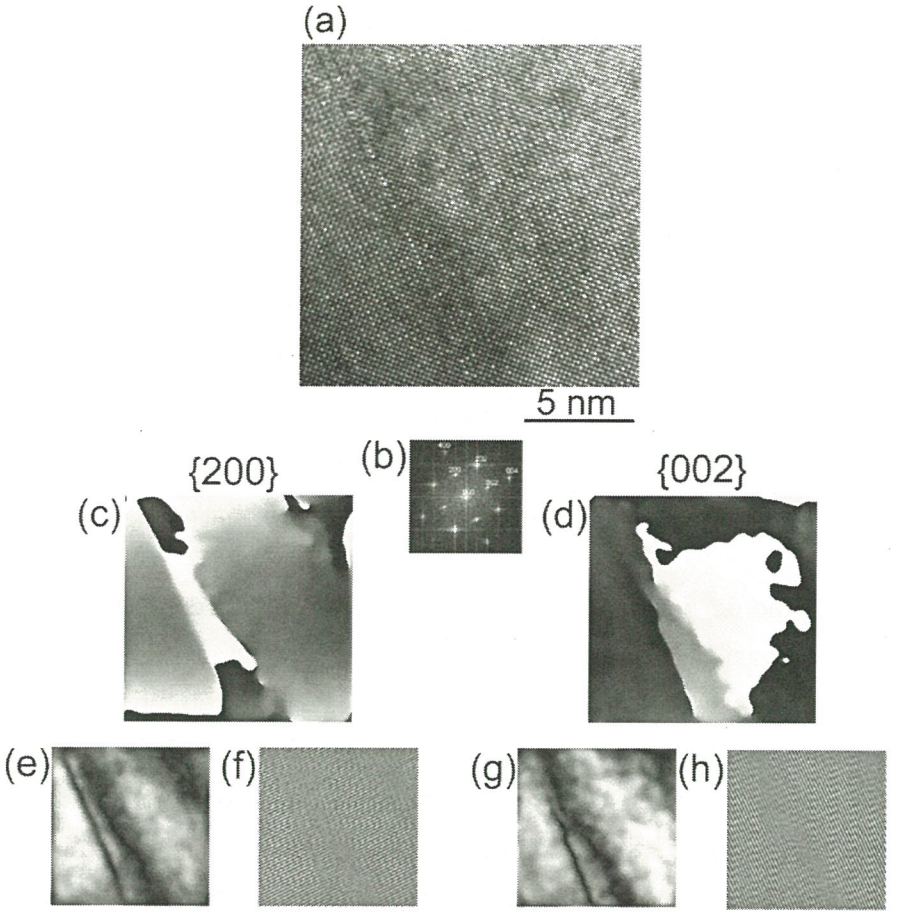

Fig. 1(a) The original HRTEM image of buried 2.4ML InAs/GaAs QDs with the wetting layer. (b) The FFT image of image (a). The GPA phase of lattice images from {200} and {002} in (c) and (d), respectively. Following the GPA process, the amplitude and Bragg filter images corresponds to the phase images.

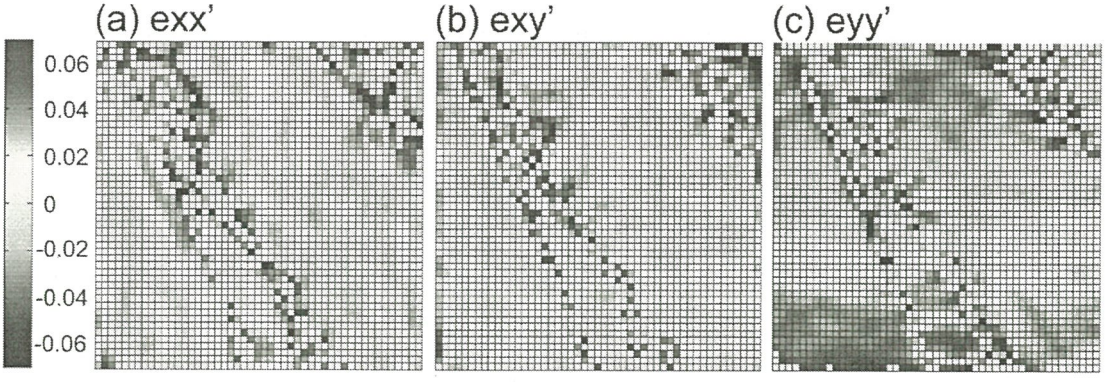

Fig. 2 The strain distribution around a QD in the symmetric strain matrix of exx', exy' and eyy'.

Second-order susceptibility
second harmonic generatio

CHEN, Wei-Liang[1]; LI, Tsung-H
Chen-Kuan[1]; FWU, Peter Tramy
SO, Peter T. C. [3,4]; and DONG, C

[1] *Department of Physics, National Taiw*
[2] *Department of Dermatology, National*
[3] *Department of Mechanical Engineeri*
[4] *Department of Biological Engineering,*

Second harmonic generatio
for minimally invasive biomedi
myosin are strong second har
second harmonic generating spe
features. In this study, we used
to determine the ratios of the s
pixel resolution. Mapping the re
additional contrast for the differe
this technique by imaging collage
human skin.

References

1. Campagnola, P. J. and Loew,
2. Plotnikov, S. V., Millard,
   Biophysical Journal 2006 (90
3. Chou, C.K., Chen, W. L., F
   Journal of Biomedical Optics

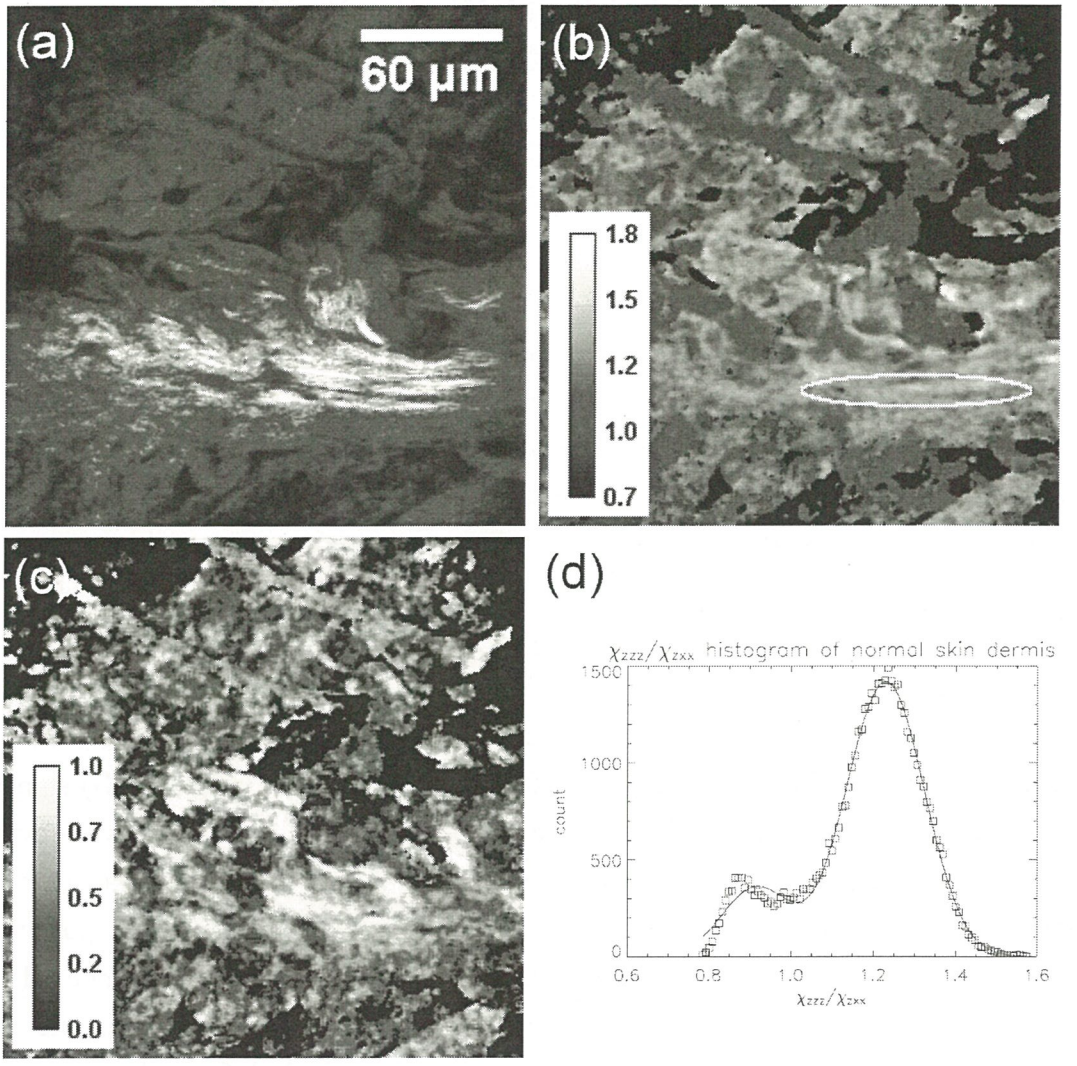

Fig. 1 (a) SHG image of the human skin dermis. (b) and (c) show respectively the second order susceptibility tensor ratios (χ_{zzz}/χ_{zxx}) and (χ_{xzx}/χ_{zxx}) displayed as an image for the same area shown in (a). The corresponding ratio value to the color displayed is shown in the calibration bar on the lower left hand corner of the image. (d) shows the histogram distribution of the χ tensor ratio (χ_{zzz}/χ_{zxx}) fitted with the sum of two Gaussian functions.

SECOND HARMONIC GENERATION MICROSCOPY CHARACTERIZATION OF CORNEAL EDEMA

HSUEH, Chiu-Mei[1](薛秋美); LO, Wen[1]; CHEN, Wei-Liang[1]; HOVHANNISYAN, Vladimir[1]; LIU, Guang-Yu[1]; WANG, Sheng-Shun[1]; TAN, Hsin-Yuan[2,3]; DONG, Chen-Yuan[1]

[1] *Department of Life Science, Institute of Ecology and Evolutionary Biology, National Taiwan University, 1 Roosevelt Rd., Sec. 4, Taipei 106, Taiwan.*

[2] *Division of Forest Biology, Taiwan Forestry Research Institute, 53 Nan-Hai Rd., Taipei 100, Taiwan*

[3] *Department of Ophthalmology, Chang Gung Memorial Hospital, College of Medicine, Chang Gung University, Linko 333, Taiwan*

The purpose of this study is to image and quantify the structural changes of corneal edema by second harmonic generation (SHG) microscopy. Bovine cornea was used as the experimental model for characterization of structural alterations in edematous corneas. Forward SHG (FWSHG) and backward SHG (BWSHG) signals were simultaneously collected from normal and edematous bovine corneas to reveal the morphological differences between them. For edematous cornea, uneven expansion in lamellar interspacing and increased lamellar thickness in posterior stroma (depth > 200 μm) were identified, while the anterior stroma composed of interwoven collagen architecture remained unaffected. Our work demonstrate the capability of SHG imaging in providing morphological information for the investigation of corneal edema biophysics and that this approach may be applied in the evaluation of advancing corneal edema *in vivo*.

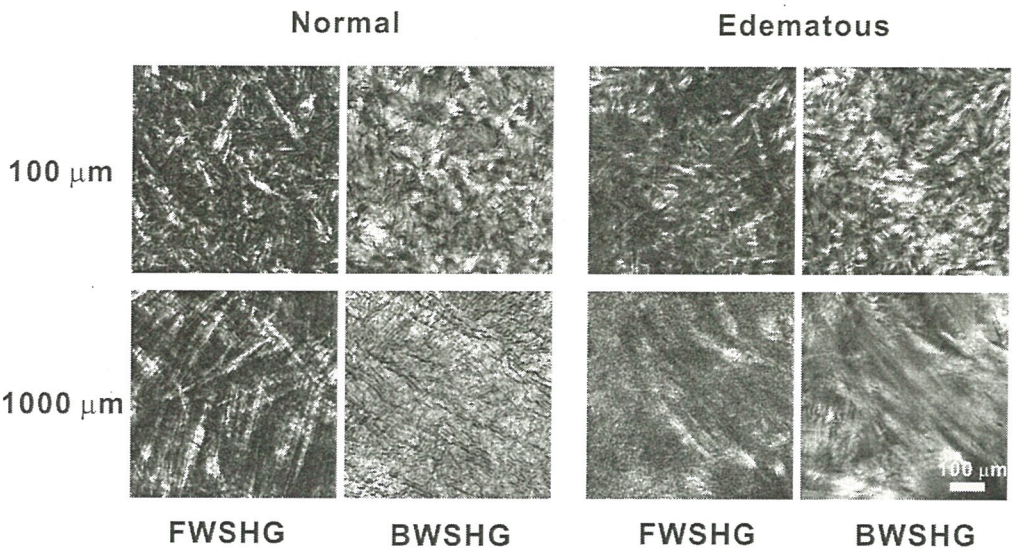

Figure 1 shows the *en face* FWSHG and BWSHG imaging of normal and edematous corneal stroma. Morphological features from the *en face* FWSHG images show that the edematous cornea has similar structural details compared to that found in the normal cornea. Furthermore, with increasing imaging depth, BWSHG image of the edematous cornea becomes similar in appearance to the FWSHG images in revealing the fibrous morphology of stromal collagen.

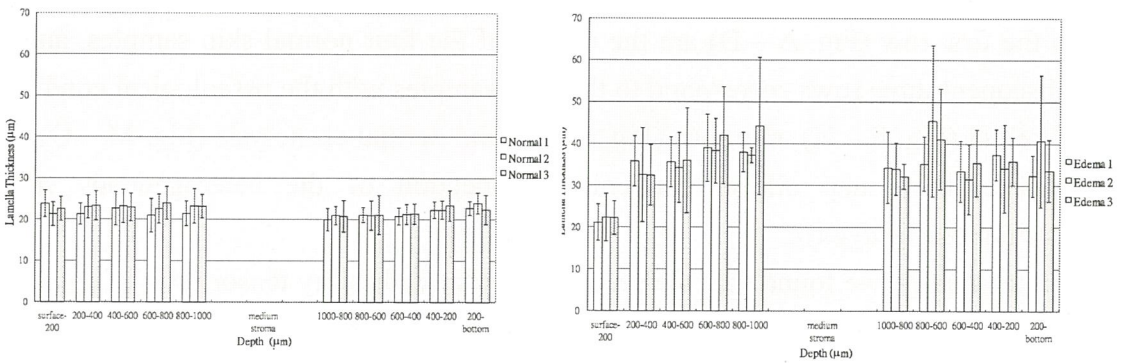

Figure 2 represents the statistics of lamella thickness between normal (left graph) and edematous (right graph) corneas. We found the increase of intralamellar spacing in edematous cornea group, and the associated lamella thickness increase occurred primarily in the posterior stroma. In the anterior region (<200 μm), the strongly cross-linked and tightly interwoven collagen matrix offers mechanical resistance to corneal expansion due to hydration.

Discrimination of Collagen in Normal and Pathological Dermis through Polarization Second Harmonic Generation

SU, Ping-Jung[1](蘇秉榮); CHEN, Wei-Liang[1]; HONG, Jin-Bon[3]; LI, Tsung-Hsien[1]; WU, Ruei-Jr[1]; CHOU, Chen-Kuan[1]; LIN, Sung-Jan[2,3]; DONG, Chen-Yuan[1]

[1] *Department of Physics, National Taiwan University, 1 Roosevelt Rd., Sec. 4, Taipei 106, Taiwan*

[2] *Institute of Biomedical Engineering, National Taiwan University, 1 Jen Ai Rd., Sec. 1, Taipei 100, Taiwan*

[3] *Department of Dermatology, National Taiwan University Hospital, 1 Jen Ai Rd., Sec. 1, Taipei 100, Taiwan*

Polarization-resolved, second harmonic generation (P-SHG) microscopy**[1, 2, 3]** at single pixel resolution is utilized for medical diagnosis of pathological skin dermis. In analyzing the large area, pixel by pixel, second order susceptibility of normal and pathological skin dermis, we found that P-SHG can be used to distinguish normal and dermal pathological condition of keloid, morphea, and dermal elastolysis**[4]**.

Fig. 1 shows the false-color map of the d_{33}/d_{31} second order susceptibility tensor element ratio for each of the sample. The palette at the upper right hand corner maps the pseudo colors corresponding to different numerical values of d_{33}/d_{31}. The images on the first row (Fig. A – D) are the results of the four normal skin samples, and the subsequent three rows correspond to the skin samples with the pathological conditions of keloid (Fig. E – H), morphea (Fig. I – L), and dermal elastolysis (Fig. M – Q). The pixel-resolved map allows convenient inspection of the heterogeneous spatial distributions of d_{33}/d_{31}.

Specifically, we found that the second order susceptibility tensor ratio of d_{33}/d_{31} for normal skins is 1.27±0.20, while the corresponding values for keloid, morphea, and dermal elastolysis are respectively 1.67±0.29, 1.79±0.30, and 1.75±0.31. We also observe that the histogram distributions of the d_{33}/d_{31} ratio for the pathological skins are 1.5 times wider than that of the normal case, suggesting that the pathological dermal collagen fibers tend to be more structurally heterogeneous.

Our work demonstrates that pixel-resolved, second-order susceptibility microscopy is effective for detecting heterogeneity in spatial distribution of collagen fibers and maybe used for future clinical diagnosis of collagen pathological conditions.

References

1. Chen, W. L., Li, T. H., Su, P. J., Chou, C. K., Fwu, P. T., Lin, S. J., Kim, D., So, P. T. C., and Dong, C. Y., Applied Physics Letters 2009 (94) 183902
2. Chu, S. W., Chen, S. Y., Chern, G. W., Tsai, T. H., Chen, Y. C., Lin, B. L., and Sun, C. K., Biophysical Journal 2004 (86) 3941
3. Plotnikov, S. V., Millard, A. C., Campagnola, P. J., and Mohler, W. A. Biophysical Journal 2006 (90) 693
4. Su, P. J., Chen, W. L., Hong, J. B., Li, T. H., Wu, R. J., Chou, C. K., Chen, S. J., Hu, C., Lin, S. J., and Dong, C. Y., Opt Express 2009 (17) 11161

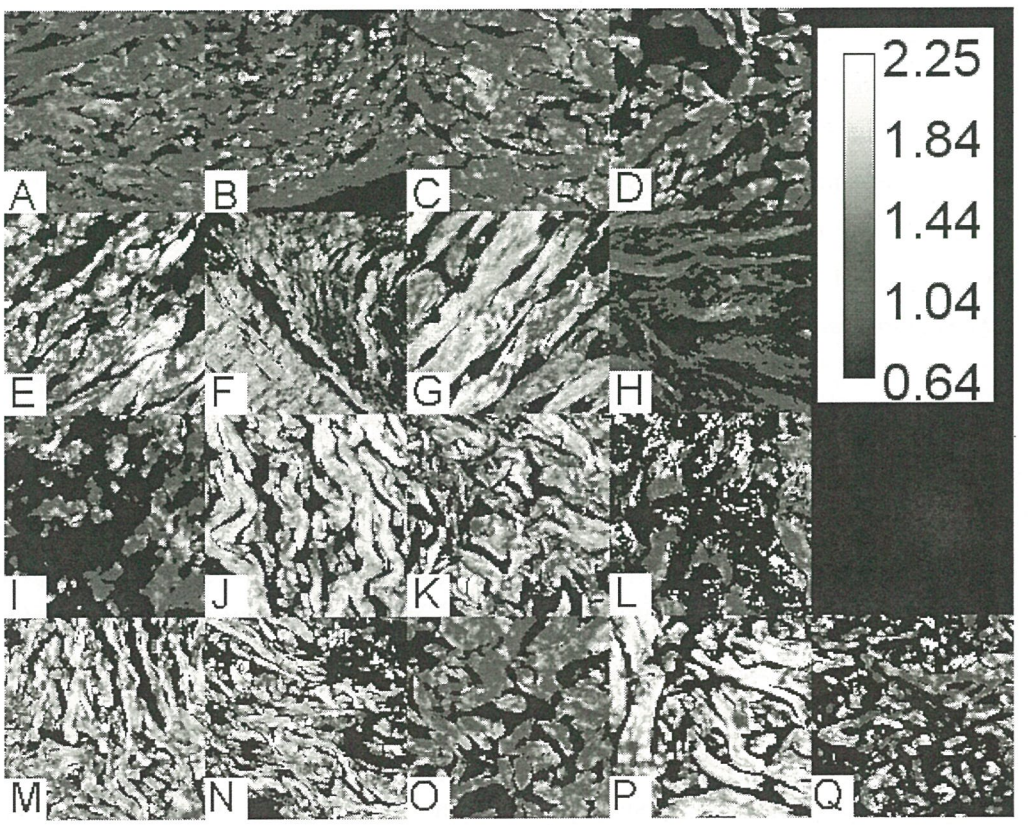

Fig. 1 Spatially resolved d_{33}/d_{31} maps for normal and pathological dermis are shown. A~D: normal, E~H: keloid, I~L: morphea, and M~Q: dermal elastolysis. The false color palette mapping the corresponding d_{33}/d_{31} values is displayed on the upper right corner. Each image size is 206×206 μm^2.

LABEL-FREE IMAGING AND CHARACTERIZATION OF *EX-VIVO* LIVER FIBROSIS USING MULTIPHOTON MICROSCOPY

SUN, Tzu-Lin[1](孫梓凌); LIU, Yuan[1]; SUNG, Ming-Chin[1]; CHEN, Hsiao-Ching[2]; YANG, Chuen-Huei[1]; HOVHANNISYAN, Vladimir[1]; CHIOU, Ling-Ling[2]; JENG, Yung-Ming[3]; LIN, Wei-Chou[3]; HUANG, Guan-Tarn[2]; KIM, Ki-Hean[4]; SO, Peter T. C.[4]; LEE, Hsuan-Shu [5,2]; DONG, Chen-Yuan[1]

[1] *Department of Physics, National Taiwan University, Taipei 106, Taiwan*

[2] *Department of Internal Medicine, National Taiwan University Hospital and National Taiwan University, College of Medicine, Taipei 100, Taiwan*

[3] *Department of Pathology, National Taiwan University Hospital and National Taiwan University, College of Medicine, Taipei 100, Taiwan*

[4] *Department of Mechanical Engineering and the Division of Bioengineering, Massachusetts Institute of Technology, MA, Cambridge 02139*

[5] *Institute of Biotechnology, National Taiwan University, Taipei 106, Taiwan*

Conventionally, liver fibrosis is diagnosed with the examination of histopathology specimens. This traditional method takes time in the specimen preparation through fixing, slicing and dying. Our goal is to apply multiphoton microscopy to efficiently obtain liver fibrosis imaging, with the advantages of label-free and high-contrast. In this work, the combined imaging modality of multiphoton autofluorescence (MAF) and second harmonic generation (SHG) was used for the qualitative imaging of liver fibrosis of different METAVIR grades under label-free, *ex-vivo* conditions. The quantification of liver fibrosis was also performed with SHG imaging to give an objective indicator in diagnosis.**[1]** We found that while MAF is effective in identifying cellular architecture in the liver specimens, it is the spectrally distinct SHG signal that allows the characterization of the extent of fibrosis. We found that without extrinsic labeling, qualitative SHG imaging can be used for the effective identification of the associated features of liver fibrosis specimens graded METAVIR 0-4 and the amount of collagen increase with the severity of liver fibrosis. Our approach demonstrates the potential of using tissue autofluorescence for hepatic cellular identification and SHG for the identification of liver fibrosis in the clinical setting and investigation of liver fibrosis in animal models *in-vivo*. **[2]**

References

1. Sun, W., et al., Nonlinear optical microscopy: use of second harmonic generation and two-photon microscopy for automated quantitative liver fibrosis studies. J Biomed Opt, 2008. 13(6): p. 064010.
2. Li, F.C., et al., In vivo dynamic metabolic imaging of obstructive cholestasis in mice. Am J Physiol Gastrointest Liver Physiol, 2009. 296(5): p. G1091-7.

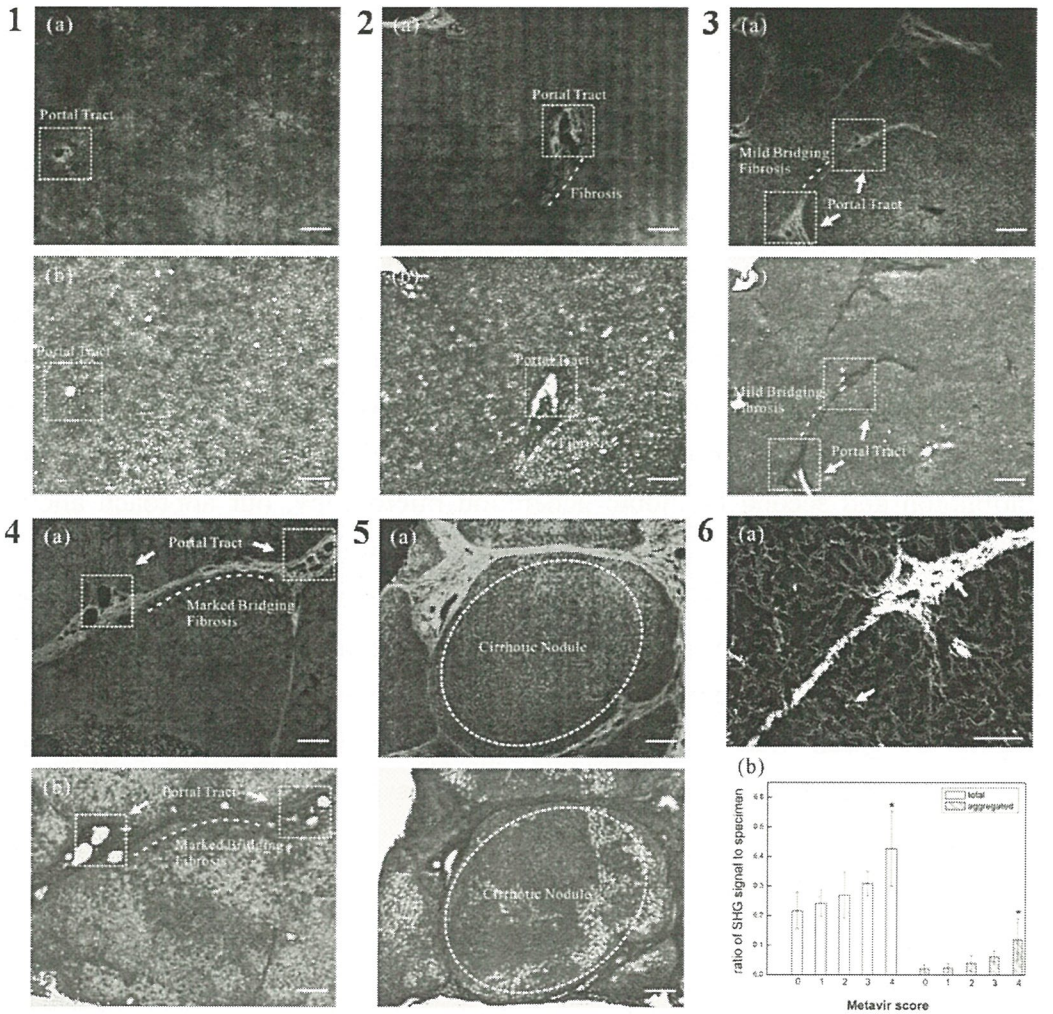

1(a) to **5(a)** show the multiphoton images of Metavir score 0 to 4 specimens, **1(b)** to **5(b)** are the respective histological comparisons of adjacent sections with Masson's trichrome staining. The green pseudo color in multiphoton image is the MAF signal from hepatocyte, the blue (380~400 nm) is the SHG form collagen fiber. **1** to **5** demonstrate the effective identification of morphological features of liver fibrosis graded 0 to 4 with multiphoton microscopy. **6(a)** is the SHG image for liver fibrosis quantification analysis, the white and yellow arrows indicate the distributed and aggregated collagen fibers respectively. We calculate the amount of total (aggregated and distributed) collagen fibers and aggregated to obtain quantitative indicators for diagnosing liver fibrosis. **6(b)** shows the amount of total and aggregated fibers increases with the severity of liver fibrosis. The two parameters have the potential to quantitatively classify progression of liver fibrosis. Scale bar is 200 μ m.

Intravital multiphoton microscopy for imaging hepatobiliary function

LI, Feng-Chieh[1](李峰杰); LEE, Yu-Yang[1]; SUN, Tzu-Lin[1]; LEE, Hsuan-Shu[2]; DONG, Chen-Yuan[1]

[1] *Department of Physics, National Taiwan University, Taipei 106, Taiwan*

[2] *Department of Internal Medicine, National Taiwan University Hospital, Taipei 100, Taiwan*

Liver is the body chemical factory, responsible for important functions such as metabolism and detoxification. When liver can not be regenerated in time to amend damages that has occurred, failure of hepatic functions such as liver failure and metabolic disease can result. Traditionally, the study of liver pathology has depended on histological techniques, but such methods are limited to ex-vivo observation. In order to study hepatic metabolism *in vivo*, we have designed a hepatic imaging chamber made of biocompatible titanium alloy (6V4Al-Ti). In combination with multiphoton and second harmonic generation microscopy, our approach allows the intravital observation of hepatic activities to be achieved.

As a demonstration of our technique, we used a non-fluorescent substance carboxyfluorescein diacetate (CFDA) as the substrate. Since the liver cells hydrolyze CFDA into carboxyfluorescein (CF) which emit green fluorescence, *in vivo* imaging of green fluorescence allows us to monitor the hepatic metabolism. Processes such as hepatic metabolism and disease progression can be studied using this methodology.

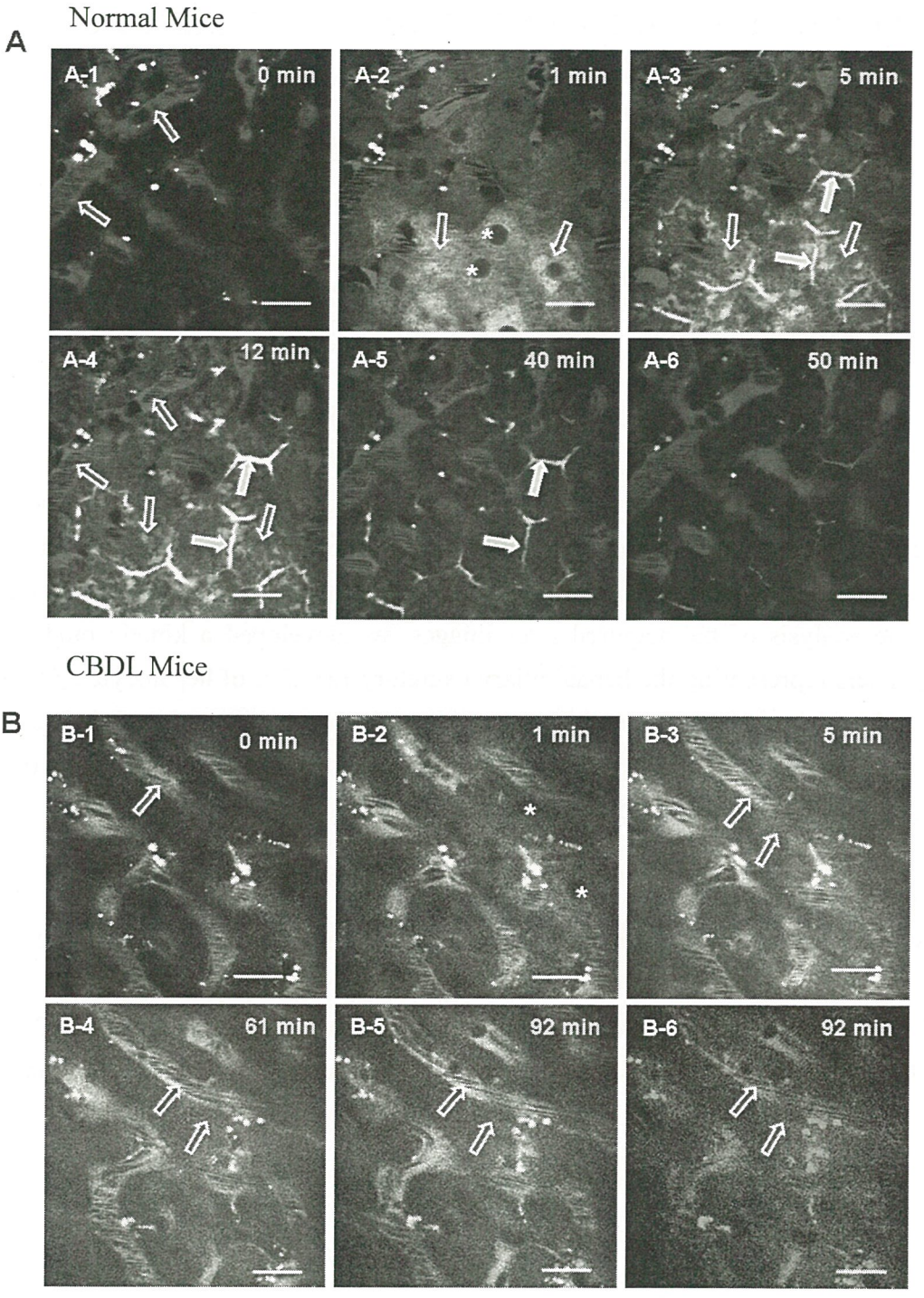

In normal mice, the green fluorescence disappeared from both the hepatocytes and the sinusoids within 50–60 min. In common bile duct ligation (CBDL) mice, by contrast, retention of the green fluorescence, especially in the sinusoid compartment, persisted within the whole observation period of 100 min. More interestingly, in CBDL mice the green fluorescence was more intense in sinusoidal veins than in hepatocytes at most time points. The fluorescence intensities in the sinusoids frequently oscillated much more than that of the hepatocytes.

UTILIZING TWO-PHOTON FLUORESCENT MICROSCOPY AND KINETIC MODEL TO MONITOR *IN VIVO* METABOLIC ACTIVITY OF MOUSE LIVER

LEE, Yu-Yang[1](李聿揚); LI, Feng-Chieh[2]; LIANG, Chih-Hueih[2]; LEE, Hsuan-Hsu[2] and DONG, Chen-Yuan[1]

[1]*Department of Physics, National Taiwan University, Taipei, Taiwan*

[2]*Department of Internal Medicine, National Taiwan University, Taipei, Taiwan*

Liver disease is an important issue in Asia, especially Taiwan, and the late phases syndromes of most chronic liver diseases are liver fibrosis. Currently, the severities of liver fibrosis are defined by the images of histological sections which are graded by their morphology. We attempt to establish a method to directly measure liver function using two-photon fluorescent microscopy**[1]** (TPFM) with a liver imaging chamber**[2]**. For the analysis of the acquired liver images, we developed a kinetic model with parameters representing the hepatobiliary excretory function of hepatocytes. Our data showed that, in the areas around fibrotic tissues, the hepatobiliary function decreases. These results demonstrate the potential of monitoring liver function by combining intravital two-photon microscopy and kinetic model of hepatic metabolism.

References:

1. So PTC, Dong CY, Masters BR, Berland KM. Two-photon excitation fluorescence microscopy. Annual Review of Biomedical Engineering 2000;2:399-429.
2. Liu Y, Chen HC, Yang SM, Sun TL, Lo W, Chiou LL, Huang GT, Dong CY, Lee HS. Visualization of hepatobiliary excretory function by intravital multiphoton microscopy. Journal of Biomedical Optics 2007;12:-.

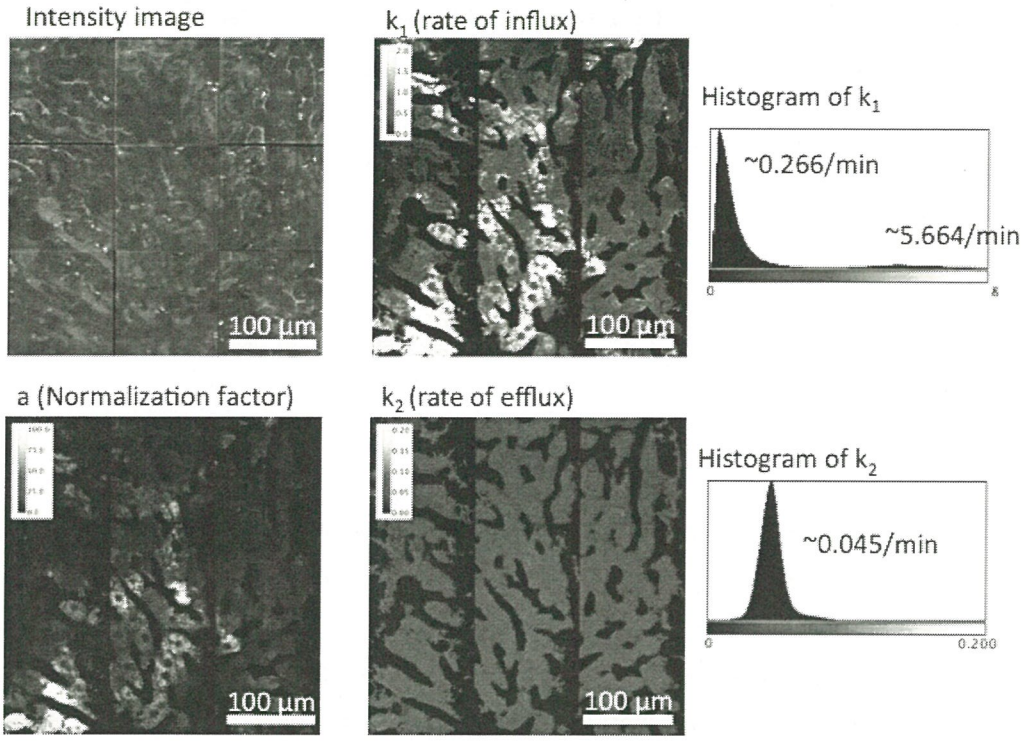

Fig 1. *in vivo* multiphoton fluorescence intensity image of normal mouse liver and the corresponding rate constants for each point in the multiphoton intensity image. k_1 and k_2 represent the rate of influx and efflux respectively. The rate constant values are represented by different colors as shown in the histogram. The parameter *a* is dependent on the total quantity of 6-CFDA flowed through the hepatocyte.

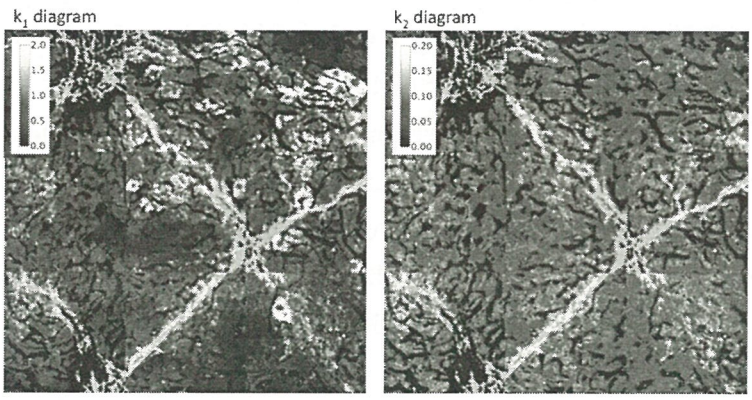

Fig 2. The k_1 and k_2 constant mapping for areas around collagen in a mouse with liver fibrosis. The images show that the rate of influx in higher around collagen. Besides, rates of efflux are similar in whole figure.

Comparison of Backscatter Electron Image (BEI) and Tradition SEM Image for the Observation of a Frafile *Lemna* (Duckeweed)

WU, Yeh-Hua（吳業華）[1]; YANG, Yuen-Po[2] and SHEUE, Chiou-Rong[1]

[1] *Department of Biological Resources, National Chiayi University（嘉義大學生物資源學系）, 300 Syeufu Rd., Chiayi 600, Taiwan.*

[2] *Department of Biological Sciences, National Sun Yat-sen University, 70 Lein-Hai Rd., Kaohsiung 804, Taiwan*

Lemna is a free-floating aquatic genus of the duckweed family (Lemnaceae). A solitary root with basal root sheath near attachment on ventral side is one of the taxonomic features. However, the feature of root sheath with somewhat transparent nature leads to the observational difficulty even with an aid of a stereomicroscope. In this study, *L. aequinoctialis* were observed by two kinds of scanning electron microscopy (SEM), a tabletop SEM combined with a pre-cryogenic EM specimen hold and liquid nitrogen treatment and a traditional SEM, for a comparison of image quality and technical requirement. In traditional SEM, we met two tough difficulties for this floating aquatic plant. One difficulty was due to *Lemna*'s floating nature which results in the samples could not sink at the stage of pre-fixation, even applied with Triton X-100. The other is the complicated procedures of dehydration and critical point drying (CPD) damaged the surface cells with evident shrinkage. However, the samples investigated with a tabletop SEM need only one treatment of rapid freezing with liquid nitrogen instead those of chemical fixation, CPD, and gold coating while with traditional SEM. These images obtained from a tabletop SEM are almost as intact as the living plants. More notable advantages including time saving, high efficiency and less cost were brought by the application of a tabletop SEM, especially for such a fragile aquatic. Certainly, this new method brings distinct benefit for acquiring morphological characteristics in this study.

References

1. Kao T. T.,Chen S. J., Chiuo W. L., Chuang Y.C., and Kuo-Huang L.L. 2008. Taiwania 53: 394- 400.
2. Landolt, E. 1986. Biosystematic investigations in the family of duckweeds (Lemnaceae), volume 2. The family of Lemnaceae—a monographic study, volume 1. Zürich: Veröffentlichungen des Geobotanischen Institutes der ETH, Stiftung Rübel, in Zürich (71 Heft).

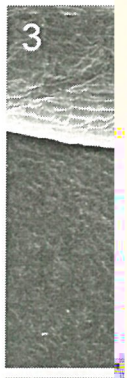

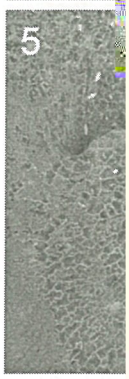

Fig. 1. Le
3. Traditi
root (R).
combined
aequinoc

The Ovule Development of Taiwanese Yew (*Taxus Sumatrana*)

LIN, Yan-You（林彥佑）[1]; CHIEN, Ching-Te[2] ; and KUO-HUANG, Ling-Long[1]

[1] *Institute of Ecology and Evolutionary Biology, National Taiwan University（臺灣大學生態學與演化生物學研究所）, 1 Roosevelt Rd., Sec. 4, Taipei 106, Taiwan.*

[2] *Division of Silviculture, Taiwan Forestry Research Institute, 53 Nan-Hai Rd., Taipei 100, Taiwan.*

Taxus L. (yew tree) is a glacial-remaining genus which can be traced back to Quaternary period. The genus includes several species around the world. The medical value of Taxane, the effective anti-cancer chemical extracted from *Taxus* L., has been highly emphasized for decades.

T. sumatrana (Miq.) de Laub. is a native yew species in Taiwan. Its nature restoration rate and seed maturing rate is quite low in wild stands. The sexual reproduction of European and Pacific yew has been well-researched in the last two decades, but that of *T. sumatrana* remains unknown. In this study, we were trying to clarify and recognize the stages of its sexual reproduction including megasporogenesis, female gametophyte development and embryo development.

The reproductive cycle of *T. sumatrana* is similar to those of European and North American species. In March, after the pollination drop appeared on the tip of micropyle, the megaspore mother cell started meiosis and developed into a female gametophyte (figure 1). By the end of May, the archegonium was well-developed (figure 2). Then, the egg cell was fertilized to form an embryo (figure 3). The embryo continued to develop until September (figure 4). The seed matured in October and its aril appeared in red.

In conclusion, during the development of ovule, the megaspore mother cell started to develop in February and the seed matured in October. The developmental stages can be recognized as the megaspore, megagametophyte, archegonium and embryo stages. Based on the result, the future work is to find out the factors affecting the seed maturing rate.

References:

1. Anderson, E. D. and Owens, J. N. Int J Pl Sci 1999(160) 459
2. Anderson, E. D. and Owens, J. N. Can J For Res 2001(31) 1046
3. Pennell, R. I. and Bell, P. R. Ann Bot 1987(59) 693
4. Pennell, R. I. and Bell, P. R. J Cell Sci 1988(89) 551

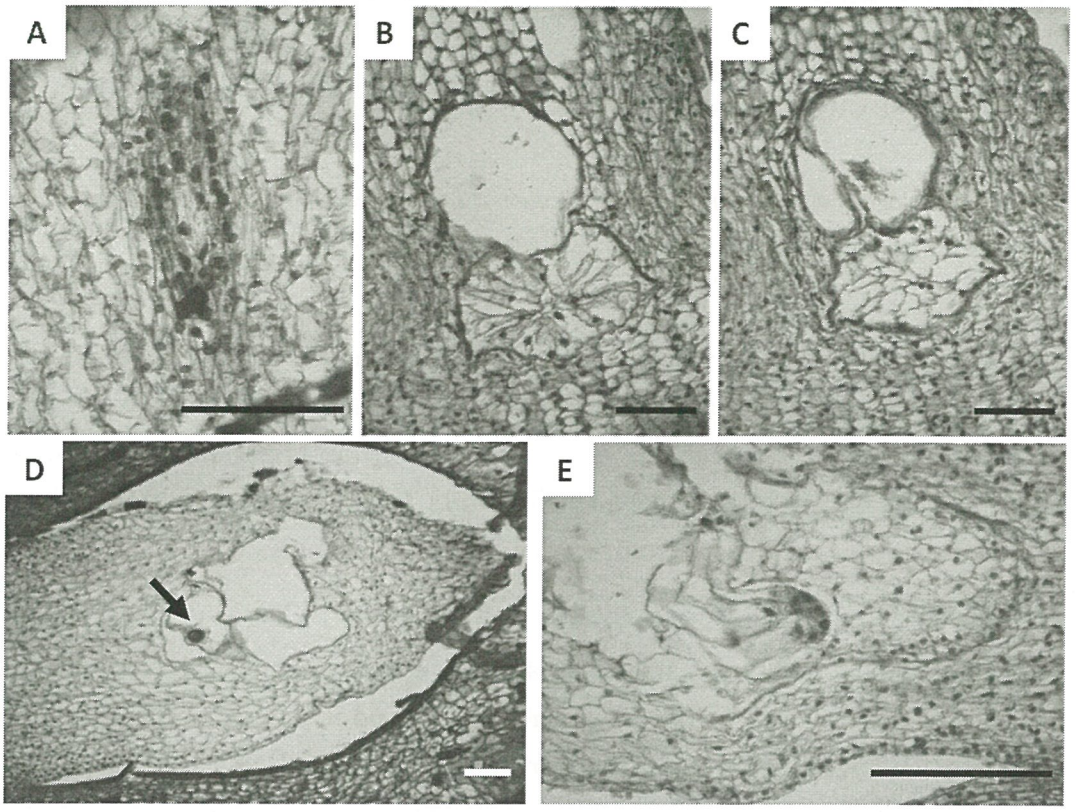

A) Four megaspores arranged linearly after meiosis in March.

B) Megagametophyte formed in April, and dividing cells arranged radially.

C) Developing megagametophyte, the cell wall of the divided cells formed in May.

D) Archegonium stage, the egg was fertilized in late May.

E) Early stage of developing embryo, mid June.

Arrow: fertilized egg; Bars = 100 μm.

Anatomical Features in Branches of *Koelreuteria henryi* Dummer

HUNG, Li-Fen（洪麗分）and KUO-HUANG, Ling-Long

Institute of Ecology and Evolutionary Biology, National Taiwan University （臺灣大學生態學與演化生物學研究所）, 1 Roosevelt Rd., Sec. 4, Taipei 106, Taiwan.

Anatomical features on the upper side and lower side of branches of *Koelreuteria henryi* Dummer were studied to understand the distribution of reaction wood. In most woody angiosperms, the reaction wood develops on the upper side of the inclined stems or branches in zones where tensile stress is large and called tension wood. Typical tension wood differs from normal wood in anatomy, with gelatinous fibers and a promoted radial growth [1].

In this study, gelatinous fiber was absent on both upper and lower side of the branches of *Koelreuteria henryi* Dummer (Fig 1). And it showed an increased radial growth on the lower side in stead of upper side (Fig 2). .

The microfibril angles (MFAs) of the S2 wall layer in fibers (Fig 3) measured by iodine method[2] were ranged from 18.28 ±2.96° to 26.93±4.40°. Six out of nine measurement sites showed significant difference of MFAs between the upper and lower sides, but no specific pattern was found. These results did not agree with the observation of Okuyama *et al*[3]. They found that in species without gelatinous fibers such as *Mangolia* and *Liriodendron*, the MFA was smaller in the tension wood than the normal wood. The fibers were similar or longer on the lower site than on the upper side (Fig 4).

In conclusion, in the branch of *Koelreuteria henryi* Dummer, gelatinous fibers was absent, the promoted radial growth and longer fibers were found on the lower side, and the MFAs showed no apparent pattern. That is, no typical tension wood anatomy was observed in the branch of *Koelreuteria henryi* Dummer.

References:

1. Evert, R. F., 2006. Esau's Plant Anatomy 3rd ed. John Wiley & Sons, Inc., Hoboken, New Jersey.
2. Senft, J. F., and Serimma, R. Wood and Fiber Science.1985 17(4) 564-567
3. Okuyama, T., Yamamoto, H., Yoshida, M., Hattori, Y., and Archer, R.R. Ann. Sci. For. 1994 (51) 291.

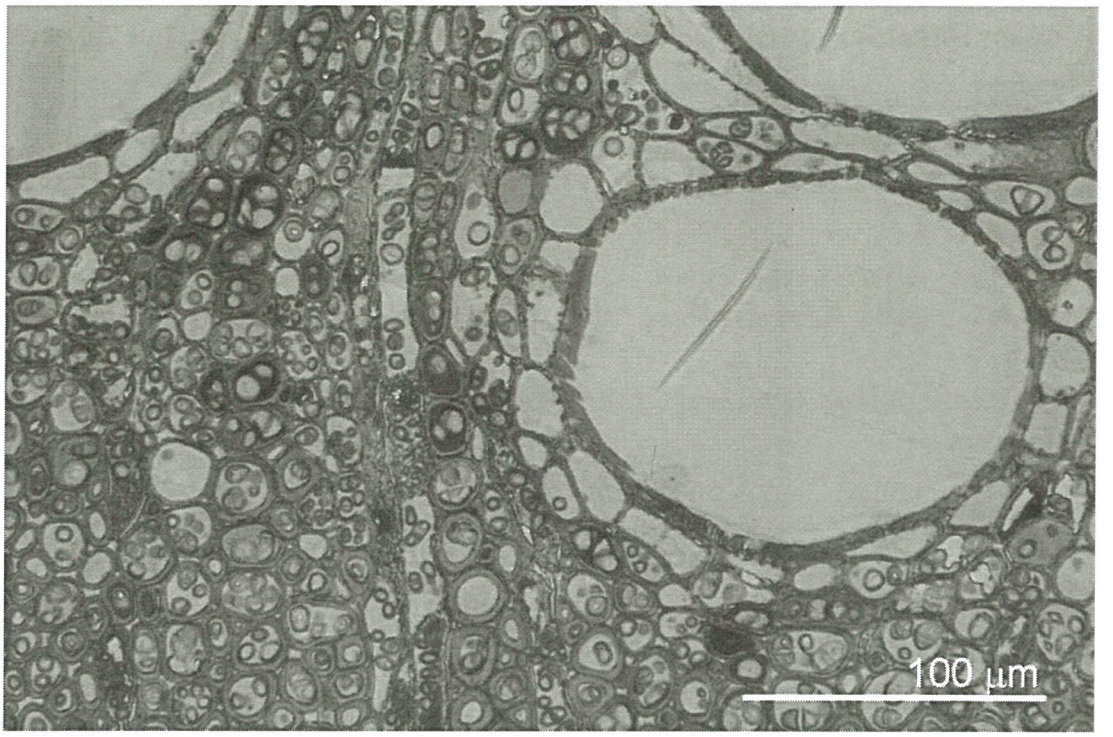

Fig 1. Secondary xylem of *K. henryi* Dummer on upper side of branch in transverse section showing no gelatinous fiber. The fibers and ray parenchyma contained starch grains. Each vessel was surrounded by a layer of axial parenchyma.

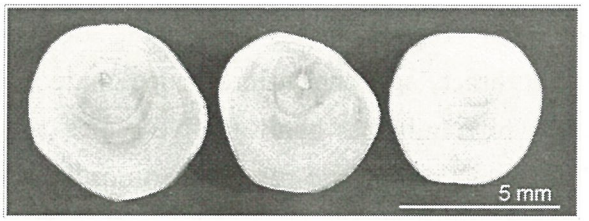

Fig 2. Cross sections of T11 branch showing eccentric growth

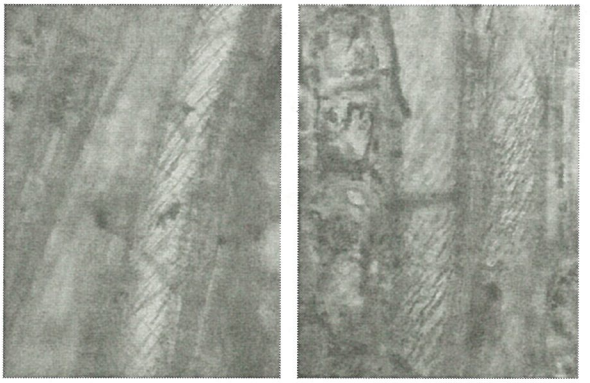

Fig 3. S2-MFA of fibers in upper side (left) and lower side (right) in site 2 of T12 branch

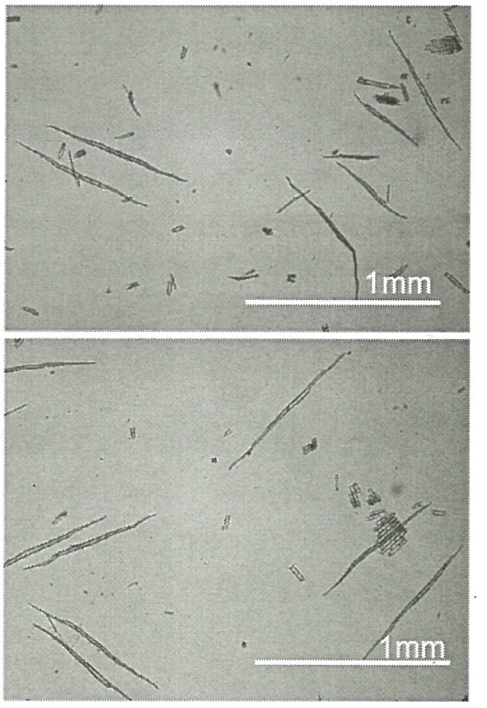

Fig 4. Fibers in upper side (up) and lower side (down) in site 3 of T11 branch

Flower Development of Pear Flower-Budwood in Lowland of Taiwan

TSAO, Ching-Wen（曹靖玟）[1]; CHEN, Shiang-Jiuun[1];SHIH, Jau-Chang[2]; and KUO-HUANG, Ling-Long[1]

[1] *Department of Life Science, Institute of Ecology and Evolutionary Biology, National Taiwan University（臺灣大學生態學與演化生物學研究所）, No. 1, Sec. 4, Roosevelt Rd., Taipei 10617, Taiwan.*

[2] *Crop Science Division, Agricultural Research Institute, No.189, Jhongjheng Rd., Wufong , Taichung 41301, Taiwan.*

Pear , *Pyrus*, is a temperate fruit tree with high economic value. In the Taiwan lowland, pears are mainly produced by top-grafed technique [1]. Research of morphology and development of pear flower bud is little, and most focused on the terminal buds of the spurs [2, 3, 4].

In this study, Materials are pear flower-budwoods of two cultivars, *Pyrus Pyrifolia* Nakai cv. Whangkeumbae from Shueili on Oct. 24, 2008 and *P. Pyrifolia* Nakai cv. Julip from Lalashan on Dec. 3, 2008. We used stereomicroscope, SEM (scanning electron microscope), and paraffin section to examine the external morphology and internal structure of pear flower buds. A flower bud of Whangkeumbae has about twelve scales, ten bracts and one inflorescence composed of nine flowers and one leaf primordium, while Julip has about twelve scales, nine bracts, and one inflorescence composed of eight flowers and two leaf primordia. On Oct. 24, 2008, Whangkeumbae (n=56) had about71.4% flower buds (Fig. D, E, F), and more than a half of flower primordia developed to the last stage (Fig. K, L) to have sepals, petals, stamens and pistils, while on Dec. 3, 2008, Julip (n=47) had about74.5% flower buds, and flowers almost developed to the last stage (Fig. L).

The result, to some degree, was coincided with the previous studies [2, 3] for the pistil initiated. However, we found that not all flower buds have the same stage on the flower-budwoods, even on the same flower-budwood. And we'll do more research to get thorough flower development of pear flower-budwood.

References

1. Liaw et al., Pro. of a Sym on Cul. Tech. and Man. in Pear, 2005
2. Kiyoshi, B., Shinji, H. and Kenji, T. J. Japan Soc. Hort. Sci. 1986 (55) 258-265
3. Shu-Ang, P. and Shuichi, I. J. Japan Soc. Hort. Sci. 1994 (63) 313-321
4. Tomoya, E., Ryutaro, T. and Keizo,Y. J. Japan Soc. Hort. Sci. 2007 (76) 210-216

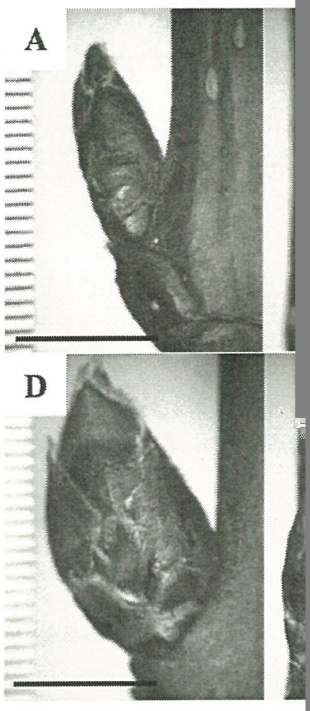

A, D. Two kinds of
flower-budwood. Leaf bu
large and plump. Bars = 1
(←) has no flower merist
C, F. The paraffin sectic
several layers of undiffer
has many flowers (only o

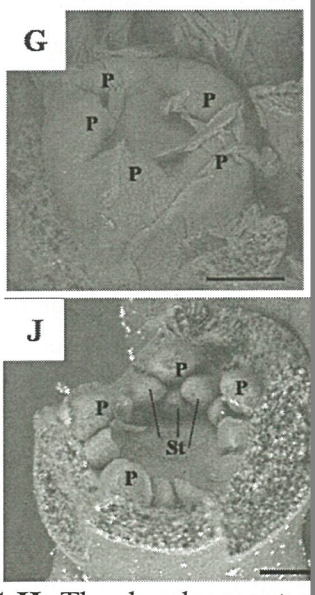

G-H. The development o
(G), then the margin becc
with the sepals (I), then
slightly raising (K) to ap
100μm.

Morphological and GFAP-Like Immunocytochemical Alterations in the Central Nervous System of the Gerbil after Heatshock and Hyperthermic Treatment

YU, Shang-Ming（游祥明） [1]; Chiang, Wei-Hui [2]; and LIN, Kwan-Hwa [3]

[1] *Department of Nursing, College of Nursing, Central Taiwan University of Science and Technology（中臺科技大學護理系）, Taichung, Taiwan*

[2] *Institute of Anatomy and Cell Biology, National Yang-Ming University, Taipei, Taiwan*

[3] *Graduate Institute of Physical Therapy, School of Physical Therapy, National Taiwan University, Taipei, Taiwan*

Pretreatment of the heat shock under the environmental stress induced neuronal protection from the stress insult and maintained the internal homeostasis. Gerbils were used in this study for heat shock and hyperthermic treatment. The heat shock experiment was processed under/ the 42^0C for 30 min (H_0) and recovered for 24 hours (H_{24h}). Thereafter, the hyperthermic treatment was processed under 45^0C for 60 min ($H_{24h}S_0$) and recovered for 4 ($H_{24h}S_{4h}$), 18 ($H_{24h}S_{18h}$) and 24 hours ($H_{24h}S_{24h}$). Animals were fixed in 6 % paraformaldehyde-lysine-periodate fixative and the brains were washed dehydrated through a series of ethanol from 50%, 70%, 95% to absolute ethanol, immersed in xylol, paraffin/xylol (1:1), and embedded in paraffin. The blocks were section by Reichert-Jung microtome at 5 μm. The sections were stained by methylene blue. Immunocytochemical staining was performed as follows: (1) incubation in rabbit antiserum to GFAP (GFAP, diluted 1:75, Zymed, CA, USA) for 14-16 hours; (2) incubation in goat anti-rabbit biotinylated gammaglobulin (Vectastain ABC kit, Vector Laboratories, Burlingame, CA, USA) for 1-2 hours; (3) incubation in ABC complex (Vectastain ABC kit, Vector Laboratories, Burlingame, CA, USA) for 1-2 hours ; (4) treatment with 3,3'-diaminobenzidine etrahydrochloride (DAB, 0.3 mg/ml, Sigma, USA) in 0.05 M Tris buffer, pH 7.6, containing 0.002% H_2O_2, until the reaction site was visible. All incubations were carried out at room temperature. Finally, the slices were dehydrated in ethanol, cleared in xylene, and coverslipped. In control samples, the first antibody was replaced by (1) normal rabbit or (2) PBS. The striking change of brain area as following：methylene blue stained cells changed from cuboidal shape to elongated at H_0 in the ependymal cell layer of the lateral ventricle. In the ependymal cell layers of the lateral ventricle, GFAP-like-IR was found moderately in the controls(Fig. A), decreased at H_0 (Fig. B), returned to that of the controls at H_{24h} (Fig. C), remained unchanged at $H_{24h}S_0$ (Fig. D), decreased at $H_{24h}S_{4h}$ (Fig. E), increased at $H_{24h}S_{18h}$ (Fig. F) similar to that of the H_{24} from the insult, and increased markedly at $H_{24h}S_{24h}$ (Fig. G).

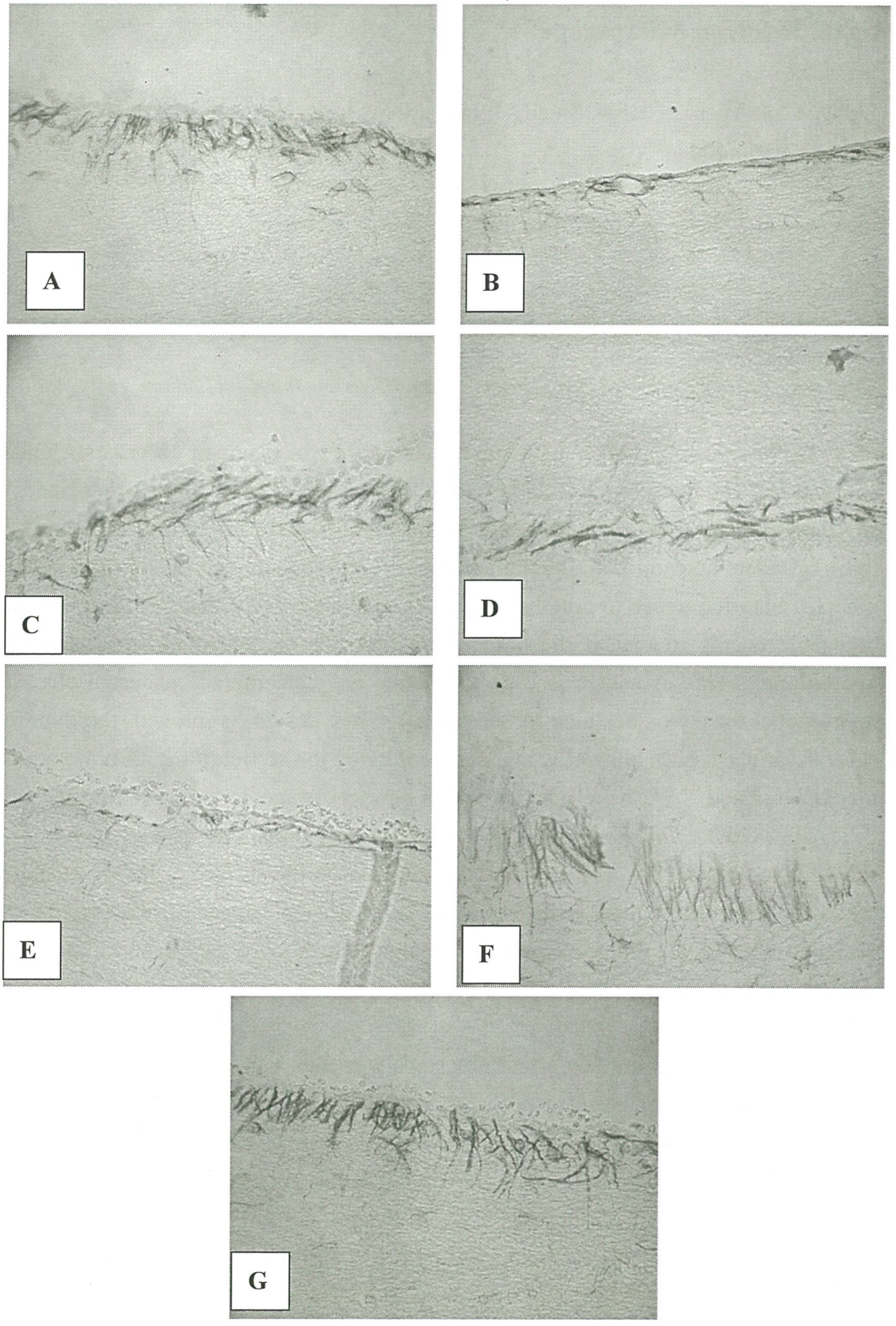
A
B
C
D
E
F
G

A Simple Cyrostage Facilitates Cryo-Specimen Observation under an Usual Electron Microscope

TANG, Chih-Yuan[1] , CHEN, Shiang-Jiuun[2], LIN, Ching-Yen[1],
HUANG, Rong-Nan[3,4](黃榮南)

[1] *Instrumentation Center, National Taiwan University, Taipei 106, Taiwan*
[2] *Department of Life Science, Institute of Ecology and Evolutionary Biology and TechComm-5, College of Life Science, National Taiwan University, Taipei 106, Taiwan*
[3] *Department of Entomology, College of Bioresources and Agriculture, National Taiwan University, Taipei 106, Taiwan*
[4] *Research Center for Plant-Medicine, National Taiwan University, Taipei 106, Taiwan*

A pre-cryogenic holder (cryostage) facilitate cyro-specimen observation under an usual electron microscope is described in these studies. This cryostage includes a specimen holding unit (the stub) and a cryogenic energy storing unit (a composite of three cylinders assembled through a screw). The cryogenic energy storing member includes a storing trench to hold liquid gas (ex. liquid nitrogen) that further supply the cryogenic energy to extend the observation time for the specimen in an electron microscope. This cyrostage is easy to operate and can upgrade an usual electron microscope for cyro-specimen observation. This design is proved feasible for several variety tissues and cells, and can be applied to the field of both biology and material science. We have employed this new cryostage for observation of yeast cells, cultured *dinoflagellates*, trichome and epidermal cells in the leaf of *Arabidopsis thaliana*, red blood cells, filiform papillae scattered on the surface of rat tongue, agar medium, water molecules, *pencillium* etc. All results suggested that the newly designed cryrostage was applicable for cryo-specimen observation under an usual electron microscope.

We have investigate the current cryostage was also applicable and function well in different module of electron microscope including Hitchi TM-1000, and S-800, both are usual electron microscope without cooling system. This cryostage could be modified and also workable to different types of electron microscope. Most importantly, the design of this cryostage is simple and easy to operate and could upgrade an usual electron microscope to a cryo-EM affordable for most laboratory.

References

1. Refshauge, S., Watt, M., McCully, M. E. and Huang, C. X. New Phytologist 2006 (172) 369
2. Tong, C. Y. Patent Pending, 2008

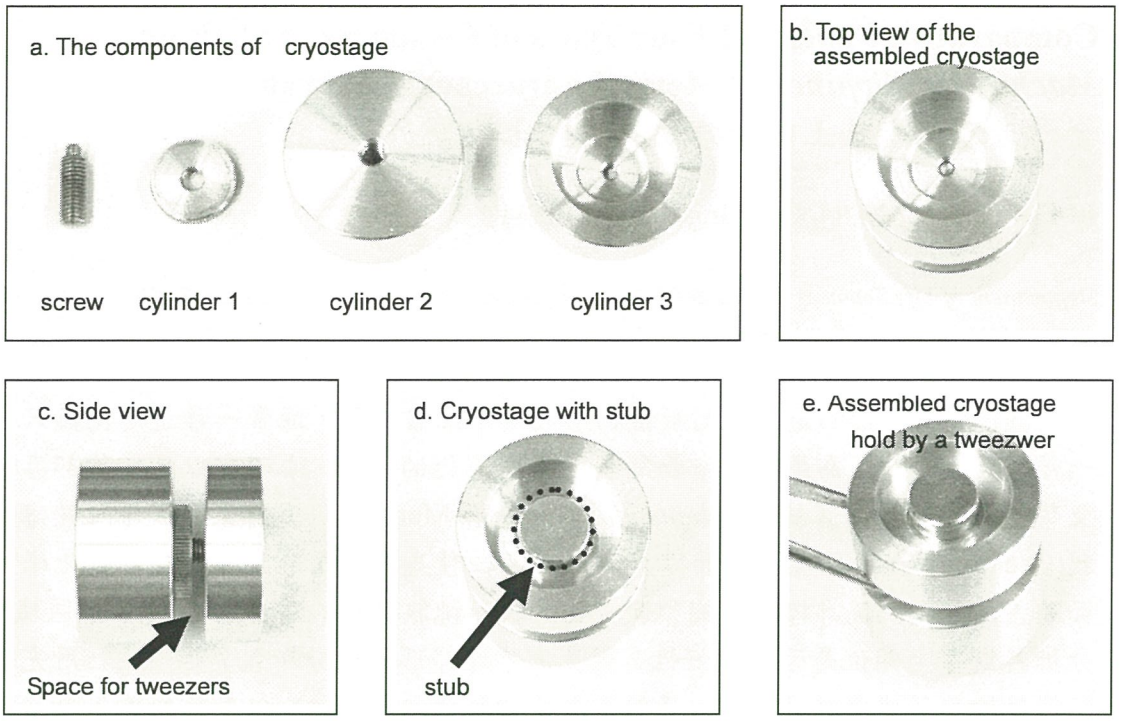

Figure 1. The components and assemble of the cryostage. The newly designed cryostage include three cylinders and one screw all made with stainless steel (a). The three cylinders were assembled together through the stainless screw (b & c). The cyclinder 2 served as the pedestal of the cryostages and cylinder 3 form a U-shape located on the top of the cyrostage to support the stub and hold back liquid nitrogen. During assembling, 0.5 cm interval was left for the cyrostage to be hold by a forcep in-between the pedestal (cylinder 2) and the cylinder 1 in the middle (d & e). The assemble of cylinders by a screw made its height adjustable for focus tuning during practicing under electron microscope. In practice, the specimen holder (stub) was screwed into the top cylinder (cylinder 3) of the cryostage (b). This cyrostage not only function as a specimen holder, but also can hold back (retain) liquid nitrogen in the fillister (trench) of the top cylinders to keep temperature low long enough (30 min) for observation under electron microscope.

Comparative Biology of Four Types of Cecidomyiid Galls on *Machilus philippinensis* Merr. (Lauraceae) in Taiwan
台灣產菲律賓楠上四種癭蚋蟲癭之比較

Jo-Fan Chao(趙若帆), Gwo-Ing Liao(廖國嫈)

Department of Life Sciences, National Cheng Kung University, Tainan 701, Taiwan, R.O.C.
國立成功大學生命科學系

蟲癭(insect gall)是昆蟲刺激植物形成的不正常組織，通常一種造癭昆蟲只在一種植物上造癭，為昆蟲與植物間長期共同演化的結果。本研究以具有葉部蟲癭及芽部蟲癭的菲律賓楠(*Machilus philippinensis* Merr.)為研究對象，探討四種癭蚋科(Cecidomyiidae)昆蟲引發菲律賓楠形成的四種蟲癭，在形態構造及組織化學方面的差異。我們統計棒狀、倒卵狀、長針狀和桃狀蟲癭在寄主植物的分布區域，分析其對寄生部位是否有偏好性；測量癭體外部形態並分析差異性；並利用光學顯微鏡檢視菲律賓楠的葉部、芽部及蟲癭切片的組織構造，以多種組織化學染色法觀察其組織化學上的差異性。結果顯示：(一)棒狀蟲癭好發於葉近軸面(89%)，倒卵狀蟲癭則好發於葉遠軸面(91.7%)，而長針狀和桃狀蟲癭皆發生於頂芽或側芽；(二)棒狀蟲癭體型最窄(1.38±0.14mm)；倒卵狀蟲癭體型最短、最寬(5.48±0.72mm×2.93±0.47mm)；長針狀蟲癭體型最長(20.6±1.23mm)；桃狀蟲癭長度次之(10.02±0.46mm)；(三)棒狀蟲癭表面有短毛及9~12條縱稜，倒卵狀蟲癭表面光滑且有不明顯縱稜，長針狀與桃狀蟲癭表面皆光滑且無稜；(四)菲律賓楠的葉肉組織分化成柵狀組織及海綿組織，但發生於葉部的棒狀及倒卵狀蟲癭之表層下的組織皆無此分化現象，通稱為皮層，且兩者內部組織構造差異大；(五)菲律賓楠的芽由多層幼葉包覆，幼葉表面上有茸毛，且芽軸的維管束仍在發育初期，然而發生於芽部的長針狀與桃狀蟲癭表面皆光滑且維管束分化完全；(六)菲律賓楠的幼葉組織內有大量的分泌細胞分布，倒卵狀和桃狀蟲癭皮層中的分泌細胞數量很少；(七)四種蟲癭在表面皆被有蠟質，而單寧、澱粉粒和蛋白質顆粒則具多寡及有無的差異。分析結果顯示癭蚋科昆蟲寄生菲律賓楠有寄生部位的偏好性，且蟲癭的表面特徵與內部組織分化異於葉部及芽部；儘管是寄生於同種植物的相同器官部位，不同種癭蚋科昆蟲引發菲律賓楠的蟲癭，在癭體的長度及寬度、表面特徵、內部組織結構與組織化學特性皆具多樣性。

References

1. Scareli-Santos, C. and Varanda, E. M. 2003. Morphological and histochemical study of leaf galls of *Tabebuia ochracea* (Cham.) Standl (Bignoniaceae). Phytomorphology (53) p.207-214.
2. Yukawa, J. and Rohfritsch, O. 2005. Biology and ecology of gall-inducing Cecidomyiidae (Diptera). *In* Biology, ecology and evolution of gall-inducing arthropods. *Edited by* A., Raman, C. W., Schaefer, T. M., Withers. Science Publishers, Inc., Vol.1, p.273-297.

圖一 菲
織中散生
細胞；C
多層幼葉
大量單寧
營養細胞
維管束。

Cryo-Electron Tomography Study of CSPIO Which Uptake by Phagocyte

Chun-Ying Tsai（蔡俊穎） [1], Hsin-Yu Lin [1], Jin-Sheng Tasi [2], Tzu-Chen Yen [3], Fu-Rong Chen [1]

[1] *Center for Electron Microscopy, Department of Engineering and System Science, National Tsing-Hua University（清華大學工程與系統科學系）, HsinChu County, Taiwan(R.O.C.)*

[2] *National Synchrotron Radiation Research Center, HsinChu County, Taiwan*

[3] *Molecular Imaging Center, Chang Gung Memorial Hospital, Taoyuan County, Taiwan*

After the concept of "magic bullet" from Nobel Prize winner (1908) Paul Ehrlich, passively targeting nanocarriers first reached clinical trials in the mid-1980s, and the first products, based on liposomes and polymer–protein conjugates, were marketed in the mid-1990s. Nanocarriers are nanosized materials that can carry multiple drugs [1] and/or imaging agents [2].

In recent years, the super paramagnetic iron oxides (SPIOs) have been widely regarded as an alternative to replace Gadolinium diethylene-triamine pentaacetic acid (Gd-DTPA) as a magnetic resonance imaging (MRI) contrast agent for its paramagnetic and non-toxic characteristic. Nanosize SPIOs are usually warped with bio-compatible materials, such as dextran or chitosan. The assembled SPIOs particle size and also its wrapping materials strongly affect its uptake mechanism by phagocyte, stability and magnetic properties.

Cryo-electron microscopy tomography of biological material images is a useful tool to reduce the radiation damage from electron beam exposures. This article has investigated the Chitosan Super Paramagnetic Iron Oxides (CSPIO) 3D structure which uptake by phagocyte use cryo-electron tomography in the JEOL 2010F electron microscope. The acquisition angle of tomography series is from -61° to +59°, 1 degree interval, and the 3D volume was reconstructed by weight back projection (WBP) method. The average particle size is about 10~15nm. The morphology and 3D structure of CSPIO before uptake by phagocyte shows in Fig.1(a) and (b), respectively. Fig 2(a) and (b) shows the result of the CSPIO that was uptaked by phagocyte after 72Hr.

References

1. Gottesman, M. M., et al., Nat. Rev. Cancer 2, 48–58 (2002).
2. Morawski, A. M., et al., Curr. Opin. Biotechnol. 16, 89–92 (2005).

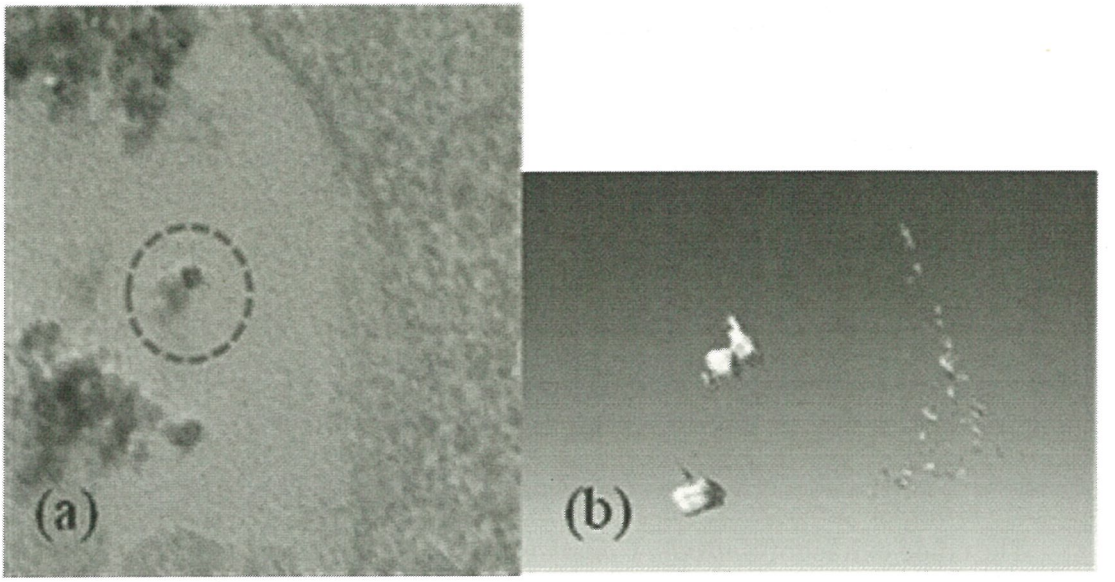

Figure 1. (a) The morphology. (b) 3D structure of CSPIO before uptake by phagocyte

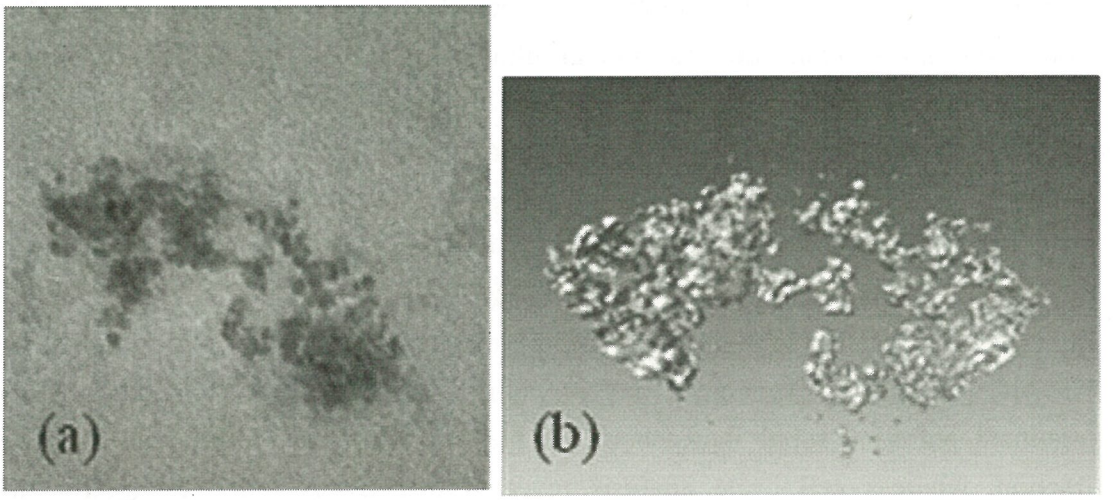

Figure 2. (a) BF image. (b) 3D structure of CSPIO which were uptake by phagocyte after 72 hour.

Cytotoxic Effects of Dehydroeburicoic Acid in Human U87MG Glioblastomas

DENG, Jhu-Yun（鄭瓊娟）[1]; CHEN, Sian-Jin[1]; JOW, Guey-Mei[2]; and JENG, Chung-Jiuan Jeng[1]

[1] *Institute of Anatomy and Cell Biology, School of Medicine, National Yang-Ming University（陽明大學解剖學暨細胞生物學研究所）, No. 155, Section 2, Li-Non Street, Taipei 12212, Taiwan*

[2] *School of Medicine, Fu-Jen Catholic University, Hsin-Chuang, Taipei County, Taiwan*

The crude extract of *Antrodia Camphorata* has been reported to display cytotoxic effects to various tumor cell lines. It remains unclear; however, what compounds within the crude extract are responsible for generating the cytotoxic effect. We therefore examined the anti-proliferation effect of 15 kinds of triterpenoids purified from *Antrodia Camphorate* on human glioblastoma U87MG cells. MTT assay indicated that three triterpenoids purified from *Antrodia Camphorat*, including methyl antcinate K, dehydroeburicoic acid, and eburicoic acid, can effectively inhibit cell proliferation. Among these three compounds, dehydroeburicoic acid (DeEA) is the most effective one. Therefore, we focused on DeEA to examine the underlying mechanisms of its cytotoxic effects on U87MG cells. MTT and LDH release assays indicated that DeEA inhibited the proliferation of the human glioblastoma cell U87MG. In addition, Annexin V and propidium iodide staining showed that DeEA treatment led to a rapid increase of glioblastomas in the necrotic/late apoptotic fraction, whereas cell cycle analysis revealed that DeEA failed to significantly enhance the population of U87MG cells in the hypodiploid (sub-G1) fraction. Using electron microscopy, we found that DeEA induced significant cell enlargements, massive cytoplasmic vacuolization, and loss of mitochondrial membrane integrity. Importantly, DeEA cytotxicity in U87MG cells was caspase-independent. DeEA treatment triggered an intracellular Ca^{2+} increase, and DeEA-induced cell death was significantly attenuated by BAPTA-AM, but not EDTA or EGTA. DeEA induced a reduction of mitochondrial transmembrane potential. Moreover, we demonstrated that calpain inhibitors effectively blocked LDH release from DeEA-treated cells. Taken together, these results suggest that in human glioblastomas, DeEA induces necrotic cell death that involves Ca^{2+} overload, mitochondrial dysfunction, and calpain activation.

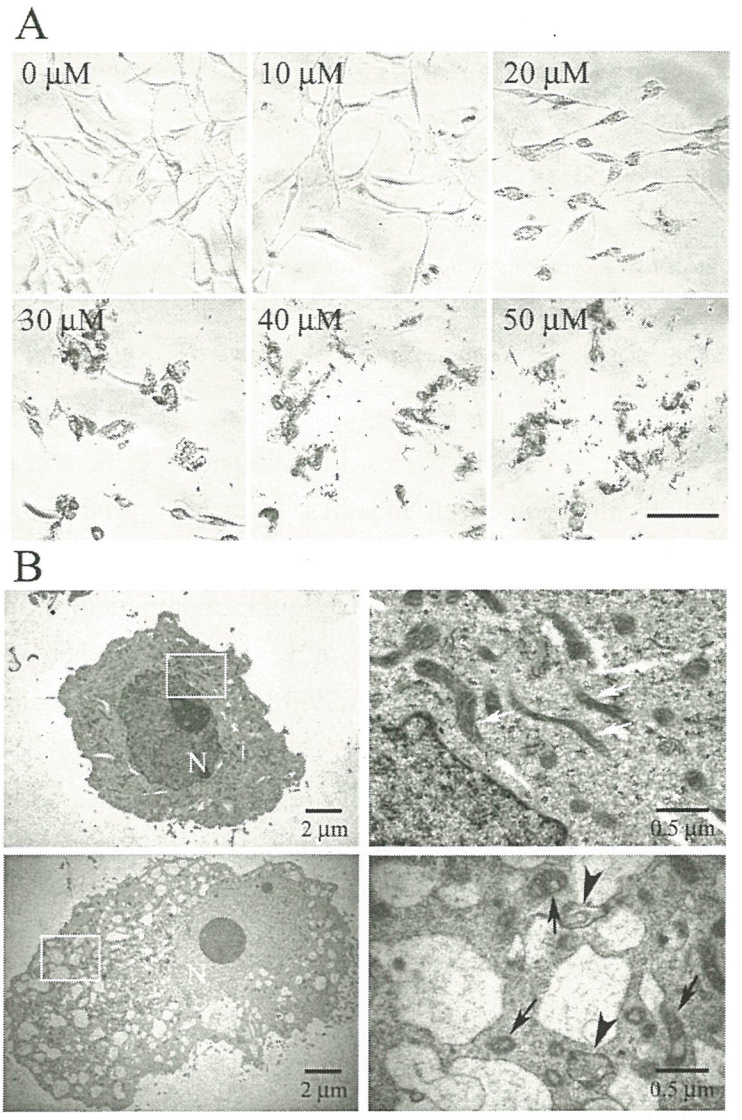

Morphological characterizations of DeEA-treated U87MG cells.

(A) U87MG cells were treated with the indicated concentrations of DeEA for 12 hours, followed analyses with phase-contrast microscopy. Scale bar: 100 μm. (B) Electron microscopic images of U87MG cells without (*upper panels*) or with (*lower panels*) 30 μM DeEA treatment for 12 hours. The areas highlighted in white boxes (*left panels*) were viewed under a higher magnification (*right panels*). Control U87MG cells (*upper panels*) displayed well-defined plasma membrane, mitochondria with intact crista structure (*white arrows*), and nuclear envelope containing nuclei (*N*). In contrast, extensive cytoplasmic vacuolization was observed in DeEA-treated cells (*lower panels*). High-power magnification of DeEA-treated cells further revealed rounded mitochondria with disrupted internal structure (*black arrows*), extensive cytoplasmic vacuolization, and autophagosomes (*arrowheads*). The autophagic vacuoles contained membranous whorls.

The Morphological Study on Pollen and Stigma Dimorphi
Limonium Sinense (Girard) Kuntze (Plumbaginaceae)

LAI, Guan-Chung（賴冠中）[1]; LIU, Ho-Yih[2]; and CHEN, Su-Hwa[1]

[1] *Institute of Ecological and Evolutionary Biology, National Taiwan University（臺灣化生物學研究所）, 1 Roosevelt Rd., Sec. 4, Taipei, Taiwan.*

[2] *Department of Biological Sciences, National Sun Yat-Sen University, 70 Lien-Hai Ro Taiwan*

Limonium sinense, a native species in Taiwan, is a perennial distributed on sandy shores and salt marshes. It usually produces t pollen grains (pollen dimorphism) and exhibits two morphs of st dimorphism) in different individuals, like many other members of Plum this plant, self-incompatibility commonly occurs when Self-incompatibility also occurs among individuals producing the sa pollen grains and stigmas (heteromorphic self-incompatibility)[1]. H morphological developments of pollen grains, stigmas, and floral parts still remain unclear. The aim of the present study was to elucidate th processes of pollen and stigma dimorphisms by using LM and EM.

Two morphs of pollen grains mainly differed in their sculptures wall: morph A with lophate exine sculpture (Fig. A) and morph reticulate exine sculpture (Fig. B). And two morphs of stigmas exhibite papillae structures, respectively (Figs. C & D). Despite the fact that th differences in pollen and stigma morphology, those individuals produ morphs of pollen grains and stigmas showed the same floral morpho And floral developmental series of *L. sinense* was as follows: a bra appeared first (Fig. F), followed by a ring-shaped sepal primordium petal primordial (Fig. H), five stamen primordial (Fig. I), and finally gy five carpel primordia (Fig. J). The floral development of this species v other members of Plumbaginaceae[2]. During microsporogenesis development, patterns of sporopollenin deposition in later stages pres distinctions between two morphs (Figs. K-P). Differences between tw stigmas also exhibited in later developmental stages.

This study showed different development serials of pollen wal formation between two morphs of this species, which resulted in the Detailed research on ultrastructural changes with the aids of EM and analysis will be studied.

References

1. Shivanna, K. R. Pollen Biology and Biotechnology. 2003.
2. De Laet, J. *et al*. J. Plant Res. 1995 (108) 289.

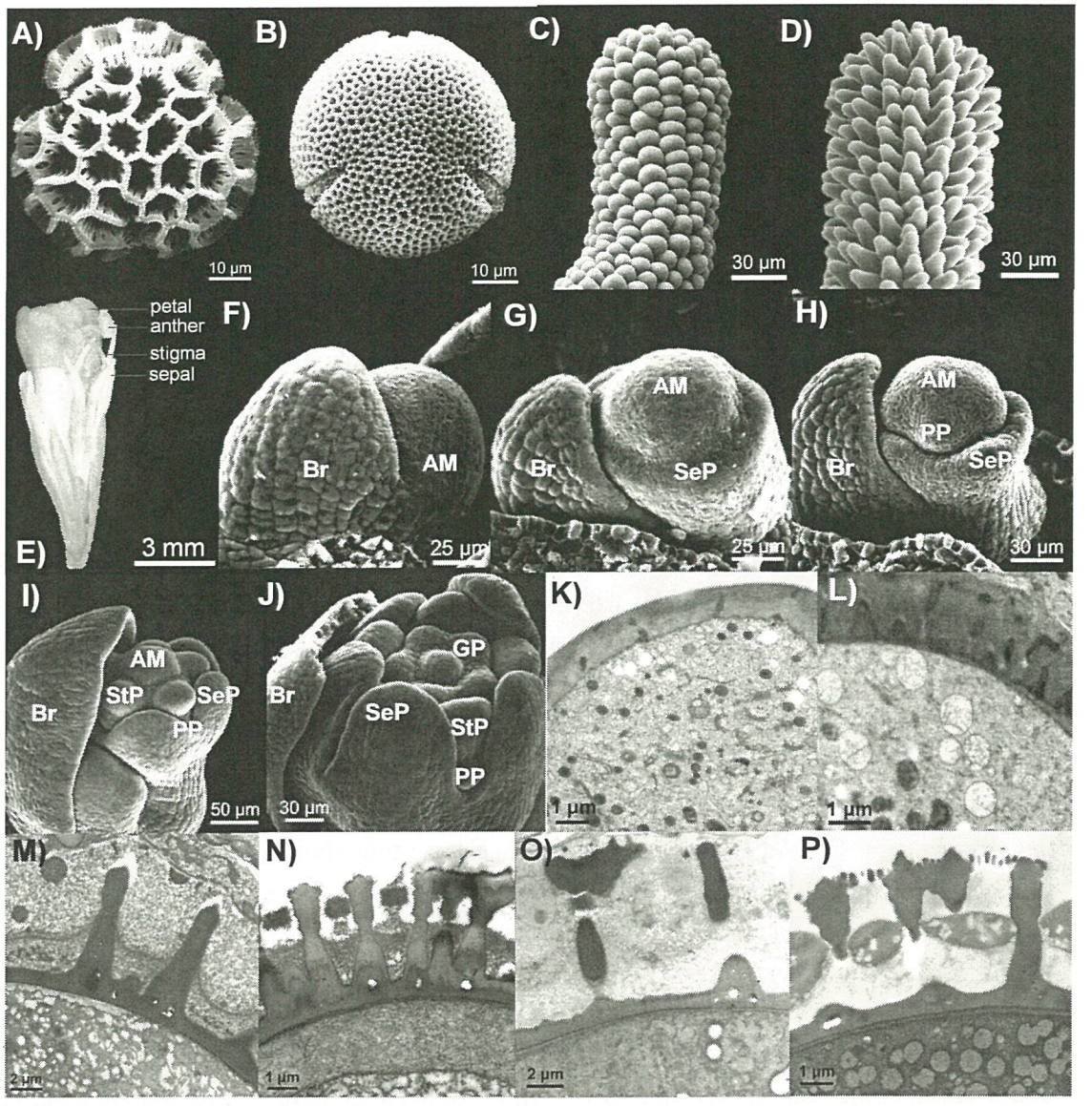

A-B Pollen grains of *Limonium sinense*. (A) Morph A with lophate exine sculpture; (B) Morph B with reticulate exine sculpture. **C-D** Stigmas of *L. sinense*. (C) Morph A with cob-like structure; (D) Morph B with papillae structure. **E** Floral morphology of *L. sinense*. **F-J** Floral development of *L. sinense*. (F) A bract primordium (Br) developed first; (G) A ring-shaped sepal primordium (SeP) appeared around the flank of the floral apical meristem (AM); (H) Five petal primordia (PP) arose on the flank of the remaining apical meristem; (I) Five stamen primordia (StP) appeared inside the petal primordia; (J) The gynoecium primordium (GP) with five carpels presented in the center of the apical meristem. **K-P** Pollen wall development of *L. sinense*. Pollen wall started formation during tetrad stage (K-L), and then sporopollenin deposited in free microspore stage (M-N) and pollen stage (O-P). K, M, and O: morph A; L, N, and P: morph B.

APLICATION OF SCANNING ELECTRON MICROSCOPE IN TAXNOMY OF RUST FUNGI

Lin Wan-Yu and Chung, Wen-Hsin

Department of Plant Pathology, National Chung Hsing University, 250 Kuo Kuang Rd., Taichung 402, Taiwan.

The rust, an obligate parasite fungus, is morphological diversity in spore. Five spore states were observed in most of rust fungi during their life cycle in nature, including spermatia (in spermogonia, 0), aecidiospores (in aecidia, I), urediniospores (in uredinia, II), teliospores (in telia, III) and basidiospores (on basidia, IV)**[1]**. Among these spore states, the morphological characters of urediniospore and teliospore almost use to classify the genus or species, especially ornamental structure of spore**[2]**.

Scanning electron microscope (SEM) is a tool to study the ultra-structure of morphology in organism, including the microbe, insect and plant**[3]**. In this study, 18 rust specimens were collected from *Hibiscus syriacus*, *Schefflera arboricola*, *Dioscorea* sp., *Prunus persica*, *Hemerocallis fulva*, *Phaseolus vulgaris*, *Zizania latifolia*, *Calocedrus formosana*, *Murdannia keisak*, *Zea mays*, *Arachis hypogaea*, *Bidens alba*, *Ficus carica*, *Perilla frutescens*, *Plumeria acutifolia*, *Ceris chinensis*, *Stachyurus himalaicus* and *Smilax china*, and the ultra ornamental structure of urediniospore were observed by SEM. The observation results showed that *Sc. arboricola* (Fig. B) and *Ca. formosana* (Fig. H) are teliospores, and other specimens were urediniospores. According the observation by SEM, the apex of urediniospores on *Pr. persica* were smooth and surface with echinulate (Fig. D). Moreover, the urediniospores on *Ph. vulgaris* (Fig. F), on *B. alba* (Fig. L) and on *Sm. china* (Fig. R) showed few and scattered echinulate, the urediniospores on *He. fulva* (Fig. E), *Zi. latifolia* (Fig. G), *F. carica* (Fig. M) and *Ce. chinensis* (Fig. P) had densely echinulate, and urediniospores on *Hi. syriacus* (Fig. A), *Dioscorea* sp. (Fig. C), *M. keisak* (Fig. I), *Ze. mays* (Fig. J), *A. hypogaea* (Fig. K) and *Si. himalaicus* (Fig. Q) were regular echinulate. In this study, the urediniospores on *Pe. frutescens* (Fig. N) and *Pl. acutifolia* were densely verrucose (Fig. O).

Our results indicated that ultra ornamental structure of urediniospore surface is highly diversity between different rust species based on SEM observation. The ultra structure will be useful morphological character to classify the species. Thus, the application of SEM in rust taxonomical study is respect.

References

1. Scott, K, J. and Chakravorty, A. K. 1982
2. Littlefield, L. J. and Heath, M. C. 1979
3. Hoppert, M. 2003

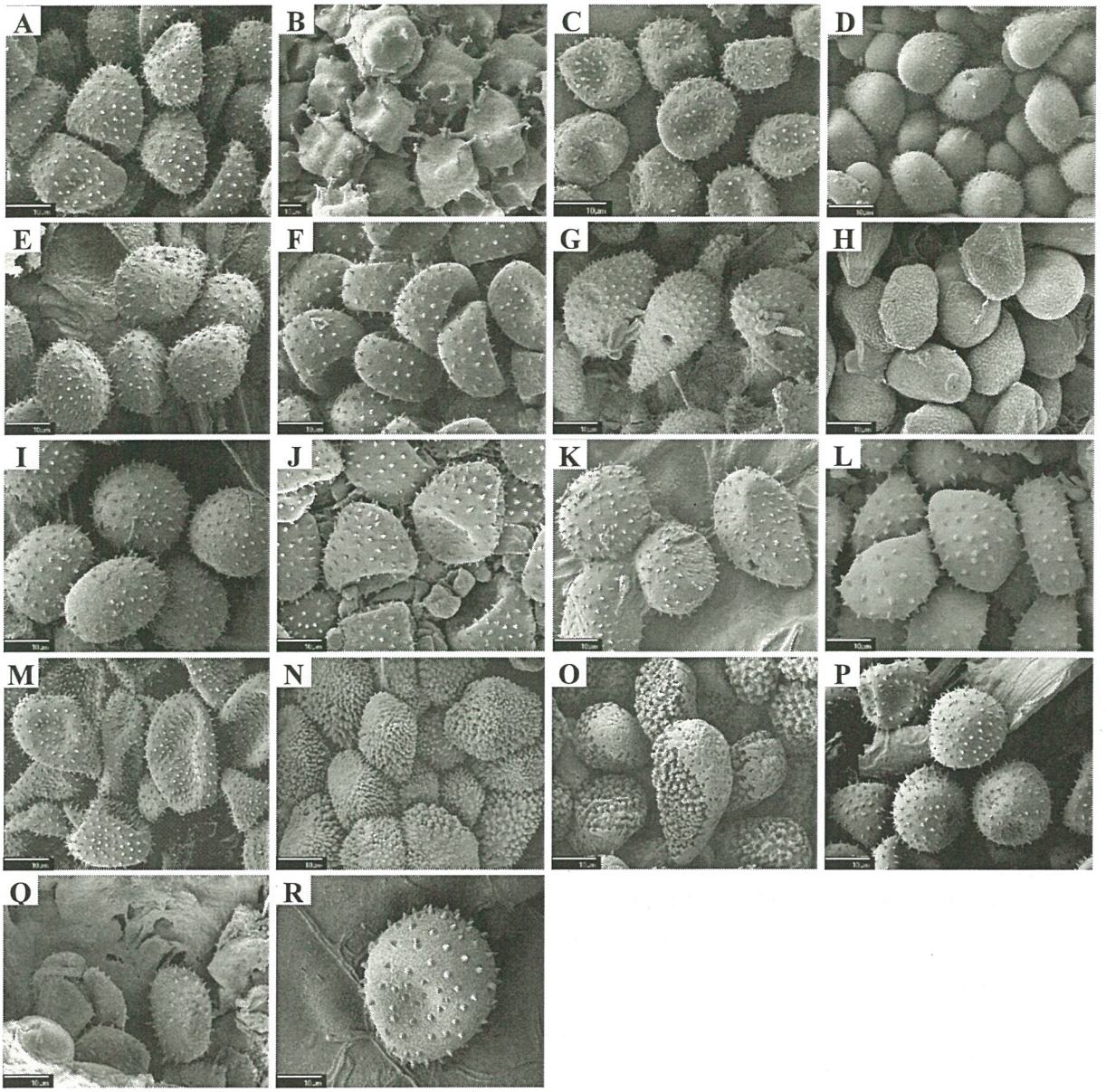

Fig. **A-R**, SEM picture of spore ornamental ultra-structure in different specimens. (A), urediniospores on *Hibiscus syriacus*; (B), teliospores on *Schefflera arboricola*; (C), urediniospores on *Dioscorea* sp.; (D), urediniospores on *Prunus persica*; (E), urediniospores on *Hemerocallis fulva*; (F), urediniospores on *Phaseolus vulgaris*; (G), urediniospores on *Zizania latifolia*; (H), teliospore on *Calocedrus formosana*; (I), urediniospore on *Calocedrus formosana*; (J) urediniospores on *Murdannia keisak*; (K), urediniospores on *Zea mays*, *Arachis hypogaea*; (L), urediniospores on *Bidens alba*; (M) urediniospores on *Ficus carica*; (N), urediniospores on *Perilla frutescens*; (0), urediniospores on *Plumeria acutifolia*; (P), urediniospores on *Ceris chinensis*; (Q), urediniospores on *Stachyurus himalaicus*; (R), urediniospore on *Smilax china*.

The Perspective of A Flagellar Tubulin Polymerization System from A Teleost on Screening of Microtubule-Associated or Anti-Mitotic Agents

JU, Tsai-Kai[1, 2], CHEN, Shiang-Jiuun[1, 3], CHUANG, Yi-Chun[2], YANG, Ya-Chan[2], HUANG, Rong-Nan[4], KUO-HUANG, Ling-Long[3]

[1] *Precision Instrumentation Center, College of Science, National Taiwan University, No. 1, Sec. 4, Roosevelt Rd., Taipei, Taiwan 10617*

[2] *Technology Commons, College of Life Science, National Taiwan University, No. 1, Sec. 4, Roosevelt Rd., Taipei, Taiwan 10617*

[3] *Department of Life Science, Institute of Ecology and Evolutionary Biology, National Taiwan University, No. 1, Sec. 4, Roosevelt Rd., Taipei, Taiwan 10617.*

[4] *Department of Entomology, National Taiwan University, No. 27, Lane 113, Sec. 4, Roosevelt Rd., Taipei, Taiwan 10617.*

Turbidity assay of tubulin polymerization has become a powerful tool for the discovery of compounds and proteins with microtubule-associating or anti-mitotic activities. Conventionally, the tubulin of the commercial source is originated from brain tissue of domestic animals that take a high cost to harvest and much care to prevent from biohazard infection. We describe here a tubulin polymerization system recovered from sperm extract of a teleost that is much accessible to routine preparation in a lab. The flagellar tubulin exhibits a typical polymerization curve, which is exclusively GTP-dependent and includes three characteristic phases, namely nucleation, growth, and steady state equilibrium, essentially identical to those of mammalian polymerization systems when kinetically assayed by optical absorbance at 340 nm during reassembly. Ultracentrifugation and immunoblotting analyses indicate that the tubulin gradually precipitates following the polymerization kinetics. Immunolabeling and negative staining further demonstrate that the change of optical absorbance is exactly resulted from microtubule reassembly. A high-throughput assay based on the flagellar tubulin and the microplate reader is now established. Through the assay, we demonstrate the flagellar tubulin polymerization also sensitive to two anti-mitotics, nocodazole and paclitaxel, though both the polymerization kinetics and the phase altered show somewhat different from the tubulin of the brain origin. In addition, two antibodies against flagellar components, β-tubulin and radial spoke protein Rsph1, also apparently interfere the microtubule reassembly. These results, together with the accessibility and cost-effectiveness, indicate that the flagellar tubulin polymerization system could become a promising platform for prescreening of anti-mitotic agents and microtubular interactome.

FEI COMPANY™
TOOLS FOR NANOTECH

Pushing the Limits with SEM and Dual Beam

Mr. William Neijssen

FEI Company

With the introduction of the first monochromated extreme high resolution (XHR) SEM it is possible to achieve sub-nanometer spatial resolution at voltages from 1 to 30kV without compromising the analytical capabilities, sample flexibility or easy of use of a traditional SEM. Not only does the XHR SEM allow achieving sub-nanometer spatial resolution using a 1kV primary beam energy on bulk specimens, but also 1.5nm spatial resolution is demonstrated at a beam landing energy of 200V. In this case the interaction volume shrinks down to only a few nanometers in depth, enabling high resolution true surface imaging. Coupling low and very low beam energy SEM to 30kV STEM-in-SEM means that highly surface sensitive and volumetric data can be rapidly obtained at the very nanometer level, from the same region of a given specimen.

The capabilities of focused ion beams (FIB) to remove and deposit materials accurately on a nanometer scale are employed for prototyping purposes across all application areas of nanotechnology. The great advantage of doing nanoprototyping in a DualBeam instrument is that one single instrument is capable of directly writing a given pattern design in any kind of substrate material with the opportunity to monitor the patterning process live with an SEM. Being able to see a nanostructure evolving and inspect the result in great detail at the moment the patterning process is completed, allows rapid process optimization and delivers in many cases a first functional prototype of a nanodevice within a very short time.

As materials are becoming increasingly complex and finer analysis is required, Dualbeams are nowadays automating the FIB slicing and SEM analysis, making it possible to acquire a precise 3D dataset from a volume ranging from less than 100mm3 to over 105mm3. Expectations regarding Dualbeam 3D characterization comprise the ability to achieve highly resolved and/or large datasets in a manageable time, as well as the possibility to achieve 3D characterization with ultimate voxel resolution.

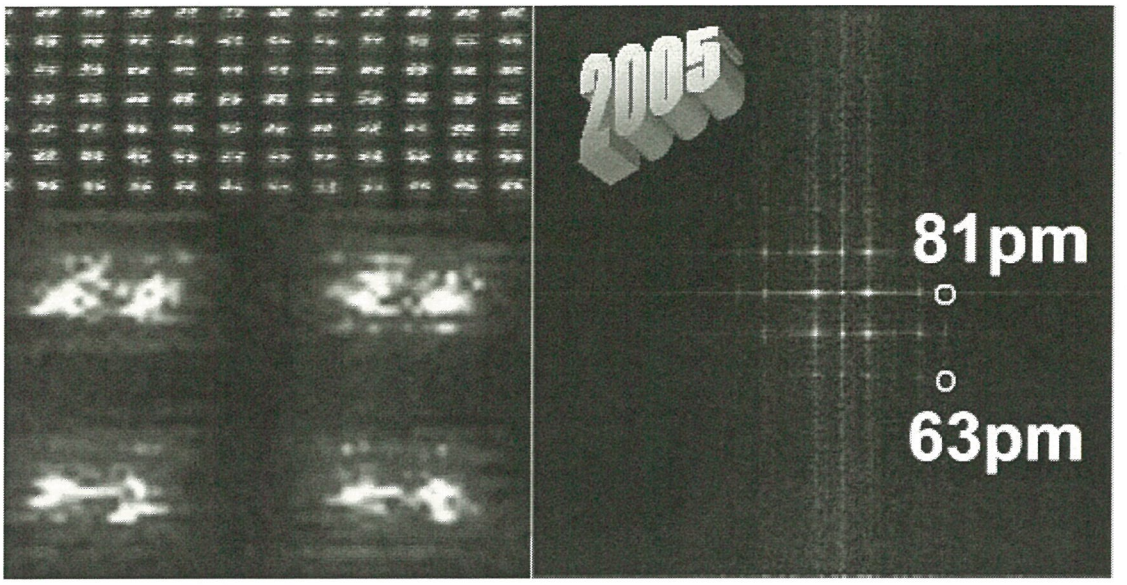

Image : S.Lopatin, FEI sample :K.Urban ER-C, Juelich Germany

Fig. 1b: STEM image of Ge<112> showing 80pm dumbbells and the diffractogram shows reflections down to 63pm. This image was recorded back in 2005

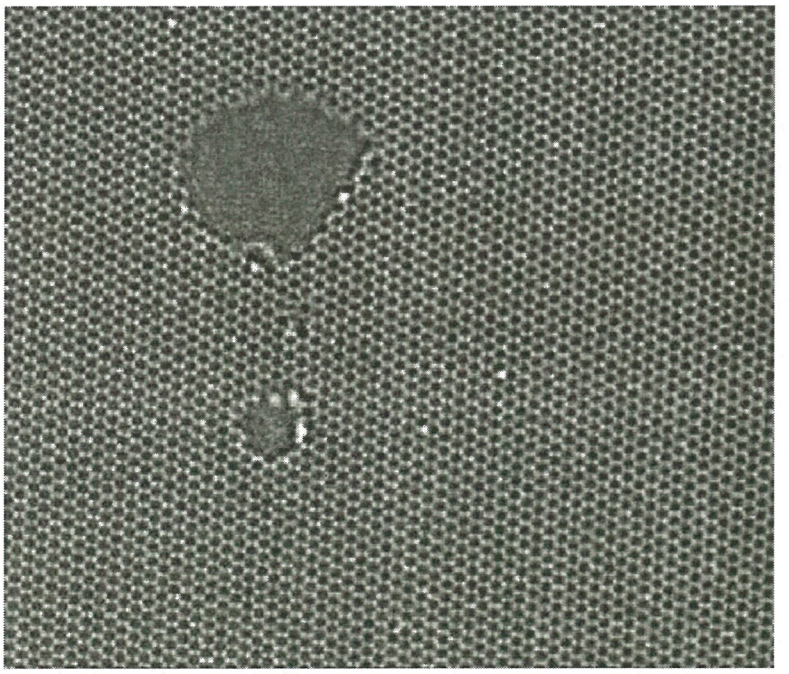

Fig. 2: TEM image of a single sheet of Graphene at 80kV

Image: P. Hartel and R. Erni; Sample: N Alam and A Zettl

Fig. 2: TEM image of a single sheet of Graphene at 80kV

FEI COMPANY™
TOOLS FOR NANOTECH

Solution for 3D imaging in life Science

Dr. Yu Yong

FEI Company

Recent developments in electron microscopy have generated a renaissance in biological imaging, allowing researchers to visualize 3D structures of biological entities at the molecular scale. Electron tomography is comparable to medical tomographic techniques like CAT, PET and MRI in the sense that it provides a 3D view of an object, yet it does so at a cellular scale and with nanometer resolution. Electron tomography has the unique ability to visualize molecular assemblies, cytoskeletal elements and organelles within cells. The three dimensional perspective it provides has revised our understanding of cellular organization and its relation with morphological changes in normal development and disease.Equally important, the refinement of cryogenic sample preparation, sample handling techniques and automation have permitted investigation of these structures in a fully hydrated state and in their native context. Cryo-TEM has been shown to be a reliable and complementary adjunct to X-ray and NMR analysis. Cryo electron tomography of vitrified samples at cryogenic temperatures combines excellent structural preservation with direct high resolution imaging. The use of cryo preparation and imaging techniques eliminates artifacts induced by plastic embedding and staining of the samples is circumvented. This review describes the technique of cryo electron tomography, its basic principles, cryo specimen preparation, tomographic data acquisition and image processing. A number of illustrative examples ranging from whole cells, cytoskeletal filaments, viruses and organelles are presented along with a comprehensive list of research articles employing cryo electron tomography as the key ultrastuctural technique.Both of electron tomography and Cryo-TEM technologies have became powerful tools for biological researchers in cellular biology, structural biology and system biology. Electron microscopy is being used today in leading research laboratories around the world to better understand virus, connectomics of the brain, protein complexes, visual proteomics and other scientific discoveries. These results are also shedding new light on mechanisms of replication, assembly and cellular entry that suggest significant opportunities for new therapeutic approaches and drug discovery. FEI is the premier provider of 3D ultrastructural imaging and Cryo-TEM solutions for the Life Sciences.

FEI focuses innovation on the creation of complete high-resolution imaging solutions for life scientists – from sample preparation to automated imaging to 3D reconstructions of biological samples and macromolecular complexes in their native hydrated state. The transmission electron microscopes of Titan and Tecnai series with Cryo-TEM and electron tomography technology from FEI are acceptable in life science around the world. Understanding complex biological systems requires knowing how cells are organized in a Three-dimensional (3D) network because their organization determines how cells can interact. 3D imaging system is requested by researchers of system biology. FEI DualBeam slice and view system provides the ideal combination of an ion beam and a scanning electron microscope (SEM) for 3D tissue imaging. With sufficient resolution and automated tissue sectioning FEI DualBeam is the microscope of choice to image larger tissue sections in three dimensions with sufficient resolution to determine the intercellular interactions. FEI products designed to perform automated tissue imaging includes the Quanta 3D and Nova 200 Nanolab, which require minimal effort to acquire a stack of images to characterize 3D tissue volume.

Key Words

3D imaging, electron tomography, Cryo electron microscopy, 3D tissue imaging, DualBeam, System biology, structural biology,

益弘儀器股份有限公司
E Hong Instruments Co., Ltd.
台北： (02) 27552266　新竹： (03)5782020　台中：(04)22452181
台南： (06) 2095135　高雄： (07)3340407　昆山：(0512)57385666

HITACHI 日立電子式顯微鏡

Field Emission SEM S-4800

解像力：1.0nm (at 15kV)
解像力：1.4nm (at 1kV)

PC Windows 全自動操作可變真空電子顯微鏡

解像力：3.0nm/4.0nm (V.P.) [S-3700N 12"含TMP]
解像力：3.0nm/4.0nm (V.P.) [S-3400N 8"含TMP]
解像力：3.0nm/4.0nm (V.P.) [SU-1510含TMP]

週邊附件及前處理設備
* HITACHI /EMITECH (QUORUM)各式
  SPUTTER 蒸鍍機及CPD
* HORIBA EDX /WDS /EBSD
* HITACHI /E-3500
  (Cross-Section Ion Milling System)

PARK XE-AFM

1. Decoupled XY and Z-scanners
2. Fast Z-servo Response
3. Direct On-Axis Optics

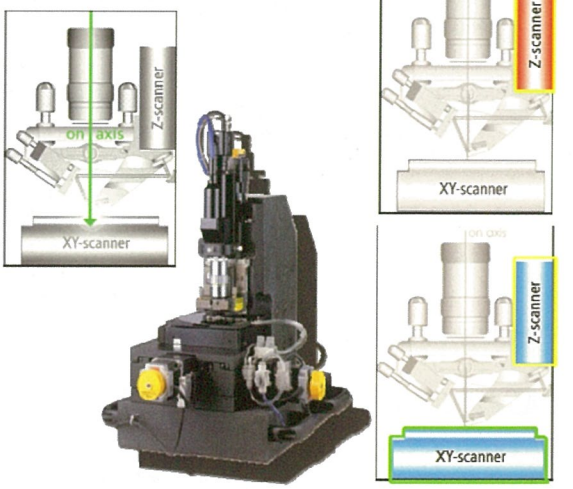

Flat Ion Milling System IM-3000

1. 離子束角度可由 0° 到90°
2. 5m5mm (H)
3. 最大樣品：
   50mm (D) x
   25mm (H)

桌上型電子顯微鏡 TM-1000

1. 最早出品桌上型節能設計者
2. 簡單易懂操作方式
3. 對無鍍金處理絕緣樣品進行觀察
4. 表現深度，展現物體的立體感

* HITACHI FIB FB-2100/NB5000(Dual Beam
* HITACHI PC-TEM H-7650 (120KV)
* HITACHI STEM HD-2700 (Cs correction)
* HITACHI HIGH/LOW FE-SEM SU-6600
* HITACHI Analystical FE-SEM SU-8000 NEW
  / SU-70

MA-tek

The Best TEM Service Prov

- ☐ Semiconductor materials and processing analysis d
- ☐ TEM Bright Field/Dark Field/High Resolution Image
- ☐ STEM Bright Field/High Angle Annual Dark Field (HA
- ☐ EELS Mapping/Line-scan/Probe Spectrum
- ☐ EDX Mapping/Line-scan/Probe Spectrum
- ☐ Selective Area Diffraction (SAD)
- ☐ Nano Beam Diffraction (NBD)


Nano materials

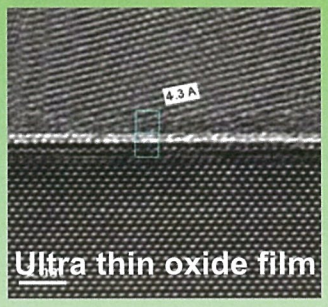

Ultra thin oxide film

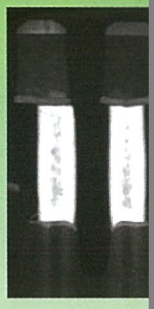

Comprehensive Materials Analysis, Failu
& Reliability Testing Service

- ☐ FIB Circuit Repair
- ☐ ESD (HBM, MM, CDM) /Latch up Testing
- ☐ Wire Bonding & IC Packaging
- ☐ Reverse Engineering
- ☐ IP Strategic
- ☐ Third Party V
- ☐ HTOL, HTS,
- ☐ TCT, TST, Pr

- ■ FIB-[FEI 201/205/800/ 986, Quanta3D-FEG, Vectra-Vision G5, Nova600, Micrio
- ■ SIMS-[Camaca IMS-6F, Atomica 4500]
- ■ ESCA/XPS -[Thermo K-Alpha]
- ■ TEM/EDX/EELS -[FEI Tecnai F20]
- ■ SEM/EDX-[HITACHI S4800, 4700, 5000, 4500]
- ■ X-Ray-[FEINFOCUS Tiger]
- ■ SAT-[HITACHI MC1]
- ■ OM-[LEICA, NIKON,OLYMPUS]
- ■ Optical Profiler-[Nano View P4050]
- ■ Decapsulator-[NSC-PS102, Nisene]
- ■ Laser Decapsulator-[Control Semi, Fatcat]
- ■ RIE-[PR2001E/NARC]
- ■ Laser cutter-[New Wave-ezlaze trilite]
- ■ ESD-[Keytek 25
- ■ CDM tester-[Or
- ■ Au Wire Bondi
- ■ Al Wire Bondin
- ■ EMMI-[Hamama
- ■ OBIRCH-[Hama
- ■ InGaAs- Hamar
- ■ Conductive AF
- ■ Probe Station-[
- ■ PIPS-[Gatan 69
- ■ Ion mill-[Gatan

閎康科技股份有限公司 www

外界AC / DC 磁場干擾消除器

AC 及DC 主動式磁場干擾消除器有多種機型適用於 SEMs,TEMs & E -Beam tools,更可消除 300mm晶片傳送裝置所產生9 KHz干擾 。

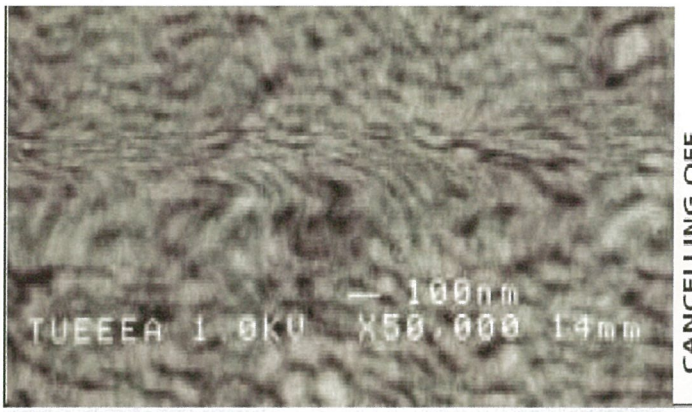

Beam 1keV Mag: 50,000 x working dist. 14mm

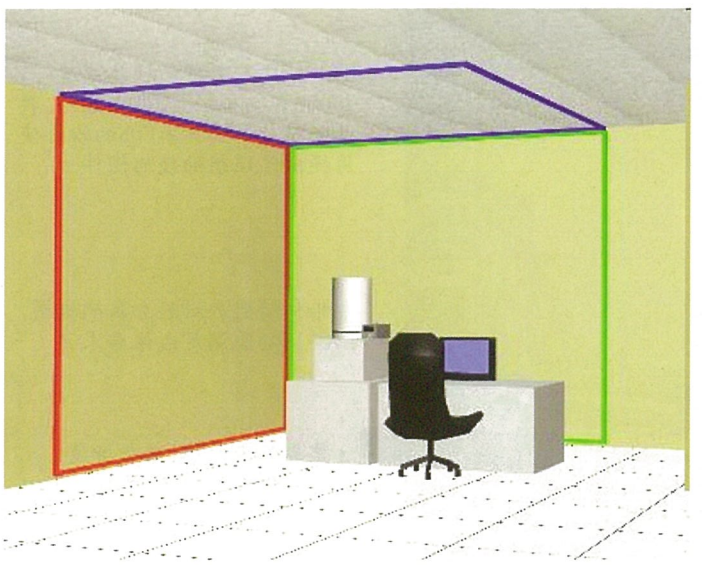

SPICER CONSULTING

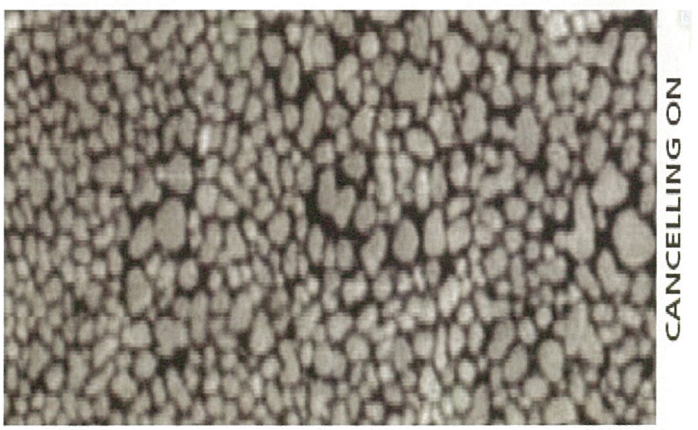

SPICER CONSULTING

台灣及中國總代理

- 超泰科技有限公司 E.B Tech Co., Ltd
- 台北市吳興街156巷16弄7號1樓
- TEL: 886-2- 2733-2576
- E-Mail : service@ebtech.com.tw
- **Web: www.spicerconsulting.com**

EVO® 18 Special Edition

Low Cost – high efficiency 材料分析掃描電子顯微鏡

EVO®18, 具有處理所有類型材料能力的分析顯微鏡為您提供卓越的成像質量。

標配能譜儀(EDS)和波譜儀(WDS)接口, 領先的X射線幾何條件對所有樣品提供最精確的分析。對於非導體採用電子束襯管技術,提高了圖像質量和分析精度。

可升級到LaB6高亮度光源, 在與X射線分析相適應的探針電流的性能上提高到一個新的水平。

EVO®18能夠處理的樣品可達250mm直徑和145mm高。此外, 共面的設計為EBSD與EDS的聯合使用提供了理想的幾何條件。

無論何時對於材料分析的挑戰, EVO®18都能滿足成像要求。

- 業界領先的X射線分析幾何條件與標配的WDS接口
- 使用可變壓力工作模式進行樣品的電荷中和
- 大的樣品台行程
- 電子束襯管用於提供增強的分析性能
- 用可選的LaB6電子源進行高性能成像

EVO®18–

圓滿的材料分析解決方案

ZEISS

Enabling the Nano-Age World®

產品系列:卡爾蔡司電子/離子顯微鏡

EVO® 系列
掃描電子顯微鏡—應用於材料分析與生命科學

SUPRA™ 系列
超高分辨率熱場發射掃描電子顯微鏡

ULTRA 系列
超高分辨率綜合分析型場發射掃描電子顯微鏡

CrossBeam® 系列
聚焦離子束最佳三維分析工具

LIBRA® 系列
配置鏡筒內OMEGA能量過濾器的穿透射電子顯微鏡

ORION™ 系列
氦離子顯微鏡

敬請參觀我們的網站: www.smt.zeiss.com/nts

台灣辦公室:
蔡司半導體有限公司
300 新竹市公道五路二段158號5樓之一
電話:+886-3-5750203 傳真:+886-3-5752406

ZEISS

Enabling the Nano-Age World®

世界最佳奈米級分析用能量分散式偵測器(EDS)

BRUKER

Nanoanalysis on TEM/STEM

特色：不須液氮冷卻、沒有震動、準確的定量結果

Best resolution ever!

X-Flash® 5000 – 123 eV at 100,000 cps

特色：不須液氮冷卻、高速 Mapping、準確的定量結果

可安裝於各廠牌 SEM/TEM(Jeol, Hitachi, FEI, Zeiss, TEscan...)

台灣布魯克生命科學股份有限公司

Bruker Taiwan Co., Ltd.
221台北縣汐止市
新台五路一段75號18樓之5
電話：(02) 86981212
傳真：(02) 86981010
info@bruker.com.tw
www.bruker.com

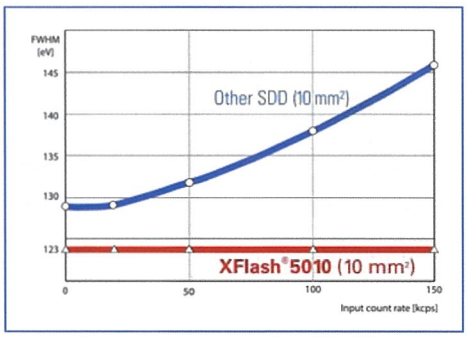

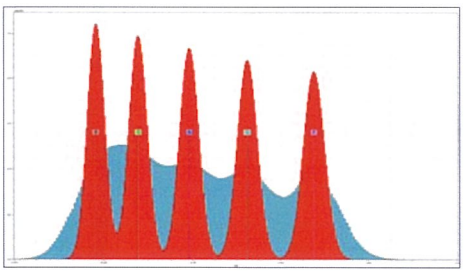

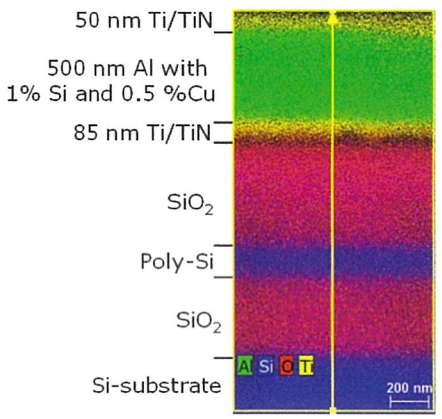

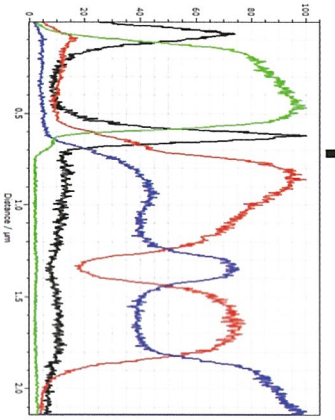

4 kV, 6 kcps, 23 min, 300*600 pixel

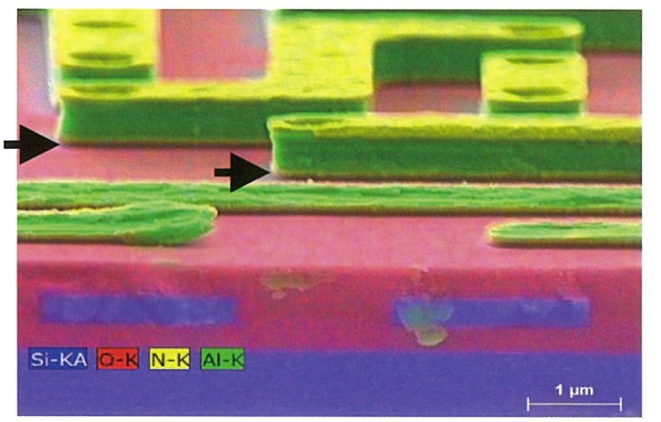

4 kV, 6 kcps, 23 min, 800*600 pixel: Arrows mark 85 nm thick layer of adhesion-promoting agent (Ti/TiN)

Nano-layer qualification at 1.3 kV Comparison with reference standards
極為準確的低加速電壓薄膜(<100nm)定量分析

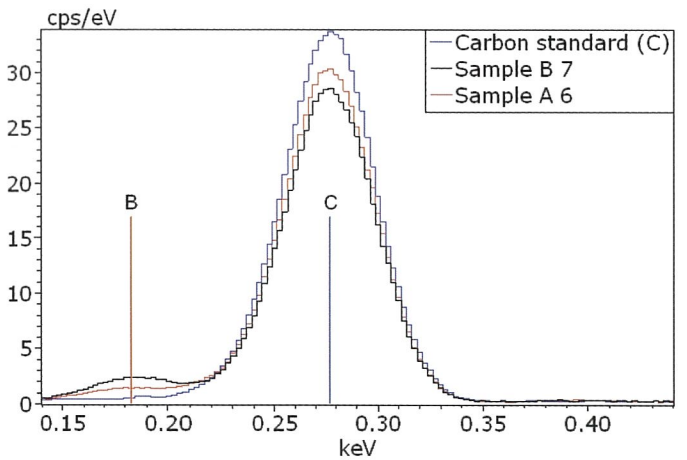

1.3 kV, 2 kcps, 30 s/spectrum

Sample 1	B	C	Sum	Sample 2	B	C	Sum
wt.%							
1-1	10,1	89,5	99,6	2-1	15,4	83,7	99,0
1-2	10,2	90,0	100,2	2-2	16,4	83,3	99,8
1-3	9,8	90,5	100,3	2-3	15,3	83,7	99,0
1-4	10,4	89,2	99,6	2-4	15,9	84,6	100,5
1-5	9,5	90,1	99,5	2-5	15,2	84,4	99,6
1-6	9,9	89,5	99,4	2-6	15,4	85,0	100,5
1-7	9,9	88,9	98,8	2-7	15,5	84,5	100,0
1-8	9,4	89,9	99,3	2-8	15,9	85,2	101,2
1-9	10,3	90,3	100,6	2-9	15,3	84,7	100,0
1-10	9,9	89,4	99,3	2-10	15,0	85,5	100,4
Mean	9,9	89,7	99,7	Mean	15,5	84,5	100,0
s (± wt.%)	0,3	0,5		s (± wt.%)	0,4	0,7	

新竹分公司：
電話:(03) 5585032
傳真:(03) 5588683

台南分公司：
電話:(06) 2706023
傳真:(06) 2704638

世界最佳奈米級分析用能量分散式偵測器(EDS)

Nanoanalysis on TEM/STEM

特色：不須液氮冷卻、沒有震動、準確的定量結果

Best solid angle and resolution – 123 eV at 100,000 cps

可安裝於各廠牌 TEM/STEM

台灣布魯克生命科學股份有限公司

Bruker Taiwan Co., Ltd.
221台北縣汐止市
新台五路一段75號18樓之5
電話：(02) 86981212
傳真：(02) 86981010
info@bruker.com.tw
www.bruker.com

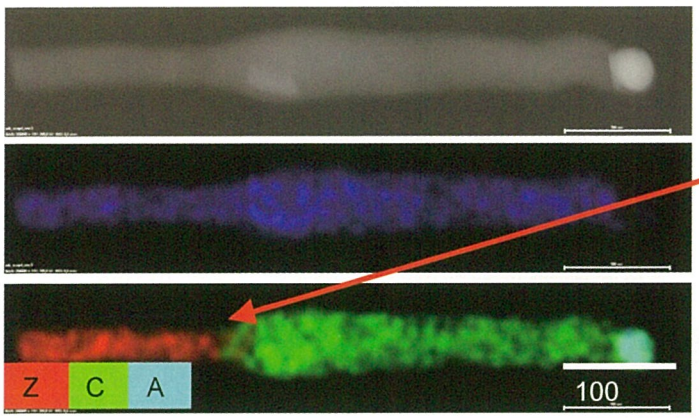

raw data, data courtesy of Dr. H. Kirmse, Prof. Neumann, Humboldt University Berlin, sample: polish academy of Science

Change in Zn to Cd contents matches lattice constant change

solid angle: 0.12sr

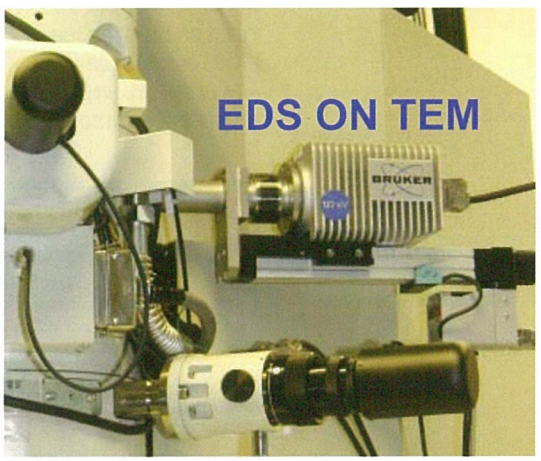

Element Profile (3090s 600x600)

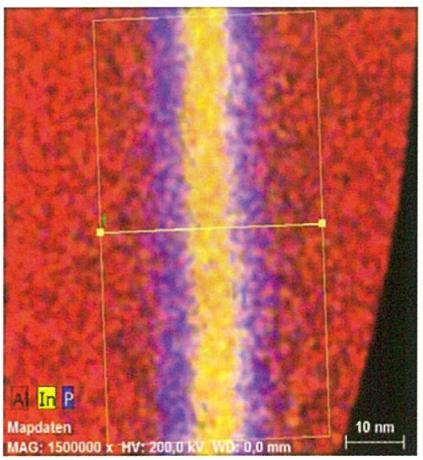

沒有震動；不影響原子等級影像

QUANTAX CrystAlign - Easy to use EBSD

特色：

- 真空下改變最佳量測角度以獲得最佳 EBSD 品質
- 超高速量測：630 patterns/s （160X120 pixels）
- 更安全的 LED 顯示 Detector 位置
- 完全的軟體整合硬體控制
- 完整的與 EDS 整合
- 簡單軟體操作介面
- 超高速重新計算 index：16,000 point/s
- 全自動最佳影像品質及量測時間校正
- 全自動量測位置校正

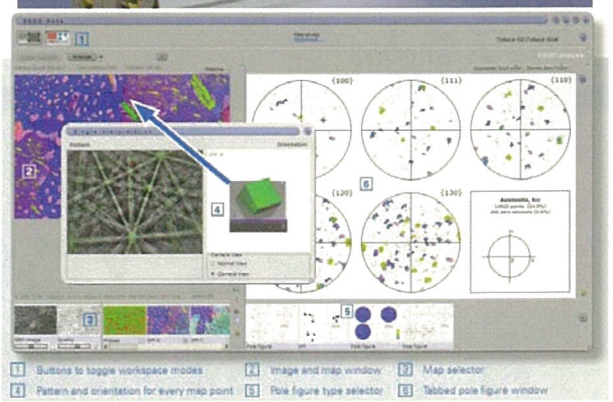

新竹分公司：
電話：(03) 5585032
傳真：(03) 5588683

台南分公司：
電話：(06) 2706023
傳真：(06) 2704638

MeX®

TURN YOUR SEM INTO A 3D MEASUREMENT DEVICE

THE REAL METROLOGY TOOL IN SEM

Pure software solution, applicable to any SEM at any magnification

Automatic calibration yields robust, accurate and traceable results

Comprehensive depth analysis according to ISO standard

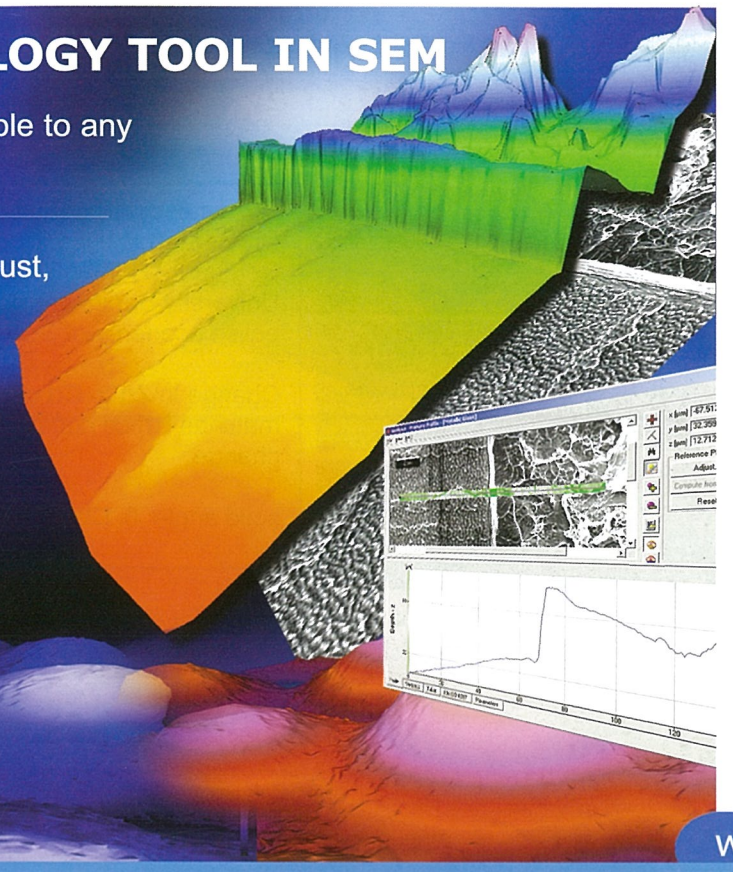

PSC 汎達科技有限公司
PENTAD SCIENTIFIC CORPORATION

新竹市光復路二段 295 號 6F 之 2
TEL : 886-3-5728466
FAX : 886-3-5728467
e-mail : pentad@pentad.com.tw
統一編號 : 86713061

www.alicona.com

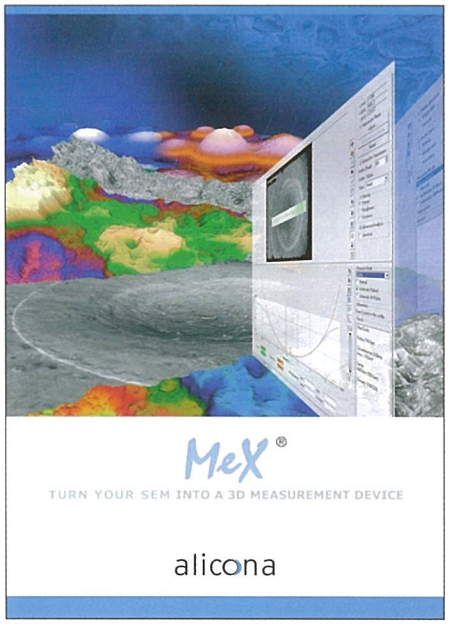

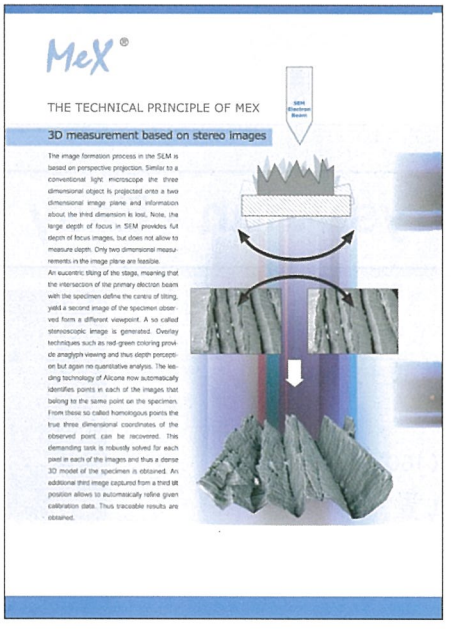

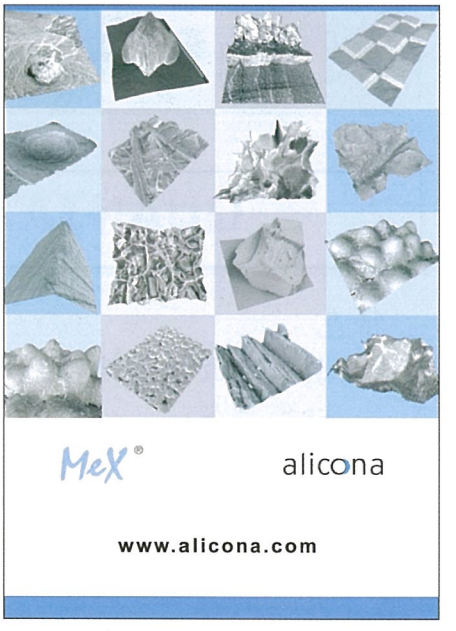

TURN YOUR SEM INTO A 3D MEASUREMENT DEVICE

第七屆海峽兩岸顯微鏡學術研討會

論文摘要彙刊

2009年8月28日-30日
花蓮 遠雄悅來大飯店

Atomic Resolution analytical Microscope

JEM-ARM200F debut

JEOL
Serving Advanced Technology

捷東股份有限公司

Leica
MICROSYSTEMS

Industrial Sample Preparation - Solid State Technology

TIC 020 Triple Ion Beam Slope Cutter

RES 101 Ion Beam Milling System

RES 120 SEM Controlled Broad Ion Beam Milling System

EM TXP Target Surfacing Device for EM & LM

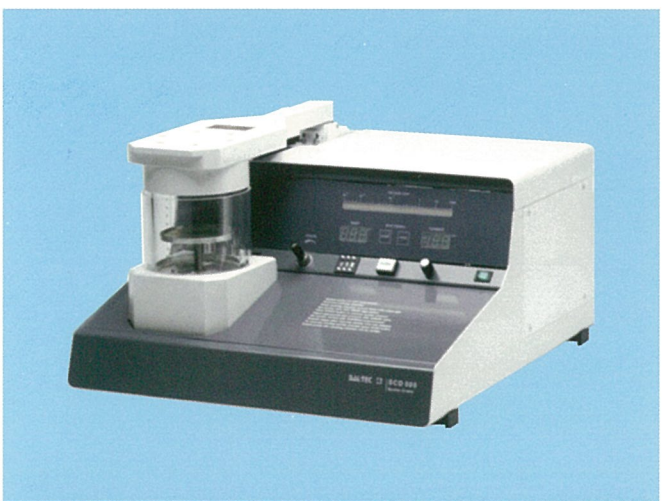

SCD 005/050 Cool Sputtering Device

SCD 500 High Vacuum Sputtering Device

台灣
總代理

友聯光學有限公司
UNION OPTICAL & INSTRUMENTS LTD.
地址：台北縣汐止市新台五路一段81號4樓之3
電話：02-26980508 E-mail：unionopt@ms11.hinet.net

Ted Pella, Inc.

電顯實驗室用耗材

Sputter Coater

Carbon Coater

Carbon Conductive Tab / Double Coated

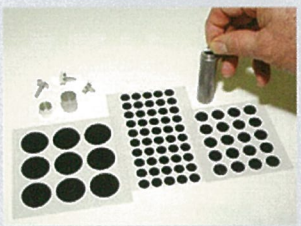

Adhesives, Conductive, SEM

Tapes

Grids Storage Boxes

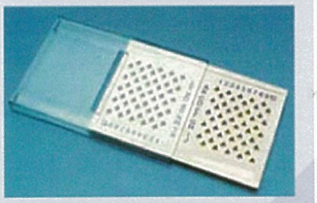

(AB 膠)G1 膠

Grids

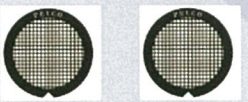

Specimen Storage: SEM

Lacey Support Films

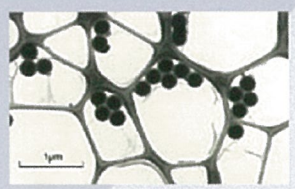

Tweezers

PSC 專業 熱忱 團隊合作
汎達科技有限公司
PENTAD SCIENTIFIC CORPORATION

新竹市光復路二段295號6F之2
TEL : 886-3-5728466 FAX : 886-3-5728467
e-mail : pentad@pentad.com.tw
www.pentad.com.tw

Solutions for enhanced performance

The winning edge in to

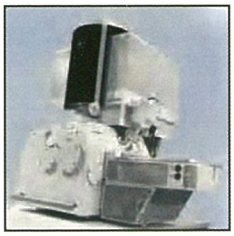

Magellan™ family

The first SEM to offer subnan
over the full 1 kV to 30 kV el
range, effectively establishing
category know as XHR SEM.
Discover a world never seen b

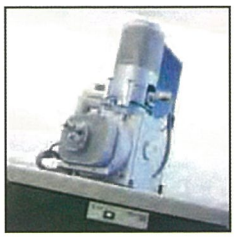

Nova™ NanoSEM 3

The most versatile ultra-high
combining very low kV imagi
capabilities with unique low va
to meet your most demandin
characterization requirements
Make your contribution to the
revolution

Quanta™ FEG 50 se

The most versatile high resolut
FEG SEM with extended low va
for the really challenging samp
experiments.
One microscope - multiple solu

Quanta™ 50 series

The ultimate low vacuum SEM
low vacuum capabilities for the
challenging samples and dyna
One microscope - multiple solu

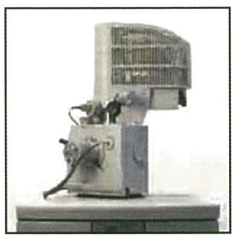

Inspect™ family

Low vacuum and FEG SEM for
material inspection and charac
Partnership begins here

FEI 台灣
新竹縣竹北市台元街28號7樓之1
Tel: +886-3-6116999
Fax:+886-3-5525998

FEI 台灣 銷售
超泰科技有限
台北市吳興街1
Tel: +886-2-2
Fax:+886-2-2